Transactions of the ASME®

Technical Editor
H. D. NELSON (2001)
Associate Technical Editors
Advanced Energy Systems
M. J. MORAN (1999)
G. REISTAD (2002)
Fuels and Combustion Technologies
S. GOLLAHALLI (2001)
Gas Turbine (Review Chair)
D. WISLER (2001)
Gas Turbine
D. COOKE (1999)
M. MIGNOLET (2002)
J. PETERS (2002)
Internal Combustion Engines
D. ASSANIS (2002)
Nuclear
R. DUFFEY (2001)
Power
D. LOU (2002)

BOARD ON COMMUNICATIONS
Chairman and Vice-President
R. K. SHAH

OFFICERS OF THE ASME
President, **R. E. NICKELL**
Executive Director, **D. L. BELDEN**
Treasurer, **J. A. MASON**

PUBLISHING STAFF
Managing Director, Engineering
CHARLES W. BEARDSLEY
Director, Technical Publishing
PHILIP DI VIETRO
Managing Editor, Technical Publishing
CYNTHIA B. CLARK
Managing Editor, Transactions
CORNELIA MONAHAN
Production Coordinator
COLIN MCATEER
Production Assistant
MARISOL ANDINO

Transactions of the ASME, Journal of Engineering for Gas Turbines and Power (ISSN 0742-4795) is published quarterly (Jan., April, July, Oct.) by The American Society of Mechanical Engineers, Three Park Avenue, New York, NY 10016. Periodicals postage paid at New York, NY and additional mailing offices. POSTMASTER: Send address changes to Transactions of the ASME, Journal of Engineering for Gas Turbines and Power, c/o THE AMERICAN SOCIETY OF MECHANICAL ENGINEERS, 22 Law Drive, Box 2300, Fairfield, NJ 07007-2300.
CHANGES OF ADDRESS must be received at Society headquarters seven weeks before they are to be effective. Please send old label and new address.
STATEMENT from By-Laws. The Society shall not be responsible for statements or opinions advanced in papers or ... printed in its publications (B7.1, par. 3).
COPYRIGHT © 2000 by the American Society of Mechanical Engineers. Authorization to photocopy material for internal or personal use under circumstances not falling within the fair use provisions of the Copyright Act is granted by ASME to libraries and other users registered with the Copyright Clearance Center (CCC) Transactional Reporting Service provided that the base fee of $3.00 per article is paid directly to CCC, Inc., 222 Rosewood Drive, Danvers, MA 01923. Request for special permission or bulk copying should be addressed to Reprints/Permission Department.
INDEXED by Applied Mechanics Reviews and Engineering Information, Inc. Canadian Goods & Services Tax Registration #126148048

Journal of Engineering for Gas Turbines and Power

Published Quarterly by The American Society of Mechanical Engineers

VOLUME 122 • NUMBER 2 • APRIL 2000

TECHNICAL PAPERS

(Contents continued on inside back cover)

This journal is printed on acid-free paper, which exceeds the ANSI Z39.48-1992 specification for permanence of paper and library materials. ♾™
♻ 85% recycled content, including 10% post-consumer fibers.

Downloaded 03 Jun 2010 to 171.66.16.159. Redistribution subject to ASME license or copyright; see http://www.asme.org/terms/Terms_Use.cfm

Journal of Engineering for Gas Turbines and Power APRIL 2000

Volume 122, Number 2

DISCUSSION

ANNOUNCEMENTS

Downloaded 03 Jun 2010 to 171.66.16.159. Redistribution subject to ASME license or copyright; see http://www.asme.org/terms/Terms_Use.cfm

Matthew J. Wagner
Air Force Research Laboratory,
Propulsion Directorate,
AFRL/PRSL Building 490,
1790 Loop Road North,
Wright-Patterson AFB, OH 45433-7103

Nelson H. Forster
Air Force Research Laboratory,
Propulsion Directorate,
AFRL/PRSL Building 490,
1790 Loop Road North,
Wright-Patterson AFB, OH 45433-7103

Kenneth W. Van Treuren
Baylor University,
Department of Engineering,
P. O. Box 97356,
Waco, TX 76798

David T. Gerardi
UES, Inc.,
4401 Dayton-Xenia Road,
Dayton, OH 45432

Vapor Phase Lubrication for Expendable Gas Turbine Engines

Vapor phase lubrication (VPL) is an emerging technology that is currently targeted for application in limited life, expendable engines. It has the potential to cut 90 percent of the cost and weight of the lubrication system, when compared to a conventional liquid lubricated system. VPL, is effective at much higher temperatures than conventional liquid lubrication (600°C versus 200°C), so considerably less cooling for the bearing is required, to the extent that the bearing materials often dictate the maximum upper temperature for its use. The hot no. 8 bearing and the cold no. 1 bearing of the T63 engine were used to evaluate the applicability of this technology to the expendable engine environment. The no. 8 bearing was a custom made hybrid with T15 steel races, silicon nitride balls, and a carbon–carbon composite cage; it was run for 10.7 h at a race temperature of 450°C at full power, without incident. Prior to engine tests, a bearing rig test of the no. 8 bearing demonstrated an 18.6 h life at a race temperature of 500°C at engine full power speed of 50,000 rpm. Cold bearing performance was tested with the standard no. 1 bearing, which consisted of 52100 steel races and balls, and a bronze cage; it was run for 7.5 h at a race temperature of 34°C at flight idle power, without incident. A self-contained lubricant misting system, running off compressor bleed air, provided lubricant at flow rates of 7–25 ml/h, depending on engine operating conditions. These tests have demonstrated for the first time that a single self-contained VPL system can provide adequate lubrication to both the hot and cold bearings for the required life of an expendable cruise missile engine. [S0742-4795(00)01302-2]

Introduction

The goal of operating gas turbines without a conventional liquid lubrication system has been a goal for nearly fifty years [1]. Benefits associated with eliminating the liquid lubrication system include a fifteen-percent reduction in engine cost and weight when using an existing expendable class engine for the comparison baseline. Engine performance benefits are also possible if the bearings can operate with reduced cooling. Most of the early work to eliminate the liquid lubrication system in gas turbines focused on rolling element bearings lubricated with powders and solid lubricant coatings [1–4]. All of these efforts met with limited success and were never tried in a full-up engine. In the 1970s, air-foil bearings became an emerging technology, and have since been successfully transitioned to production auxiliary power units [5,6]. However, the success of foil bearings has not scaled to larger engines, although recent efforts are showing promise. Realizing the difficulties in powder and solid lubrication for rolling element bearings, and the load carrying limits of foil bearings, a concentrated effort was begun during the early 1990s to develop vapor phase lubrication for use in expendable class engines [7–10]. Vapor lubricants chemically react with the bearing steel to form films composed of organic constituents and polyphosphates. Specific advantages over passive solid lubricants are the relatively fast replenishment process, and the increased thickness (0.10 μm) of the lubricating film. By 1996, this technology had matured to the point where it was successfully demonstrated in the no. 8 bearing position of the T63-A-700 engine at idle condition [11]. To the knowledge of the authors, this was the first test without liquid lubrication in a gas turbine of this size.

The objective of the research described in this paper was to extend the prior testing of Van Treuren to include the no. 1 and no. 8 bearings, demonstrating a full-range of temperatures from cold to very hot. As shown in Fig. 1, the no. 1 bearing supports the compressor at the inlet, and the no. 8 bearing supports the first stage (gas producer) turbine. Also, as shown in Fig. 1, the T63 has an unusual design where the hot combustion gas blows directly on a heat shield buffering the no. 8 sump. Consequently, the no. 8 bearing runs very hot, providing a reasonable simulation of thermal conditions expected for a much more advanced engine cycle. Additionally, it is easy to isolate the no. 1 and no. 8 bearings from the rest of the lubrication system, and thus, the T63 engine itself can be used as a slave system to test the bearings in a realistic engine environment. Unlike the earlier engine test, which used shop air to deliver the vapor lubricant, the air in these tests was supplied from the engine. Aside from an initial startup period where a minimal amount of external support was provided, the system was totally self-sustained. The air used in these tests was taken from the compressor discharge to better simulate pressures and temperatures expected in earlier stages of a compressor from a more advanced engine. Higher temperature bearing materials were also used in this evaluation to extend beyond the idle condition reached in the previous paper to achieve the engine normal rated power (NRP) condition. The no. 1 bearing test described in this paper was performed at the Aeronautics Laboratory, U.S. Air Force Academy, and the no. 8 bearing tests were performed at the Propulsion Directorate, Air Force Research Laboratory, Wright-Patterson AFB.

High Speed Bearing Rig Test of Hot No. 8 Bearing

Prior to engine testing, single bearing rig tests of the no. 8 bearing were performed to establish safe operating limits, and to confirm that sufficient lubricant would be delivered by the mister at all engine compressor discharge conditions, thereby reducing risk to the engine. This was considered necessary because the engine is designed to operate with standard liquid lubrication at outer race temperatures below 204°C, and no. 8 bearing temperatures with VPL were expected to be in excess of 500°C.

Contributed by the International Gas Turbine Institute (IGTI) of THE AMERICAN SOCIETY OF MECHANICAL ENGINEERS for publication in the ASME JOURNAL OF ENGINEERING FOR GAS TURBINES AND POWER. Paper presented at the International Gas Turbine and Aeroengine Congress and Exhibition, Indianapolis, IN, June 7–10, 1999; ASME Paper 99-GT-28. Manuscript received by IGTI March 9, 1999; final revision received by the ASME Headquarters January 3, 2000. Associate Technical Editor: D. Wisler.

Copyright © 2000 by ASME

Downloaded 02 Jun 2010 to 171.66.16.119. Redistribution subject to ASME license or copyright; see http://www.asme.org/terms/Terms_Use.cfm

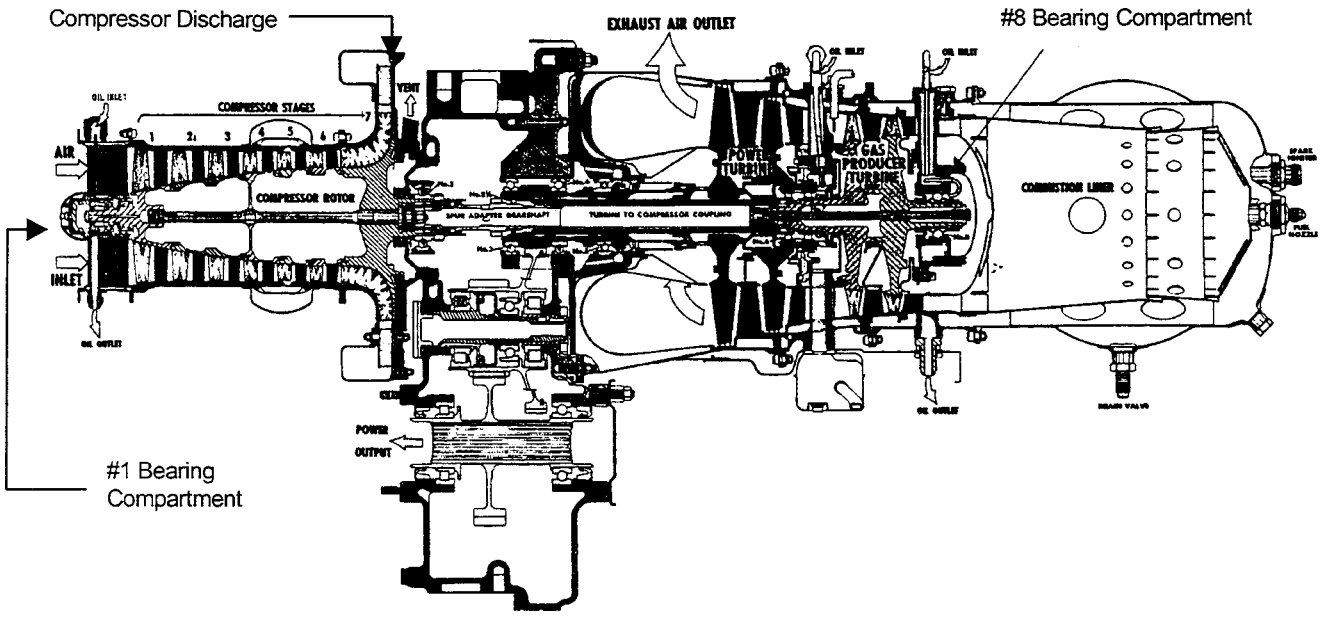

Fig. 1 Allison T63 turboshaft engine [12]

Hybrid no. 8 engine bearings were custom made for these tests. They consisted of a 20 mm bore split inner race, a 42 mm diameter outer race, a one-piece cage, and nine 7.144 mm (9/32 in.) diameter balls. The race material was T15 steel, the balls were NBD 200 silicon nitride, and the cage was carbon-carbon (C–C) composite. The cages were fabricated from a two-dimensional weave tube stock, developed in conjunction with BF Goodrich. The weave was optimized for circumferential and radial cage strength. After machining, the cages were redensified, and the surfaces treated with a proprietary antioxidant. The computed angles, loads, and stresses at the rolling element contact are shown in Table 1.

The lubricant used was a blend of tertiary-butyl phenyl phosphate (TBPP) isomers, commercially known as FMC Corporation's Durad 620B. It was misted using an engine rated venturi-type oil mist generator from a Williams International model WR24-6 target drone engine. The mister dry weight was 573 g, with a reservoir capacity of 190 ml. The lubricant was heated to above 55°C to reduce its viscosity for better misting. This was accomplished in the test rig by using electrically heated shop air at the mister inlet. Shop air conditions were set to match nominal engine compressor discharge air conditions that would be at the mister inlet in the operating engine. The mister was instrumented to measure inlet air pressure (P_{ai}) and temperature (T_{ai}), and reservoir liquid temperature (T_{liq}). The inlet air mass flow was measured to within ± 0.1 g/s, and the liquid flow rate was calibrated to within ± 2 ml/h. Mister operating conditions are shown in Table 2.

The T63 no. 8 bearing, its support, and the vapor mist system were installed in the high-speed bearing rig (Fig. 2). The rig is an air turbine driven test stand designed to test full-scale bearings at speeds up to 55,000 rpm. The T63 support for the no. 8 bearing was mounted to the front of the rig. The sump cap was modified so that the normal engine thrust load of 267 N could be applied to the bearing outer race via a wave spring washer made of A-286 alloy steel. A plate mounted to the front of the support directed 23 g/s of air at 0.8 bar gauge, from an electric heater to the top of the sump cap to heat the bearing compartment.

The misted lubricant used the existing flow path for liquid lubricant (Fig. 2). The mist entered through the oil inlet strut and passed through a nozzle directed at the bearing. It then passed through the hot bearing, which vaporized the lubricant and initiated the chemical reaction with the bearing surface to form the lubricating film. After it passed through the bearing, the vapor mixed with the labyrinth seal buffer air. The combined flows entered the bearing sump, and then exited through the oil scavenge strut. The residual vapor was vented out of the room through an exhaust hood. Two components in the standard flow path were modified. First, the nozzle inside diameter was enlarged from 1.27 to 3.15 mm to accommodate the air mass flow rate and to reduce the risk of clogging. Second, the bearing retainer plate was modified so that it completely sealed the top side of the sump to create a pressure differential to draw the vapor through the bearing.

Instrumentation included sheathed thermocouples on the bearing outer race (T_{race}), vapor inlet (T_{vi}), vapor outlet (T_{vo}), nozzle inlet (T_{noz}), dry sump outlet (T_{sump}), and air heater outlet (T_{air}). Shaft speed was measured with a proximity pickup on the air turbine hub. The bearing thrust load of 267 N was computed from the wave spring stiffness and applied compression of the spring at room temperature. At NRP operating temperatures, the combined

Table 1 Computed contact parameters for hybrid T63 #8 Bearing (267 N applied thrust load)

Speed (rpm)	Race	Contact Angle (deg)	Contact Load (N)	Contact Stress (GPa)	Spin/ Roll Ratio
35,000	Inner	43.1	43	1.09	0.46
"	Outer	28.6	62	0.95	4E-17
51,000	Inner	46.4	41	1.06	0.65
"	Outer	20.0	86	1.05	4E-17

Table 2 Mister operating conditions in rig tests (simulated T63 engine conditions)

Parameter	Ground Idle	Normal Rated Power
Rig rpm (Ref)	35,000	50,000
P_{ai} (bar gauge)	1.0	3.4
T_{ai} (°C)	150	150
T_{liq} (°C)	55	75
Air flow (g/s)	0.4	1.0
Lube flow (ml/hr)	7	21

Downloaded 02 Jun 2010 to 171.66.16.119. Redistribution subject to ASME license or copyright; see http://www.asme.org/terms/Terms_Use.cfm

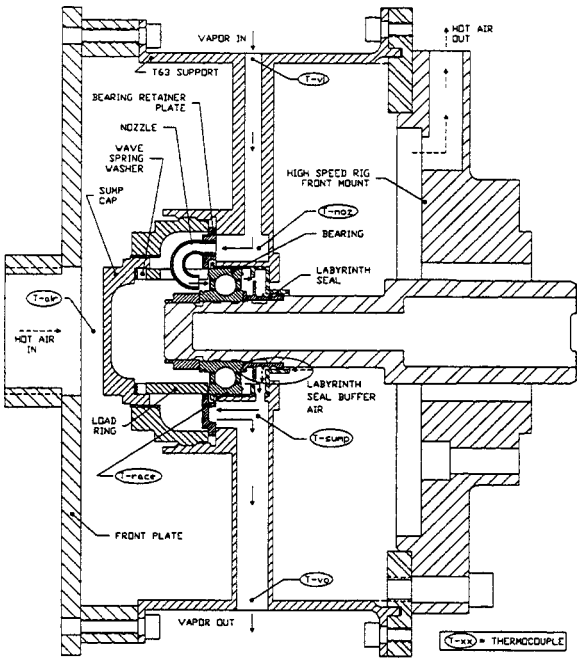

Fig. 2 High speed bearing rig test setup, side view

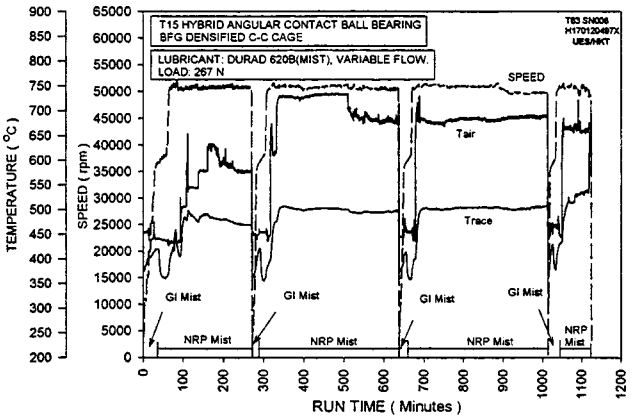

Fig. 3 High speed bearing rig no. 8 bearing test results

effects of reduced spring stiffness and increased spring compression due to expansion of the load ring (Fig. 2) resulted in a net 15 percent increase in computed thrust load.

Prior to testing, a new bearing was cleaned and coated with approximately 2 ml of liquid Durad, installed in the support strut and thrust loaded to 267 N. In the rig, it was not possible to duplicate the rapid heating experienced in the engine during startup. Instead, the bearing was preheated with the air heater for approximately one hour until a steady state temperature of 370°C was obtained at the bearing outer race. During the preheat cycle, the lubricant mist was run through the bearing while slowly rotating it, to avoid oxidation of the T15 steel races. With mister flow at engine ground idle (GI) conditions, the test was initiated with a slow (10–15 min) ramp up to 35,000 rpm, which was just above the engine GI speed. The bearing temperature was then allowed to stabilize. Mister flow was then increased to engine normal rated power (NRP) conditions, and the bearing temperature was again allowed to stabilize. From there, speed was increased to engine NRP speed of 50,000 rpm and the bearing temperature was again allowed to stabilize. Finally, the heater temperature was increased to maximum (690°C to match engine intra-turbine temperature at NRP), resulting in stable bearing temperatures of 490°C–510°C. Testing proceeded at this condition for approximately six hours, or until signs of bearing distress were observed. Bearing speed was controlled to within ±1000 rpm.

Results of the no. 8 bearing rig test are shown in Fig. 3. The bearing was run over a period of four days, including four start/stop cycles, for a total of 18.6 h. The majority of the run time (16 h) was spent at engine NRP conditions. The outer race temperature remained steady at 490°C–510°C throughout the first three days of testing, and only began to fluctuate on the final day, just prior to test suspension. The test was terminated after a sharp bearing temperature rise to 680°C, indicating bearing distress.

Despite the sharp temperature rise, the bearing was in relatively good condition after the test. The C–C cage had little wear and a highly polished condition on the sliding surfaces. The silicon nitride balls had what appeared to be regions of material transfer from the lubricant and/or race. Similarly, the bearing races had what appeared to be carbonaceous deposits. Surface analyses are underway to further define these deposits. The increase in bearing temperature is attributed to these deposits, which are thought to have increased the friction at the ball/race contact.

In the previous work [11], which used standard bearing materials (i.e., M50 steel races/balls and silver-plated 4340 steel cage), it was deemed that the maximum race temperature for safe operation was 379°C. One of the primary reasons for this was excessive wear on the land surfaces of the silver-plated 4340 steel cage. This problem was significantly reduced in this test by use of the in-house developed C–C cage.

From this test, it was concluded that the vapor phase lubricated bearing could safely be operated in the engine for at least 10 h at 490°C–510°C outer race temperature, at full engine speed (50,000 rpm), with the mister operating from compressor discharge air.

T63 Engine Tests of Hot No. 8 Bearing

For the high temperature engine tests, the no. 8 bearing was lubricated with Durad 620B mist while the remainder of the engine operated with standard liquid lubrication (MIL-L-7808). The liquid lubrication system was replumbed to bypass the no. 8 bearing. The misting system hardware, flow rates, and flow path for the no. 8 bearing were identical to the HS rig tests. Operating air for the mister was now bled from the engine compressor discharge, rather than heated shop air, so mister flow rates varied directly with engine speed. The residual mist was routed from the no. 8 scavenge outlet to the compressor inlet gas path to be burned in the combustor. Instrumentation locations are shown in Fig. 4. The mister was instrumented to monitor inlet air pressure (P_{ai}), temperature (T_{ai}), and reservoir liquid temperature (T_{liq}). Sheathed thermocouples were added to the engine on the vapor inlet (T_{vi}), vapor outlet (T_{vo}), nozzle inlet (T_{noz}), dry sump outlet (T_{sump}), sump outer wall (T_{wall}), and buffer air (T_{air}). Three bearing outer race thermocouples were oriented circumferentially 90 deg apart at 3, 6, and 9 o'clock positions (T_{race3}, T_{race6}, T_{race9}) such that the 6 o'clock position was in line with the static rotor load due to gravity.

One new hybrid no. 8 engine bearing was tested. It was cleaned and coated with 2 ml of liquid Durad 620 B before installation in the engine. Prior to engine startup, the bearing was premisted for ten minutes using heated shop air; this served to prelubricate the bearing and heat the lubricant so it would mist at engine startup. Engine startup from 0 to 32,000 rpm (GI) was accomplished in one minute. At this condition, the bearing temperature was monitored until a steady-state condition was reached. Engine power was then slowly increased to 75 percent NRP and then to NRP. The bearing temperature was monitored and the engine power maintained for a specified amount of time and then a normal shutdown performed.

Results are shown in Fig. 5. The bearing was run over a period of two days, including two start/stop cycles, for a total of 10.7 h. The majority of the run time (8 h) was spent at NRP conditions.

Downloaded 02 Jun 2010 to 171.66.16.119. Redistribution subject to ASME license or copyright; see http://www.asme.org/terms/Terms_Use.cfm

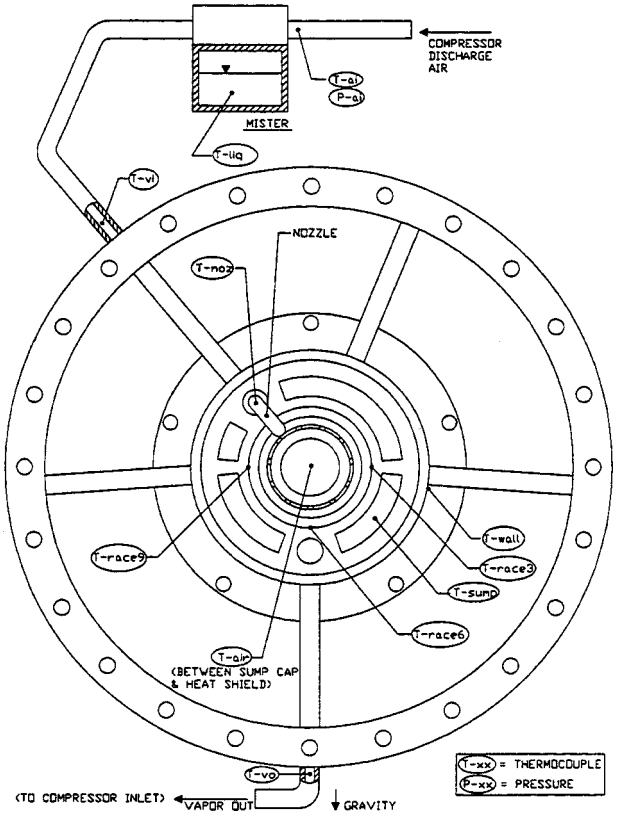

Fig. 4 T63 no. 8 bearing housing instrumentation

The bearing was still operating well at the completion of the runs. In Fig. 5, the temperatures of the vapor and buffer air in the vicinity of the bearing are plotted along with race temperature, speed, and mister operating parameters. The three bearing temperatures generally agreed within ±3°C, so only T_{race6} is plotted for clarity.

Some system characteristics should be noted. First, consider mister operation. As power was increased, compressor discharge pressure increased (P_{ai}), thus increasing the air and lubricant flows through the mister and into the bearing sump. Higher power settings also gave higher compressor discharge temperatures and higher T_{ai}. Note however, that T_{ai} was 50°C–130°C cooler than the compressor discharge temperature, due to convective cooling of the tube between the compressor discharge and mister inlet. This tube cooling was even higher at power settings above GI

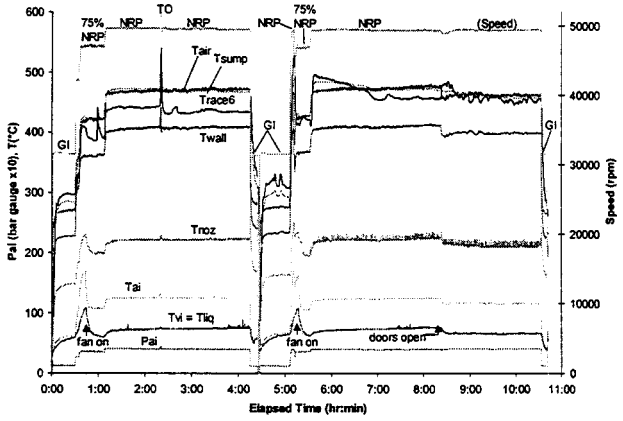

Fig. 5 T63 engine no. 8 bearing test results

Table 3 Comparison of lubrication systems in T63 engine

Parameter	Liquid	Vapor Phase
Max Allowable Bearing temp (°C)	204	540
#8 Bearing Avg. Temp at NRP (°C)	186	450
# 8 Lube flow rate at NRP (ml/min)	1250	0.35
# 8 Sump lube cooling at NRP (W)	1420	260
Lube System Dry Weight (kg)	10	0.6
Lubricant Capacity (liters)	10	0.2
Total Weight (kg) (Dry + Lubricant)	20	0.8

because a facility cooling fan was turned on, as noted. A decrease in compressor discharge temperature is again seen at 8:22, when outside doors to the test cell were opened, thus lowering the compressor inlet temperature. Finally, as the air passed through the mister, its temperature dropped as it heated the liquid lubricant, so that the exiting mist (vapor) was in equilibrium with the liquid ($T_{vi}=T_{liq}$). In the engine, the mist (vapor) was heated from T_{vi} to T_{noz} as it passed through the inlet strut. The temperature then increased from T_{noz} to T_{sump} as it absorbed heat from the bearing and the sump cap and walls. Finally, note that the engine buffer air was heated from T_{wall} to T_{air} as it passed from its entry point at the side of the sump to the center of the combustor heat shield.

When at GI at the start of both run days, T_{race6} was hottest, then T_{sump}, T_{air}, and T_{wall}. This was because vapor flow rate was low and the bearing self-generating heat rate was higher than the vapor convective cooling rate. When power was increased to 75 percent NRP and NRP, T_{air} and T_{sump} were equal and the hottest, and T_{race6} settled between them and T_{wall}. This was because the vapor flow rate had increased to the point where vapor convective cooling was greater than or equal to bearing self-generating heat.

There were four instances where T_{race6} digressed from the above. First, at 2:20–2:21, power was increased from NRP to take-off (TO), causing T_{race6} to reach 540°C, which was the maximum allowable limit for the race material, so power was decreased to NRP. Second, at 5:08–5:11, power was increased directly from GI to NRP, again causing T_{race6} to reach 540°C, so power was decreased to 75 percent NRP. In this case, the rapid increase in speed and heat without a preceding increase in lubricant flow may have caused borderline lubrication starvation. Third, at 5:35–6:35, when power was increased from 75 percent NRP to NRP, T_{race6} was higher than T_{sump} and T_{air}, indicating that the bearing self-generating heat was greater than the vapor convective cooling. This may have been a residual effect from the 5:08–5:11 event. Fourth, at 8:22, T_{race6} increased by 20°C when the doors were opened. This is believed to be due to a sudden increase in thrust load, as indicated by increased engine power output, which was due to the higher density of the cooler compressor inlet air.

In Table 3, characteristics of the VPL system are compared to the liquid lubrication system, using data from a previous oil test with this engine. The cooling provided by the lubricant passing through the no. 8 sump was calculated as:

$$Q=mC_p(T_{sump}-T_{noz})$$

For the vapor, C_p was for air and the air mass flow (1.0 g/s) was obtained from the mister calibration at NRP. The energy absorption due to vaporization of the Durad was several orders of magnitude less than that due to the airflow, and therefore was considered negligible. For the liquid, C_p was for turbine engine oil (MIL-L-7808J), and the oil mass flow (18.9 g/s) was obtained from the no. 8 nozzle specification. Since the VPL bearings could run at much higher temperatures, large flow rates of lubricant were not required for cooling; less than one-fifth of the cooling capacity was required, and the air carrier provided this for the vapor lubricant. The lubricant flow rate required for adequate lu-

Downloaded 02 Jun 2010 to 171.66.16.119. Redistribution subject to ASME license or copyright; see http://www.asme.org/terms/Terms_Use.cfm

brication was only 0.03 percent of the liquid system rate, which is on the order of what the engine normally consumes due to seal leakage, etc. Therefore, a single-pass VPL system was used, which eliminated the majority of the recirculating liquid system components with their associated weight and complexity. If VPL were to replace liquid lubrication in this example, the result is a 19.2 kg (96 percent) reduction in total lubrication system weight. Additionally, the oil mister is driven by compressor bleed air (0.07 percent engine flow), so a power takeoff shaft and accessory gearbox are no longer required.

T63 Engine Test of Cold No. 1 Bearing

If a single lubrication approach is to be used for all bearings in a gas turbine engine, it must perform in both the hot aft section and the cooler forward section. The objective of the cold no. 1 bearing test was to demonstrate that Durad mist would provide adequate lubrication in the cooler forward position. The bearing temperatures in these tests were well below the vapor point of Durad, so the lubrication mechanism was that of conventional oil mist lubrication with full EHD film at the contacts, rather than the chemical reaction mechanism of the high temperature tests.

Baseline tests were run with the standard recirculating oil system, and then Durad mist tests were run for comparison. The bearings used in these tests were standard no. 1 engine bearings with a 10 mm bore, 52100 steel races and balls, and a bronze cage. They were installed in the no. 1 bearing housing shown in Fig. 6. The bearing was instrumented with six *K*-type thermocouples (Fig. 7). Three thermocouples were in contact with the bearing outer race at the 2, 6, and 10 o'clock positions as viewed from the front of the engine (nos. 1, 2, and 3). One thermocouple was placed aft of the bearing to read the temperature of the exiting Durad mist (no. 4), but during testing it was found to be unreliable. A thermocouple was also placed on the bullet nose of the bearing hub to record the surrounding temperature (no. 5). These five thermocouples were positioned in the bearing compartment through small holes drilled in the bullet nose of the hub. The sixth thermocouple was positioned inside the Durad mist delivery tube, just prior to the hub.

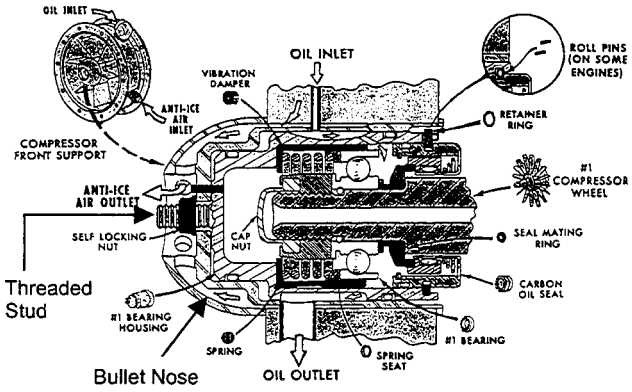

Fig. 6 Side view of no. 1 bearing housing [12]

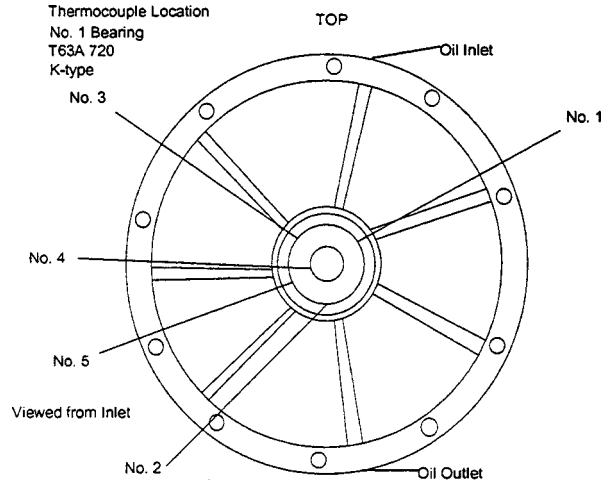

Fig. 7 T63 no. 1 bearing housing instrumentation

Table 4 No. 1 bearing oil baseline test temperatures

Condition	Ground Idle	Flight Idle	Normal Rated
Oil Inlet (°C)	39.4	46.1	54.4
Oil Outlet (°C)	33.3	39.4	46.7
Bearing Avg (°C)	51.7	62.2	76.1
Ambient (°C)		27.2	

During the baseline oil tests, oil temperatures were measured at the oil inlet and outlet struts (Fig. 7). Results for the three operating conditions tested are shown in Table 4. Note that at all operating conditions, the oil outlet temperature was consistently cooler than the oil inlet temperature by $6.9°C \pm 0.8°C$. This occurred even though the bearing was consistently hotter than the oil, due to self-generated heat. This indicates that the majority of the oil heat transfer was from the oil to the surroundings through the oil inlet and outlet struts, rather than from the bearing to the oil.

After the baseline oil tests were accomplished, the no. 1 bearing was isolated from the engine oil system by coupling the no. 1 oil inlet line to the outlet line, which completed the recirculating oil circuit. The Durad 620B lubricant was misted with an Alemite Model 4955 oil mist generator. The Durad was electrically preheated to 93°C in the reservoir to reduce its viscosity and allow better misting. The mister was supplied by 0.63 g/s of compressor bleed air at 1.02 bar gauge and was set to deliver 13 ml of lubricant per hour. The outlet line from the mister was routed in front of the engine inlet and connected to the threaded stud in the bullet housing. A front tap drilled in this threaded stud provided a path for the Durad mist to the bearing (Fig. 6). The carbon oil seal from the aft end of the bearing compartment was removed so that unused mist from the bearing would enter the compressor and go through the combustor. The engine was run at ground idle (GI) and flight idle (FI) operating conditions for the Durad mist test, and was not run at NRP because of a problem with the data acquisition control systems.

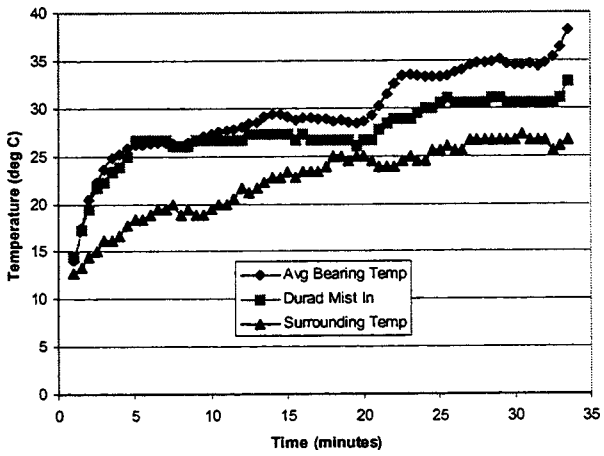

Fig. 8 T63 no. 1 bearing, Durad mist test results

Downloaded 02 Jun 2010 to 171.66.16.119. Redistribution subject to ASME license or copyright; see http://www.asme.org/terms/Terms_Use.cfm

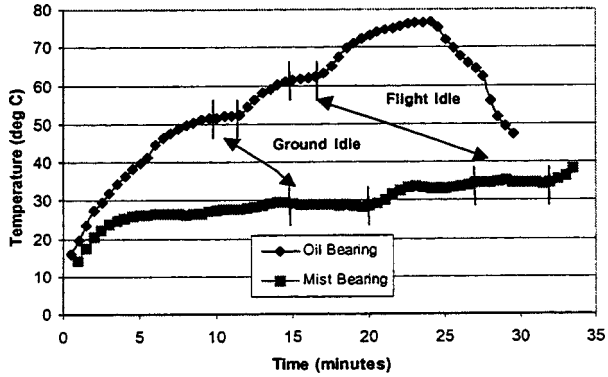

Fig. 9 T63 no. 1 bearing, oil versus Durad mist comparison

Table 5 Comparison of key engine operation parameters

Flight Condition	Parameter	Liquid Lubrication	Durad Mist Lubrication
Ground Idle	Shaft Speed (rpm)	32,000	32,000
	Shaft Torque (N-m)	33.5	39.5
	T_{t5} (°C)	502	493
	#1 Bearing Temp (°C)	52	29
Flight Idle	Shaft Speed (rpm)	43,000	43,000
	Shaft Torque (N-m)	67.7	71.3
	T_{t5} (°C)	554	534
	#1 Bearing Temp (°C)	62	34

The initial Durad mist lubrication test of the no. 1 bearing lasted approximately 40 min. After 16 min into the test, the bearing temperature reached equilibrium at the GI condition. At 19 min into the test the engine went to the FI condition, and the bearing temperature stabilized after 27 min elapsed time. Subsequently, 7.5 h of total elapsed time was put on the engine with 12 start cycles.

Figure 8 shows the average bearing temperature, the temperature of the Durad mist coming into the bearing, and the temperature of the surrounding hub. The average bearing temperature was similar to both the mist inlet temperature and the surrounding temperature, indicating very little bearing self-heat generation. Figure 9 shows that the bearing temperature of the mist lubricated bearing was lower than the liquid lubricated bearing, at the same engine conditions. At stable GI operation, the misted bearing was 23°C cooler, while at stable FI operation, the misted bearing was 28°C cooler. This indicates that most of the heat generation in the liquid lubricated bearing was due to churning of the oil. The mist system provided only enough Durad for lubrication, thus eliminating energy losses due to oil churning in the cold bearing compartment.

A comparison of the oil baseline test and the Durad mist lubrication test shows little difference in key engine operating parameters (Table 5). Minor differences can be justified by the difference in ambient air temperature on the two test days. The engine operated at approximately the same performance levels, showing that Durad mist operated as a satisfactory replacement for liquid lubrication in the cold no. 1 bearing.

Conclusions

In conclusion, a revolutionary concept in rotor support has been demonstrated in an operational gas turbine engine. The system includes the advantages of high load carrying capacity inherent to rolling element bearings, without the weight and cost penalties of a recirculating liquid lubrication system. Although bearing life may be limited to less than 20 h, the approach is applicable to limited life expendable cruise missile engines.

This is the first time that VPL has been accomplished in an actual engine at full power and at steady-state bearing temperatures of 430°C–460°C with sufficient life for an expendable cruise missile engine (10 h). This is also the first time it has been accomplished with a completely self-contained oil misting system running off of engine compressor bleed air. Additionally, the use of Durad 620B mist to lubricate an engine bearing at temperatures of 10°C–40°C has demonstrated the suitability of this approach for low temperature, as well as high temperature regimes. Finally, this is the first engine to operate with a bearing containing a C–C composite cage. The C–C cage resolved the sliding wear problems encountered with the silver-plated 4340 steel cage in previous VPL tests [11].

Future Work

Future VPL work will include studies of the fundamental mechanisms, with the goal of extending bearing life to hundreds of hours for application in limited life vehicles such as uninhabited air vehicles. Material analyses of the bearings from these tests are in progress for this purpose.

Nomenclature

C_p = specific heat (J/g-°C)
FI = flight idle power
GI = ground idle power
m = fluid mass flow (g/s)
NRP = normal rated power (maximum continuous power)
P_{ai} = mister air inlet pressure (bar gauge)
Q = heating rate (W)
TO = take-off power=maximum engine power (5 min limit)
T_{ai} = mister air inlet temperature (°C)
T_{air} = buffer air temperature forward of sump cap (°C)
T_{liq} = mister reservoir liquid temperature (°C)
T_{noz} = vapor temperature at nozzle inlet (°C)
T_{race} = bearing outer race temperature (°C)
T_{sump} = vapor temperature at dry sump outlet (°C)
T_{t5} = intra-turbine temperature (°C)
T_{vi} = vapor inlet temperature (°C)
T_{vo} = vapor outlet temperature (°C)
T_{wall} = sump outer wall temperature (°C)

References

[1] Macks, E. F., Nemeth, Z. N., and Anderson, W. J., 1951, ''Preliminary Investigation of Molybdenum Disulfide-Air-Mist Lubrication of Roller Bearings Operating to DN Values of 1×10^6 and Ball Bearings Operating to Temperatures of 1000°F,'' NASA Report NACA RM ES1 631.
[2] Wallerstein, S., 1965, ''Application of a Gas Powder Lubrication System to a Gas Turbine Engine,'' Air Force Report AFAPL-TR-65-43.
[3] Boes, D., 1978, ''Development of Light Weight Solid Lubricated Bearing Retainers,'' Air Force Report AFAPL-TR-78-72.
[4] Gardos, M. N., 1984, ''Solid Lubricated Rolling Element Bearings Final Report,'' Air Force Report AFWAL-TR-83-4129.
[5] Agrawal, G. L., 1997, ''Foil Air/Gas Bearing Technology—An Overview,'' ASME Paper No. 97-GT-347.
[6] Heshmat, H., Shapiro, W., and Grey, S., 1981, ''Development of Foil Journal Bearings for High Load Capacity and High Speed Whirl Stability,'' ASME Paper No. 81-Lub-36.
[7] Forster, N. H., 1997, ''High Temperature Lubrication of Rolling Contacts with Lubricants Delivered from the Vapor Phase and as Oil-Mists,'' Air Force Report WL-TR-97-2003.
[8] Forster, N. H., and Trivedi, H. K., 1997, ''Rolling Contact Testing of Vapor Phase Lubricants: Part I—Material Evaluation,'' Trib. Trans., **41**, No. 3, pp. 421–428.
[9] Forster, N. H., and Trivedi, H. K., 1997, ''Rolling Contact Testing of Vapor Phase Lubricants: Part II—System Performance Evaluation,'' Trib. Trans., **41**, No. 3, 493–499.
[10] Forster, N. H., and Givan, G. D., 1999, ''Computer Modeling of Heat Generation in Vapor Lubricated Bearings for Gas Turbines,'' RTO MP-8, pp. 9–1 to 9–10.
[11] Van Treuren, K. W., Barlow, D. N., Heiser, W. H., Wagner, M. J., Forster, N. H., 1998, ''Investigation of Vapor-Phase Lubrication in a Gas Turbine Engine,'' ASME J. Eng. Gas Turbines and Power, **120**, No. 2, pp. 257–262.
[12] Allison Gas Turbine Division, 1981, TM55-2840-231-23.

Downloaded 02 Jun 2010 to 171.66.16.119. Redistribution subject to ASME license or copyright; see http://www.asme.org/terms/Terms_Use.cfm

Pioneering Turbojet Developments of Dr. Hans Von Ohain—From the HeS 1 to the HeS 011

Cyrus B. Meher-Homji
Bechtel Corporation,
Houston, TX 77252

Erik Prisell
Defence Materiel Administration (FMV),
Stockholm, Sweden

On March 13, 1998, Dr. Hans Joachim Pabst von Ohain, co-inventor of the turbojet, passed away at the age of 86. As a young doctoral student, von Ohain conceived of and built a demonstrator turbojet engine. He was hired by the Heinkel Aircraft Company in 1936 and under intense time pressure imposed by Ernst Heinkel, designed the world's first flight turbojet engine. This paper traces the technical antecedents leading to historic jet-powered flight made on August 27, 1939 by a Heinkel He 178 aircraft powered by von Ohain's HeS 3B turbojet. During his tenure at Heinkel and thereafter at the Heinkel-Hirth Company, he was responsible for a series of turbojet engines culminating in the advanced second generation HeS 011 with a thrust of 2860 lbs. This paper is a tribute to an outstanding scientist who made possible the turbojet revolution and who will forever be remembered as the inventor of the world's first flight turbojet. [S0742-4795(00)02102-5]

1 Introduction

Early morning on August 27, 1939, five days before the outbreak of the Second World War, a small group of people assembled at the Heinkel airfield at Marienehe close to Rostock to witness the first flight of a He 178 turbojet powered aircraft flown by test pilot Erich Warsitz. Among those present were Ernst Heinkel, von Ohain the young and brilliant designer of the turbojet, Max Hahn and Wilhelm Gundermann who worked on the small team that developed the world's first flight engine, the HeS 3B. The flight, which lasted approximately 6 minutes, changed the course of aircraft and propulsion history. An account of Dr. von Ohain's work is presented with technical details of his turbojet designs culminating in the HeS 011 which was considered the most advanced jet engine design at the end of the Second World War.

1.1 Antecedents. Dr. Hans von Ohain in Germany and Sir Frank Whittle in England, both of whom are considered co-inventors of the turbojet engine, pioneered the turbojet revolution. Constant [1], Schlaifer [2], von Ohain [3], Scott [4], Jones [5], and Meher-Homji [6] have documented their work. Both Whittle and von Ohain independently envisioned flight speeds in excess of 500 mph at altitudes of 30,000 feet, had revolutionary ideas as students, and developed their engines without the help of the traditional aeroengine companies. In order to put the development of Ohain's jet engines built prior to and during the Second World War into a historical perspective, it is necessary to trace the course of Ohain's thinking and the theoretical and practical developments relating to gas turbines before the Second World War and examine the factors that led Heinkel into taking on the risk of turbojet development.

1.2 Overview of Turbojet Development in Germany. Turbojet development in Germany initially included two independent programs that were not, at least initially, under the auspices of the German Air Ministry (RLM[1]). As is typical of revolutionary technological changes, these two programs did not initiate at the traditional aeroengine companies but started at Heinkel Airframe and at Junkers Airframe Company. Ultimately, both these developments ended up under Heinkel, but as we will see later, despite a pre-eminent position in the area of turbojet engine and jet aircraft development, Heinkel could not capitalize on his position as a jet age pioneer.

1.2.1 Engine Development Sponsored by Ernst Heinkel. Von Ohain developed the idea of his jet engine while he was a doctoral student at the University of Gottingen. By 1934, he had completed rudimentary design calculations that indicated speeds of 500 mph were possible. He initiated patent procedures and decided to build a working model of the engine. Working with Max Hahn, an expert mechanic and machinist and a natural engineer, he built his first model engine which was plagued by combustion problems. Von Ohain's Professor R. W. Pohl, introduced von Ohain to Ernst Heinkel, the legendary aircraft manufacturer whom, Pohl knew, was obsessed with high-speed flight. As a result, the 24 year old Ohain was interviewed by Heinkel and his leading engineers, and was hired by Heinkel.

Ernst Heinkel had come into prominence during the First World War when he was the chief designer of the Hansa-Brandenburgischen Flugzeugwerke and he was noted as a designer of a wide variety of marine aircraft. Heinkel formed his own company in 1922 and produced several well-known aircraft. His obsession with speed was triggered in September 1927 when he visited Venice to see the famous Schneider Cup race. When viewing the fast aircraft on display, Heinkel was seized with an intense desire to build fast aircraft [7]. It was at this event that Claudius Dornier, while standing with him viewing a high performance Fiat engine, uttered the following prophetic words to Heinkel ''If only we had a single engine like that, we could be in this race, but the way our aviation industry is going, we shall never get a decent one.'' Heinkel stated in his memoirs that this was indeed a true statement and that German engines, as the result of the setbacks suffered between 1918 and 1933, never caught up with the rest of the world nullifying the advantages achieved in the field of airframe aerodynamics. This disillusionment with the German aircraft en-

Contributed by the International Gas Turbine Institute (IGTI) of THE AMERICAN SOCIETY OF MECHANICAL ENGINEERS for publication in the ASME JOURNAL OF ENGINEERING FOR GAS TURBINES AND POWER. Paper presented at the International Gas Turbine and Aeroengine Congress and Exhibition, Indianapolis, IN, June 7–10, 1999; ASME Paper 99-GT-228. Manuscript received by IGTI Mar. 9, 1999; final revision received by the ASME Headquarters Jan. 3, 2000. Associate Technical Editor: D. Wisler.

[1]The German National Ministry of Aviation was known as the Riechluftfahrtministerium or RLM for short.

Copyright © 2000 by ASME

Downloaded 02 Jun 2010 to 171.66.16.119. Redistribution subject to ASME license or copyright; see http://www.asme.org/terms/Terms_Use.cfm

gine industry persisted with Heinkel and was *certainly a factor in his plunging forth with the bold new concept proposed by the young von Ohain nine years later*.

After getting intoxicated by speed, Heinkel hired Siegfried and Walter Guenther who were identical twins. The Guenther brothers were brilliant and gifted designers responsible for several of Heinkel's competition winning designs and also for the graceful jet aircraft designs developed by Heinkel. They were responsible for the famous He 70 (the Heinkel Blitz) which won eight international speed records in 1933. This aircraft was fitted with a 600 HP BMW engine, which represented a technology lag from the US, English, and French engines at that time. The He 70 had such good aerodynamics that one was actually purchased by Rolls Royce to test and demonstrate their 810 HP Kestrel V engine.[2] The Gunther brothers were present at von Ohain's initial interview with Heinkel and recognizing the limitations of propellers for high-speed flight, were enthused by his jet concept.

As described in detail below, Heinkel hired von Ohain in 1936 and this brilliant young physicist put him in the position to fly the world's first turbojet powered aircraft in August 1939. Von Ohain and Max Hahn started work at Heinkel Marienehe Works under a shroud of secrecy and were given instructions to develop a jet engine as rapidly as possible with the stipulation that ground tests were to begin within a year. The first engine designated as the He S1, was a demonstrator engine that operated on hydrogen fuel and was successfully test run in March 1937. Continuing development, von Ohain's team had the HeS 3B engine operational and the historic first pure jet-powered flight of the He 178 powered by a HeS 3B turbojet occurred on August 27, 1939, a few days before the start of the Second World War. Heinkel immediately informed high air ministry officials of this momentous event, but was met with indifference. The German Air Ministry ordered Heinkel to cease all research on jet engines but Heinkel, convinced that his political connections would ultimately result in a profitable contract, kept von Ohain's team working on turbojets. A few months later, Heinkel's proposal for a jet fighter (the He 280) was accepted by the RLM. This aircraft was to be powered by two HeS 8A engines designed by von Ohain.[3] After the first flight of the He 280, the RLM allowed Heinkel to purchase the Hirth Motoren and in doing so Heinkel had full-fledged engine manufacturing capability. Von Ohain moved to the Heinkel-Hirth Company and continued engine development work there. The RLM cancelled the He 280 on March 27, 1943 and development of the HeS8A was curtailed by the RLM in mid 1942 in favor of the Jumo 004 and BMW 003 engines.

1.2.2 Turbojet Engine Development Initiated at Junkers Aeroplane Company. During 1936 and 1939, engineers at another aircraft manufacturer, Junkers Aeroplane Company, were working on jet engines under the guidance of Prof. Herbert Wagner. Wagner, a brilliant airframe designer was well-versed in steam turbine design and wanted to develop jet engines which, he felt, would make Junkers a pre-eminent aircraft company. By 1938, Junkers had 30 designers and draftsmen working on the project at their Magdeburg plant and were in the process of developing a demonstrator, that had a 12 stage axial compressor, single combustor and a two-stage turbine. This team included Max Adolf Mueller who was at one time an assistant to Prof. Wagner at the Technical University in Berlin and was now project manager for the Wagner jet engine studies. Later, the RLM insisted that engine development work be taken over by Junkers engine company (Junkers Motoren at Dessau). Mueller, who objected to the organizational changes, and 12 members of his team, left Junkers and were hired by Heinkel in the summer of 1939, thus bringing the Wagner engine program to Heinkel. Included in this team was Dr. R. Friedrich, an outstanding compressor aerodynamist.

1.2.3 Official Turbojet Programs of the RLM (German Air Ministry). A pictorial overview of the course and chronology of German turbojet development is shown in Fig. 1 including the key aircraft developed. Also shown are aircraft that were planned for deployment using the second generation HeS 011 engine.

In 1938, Helmut Schelp and his senior, Hans Mauch in the German Air Ministry (RLM) had ambitious jet engine development programs in mind and were trying to work with the aeroengine manufacturers to interest them in jet engine development. Schelp was aware of the limitations of piston engines for higher speeds and had concluded that jet propulsion was the solution.[4] Schelp was unaware of the ongoing research at Heinkel Airframe or Junkers Airframe Company. The prevailing feeling at that time was that compressor and combustor efficiencies were too low to permit a practical jet engine. Schelp, however, knew of three leading compressor engineers; Professors Prandtl, Betz and Encke who worked at the Aerodynamic Research Establishment (AVA) at Göttingen and had been successful in designing compressors based on aerodynamic airfoil theory. Schelp recognized that their work could provide the impetus required in developing a practical engine.

In 1938, Schelp and Mauch visited four dominant aeroengine manufacturers—BMW, Junkers Aeroengine Company, Daimler Benz, and Bramo. The head of Junkers Aeroengine, Otto Mader, reluctantly accepted a small development engineering contract. He was not aware of Wagner's ongoing program at Junkers *Airframe* Company mentioned above. Daimler Benz refused Schelp's offer for funding. Bramo, fearful that they would soon to face severe competition in piston engine orders to their rivals BMW, agreed to perform a study. BMW took on a study contract. Later during the war, the BMW company developed the 003 engine under the leadership of Dr. Herman Oestrich.

Ultimately, all German turbojet development work came under RLM control. The RLM insisted that all engine development be done at engine companies.[5] At the Junkers Aeroengine Company (Junkers Motoren or Jumo for short), work proceeded on the deliberately conservative Junkers Jumo 004 engine under the leadership of Anselm Franz. This engine, which powered the Me 262, was the world's first high volume production turbojet and is described by Meher-Homji [8]. As mentioned above, Heinkel was permitted to purchase the Hirth Corporation, which gave him access to engine manufacturing technology. Both the von Ohain and Mueller engine programs were moved to the Heinkel-Hirth Corporation essentially under RLM control.

2 Von Ohain's Early Work

Von Ohain developed the idea of his jet engine while he was a doctoral student at the University of Göttingen when he was working towards his Ph.D. under the renowned Professor Pohl. During a flight on a Junkers Trimotor aircraft, von Ohain was appalled by the high noise and vibration caused by the reciprocating engines and instinctively felt that the combination of aerodynamic aircraft would be more matched, in an aesthetic sense, with a continuous flow aerothermodynamic engine. Spurred on by this initial feeling, von Ohain, in the Fall of 1933, started thinking about a steady aerodynamic flow process involving a project

[2]Heinkel actually tried to negotiate a deal with the British Air ministry to trade license of the He 70 manufacture for the license to build and develop Rolls Royce Engines in Germany. This deal was not permitted by the German Air Ministry who assured Heinkel that German aeroengine development was soon to ''surpass the achievements of the foreign aircraft engine builders.''

[3]Nine prototypes of the He-280 were built and in the spring of 1942 the prospects for this aircraft were favorable as the Jumo 004 was, at that time, plagued by compressor blade vibratory problems. Once these problems were resolved by Franz and Bentele, the Me 262 proved to be superior to the He-280 and was thus chosen for production.

[4]Schelp was aware of the work of Armengaud and Lemale published before 1910 in which jet propulsion was put forward.

[5]Mauch had actually suggested that Heinkel's jet engine team be the nucleus of a jet development effort to be established at Daimler-Benz, an offer which Heinkel refused.

Downloaded 02 Jun 2010 to 171.66.16.119. Redistribution subject to ASME license or copyright; see http://www.asme.org/terms/Terms_Use.cfm

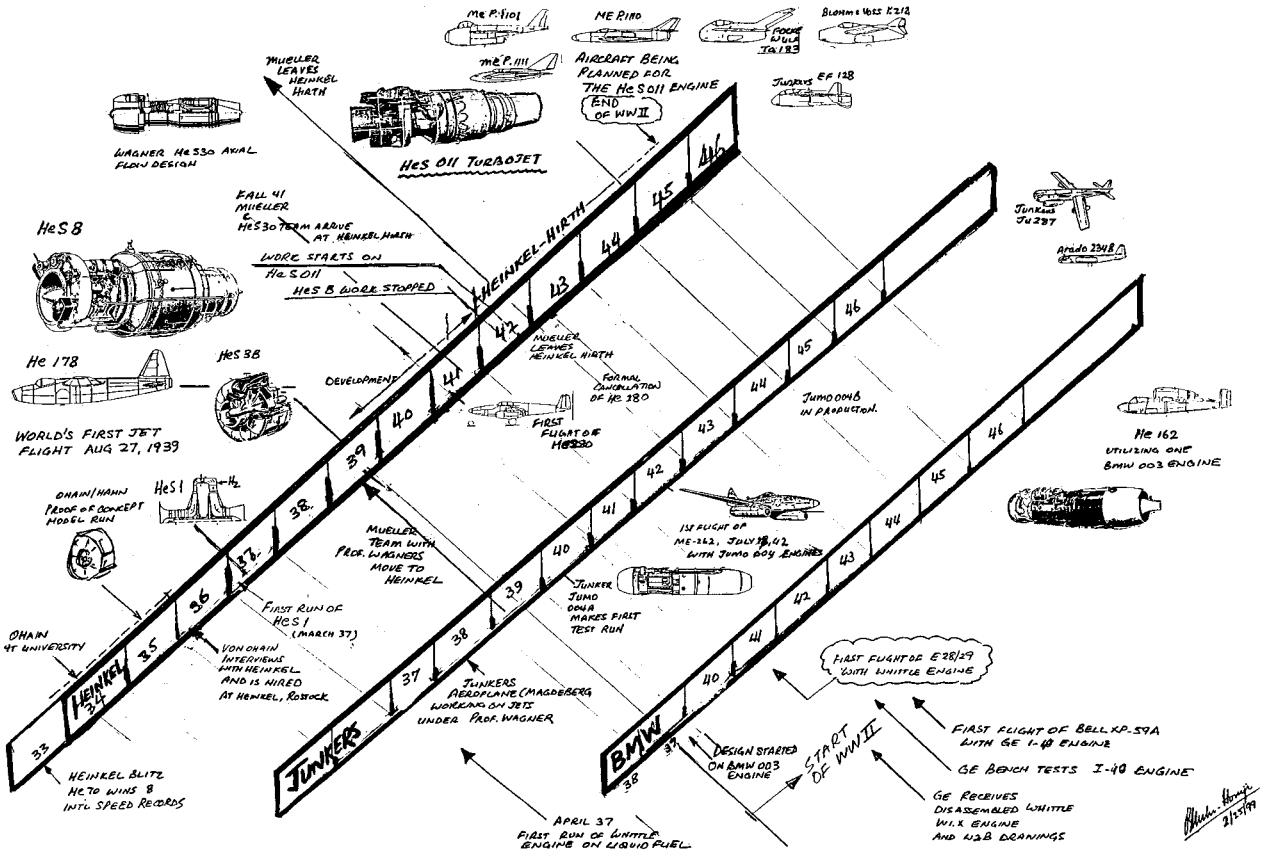

Fig. 1 Timeline showing German jet engine development program and operational and planned turbojet aircraft

based on a modified ''Nernst'' turbine[6] and his preliminary calculations indicated that such a system would have great advantages in terms of power to weight ratio. With his design goal of simplicity for a working model, he chose a centrifugal compressor and radial inflow turbine layout to minimize matching problems. Even at this early date, von Ohain recognized that importance of minimizing frontal area by the use of axial flow compressors but opted for the simpler radial design for the initial models.

By 1934, he had completed rudimentary design calculations that indicated speeds of 500 mph were possible based on a pressure ratio of 3:1 and a turbine inlet temperature of 1200 to 1400°F. Although the fuel consumption was high, von Ohain calculated that the turbojet's weight would be about a fourth that of a reciprocating engine. He initiated patent procedures and decided to build a working model of the engine at his own expense. Von Ohain developed a friendship with Max Hahn an expert mechanic, machinist and a natural engineer,[7] who was the chief mechanic at the Bartells and Becker car repair shop in Gottingen where he used to have his car repaired. Von Ohain showed Hahn his initial sketches and Hahn made suggestions for simplification to enable manufacture. The prototype model was built by Hahn and funded by von Ohain with the initial estimate being 1000 marks. The engine is shown in Fig. 2. This engine did not self sustain due to combustion problems but did result in unloading of the starter. Ohain made temperature and pressure distribution measurements and recounted that Hahn, who was normally most stern and skeptical, was in this instance most optimistic because of the unloading of the starter and the high velocity flame emanating from the jet pipe![8] Ohain realized right away that liquid fuel combustion would be a formidable challenge that would take considerable financial and technical resources to overcome.

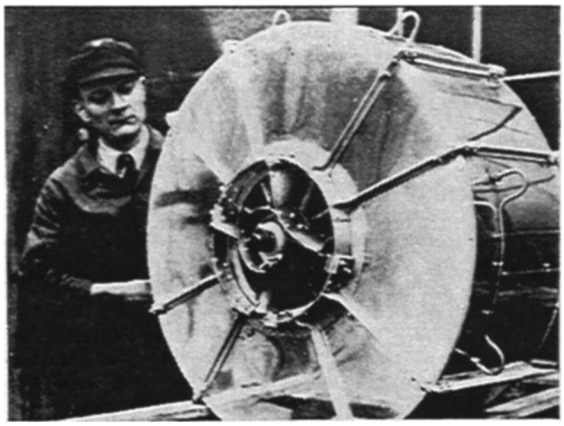

Fig. 2 Prototype model (1934) which did not self sustain

Professor R. W. Pohl[9] at Göttingen University was very supportive of this extracurricular work and permitted experiments to be conducted in the backyard of his institute, supplying von Ohain with instrumentation and a starter motor. Convinced that von Ohain's theory was right and that this concept had a future, he

[6]Von Ohain initially investigated concepts not involving moving machinery by bringing incoming ram air in contact with the expanding gas but the problems with heat transfer and losses caused these ideas to be replaced by a compressor—turbine concept.

[7]Von Ohain always had the greatest respect for Max Hahn's natural engineering and practical skills and being a man of great humility, always mentioned Hahn's contribution in both his talks and subsequent papers. Max Hahn followed Ohain to Heinkel and worked closely on the development of the early engines till the end of the war.

[8]As described by Ohain—this was like a flame thrower!

[9]Prof. R. W. Pohl was von Ohain's Professor for his doctorate which was in physics. Von Ohain had minored under Prof. L. Prandtl in the area of applied mechanics.

Downloaded 02 Jun 2010 to 171.66.16.119. Redistribution subject to ASME license or copyright; see http://www.asme.org/terms/Terms_Use.cfm

recommended to von Ohain that industrial sponsorship would be needed for further development and indicated his willingness to write a letter of recommendation to an aeroengine company of von Ohain's choice. Von Ohain wisely chose the aircraft manufacturer Ernst Heinkel as he was aware of Heinkel's obsession for high-speed aircraft and that his reputation as a risk taker.[10] Another factor in this choice was the fact that von Ohain loved the Baltic Sea and sailing and the Heinkel works at Rostock was perfect for this. Von Ohain intuitively recognized that the traditional aeroengine companies would resist the revolutionary design that he was proposing.

3 Turbojet Engine Development Work at Heinkel

In February 1936 Pohl wrote to Heinkel and as a result, the 24 year old von Ohain was summoned to Heinkel's house on the Baltic Coast. According to von Ohain [9] during his discussion with Heinkel on the evening prior to the day-long interview, Heinkel listened to his proposal and asked him point blank as to what the problem areas were with his proposed engine as he wanted to know if this young Ph.D. had a sense of reality. Von Ohain indicated to him that the problem was the high fuel consumption but that this could be improved as development efforts proceeded.

The next day, von Ohain met with the leading engineers at Heinkel and after a grueling one-day interview, in which he skillfully addressed all questions, he succeeded in convincing Heinkel to hire him.[11] Included in this group were Walter and Siegfried Guenther, Heinkel's leading aerodynamicists, who instantly recognized the importance of jet propulsion for high-speed flight. An employment contract was issued to von Ohain on April 15, 1936.

3.1 The HeS 1 Demonstrator Engine. Von Ohain and Max Hahn (whom von Ohain insisted be hired) started work under a shroud of secrecy in a special building in Marienehe and were given instructions to develop a jet engine as rapidly as possible with the stipulation from Heinkel that bench tests were to begin within a year. The project was deliberately given a vague name of ''Sonder-Entwicklung'' (''Special Development'') and the work started with a team including Max Hahn and Wilhelm Gundermann, a gifted Heinkel designer, and two draftsmen. Heinkel kept this work secret from the German Air Ministry (RLM), the Luftwaffe, and engine manufacturers.[12]

The rather over-ambitious schedule stipulated by Heinkel forced von Ohain to deviate from his original plan which was to systematically conduct studies and tests and solve the combustion problems. Recognizing the politics of the situation, von Ohain made the conscious decision that a simple engine run on hydrogen fuel would provide the impetus needed for such a project, quickly demonstrate a tangible running engine to Heinkel[13] and buy him some time for systematic combustion investigations. After this decision was made, he started parallel investigations into the use of liquid fuels and even visited industrial fairs in Leipzig in order to elicit support from burner manufacturers for the design of a high intensity combustor. Not finding any support, he realized that this formidable problem would have to be solved by his own team. Work proceeded, with von Ohain providing the overall technical direction, laying out the engine and conducting thermodynamic studies, Gundermann working on the mechanical design and stress analysis and Hahn working on manufacturing techniques and combustion.

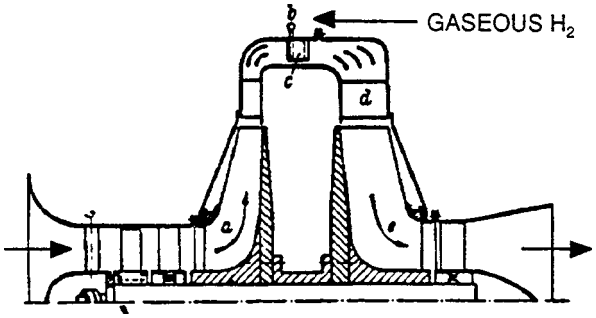

Fig. 3 HeS 1 Demonstrator run on hydrogen fuel

The HeS 1[14] layout is shown in Fig. 3. It consisted of a back-to-back radial compressor and a radial inflow turbine. The rotor diameter was 12 in. The centrifugal compressor was preceded by an axial entry stage. The hydrogen combustor consisted of a large number of hollow vanes with blunt trailing edges placed within the air duct between the compressor and the radial inflow turbine. The engine was made essentially of sheet steel fabricated at the Marienehe works and disks fabricated at a nearby shipyard. The engine operated at a speed of 10,000 rpm and produced a thrust of 1.1 kN (250 lbs.) Von Ohain's choice of hydrogen as a fuel was wise, as the demonstrator combustor did not present any significant problems because of the high flame velocity and the wide combustion range of hydrogen. It also performed flawlessly under off design conditions and during transient acceleration and deceleration.

In the Spring of 1937 the engine was demonstrated early one morning in front of Ernst Heinkel, and this had a major impact on von Ohain's position at Heinkel. The young von Ohain was now established as a brilliant engineer and received a letter of recommendation and a pay increase from Heinkel. Dr. von Ohain received a permanent contract and was named head of the Heinkel jet propulsion development. After this successful engine run, Heinkel pushed hard for a flight engine operating on liquid fuel. This led to the design and development of the HeS.2[15] engine and finally the HeS 3 engine.

3.2 Design and Development of the HeS 3A and HeS 3B Engine. Starting in May 1937, after the running of the HeS. 1 engine, work was intensified on the combustor development. The combustor investigation program included the following elements [3]:

- installation of a 2 HP blower with controllable bypass to allow testing
- investigations on segments of annular combustors to evaluate influence of combustor shape, flame holding mechanisms and optimization for minimizing pressure drop[16] fuel vapor generation and injection into the combustor by electrical heating
- atomization studies

By 1938 a combustor with excellent operational characteristics was developed. This combustor used vaporized fuel, but there were still difficulties with atomizing that had to be overcome.

Design work had begun on the flight engine (designated as the HeS 3) in May 1937, and in September 1937, Max Hahn sug-

[10]This choice was very correct as the traditional aircraft engine companies were reluctant to study jet propulsion as Schelp would find out at a later date. All the initial jet development work in Germany was done by aircraft companies and not aeroengine companies.

[11]Part of the reason for Heinkel hiring von Ohain was to prevent him from going to his archrival, Messerschmitt. This rivalry continued throughout the war in the race to produce the first jet fighter. For example, in 1940/41, Messerschmitt delayed for months, by political means, Heinkel's acquisition of Hirth Motoren GmbH [2].

[12]Hans Mauch of the RLM actually visited Heinkel in the summer of 1938 about one year prior to the first jet powered flight. He witnessed the operation of the hydrogen fueled demonstrator engine, and this helped convince him of the need for turbojets for high speed flight.

[13]An important attribute of an innovator is the recognition that design compromises are often required for success and that often a technically elegant design may not lead to long term success. Both Dr. von Ohain and Sir Frank Whittle had this insight.

[14]The designation stands for He=Heinkel, S=Strahltriebwerk=Jet engine. This same designation was continued when Heinkel purchased Hirth.

[15]The HeS 2 had the same turbomachinery components as did the HeS 3 but utilized hydrogen in its combustor.

[16]Since the segments were circumferentially small, the sidewall effects reduced the usefulness of the tests.

Downloaded 02 Jun 2010 to 171.66.16.119. Redistribution subject to ASME license or copyright; see http://www.asme.org/terms/Terms_Use.cfm

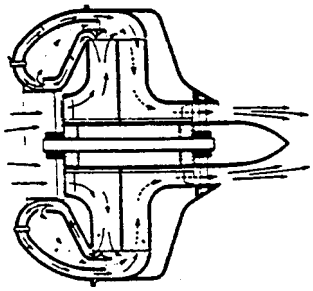

Fig. 4 Patent drawing of Hahn showing combustor located in front of centrifugal compressor

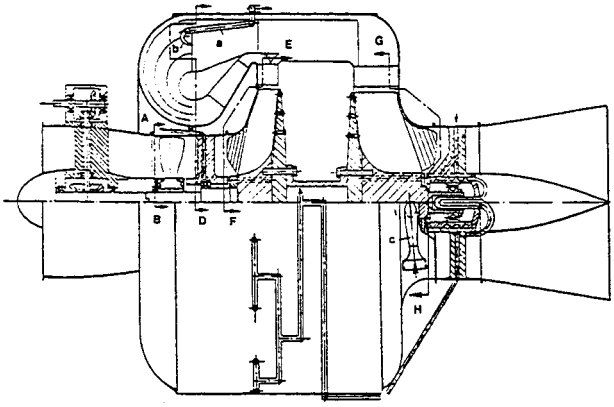

Fig. 5 Layout of the HeS 3B flight engine [10]

gested the idea of arranging the combustor in the large unused space in front of the centrifugal compressor a concept that would reduce shaft size and engine weight. Dr. von Ohain was very impressed by Hahn's idea and encouraged him to apply for a patent and the idea was incorporated in the engine layout by von Ohain. The patent drawing is shown in Fig. 4 [10].

The first HeS 3A was tested in 1938, but did not produce the design thrust required because a small compressor and combustor had been used to reduce the frontal area. The engine was, therefore, completely redesigned and resulted in the HeS 3B. This engine attempted to increase the mass flow by having a high hub/tip ratio and von Ohain minimized the inlet losses by using an axial inducer stage which, in addition to contributing to an increased pressure ratio, also provided a counter swirl thus decreasing the inlet relative Mach number and curvature of the inlet blade. The layout of the flight engine is shown in Fig. 5 [11]. The inlet section of the HeS 3 is shown in Fig. 6. The wraparound combustor is shown in Fig. 7 and the radial inflow turbine is shown in Fig. 8.

The engine had a speed of 13,000 rpm, a weight of 360 kg (793 lbs), and frontal area of 0.68 m^2 (7.31 sq. ft.). Figure 9 shows the performance characteristics of this engine presented by Carter [12].

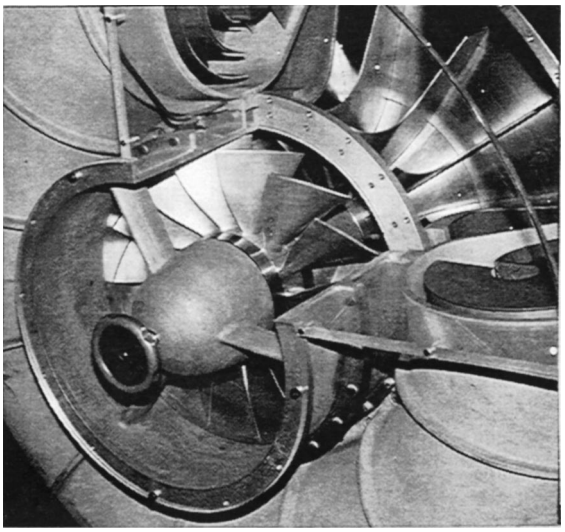

Fig. 6 Inlet section of the HeS 3B showing inducer and centrifugal compressor

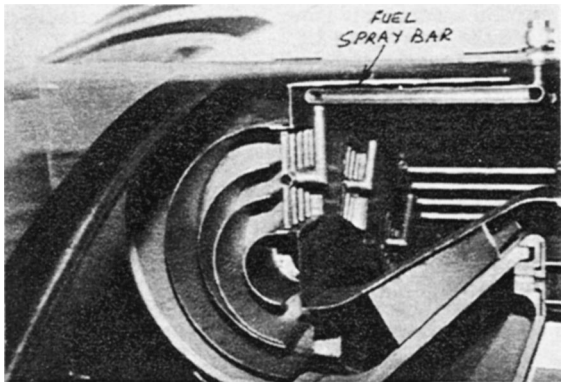

Fig. 7 Combustor section of the HeS 3B

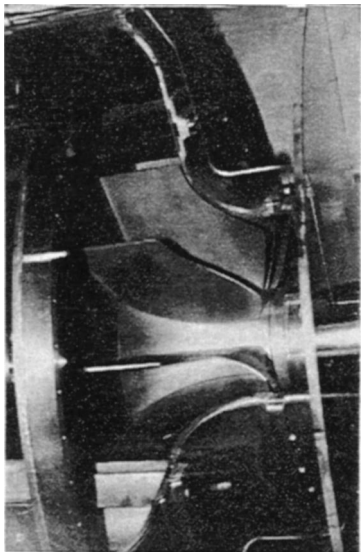

Fig. 8 Radial inflow turbine of the HeS 3B

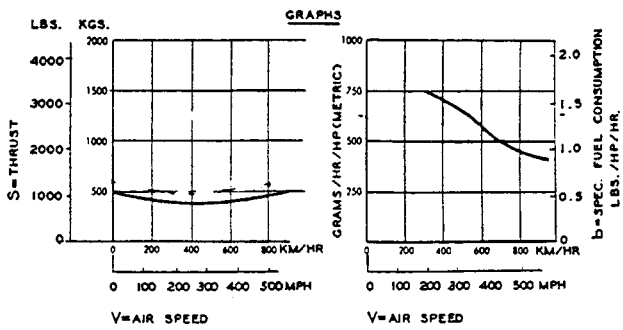

Fig. 9 Performance characteristics of the He S3B

Downloaded 02 Jun 2010 to 171.66.16.119. Redistribution subject to ASME license or copyright; see http://www.asme.org/terms/Terms_Use.cfm

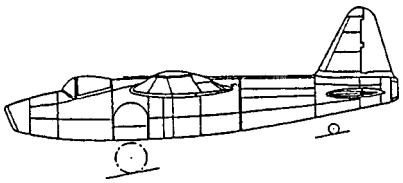

Fig. 10 The He 178—world's first jet powered aircraft

4 The He 178: the World's First Jet Aircraft

Design on the He 178 was led by Dr. Heinrich Hertel and worked on by the Guenther twins. The basic design was laid out by Walter Guenther but after his tragic death in a car accident in September 1937, the work was carried out by Heinrich Helmbold and Siegfried Guenther who kept Walter Guenther's design concept unchanged. The aircraft was to use the HeS 3 engine. The He 178 (Fig. 10) was a small shoulder winged airplane having a wing span of 7.2 m (23 ft 7 in) and a length of 7.48 m (24 ft 6 in). The wings were mostly of wooden construction with a small dihedral angle. Air for the single HeS 3B engine was drawn in from a nose intake and routed to the engine via a duct that went below the pilot's seat. The fuel tank was located behind the pilot's seat. The aircraft had a loaded weight of 1950 kg (4295 lbs) and was designed for a maximum speed of 640 Km/h (498 mph) at sea level.

On August 27, 1939, the He 178 piloted by Erich Warsitz made a historic 6 minute flight from the Heinkel airfield in Marienehe at about 4 am. There was great jubilation after this historic event. Heinkel rushed to inform the RLM of this achievement, but met with indifference as the RLM had more immediate problems of gearing up for the war which was to start within a few days. Later, Heinkel arranged for a demonstration of the He 178 that was observed by Schelp, Milch, and Udet. The aircraft experienced a fuel pump leakage problem initially prior to takeoff and Heinkel had to improvise by claiming a tire blow out to keep the skeptical group interested while the fuel pump was replaced [5]. Finally, a successful demonstration was made, but there was little enthusiasm displayed by the Air Ministry representatives.

This was the first aircraft in the world to fly utilizing a turbojet and was also the first to experience a bird ingestion problem![17] To put the date into perspective, the first flight was one year before the Caproni-Campini CC2[18] and 20 months before the British Gloster E28/39 first took to the air with Whittle's W1 engine.

5 The HeS 6 Engine

The HeS 6 was a refinement of the HeS 3 engine with increased thrust up to 2860 kg (1300 lbs) at 13,300 rpm. The specific fuel consumption was essentially the same as the HeS 3. While this engine itself was successful, the combination of the HeS 6 within the He 178 airframe resulted in poor performance. Problems with the airframe and a persistent problem wherein the undercarriage would not retract finally caused Heinkel to retire the He 178 which was moved to the Air Museum in Berlin and subsequently destroyed during an Allied bombing raid.

6 Engine Development for the He 280 Jet Fighter

Shortly after the demonstration of the He 178 to the RLM, Heinkel started development of a twin engine fighter which was designated the He 280. The aircraft could not use engines of the HeS 3B type because of the large engine diameter and low performance. At this time, however, the axial flow engine (designated the HeS 30) that was being developed by Mueller who had arrived at the Heinkel Rostock plant, was experiencing serious development problems. Recognizing that this engine would not be ready in time, von Ohain took a gamble in designing a back up solution designated the HeS8 which would employ a radial rotor similar to the HeS 3B combined with an axial vane diffuser and a straight through flow combustor. Only 14 months were available for this development, as the He 280 airframe was developed much faster than its engines.

It is interesting to examine the history of the Mueller engine in context of von Ohain's work. Mueller had his initial contacts with Heinkel and Dr. von Ohain in early 1939 when he offered to bring Heinkel the Wagner engine and the project team. At this time, Mueller gave the impression that the engine program was well advanced and Heinkel and von Ohain believed that this program together with their own He S 3 engine would place Heinkel in a leading position as a jet engine maker. Mueller and his team were hired by Heinkel and came over in the summer of 1939. The Wagner engine took on the Heinkel designation of HeS 30. Mueller and his team were incorporated in Dr. von Ohain's propulsion group and given the task to finalize the development of the HeS 30. Dr. von Ohain and Heinkel soon realized that this engine program was nowhere near the advanced stage, implied by Mueller. Heinkel pushed hard for the effort to make this program successful especially as the HeS 30 was to be the propulsion plant for Heinkel He 280 fighter. During contract negotiations with the RLM, Udet, who was supportive of Heinkel and who had recognized that Heinkel needed engine manufacturing capability and skilled manufacturing manpower to compete with the established engine companies, made Heinkel a gentlemen's agreement that if the He 280 succeeded in flying before April 1941 Heinkel could buy the Hirth Motoren company in Stuttgart.

By the end of 1939 the HeS 30 progress was very slow and Heinkel, concerned of the adverse impact on the He 280 program, approached Dr. von Ohain to develop a backup solution. Dr. von Ohain's solution, designated the HeS 8A, was a design based on the HeS 3B but with an axial diffuser and a straight through flow combustor. The engine program was done under a RLM contract giving the engine the first RLM designation of a German turbojet the 109-001. It was not without risks because the specification of the aircraft limited the engine diameter and therefore the axial diffuser function and efficiency together with the straight through combustor became very critical. Luckily for Heinkel, von Ohain's HeS 8 engine managed to meet the minimum requirements and was ready in time for the first flight of the He 280 which took place in late March 1941. The He S 30 program still suffered several problems including a mismatch between the compressor and turbine. Thus, it is thanks to von Ohain's HeS 8 that the He 280 flew on schedule and the RLM allowed Heinkel to purchase Hirth Motoren company which could then give the Mueller team support with the HeS 30 program.

7 The HeS 8A Engine Description

The HeS8 (RLM Designation 109-001) was designed with the specific objectives mentioned above and was based on the HeS 3 and HeS 6 engines. The reduction in diameter was accomplished by redesign of the compressor diffuser into an axial design and combustion chamber by making it a ''straight through'' design as shown in Fig. 11. The leading particulars of this engine are shown in Table 1.

The HeS 8A comprised of a 14-blade axial flow inducer having airfoil type blades, which were made from aluminum alloy forgings. The inducer was followed by a 19-vane radial flow impeller of composite construction consisting of aluminum alloy blades retained in a steel hub and rear shrouding plate. Leaving the combustor, the working fluid passed through a 14-blade radial inflow turbine, also built up of steel blades retained in a steel hub. The compressor-turbine shaft was mounted on two bearings, one between the inducer and impeller and the second aft of the turbine.

The combustion chamber was a ''straight through'' annular design with compressor discharge passing through two sets of diffuser vanes prior to entering the combustor. The vaporizing fuel

[17]Luckily this was a small bird and did not pose a problem.

[18]This aircraft used a ducted fan jet system but utilized a reciprocating compressor and consequently was not a true turbojet.

Downloaded 02 Jun 2010 to 171.66.16.119. Redistribution subject to ASME license or copyright; see http://www.asme.org/terms/Terms_Use.cfm

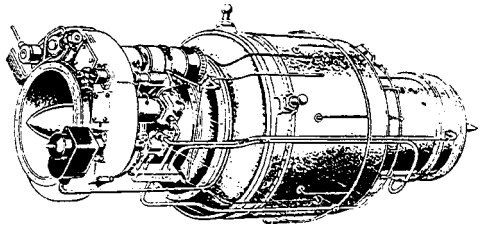

Fig. 11 The HeS 8 engine

Table 1 Leading particulars of the HeS 8 turbojet

PARAMETER	HES8 ENGINE
RPM	13,500
Weight	837 lbs, (380 kg)
Frontal Area	5.05 sq. f; (0.47 m2)
Specific Thrust.	1.89Lb thrust/Lbs; (18.5 N/kg)
Specific fuel consumption	1.6 Lbs/Lbs thrust hour;(0.163 kg/Nh)

system injected fuel into the chamber through 16 sets of eight nozzles giving a total of 128 nozzles. Each nozzle was a tube approximately 1/16th inch in diameter. Initially, no attempts were made to provide any secondary air distribution but later models had such provisions.

The propelling nozzle was of fixed area and a tailpipe was used on the He 280 installation. The exact number of engines of this type actually built is not known but several versions were built.

Even though the HeS 8A was a good engine, its power was marginal for the He 280, and it lost out to the Jumo 004, which had been chosen for the production of the Me 262 jet fighter. While the performance in terms of thrust and fuel consumption and length was superior,[19] the HeS 8A engine also had a problem relating to the radial inflow turbine which represented a technology leap for the time and the overall need for strategic materials was higher than for the axial cooled blading of the Jumo 004. Consequently, thrust growth by means of increasing turbine inlet temperature was limited for the HeS 8A without the use of strategic materials such as nickel. The radial inflow turbine blades also suffered from fatigue failures and blade-to-hub attachment problems.

8 The Worlds First Jet Fighter the He 280

The He 280 was a graceful twin engined fighter designed by Robert Lusser.[20] It was designed as an all metal mid-wing monoplane powered by two turbojets located in nacelles under the wings. The wing had a straight leading edge and then a dihedral outboard of the engines. The tail consisted of a high mounted tailplane carrying a fin and rudder on each tip. The latest variant had a V tail. Nose armament consisted of three 20 mm cannon. The aircraft had a wingspan of 12 m (40 ft) and a length of 10.04 m (34 ft).

The He 280 was itself a revolutionary design in that it had a tricycle undercarriage and a compressed air-operated ejection seat. By March 1941, the first experimental aircraft V1 had made 40 gliding flights and on March 30, 1941 it took off for the first time powered by von Ohains's HeS 8 Engines with Heinkel's test Pilot Fritz Schaffer at the controls. No engine cowlings were fitted for this flight due to fuel leakage which was noticed prior to the flight. On April 5, 1941, the aircraft was successfully demonstrated in front of RLM officials. The He 280 was also flown in test combat against a Focke Wolfe 190.

[19]The axial flow Jumo 004 was, however, superior to the HeS8A in thrust per unit projected frontal area.

[20]Heinkel had hired Robert Lusser away from Messerschmitt. Lusser had done preliminary design work on the ME 262.

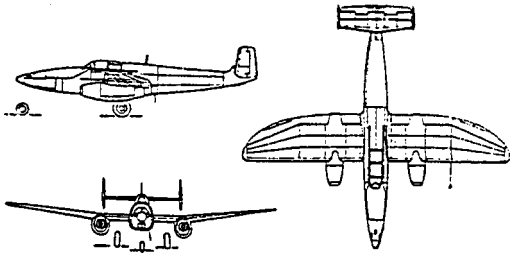

Fig. 12 The graceful twin engined He 280 jet fighter powered by von Ohain's HeS 8 engines

There is an interesting anecdote on the He 280 reported in Jones [5]. Just before a take-off, test pilot Bader, was handed a small hammer by Robert Lusser. Lusser, explained to Bader apologetically that there was as yet no means of jettisoning the cockpit canopy and that should he have to leave in an emergency, he would need the hammer to smash his way out. The He 280 is shown in Fig. 12.

9 Acquisition of Hirth Motoren and Formation of Heinkel Hirth

Working at Heinkel gave von Ohain complete technical freedom and the ability to choose his own path without constraints related to funding or test facilities or interference by the RLM. Further, he had the direct and enthusiastic support of the owner of the company. This was an excellent environment for innovation for the early engines but as the needs turned to production, the disadvantages of working for an airframe company began to show. There was a lack of expertise in the area of engine design in the areas of materials, blading vibrations, aeromechanics, manufacturing techniques. Heinkel wished to buy an engine manufacturer to enhance his position as an engine company and to derive the required technical manpower.

After the demonstration flight of the He 280 Heinkel finally received permission to purchase Hirth–Motoren[21] which was a reputable manufacturer of reciprocating aero engines and turbochargers located at Zuffenhausen near Stuttgart. This acquisition was fraught with politics, with Heinkel's rival Messerschmitt reportedly delaying the acquisition for several months.[22] With the acquisition of Hirth, Heinkel had access to the engineering capabilities and manufacturing know-how of this small but well known engine company.

The formal name of the company formed when Heinkel took over Hirth Motoren was Ernst Heinkel AG-Werk Hirth Motoren and was called Heinkel–Hirth for short. It is interesting to note that when asked during a conference in 1978 what single item von Ohain would have asked for during his early development days, he stated that the greatest need was for expertise in the area of blade vibrations which he said he got from the Hirth Company in the form of Dr. Bentele[23] [13].

After the acquisition of Hirth, Heinkel started moving his jet engine team to Zuffenhausen. Mueller and his HeS 30 axial flow engine being the first to arrive in the Fall of 1941. Shortly thereafter in 1942, von Ohain and his propulsion team also relocated to the Heinkel–Hirth facilities. Von Ohain immediately struck up an excellent working relationship with the Hirth engineers and the combined team worked closely in engine development. Von Ohain's brilliance, modesty and fairness immediately caused a

[21]Hirth–Motoren GmbH was owned by Hellmuth Hirth and was founded in 1931. Hirth himself died in 1938.

[22]Heinkel's friend Udet in the Luftwaffe had by now realized that the Luftwaffe could not maintain parity with allied air development and a radical technological innovation was called for. Udet committed suicide in 1941.

[23]Dr. Max Bentele was at the time, a leading expert in Germany specializing in aeromechanics and blade vibration. In the Fall of 1943, he had resolved a complex blade failure problem on the Junkers Jumo 004 engine.

Downloaded 02 Jun 2010 to 171.66.16.119. Redistribution subject to ASME license or copyright; see http://www.asme.org/terms/Terms_Use.cfm

bond to develop between the Hirth engineers. Mueller on the other hand, was not receptive to help for his problematic HeS 30 axial flow machine [14]. The HeS 8 engine was in the stage where itwas being developed for manufacture and Hirth engineers contributed towards this task. In July 1942, the HeS 8A was running well, but by this time the Me 262 and its Junkers 004 engines had been chosen to be the first production jet for the Luftwaffe. Ultimately, the HeS 8 program, the HeS 30 program, and the He 280 fighter aircraft were officially cancelled in early 1943. Shelp of the RLM decided that von Ohain's team at Heinkel–Hirth should start work on a second-generation turbojet the HeS 011. At this juncture, Heinkel, who in the early years of the war had a preeminent position in turbojet engine and jet aircraft technology, had now lost his dominant position.[24]

10 Design and Development of the Heinkel–Hirth HeS 011 Engine

In 1942 the RLM granted Heinkel-Hirth the contract for a second-generation engine known as the HeS 011 (RLM designation 109-011) which provided a quantum step in specific power and performance. The specifications of this engine were as follows [13]: Max thrust 12.75 kN (2863 lbs) with a growth to 14.7 kN (3307 lbs) weight under 900 kg (1985 lbs) pressure ratio 4.2:1, altitude capability 15 km (50,000 ft) specific fuel consumption less than 1.4 lb/lb-hr. Dr. von Ohain was in charge of the development and Dr. Max Bentele was responsible for component development and managed the development on the compressor and turbine sections of the engine.

As reported by Bentele [14], in December 1944 the best performance parameters attained for the engine were a thrust of 13 kN (2940 lbs) at a rotor speed of 10,205 rpm. The leading particulars of the first generation Jumo 004B engine which was in production and this advanced engine developed at Heinkel–Hirth are compared in Table 2. A photograph of the engine is shown in Fig. 13 [14] and the layout depicted in Fig. 14 [15].

10.1 Compressor Section. The concept and aerodynamic design of the compressor was by Dr. von Ohain. The compressor had a single stage inducer row followed by a diagonal compressor[25] (mixed flow) stage and then three symmetric (50 percent reaction) axial flow compressor stages. As the air exited the first axial inducer stage, the annular passage was reduced by a shaft fairing to the diagonal compressor. The combination of a diagonal stage with axial flow stages was ingenious as it made the operating line very flat and imparted growth potential without incorporating variable geometry which would be required for higher pressure ratios.

The double-skinned intake hoods served the dual function of straightening the airflow and housing the accessories, oil tank, and lube oil pump. Both warm air and electric heating were available for anti-icing. A photograph of the compressor section is shown in Fig. 15 which shows the mixed flow stage.

To develop this compressor, a 1600 kW electric test stand in Zuffenhausen and a steam turbine driven 15,000 hp stand in Dresden were utilized. The rigs allowed the measurement of flow, pressure and temperature distributions in the flow path and considerable challenges had to be met in designing the mixed flow compressor section. Rather than arriving at an optimal configuration for the axial stages analytically, this was done experimentally using adjustable stators. A variety of settings were tested on the stand and finally this led to satisfactory performance as shown in the compressor map of Fig. 16 [14]. Bentele recounts that during one test, in spite of smooth running of the engine, the occurrence of discrepancies in pressure and temperature readings puzzled the test team. The issue was resolved when a technician appeared with some broken aluminum blades which he had found at the compressor air exit and inquired if this might be the problem! Evidently, the uniform breakage of the blades did not result in significant unbalance.

Table 2 Comparison between the Junkers Jumo 004B and the Heinkel Hirth HeS 011 engines

Parameter	Jumo 004 B	HeS-011A
Manufacturer	Junkers Engine	Heinkel-Hirth
Thrust, Lbs	2000; (8.927 kN)	2863 , (12.75 kN)
Weight, Lbs	1650; (750 kg)	1950; (885 kg)
T/W Ratio	1.21	1.44
Length	152" (3860 mm)	131.6" (3343 mm)
Frontal dia.	30"; (760 mm)	32";(805 mm)
Air mass flow rate, lb/sec	46.7; (21.2 kg/sec)	64; (29 kg/sec)
Pressure Ratio	3.1:1	4.2:1
RPM	8700	10,205
Compressor configuration	8 stage axial flow	Diagonal stage +3 axial stages
Turbine Configuration	1 stage turbine	2 stage air cooled
Fuel Consumption Lb/Lb thrust	1.4-1.48	1.35
Turbine inlet temperature, F	1427F;(775C)	1427 F (775C)

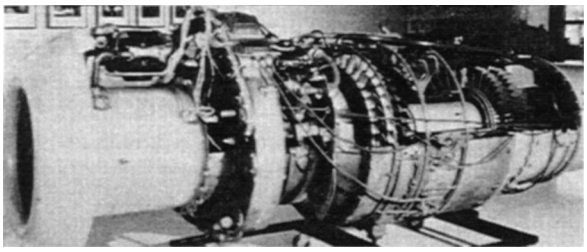

Fig. 13 The Heinkel Hirth HeS 011 engine

10.2 Combustor. The combustor was an annular design with airflow being divided into two flow streams by an annular headpiece with a small airflow being routed into the head piece for mixture preparation and combustion. Most of the air was routed through two of the outer and inner rows of vented at the end of the combustion chamber and into the missing chamber to attain the required temperature. The housing wall located around the combustor was protected against radiant heat transfer by an annular insulator around which was circulated fresh air from the chamber. Sixteen equispaced fuel nozzles were utilized with four igniter plugs, two on the lateral axis and two 45 deg upwards. Bentele indicated that the combustor was a great design challenge and obtaining a satisfactory radial and circumferential temperature profile was not easy given the flow profile emanating from the mixed flow compressor wheel. The combustor was, therefore, a design compromise, but one that worked.

10.3 Turbine Section. The HeS 011 had a really remarkable two stage air-cooled turbine section (Fig. 17) designed by Dr. Max Bentele. Two rows of hollow turbine nozzle blades were cooled by air bled off through the annulus after the final compressor stage. This nozzle cooling air was ducted between the combustion chamber and the rotor shaft, which was shielded by an annular insert. The two-stage axial turbine was cooled by compressor bleed air. Both of the discs had hollow vanes with air being routed to the second stage through holes bored in the first stage. The airflow exited the blades at the tip.

The development of the turbine section was most challenging. Initially solid blades were employed and stress rupture occurred at

[24]Unlike Udet, Milch was not as supportive of Heinkel and was disappointed in Heinkel's problems relating to the He 177 long range bomber. This aircraft was a disaster because of absurd requirements imposed on it by the RLM. Further, political lobbies in Berlin resented Heinkels freewheeling style.

[25]This was called ''kombination sverdichter.''

Downloaded 02 Jun 2010 to 171.66.16.119. Redistribution subject to ASME license or copyright; see http://www.asme.org/terms/Terms_Use.cfm

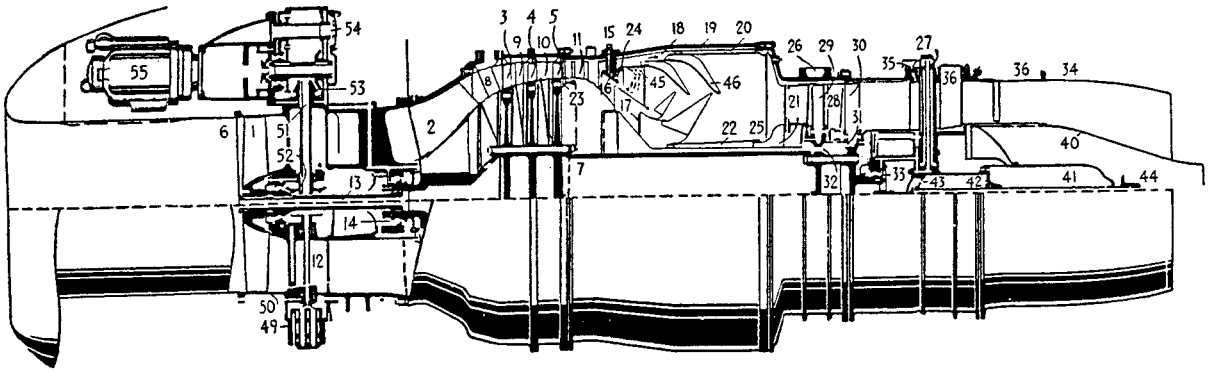

(1) Front axial rotor; (2) diagonal rotor; (3, 4, 5) third, fourth, fifth rotors; (6) air-intake hood; (7) main shaft; (8, 9, 10) guide grids; (11) triple grid; (12) pump drive shaft; (13) floating rod; (14) front main bearing; (15) connection for fuel pipe; (16) arrow-shaped ring (nozzle ring); (17, 18) air flows between compressor and turbine; (19) housing wall; (20) circular chamber; (21) guide grip in front of turbine wheel; (22) circular chamber; (23) annular cool-air gap; (24) injection nozzles; (25) cool-air passage to guide grids; (26) fastening flange; (27) connection for lubricant pipe; (28) guide grids between turbine rotors; (29, 30) turbine rotors; (31) cool-air holes; (32) cool-air holes; (33) rear main bearing; (34) thrust-nozzle housing; (35) cool-air connection; (36) ventilation tube; (37) pressure-measurement place; (38) (not shown—not identified); (40) thrust-nozzle sleeve; (41) piston rod; (42) pressure cylinder; (43) piston; (44) piston-rod bearing; (45) mixers; (46) scoops; (47, 48) (not shown—not identified); (49) lubricant pump set; (50) front compressor housing; (51) vertical shaft; (52, 53) bevel gears; (54) drive connection for turbine's extension shaft; (55) starter

Fig. 14 Layout of the advanced HeS 011 engine [15]

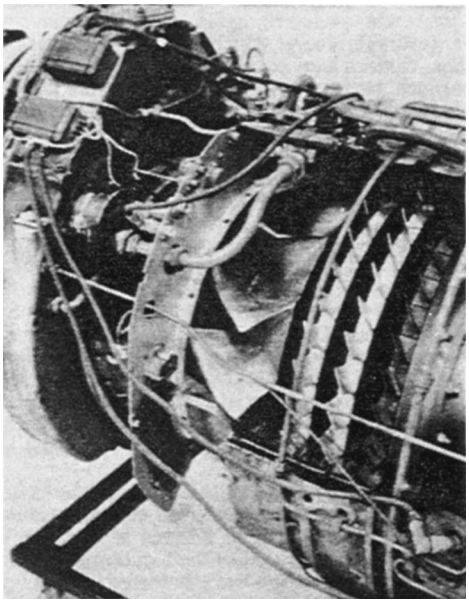

Fig. 15 Compressor section of the HeS 011 [14]

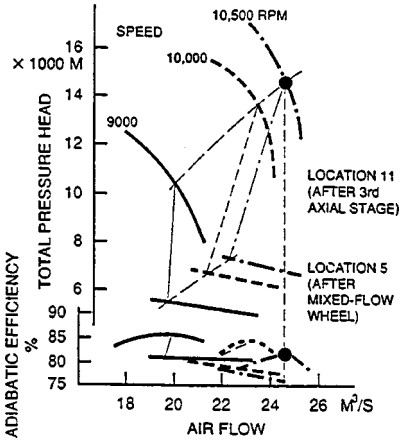

Fig. 16 HeS 011 Compressor map [14]

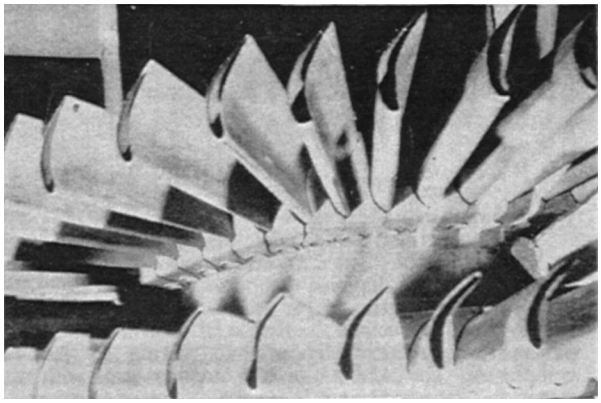

Fig. 17 Details of the HeS 011 2 stage air cooled turbine section [14]

the first stage and fatigue failures at the second stage. The resonance failure was traced to the location of four struts of the rear bearing support and these were eliminated by spacing the struts at unequal angles thus minimizing the forced excitations which were in resonance with the second-stage rotor blades. Some of the strut arrangements analyzed are shown in Fig. 18. A Bentele Diagram[26] of the blading is depicted in Fig. 19 [16].

The final air-cooled blade designed by Dr. Bentele did not utilize any strategic materials and were called ''topfschaufel.'' These blades were manufactured starting with a circular plate of austenetic chrome-moly sheet steel from which a closed end tube was drawn in several stages with intermediate heat treatments. As seen in Fig. 20 [17], wall thickness diminished from 2 mm (0.079 in) at the root to 0.45 mm (0.017 in) at the blade tip, so as to match the stresses with the prevailing radial temperature profile. The airfoil shape was then induced and finish machining done. Both the first and second turbine stages utilized this construction and contained an insert for the proper distribution of the cooling air and for damping blade vibration.

10.4 Mechanical Features and Accessories

10.4.1 Bearings and Accessories. There were two main bearings on the HeS 011. The front main ball bearing was located

[26]Bentele developed this diagram independent of knowledge of Campbell's work on steam turbine disk vibration in the US.

Downloaded 02 Jun 2010 to 171.66.16.119. Redistribution subject to ASME license or copyright; see http://www.asme.org/terms/Terms_Use.cfm

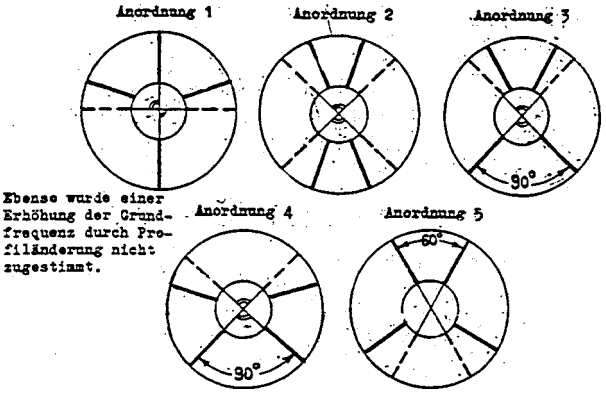

Fig. 18 Some rear bearing support strut arrangements evaluated in resolving blade vibration problem

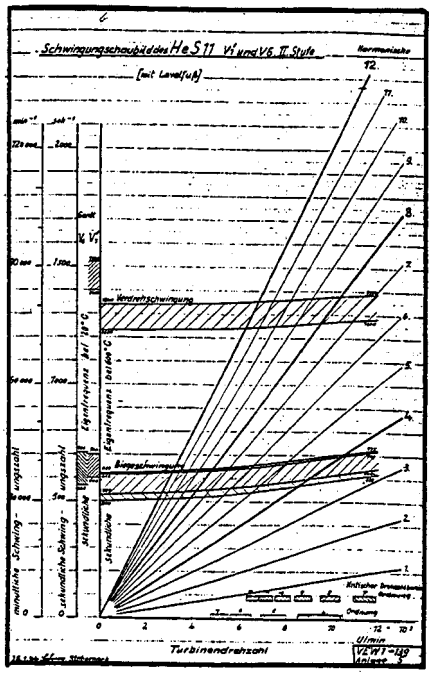

Fig. 19 Bentele diagram showing excitation and natural frequencies [16]

just ahead of the diagonal compressor and was both a radial and thrust bearing. A floating shaft extended from it to drive the front axial compressor and, via bevel gearing and vertical take off shafts, the accessories. Accessories located above the engine included the Riedel starter,[27] a Siemens or Bosch generator, a Barmag fuel pump, Knorr air compressor and tachometer. The rear bearing located aft of the two-stage turbine was cooled as well as lubricated by pressurized oil.

10.4.2 Fuel System. The fuel system was controlled by the throttle, which operated a constant speed governor to control fuel and thus engine speed. Fuel was routed to a low-pressure fuel pump which was a double gear pump with two independent suctions. The delivery of this pump was fed to the Barmag high-pressure fuel pump, which delivered about 51.6 1/min (13.7 gpm) at a pressure of 40 kg/cm^2 (570 psi). A pressure control valve diverted excess flow back to the suction side of the low-pressure pump. The high-pressure fuel was then fed to the governor and

[27]This was similar to the starter used in the Junkers Jumo 004 and BMW 003 engines.

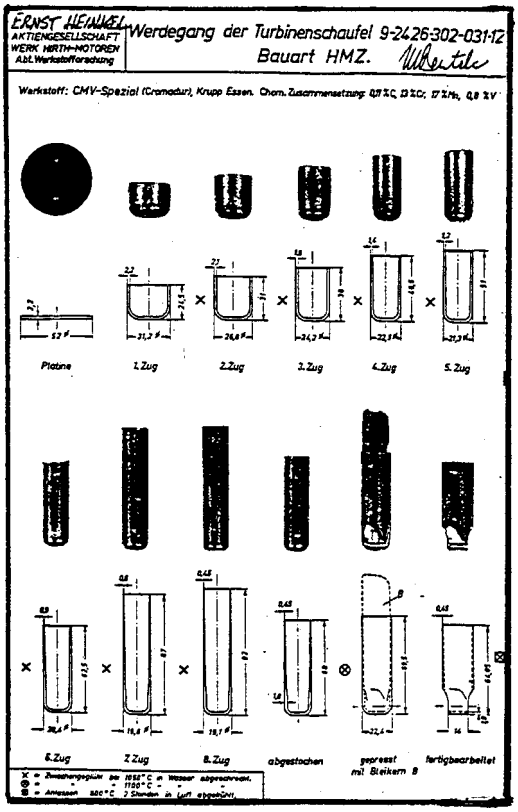

Fig. 20 Ingenious method of developing air cooled turbine blade starting with a circular plate 25 mm diam

through two annular pipes to the 16 fuel injectors in the combustor. A pressure valve on the delivery pipes ensured that the appropriate pressure to sustain operation would be admitted to the combustor.

10.4.3 Lubrication System. Lube oil tanks with a capacity of 12 liters (3.18 gal) were located on the lower part of the accessory support on both sides of the pumpset which consisted of a delivery and 2 scavenge units. An additional return (scavenge) pump was located behind the rear bearing. The oil flow rate was 35 L/min (9.24 gpm) at an operating pressure of (3.5–4 kg/cm^2 (50–57 psi). Oil was gravity fed from the tanks to the delivery pump, which routed it through a filter and collector. Both the two main bearings and the accessory bearings were lubricated by the pressurized collector through two distributor pipes. The gearing and bearings of the front axial compressor were centrifugally lubricated while the bevel gears were spray lubricated.

10.4.4 Tail Cone Bullet. The HeS 011 had an adjustable tail cone bullet moved by a piston within the cone.[28] In the original configuration, the bullet was linked to the throttle control to control the piston feed and drain pressure oil pipe. This was later changed to an electrically controllable crossfeed valve connected so that when switched off, it moved to the operating or extended position and when switched on, brought the bullet to the retracted position for startup.

11 Hans Von Ohain, Co-Inventor of the Turbojet

Dr. Hans Joachim Pabst von Ohain was born on December 14, 1911 in Dessau Germany. He received his Doctorate in Physics and Applied Mechanics in 1935 at the University of Göttingen and remained at the University for a year while he developed a theory of jet engines and built a demonstration model. In April 1936, he joined the Heinkel company in Rostock moving to the

[28]Similar to the BMW 003 engine.

Downloaded 02 Jun 2010 to 171.66.16.119. Redistribution subject to ASME license or copyright; see http://www.asme.org/terms/Terms_Use.cfm

Heinkel-Hirth company in Stuttgart in the Fall of 1942. He directed a research and development program that resulted in the HeS 3B engine that powered the Heinkel He 178 which made the world's first turbojet powered flight on August 27, 1939 at the Heinkel Airfield near Rostock. He also developed the HeS 8A, which powered the world's first twin jet fighter, the He280 that flew in April 1941. Thereafter, he was instrumental, along with Dr. Max Bentele, in the development of what would be the world's most powerful and sophisticated turbojet at the end of the Second World War, the HeS 011.

Being considered one of the most outstanding engineers in Germany in the field of turbojet engineering, Dr. von Ohain was invited to the US in 1947, where he became a research scientist at Wright-Patterson AFB. In 1963, he rose to the position of Chief Scientist in the Air Force Aerospace Research Laboratories, which conducted virtually all Air Force in-house basic research in the physical and engineering sciences. In 1975 he became Chief Scientist of the Aero Propulsion Laboratory, assuming responsibility for maintaining the technical quality of Air Force research and development in air-breathing propulsion, power and petrochemicals.

Dr. von Ohain's accomplishments in these positions won national and international recognition. He retired from government service in 1979 and became Research Professor in Aerothermodynamics at the University of Dayton Research Institute and also a Visiting Professor at the University of Florida. He was immensely popular with his students and always interested in helping young people with their education.

Dr. Hans von Ohain was a man of great humility and modesty. Throughout his life and in his many lectures and papers covering early turbojet history, he always made it a point to mention the contributions of others, at times understating his contributions.

During his 32 years of service in the United States, Dr. von Ohain published more than 30 technical papers and registered 19 U.S. patents. He had registered over 50 patents while working for Heinkel. Dr von Ohain was honored for his contributions to aviation with many awards which include the election to member of Deutsche Akademie der Luftfahrt Forschung, the coveted Goddard Award for the American Institute of Aeronautics and Astronautics (AIAA) and numerous Air Force awards. He received the ASME Tom Sawyer Award in June 1990 and was inducted into the National Hall of Fame for Aviation in 1990. Von Ohain and Sir Frank Whittle were awarded the Charles Draper Prize in 1992 for their monumental contributions to aviation. This coveted award is considered the ''Nobel Prize'' for technology. He was awarded three honorary Doctorates from the Universities of Dayton, West Virginia, and University of Florida. He was the recipient of several prestigious German Awards including the Prandtl Ring for his contributions to jet aviation. Dr. von Ohain passed away at the age of 86 in Melbourne, Florida and will forever be remembered as the co-inventor of the turbojet and developer of the world's first flight jet engine.

A photograph of Dr. von Ohain, Sir Frank Whittle, and Dr. Max Bentele [14] is shown in Fig. 21. This is the last known photograph of these jet pioneers together and was taken in 1978.

12 Closure

This paper has covered the pioneering work of Dr. Hans von Ohain, co-inventor of the turbojet and a man who changed the future of flight and brought us into the jet age. His seminal work at Heinkel provided the impetus for the jet engine programs in Germany. The paper has covered his historic engines including the HeS 3B world's first turbojet to fly, the HeS 8 which was to power the graceful He 280 fighter and the world's most advanced turbojet at the end of the Second World War, the HeS 011. Notwithstanding his subsequent contributions to jet engine technology through the 1980s, he will always be remembered and will go down in history as a pioneer who made possible the turbojet revolution.

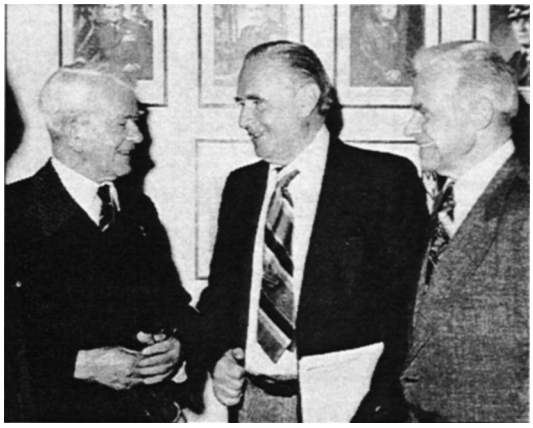

Fig. 21 Photograph of three jet engine pioneers taken in 1978. Left to right, Sir Frank Whittle, Dr. Hans von Ohain, and Dr. Max Bentele [14].

Acknowledgments

We are grateful to Dr. Max Bentele for his help and communications and for providing us his papers on the subject. His excellent autobiography ''Engine Revolutions'' covers several interesting details of the dawn of the jet age in which he played a major role and which has been a valuable reference. We acknowledge the help at the American Heritage Center in providing archival data from Dr. Bentele's archives and also the archival staff at the Smithsonian Institute's National Air and Space Museum. The excellent works of Bentele, Constant, Jones, and Gunston are recommended to those wishing to pursue this topic further.

References

[1] Constant, E. W., II, 1980, *The Origins of the Turbojet Revolution*, Johns Hopkins Univ. Press, Baltimore, MD.

[2] Schlaifer, R., 1950, *Development of Aircraft Engines*, Graduate School of Business Administration, Harvard University, Boston, MA.

[3] von Ohain, H., 1979, ''The Evolution and Future of Aeropropulsion Systems,'' *The Jet Age–40 Years of Jet Aviation*, Walter J. Boyne and Donald S. Lopez, eds., Smithsonian Institute, Washington, DC.

[4] Scott, P., 1995, ''Birth of the Jet Engine,'' Mechanical Engineering, January, ASME, New York, pp. 66–71.

[5] Jones, G., 1989, *The Birth of Jet Powered Flight*, Methuen, London.

[6] Meher-Homji, C. B., 1998, ''The Development of the Whittle Turbojet,'' ASME J. Eng. Gas Turbines Power, **120**, No. 2, ASME, New York.

[7] Heinkel, E., 1956, *Stormy Life–Memoirs of a Pioneer of the Air Age*, E. P. Dutton and Co., New York.

[8] Meher-Homji, C. B., 1997, ''The Development of the Junkers Jumo 004B-the World's First Production Turbojet,'' ASME J. Eng. Gas Turbines Power, **119**, No. 4, ASME, New York.

[9] von Ohain, H., 1989, talk made at the 50th Anniversary of Jet Powered Flight, video cassette, Vol. No. 1, AIAA, Dayton Chapter.

[10] Bamford, L. P., and Robinson, S. T., 1945, ''Turbine Engine Activity at Ernst Heinkel Atiengesellschaft Werk Hirth-Motoren, Stuttgart/Zuffenhausen,'' report by the Combined Intelligence Objectives Sub-Committee dated May 1945.

[11] Gunston, B., 1995, *The Development of Jet and Turbine Aero Engines*, Patrick Stephens, Ltd., UK.

[12] Carter, J. L., 1945, *Ernst Heinkel Jet Engines*, Aeronautical Engine Laborotory (AEL), Naval Air Experimental Station, Bureau of Aeronautics, US Navy, June, 1945.

[13] *An Encounter Between the Jet Engine Inventors Sir Frank Whittle and Dr. Hans von Ohain*, 1978, Wright-Patterson Air Force Base, OH, History Office, Aeronautical Systems Division, US Air Force Systems Command.

[14] Bentele, M., 1991, *Engine Revolutions: The Autobiography of Max Bentele*, Society of Automotive Engineers, Warrendale, PA.

[15] Neville, L. E., and Silsbee, N. F., 1948, *Jet Propulsion Progress*, McGraw Hill Inc, New York.

[16] Hirth Motoren G.m.b.H. Report, 1944, VEW 1-139, ''Schwingungsuntersuchungen an der He S 11-Turbine V1 aund V6 mit Vollschaufeln,'' dated Jan 31, 1944; Max Bentele Papers, American Heritage Center, University of Wyoming, Laramie, WY.

[17] Hirth Moteren G.m.b.H. Report, 1944, VEW 1-140, ''Untersuchung der Fussbefestigung von Topf-und Falt-schaufeln durch Kaltschleuderprufung,'' dated April 16, 1944; Max Bentele Papers, American Heritage Center, University of Wyoming, Laramie, WY.

Downloaded 02 Jun 2010 to 171.66.16.119. Redistribution subject to ASME license or copyright; see http://www.asme.org/terms/Terms_Use.cfm

Advances in Oxide-Oxide CMC

Robert A. Jurf
Steven C. Butner
Composite Optics, Inc.,
9617 Distribution Avenue,
San Diego, CA 92121

Recent advances in COI's oxide–oxide CMC materials will be presented including basic processing steps, updated material properties, and fabrication techniques. Material properties of COI's alumino-silicate system reinforced with various oxide fabrics will be compared, along with progress in developing a 1200°C oxide matrix system for future turbine system applications. Examples of fabricated hardware, including a subscale combustion liner, will be shown. Recent test and evaluation data will be provided.
[S0742-4795(00)01802-0]

Introduction

During the past three years, Composite Optics, Inc. (COI) has developed oxide–oxide ceramic matrix composites (CMCs) for advanced military aircraft, with potential applications in commercial gas turbine engine systems. Extreme temperature conditions are realized for very brief periods of time for missile applications (less than one hour) and up to 100 h for a military engine in afterburner conditions. These temperatures are relatively short compared to the 10,000's of hours of steady-state operation in commercial gas turbines and other industrial applications [1]. COI has explored the viability of using an oxide system in commercial energy applications by characterizing coupons in ways directed toward commercial requirements. The baseline alumino-silicate system has shown early promise in both basic properties, producibility, and environmental resistance. As COI proceeds with testing and evaluation of subscale rig components, a more refractory oxide system aimed at satisfying the higher temperatures and longer durations of the gas turbine engine community is being developed.

CMC Development Objectives and Approach

The original development goals were established for current and future military exhaust systems. In addition to meeting aircraft thermomechanical demands, CMC systems must have a simple robust process in order to be economically viable. Specific targets were identified at the onset of development:

1 tensile strength of 140 MPa at 1000°C with 1100°C excursions
2 mechanical property stability with temperature
3 low cost manufacturing process

COI's ceramic matrix composite baseline approach is a sol-gel derived alumino-silicate matrix that can be combined with a variety of commercially available fiber reinforcements such as Nextel 550, Nextel 610, and Nextel 720 [2]. The baseline oxide–oxide system relies on controlled matrix porosity for toughness, thereby eliminating the need for fiber coatings. Recent findings support the conclusion that high strength, damage tolerant oxide–oxide CMC's can be made without the use of fiber coatings [3–5].

Reinforcement Selection. The fibers used are all in fabric form and are selected based on the advantages that each type offers when laminated in COI's ceramic composite (Table 1). The maximum use temperature of COI's CMCs is largely determined by the fabric reinforcement system. Of the oxide fibers currently available in the commercial market, Nextel 720 has the best temperature capability and creep resistance.

Typical Properties of Nextel 720 CMC. Mechanical testing has been an ongoing part of the maturation process for this CMC system. Table 2 summarizes basic mechanical strength and modulus values compiled to date on the Nextel 720 alumino-silicate system [6]. All tests used typical ASTM standards for organic composites and/or ceramic matrix composites.

Creep and Fatigue Properties. Resistance to creep rupture and fatigue is an important material characteristic for both military and commercial gas turbine engines. Larry Zawada at the Air Force Research Laboratory (AFRL) Materials and Manufacturing Directorate, Wright-Patterson AFB, OH, has characterized COI's Nextel 720 alumino-silicate system at 1000°C and 1100°C [7]. Preliminary results summarized in Table 3 are very encouraging. The residual strengths after fatigue are equal or greater than the virgin untested material, suggesting that repeated loading may have a work-hardening toughening phenomenon. The creep rupture tests are just as encouraging, with residual strengths after 100 h at 150 MPa equal to 209 MPa. Tests are continuing, and data will be reported as it becomes available.

Environmental Resistance. Rob Kowalik at NAVAIR Materials Division at Patuxent River, Maryland completed preliminary hot corrosion studies in March 1998 of COI's Nextel 550 and 720 reinforced CMC [8]. The first test run on the materials was a 500 cycle oxidation resistance test to 900°C in air only; each cycle consisting of 55 min at 900°C and 5 min at room temperature. As expected, the CMC was extremely inert to the oxidation exposure; there was no weight change or visible change in the CMC samples.

The second test run on the material was a hot corrosion thermal exposure. When salt water is ingested into aircraft turbine engines and mixed with sulfur residue, corrosive salts are deposited on nozzle parts, greatly reducing their useful operating life. To model this behavior, Na_2SO_4 is deposited on the CMC coupon surfaces at 5 gm/cm^2. The 500 cycle thermal exposure to 900°C is repeated. In materials such as SiC/SiC, a thick film of sodium silicate forms on the surface which spalls off during continued thermal cycling [9]. After completing 500 cycles of cycling, no visible glass formation and no significant weight changes were reported. Initial analysis gave no indication of any sodium silicate layer formation. The surface topography and morphology looked unchanged. The results showed COI's CMC materials were well-behaved at 900°C and are very promising. Additional evaluation is being pursued by the Navy. National Aeronautics and Space Administration (NASA), and Oak Ridge National Laboratory (ORNL) at this time, and will be reported in future publications.

Effects of Long-Term Aging. Siemens-Westinghouse has carried out long-term aging studies on COI's Nextel 720 alumino-silicate system. Samples were exposed up to 1000 h at tempera-

Contributed by the International Gas Turbine Institute (IGTI) of THE AMERICAN SOCIETY OF MECHANICAL ENGINEERS for publication in the ASME JOURNAL OF ENGINEERING FOR GAS TURBINES AND POWER. Paper presented at the International Gas Turbine and Aeroengine Congress and Exhibition, Indianapolis, IN, June 7–10, 1999; ASME Paper 99-GT-190. Manuscript received by IGTI March 9, 1999; final revision received by the ASME Headquarters January 3, 2000. Associate Technical Editor: D. Wisler.

 Copyright © 2000 by ASME

Downloaded 02 Jun 2010 to 171.66.16.119. Redistribution subject to ASME license or copyright; see http://www.asme.org/terms/Terms_Use.cfm

Table 1 Features of different CMC fabric reinforcements

	Oxide CMC Properties with Various Oxide Fabrics				
	Astroquartz	Nextel 312	Nextel 550	Nextel 720	Nextel 610
Composite Density (gm/cc)	1.50	2.30	2.41	2.60	2.83
Nominal Fiber Volume (%)	50	48	38	48	51
RT Tensile Modulus (GPa)	22 (est)	31.0	40.0	76.5	124.1
RT Tensile Strength (MPa)	46 (est)	124.8	147.6	179.0	366.1
CTE (ppm/C)	0.40	4.85	5.40	6.30	7.92

Table 2 Typical properties of Nextel 720 reinforced alumino-silicate CMC system

	Temp	Strength (MPa)	Modulus (GPa)	Strain (%)
Tension (17)	RT	179	76.5	0.30
Tension (after 100 hours at 1000°C) (6)	RT	187	82.1	0.29
Tension (4)	1000°C	170	73.1	0.27
Tension (after 100 hours at 1000°C) (4)	1000°C	176	78.6	0.28
Flexure (48)	RT	216	97.9	0.22
Compression (12)	RT	186	80.0	0.22
In-Plane Shear (12)	RT	31	14	0.49
Interlaminar Shear Strength (45)	RT	11.5	-	-
(*) Quantities of test specimens				
Elevated Tensile Data[6]				

Table 3 Residual tensile strengths after fatigue and creep loadings in air

	Test Temperature	Stress Level	Loading Conditions	Residual Tensile Strength
Fatigue	1000°C	125 MPa	100,000 cycles	193 MPa
	1000	150	100,000	211
	1000	160	100,000	195
	1100	150	100,000	168
Creep Rupture	1000	150	100 hours	209

tures ranging from 1000°C to 1200°C (Fig. 1) in air [10]. The data indicates that the properties of the Nextel 720 composite are stable for very long-term exposures (1000 h) up to 1000°C, then degrade rapidly beginning at 1100°C. COI has carried out similar aging studies for durations up to 100 h and temperatures up to 1200°C. While the results were very similar to the Siemens-Westinghouse data at 1200°C, the results at 1100°C differed substantially. COI's results indicated less than a 10 percent degradation in strength after 100 h exposure to 1100°C. Siemens-Westinghouse found over a 40 percent degradation in strength under the same conditions. While the details of the results differ, the overall conclusions are the same.

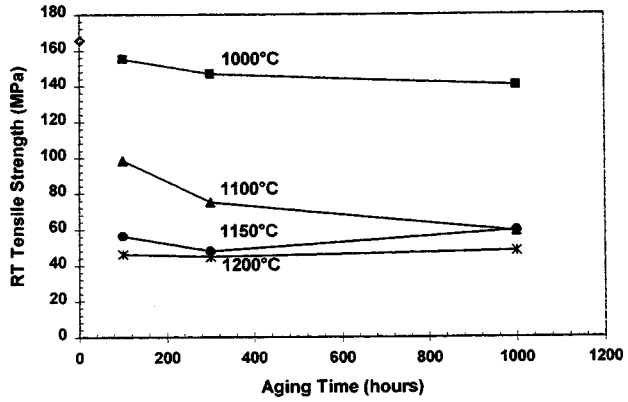

Fig. 1 Tensile strength retention after 1000 h of exposure up to 1200°C [10]

Along with the degradation in strength with temperature exposure beyond 1100°C, there is a transition from fibrous to brittle failure (Fig. 2). While the mechanism for the strength/microstructural degradation has not been fully characterized, COI currently believes that the primary loss in strength is a result of additional matrix densification rather than fiber degradation. As the matrix is further densified (through sintering) it shrinks, becomes stronger, and bonds more extensively to the reinforcement fibers thereby degrading the toughness mechanism.

The data strongly suggests that COI's alumino-silicate Nextel 720 system will not satisfy the 10,000 h 1200°C demands of next generation gas turbine engines. The ''Future Work'' section presents basic research COI has initiated on more refractory oxide systems that are aimed at commercial gas turbine engine applications.

Component Design and Manufacturing

COI's process for manufacturing oxide–oxide CMCs is simple and low cost. The fabrication process does not require repetitive reinfiltration or pyrolyzation steps. No thin fiber coatings or exterior oxidation protection coatings are required for COI's baseline

Downloaded 02 Jun 2010 to 171.66.16.119. Redistribution subject to ASME license or copyright; see http://www.asme.org/terms/Terms_Use.cfm

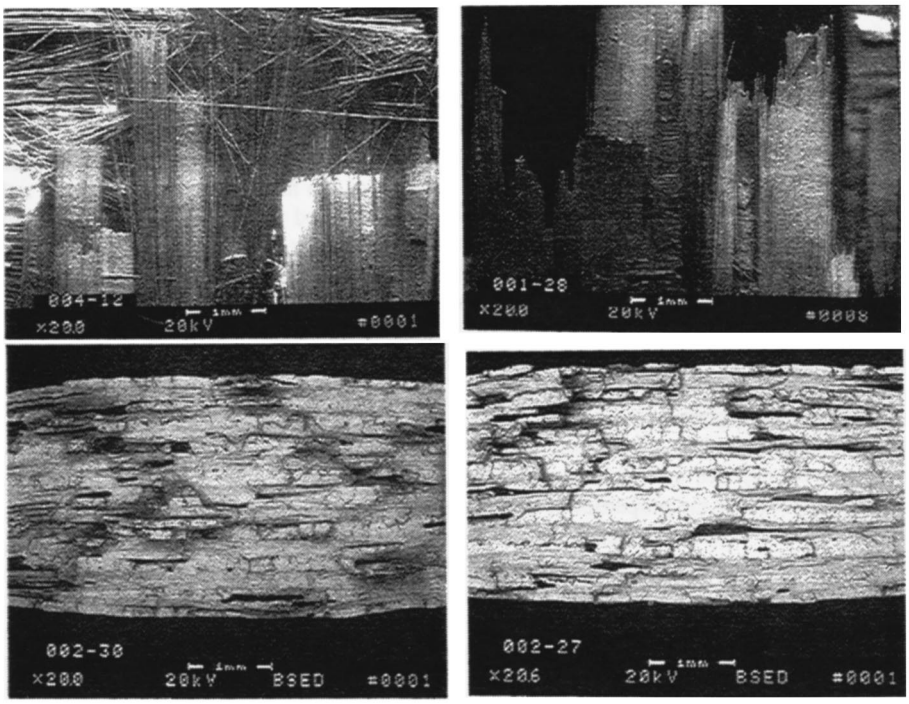

Fig. 2 Fracture surfaces as fabricated (top-left), and after 1000 h exposure to 1000°C (top right), 1100°C (bottom left), and 1200°C (bottom right) [10]

alumino-silicate process. This lowers the fabrication costs and eliminates coating compatibility and thermal stability problems. Even ''low cost'' CMCs can be prohibitively expensive due to tooling and complex stiffener arrangements. A conventional approach to fabricating a complex shaped component is shown in Fig. 3.

The matrix is a viscous slurry that is prepregged into the fabric and staged to a tacky consistency. Components are laid-up using organic composite techniques and cured (dried) using low pressures (<0.7 MPa) and temperatures (<150°C). Composite parts have sufficient strength at this point to be demolded. The final step required is a free standing pressureless sinter of about 1150°C to sinter the matrix to final density listed in Table 1.

We applied this process to a subscale liner to be tested by Solar Turbines in San Diego, CA. This liner test has been used by Solar to screen various CFCC's for suitability in gas turbine engines [1]. The liner COI produced was nominally 20 cm in diameter and 20 cm in length. The wall architecture was six plies, and about 1.65 mm thick. The manufacturing sequence is shown in the sequence of photos, Fig. 4.

With the tooling in-hand, the time required to prepare the material, lay-up and cure the composite, and trim the ends was six working days. In a production environment, this could be reduced even further, making this type of manufacturing process economically attractive.

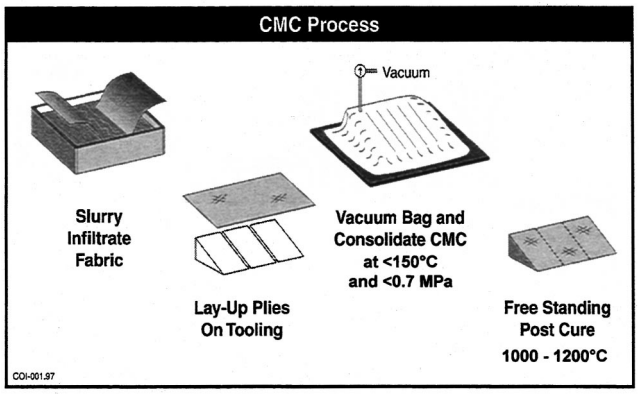

Fig. 3 COI's CMC fabrication process

Future Work

In May of 1998, COI was awarded a Phase I Small Business Innovative Research (SBIR) contract by AFRL to investigate the development of a low cost oxide matrix that is stable for long term exposures to 1200°C. The primary objective is to develop and demonstrate an oxide matrix composite using commercially available refractory fibers (Nextel 720) that will retain better than 90 percent of its original composite strength after 100 h of exposure to 1200°C. The mechanical property goals were to achieve a 175 MPa tensile strength, 200 MPa flexural strength, and a 12 MPa interlaminar shear strength in a zero degree warp aligned fabric layup. Several oxide matrices were investigated including an alumina and mullite based system. Preliminary Phase I results have shown promise in the approach. Some early laminate test results are in Table 4.

All of the laminates produced in the first iteration achieved better than 90 percent strength retention after 100 h exposure to 1200°C. In Table 4 the strength retention of COI's baseline Nextel 720 system is shown for comparison. The alumina based system has shown better initial structural performance while the mullite system showed better microstructural development. Both systems showed very good strength retention properties. Future work will focus on improving the strength and more extensively characterizing the temperature stability of the materials. A follow-on to the SBIR Phase I program has been awarded by AFRL. The Phase II effort will involve research activities at AFRL, Siemens-Westinghouse, Solar Turbines and ORNL.

Downloaded 02 Jun 2010 to 171.66.16.119. Redistribution subject to ASME license or copyright; see http://www.asme.org/terms/Terms_Use.cfm

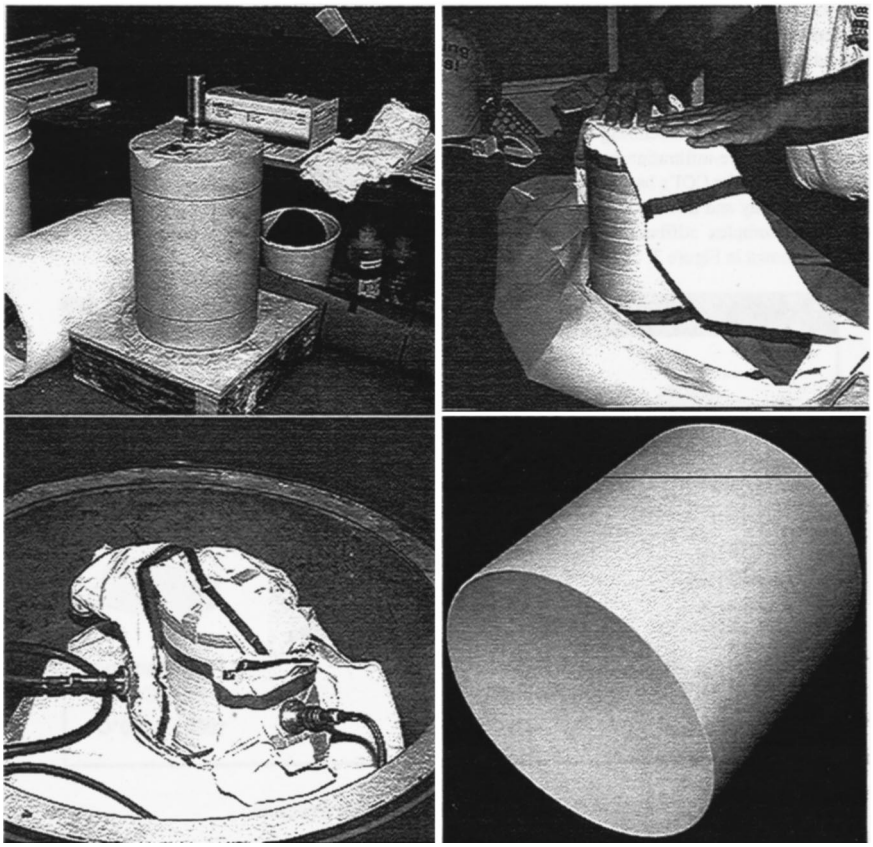

Fig. 4 The tooling (top-left), ply lay-up (top-right), bagging process (bottom left), and finished part (bottom right)

Table 4 Phase I SBIR results using Nextel 720 fabric

	Flexure Strength (MPa)		
Matrix Composition	As Cured	100 hours at 1200C	% Strength Retention
Baseline System	208.6	88.3	42%
Alumina	182.0	190.3	105%
Mullite	124.8	115.1	92%

Acknowledgments

We gratefully acknowledge the support of the Air Force Research Laboratory under SBIR Contract F33615-98-C-5210, and we wish to thank Larry Zawada of AFRL for performing fatigue and creep rupture tests and for providing these data. We also acknowledge Jay Lane and Eric Carelli, Siemens Westinghouse Power Corporation in Pittsburgh, PA for the long-term aging and photomicrographs. Lastly, we acknowledge Solar Turbines for funding to manufacture the subscale liner.

References

[1] Simpson, J., et al., 1997, ''Testing of Monolithic Ceramics and Fiber Reinforced Ceramic Composites for Gas Turbine Combustors,'' Ceram. Eng. Sci. Proc., **18**, No. 4, pp. 1–3.
[2] 3M Ceramic Fiber Technical Data Brochure, 1998, published by 3M Ceramic Fiber Products, 3M, St. Paul, MN.
[3] Tu, W. C., et al., 1996, ''Concept for a Damage-Tolerant Ceramic Composite with ''Strong'' Interfaces,'' J. Am. Ceram. Soc., **79**, No. 2, pp. 417–24.
[4] Cazzato, A., et al., 1997, ''Monazite Interface Coatings in Polymer and Sol-Gel Derived Ceramic Matrix Composites,'' presented at the 21st Annual Cocoa Beach Conference.
[5] Levi, C., 1997, ''Damage Tolerant All-Oxide CMC's Without Fiber Coatings,'' presented at the 21st Annual Cocoa Beach Conference.
[6] French, J., personal communication, Boeing, St. Louis, MO.
[7] Zawada, L., personal communication, AFRL, Dayton, OH.
[8] Kowalik, R., personal communication, NAVAIR, Patuxent River, MD.
[9] Wang, S. W., et al., 1994, ''High Temperature Behavior of Salt Coated Nicalon Fiber Reinforced Calcium Alumino-Silicate Composite,'' Ceram. Eng. Sci. Proc., **15**, No. 4, pp. 465–474.
[10] Lane, J., and Carelli, E., personal communication, Siemens Westinghouse, Pittsburgh, PA.

Downloaded 02 Jun 2010 to 171.66.16.119. Redistribution subject to ASME license or copyright; see http://www.asme.org/terms/Terms_Use.cfm

David A. Woodford
Materials Performance analysis (MPa), Inc.,
1707 Garden Street,
Santa Barbara, CA 93101

Andrew A. Wereszczak
High Temperature Materials Laboratory,
Oak Ridge National Laboratory,
Oak Ridge, TN 37831-6069

Wate T. Bakker
Electric Power Research Institute,
3412 Hillview Avenue,
Palo Alto, CA 94303-1395

Stress Relaxation Testing as a Basis for Creep Analysis and Design of Silicon Nitride

A new approach to tensile creep testing and analysis based on stress relaxation is described for sintered silicon nitride. Creep rate data covering up to five orders of magnitude were generated in tests lasting less than one day. Tests from various initial stresses at temperatures from 1250°C to 1350°C were analyzed and compared with creep rates measured during conventional constant load testing. It was shown that at least 40 percent of the creep strain accumulated under all test conditions was recoverable, and that the deformation could properly be described as viscoelastic/plastic. Tests were conducted to establish the level of repeatability and the effects of various thermomechanical histories. It was shown that none of the prior exposures led to significant impairment in creep strength. The results were used for three different grades to establish the value of the accelerated test to compare creep strengths for acceptance and for optimization. Several useful correlations were obtained between stress and creep rate. The systematic creep rate dependence as a function of loading strain prior to relaxation provided a possible basis for design in terms of a secant modulus analysis. [S0742-4795(00)02302-4]

Introduction

Ceramics offer a number of potential advantages for high temperature components in gas turbines. Their low density, high stiffness, low thermal conductivity and, in most cases, higher creep strength at temperatures in excess of 1000°C, make them good candidates for a number of components. The greatest payoff is for those components which require the use of turbine air cooling, such as first stage turbine blades and shrouds. Other components which could substantially benefit from the replacement of superalloys are the combustor, transition piece and first stage turbine nozzle. Tensile creep testing of ceramics can be difficult and expensive because of the need to use sophisticated specimen gripping, precision extensometry and stable temperature control at very high temperatures. However, a number of laboratories, worldwide, are now developing the capabilities, and beginning to report the results, of careful and accurate tensile creep tests on engineering ceramics [1–3]. This requires a major commitment in time and expense to generate the extensive data using traditional creep testing of the many specimens necessary to provide a basis for both statistical analysis and extrapolation to the required design life. Consequently, in recent years such studies have often been part of major collaborative programs [4].

An alternative approach to generating creep data, which is far more efficient in terms of numbers of test specimens and test duration, involves the generation of stress versus creep rate responses derived from stress relaxation tests (SRT). This methodology was strongly promoted several years ago by Hart [5] as a basis for his plastic equation of state, and has been developed and applied subsequently to a wide variety of metallic materials [6–8]. Very recently, it has been applied as part of a new framework for materials development, design and remaining life assessment of operating components [9]. This use of a high precision short time stress relaxation test has also been successfully applied to creep analysis for engineering polymers [10].

Some preliminary work on stress relaxation testing of alumina and silicon nitride has been reported [11,12]. This was sufficiently promising to justify a more detailed study of a ceramic from a design perspective using this methodology. Two of the most promising monolithic silicon nitride materials have been evaluated for stage one turbine stator shroud components for large utility gas turbines with turbine inlet temperatures in the range of 1250–1300°C [4]. SN-88, supplied by NGK Insulators, Ltd., was extensively tested and evaluated, and the results compared with those generated in conventional creep tests [13]. The second material, AS-800, was supplied by AlliedSignal Ceramic Components, and results on an earlier vintage of this material have also been reported [14].

The AS800 has now been improved significantly compared with previous vintages. The present work is a more comprehensive study of new (1997) AS800. In addition to generating basic data at temperatures between 1200°C and 1350°C and comparing with the previous results, tests were conducted to examine repeatability and the effects of prior thermomechanical exposures.

Experimental Procedure

Tests were performed at Oak Ridge National Laboratory on an Instron electromechanical series 1380 test system fitted with self-aligning grips, a 1500°C short furnace, and contacting capacitive extensometry. Specimens, designed for use with the grips, were 165 mm long, and featured a reduced section of 40 mm and diameter of 6 mm. Temperature calibration along a 25.4 mm gage length was maintained and controlled to 1°C at temperatures to 1350°C. With the closed-loop strain control the set strain was held to $\pm 15\times 10^{-6}$.

Standard procedure involved loading at a rate of 10 MPa/sec to a prescribed stress and switching to strain control on the specimen and monitoring the relaxation of stress. The stress versus time response fitted to a fourth order polynomial was converted to a stress versus creep strain-rate response by differentiating and dividing by the modulus measured on loading according to the following:

$$e_e + e_i = e_t = \text{constant}$$

$$\frac{de_i}{dt} = \frac{-de_e}{dt} = \frac{-1}{E} \cdot \frac{ds}{dt},$$

Contributed by the International Gas Turbine Institute (IGTI) of THE AMERICAN SOCIETY OF MECHANICAL ENGINEERS for publication in the ASME JOURNAL OF ENGINEERING FOR GAS TURBINES AND POWER. Paper presented at the International Gas Turbine and Aeroengine Congress and Exhibition, Indianapolis, IN, June 7–10, 1999; ASME Paper 99-GT-291. Manuscript received by IGTI March 9, 1999; final revision received by the ASME Headquarters January 3, 2000. Associate Technical Editor: D. Wisler.

 Copyright © 2000 by ASME

Downloaded 02 Jun 2010 to 171.66.16.119. Redistribution subject to ASME license or copyright; see http://www.asme.org/terms/Terms_Use.cfm

where

e_e = elastic strain
e_i = inelastic creep strain
e_t = total strain
s = stress
E = elastic modulus

This is, in effect, a self-programmed variable stress creep test. Typically, a test lasting less than one day may cover up to five decades in creep rate. The accumulated inelastic strain was usually less than 0.1 percent, so that several relaxation runs at different stresses could be made on a single specimen with minimal change in the mechanical state. Thus, an enormous amount of creep data was generated in a short time on a single specimen. Separate specimens were used for different temperatures of 1200°C, 1250°C, 1300°C, and 1350°C.

The test sequence involved relaxation runs from progressively increasing set stresses. Each run was unloaded after approximately twenty hours and the residual strain was monitored for at least two hours to measure any anelastic creep recovery.

Basic tensile and creep data on AS800 were obtained from AlliedSignal Ceramic Components. These data were used to set stresses for the SRT tests. All tensile testing had been done at the University of Dayton, at a stressing rate of 150 MPa/sec. Round bar creep testing was also done at the University of Dayton and flat specimen testing was done at NIST. These data were used for comparison and were not separately identified since there appeared to be no systematic effect of specimen geometry.

The test matrix is described next.

1 1200°C, one-day tests at stress levels of 300 MPa, 350 MPa, and 400 MPa
2 1250°C, one-day tests at stress levels of 250 MPa, 300 MPa, and 350 MPa
3 1300°C, one-day tests at stress levels of 200 MPa, 250 MPa, and 300 MPa
4 1350°C, one-day tests at stress levels of 150 MPa, 200 MPa, and 250 MPa
5 1200°C, 3 one-day tests from 300 MPa for repeatability
6 1350°C, 3 one-day tests from 200 MPa for repeatability
7 Testing in sequence 1200°C at 350 MPa and 1350°C at 200 MPa
8 Testing in sequence 1350°C at 200 MPa and 1200°C at 350 MPa
9 Preexpose 20 h at 1250°C then test at 1200°C at 300 MPa and 350 MPa.
10 Preexpose 20 h at 1300°C then test at 1200°C at 300 MPa and 350 MPa
11 Preexpose 20 h at 1350°C then test at 1200°C at 300 MPa and 350 MPa
12 1300°C, run test for three days at 300 MPa

The objectives were as follows:

- tests 1 to 4 were analyzed for basic design and comparison with creep data
- tests 5 and 6 were to determine repeatability
- tests 7 and 8 examined the effect of temperature sequence
- tests 9 to 11 examined the effect of preexposure on creep strength
- tests 12 was a longer test run

Results

Examples of the tensile curves at 1200°C and 1350°C are shown in Figs. 1 and 2. In addition to the relaxation at a fixed strain these figures also show the anelastic recovery which occurs on unloading. During the two hour hold at near zero stress up to 50 percent of the accumulated creep strain recovered. During relaxation the strain was held within a band of approximately 3 $\times 10^{-5}$, i.e., ± 15 microstrain. For a modulus of about 300,000 MPa this would lead to a stress uncertainty of ± 4.5 MPa. An example of the stress versus Ln time curves at 1200°C which reflect these stress variations is shown in Fig. 3.

Examples of the derived log stress versus creep rate curves at 1200°C and 1350°C are shown in Figs. 4 and 5. These typically cover nearly four decades in rate and show systematic dependence on the initial stress. Figure 6 compares the derived data for three successive tests from 300 MPa and 1200°C with that from the first run in a separate specimen. Repeatability between the separate specimens 5-1 and 1-1 is good. However, subsequent repeat tests on the same specimen (5-2 and 5-3) indicate an appreciable effect of prior history; the subsequent runs indicate lower creep rates of

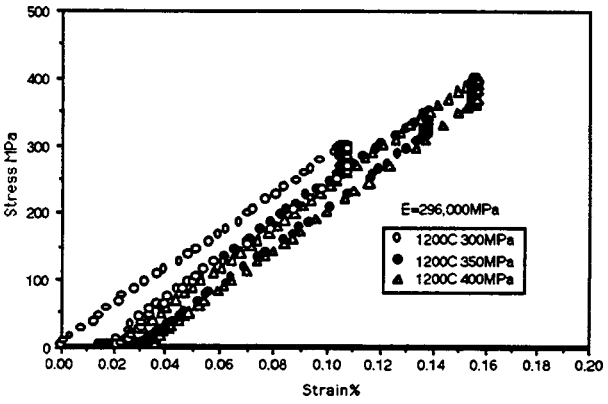

Fig. 1 Stress-strain for specimen #1 1200°C

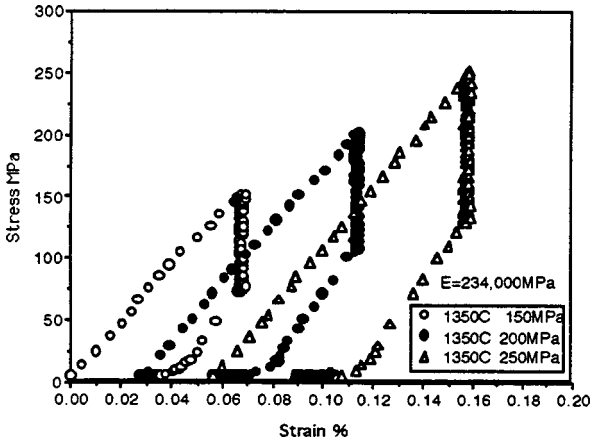

Fig. 2 Stress-strain for specimen #4 at 1350°C

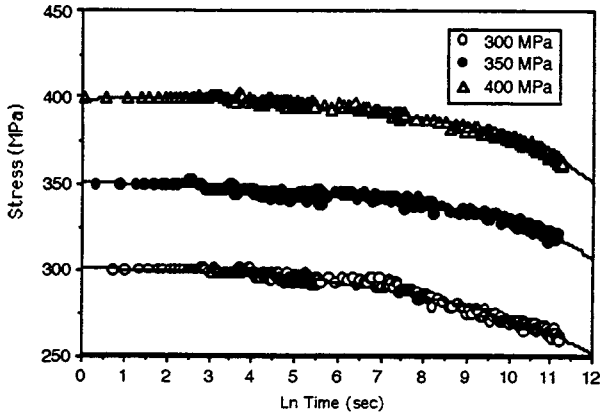

Fig. 3 Stress relaxation in specimen #1 at 1200°C

Downloaded 02 Jun 2010 to 171.66.16.119. Redistribution subject to ASME license or copyright; see http://www.asme.org/terms/Terms_Use.cfm

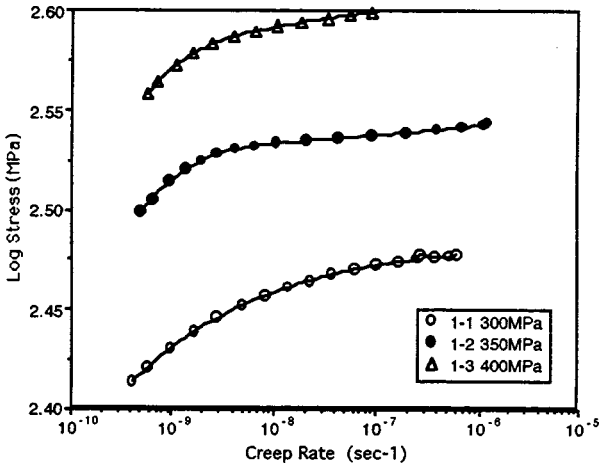

Fig. 4 Stress versus creep rate at 1200°C for specimen #1

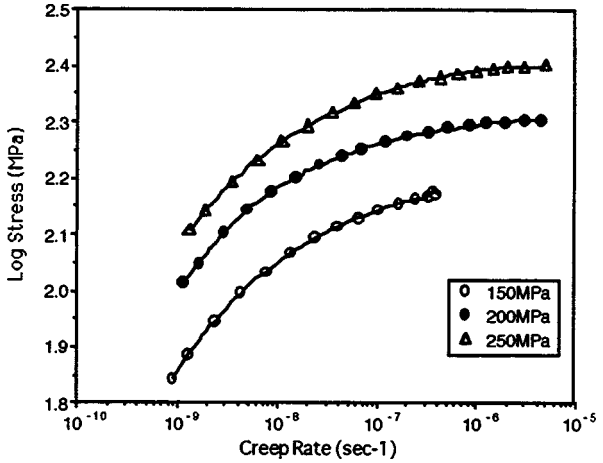

Fig. 5 Stress versus creep rate at 1350°C for specimen #4

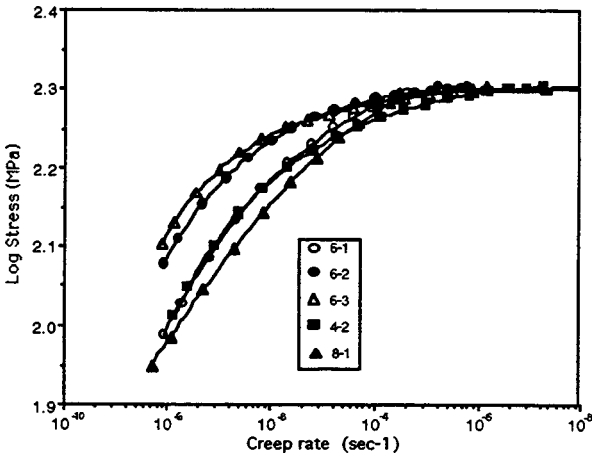

Fig. 7 Specimens 6, 4, and 8 relaxed from 200 MPa and 1350°C

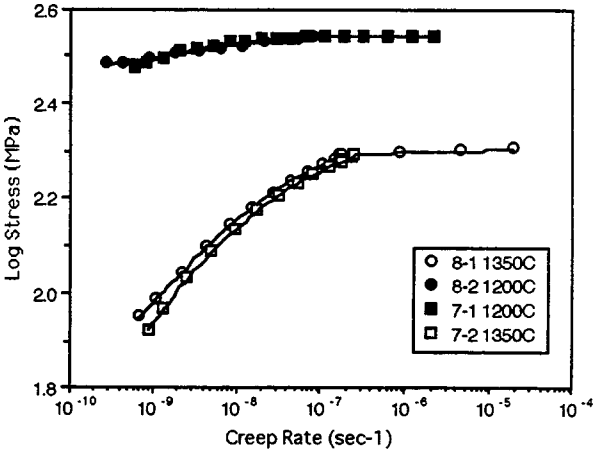

Fig. 8 Effect of test sequence in specimens 7 and 8

nearly a factor of ten. A similar effect is shown in Fig. 7 for tests from 200 MPa and 1350°C. Tests 6-1, 4-2, and 8-1 on separate specimens are quite repeatable, whereas 6-2 and 6-3 indicate a substantial reduction in creep rate. In this sequence 4-2 is the second run in a sequence but is from a higher stress than 4-1 and apparently is not influenced by the first run in that case.

Figure 8 indicates there is no effect of test sequence for relaxation from 1200°C and 350 MPa and 1350°C and 200 MPa. This result appears to indicate that for large changes of stress and temperature prior history effects are wiped out. For thermal exposure alone, however, a small systematic strengthening effect was observed with increasing temperature of prior exposure for testing at 1200°C and 300 MPa (Fig. 9). This systematic behavior was not observed for the tests from 1350°C and may be within the level of

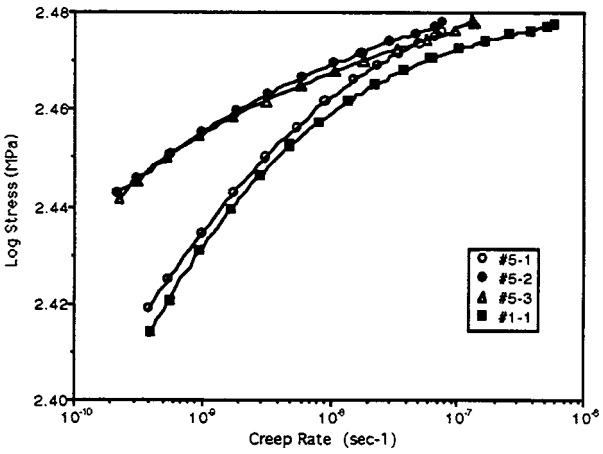

Fig. 6 Specimens 5 and 1 relaxed from 300 MPa and 1200°C

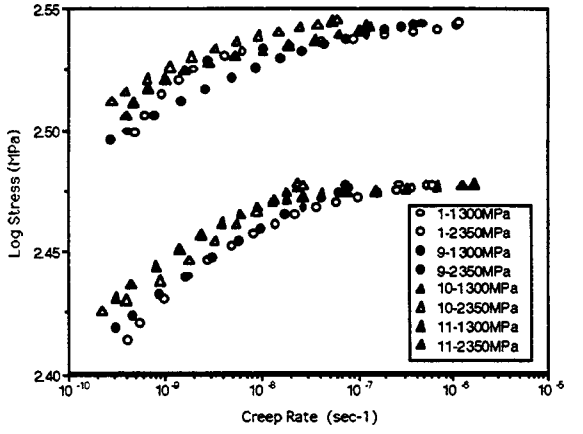

Fig. 9 Effect of thermal exposure on relaxation from 300 MPa and 350 MPa in specimens 1, 9, 10, and 11

Downloaded 02 Jun 2010 to 171.66.16.119. Redistribution subject to ASME license or copyright; see http://www.asme.org/terms/Terms_Use.cfm

repeatability. In no case in any series of these experiments was there evidence that prior thermomechanical exposure could lead to a reduced creep strength.

Discussion

Five areas are covered in this discussion: comparison with previous SRT results, comparison with Allied Signal creep data, viscoelastic/plastic behavior, effect of prior thermal/mechanical history, and creep design for silicon nitride.

Comparison With Other SRT Data. Comparisons were made at three test temperatures with previously generated data for silicon nitride on the GE/EPRI Ceramics for Gas Turbines Program. Examples at 1200°C and 1300°C are shown in Figs. 10 and 11. The filled circles are the new data. In these figures AS800 is an earlier vintage of the Allied Signal material and SN88 is from NGK insulators. The current AS800 was clearly superior in creep strength to both of the other tested materials at all three temperatures. At the lowest stresses the creep rates were more than an order of magnitude lower than those for the other materials.

Comparison With Allied Signal Creep Data. Creep data were generated both on NIST dogbone specimens and ORNL buttonhead specimens. The data were supplied by John Pollinger of Allied Signal and the creep rates were used in comparison with the SRT data. No distinction was made between the two specimen types in the comparison. The Allied Signal minimum creep rate data at 1300°C are compared with two SRT tests from 300 MPa in Fig. 12. Test #12 was a three day test and extended almost to $10^{-10}\,s^{-1}$. The creep data split the trends for the two SRT tests and gave a stress exponent of 6.25. Test 3-3 has lower creep rates after prior SRT tests at 200 MPa and 250 MPa than does test 12. This result is consistent with the results shown in Figs. 6 and 7 in that prior SRT runs lead to increased creep resistance. Less extensive data at 1250°C and 1350°C gave stress exponents of 6.5 and 7.8, respectively.

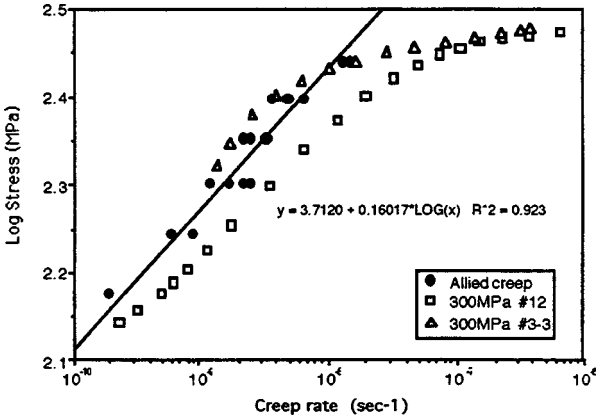

Fig. 12 Comparison with creep data at 1300°C

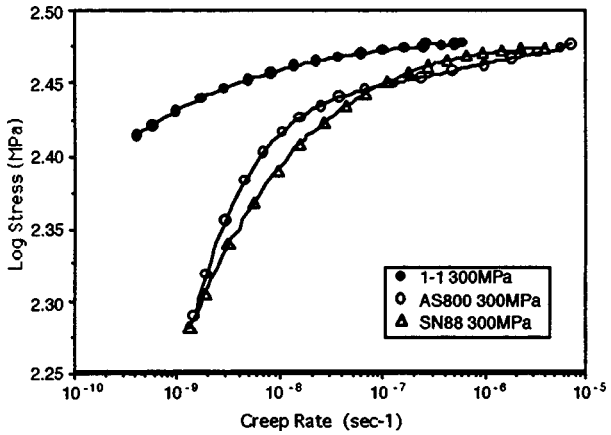

Fig. 10 Comparison data at 1200°C from 300 MPa

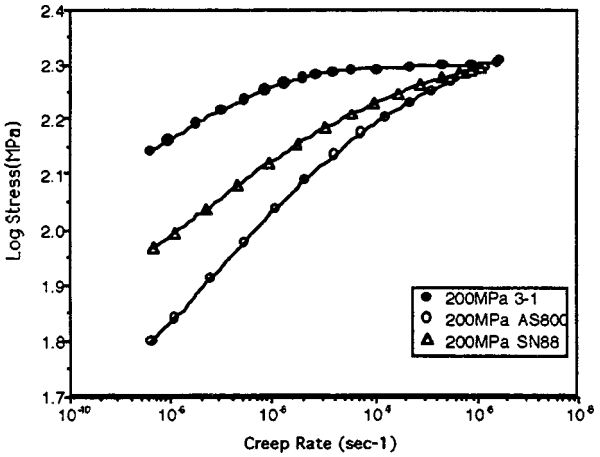

Fig. 11 Comparison data at 1300°C from 200 MPa

Viscous Elastic/Plastic Deformation. After unloading at the end of the test the strain was monitored for two hours in each run to estimate the anelastic recovery rate. Between one third and two thirds of the accumulated inelastic strains were recovered during this period. The fraction recovered did not clearly depend on test temperature. However, there was some indication that a higher fraction recovered in later tests of a series at increasing stress or constant stress. These observations demonstrate that an appreciable, and perhaps a major portion of the creep strain, is recoverable. It was found that the creep recovery could be empirically fit to a time to the one third law quite well. This is illustrated in Fig. 13 for specimen #12 at 1300°C.

In previous studies on similar material the first significant stress relaxation and subsequent creep recovery was observed at 800°C and progressively increased to 1300°C [14,13]. It appears that linear elastic behavior may be assumed up to about 800°C and that viscoelastic/plastic behavior becomes increasingly important at higher temperatures.

For conventional creep testing the anelastic component would affect the magnitude of the transient strain depending on the loading rate as well as the temperature and stress. In addition, if much of the creep strain is recoverable, then its magnitude is expected to be history dependent. Even in metals, the relative contribution of

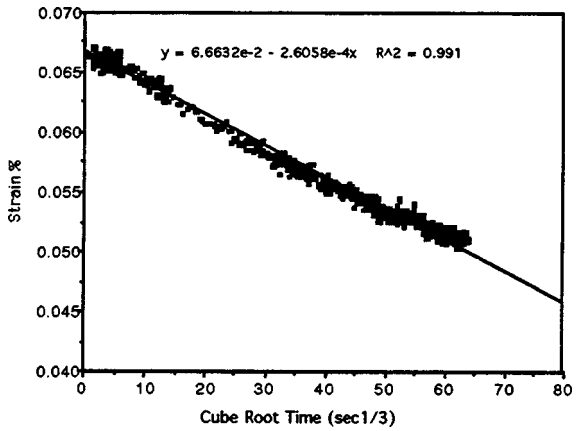

Fig. 13 Anelastic contraction at 1300°C

Downloaded 02 Jun 2010 to 171.66.16.119. Redistribution subject to ASME license or copyright; see http://www.asme.org/terms/Terms_Use.cfm

anelastic strain to total creep strain increases as the stress decreases and may become significant under equipment operating conditions. Therefore, unless a concerted effort is made to separate the components of creep strain, the conventional creep analysis could not provide a useful basis for analysis of non-steady test conditions.

For viscoelastic flow, all or part of the inelastic creep strain is recoverable. Whereas plastic shortening never occurs, anelastic strain may lead to an extension on loading and a shortening or contraction on unloading. Clearly, the extent of creep recovery is going to depend on the stress, temperature and previous deformation history.

The fact that repeat runs at the same stresses (#5 at 1200°C and #6 at 1350°C in Figs. 6 and 7) creep much more slowly than the first run may be because of continued anelastic contraction stemming from the previous test in each case. Since full recovery was not allowed after the first run, some anelastic contraction is expected during the second run. This in turn would lead to the lower than expected creep rates.

Whereas the importance of creep recovery is well recognized in polymer design, it is usually ignored in metal design. On the basis of the current experiments, it appears that the phenomenon may be very important for ceramics design, at least for the silicon nitride studied in this program.

Effect of Prior Thermal/Mechanical History. The first run tests in Figs. 6 and 7 (e.g., #5-1 and #1-1, and #6-1 and #8-1) indicate good repeatability in separate specimens. However, subsequent tests on the same specimen at the same stress for both 1200°C and 1350°C show a reduced creep rate (e.g., #5-2,3 and #6-2,3). As indicated above this most likely stems from the complexity of anelastic deformation. However, for large changes in test conditions there is no effect of test sequence history. This is clearly shown in Fig. 8 for tests between 1200°C and 1350°C. The fact that testing at 1200°C has no significant effect on the response at 1350°C may be easier to accept than the reverse sequence, but the results are clear. Figure 9 shows, especially for the first run from 300 MPa, that unstressed thermal exposure may lead to reduced creep rates at 1200°C. It is interesting to note that in no case did prior thermal or thermal/mechanical treatment lead to a significant reduction in creep strength. Figure 12 shows another example where the third run in a test sequence, #3-3, has a higher creep strength than the first run from the same stress, #12.

Creep Design for Silicon Nitride. Creep testing and analysis of ceramics have tended to follow methods and procedures developed for metallic materials. Thus parametric correlations of minimum creep rates and rupture times are normally used as bases for comparison and optimization. These have required the use of expensive and time consuming tests. Moreover, because of the major contribution of anelastic strain to creep deformation the methodology may not be appropriate. The phenomenology and the mechanism of deformation in polymers are recognized to be quite different from those in metals. The dominant role of viscoelasticity in polymers, with complete recovery of strain after unloading possible in many situations, has led to different design approaches [15]. Based on the current and previous tests [14,13] it is believed to be more appropriate to draw from these approaches rather than the traditional approaches to metallic alloy mechanical design. Thus, the ceramic is viewed as a viscoelastic/plastic material.

Polymer components are often designed using a Pseudo Elastic Method. The classical equations for the design of springs, beams, plates, cylinders etc. have all been derived under the assumptions that:

1 the strains are small
2 the modulus is constant
3 the strains are independent of loading rate or history and are immediately reversible
4 the material is isotropic
5 the material behaves the same way in tension and compression

In the Pseudo Elastic Method appropriate time-dependent values of properties such as modulus are selected and substituted into the classical equations. It is common to generate stress-strain curves as a function of rate (or time) either directly or indirectly. The latter may be done by crossplotting using constant time sections through conventional creep curves. These produce isochronous curves. Alternatively, pseudo stress-strain curves as a function of strain rate or stress rate may be generated from stress relaxation tests in polymers [10] or ceramics [14]. The appropriate time-dependent modulus is then the stress divided by the strain for a particular strain. This is referred to as the secant modulus.

In the previous studies [14,13] it was shown that stress relaxation was insignificant up to about 800°C and that a linear elastic design analysis based on a tangent (Young's) modulus was appropriate. At higher temperatures it is proposed that an elastic analysis using a time dependent secant modulus may be most appropriate.

To generate the secant modulus curves it was first necessary to plot pseudo stress strain curves. These could be done either as a function of inelastic (creep) strain rate or stress rate. The latter was chosen since it is much easier, if necessary, to run actual tests under stress rate control. Also, since the initial loading was under stress rate control this allowed an additional high rate point to be included. The procedure involved curve fitting of derived stress versus stress rate curves. These were then used to generate pseudo stress-strain curves as a function of stress rate as shown in the example at 1350°C in Fig. 14. The secant modulus values for each

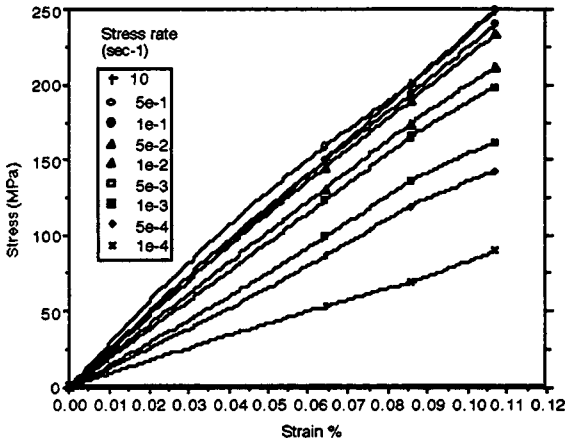

Fig. 14 Pseudo stress strain curves for specimen #4 at 1350°C

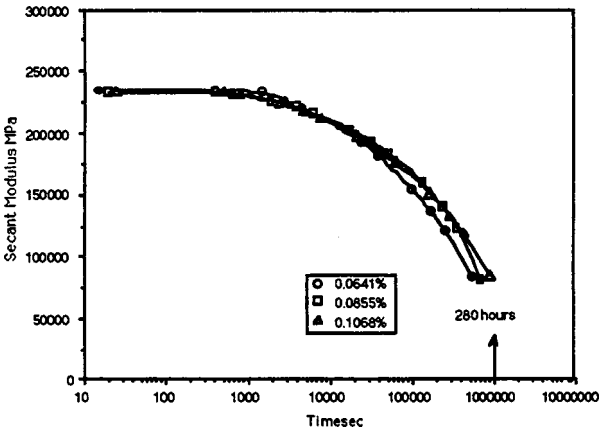

Fig. 15 Secant modulus for #4 at 1350°C

Downloaded 02 Jun 2010 to 171.66.16.119. Redistribution subject to ASME license or copyright; see http://www.asme.org/terms/Terms_Use.cfm

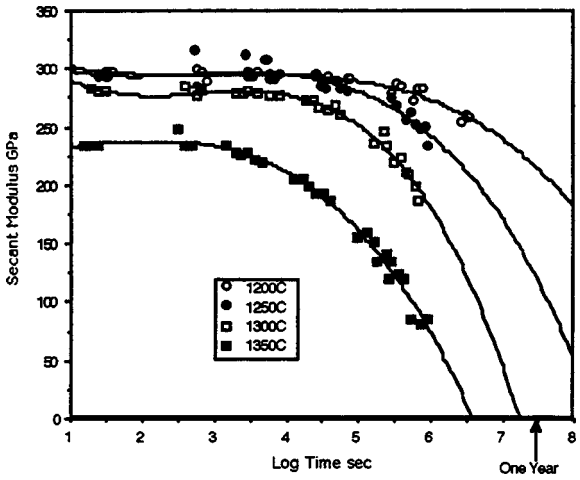

Fig. 16 Secant modulus curves for all temperatures

of the three tests at each temperature were then plotted against pseudo time (stress divided by stress rate). It was found that there appeared to be no clear effect of strain (see Fig. 15 at 1350°C). Accordingly, all the results of secant moduli could be plotted on unique temperature dependent but strain independent curves versus log time. The resulting plot is shown in Fig. 16.

Time-dependent design in this approach would simply use pseudo elastic analysis with the appropriate modulus being selected from Fig. 16. For example, the value at one year indicates that the allowable tensile loading at 1250°C for a strain of 0.1 percent would be 115 MPa (i.e., 115 GPa$\times$0.001).

Conclusions

1 Stress relaxation tests with a strain control to $\pm 1.5\times 10^{-5}$ were successfully conducted to produce stress versus creep rate curves covering between three and four decades in rate.

2 After unloading, all tests showed between 40 percent and 60 percent recovery of the inelastic strain in two hours, demonstrating the importance of viscoelasticity in the overall deformation.

3 Prior SRT testing, depending on the particular test sequence, either had no effect or resulted in increased creep strength (reduced creep rate).

4 Prior thermal exposure also resulted in increased creep strength.

5 None of the prior exposures led to a reduction in creep strength. This offers a new perspective on remaining life assessment of components.

6 An SRT test conducted at 1300°C for three days clearly showed a sigmoidal shape.

7 Comparison with previous data on silicon nitride indicated that the present material is the strongest tested so far.

8 Long time creep data on similar pedigree material showed comparable creep rates.

9 Creep recovery at a fixed stress obeyed a time to the one third law quite well.

10 Pseudo stress strain curves were constructed as a function of stress rate. These were used to measure secant modulus values which were found to be essentially independent of strain for a fixed time.

11 It was proposed that a master plot of secant modulus versus log time could be used in a pseudo elastic design framework for silicon nitride at temperatures above about 800°C.

Acknowledgment

This work is part of a project entitled ''Creep Strength and Fracture Resistance Evaluation of High Temperature Materials'' supported by EPRI under contract #8512-10.

References

[1] Carroll, D. F., Wiederhorn, S. M., and Roberts, D. E., 1989, ''Technique for Tensile Creep Testing of Ceramics,'' J. Am. Ceram. Soc., **72**, No. 9, pp. 1610–1614.
[2] Dyson, B. F., Lohr, R. D., and Norrell, R., eds., 1989, *Mechanical Testing of Engineering Ceramics at High Temperatures*, Elsevier Applied Science, London and New York.
[3] Ferber, M. K., Jenkins, M. G., and Nolan, T. A., 1994, ''Comparison of the Creep and Creep Rupture Performance of Two HIPed Silicon Nitride Ceramics,'' J. Am. Ceram. Soc., **77**, pp. 657–665.
[4] Hecht, N. L., Orenstein, R. M., Rajiyah, H., Tressler, R. E., Wiederhorn, S. S., and Woodford, D. A., 1997, ''Ceramics for Gas Turbines Program,'' EPRI WO3979-01.
[5] Hart, E. W., 1970, ''Constitutive Relations for the Nonelastic Deformation of Metals,'' J. Eng. Mater. Technol., **93**, pp. 599–607.
[6] Hart, E. W., and Solomon, H. D., 1973, ''Load Relaxation Studies of Polycrystalline High Purity Aluminum,'' Acta Metall., **21**, pp. 295–307.
[7] Li, C. Y., 1981, *Metallurgical Treatises*, J. K. Tien and G. F. Elliot, eds., TMS-AIME, pp. 469–485.
[8] Woodford, D. A., 1975, ''Measurement of the Mechanical State of A Low Alloy Steel at Elevated Temperatures,'' Metall. Trans. A, **6**, p. 1693–1697.
[9] Woodford, D. A., 1993, ''Test Methods for Accelerated Development, Design, and Life Assessment of High-Temperature Materials,'' Mater. Des., **14**, No. 4, pp. 231–242.
[10] Grwzwinski, G. G., and Woodford, D. A., 1995, ''Creep Analysis of Thermoplastics Using Stress Relaxation Data,'' Polym. Eng. Sci., **35**, No. (24), pp. 1931–1937.
[11] Woodford, D. A., VanSteele, D. R., and Hyder, M. J., 1991, ''Stress Relaxation of Alumina at High Temperature,'' J. Am. Ceram. Soc., **74**, No. 12, pp. 3142–3144.
[12] Wereszczak, A. A., Ferber, M. F., Kirkland, T. P., and Lara-Curzio, E., 1995, ''Stress Relaxation of Silicon Nitride at Elevated Temperature,'' Ceram. Eng. Sci. Proc., **16**, pp. 1–10.
[13] Woodford, D. A., 1998, ''Stress Relaxation, Creep Recovery, and Newtonian Viscous Flow in Silicon Nitride,'' J. Am. Ceram. Soc., **81**, No. 9, pp. 2327–2332.
[14] Woodford, D. A., 1996, ''Creep Design Analysis of Silicon Nitride Using Stress Relaxation Data,'' Mater. Des., **17**, No. 7, pp. 127–132.
[15] Crawford, R. J., 1987, *Plastics Engineering*, Pergamon Press, New York.

Downloaded 02 Jun 2010 to 171.66.16.119. Redistribution subject to ASME license or copyright; see http://www.asme.org/terms/Terms_Use.cfm

Exposure of Ceramics and Ceramic Matrix Composites in Simulated and Actual Combustor Environments

Karren L. More
Peter F. Tortorelli
Mattison K. Ferber
Larry R. Walker
James R. Keiser
Oak Ridge National Laboratory,
Oak Ridge, TN 37831-6064

Narendernath Miriyala
William D. Brentnall
Jeffrey R. Price
Solar Turbines Incorporated,
San Diego, CA

A high-temperature, high-pressure, tube furnace has been used to evaluate the long term stability of different monolithic ceramic and ceramic matrix composite materials in a simulated combustor environment. All of the tests have been run at 150 psia, 1204°C, and 15 percent steam in incremental 500 h runs. The major advantage of this system is the high sample throughput; >20 samples can be exposed in each tube at the same time under similar exposure conditions. Microstructural evaluations of the samples were conducted after each 500 h exposure to characterize the extent of surface damage, to calculate surface recession rates, and to determine degradation mechanisms for the different materials. The validity of this exposure rig for simulating real combustor environments was established by comparing materials exposed in the test rig and combustor liner materials exposed for similar times in an actual gas turbine combustor under commercial operating conditions. [S0742-4795(00)02402-9]

Introduction

Continuous fiber-reinforced ceramic matrix composites (CFCCs) are being developed to replace several metal components in industrial stationary gas turbines. One such application that has received a significant amount of attention in the past few years is the uncooled CFCC combustor liner. The use of CFCC materials for this component can result in significantly decreased CO and NO_x emissions even at increased combustor wall temperatures; i.e., ~1200°C or higher [1].

In May 1997, Solar Turbines began field tests of its Centaur 50S natural gas engine fitted with first stage monolithic ceramic blades and CFCC combustor liners at Atlantic Richfield Company (ARCO) Western Energy, Bakersfield, CA [2,3]. This test was a major milestone for Solars' Ceramics for Stationary Gas Turbines (CSGT) Program under the sponsorship of the U.S. Department of Energy (DOE). It was also one of the first application-specific tests under DOE's CFCC Program.

Full acceptance of ceramic materials for this particular application, however, is still a daunting task. There is a lack of long-term exposure/testing data for many of the commercially-available and proprietary CFCC materials, especially in corrosive environments similar to those encountered in an actual turbine combustor. It is desirable to use a laboratory test to screen the viability of the different CFCC compositions; using actual CFCC combustor liners (even sub-scale) in real engine tests to generate data is an exceptionally expensive undertaking. Prior knowledge of a CFCC's stability is extremely important before placing that material in a field test. Burner rig studies have been conducted on different SiC materials [4,5] however, these tests are somewhat limited in that only a few samples can be exposed simultaneously and typical runs are only 100 h. Long term data is then extrapolated from the 100 h results. No burner rig data are currently published for SiC-based composites. Since the operating lifetime goal for the CFCC combustor liners will ultimately be >30,000 h, a complete understanding of the microstructural stability for the many CFCC materials after long exposures in these environments is critical for their future placement in this application and other hot-section components.

The major goals of this program were twofold: (1) to provide a means for exposing large numbers of different CFCC materials to a simulated combustor environment for long periods of time (initially up to at least 3000 h) and (2) to determine the primary degradation/recession mechanisms for individual CFCC compositions as a function of time at the maximum temperature the CFCC liners experience during engine tests. This is being accomplished using a high-temperature, high-pressure, tube furnace which was originally constructed to conduct corrosion/leak tests on ceramic materials for a steam reformer application [6]. This furnace permits simultaneous exposure of many specimens at temperatures up to 1550°C and pressures as high as 500 psia. As described below, the Oak Ridge National Laboratory (ORNL) rig has been used to successfully duplicate the materials degradation/recession observed for a 1000 h field test of a CFCC combustor liner run in a Solar Turbines Centaur 50S engine at ARCO Western Energy (referred to as the ARCO test). Microstructural analyses of the CFCC liners removed from the ARCO test as well as samples from the first exposure tests (verification runs) in the ORNL rig will be described here.

Experimental Procedure

The ORNL rig consisted primarily of a furnace and gas supply system [6]. The furnace, capable of operating at temperatures up to 1550°C, accommodated six vertically loaded, 8.9 cm diameter tubes, two of which were dedicated to this study. The 1.2 m long tubes, used to hold the samples and contain the pressurized test atmosphere, were composed of SiC (Hexoloy SA™). The tubes were supported by a metal flange which also provided a gas-tight seal. A combination of flexure and tensile CFCC specimens were loaded into a 3.2 cm diameter alumina carrier tube which was then inserted into the SiC tube and suspended at the top by the flange. A ''slow flow'' gas supply system provided a pressurized mixture of steam and premixed gas to each tube. A schematic of a SiC tube assembly is shown in Fig. 1 and a typical specimen loading configuration for the alumina carrier tube is shown in Fig. 2. Each alumina tube can hold as many as 30 combined tensile and flexure

Contributed by the International Gas Turbine Institute (IGTI) of THE AMERICAN SOCIETY OF MECHANICAL ENGINEERS for publication in the ASME JOURNAL OF ENGINEERING FOR GAS TURBINES AND POWER. Paper presented at the International Gas Turbine and Aeroengine Congress and Exhibition, Indianapolis, IN, June 7–10, 1999; ASME Paper 99-GT-292. Manuscript received by IGTI March 9, 1999; final revision received by the ASME Headquarters January 3, 2000. Associate Technical Editor: D. Wisler.

 Copyright © 2000 by ASME

Downloaded 02 Jun 2010 to 171.66.16.119. Redistribution subject to ASME license or copyright; see http://www.asme.org/terms/Terms_Use.cfm

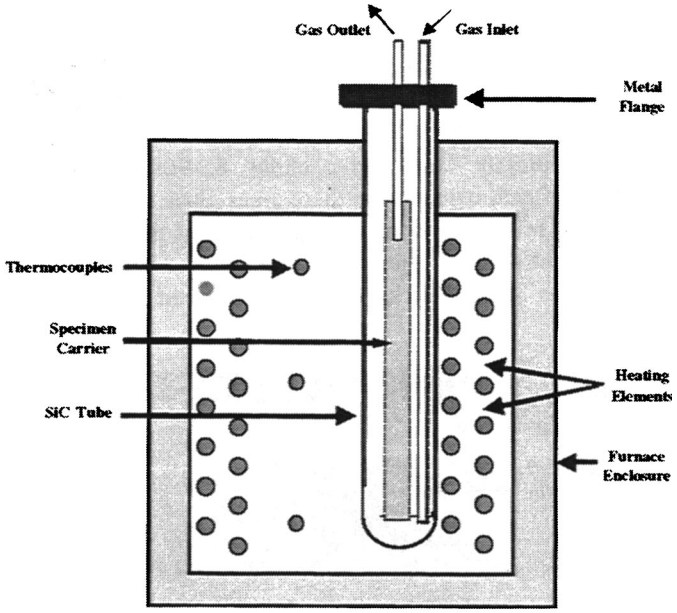

Fig. 1 Schematic of SiC tube and gas assembly in ORNL rig. Furnace holds six vertically loaded tubes.

specimens. In order to best simulate the combustor environment, all tests were conducted in air at 1204°C (2200°F), 15 percent water vapor (balance air), and 150 psia. Each test was run for 500 h, after which the specimens were carefully removed, weighed and measured, and selectively cut for microstructural analysis. Depending on the amount of degradation observed, the specimens were either placed back in the furnace for additional 500 h exposures under the same conditions or removed from the test. In this way, the most promising materials could be exposed for very long times and new materials could replace less stable materials removed from the tests.

The CFCC liners from the ARCO field test were used as the microstructural ''standard'' for the first several runs in the ORNL rig. The ability of the ORNL rig to simulate a combustion envi-

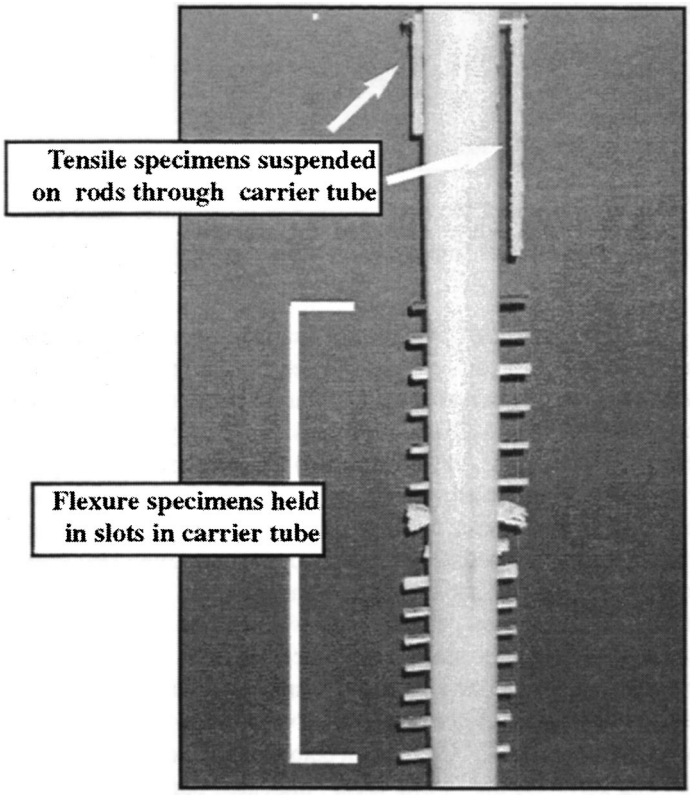

Fig. 2 Alumina carrier tube that holds tensile and flexure specimens for exposure in ORNL rig

Downloaded 02 Jun 2010 to 171.66.16.119. Redistribution subject to ASME license or copyright; see http://www.asme.org/terms/Terms_Use.cfm

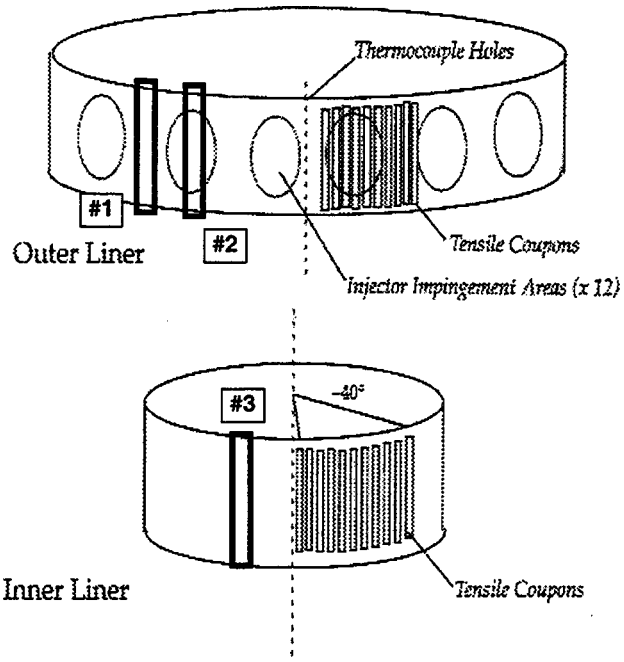

Fig. 3 Schematic of specimens cut from inner and outer CFCC combustor liners after ARCO test

ronment and reproduce the microstructural damage observed in the ARCO liners was one of the most important goals of this study. The dimensions of the inner and outer liners used in the ARCO test were nominally 33 cm and 76 cm in diameter, respectively, with a height of 20 cm and a thickness of 2.5 mm. The outer surface of the inner liner and the inner surface of the outer liner were the working surfaces of the two liners. Both the inner and outer liners were made of AlliedSignal Composites Inc. (ACI) Enhanced SiC/SiC CFCC which had Ceramic Grade (CG) Nicalon™ fibers, a pyrocarbon interfacial coating, a SiC matrix produced by isothermal chemical vapor infiltration (CVI), and a thin ($\sim$60 μm thick) SiC seal coat [7]. This material was selected to be used in the first field test because of its performance in several 100 h sub-scale combustor tests at Solar Turbines [8]. During the ARCO test, the liners were periodically inspected for surface damage about every two weeks using a borescope. The extent of damage, usually in the form of visible changes in surface color or structure, dictated the point at which the liners were removed from the engine test. In the case of the ARCO test, the engine test was actually stopped after $\sim$948 h as a result of foreign object damage (FOD) and subsequent failure of the monolithic ceramic blades. Visual inspection of the liners showed considerable surface damage and the decision was made to remove them from the test for examination. Both liners were still completely intact.

The engine tested liners were first sent to Argonne National Laboratory (ANL) for non-destructive evaluation (NDE). After NDE, both liners were sent to ACI where tensile specimens (all residual strength measurements were performed at ACI) and sections for microstructural analysis were cut. ORNL received a total of three 2.54 cm wide sections; two full (top to bottom) sections from the outer liner and one full section from the inner liner, as illustrated in Fig. 3. Several samples were cut from each section at ORNL with each sample representing different amounts of visually observed surface damage. Metallographic cross-sections were prepared from each to examine damage as a function of depth from the exposed surface. The samples were structurally and compositionally analyzed using an electron microprobe equipped with energy and wavelength dispersive spectrometers. Selected samples were also prepared for transmission electron microscopy to determine the extent of thermal damage to the fibers.

The primary purpose of the first few ORNL rig exposures was to verify the ability of these tests to simulate the combustor environment. Enhanced SiC/SiC tensile bars, which were co-processed with the ARCO liners (and thus assumed to have the same starting microstructure) were exposed in two successive 500 h runs to match the total time that the ARCO liners were engine tested. SiC Hexoloy SA™ flexure bars and several different Si_3N_4 bars were also included as standards in order to assess the oxidation kinetics of known materials. The oxidation behavior of these monolithic ceramics in the presence of water vapor, albeit at lower pressures, has been well documented in the literature (see, for example, [9,10]).

After each 500 h exposure, the specimens were removed from the ORNL rig, weighed, and sectioned. Microstructural examinations were systematically conducted to measure oxide product thickness and surface recession. It was determined from these initial runs that the weight and dimensional measurements were not reliable as a result of unavoidable handling during removal from the furnace. Such handling could result in loss of oxide product. Thus, microstructural measurements were used to determine the oxidation kinetics.

Results and Discussion

Microstructural Analysis of ARCO Liners. Visual inspection of the ARCO liners after 1000 h showed ''white'' areas on the working surfaces of both the inner and outer liners. These white areas were initially observed on the exposed liner surfaces after $\sim$500 h during a visual borescope inspection. The localized white spots on the outer liners corresponded directly with the 12 injector impingement areas on the inner surface of this liner. The white spots indicated a range of localized temperatures since the surfaces between and around these white spots appeared relatively unchanged. The exposed surface of the inner liner, in particular, exhibited severe damage over most of its surface. Figure 4 shows the inner surface of the outer liner; note the localized white damaged regions that corresponded directly with the injector impingement areas.

Microstructural examination of the inner liner showed that significant surface recession occurred during the ARCO test. As shown in Figs. 5(*a*) and 5(*b*), comparing sections of the inner liner from the top surface (CFCC exposed to the lowest temperature during the engine test) and from the center of the exposed surface of the inner liner (near maximum damage area), respectively, recession of about 20 percent of the inner liner thickness was ob-

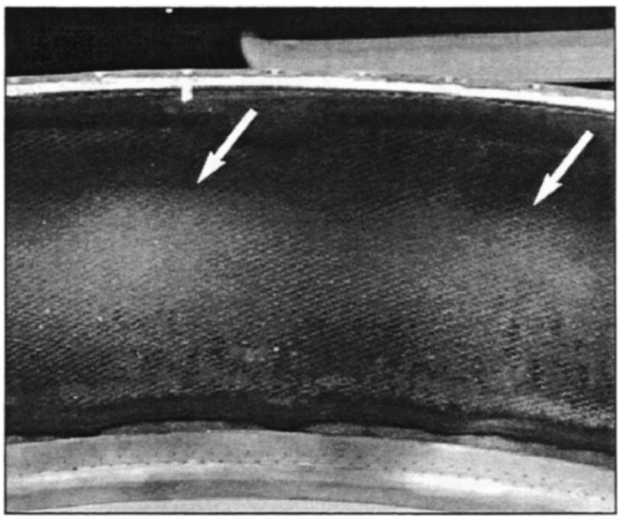

Fig. 4 Portion of the inner surface of outer liner; note two of the localized white damaged regions that corresponded directly with injector impingement areas (arrows)

Downloaded 02 Jun 2010 to 171.66.16.119. Redistribution subject to ASME license or copyright; see http://www.asme.org/terms/Terms_Use.cfm

(a) Unexposed inner liner

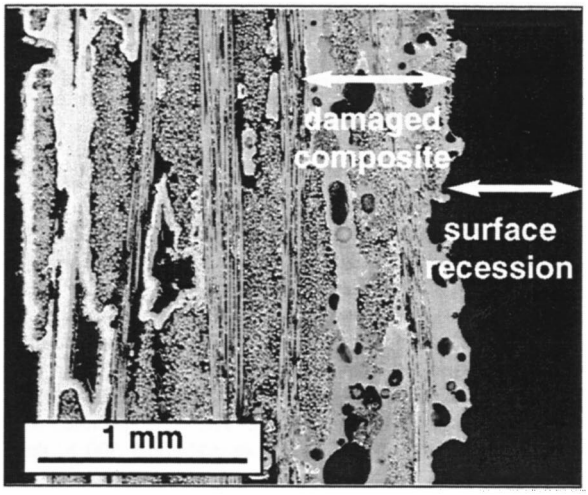

(b) Inner liner after ARCO field test

Fig. 5 Microstructural damage at outer surface of inner liner after the ARCO test. (*a*) Section of liner taken from top (cooler) edge of liner showing intact SiC seal coat and non-damaged composite, and (*b*) section taken from center of exposed surface showing significant surface recession, loss of most of the seal coat, and extensive composite damage below the surface. Damage regions below surface consist primarily of reacted matrix constituents that form glass and loss of fibers.

served and another 25 percent of the CFCC exhibited microstructural damage (see arrows in Fig. 5(*b*)). The damage assessment indicated that not only was the protective SiC seal coat (initially ~60 μm thick) completely removed during engine testing, but the CFCC constituents themselves had reacted to form a low melting point glass at the liner surface. The oxidation of the SiC seal coat (and matrix) resulted in the rapid formation of surface silica; the silica then formed volatile reaction products in the water containing environment [11,4] resulting in accelerated SiC recession. The projected CVD SiC recession after 1000 h under lean-burn conditions, estimated from burner rig studies performed at NASA Glenn, is ~150 μm at 1200°C, 0.6 atm H_2O, and a gas velocity of 33 m/s [4]. The maximum temperature during the ARCO test could not be accurately measured since the thermocouples failed in the early stages of the field test. However, based on the intermittent visual inspections of the liners during the ARCO test, the seal coat on the inner liner (and locally on the outer liner) was

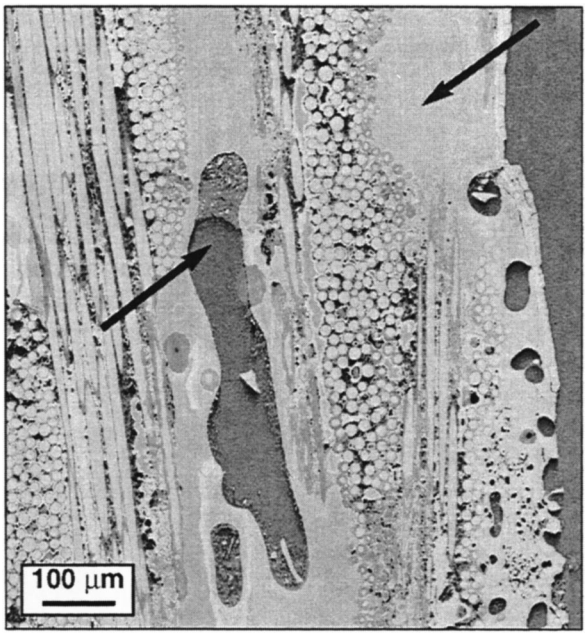

Fig. 6 Typical microstructural damage observed at the outer surface of the inner liner. Arrows indicate areas of ''pooled'' glass observed throughout damaged region.

breached relatively early in the test indicating that the temperature was ~1200°C, and possibly as high as 1260°C at the hot spots on the inner liner.

Typical microstructural damage observed at the outer surface of the inner liner is shown in Fig. 6. Large ''pools'' of glass were observed; the CG Nicalon™ fibers and associated matrix constituents reacted with the glass and entire fibers tows were consumed during glass formation (as shown in Fig. 7). While most of the glass was primarily silica, small amounts of boron were found in

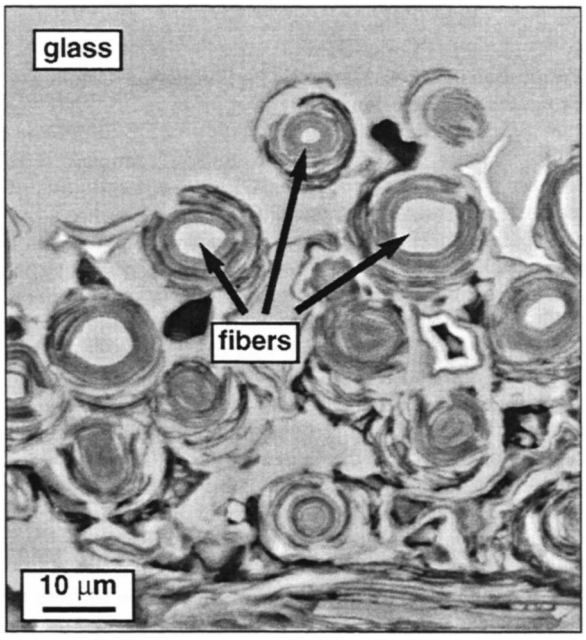

Fig. 7 CG Nicalon™ fibers were consumed during extensive matrix glass formation within damaged regions near exposed surface of inner liner. Arrows indicate fibers at different stages of reaction with glass.

Downloaded 02 Jun 2010 to 171.66.16.119. Redistribution subject to ASME license or copyright; see http://www.asme.org/terms/Terms_Use.cfm

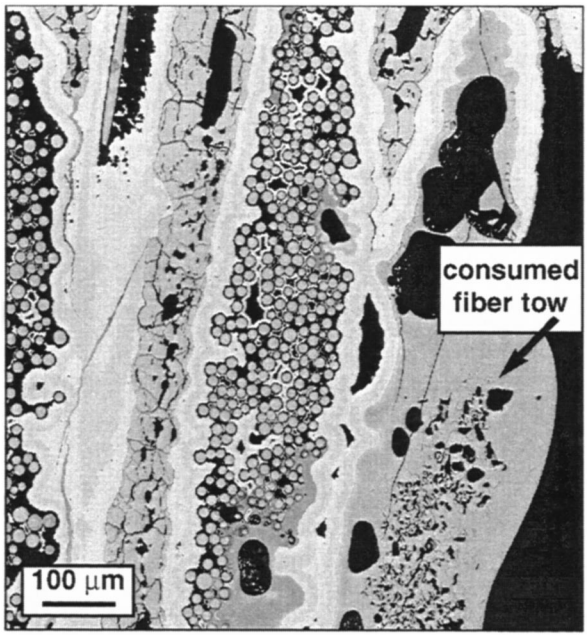

Fig. 8 Typical microstructural damage observed at the inner surface of the outer liner after the ARCO test. Microstructural degradation was similar to that observed for the inner liner.

these areas (additional matrix constituents were the source of the B), which caused a reduction in the glass melting point. Matrix constituents containing boron therefore contributed significantly to the glass formation. Similarly damaged areas were also identified well below the exposed surface of the inner liner (arrows in Fig. 6) and were primarily associated with areas of large porosity (these composites typically were only about 85–90 percent dense), indicating significant oxidation in these areas also. Formation and subsequent recession of the glass product was the primary degradation mechanism of the outer surface of the inner liner. The process was accelerated by the damage formed below the surface.

Evaluation of the injector impingement areas on the inner surface of the outer liners showed similar microstructural damage as that observed on the inner liner, albeit to a much lesser extent; the SiC seal coat was completely removed in these localized areas, but only the top CG Nicalon™ fiber ply was adversely affected, as shown in Fig. 8. In the areas surrounding the injector impingement regions, the SiC seal coat was somewhat thinned (the thickness of the remaining seal coat depended primarily on the local temperature), but remained intact. The surfaces of pores below the liner surface were oxidized (this was most pronounced below the injector impingement areas) and in many instances, matrix and fiber damage around these pores was observed well into the bulk of the underlying CFCC. Clearly, on both the inner and outer liner working surfaces, the ''white areas'' indicated complete loss of the protective SiC seal coat. This will be used in future borescope inspections as an indication of the point at which the protective seal coat is breached.

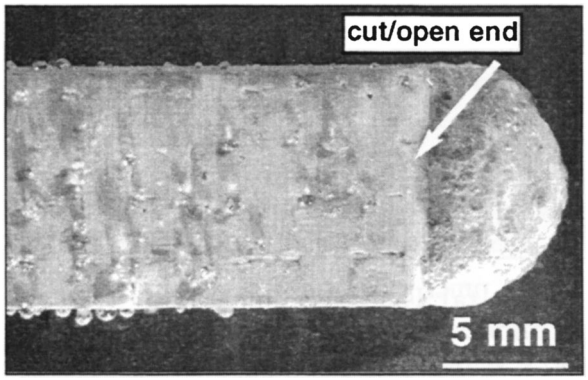

Fig. 9 Surface of Enhanced SiC/SiC specimen after 500 h exposure in ORNL rig. Material was co-processed with CFCC liners in ARCO test. Specimen geometry contributed to significant glass formation at cut/open edges.

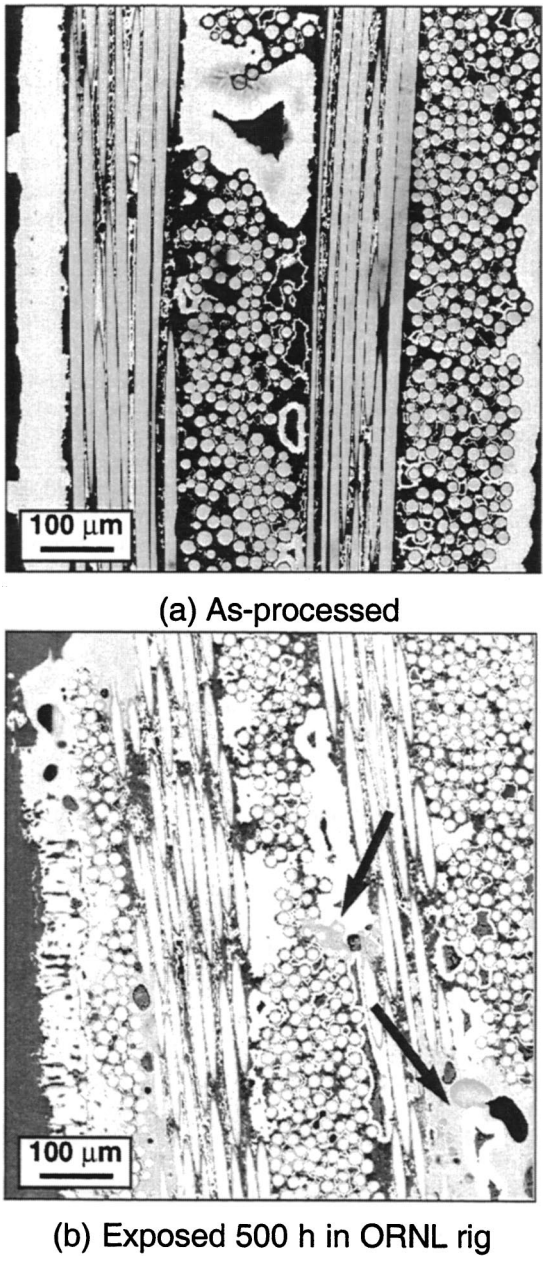

Fig. 10 A comparison of cross-sections of the (*a*) as-processed Enhanced SiC/SiC material, and (*b*) the Enhanced SiC/SiC CFCC after exposure in the ORNL rig for 500 h. Compare localized microstructural degradation (reacted matrix constituents) in Fig. 10(*b*) (indicated by arrow) to inner liner degradation shown in Fig. 6.

Verification of ORNL Steam Rig for Simulating Combustor Environment Corrosion. Two types of Enhanced SiC/SiC samples were included in the initial run of the ORNL rig: tensile

Downloaded 02 Jun 2010 to 171.66.16.119. Redistribution subject to ASME license or copyright; see http://www.asme.org/terms/Terms_Use.cfm

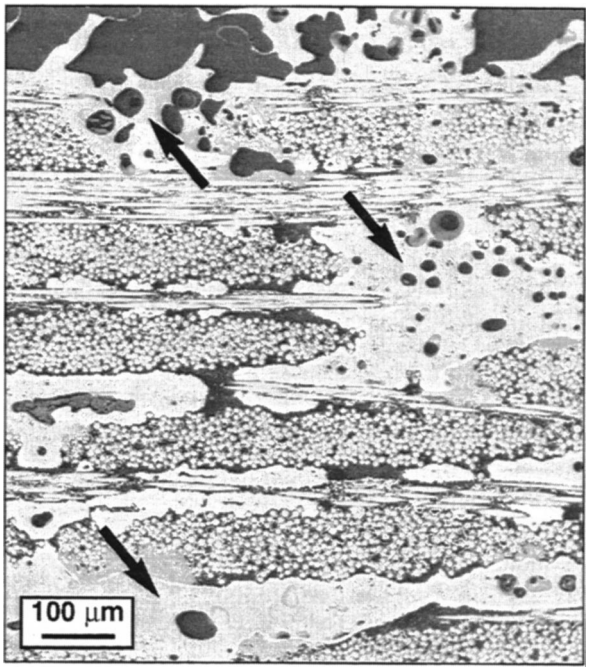

Fig. 11 Microstructural degradation of Enhanced SiC/SiC CFCC after exposure in the ORNL rig for 1000 h. Compare microstructural degradation (reacted matrix constituents) in Fig. 11 (indicated by arrow) to inner liner degradation in Fig. 6.

bars of material co-processed with the ARCO liners which had a SiC seal coat thickness of ~60 μm and a similar composite with a much thicker ~300 μm SiC seal coat. The second material provided additional data for the rig assessment; kinetic data for CVD SiC could be accumulated in addition to data for SiC (Hexoloy SA™) for comparison with existing burner rig data [4,9]. The primary goal of the first two ORNL runs, however, was to verify that the ORNL rig could reproduce the microstructural degradation observed in the liners after the ARCO test.

Visual inspection of the Enhanced SiC/SiC tensile specimen after the first 500 h run showed that all the surfaces were covered with a white oxide product and glass bubbles. An important observation made after the first 500 h exposure was that extensive degradation occurred at cut or open surfaces of the specimens. These areas had to be carefully avoided during microstructural evaluation since these could lead to excessive amounts of materials degradation that would not be representative of the extent of damage found in combustor liners (which have no open or cut ends). Figure 9 is a photograph of the Enhanced SiC/SiC specimen removed after 500 h. Note the excessive amount of glass protruding from the surface cut after the test; not only is there usually no seal coat on these ends, but the exposed fiber ends and open areas into the matrix contribute to accelerated degradation. The specimen for microstructural analysis was cut at least 1 cm below this open surface.

Cross-sections of the as-processed Enhanced SiC/SiC composite before and after exposure in the ORNL rig for 500 h are shown in Figs. 10(*a*) and 10(*b*), respectively. The SiC seal coat was fully oxidized across the specimen surface and fiber tows below the surface showed areas of constituent reaction (arrows in Fig. 10(*b*)). The damaged composite areas in the ORNL-exposed specimen were structurally similar to those observed for the same material after the ARCO test (see Fig. 6); localized areas of constituent reaction (glass formation) are noted in Fig. 10(*b*). The same specimen was placed back in the ORNL rig for an additional 500 h, thus exposing the material for approximately the same amount of time achieved in the ARCO test. After 1000 h in the ORNL rig, the microstructural degradation was extensive, as

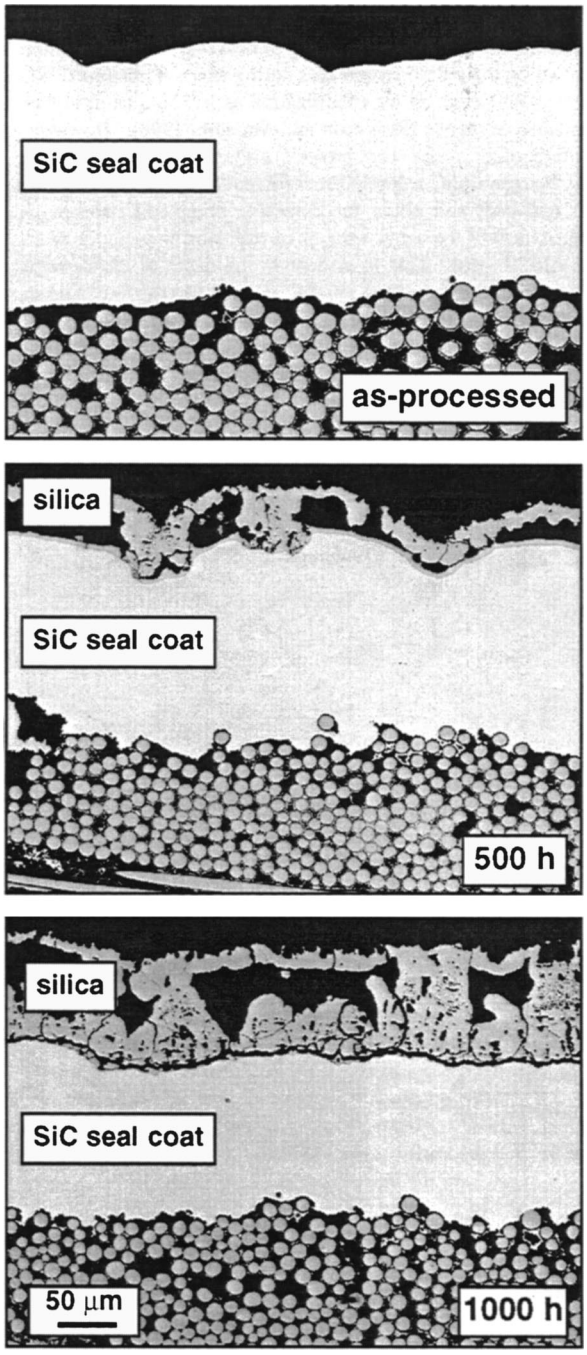

Fig. 12 CVD SiC seal coat oxidized for 500 and 1000 h. It was determined from direct microstructural measurements that the SiC seal coat recessed by oxidation at a linear rate of approximately 45 μm/500 h.

shown in Fig. 11, and was nearly identical to that observed for the same material engine tested at ARCO. There was significant glass formation at the surface.

The Enhanced SiC/SiC sample with a thick CVD SiC seal coat was used to determine the CVD SiC oxidation/recession rate in the ORNL rig. Figure 12 shows the oxidation of the SiC seal coat for three sequential 500 h exposures. It was determined from direct microstructural measurements that the SiC seal coat recessed by oxidation at a maximum linear rate of approximately 45 μm/500 h. Clearly, the oxidation/recession rate of the SiC was accelerated in the ORNL rig compared to rates reported previously for CVD SiC exposed at lower water vapor pressures [12,13]. A com-

Downloaded 02 Jun 2010 to 171.66.16.119. Redistribution subject to ASME license or copyright; see http://www.asme.org/terms/Terms_Use.cfm

plete kinetic analysis of this phenomenon is currently ongoing. It is interesting to note that most of the silica formed on the specimen surfaces during exposure in the ORNL rig was not removed by volatilization as it would be at higher gas flow velocities [4]. However, the bulk of this silica is not protective against ongoing oxidation and the rate of SiC recession is sufficiently high to compromise the seal coat and allow for extensive composite damage in approximately the same amount of exposure time as found in the ARCO test. This is evident in the depth of the damage observed in the Enhanced SiC/SiC composite after exposure in the ORNL rig; the amount of material lost is not indicative of total damage because the environment penetrates into the composite and causes the same type of microstructural degradation below the surface.

Conclusions

Comparison of results from laboratory and combustor exposures demonstrated that the ORNL rig provides a valid simulation of CFCC microstructural degradation at a rate which is comparable to that observed in actual combustor environments. The rig allows for the necessary high sample throughput to assess damage accumulation and corrosion mechanisms for extended periods of time.

Acknowledgments

Research sponsored by U.S. DOE, Office of Energy Efficiency and Renewable Energy, Office of Industrial Technologies, for both the CFCC Program under contract DE-AC05-96OR22464 with Lockheed Martin Energy Research Corp. and the CSGT Program under contract DE-AC02-92CE40960 with Solar Turbines Inc. Our gratitude is extended to D. W. Coffey, M. Howell, and T. S. Geer for technical assistance.

References

[1] van Roode, M., Brentall, W. D., Norton, P. F., and Pytanowski, G. P., 1993, ''Ceramic Stationary Gas Turbine Development,'' ASME Paper 93-GT-309.
[2] Price, J. R., Jiminez, O., Faulder, L., Edwards, B., and Parthasarthy, V., 1998, ''Ceramic Stationary Gas Turbine Development Program—Fifth Annual Summary,'' ASME Paper 98-GT-181.
[3] Stambler, I., 1997, ''ARCO Operating Ceramics Centaur to Evaluate Actual Field Service,'' Gas Turbine World, Sept.–Oct., pp. 20–22.
[4] Robinson, R. C., and Smialek, J. L., 1998, ''SiO_2 Scale Volatility and Recession of CVD SiC in a High Pressure Burner Rig,'' *Electrochemical Society Proceedings*, P. Y. Hou, et al., eds., The Electrochemical Society, Pennington, NJ, **98-9**, pp. 406–417.
[5] Etori, Y., et al., 1997, ''Oxidation Behavior of Ceramics for Gas Turbines in Combustion Gas Flow at 1500°C,'' ASME Paper 97-GT-355.
[6] Keiser, J. R., Howell, M., Williams, J. J., and Rosenberg, R. A., 1996, ''Compatability of Selected Ceramics with Steam-Methane Reformer Environments,'' *Proceedings of Corrosion/96*, NACE International, Houston, TX, Paper 140.
[7] Gray, P., Headinger, M., and Miller, A., 1996, ''Long Term Tensile Stressed Oxidation and Fatigue Life of Enhanced SiC/SiC CMCs,'' *Proceedings of the 20th Annual Conference on Ceramic, Metal and Carbon Composites, Materials and Structures*, M. Opeka, ed., pp. 865–877.
[8] Simpson, J. F., Parthasarathy, V., and Fahme, A., 1997, ''Testing of Monolithic Ceramics and Fiber-Reinforced Ceramic Composites for Gas Turbine Combustors,'' *Ceramic Engineering and Science Proceedings*, **18**, No. 4, pp. 229–238.
[9] Opila, E. J., and Hann, R. E., 1997, ''Paralinear Oxidation of CVD SiC in Water Vapor,'' J. Am. Ceram. Soc., **80**, No. 1, pp. 197–205.
[10] Fox, D. S., 1998, ''Oxidation Behavior of CVD SiC and Si_3N_4 from 1200°C–1600°C,'' J. Am. Ceram. Soc., **81**, No. 4, pp. 945–950.
[11] Opila, E. J., and Jacobsen, N. S., 1998, ''Volatile Si-O-H Species in Combustion Environments,'' *Electrochemical Society Proceedings*, P. Y. Hou, et al., eds., The Electrochemical Society, Pennington, NJ, **98-9**, pp. 524–534.
[12] Opila, E. J., 1994, ''Oxidation Kinetics of CVD SiC in Wet Oxygen,'' J. Am. Ceram. Soc., **77**, No. 3, pp. 730–736.
[13] Opila, E. J., 1999, ''Variation of the Oxidation Rate of SiC with Water-Vapor Pressure,'' J. Am. Ceram. Soc., **82**, No. 3, pp. 625–636.

Downloaded 02 Jun 2010 to 171.66.16.119. Redistribution subject to ASME license or copyright; see http://www.asme.org/terms/Terms_Use.cfm

A New Technique for Identifying Synchronous Resonances Using Tip-Timing

Steve Heath
Electronic and Measurement
Technology Department,
Rolls Royce plc,
PO Box 31,
Derby DE24 8BJ, UK

Non-contact measurement of vibration at turbomachinery rotor blade tips using blade tip-timing has become an industry-standard procedure. Current research focuses on analysis methods for interpretation of the measured vibration data from a limited number of probes. The methods are classified by the form of the vibration they can identify. Identification of asynchronous response amplitude and frequency is well documented. Whilst a method for identifying maximum synchronous resonance amplitude has existed since the early 1970s, there is no published evidence of a method for directly identifying frequency or engine order using a small number of probes. This paper presents a new analysis method for identifying synchronous resonance engine order using two tip-timing vibration measurements. The measurements are made at different locations on the turbomachinery casing using a minimum of two probes. A detailed description of the method and results from its practical application are given. The potential of the method to identify the amplitude and frequency of close modes, not possible with current methods, is demonstrated. The effect of blade mistuning on the accuracy of the method is investigated. Existing synchronous response analysis methods and the new method presented here give the response amplitude and frequency after the resonance has been traversed. Real-time identification of synchronous response amplitude and frequency would allow tip-timing to be used as a safety monitor of all blades. Real-time methods, their limitations and practical application are discussed. The future use of tip-timing as the dominant vibration measurement system is discussed with reference to experience on measurements made solely with tip-timing on assemblies with undefined vibration characteristics.
[S0742-4795(00)02602-8]

1 Introduction

Rotating blade vibration measurements are a key part of any turbomachinery research and development program. Contacting measurement techniques, such as strain gauges, are well established but monitor a limited number of blades, are costly and time consuming to install, have a limited operating life and can interfere with the aerodynamic and mechanical properties of the assembly. Tip-timing is a non-contacting measurement technique which uses casing mounted probes to determine the vibration of all blades. The technique uses the time at which the blade tips pass the probes to give the blade vibration at the probes. Whilst tip-timing can completely characterize rotating assembly vibration using many probes as demonstrated by Endoh et al. [1], routine application requires a limited number of probes per rotor stage (normally 3 or 4). Typically, tip-timing is used to confirm vibration of assemblies and their derivatives already characterized using strain gauges or when measurements using strain gauges are impractical or untimely.

The typical elements of a tip-timing system are shown in Fig. 1 and are (i) the acquisition of raw arrival time data by a number of stationary probes placed in the casing, (ii) the derivation of characteristic vibration parameters, such as blade displacement from the measured data, and (iii) the analysis of the characteristic parameters to describe the vibration properties of the bladed-disk assembly.

The reluctance to use tip-timing for primary vibration measurement results from the limited capabilities and unreliability of the technique when a limited number of probes are used. The focus of research in recent years has been to enhance and supplement the tip-timing data analysis methods to give capability comparable to strain gauges and improved results reliability. As capability and reliability have improved, confidence in use of the technique has risen and it is now routinely used as an adjunct to or instead of strain gauges. The capabilities of current tip-timing analysis techniques using two independent measurements of blade vibration

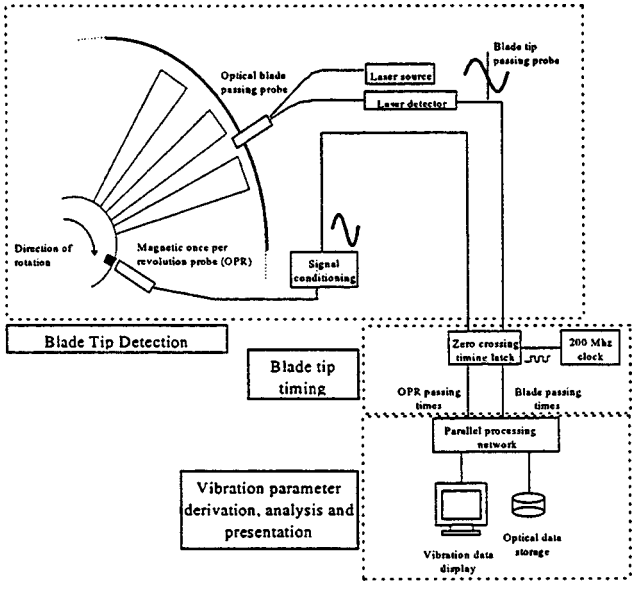

Fig. 1 Typical blade tip-timing system elements

Contributed by the International Gas Turbine Institute (IGTI) of THE AMERICAN SOCIETY OF MECHANICAL ENGINEERS for publication in the ASME JOURNAL OF ENGINEERING FOR GAS TURBINES AND POWER. Paper presented at the International Gas Turbine and Aeroengine Congress and Exhibition, Indianapolis, IN, June 7–10, 1999; ASME Paper 99-GT-28. Manuscript received by IGTI March 9, 1999; final revision received by the ASME Headquarters January 3, 2000. Associate Technical Editor: D. Wisler.

Copyright © 2000 by ASME

Downloaded 02 Jun 2010 to 171.66.16.119. Redistribution subject to ASME license or copyright; see http://www.asme.org/terms/Terms_Use.cfm

Table 1 Current two parameter analysis method capability

Vibration Type	Vibration Characteristics Uniquely Identified	
	Amplitude	
	Constant Speed	Speed Traverses Resonance
Asynchronous	Yes	Yes
Synchronous	No	Yes
	Frequency	
Asynchronous	Yes	Yes
Synchronous	No	No

(parameters) are summarized in Table 1. A detailed review of all these analysis methods was performed by Heath and Imregun [2]. The capability of the analysis methods clearly depends on the assembly vibration type, synchronous and asynchronous. Synchronous (or integral order) resonances are assembly modes that are excited at multiples of the rotational speed. Asynchronous resonances are mainly due to aerodynamic instabilities such as rotating stall and flutter.

Improved methods for identification of synchronous vibration are necessary for tip-timing measurements using a limited number of probes to be comparable to those from strain gauges. These methods are a key part of tip-timing research. This paper details a new ''two parameter analysis method'' for identifying synchronous vibration frequency when the assembly speed traverses a resonance. Experience with methods for identifying synchronous vibration at constant speed are discussed and current and future research outlined.

2 Synchronous Vibration Analysis Methods

Synchronous response analysis methods have been classified as direct and indirect. Direct analysis methods use a number of response measurements from each assembly rotation to identify the instantaneous assembly vibration characteristics. It is assumed that assembly operating conditions are approximately constant for each measurement set. These methods have the potential of identifying continuous amplitudes for single or multiple resonances in real-time.

Indirect analysis methods use response measurements from each assembly rotation as a synchronous assembly resonance is traversed. These methods typically give the maximum resonance amplitude and frequency for the speed range over which the resonance occurs. As the assembly response is synchronous, the engine order of the response remains constant as the resonance is traversed. The actual response frequency is the product of the assembly rotation frequency and response engine order. Typically, indirect methods give the engine order of the resonance and a mean value of the associated frequency has to be calculated from the assembly rotation speed range over which resonance occurs.

2.1 Indirect Amplitude Identification Analysis Methods. Prior to this research program, a single indirect method proposed by Zablotsky and Korostelev [3] was a de-facto standard method for determining the amplitude of single synchronous resonances, with recent applications being reported by Chi and Jones [4]. The analysis technique is based on measuring a single tip response parameter, such as displacement (or velocity, or acceleration), using a minimum of one probe. The method requires the resonance to be excited by varying the assembly rotation speed in such a way that the assembly is forced to traverse the resonance of interest. The form of the measured displacement versus rotational speed characteristic depends on the position of the measurement probe relative to the assembly forcing function. Typical plots at different measurement positions for the same forcing term are shown in Fig. 2.

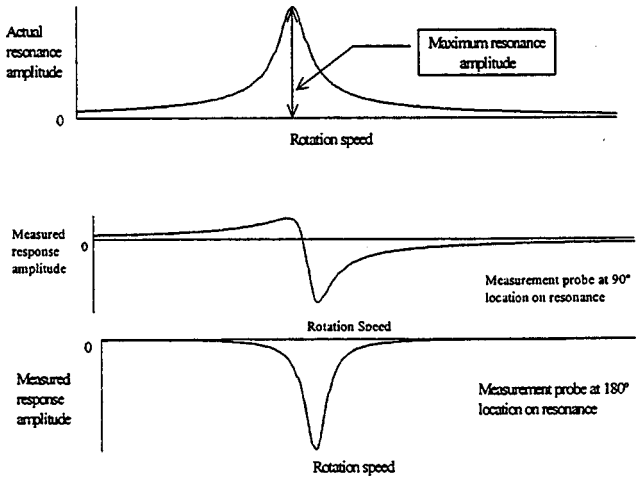

Fig. 2 Comparison of actual and measured response amplitudes for different measurement positions

It is usually assumed that the maximum (zero-to-peak) resonant response amplitude is given by the maximum-to-minimum values of the measured displacement versus speed characteristic. It is further assumed that this value is independent of the location of the measurement point. The mathematical basis of the Zablotsky and Korostelev method is described by Heath and Imregun [5]. It has also been shown by Heath and Imregun [5] that there are inherent errors associated with such assumptions but that the magnitude of these errors is acceptable for practical measurements and can be corrected if necessary.

The shape of the measured displacement versus speed plot is a determined by the location of the measurement probe. For the purposes of this paper, the angular location of the probes refers to a fixed position expressed in terms of the wavelength of the response. Consider a forced response of order n and two probes separated by an angle α on the resonance. This corresponds to an angular separation of α/n on the casing.

2.2 Indirect Frequency Identification Analysis Methods. Measurements using a number of probes equally spaced around the casing have been reported, Zielinski and Ziller [6]. These systems are truly direct analysis methods as they give response amplitude and frequency using Fourier analysis over a number of rotations. Determination of response frequency uses theoretical predicted values and with a limited number of probes the method is insensitive to certain response orders. Installation of equally spaced probes can be impractical and theoretical predictions may be inaccurate such that the method has limited usefulness for general turbomachinery applications. It is, however, able to resolve low response amplitudes by virtue of using Fourier analysis.

As part of an on-going research program, a new indirect analysis method capable of identifying resonance order using two response measurements and a minimum of two probes has been developed. The method does not rely on theoretical vibration response predictions and has been successfully applied to measurements from operating turbomachines. Current partially automated implementations of the method are not suitable for real-time identification of resonance order. The method uses two response measurements on the same axial line and has been designated the ''*two parameter method.*''

2.2.1 Description of Two Parameter Analysis Method. The two parameter method was developed from observation of two measurements of a synchronous resonance from probes on the same axial position on the assembly casing. It was developed

Downloaded 02 Jun 2010 to 171.66.16.119. Redistribution subject to ASME license or copyright; see http://www.asme.org/terms/Terms_Use.cfm

using a multi-degree-of-freedom numerical simulator, which includes the structural and geometric properties of the bladed-disk assembly, the external forcing terms and the characteristics of the optical probe.

Consider two probes denoted A and B located on the assembly periphery. Probe A is located before probe B in the direction of assembly rotation and angular measurements are positive in the direction of rotation. Let probe A be at angular position, θ_A on the assembly periphery and let $\Delta\theta$ be the angular spacing between probes A and B. Given that the assembly vibration response displacement amplitude at the probes x_A and x_B can be calculated from the timing measurements. For a synchronous resonance of order n, x_A, and x_B are given by

$$x_A = A(\omega)\cos(n\theta_A + \psi(\omega)) + C \tag{1}$$

$$x_B = A(\omega)\cos(n\theta_A + \psi(\omega) + n\Delta\theta) + C, \tag{2}$$

where $A(\omega)$ and $\psi(\omega)$ are the amplitude and phase of the assembly response and C is a constant offset. If $\Delta\psi$ is the angular separation of the measurements on the resonance, Eq. (2) can be rewritten as

$$x_B = A(\omega)\cos(n\theta_A + \psi(\omega) + \Delta\psi) + C. \tag{3}$$

When the sensor spacing $\Delta\psi$ on the resonance is 90 deg, (3) becomes

$$x_B = -A(\omega)\sin(n\theta_A + \psi(\omega)) + C. \tag{4}$$

For a single-degree-of-freedom system, a polar plot of the system's response forms a circle as the resonance is traversed. Such a situation is shown in Fig. 3 by considering variations in the excitation frequency and the resulting response amplitude and phase.

The polar plot of Fig. 3 and the form of (1) and (4) mean that a plot of x_A against x_B will also describe a circle if the assembly response can be approximated to that of a single-degree-of-freedom system and the probes are separated by 90 deg on the resonance. Tuned synchronous resonances can be modelled using a single-degree-of-freedom system and a plot of x_A against x_B for a 90 deg spacing will be a circle. The location of the circle relative to the plot origin will be determined by the fixed offset C which may be different at each probe. The location of the point on the circle corresponding to excitation frequencies significantly away from resonance will be determined by the angular position of the probes relative to the resonance $n\theta_A$.

Equations (1) and (3) were used with a single-degree-of-freedom system response model for $A(\omega)$ and $\psi(\omega)$ with zero offset, C, to produce plots of x_A versus x_B for various probe spacings on the resonance with frequencies which traverse the resonance frequency defined by the single-degree-of-freedom model, Fig. 4.

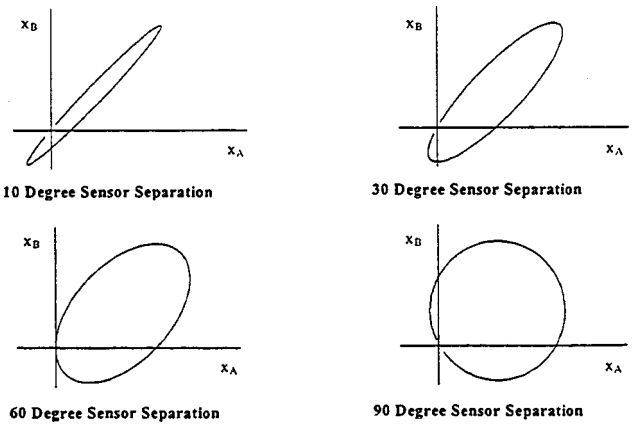

Fig. 4 Plots of x_A versus x_B for differing probe spacing

The plots in Fig. 4 were termed ''two-parameter'' plots and described using the following terms:

Major axis = straight line joining the two points furthest apart on the plot

Minor axis = maximum length straight line joining two points on the plot normal to the major axis

Major axis angle = angle between major axis and horizontal plot axis

$$\textit{Axis ratio} = \frac{\text{length of minor axis}}{\text{length of major axis}}$$

These terms are illustrated in Fig. 5.

Although the two-parameter plots are defined in terms of ellipse geometry, these plots are not true ellipses in that there is no symmetry about the major axis. The lack of symmetry is caused by the single-degree-of-freedom nature of the blade resonance and is a feature of the two-parameter analysis method.

The resonance order, n, can be calculated from

$$n = \frac{\Delta\psi}{\Delta\theta} \tag{5}$$

Analysis of the two-parameter plots revealed a relationship between probe spacing and the two-parameter plot axis ratio and the major axis angle. The relationship was independent of the location of probe A and is illustrated in Fig. 6. The major axis angle is always ± 45 deg except for probe spacings of 90 deg and 270 deg where it is undefined as the two-parameter plots form circles for these spacings.

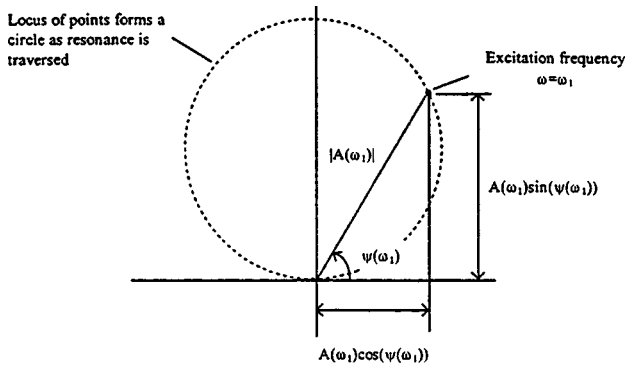

Fig. 3 Polar plot for single-degree-of-freedom-system resonance

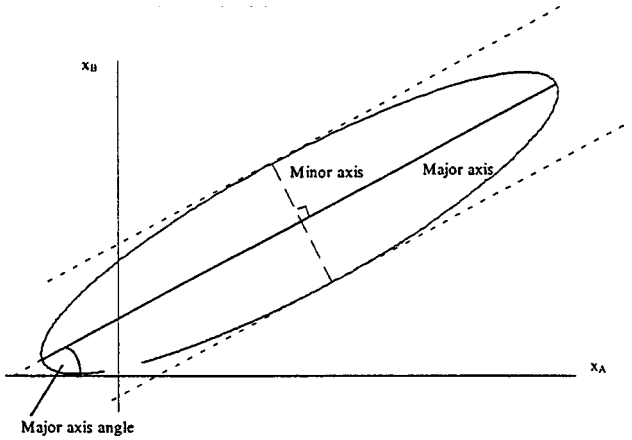

Fig. 5 Definition of two-parameter plot terms

Downloaded 02 Jun 2010 to 171.66.16.119. Redistribution subject to ASME license or copyright; see http://www.asme.org/terms/Terms_Use.cfm

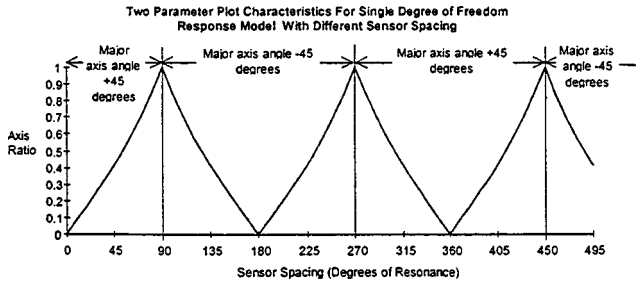

Fig. 6 Relationship between axis ratio, major axis angle, and probe spacing

There is a region on each two-parameter plot where there are no data points. This absence of points is due to the simulated assembly rotation speed range producing a finite range of assembly excitation frequencies, the extremes of which do not give zero response amplitude. Such a region can be expected in all two-parameter plots. The region may cause inaccuracies in the determination of the plot parameters when it is coincident with the axis end point.

The relationship between the probe spacing, axis ratio and major axis angle repeats itself at sensor spacing intervals of 360 deg. Four regions can be identified within each 360 deg interval. Table 2 lists the probe spacing ranges for each region.

Within each region there is an almost linear relationship between the probe spacing and the axis ratio. In practice, the axis ratio and the major axis angle are identified from a two-parameter plot and the possible spacings calculated using Fig. 6. To enable direct calculation of probe spacing a third order polynomial fit of axis ratio to probe spacing for a single-degree-of-freedom resonance model was performed for each region. The polynomial used is given in (6) and the polynomial coefficients for each region are given in Table 3.

$$\text{Sensor spacing} = P \times (\text{axis ratio})^3 + Q \times (\text{axis ratio})^2 + R \times (\text{axis ratio}) + S \tag{6}$$

Multiple values of probe spacing will be determined using the relationship of Fig. 6 but the true resonance order should be a positive integer. It is possible that a number of probe spacing values will satisfy this condition and, in such cases, a knowledge of the expected or reasonable resonance order is necessary to identify the correct spacing.

Table 2 Sensor spacing region definitions

Region	Sensor Spacing Range
1	0° to 90°
2	90° to 180°
3	180° to 270°
4	270° to 360°

Table 3 Polynomial coefficients for each sensor spacing region

Region	P	Q	R	S
1	-7.22644	-21.82787	119.08946	-0.16976
2	7.27262	21.84211	-119.16418	180.17559
3	-7.28363	-21.82579	119.15622	179.82559
4	7.21876	21.84879	-119.10273	360.17127

2.2.2 Evaluation of Two Parameter Analysis Method. The two-parameter method was evaluated using a multi-degree-of-freedom assembly model with different probe spacing and relative resonance amplitude, A_{rel}, Table 4. Relative resonance amplitude is defined as

$$A_{rel} = \frac{A_{max}}{R}, \tag{7}$$

where A_{max} is the maximum resonance amplitude and R is the assembly tip radius.

Relative resonance amplitude was used in the parametric evaluation as it has been shown to influence the accuracy of the Zablotsky-Korostelev method, Heath and Imregun [5].

Table 4 shows that as relative resonance amplitude increases, the axis ratio for a given probe spacing changes. Using the relationship of Fig. 6 this means that an incorrect probe spacing can be identified from a measured axis ratio with resulting inaccuracies in the derived resonance order. If the relationship between probe spacing and axis ratio is assumed to be approximately linear and correct at low values of relative resonance amplitude, the percentage error in axis ratio will be the same as the percentage error in probe spacing and resonance order. When the absolute value of the resonance order error exceeds 0.5, the identified resonance order will be incorrect. Measurements on steam turbines have shown typical maximum relative resonance amplitudes of 0.005 which would result in axis ratio errors of less than 2 percent and would not affect the correct identification of resonance orders up to 20. Practical applications of the two-parameter plot method for identifying the sensor spacing should consider the observed relative resonance amplitude when quantifying the accuracy of the results obtained, particularly as some modern fan blades are designed to withstand relatively large vibration amplitudes. Inaccuracies in the two-parameter method can be minimized by choosing probe spacings which produce large changes in axis ratio for increments in resonance order and using measurements from more than two probes to give a number of two-parameter analysis results which can be cross checked. One approach to choosing a probe configuration is given in 2.2.3.

The inaccuracies in the two-parameter method are caused by the spacing of the measurements on the synchronous response, $n\Delta\theta$, changing as the resonance is traversed. At low relative resonance amplitude values this change is negligible but as relative resonance amplitude increases the change becomes significant. For a probe spacing of 90 deg on the resonance, a relative resonance amplitude of 0.00014 gives a change in spacing on the response of 0.02 deg whereas a relative resonance amplitude of 0.04 gives a change of 8.02 deg. The change in spacing is a feature of the indirect tip-timing analysis approach where the

Table 4 Variation of axis ratio with relative resonance amplitude

Probe spacing (degrees)	Relative Resonance Amplitude				
	0.00014	0.000335	0.0083	0.0166	0.0332
	Axis Ratio				
10	0.0875	0.0876	0.0868	0.0861	0.0905
20	0.1764	0.176	0.175	0.1738	0.1816
30	0.268	0.267	0.2662	0.2645	0.2749
40	0.364	0.3636	0.3619	0.3598	0.3718
50	0.4664	0.4658	0.464	0.4617	0.4741
60	0.5775	0.5754	0.575	0.5725	0.5838
70	0.7003	0.6974	0.698	0.6953	0.7029
80	0.8393	0.8393	0.8372	0.8343	0.8322
90	1	0.9991	0.9825	0.9654	0.9322

Downloaded 02 Jun 2010 to 171.66.16.119. Redistribution subject to ASME license or copyright; see http://www.asme.org/terms/Terms_Use.cfm

Table 5 Tuned and mistuned two-parameter plot analysis for differing relative resonance amplitudes

	Relative Resonance Amplitude 0.000335			
	Tuned		Mistuned	
Blade number	Axis ratio	Major Axis Angle (degrees)	Axis Ratio	Major Axis Angle (degrees)
1	0.087	45.00	0.088	45.08
4	0.087	45.00	0.087	45.00
9	0.087	45.00	0.088	44.94
11	0.087	45.00	0.089	44.95
	Relative Resonance Amplitude 0.0335			
	Tuned		Mistuned	
Blade number	Axis ratio	Major Axis Angle (degrees)	Axis Ratio	Major Axis Angle (degrees)
1	0.090	45.00	0.091	44.61
4	0.090	45.00	0.090	44.73
9	0.090	45.00	0.093	44.21
11	0.090	45.00	0.095	44.69

change in measured response phase does not track the actual change in response phase as the resonance is traversed, Heath and Imregun [5].

Mistuning, or small blade-to-blade manufacturing differences, will cause the blades in the assembly to have dramatically different response levels and the assembly will exhibit many close modes because of the splitting double modes. Mistuning will distort the two-parameter plots and hence adversely affect the results of the analysis. The effects of mistuning were quantified using a numerical simulation of a 12-bladed disk, running in the vicinity of a split 3 nodal-diameter mode[1] and subject to a 3 engine-order excitation. Initially a ± 1 percent variation in blade cantilever frequency and 10 deg probe spacing were used and the two-parameter plots for four blades at two relative resonance amplitudes analyzed, Table 5.

The same assembly mistuning was used in each case, implying that the axis ratio depends on both the level of mistuning and relative resonance amplitude which is different for each blade in the mistuned case. Detailed analysis shows that in the mistuned case there is no correlation between the variation in relative resonance amplitude and the variation in axis ratio for the selected blades. For ± 1 percent frequency mistuning, the maximum axis ratio error is $+2$ percent for a relative resonance amplitude of 0.000335 and $+9$ percent for a relative resonance amplitude of 0.0335. The presence of mistuning is readily identified in the two-parameter plot and if the plots are distorted the validity of the two-parameter analysis needs to be carefully examined.

Figure 7 shows the effects of increased and probably unrealistic assembly mistuning on a two parameter plot for a 90 deg probe spacing.

The smaller circles in Fig. 7 are caused by close modes resulting from assembly mistuning. However, the overall plot still describes a circle implying that a single mode will dominate each blade response. Ignoring the low amplitude modal circles, Fig. 7 has an axis ratio of 0.95 which is comparable with the results obtained at lower levels of mistuning. In all cases, mistuning does affect the axis ratio and hence the accuracy of the resonance order

[1]Double modes split into two single ones with close frequencies and similar but not identical mode shapes.

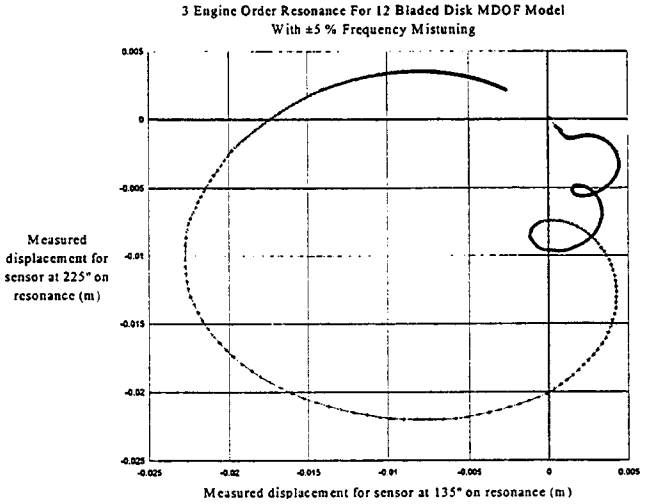

Fig. 7 Plot for increased assembly mistuning

identified from the two-parameter plots. A detailed discussion of mistuning and its effect on tip-timing measurements can be found in Schaber [7].

2.2.3 Application of Two Parameter Analysis Method. The two-parameter method has been successfully applied to a number of turbomachines. One such application will be discussed here for illustrative purposes. Tip-timing measurements were made during the commissioning of a low pressure (LP) steam turbine. Three probes were installed on the same axial line in the turbine casing. The probes are denoted probes 1, 2, and 3 with a given blade arriving first at probe 1, next probe 2, and last probe 3. The nominal spacing between probes 1 and 2 was 5.625 deg and between probes 2 and 3 was 16.875 deg. Accurate values for probe spacing were obtained from blade arrival times under non-vibrating conditions. The probe spacings were chosen to allow identification of resonances up to 10 engine order using two-parameter plots from different probe combinations. The predicted two-parameter plot characteristics using measurements from different probes are given in Table 6.

Tip-timing data was acquired from a number of controlled decelerations of the turbine with an air jet providing excitation of synchronous assembly resonances. A non-vibrating once-per-revolution probe (OPR) was used and the displacement of all blade tips relative to the OPR calculated at each probe on every assembly rotation. A typical blade displacement versus speed plot is shown in Fig. 8. Visual analysis of these measurements shows three synchronous resonances which are summarized in Table 7.

Table 6 Two-parameter plot characteristics for different probe combinations

Resonance Engine Order	Probes Measurements Used For Two-Parameter Plot					
	1 and 2		1 and 3		2 and 3	
	Angle	Ratio	Angle	Ratio	Angle	Ratio
1	+45	0.049	+45	0.198	+45	0.147
2	+45	0.098	+45	0.415	+45	0.303
3	+45	0.147	+45	0.668	+45	0.474
4	+45	0.198	-	1	+45	0.668
5	+45	0.25	-45	0.668	+45	0.905
6	+45	0.303	-45	0.415	-45	0.819
7	+45	0.358	-45	0.198	-45	0.6
8	+45	0.415	-45	0	-45	0.415
9	+45	0.474	-45	0.198	-45	0.25
10	+45	0.536	-45	0.415	-45	0.098

Downloaded 02 Jun 2010 to 171.66.16.119. Redistribution subject to ASME license or copyright; see http://www.asme.org/terms/Terms_Use.cfm

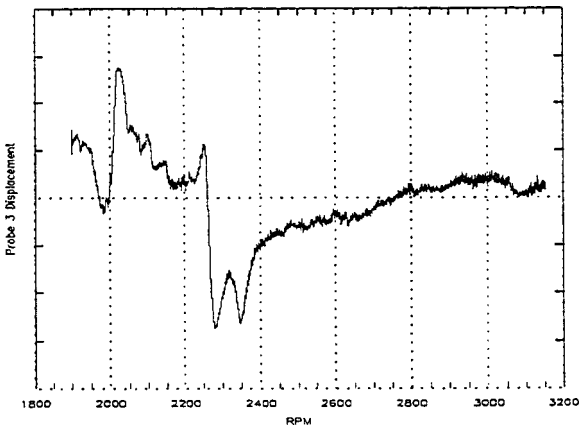

Fig. 8 Measured displacement versus speed plot

The actual measured displacement values will not be given in this discussion as the purpose is to illustrate the application of the two-parameter method.

The turbine vibration was measured solely using tip-timing but the characteristics of each resonance can be inferred from previous measurements and theoretical predictions. Using this prior knowledge, mode 1 in Table 7 can be identified as a 4 engine order resonance whilst modes 2 and 3 can be identified as 2 engine order resonances each with distinct mode shapes.

A typical two-parameter plot for the speed range 2200 to 2450 RPM is shown in Fig. 9. There are two distinct but incomplete ellipse shapes in the two parameter plot, the smaller ellipse being due to mode 3. For the purposes of this study and to show the benefits of the two-parameter analysis method, identification of the two close modes numbers 2 and 3 will be considered. Automated analysis of the two parameter plots was performed using an ellipse fitting procedure.[2] The data to be analyzed should contain a single distinct ellipse shape and therefore data in the speed ranges 2200 to 2315 RPM and 2300 to 2450 RPM were analyzed separately. Figure 10 shows the results of an automated ellipse fit to a two-parameter plot for measurements taken between 2200 and 2315 RPM.

Table 7 Resonances identified from displacement versus speed plots

Mode Number	Speed Range (RPM)
1	1950-2100
2	2200-2315
3	2300-2450

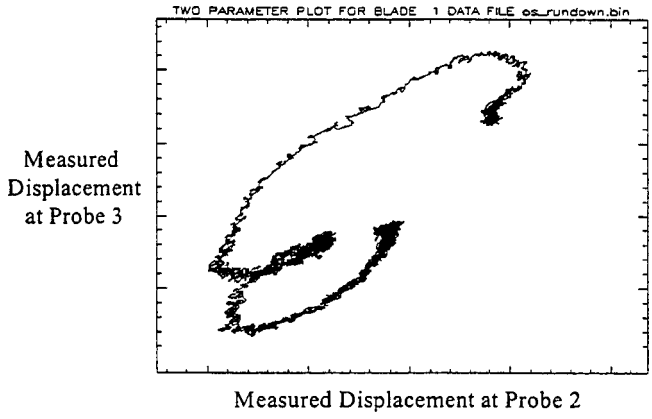

Fig. 9 Measured two-parameter plot for speed range 2200 to 2450 RPM

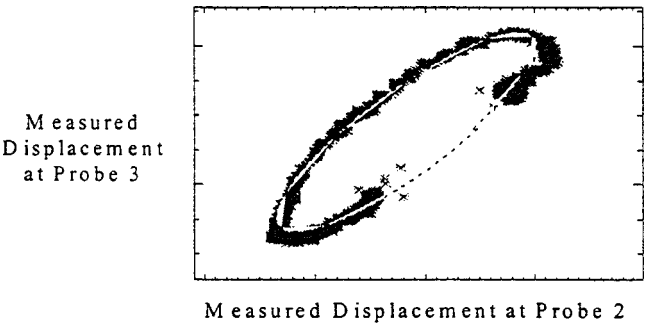

Fig. 10 Results of ellipse fit to two-parameter data for speed range 2200 to 2315 RPM

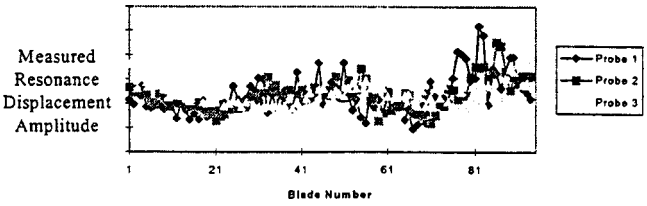

Fig. 11 Mode 2 amplitude at probes 1 to 3

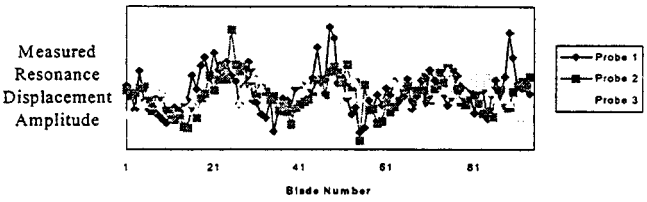

Fig. 12 Mode 3 amplitude at probes 1 to 3

The ellipse fit of Fig. 10 shows how the two-parameter plot method can be used to identify the characteristics of close modes. The maximum amplitude of the resonance was taken as the average of the maximum to minimum values of the ellipse in the x and y-axis directions. For an axis angle of 45 deg the maximum to minimum value in the x-axis direction should be the same as the maximum to minimum value in the y-direction. The closeness of the axis angle to ± 45 deg can be used as an indicator of the quality of the ellipse fit. The relative resonance amplitude for modes 2 and 3 has a maximum value of 0.0015 implying that the errors in the two-parameter plot analysis will be small. The results of the amplitude and order analysis for modes 2 and 3 are given in Figs. 11–14. The two-parameter analysis correctly identifies the resonance order for modes 2 and 3 and allows the resonance amplitude to be determined when this would not have been possible from the displacement versus speed plots using the Zablotsky-Korostelev analysis method. The resonance order will be the same for all blades and is taken as the integer value closest to the mean of the plots of order versus blade number. The automated two-

[2]The use of ellipses to characterize two-parameter plots had been previously shown to produce minimal errors in derived axis ratio and angle using multi-degree-of-freedom response data.

Downloaded 02 Jun 2010 to 171.66.16.119. Redistribution subject to ASME license or copyright; see http://www.asme.org/terms/Terms_Use.cfm

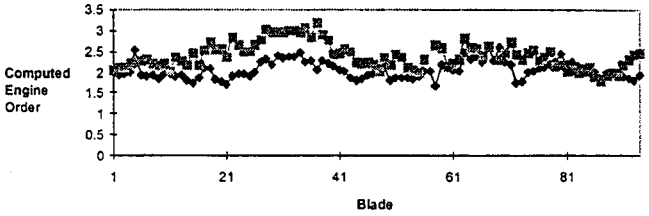

Fig. 13 Mode 2 order from two-parameter analysis of two decelerations

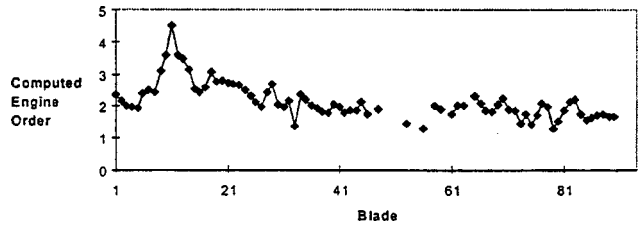

Fig. 14 Mode 3 order from two-parameter analysis of one deceleration

parameter ellipse analysis is currently performed off-line as it can take several hours depending on the number of data points and blades to be analyzed.

3 Future Tip-Timing Research and Application

Real-time analysis methods for synchronous resonances give continuous values for synchronous response amplitude and order. There is minimal published information on these methods and the author in common with other workers in the field has considered the use of curve fitting techniques using response parameters from four probes. This approach comes from considering the response to be of the form:

$$x = A_n \cos(\omega_n t + \psi_n) + C_n, \tag{8}$$

where x is the response amplitude at time t, A_n, and ψ_n are the response amplitude and phase, C_n is a fixed measurement offset, and ω_n is the response frequency. The measurements of displacement and time at each probe give four equations of the form of (8) which can be solved for response frequency, amplitude, phase and offset. Evaluation of the method using numerical response data has shown it to be sensitive to measurement noise. Alternative curve fitting methods using up to six probes are currently being investigated.

The author's group currently have no tip-timing analysis methods for continuous calculation of synchronous response amplitude and frequency using a practical number of probes. Consequently, tip-timing cannot be used as a vibration safety monitoring system when damaging synchronous resonances may be present. The applications of tip-timing are therefore limited and potential users of the measurement system data always see a clear advantage in using strain gauges. Nevertheless, as users see the advantages of having vibration data for all blades and thus knowing the true maximum operating stresses, the pressure to improve synchronous resonance identification capability increases. In addition, users can also see the financial, and time-scale, benefits of routinely using tip-timing instead of strain gauges.

Ongoing tip-timing research is focusing on direct synchronous response identification techniques using a variety of methods and a maximum of six probes (initially). It is hoped that the fruits of this research program will be harvested in the year 2000 and that the use of tip-timing vibration measurements systems and acceptance of the technique will grow even more rapidly thereafter.

4 Concluding Remarks

1 A new indirect tip-timing analysis method, the two-parameter plot method, has been developed for identifying the maximum resonance amplitude and order of synchronous resonances. The method requires only two casing mounted probes and has been successfully applied to turbomachinery tip-timing vibration measurements.

2 The accuracy of the two-parameter method is affected by relative resonance amplitude and mistuning. The errors have been quantified and are considered generally acceptable but the form of two-parameter plot must be used as a guide to the validity of the results obtained. The accuracy of the method can be improved by considering sets of measurements from more than two probes.

3 The two-parameter method allows the amplitude and order of close modes to be identified which is not possible using the industry standard Zablotsky-Korostelev analysis method.

4 Ongoing tip-timing research is focused on providing direct synchronous response analysis techniques for the year 2000. Once these techniques are available, tip-timing will be a realistic alternative to strain gauging for all rotating assembly vibration measurements.

5 Refinement and upgrading of the tip-timing acquisition and display system is taking place and is scheduled to be completed in the year 2000. The resulting tip-timing measurement system ought to be usable by people other than vibration measurement specialists and consequently more widely used within and outside Rolls-Royce.

Acknowledgments

Part of this research program was jointly funded by EPSRC and Rolls-Royce plc and carried out at Imperial College, London between October 1992 and October 1995. The remainder of the research since October 1995 has been funded by Rolls-Royce plc. The author is grateful to Dr. M. Imregun of Imperial College and Mr. P. Loftus of Rolls-Royce plc for their continuing support and encouragement of this tip-timing analysis method research program. The opinions expressed in this paper are those of the author and are not necessarily the opinions of Rolls-Royce plc.

References

[1] Endoh, M., Matsuda, Y., and Matsuki, M., 1983, ''Non-Contact Measurement of Rotating Blade Vibrations,'' *International Gas Turbine Congress*, Tokyo, pp. 953–960.

[2] Heath, S., and Imregun, M., 1997, ''A Review of Analysis Techniques for Tip-Timing Measurements,'' ASME Paper 97-GT-213.

[3] Zablotsky, I. Ye., and Korostelev, Yu. A., 1970, ''Measurement of Resonance Vibrations of Turbine Blades with the ELURA Device,'' Energomashinostroneniye, **2**, No. 2, pp. 36–39.

[4] Chi, R. M., and Jones, H. T., 1988, ''Demonstration Testing of a Non-Interference Technique for Measuring Turbine Engine Rotor Blade Stresses,'' *AIAA/SAE/ASME/ASEE 24th Joint Propulsion Conference*, Boston, MA, AIAA-88-3143.

[5] Heath, S., and Imregun, M., 1996, ''An Improved Single-Parameter Tip-Timing Method for Turbomachinery Blade Vibration Measurements Using Optical Laser Probes,'' Int. J. Mech. Sci., **38**, No. 10, pp. 1047–1058.

[6] Zielinski, M., and Ziller, G., 1997, ''Optical Blade Vibration Measurement at MTU,'' AGARD PEP Symposium—Advanced Non-Intrusive Instrumentation for Propulsion Engines, Brussels.

[7] Schaber, U., 1997, ''Non-Contact Vibration Measurement of Mistuned Coupled Blades,'' ASME Paper 97-GT-190.

Downloaded 02 Jun 2010 to 171.66.16.119. Redistribution subject to ASME license or copyright; see http://www.asme.org/terms/Terms_Use.cfm

Active Control of Discrete-Frequency Turbomachinery Noise Using a Rotary-Valve Actuator

Scott D. Sawyer
Department of Mechanical Engineering,
University of Akron,
Akron, OH 44323

Sanford Fleeter
Department of Mechanical Engineering,
Purdue University,
West Lafayette, IN 47907

Turbomachine discrete-frequency tones, a significant environmental concern, are generated by rotor-stator interactions. Specific spatial modes are generated, but not all generated modes propagate to the far field. It is the propagating spatial modes generated by rotor-stator interaction that represent the community-disturbing far field discrete-frequency noise. Fundamental active airfoil source discrete-frequency noise control experiments are performed, with the active airfoil source control optimized to generate propagating spatial modes to cancel the propagating spatial modes generated by the rotor-stator interaction. These experiments demonstrate the viability and effectiveness of rotary-valve discrete-frequency noise control. Specifically, the active noise control system combines the active airfoil source control with in-duct spatial mode measurement. In this unique design, the active airfoils of the stator vane row are driven by a remote centerbody-mounted rotary-valve system. Propagating spatial mode reductions of 5 dB and 9 dB upstream and downstream with negligible modal spillover are demonstrated. [S0742-4795(00)02702-2]

Introduction

In the design of advanced gas turbine engines, aeroacoustics is an increasingly important issue. In addition to meeting the long term performance requirements of increased fuel efficiency, decreased weight, and improved reliability and maintainability while being competitively priced, engine certification requires meeting prevailing noise regulations such as the U.S. FAR 36 Stage 3 rules which are to be implemented through the end of this decade. In addition, more stringent noise level guarantees are often required of the engine manufacturer by airlines to meet tougher local airport noise requirements. Also, there is a near certainty that more stringent Stage 4 requirements will require an additional reduction of 5–10 dB in the effective perceived noise level.

Figure 1 shows the primary noise sources for a high bypass turbofan engine: the fan, the low-pressure or boost compressor, and the low-pressure turbine [1,2]. Their noise signatures include a broadband noise level with large spikes or tones at multiples of blade passing frequencies. For subsonic fans, the acoustic spectrum discrete tones are usually 10–15 dB above the broadband level. The discrete-frequency tones may not contribute significantly to the overall noise level but are the main source of objectionable noise at take-off and landing.

Current cutting edge fan designs have high-bypass-ratio, wide-chord fans with low blade counts. These designs feature closely spaced blade rows with short length-to-diameter ratio nacelles that limit the effectiveness of the traditional combination of passive turbomachinery noise source control and suppression. Hence, engine broadband and discrete-frequency noise characteristics are often determined very early in the design, with further noise reduction only achievable through active noise control.

Active noise control by nature provides no performance benefit. Thus, the design of the active noise control system must limit the performance detriment while maintaining acceptable noise control and minimizing the complexity and weight of the system to maximize robustness and minimize cost.

Contributed by the International Gas Turbine Institute (IGTI) of THE AMERICAN SOCIETY OF MECHANICAL ENGINEERS for publication in the ASME JOURNAL OF ENGINEERING FOR GAS TURBINES AND POWER. Paper presented at the International Gas Turbine and Aeroengine Congress and Exhibition, Indianapolis, IN, June 7–10, 1999; ASME Paper 99-GT-403. Manuscript received by IGTI March 9, 1999; final revision received by the ASME Headquarters January 3, 2000. Associate Technical Editor: D. Wisler.

Active noise control has also been analytically modeled and experimentally demonstrated. Smith et al. [3] applied an active control system to reduce inlet noise radiating from the fan of a JT15D turbofan engine. The control sound field was generated by a circumferential array of 12 actuators mounted on the inlet. Large area microphones placed outside the inlet in the acoustic far field provided the error signals. The control system utilized a feedforward adaptive filtered algorithm. The 28 bladed rotor was excited by 27 rods mounted upstream of the rotor, generating four propagating spatial modes. With the three error microphones placed outside the engine, global discrete-frequency noise control was achieved in real-time.

Before an active noise control system can be realized, it is beneficial to consider the character of the discrete-frequency noise problem. Discrete-frequency tones are generated by periodic unsteady aerodynamic interactions between adjacent blade rows. Namely, turbomachine blade rows are subject to temporally nonuniform flow fields resulting from either potential or viscous wake interactions of upstream and downstream blade rows or inlet distortions. Thus, the airfoils exist in an unsteady velocity field. The no through-flow boundary condition at the airfoil surface results in unsteady surface pressure distributions in response to these excitations. Due to the harmonic nature of the excitation, the surface pressure response on adjacent airfoils is equal in amplitude and shifted in phase by the interblade phase angle. The airfoil unsteady surface pressures couple with the duct and produce spatially periodic acoustic waves that may propagate or decay with axial distance in the duct. Acousticians know these spatially periodic acoustic waves as spatial modes.

The goal of active airfoil source control is the cancellation of the propagating modes generated by a rotor-stator interaction. This is accomplished with actuators mounted one per stator airfoil [4,5]. These actuators are driven at blade pass frequency, where the control signal of adjacent actuators is equal in amplitude and shifted in phase by the interblade phase angle. Thus, the rotor-stator interaction is directly analogous to the active airfoil, with the active airfoil generating the same spatial modes. The active control spatial modes have the same propagation/decay characteristics as the rotor-stator generated spatial modes. Sawyer and Fleeter [6] demonstrated active airfoil source control for the simultaneous control of both upstream and downstream propagating spatial modes. This system is optimized for the control of rotor-

 Copyright © 2000 by ASME

Downloaded 02 Jun 2010 to 171.66.16.119. Redistribution subject to ASME license or copyright; see http://www.asme.org/terms/Terms_Use.cfm

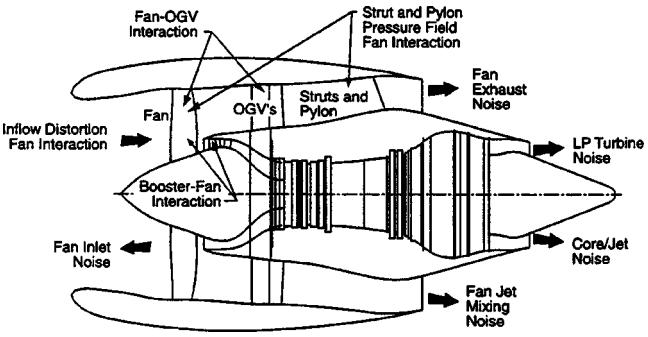

Fig. 1 Turbomachine noise sources

stator generated propagating spatial modes that represent the discrete-frequency noise received by an observer.

The above noise control techniques have one thing in common: the use of compression driver type acoustic elements. These drivers and the required control and amplification hardware are complex, expensive and heavy. Thus, the overall objective of this paper is to develop and demonstrate the viability of a relatively simple and inexpensive but robust rotary-valve actuator. In this unique design, the active airfoils of the stator vane row are driven by a remote centerbody-mounted rotary-valve system. This is accomplished through fundamental experiments performed in the Purdue Rotating Annular Cascade Facility directed at investigating the characteristics, performance and viability of the rotary-valve actuator.

Discrete-Frequency Noise Generation and Control

The classical model of discrete-frequency noise in a turbomachine considers a rotor and stator in an annular duct [7]. For example, in a multistage turbomachine unsteady pressure is generated on stator rows due to the periodic wakes of an upstream rotor blade row and the potential fields of upstream and downstream rotor blade rows. These unsteady stator vane surface pressures are the source of turbomachine discrete-frequency noise at multiples of the rotor blade pass frequency. The stator row unsteady loading then couples to the duct to produce acoustic waves.

The acoustic response of the stator row is characterized as the superposition of spatial modes, where the generated spatial modes are a function of the number of rotor blades and stator vanes. A spatial mode is described as a lobed pressure pattern where the spatial mode order is equal to the number of lobes. The propagation, resonance, or decay of a spatial mode is specified by the axial wave number. Of the generated modes, only certain modes propagate to the far field. It is these propagating modes which represent the discrete-frequency noise received by an observer. These acoustic response characteristics are important to properly explain the measured acoustic response due to rotor-stator interactions and to provide the necessary understanding of the basic concepts of an active discrete-frequency noise control system.

Annular Duct Acoustics

The unsteady flow in an annular duct is described by the wave equation for a uniform axial flow, derived by considering the inviscid, compressible flow with small unsteady perturbations.

$$\left(\frac{\partial}{\partial t}+U_\infty\frac{\partial}{\partial \xi}\right)^2 p=A_\infty^2\left(\frac{1}{r}\frac{\partial}{\partial r}\left(r\frac{\partial}{\partial r}\right)+\frac{1}{r^2}\frac{\partial^2}{\partial \theta^2}+\frac{\partial^2}{\partial \xi^2}\right)p, \quad (1)$$

where p is the acoustic pressure, A_∞ is the freestream speed of sound, U_∞ is the freestream axial velocity, and ξ, r, and θ are the axial, radial and circumferential coordinates.

The acoustic pressure is a function of radius and is harmonic in time, axial distance and polar angle.

$$p(\xi,r,\theta,t)=\overline{p}(k_\mu r)e^{i(k_\xi\xi+k_\theta\theta-nN_{\text{Blades}}\Omega t)}, \quad (2)$$

where $\omega=nN_{\text{Blades}}\Omega$ is a multiple of blade pass frequency, n is the rotor harmonic, k_θ is the spatial mode order, k_ξ is the axial wave number, $\overline{p}(k_\mu r)$ describes the radial variation of the pressure, and k_μ is a radial eigenvalue.

The spatial modes generated by a rotor-stator interaction are a function of the number of rotor blades and stator vanes $k_\theta=nN_{\text{Blades}}+mN_{\text{Vanes}}$, where $m=0,\pm1,\pm2,\ldots$ is an arbitrary integer. Not all of the generated modes will propagate to the far field. The propagation, resonance or decay of a spatial mode is determined by the axial wave number k_ξ.

Far Field Discrete-Frequency Noise

Although an infinite number of spatial modes are generated by the rotor-stator interaction at the harmonics of blade passage frequency, only certain of these modes propagate to the far field, with the rest decaying before reaching the far field. Thus it is only those propagating spatial modes that represent the discrete-frequency noise received by an observer. The propagation of the acoustic pressure modes is specified by the axial dependence of the duct pressure waves, i.e., the axial wave number, specifically the expression under the radical of

$$k_\xi=\frac{k_\omega M}{1-M^2}\pm\sqrt{\left(\frac{k_\omega M}{1-M^2}\right)^2+\frac{k_\omega^2-k_\mu^2}{1-M^2}}, \quad (3)$$

where M is the freestream Mach number and $k_\infty=\omega/A_\infty$ is the compressible reduced frequency.

- $k_\omega^2-k_\mu^2(1-M^2)>0$. There are two real k_ξ values corresponding to two propagating pressure waves, one upstream and the other downstream.
- $k_\omega^2-k_\mu^2(1-M^2)<0$. There are two complex k_ξ values corresponding to two decaying waves, one upstream and the other downstream.
- $k_\omega^2-k_\mu^2(1-M^2)=0$. This is a resonance condition, with the resonant frequency known as the cut-off frequency because below the cut-off frequency the pressure waves decay in the axial direction or are ''cut-off.''

Experimental Facility and Instrumentation

The experiments were performed in the Purdue Rotating Annular Cascade Research Facility, Fig. 2. This facility is an open loop draw through type wind tunnel capable of test section velocities of 220 ft/s. The flow, conditioned by a honeycomb section and an acoustically treated inlet plenum, accelerates though a bellmouth inlet to the constant area annular test section. The flow exiting the test section is diffused into a large acoustically treated exit plenum. The flow is drawn through the facility by a 300 hp centrifugal fan located downstream of the exit plenum. An optical pickup on the rotor shaft is utilized to determine the rotor shaft speed.

Two arrays of 10 Piezotronics Inc. PCB 103A piezoelectric microphones with uniform circumferential spacing are mounted via static pressure taps in the outer wall of the inlet annulus, Fig. 2. The microphones have a nominal sensitivity of 1500 mV/psi and a natural frequency of 13 kHz. The microphones are calibrated as installed in the rig and show linear amplitude response and flat frequency response in the region of interest. Experimental error in the pressure measurement is within 3 percent amplitude and 5 deg phase. The Nyquist critical mode $k_{\theta,\text{critical}}$ is 5 for the ten-microphone array, with all spatial modes above the Nyquist critical mode aliased below the Nyquist mode.

The annular test section is configured with a rotor with 16 NACA 0024 airfoils upstream of a stator with 18 NACA 65A012 airfoils with a 15.24 cm (6.00 in.) chord. The 16 rotor blades and 18 stator vanes generate $k_\theta=n16+m18$ spatial modes, where n is the rotor harmonic, and m is an arbitrary integer. Therefore, the

Downloaded 02 Jun 2010 to 171.66.16.119. Redistribution subject to ASME license or copyright; see http://www.asme.org/terms/Terms_Use.cfm

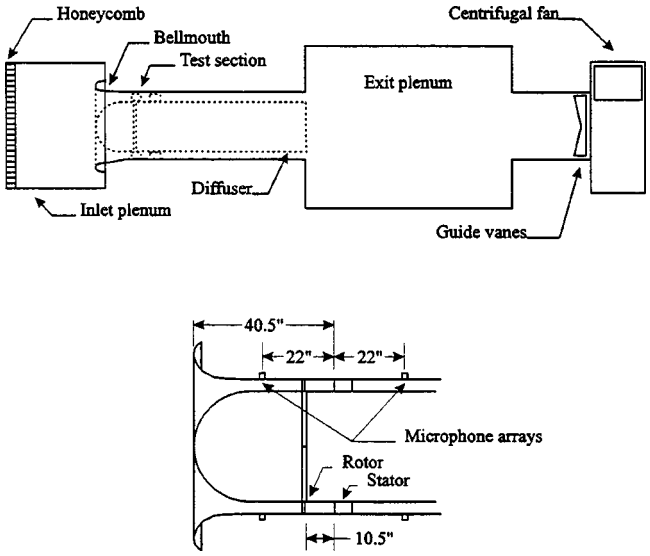

Fig. 2 Purdue annular cascade facility

spatial modes $k_\theta = \ldots, -20, -2, 16, \ldots$ are generated at blade pass frequency. At twice blade pass frequency, the spatial modes $k_\theta = \ldots, -22, -4, 14, \ldots$ are generated by the rotor-stator interaction. For typical operating conditions from 800 to 1000 rpm, only the $k_\theta = -2$ mode at blade pass frequency and the $k_\theta = -4$ at twice blade pass frequency are cut-on. The interblade phase angle of the 16 bladed rotor and the 18 vaned stator is -320 deg.

Active Discrete-Frequency Noise Control

The far field discrete-frequency noise of a turbomachine received by an observer is composed of spatial modes generated at multiples of rotor blade pass frequency that have propagated in the duct and have radiated to the acoustic far field. These discrete-frequency tones are generated by rotor-stator interactions and can be characterized through the measurement of the modal structure in the duct both upstream and downstream of the airfoil rows. The function of the active noise control system is the cancellation or reduction of the propagating acoustic modes in the duct, i.e., before the modes are radiated to the far field. The active noise control system utilizes active airfoil source control that mimics the rotor-stator interaction and is optimized for control of the propagating acoustic modes generated by the rotor-stator interaction. Additionally, on-airfoil actuators minimize the actuator power requirements.

The spatial modes and the excitation frequency characterize an acoustic wave generated by the rotor-stator interaction. The number of rotor blades and stator vanes specifies the spatial modes generated $k_\theta = nN_{\text{Blades}} + mN_{\text{Vanes}}$. Ideally, the active control system and the rotor-stator interaction produce the same propagating acoustic waves. This enables the active control system to cancel the rotor-stator generated propagating waves, resulting in no discrete-frequency noise in the far field. The interaction of a 16 blade rotor and an 18 vane stator generates a $k_\theta = -2$ propagating spatial mode at blade pass frequency. The stator equipped with active source control also generates a $k_\theta = -2$ propagating spatial mode at blade pass frequency. If the noise generated by the active source control is properly phased relative to the noise generated by the rotor-stator interaction, the result is complete cancellation of the discrete-frequency noise in the duct.

The source of the discrete-frequency noise is the unsteady loading on the stator airfoils, with the unsteady loading of adjacent airfoils equal in magnitude and shifted in phase by the interblade phase angle. The active noise control system is realized by placing an acoustic source on each stator vane. Driving successive acoustic sources on adjacent stator vanes by signals that are equal in magnitude and shifted in phase by the interblade phase angle, the acoustic sources and the rotor-stator interactions generate the same spatial modes. Note that cancellation of the rotor-stator interaction noise at a location upstream or downstream implies that that spatial mode is cancelled everywhere in the duct. Since the control and source are coincident (i.e., on the stator vane), the control and source spatial modes will have exactly the same reflection, transmission and scattering characteristics.

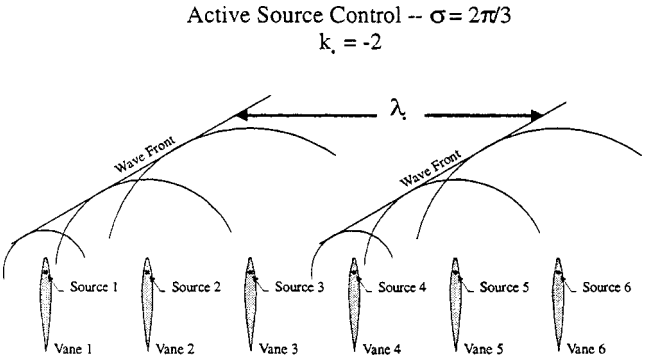

Fig. 3 Vane to vane phase shift of acoustic pressure and active control voltage

The generation of a propagating spatial mode can be considered as a coalescence of waves from the stator vanes. This is shown schematically in Fig. 3 where a $k_\theta = -2$ spatial mode is generated by a six airfoil stator. The spatial modes generated by the acoustic sources will propagate or decay upstream and downstream in the same manner as the spatial modes generated by the rotor-stator interactions.

For example, a 16 blade rotor interacting with an 18 vane stator generates the $k_\theta = \ldots, -20, -2, 16, \ldots$ spatial modes at blade pass frequency. At 1000 rotor shaft rpm, only the $k_\theta = -2$ mode propagates to the far field. The spatial modes propagating upstream and downstream are characterized by the complex amplitudes $P_{\text{gust,up}}(k_\theta = -2)$ and $P_{\text{gust,down}}(k_\theta = -2)$. The propagating modes that will be canceled through active control, as illustrated in Fig. 4.

The control system is assumed to be linear with the control signal input amplitude. Therefore, the active control system is characterized by the generated complex amplitudes $P_{A,\text{up}}(k_\theta = -2)A$ and $P_{A,\text{down}}(k_\theta = -2)A$, where $P_{A,\text{up}}(k_\theta = -2)$ and $P_{A,\text{down}}(k_\theta = -2)$ are the influence coefficients generated by the actuator, and A is the complex amplitude of the control signal. The measured response due to the active control system and the rotor stator interactions are

$$P_{\text{measured,up}} = P_{\text{gust,up}} + P_{A,\text{up}}A$$
$$P_{\text{meaured,down}} = P_{\text{gust,down}} + P_{A,\text{down}}A. \tag{4}$$

The amplitude and phase of the source control signal can be set to reduce the upstream $P_{\text{measured,up}} = 0$ or the downstream

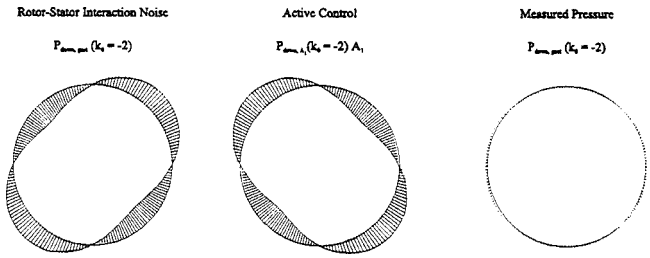

Fig. 4 Active control of $k_g = -2$ mode in the downstream duct

Downloaded 02 Jun 2010 to 171.66.16.119. Redistribution subject to ASME license or copyright; see http://www.asme.org/terms/Terms_Use.cfm

$P_{\text{measured,down}}=0$ propagating mode. Solving Eq. 4 for the complex control signal amplitude to reduce the upstream propagating mode $P_{\text{measured,up}}=0$ yields

$$A=-\frac{P_{\text{gust,up}}}{P_{A,\text{up}}}. \tag{5}$$

Solving Eq. 4 for the complex control signal amplitude to reduce the downstream propagating mode $P_{\text{measured,down}}=0$ yields

$$A=-\frac{P_{\text{gust,down}}}{P_{A,\text{down}}}. \tag{6}$$

To reiterate, the cancellation of one rotor-stator generated propagating spatial mode $P_{\text{gust,up}}$ or $P_{\text{gust,down}}$ requires a set of acoustic sources. The acoustic sources will produce upstream and downstream going spatial modes. When the acoustic sources are driven at the proper amplitude and phase, cancellation of a propagating spatial mode is possible. The measured acoustic pressure of the propagating mode is equal to the superposition of the rotor-stator noise with that due to the active control system.

Active Airfoil Source Control

The central components of this active noise control system are the active stator airfoils that generate propagating spatial modes analogous to those of the rotor-stator interaction. The acoustic sources are driven at the excitation frequency and have the same phase shift from stator vane to stator vane. Thus, the active control system mimics the rotor-stator interaction and generates a $k_\theta=-2$ spatial mode.

The twin-cavity active airfoil with perforated metal sheathing is shown in Fig. 5. The cavity access ports located on the airfoil hub allow the airfoil to be driven by a remote centerbody-mounted acoustic source. The microperforated sheathing minimizes the disturbance of the stator vane aerodynamics while providing only minor resistance to the acoustic radiation from the cavity. The perforated screen has 0.010 in. diameter holes and a 30 percent open area.

The dimensions of the connector and vane cavity were selected such that the cavity and the tube formed a resonator tuned to the rotor blade pass frequency at 1000 rotor shaft rpm (267 Hz). This resonator configuration provided an amplification of 12 dB relative to the compression driver alone. This configuration is also characterized by a sufficiently broad bandwidth necessary to achieve a useful operating range in the laboratory environment.

Both the upper and lower surface actuators generate upstream and downstream going propagating spatial modes. The active control system is setup to naturally mimic the rotor-stator interaction noise, with the physics that governs the rotor-stator interactions also applying to the active noise control system.

Rotary-Valve Actuator

A schematic of the rotary-valve assembly is shown in Fig. 6. The major components are the step motor drive, the rotary-valve and the optical encoder. The step motor synchronizes the rotor shaft with the shaft of the rotary-valve. The optical encoder monitors rotation of the rotary-valve shaft to ensure the synchronicity of the rotor shaft and the rotary-valve shaft. The components of the rotary-valve are the rotating disk, the valve outer body, the air supply inlet ports and the outlet ports. The outlet ports are connected via flexible tubing to the active airfoils of the stator vane row.

A cross-section of the rotary-valve, Fig. 7, shows the notched rotary disk and the valve outer body with the 18 hose-barb outlet ports that are connected to the 18 active airfoils of the stator vane row. As the rotary-valve shaft rotates with the rotor shaft, the 16 notches of the rotary disk naturally open and close the outlet ports at blade pass frequency. For a 3.375 in. diameter disk, a 0.331 in. wide notch in the rotating disk in Fig. 8 gives a 50 percent duty cycle.

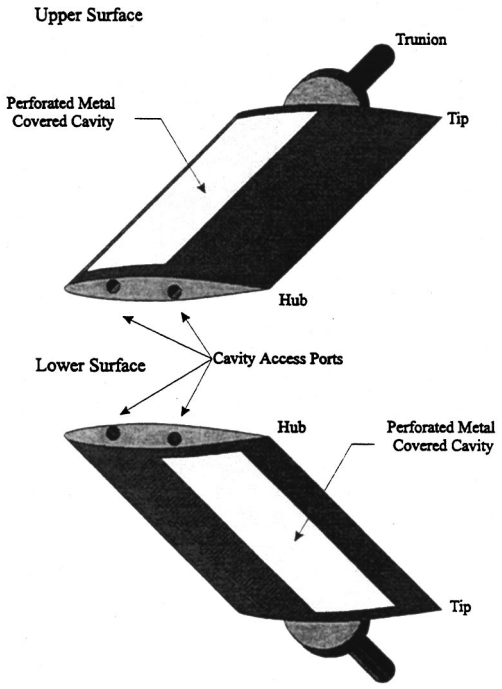

Fig. 5 Active stator airfoil

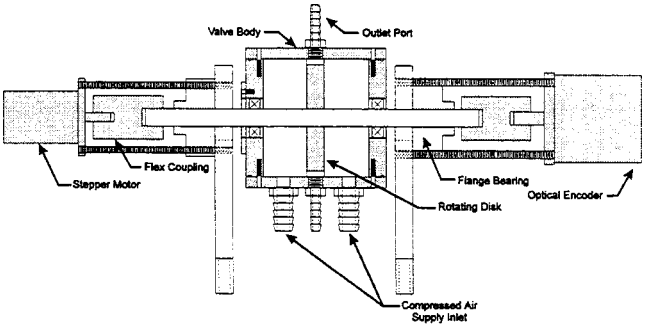

Fig. 6 Pressure pulse generator rotary-valve assembly schematic

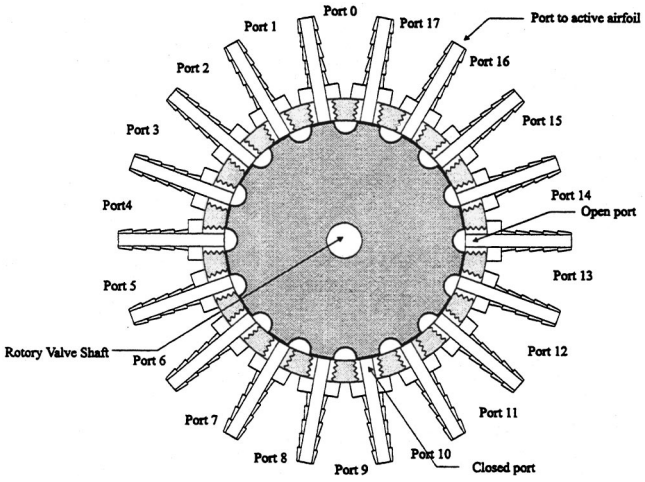

Fig. 7 Rotating disk and active airfoil ports

Downloaded 02 Jun 2010 to 171.66.16.119. Redistribution subject to ASME license or copyright; see http://www.asme.org/terms/Terms_Use.cfm

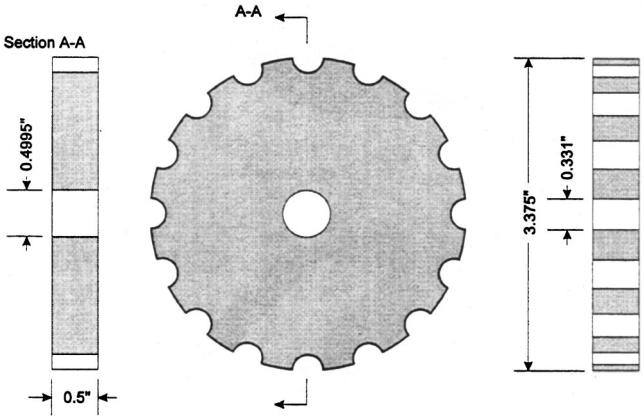

Fig. 8 Rotating disk

In correspondence with Fig. 7, Fig. 9 shows the open area of the outlet ports as the intersection of the rectangular notches in the rotating disk with the circular outlet ports. As the rotating disk rotates the outlet ports cycle from fully closed to fully open and back to closed.

The unsteady flow rate to an active airfoil is periodic in time where the flow rate to adjacent airfoils is equal in magnitude and shifted in phase. The number of notches and ports of the rotary-valve ensures the relative phase from airfoil to airfoil is equal to the interblade phase angle. Thus, the notch-port interaction is directly analogous to the rotor-stator interaction and, this system is mechanically optimized to cancel the propagating spatial mode generated by the rotor-stator interaction. In fact, this is apparent in Fig. 9 where a distinct two lobed interference pattern is formed as the outlet ports transition from fully closed to fully open. Rotation of the outer valve body shifts the phase of the open area curve, thus affecting the phase of the active control.

The shaft of the rotary-valve is driven by an Oriental Vextra step motor controlled by a Panther LD microstepping drive. The microstepping drive provides 800 steps per revolution. Proper phase and speed reference to the rotor drive shaft is insured by an 800 pulse per revolution optical encoder. The encoder output acts as the microstepping drive ''step'' input. Hence, the rotor drive shaft and the step motor are perfectly synchronized.

The acoustic response amplitude is controlled by the mass flow rate of air going through the system. The 18 active airfoil ports provide a steady flow rate going into the valve. This steady flow rate is measured using a rotameter. The phase of the acoustic excitation varies with the relative position of the rotary-valve disk and the valve outer body. The phase of the acoustic excitation is controlled using a belt attached to the valve outer body and a Hurst gear-head step motor with a ten-to-one reduction gear set.

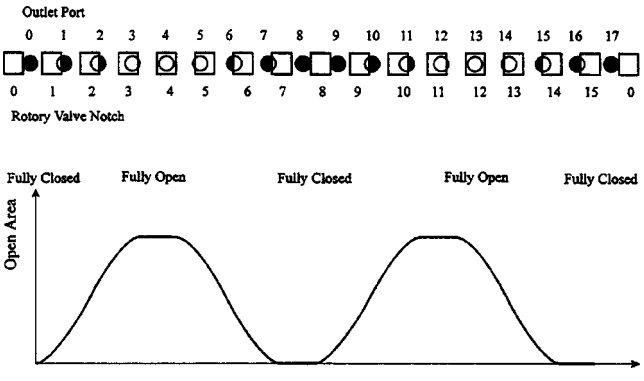

Fig. 9 Rotary-valve outlet port open area at an instant in time

The second step motor holds the outer valve body stationary while allowing phase adjustment. One step of the Hurst gear head motor corresponds to a 0.1 deg rotation of the valve body. Thus, the phase of the acoustic excitation can be controlled to within 1.8 deg.

In summary, the propagating spatial mode control is accomplished using active airfoil source control and in-duct spatial mode measurement. The active airfoil design allows the airfoil to be driven using a remote centerbody-mounted rotary-valve actuator.

Data Acquisition and Signal Processing

Acquisition and digitization of the microphone signals and the shaft trigger signal is accomplished using five National Instruments NB-A2000 analog-to-digital boards installed in an Apple Macintosh Quadra 950 computer. This system allows the simultaneous acquisition of twenty channels of data, initiated by the shaft trigger signal. Ensemble averaging over 100 rotor revolutions is utilized to reduce the random noise not phase-locked to the rotor.

A primary component of the active noise control system is the measurement of the propagating spatial modes [8,9] generated by both the rotor-stator interaction and the active airfoil source control system. The measured spatial modes not only characterize the baseline rotor-stator response, but also quantify the effectiveness of the active noise control system.

The discrete-frequency acoustic response is the superposition of spatial modes generated at the multiples of rotor blade pass frequency, with the acoustic modes at blade pass and twice blade pass frequency of primary concern. An array of microphones is required to determine the measured acoustic response as a function of both frequency and spatial mode. This temporal-spatial transform is accomplished using two discrete Fourier transforms. The first determines the frequency content of the microphone signals, and the second determines the amplitude of spatial modes at each frequency. The spatial transform, operating on the complex results of the temporal Fourier transform, separates the forward and backward spinning modes.

Results

To demonstrate the viability and the effectiveness of the airfoil rotary-valve discrete-frequency active noise control system, fundamental experiments are performed in the Purdue Rotating Annular Cascade Research Facility. Initial data sets were acquired without a rotor row installed and indicate the control air flow rate necessary to achieve significant noise reductions. The effect of high control air supply rates were also investigated in a sans rotor configuration. High control air flow rates per active airfoil were achieved using the 18-airfoil stator vane row with only two active airfoils. Thus, two opposing pressure ports were left attached to the two active airfoils while the remaining pressure ports were disabled. Hence, the flow rate available to the active airfoils was maximized.

Active discrete-frequency noise control was demonstrated using 16 NACA 0024 rotor wake generators. The experiments were performed at 1000-rpm rotor shaft rotation, and an axial freestream velocity of 36 ft/s. At this condition, the rotor-stator acoustic response is 0.001791 psi or 116 dB in the upstream duct and 0.00087 psi or 109 dB in the downstream duct. These represent the magnitude of the propagating spatial mode and are the quantities to be cancelled.

Figure 10 shows the propagating spatial mode measurements as a function of the rotary-valve air supply. These data were acquired in the absence of the rotor and represent the control authority of the control system. The maximum noise levels of 0.00021 psi (97 dB) and 0.00014 psi (94 dB) upstream and downstream, respectively are generated at the 18 cfm flow rate. As generated modes are smaller than the measured modes generated by the rotor-stator interaction, more air is required by the system to achieve a significant noise reduction.

Downloaded 02 Jun 2010 to 171.66.16.119. Redistribution subject to ASME license or copyright; see http://www.asme.org/terms/Terms_Use.cfm

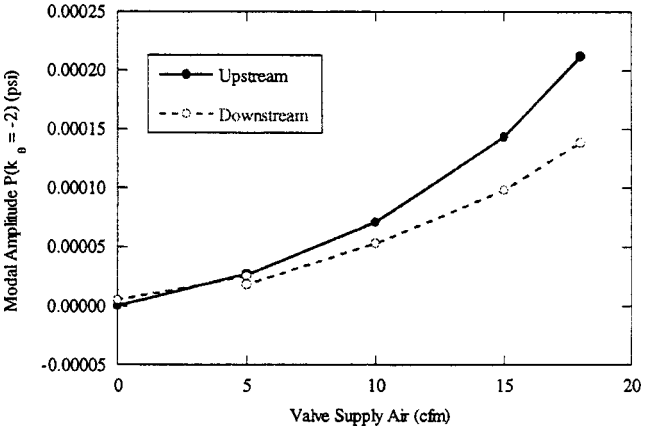

Fig. 10 Active control authority spatial mode magnitude as a function of rotary-valve flow rate

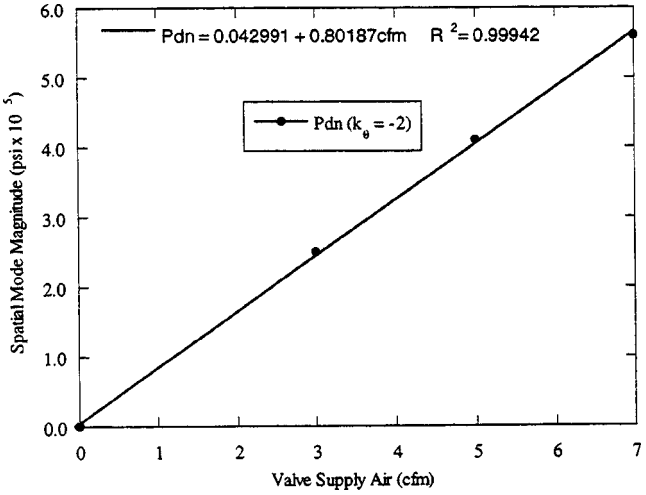

Fig. 12 Spatial mode magnitude as a function of rotary-valve air supply

The influence of a high flow rate per active airfoil was determined by closing all but two opposing ports of the rotary-valve. Figure 11 shows the propagating spatial mode measurements using only two active airfoils in the vane row. Notice the $k_\theta = -2$ through 2 spatial modes are cut-on at blade pass frequency, but only the $k_\theta = -2$, 0 and 2 spatial modes are generated by the two active vanes. For control air flow rates up to 7 cfm, there is a consistent character of the generated noise with very little modal spill over. The magnitude of the $k_\theta = -2$ spatial mode is shown in Fig. 12 as a function of the valve air supply for the two active vanes. Thus, these data show that the full vane cascade can be improved upon by increasing the flow rate available to the valve.

With the rotor fitted with 16 NACA 0024 airfoils, the interaction with the 18 active stator vanes produces a $k_\theta = -2$ propagating spatial mode at blade pass frequency. The influence of the valve phase angle on the spatial mode magnitude was determined at the maximum sustainable flow rate of 30 cfm (0.2 percent of total flow rate). This is shown in Fig. 13 using a linear scale and in Fig. 14 using a decibel scale.

A sinusoidal variation of spatial mode magnitude is seen in Fig. 13 where the control constructively and destructively interferes with the rotor-stator generated discrete-frequency noise. This corresponds to Fig. 14 where significant noise reduction is seen over a small range of valve phase angles. Assuming the measured response follows Eq. 4 $P_{\text{measured}} = P_{\text{gust}} + P_{A_1} A_1$, where A_1 is the

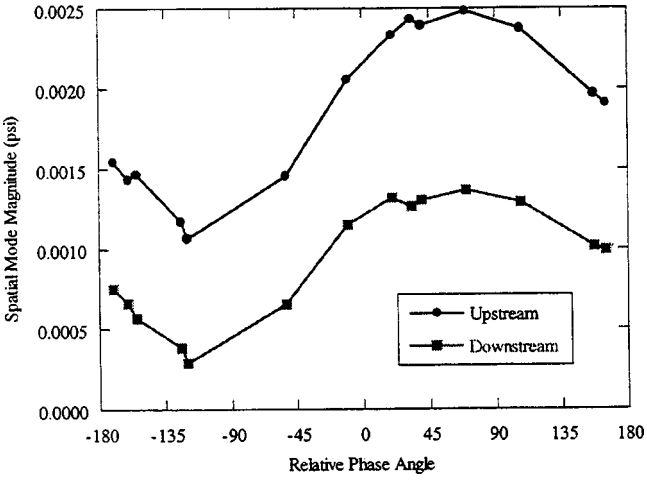

Fig. 13 Influence of valve phase angle on spatial mode magnitude

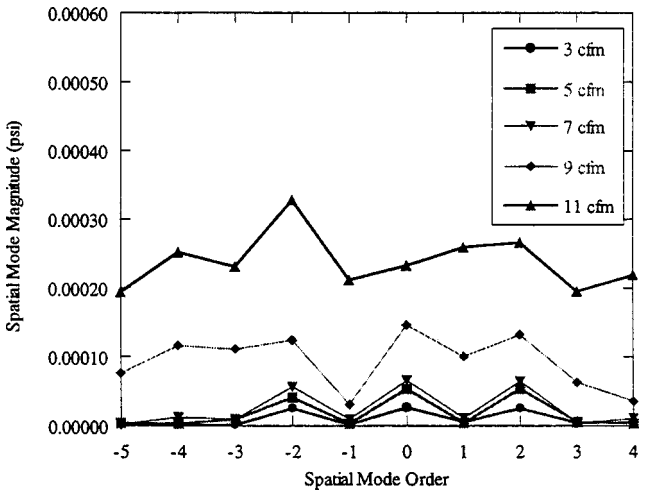

Fig. 11 Two vane rotary-valve discrete-frequency noise generation

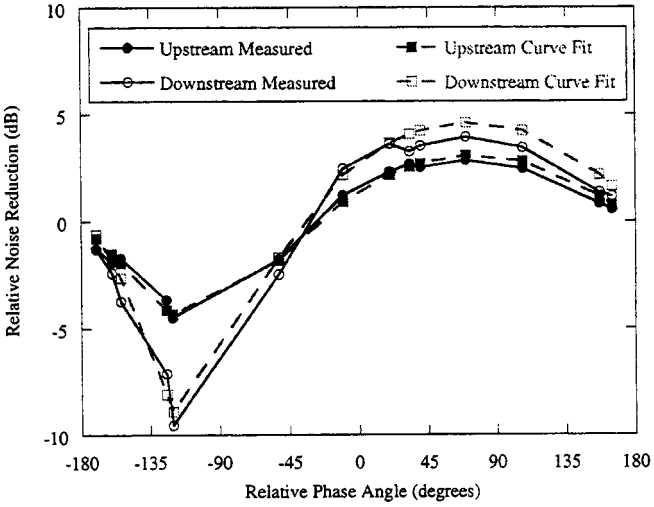

Fig. 14 Influence of valve phase angle on spatial mode magnitude

Downloaded 02 Jun 2010 to 171.66.16.119. Redistribution subject to ASME license or copyright; see http://www.asme.org/terms/Terms_Use.cfm

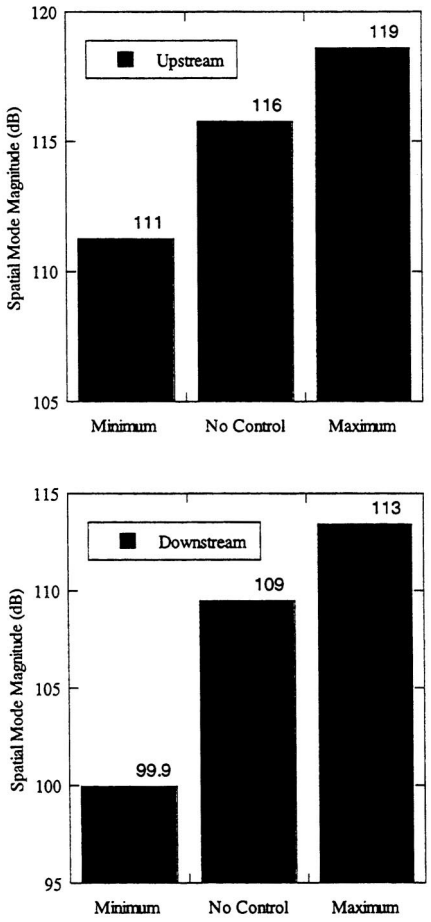

Fig. 15 Upstream control using rotary-valve active noise control system

control air flow rate, it is possible to determine the influence coefficient P_{A_1}. Equations 5 and 6 can then be used to estimate the control flow rate A_1 necessary for complete cancellation. Thus, the data indicate 71 cfm and 43 cfm are necessary for the complete cancellation of the upstream and downstream propagating spatial modes. Recall that two rotary-valves would be required to control the propagating spatial mode both upstream and downstream.

These active discrete-frequency noise control results are summarized in Fig. 15 that shows the uncontrolled, minimum and maximum levels achieved in Fig. 14. In the upstream duct, the 116 dB $k_\theta = -2$ propagating spatial mode is reduced to 111 dB for a 5 dB reduction. More control is exhibited in the downstream duct where the 109 dB $k_\theta = -2$ propagating spatial mode is reduced to 100 dB for a 9 dB reduction.

Summary and Conclusions

Advanced design high bypass turbomachines generate prominent discrete-frequency tones. These tones are generated by rotor-stator interactions, with specific spatial modes generated. However, only certain of these generated modes propagate to the far field, with the propagating spatial modes representing the far field discrete-frequency noise. High bypass turbomachines limit the effectiveness of current state-of-the-art acoustic treatments for suppression and source control. As prevailing noise regulations become ever more stringent, innovative control of turbomachine noise sources is increasingly important. Thus, a series of fundamental experiments was performed to demonstrate the effectiveness of active airfoil source control excited by a rotary-valve actuator.

In the active airfoil source control technique, the propagating spatial modes, i.e., the far field tone noise, are canceled through the generation of control propagating waves that cancel those modes generated by the rotor-stator interaction. The active airfoil source control is optimized for the control of propagating spatial modes. The active noise control system incorporates active airfoil source control with in-duct spatial mode measurements. The mechanical design of the rotary-valve actuator assures the generation of a $k_\theta = -2$ propagating spatial mode. The rotary-valve is simply controlled via the total flow rate and the relative position of the rotary valve body. The rotary-valve actuator demonstrated 5 dB and 9 dB reductions upstream and downstream at a flow rate equivalent to 0.2 percent of the freestream flow.

Nomenclature

A_∞ = freestream speed of sound
Q_μ = an eigenvalue
k_ξ = axial wave number
k_θ = tangential wave number
$k_{\theta,\text{critical}}$ = critical Nyquist mode
k_μ = an eigenvalue
M = axial mean flow Mach number
n = rotor harmonic
N = number of microphones
N_{Blades} = number of rotor blades
N_{Vanes} = number of stator vanes
p = acoustic pressure
r = radial coordinate
U_∞ = mean axial velocity
x = axial direction
θ = circumferential coordinate
ω = frequency $\omega = nN_{\text{Blades}}\Omega$
Ω = rotor circular frequency
Ω_p = pressure pattern phase speed
ξ = axial coordinate

References

[1] Gliebe, P. R., 1992, ''Aeroacoustics in Turbomachines and Propellers—Future Research Needs,'' *6th International Symposium on Unsteady Aerodynamics, Aeroacoustics, and Aeroelasticity of Turbomachines and Propellers*, H. F. Atassi, editor Springer-Verlag, New York and Berlin.
[2] Groeneweg, J. F., and Rice, E. J., 1987, ''Aircraft Turbofan Noise,'' ASME J. Turbomach., **109**, No. 1, pp. 130–141.
[3] Smith, J. P., Burdisso, R. A., and Fuller, C. R., 1996, ''Experiments on the Active Control of Inlet Noise From a Turbofan Jet Engine Using Multiple Circumferential Control Arrays,'' AIAA Paper 96-1792.
[4] Kousen, K. A., and Verdon, J. M., 1994, ''Active Control of Wake/Blade Row Interaction Noise,'' AIAA J., **32**, No. 10, pp. 1953–1960.
[5] Kousen, K. A., 1993, ''Multiple Mode Minimization of Wake/Blade-Row Interaction Noise Using a Single Actuator Per Blade,'' AIAA Paper 96-1691.
[6] Sawyer, S., and Fleeter, S., 1997, ''Active Control of Discrete-Frequency Noise Generated by Rotor-Stator Interactions,'' AIAA Paper 97-1689.
[7] Tyler, J. M., and Sofrin, T. G., 1962, ''Axial Flow Compressor Noise Studies,'' SAE Trans., **70**, pp. 309–332.
[8] Sawyer, S., and Fleeter, S., 1994, ''Mean Stator Loading Effect On The Acoustic Response Of A Rotating Cascade,'' AIAA Paper 94-2953.
[9] Sawyer, S., Feiereisen, J. M., and Fleeter, S., 1996, ''The Influence of Rotor Detuning on the Acoustic Response of an Annular Cascade,'' AIAA Paper 96-1689.

Downloaded 02 Jun 2010 to 171.66.16.119. Redistribution subject to ASME license or copyright; see http://www.asme.org/terms/Terms_Use.cfm

Exergy Analysis of Combined Cycles Using Latest Generation Gas Turbines

Bruno Facchini
e-mail: bruno@brun.de.inifi.it

Daniele Fiaschi
e-mail: danif@fias.de.unifi.it

Giampaolo Manfrida
e-mail: gpm@dicnet.ing.unifi.it

Dipartimento di Energetica 'Sergio Stecco',
Università degli Studi di Firenze,
Via Santa Marta, 3 50139, Firenze, Italy

The potential performance of optimized gas-steam combined cycles built around latest-generation gas turbine engines is analyzed, by means of energy/exergy balances. The options here considered are the reheat gas turbine and the H-series with closed-loop steam blade cooling. Simulations of performance were run using a well-tested Modular Code developed at the Department of Energy Engineering of Florence and subsequently improved to include the calculation of exergy destruction of all types (heat transfer, friction, mixing, and chemical irreversibilities). The blade cooling process is analyzed in detail as it is recognized to be of capital importance for performance optimization. The distributions of the relative exergy destruction for the two solutions—both capable of achieving energy/exergy efficiencies in the range of 60 percent—are compared and the potential for improvement is discussed. [S0742-4795(00)00902-9]

Introduction

The appearance on the exergy market of gas/steam combined cycles with efficiency exceeding 60 percent when fueled with natural gas [1] has posed the serious question of what is the actual limit of efficiency reachable by these up-to-date energy systems: even more important is to understand if there is still a margin for thermodynamic optimization within these plants, or if further improvements can only be obtained by major technological steps (such as water/steam closed loop cooling of turbine blades; hydrogen fueling with higher maximum cycle temperature [2]; addition of topping fuel cell modules; etc.) As for all new technologies, these steps need major expenditure on research and experimentation, and at the development stage offer lower reliability—which is a major concern to potential users, who would often rather select a mature technology if this could reach similar performance levels.

In order to provide an answer, a detailed study was performed considering two of the options of major interest to the present and near-future market:

(a) the Reheat Gas Tubine/Combined Cycle (RGT/CC), a solution represented on the market by the ABBGT24 and its developments
(b) the Closed-Loop Steam Cooled Gas Turbine/Combined Cycle (CLSCGT/CC), a technology being introduced on the market by GE and Siemens and known as H-series development

Even if the basic operating data of the two engines were kept as close as possible to published data (compressor flow rate, turbine inlet temperature, coolant flows, etc.), the possibility of adjusting the pressure ratio around the design value was considered in the light of improving the matching with the steam bottoming cycle. The model employed for simulation is that developed by Carcasci and Facchini [3], which has undergone thorough validation in many configurations and for different gas turbine engines; a distinctive feature of this model is its fully implicit nature, that is, there is no deterministic distinction between input and output data, but the model can operate effectively provided any set of consistent data. This has allowed a satisfactory prediction of performance even when many necessary data were missing from the manufacturer; this feature is also used for cross-checking the validity of the published data and to reconstruct the actual operating data from measured performances.

The model includes full treatment of cooling flows and the separate evaluation of the effects of blade cooling with a high degree of detail [4]. The modular code includes also the possibility of varying compressor and turbine sections efficiency as well as cooling-air flow as a function of pressure ratio for off-design analysis: for the present work, these features don't have relevance, since a simply thermodynamic study was carried on. The blade-cooling flowrate is only T_{Max} dependent (only adjusted to maintain fixed metal temperatures) and doesn't have any influence on the compressor pressure ratio, that is fixed at design operating conditions. Obviously, all the operating conditions and parameters are tuned with the ones relative to the studied machines—in the present study the GT24 and M9001 gas turbines—with a full agreement in the operating conditions. A recent addition to the code has been the complete exergy balance, including evaluation in all plant components of the effects of irreversibilities arising from different sources, such as the following

- heat transfer
- friction
- mixing of streams
- chemical reactions
- interaction with the environment

The detailed exergy balance is used in this study to compare the performance of plant sections and to understand the margins for potential performance improvement.

Cycle with Reheat Gas Turbine (RHGT/CC)

The RHGT gas turbine cycle is sketched schematically in Fig. 1. It looks like a conventional gas turbine cycle, except for the second combustion, realized after the first expansion in the high pressure turbine. The optimizing efficiency pressure ratio is displaced to relatively high values with reheat ($\beta \approx 30$ for $T_{\mathrm{IT}} = 1508$ K, as for the ABBGT24 engine).

The practice of reheat introduces some additional losses with respect to an equivalent simple cycle, that typically reduce by about $1 \div 2$ percentage points the improvement in efficiency; basically:

Contributed by the International Gas Trubine Institute (IGTI) of THE AMERICAN SOCIETY OF MECHANICAL ENGINEERS for publication in the ASME JOURNAL OF ENGINEERING FOR GAS TURBINES AND POWER. Paper presented at the International Gas Turbine and Aeroengine Congress and Exhibition, Indianapolis, IN, June 7–10, 1999; ASME Paper 99-GT-10. Manuscript received by IGTI March 9, 1999; final revision received by the ASME Headquarters January 3, 2000. Associate Technical Editor: D. Wisler.

Copyright © 2000 by ASME

Downloaded 02 Jun 2010 to 171.66.16.119. Redistribution subject to ASME license or copyright; see http://www.asme.org/terms/Terms_Use.cfm

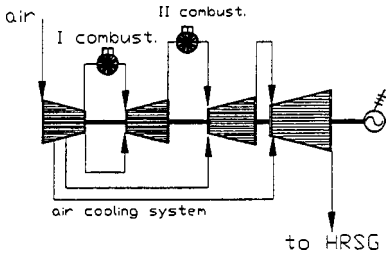

Fig. 1 Reheat gas turbine cycle

• a larger pressure drop is present with two combustion chambers;

• pressure losses are also added by the diffuser, needed to allow the correct fuel-gas aerodynamic conditions at the inlet of the second combustion chamber;

• the whole first turbine must be cooled because of the high operating temperature;

• the isentropic efficiency of the whole compression process is decreased (for equal levels of polytropic efficiency) due to the higher optimizing pressure ratio with respect to the simple cycle.

The main operating parameters and results for the cycle (representing closely data for the ABB GT24) with and without reheat (in this case for $\beta \approx 30$ and $\beta \approx 16$; this last is the value maximizing power output for the simple cycle) are summarized in Table 1. Increasing pressure ratio produces a 3 percent improvement in efficiency for the simple cycle, which is paid by a reduction in specific work (15 percent); the practice of reheat allows improvement efficiency of about 2.5 percent over the $\beta = 16$ solution, with a substantial recovery in specific work. Moreover, the reheat cycle exhaust gas temperature is high enough to allow a highly efficient Heat Recovery Steam Generator (HRSG).

Figure 2 shows the exergy destruction balance of the reheat gas turbine cycle, compared with that of the simple cycle. The sum of the two combustion chamber exergy destructions amounts to about 28.3 percent of the fuel exergy input, while in the simple, single combustor cycle the combustion irreversibility reaches 30.8 percent with $\beta = 16$ and 29.5 percent with $\beta = 30$. This beneficial effect is due to preheating in the second combustion (the oxidant stream enters the combustion chamber at 1200 K).

In order to reach comparable values of efficiency and specific work without reheat, the firing temperature should be raised to 1700 K, with significant drawbacks in terms of investment and maintenance costs. Reheat seems thus to be an effective way to improve the thermodynamic performance of gas turbine cycles avoiding relevant development problems.

An interesting feature of the reheat cycle is the possibility of altering the exhaust gas temperature by varying the reheat pressure level: this can be useful to improve coupling with the bottoming cycle. Figure 3 shows the behavior of the main performance parameters as a function of reheat pressure; good performance can be achieved at 16 bars, which represents a good compromise between specific work and efficiency. A reheat pressure value optimizing specific work (14 bars) was found. For each case, cooling flow to the reheat turbine section was adjusted to maintain correct values of metal temperature.

Table 1 GT cycle performance for three reference cases

	Simple Cycle	Simple Cycle	Reheat Cycle
Pressure Ratio β	16	30	30
H.P. GT Cycle firing Temp. [K]	1508	1508	1508
I.P. GT Cycle firing Temp. [K]	-	-	1508
Reheat Pressure [Bar]	-	-	16
Coolant flowrate / compressor flowrate	17.1	22.5	26.3
Gas Turbine Exhaust Temp. [°C]	512.1	395.6	509.8
Energy Efficiency [%]	36.3	39.5	38.7
Exergy Efficiency [%]	34.6	37.5	37.0
Specific Work [kJ/kg]	323	276	367

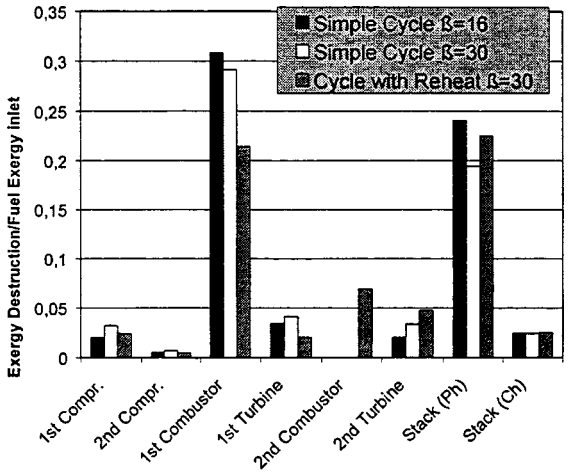

Fig. 2 Exergy destruction in reheat GT cycle

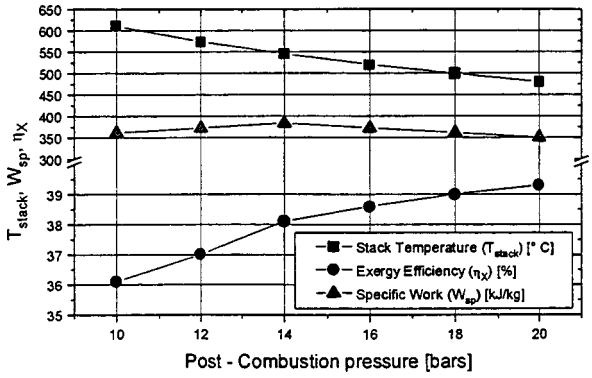

Fig. 3 Effect of reheat pressure on cycle performance

With values of reheat pressure in the range of 14 to 16 bars, however, the exhaust gas temperature is too low (512°C) to obtain good performance from the bottoming cycle. The reheat pressure level should be lowered down to 11 bars (which is the value for the ABB GT24 gas turbine); in this way, the efficiency of topper cycle is penalized, but a consistent heat recovery takes place in the combined cycle.

H-Technology Cycle

The beneficial effects of raising the maximum cycle temperature T_{Max} are well known. Current generation blade cooling techniques allow a difference (ΔT_{nozzle}) between T_{Max} and T_{IT} of about 150°C: this means that, if a high value of $T_{IT} = 1700$ K is considered, a T_{Max} of at least 1850 K should be reached in the combustion chamber. Such high values involve remarkable problems for cooling the combustion chamber walls and the first nozzle blades. The H-generation gas turbine, operating necessarily with combined cycle configuration and closed loop water/steam nozzle cooling, can strongly limit ΔT_{nozzle} (50°C) with evident advantages in terms of performance and NOx emissions.

A simplified schematic of a steam cooled gas turbine cycle is represented in Fig. 4. The GT cycle is closely coupled with a bottoming steam cycle, both at the HRSG and inside the gas tur-

Downloaded 02 Jun 2010 to 171.66.16.119. Redistribution subject to ASME license or copyright; see http://www.asme.org/terms/Terms_Use.cfm

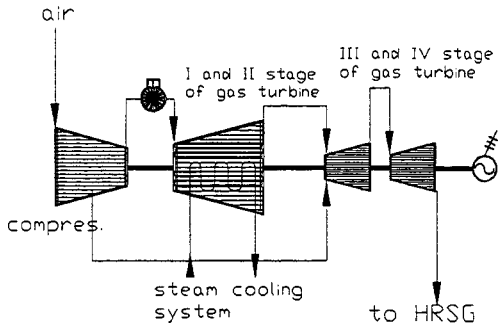

Fig. 4 Schematic of the LM9001 H with closed loop blade cooling

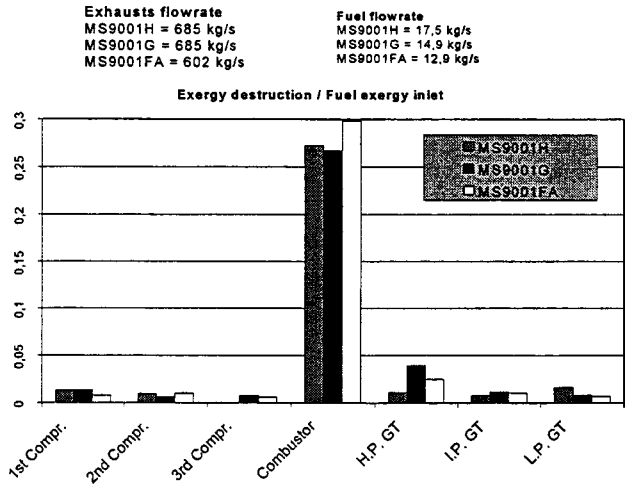

Fig. 5 MS9001 Gas Turbine relative exergy destruction

bine, where heat is removed from the hot combustion gas stream and transferred to superheated intermediate pressure (IP) steam. The steam exiting the HP turbine is thus split into two flows: one is directed to the cooling system of the gas turbine, the other to the reheat section of the HRSG. The two flows are remixed at the IP steam turbine inlet. Steam is a very efficient heat transfer fluid, so that a limited amount is required to cool the turbine. In this way, also a limited amount of air must be bled at compressor discharge for blade cooling (only the third stage is cooled with traditional techniques—film cooling, impingement, etc.).

The component-level exergy destruction balance (Fig. 5) is illustrated with reference to a LM9001H gas turbine, and compared with that of previous-generation machines (F and G series).

The combustion chamber shows relatively low values of exergy destruction in the H-configuration with respect to commonly encountered values [5,6]; a similar performance (slightly lower exergy destruction) is achieved by the G-engine, which however features higher values of T_{Max}(K). For each of the three cases, T_{IT} was fixed at the same level and then T_{Max} calculated: since the H-series is steam cooled, a temperature drop between the 1st stator and the 1st rotor of only 60–70°C occurs, while for the G-series this drop is about 150–180°C. So, T_{Max} is higher and the related combustion chamber exergy destruction slightly lower (referred to fuel exergy inlet) for the G one.

The HRSG and Bottoming Cycle

A schematic of the HRSG and bottoming cycle is shown in Fig. 6. The three-pressure-level heat recovery steam generator was simulated using the same values of the basic thermodynamic pa-

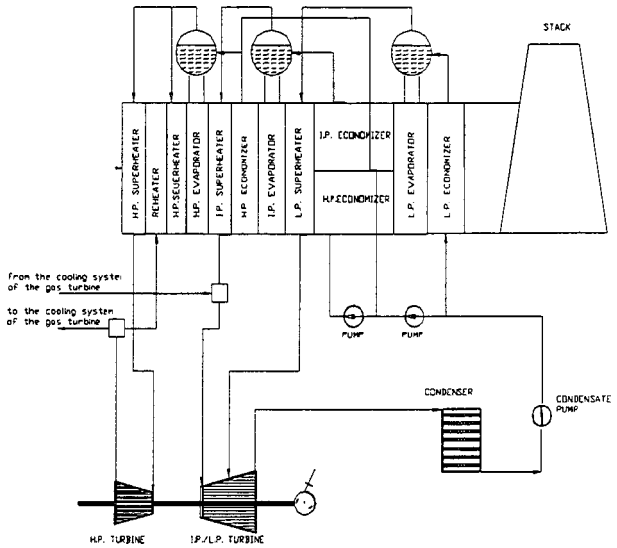

Fig. 6 Schematic of the heat recovery steam generator (3 pressure levels)

Table 2 HRSG and bottoming steam cycle operating data

PARAMETER	SYMBOL	VALUE	UNIT
Pinch point economizer Temp. Diff.	ΔT_{pp}	14	K
Pinch point evaporator Temp. Diff.	ΔT_{pp}	20	K
Evaporator subcooling Temp. Diff.	ΔT_{ap}	8	K
Superheater approach Temp. Diff.	ΔT_{ap}	20	K
Maximum steam temperature	$T_{max,steam}$	833	K
Efficiency, HP steam turbine	η_{is}	88	%
Efficiency, IP steam turbine	η_{is}	90	%
Efficiency, LP steam turbine	η_{is}	90	%
Condenser pressure	p_{cond}	7 (5,10)	kPa
Gas side pressure loss	Δp_{tot}	5.6	kPa
Efficiency of all heat exchangers	η_{ex}	99	%
Efficiency of AC generators	η_{gen}	99	%

rameters for the M9001H and GT24 plants (Table 2). The values are not exactly those optimizing the performance of each of the two reference plants, which are however relatively close as the GT exhaust temperature level is quite similar. Selecting the same values for the two cases allows an easier comparison between the two solutions.

If the bottomer and HRSG sections were changed, the performance of the combined cycle would not change heavily (until the bottomer conditions allow to operate at the same temperature and pressure levels) because similar vaues of the gas turbine exhaust temperature were found.

Exergy Analysis of the GT24 and MS9001 Combined Cycles

The exergy efficiency is calculated as

$$\eta_x = W/e_{\mathrm{in}}$$

Downloaded 02 Jun 2010 to 171.66.16.119. Redistribution subject to ASME license or copyright; see http://www.asme.org/terms/Terms_Use.cfm

and also by an indirect approach

$$\eta_x = 1 - \Sigma L/e_{\text{in}}.$$

L/e_{in} is the relative exergy loss, which is evaluated separately for each component; the distributions of L/e_{in} for the two reference cases here considered are presented in Figs. 7 and 8. The results hereafter presented include in global terms the effects of turbine cooling; details of exergy accounting in cooled expansions are provided in a subsequent paragraph.

With reference to the combined cycle, the choice of a reheat configuration (Fig. 7) allows the gain of about 2 to 3 percentage points in exergy efficiency with respect to conventional air-cooled gas turbine combustion processes, under similar conditions of T_{Max}.

The reduction in combustion irreversibility allows the plant based on the reheat option to reach interesting figures for exergy efficiency (54.3 percent) even with limited T_{IT} values (1508 K), and with a thermomechanical loading which is lower than that of many aero-derivative or even industrial gas turbines.

Some other losses (e.g., the air-cooled turbine expansion, which is discussed in detail separately) are relatively large with respect to what could be achievable with more advanced technologies. However, a partial recovery takes place at combined cycle level, because the reheat allows the selection of high GT pressure ratios yet maintaining relatively high exhausts temperature, which are beneficial for the HRSG performance.

The H-technology combined-cycle power plant (Fig. 8) features a better exergy efficiency (58.1 percent), which reflects the high value of thermal efficiency (exceeding 60 percent). Data for current-generation air-cooled versions of the same engine (MS 9001-FA and MS 9001-G) are also shown.

The high efficiency is a result of the following three basic features:

1 The maximum cycle temperature is very high (especially in comparison to the GT 24), which allows limiting the combustion irreversibility to values even lower than that of the reheat gas turbine (about 27.2 percent). When considering the air-cooled (FA and G) versions of this engine, the combustion exergy loss was evaluated respectively at 29.8 percent for the MS 9001-FA ($T_{\text{Max}} = 1570$ K) and 26.6 percent for the MS 9001-G ($T_{\text{Max}} = 1700$ K).

2 The steam cooling allows achievement of very good efficiencies even for high-temperature, cooled turbine stages, in comparison with conventional (air-cooled) gas turbines.

3 Steam cooling is regenerative, and this is reflected in the very small exergy destruction in the heat transfer process of the HRSG reheater, whose rating and size are reduced as a relevant flowrate of reheated steam results from the cooling stream of the gas turbine blades.

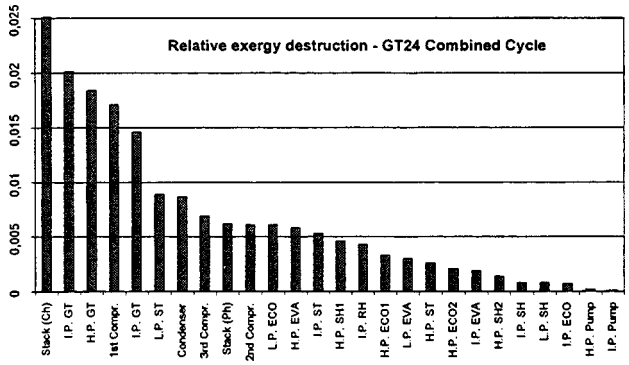

Fig. 7 Exergy balance of the reheat-GT combined cycle reheat gas turbine

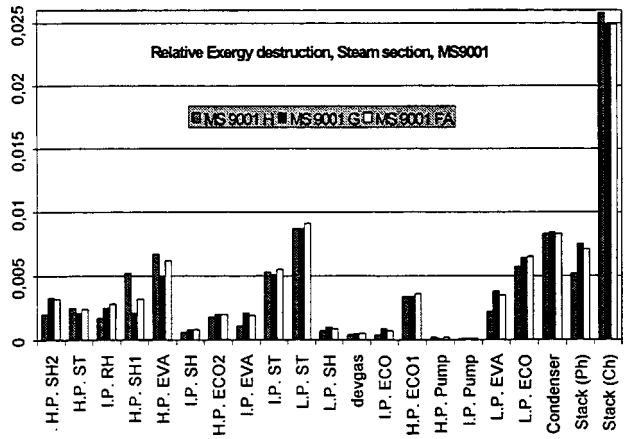

Fig. 8 Exergy balance of the H-technology HRSG and steam cycle (data also shown for conventional, air-cooled)

Exergy Analysis of Closed Loop Blade Cooling and Standard Air Cooling

Even if cooling is very effective with steam, the gas turbine design undergoes several complications and new problems arise (designing coolant return ducts and sealing systems; less uniform blade temperature profiles with respect to film cooling).

The exergy destruction in the closed loop blade cooling is principally due to heat transfer between hot gas and steam. The closed loop cooling model includes the following sub-processes, shown schematically in Fig. 9:

Stator: heat transfer between hot gas and coolant expansion (friction loss)

Rotor: heat transfer between hot gas and coolant expansion (friction loss)

Reversing the order of heat transfer and gas expansion corresponds to the physical process and was suggested in the first models of cooled gas turbines [7].

The thermodynamic model for expansion across an air-cooled gas turbine stage is derived from that originally presented by Horlock [7], and considers the following processes:

Stator

1 Heat transfer between hot gases and coolant up to thermal equilibrium conditions ($T_{\text{gas}} \rightarrow T_{\text{refr}} T_{\text{cool}} \rightarrow T_{\text{refr}}$).

2 Mixing of the hot gases with the coolant stream ($m_{\text{gas}} = m_{\text{gas}} + m_{\text{cool}}$; concentrations of chemical species are also adjusted).

3 Total pressure loss ($p \rightarrow p - \Delta p_{\text{loss}}$) connected to friction in the blade coolant passages, and to irreversible effects connected with momentum exchange between the two streams (hot gases and coolant). External blockage effects eventually introduced by film cooling are also approximately accounted in this total pressure loss.

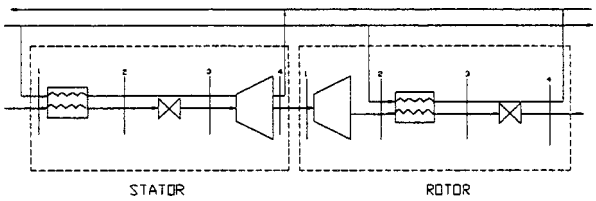

Fig. 9 Thermodynamic model for a steam-cooled turbine stage

Downloaded 02 Jun 2010 to 171.66.16.119. Redistribution subject to ASME license or copyright; see http://www.asme.org/terms/Terms_Use.cfm

4 Irreversible expansion (as for an uncooled stator, referred to unit mass flowrate). This loss is linked to the uncooled expansion pressure loss coefficient, as can be estimated by one of the well-tested correlations for turbine efficiency.

Rotor

1 Irreversible expansion (as for an uncooled rotor, cfr. point 4 of stator).
2 Heat transfer between hot gases and coolant up to thermal equilibrium conditions ($T_{gas} \rightarrow T_{refr} T_{cool} \rightarrow T_{refr}$).
3 Mixing of the hot gases with the coolant stream ($m_{gas} = m_{gas} + m_{cool}$; concentrations of chemical species are also adjusted).
4 Total pressure loss ($p \rightarrow p - \Delta p_{loss}$).

The computer code determines automatically the number of cooled stages which are needed to maintain a blade metal temperature of 1123 K. The results are summarized in Table 3.

Figure 10 collects the detailed exergy destructions for all the cases examined, per unit mass flowrate through the turbine. It shows that, for simple gas turbine cycles with air-cooled turbines, the exergy destruction connected with blade cooling is increased with raising T_{Max}. The opposite happens for the expansion irreversibility (which is the basic loss for an uncooled stage).

With specific reference to blade cooling, the largest contributions to exergy destruction are those associated with the irreversible heat transfer process, which reach 1.5 percent of the inlet exergy for $T_{Max} = 1800$ K.

The limits of air cooling are clearly stated in Fig. 10, which for $T_{Max} = 1800$ K confirms a cumulative relative exergy destruction due to blade cooling of the order of 3 percent, which is even larger than the effects of the expansion irreversibility (uncooled turbine).

Table 3 Results of turbine blade cooling model (Key: 1SS=1st Stage Stator; 2SR=2nd Stage Rotor, etc., AC=Air Cooling, SC=Steam Cooling, NC=No Cooling)

Cycle	T_{max} [K]	1SS	1SR	2SS	2SR	3SS	3SR	4SS	4SR
Simple	1500	AC	AC	AC	NC	NC	NC	-	-
Simple	1650	AC	AC	AC	AC	NC	NC	-	-
Simple	1800	AC	AC	AC	AC	NC	NC	-	-
GT24 RH	1500	AC	AC	AC	AC	AC	NC	-	-
MS9001 H	1700	SC	SC	SC	SC	AC	AC	NC	NC
MS9001 H	1800	SC	SC	SC	SC	AC	AC	NC	NC

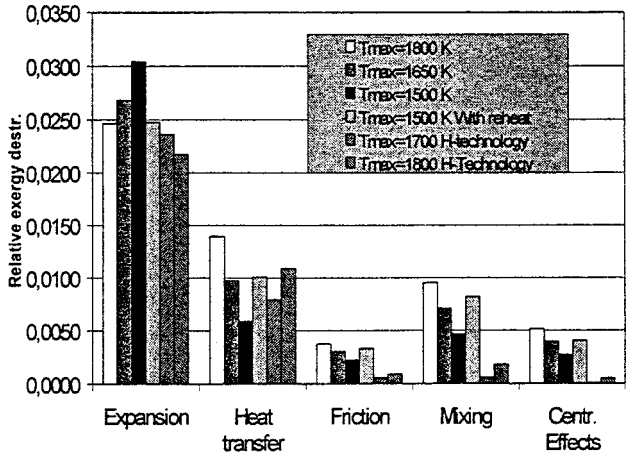

Fig. 10 Distribution of relative exergy destruction—cooled expansion

Closed-loop steam cooling allows to combine small levels of expansion irreversibility with a reduced exergy destruction for blade cooling. Among the various contributions of blade cooling to exergy destruction, the heat transfer one is relatively large, but all other contributions are very small in comparison to the case of air cooling. A significant difference between air and steam cooling is the internal regeneration of the process: by air-cooled stages, only about 20 percent of the exergy of the coolant stream at inlet is recoverable after mixing with the hot gases (recovery is in turn affected by inefficiencies in the following stages), while by steam cooled stages the exergy transferred to the bottoming steam cycle is a significant fraction (of the order of 80 percent) of the exergy decrease of the gas stream.

Even if one air-cooled stage is retained for the MS 9001 H configuration, the benefits of steam cooling are substantial and—together with a small reduction of the combustion irreversibility and of other minor losses—contribute significantly to the high exergy efficiency of the combined cycle.

Conclusions

The analysis of simulated results (thermodynamic analysis) indicates that both H-technology and reheat lead to a relevant increase of performance in terms of specific work and efficiency (57.5 percent for the GT24 and 60 percent for the MS9001H). A supplementary simulation showed that the combination of the two technologies could lead to an efficiency of about 62 percent at the present technological level

Power plants based on an H-technology gas turbine have potential for attaining efficiency levels which are presently beyond the limits of conventionally cooled gas turbine plants; however, this choice entails consistent technological problems which will certainly be reflected in the higher plant investment costs, and some degree of uncertainty about reliability at least for the first plants built. On the other hand, the GT24 uses consolidated technology with lower investment expenditure, but also a lower performance potential. The opportunity of the utilization of the H-technology is strictly dependent on the breakdown of the financial investment in terms of purchase and operation of the plant.

Acknowledgments

Mr. Enrico Morelli performed a large work in the implementation of the exergy balance in the Modular simulation code, while working as a graduate level student. His contribution is gratefully acknowledged.

Nomenclature

T_{Max} = maximum cycle temperature
T_{IT} = turbine inlet temperature (1st rotor)
T_{gas} = combustion gas temperature
T_{refr} = cooled gas temperature
T_{cool} = cooling gas (or steam) temperature
β = pressure ratio
ΔT_{nozzle} = temperature drop across stator nozzle after the combustion chamber
η_x = cycle exergy efficiency
W = cycle power output
e_{in} = cycle exergy inlet
L = exergy destruction
p = pressure
Δp_{loss} = pressure drop due to the exergy destruction
m_{gas} = hot gas flowrate
m_{cool} = cooling gas (or steam) flowrate
(Ph) = physical exergy destruction
(Ch) = chemical exergy destruction

Downloaded 02 Jun 2010 to 171.66.16.119. Redistribution subject to ASME license or copyright; see http://www.asme.org/terms/Terms_Use.cfm

References

[1] MPS (Modern Power Systems), 1998, ''501 ATS Compressor Tests Show Progress,'' staff reports, Gas Turbine Research at Whittle's Test Site, Porvoo Proves 6FA Niche, pp. 41–55.

[2] Aoki, S., Uematsu, K., Suenaga, K., Mori, H., and Sugishita, H., 1998, ''A Study of Hydrogen Combustion Turbines,'' ASME Paper 98-GT-394.

[3] Carcasci, C., and Facchini, B., 1995, ''A Numerical Method For Power Simulations,'' presented at the GTI TURBO Expo Houston 1995.

[4] El Masri, M. A., 1997, ''Exergy Balance Analysis of the Reheat Gas Turbine Combined Cycle,'' presented at the 2nd ASME-JSME Thermal Engineering Conference, Honolulu, Hawaii.

[5] Kawaike, K., et al., 1984, ''Effect of New Blade Cooling System with Minimized Gas Temperature Diluition on Gas Turbine Performance,'' ASME Paper 84-GT-89.

[6] Koellen, O., and Koschel, W., 1986, ''Effect of Film Cooling on the Aerodynamic Performance of a Turbine Cascade,'' *Heat Transfer and Cooling in Gas Turbine*, AGARD Rep.

[7] Horlock, J. H., 1966, *Axial Flow Turbines*, Butterworths, London.

Downloaded 02 Jun 2010 to 171.66.16.119. Redistribution subject to ASME license or copyright; see http://www.asme.org/terms/Terms_Use.cfm

Full Load and Part-Load Performance Prediction for Integrated SOFC and Microturbine Systems

Stefano Campanari
Research Assistant,
Energetics Dept., Politecnico di Milano,
Piazza Leonardo da Vinci 32,
20133 Milano, Italy
e-mail: stefano.campanari@polimi.it

During the last years, two new subjects among the others have raised interest in the field of small scale electric power generation: advanced microturbines and solid oxide fuel cells. This paper investigates the thermodynamic potential of the integration of the solid oxide fuel cell technology with microturbine systems, in order to obtain ultra-high efficiency small capacity plants, generating electric power in the range of 250 kW with 65 percent LHV net electrical efficiency and with the possibility of cogenerating heat. A detailed description of the calculation model is presented, capable of full and part-load performance analysis of the microturbine and of the integrated SOFC+microturbine system. [S0742-4795(00)01702-6]

1 Introduction

It is well known that recuperated microturbine units generating 50–200 kW are projected to achieve net electrical efficiencies approaching 30 percent (LHV), with low pressure ratios, uncooled operation and turbine inlet temperatures close to 900°C [1,2]. Solid oxide fuel cells (SOFCs) on their own achieve 50 percent net electrical efficiencies and have already been considered for integration with multi-MW gas turbine cycles, projected to achieve extremely high efficiencies for electric power production [3–6]. The recent successful operation of a 100 kW SOFC plant [7], with direct natural gas feeding and internal reforming, offers the basis for considering small size plants, based on the successful integration of these two technologies, which could open new market spaces for the beginning of their commercialization [8].

The SOFC system exhaust temperatures (in the range of 800–900°C) are adequate for an exploitation in a microturbine with the above-mentioned characteristics, and no kind of difficulty has emerged for operating the SOFC system at the pressure required by a microturbine [9]. It is therefore possible to design a small recuperative gas turbine cycle, where the combustor is ''substituted'' by a SOFC system, fed with preheated and compressed air, and generating hot exhaust gases expanded by the gas turbine.

As the interest in such small power systems is not restricted to full load operation only, this paper deals with a full load and part-load performance prediction for these plants.

In the first section of the paper, a model for predicting the performances of a single-stage, high-speed radial-to-radial microturbine is discussed, with recuperative operation, absence of variable-inlet-guide-vanes systems (typically not used on this kind of turbomachine) and with variable speed optimization. Subsequently, the part-load modeling of the SOFC is discussed. In the second section of the paper an integrated SOFC and recuperative microturbine plant is proposed, with a detailed analysis of the fuel cell operating parameters and of the other components characteristics (pressure drops, efficiencies), together with their effects on the plant efficiency. The performances at full and part-load of such a system are predicted, together with the influence of the ambient temperature. Calculations are performed based on state-of-the-art performances of small turbomachinery and on the most advanced SOFC tubular technology, with natural gas feeding, internal reforming of hydrocarbons and internal air preheating.

Contributed by the International Gas Turbine Institute (IGTI) of THE AMERICAN SOCIETY OF MECHANICAL ENGINEERS for publication in the ASME JOURNAL OF ENGINEERING FOR GAS TURBINES AND POWER. Paper presented at the International Gas Turbine and Aeroengine Congress and Exhibition, Indianapolis, IN, June 7–10, 1999; ASME Paper 99-GT-65. Manuscript received by IGTI March 9, 1999; final revision received by the ASME Headquarters January 3, 2000. Associate Technical Editor: D. Wisler.

2 Calculation Model

2.1 The Microturbine Model: Part-Load Operation. The developed model makes reference to a single stage gas turbine, with radial compressor and radial turbine and with a recuperative cycle arrangement. With an inlet mass flow rate of 0.4–1.0 kg/s this model is representative for the 40–80 kW-class microturbines actually developed by many manufacturers [2,1]: as an example General Electric–Elliott Energy Systems distributes a 45 kW and an 80 kW recuperated gas turbine, with a pressure ratio of 4:1 and net electrical LHV efficiency of 30 percent, rated with a design speed of 116,000 and 68,000 rpm respectively and with a 0.41–0.84 kg/s mass flow rate [10]; Allied Signal Aerospace Co. manufactures a 50 kW engine for vehicle applications with $\beta=3.3$ at 75,000 rpm [11] and a 75 kW genset with a pressure ratio of 3.8:1 and a design speed of approximately 85,000 rpm.

The high rotating speed of these compact machines requires a rectifier+inverter power control system, flattening the high frequency AC output of the high speed generator and subsequently generating the requested grid frequency from the rectified direct current. It is interesting to note that this kind of process could be suitable for integration with the power conditioning system of a fuel cell, typically generating an AC output starting from the cell DC electrical generation.

The model adopts as a reference the compressor map given by Uchida et al. [12] for a centrifugal compressor developed and tested for application in a 100 kW gas turbine, elaborated according to the similarity rules. This map shows an isentropic efficiency of about 79.5 percent at the manufacturer design point, which is rated at a pressure ratio of 5.0, 0.445 kg/s and 100,000 rpm, and values somewhat higher (80–82 percent) at lower speed. For the application discussed here, the design point has been set to a pressure ratio of 3.8 and a specific speed of 0.13 (85,000 rpm at 0.5 kg/s): the resulting operating point, together with the partial load operating curve, is shown in Fig. 1. The maximum efficiency was set to 79.5 percent at the design point, with a surge margin (in terms of mass flow) of about 15 percent.

Copyright © 2000 by ASME

Downloaded 02 Jun 2010 to 171.66.16.119. Redistribution subject to ASME license or copyright; see http://www.asme.org/terms/Terms_Use.cfm

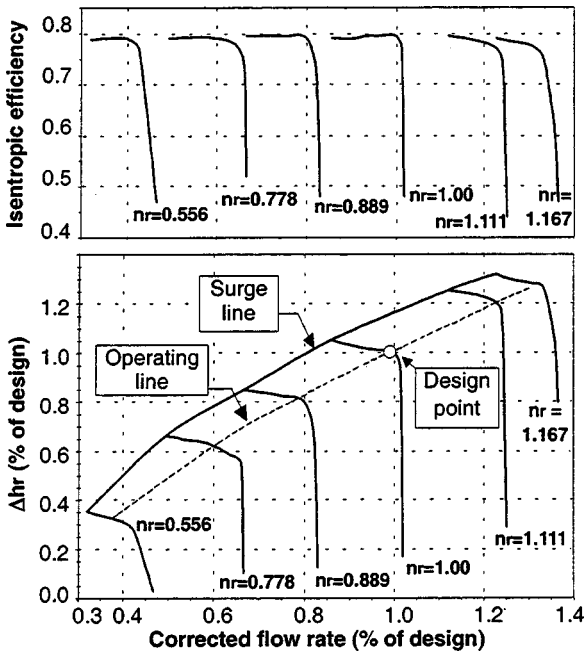

Fig. 1 Characteristics of the centrifugal compressor

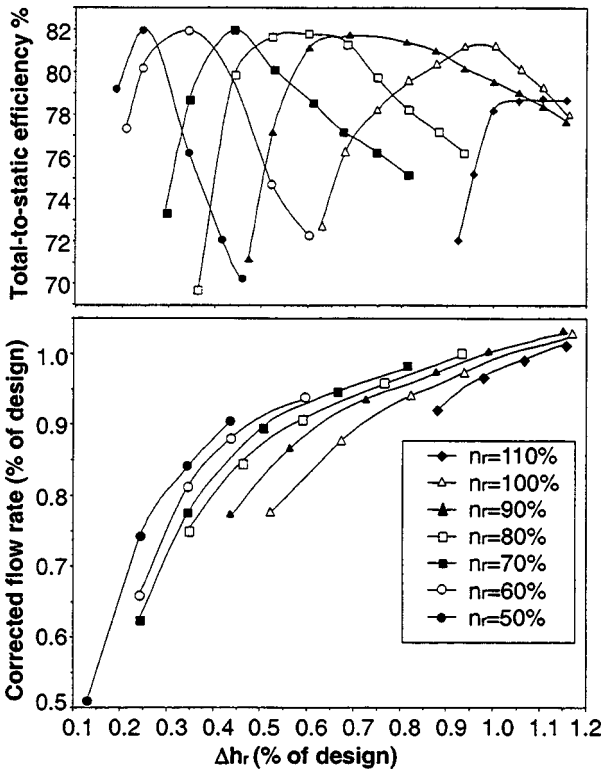

Fig. 2 Characteristics of the radial turbine

The curves are adimensionalized with respect to the design conditions, and recalculated in terms of corrected enthalpy change (instead of pressure ratio), corrected flow rate and corrected speed, defined as following (with T, p, and m_C at the compressor inlet):

$$\Delta h_r = \frac{\Delta h_{\mathrm{re}}}{c_{p,0} T_{\mathrm{ref}}} \tag{1}$$

$$m_r = m_C \frac{\sqrt{T/T_{\mathrm{ref}}}}{p/p_{\mathrm{ref}}} \tag{2}$$

$$n_r = \frac{n}{T/T_{\mathrm{ref}}}. \tag{3}$$

Besides, the model includes a turbine map based on the works of Pullen et al. [13] for a high pressure ratio radial inflow uncooled turbine, suitable with necessary scaling for engines in the 50–300 kW range. The design point for the turbine, tested and developed for power generation purposes and for small aircraft application, was originally set at a mass flow rate of 0.387 kg/s, 100,000 rpm, TIT=1200 K, total-to-static pressure ratio of 4.7 and total-to-static efficiency of about 82 percent.

For the application of this work it is considered to operate with the curves illustrated in Fig. 2, derived with appropriate scaling from the original map and recalculated as above in terms of corrected quantities (with T, p, and m_T at the turbine inlet); all the values are then adimensionalized with respect to the design conditions chosen here, which is characterized by a pressure ratio of 3.4, a specific speed of 0.11 (85,000 rpm at 0.5 kg/s) and a 0.82 total to static efficiency. The turbine efficiency is assumed to gain 2.5 percent with the diffuser recovery of the exhaust gas kinetic energy at the nominal point; at partial load the efficiency gain is reduced as the square of the flow rate.

The resulting design point turbine isentropic efficiency is therefore 84.5 percent. These values are in good agreement with the works of Jones [14] and Kim et al. [15] on microturbine development.

The other assumptions for the GT cycle calculation are shown in Table 1. The minimum temperature difference on the recuperator is set to 45°C; partial load calculation are made by keeping the heat exchanger area as a constant and assuming a dependence of the global heat transfer coefficient on the Reynolds number elevated by 0.6. According to these assumption, the resulting minimum temperature difference becomes lower when the thermal duty of the heat exchanger is reduced.

The air and gas side pressure drops are set to 3 percent and 6 percent respectively at design conditions (accounting for different density and gas speed), and they are varied at partial load as a function of the mass flow and density according to the following relation:

$$\Delta P \cong \mathrm{Const} \times \frac{m^2}{\rho}, \tag{4}$$

as by the Darcy equation for turbulent flows, assuming a negligible variation of the friction factor.

The total amount of the recuperator heat loss is kept constant and independent with respect to the load, assuming that it is mostly influenced by the external temperature of the insulation,

Table 1 Gas turbine cycle model assumptions

Pressure ratio (design point)	3.8
Combustor outlet temperature (design point)	900 °C
Recuperator Δp/p air/gas side (design point)	3% / 6%
Minimum ΔT recuperator (design point)	45°C
Heat loss recuperator (design point; T_{amb}=15°C)	2%
Combustor Δp/p	6%
Combustion efficiency	98.5%
Organic efficiency (design point)	96%
Electric generator efficiency (design point)	95%
Power control system efficiency (design point)	96%
Fuel compressor efficiency	70%
Fuel (natural gas) composition: CH_4 98% - C_2H_6 0.7% - C_3H_8+C_4H_{10} 0.3% - Sulfur compounds 50 ppmv - N_2 1%	

Downloaded 02 Jun 2010 to 171.66.16.119. Redistribution subject to ASME license or copyright; see http://www.asme.org/terms/Terms_Use.cfm

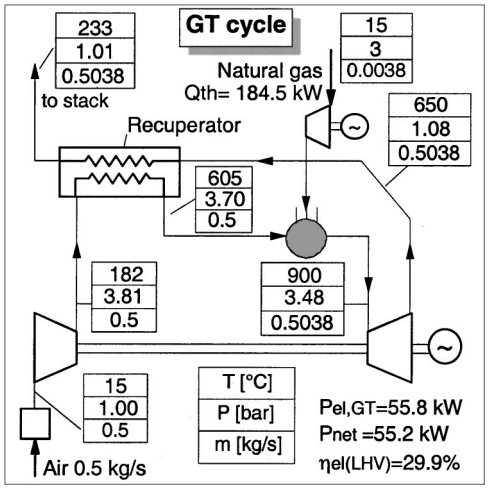

Fig. 3 The recuperated gas turbine cycle

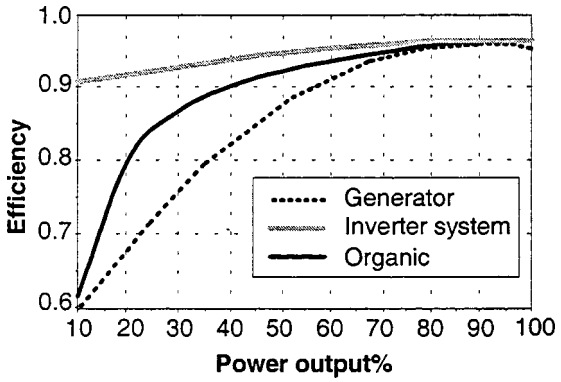

Fig. 4 Electric and organic efficiencies at partial load

which is almost constant at partial loads. The same applies for the SOFC heat losses. The combustor pressure drop is kept for simplicity constant at partial load.

The combustor outlet temperature is set to 900°C, even if some manufacturers declare higher values, close to 1000°C [11,16]. The resulting design point configuration is shown in Fig. 3, with an LHV net electrical efficiency of about 30 percent and a 55.2 kW output.

The electrical generator efficiency, together with the power conditioning (rectifier and inverter) system efficiency and the gas turbine organic efficiency are reduced at partial load as shown in Fig. 4. The organic efficiency curve is generated assuming that the design point loss amount is constant at partial load. The generator design efficiency of 95 percent is consistent with latest prototype test results [17]. The inverter system efficiency has been set to 96 percent [18], a value lower than the maximum efficiency (97 percent) quoted by some manufacturer [19]; an efficiency decay of about 5 percent at 10 percent load was assumed to quantify the effects of auxiliary losses (ventilation etc.), of main bridge and thyristors losses, etc.

The combustion efficiency is set to the conservative value of 98.5 percent, while even 99.5 percent appears to be feasible [11].

The operation at reduced power can be made as follows:

- By a reduction of fuel flow and TIT at constant speed: the operating point on the compressor curve is moved to the right, and the pressure ratio is reduced to accommodate the mass flow requested by the turbine. The operating point on the turbine curves move towards lower TITs, higher n_r (Eq. (3)), lower Δh_r (or pressure ratio) and m_r. The compressor/turbine matching requires a working condition characterized by a little increase in the air mass flow, a reduction of the turbine and compressor efficiency and great penalties on the cycle efficiency.
- By a reduction of speed at constant TIT (or with a moderate reduction of TIT): the new operating point for the compressor follows the dashed curve in Fig. 1, resulting in a lower pressure ratio and a corrected mass flow on the turbine compatible with the requested TIT. The operating point on the turbine curves moves towards lower n_r and lower Δh_r. The new working condition is characterized by high compressor and turbine polytropic efficiency and yields almost constant cycle efficiency; the compressor surge margin is always kept around 15 percent.
- The results of these calculations are presented in Fig. 5. It is possible to note that the variable speed operation with constant TIT, or with small TIT reduction, should give the best partial load performances for this machine. At 50 percent of the full power output it is than possible to achieve a still very high system efficiency, just about 3 percentage points lower than the design efficiency. This is possible because

1 the sensible mass flow reduction leads to reduced pressure losses;

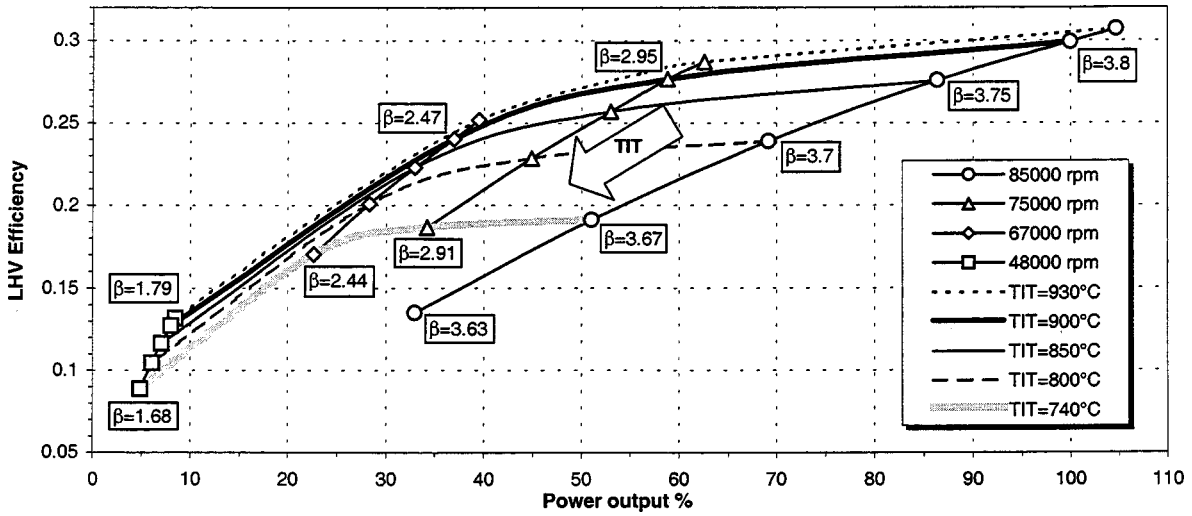

Fig. 5 Calculated gas turbine performances at partial load

Downloaded 02 Jun 2010 to 171.66.16.119. Redistribution subject to ASME license or copyright; see http://www.asme.org/terms/Terms_Use.cfm

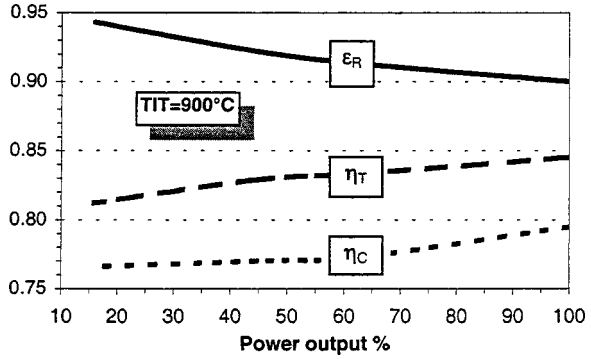

Fig. 6 Compressor and turbine isentropic efficiencies and recuperator effectiveness for the gas turbine cycle at partial load (constant TIT operation)

2 the reduced duty on the recuperator leads to a higher heat exchange effectiveness (Fig. 6), ranging from about 89 percent to over 93 percent at the lower loads; and

3 the compressor and turbine efficiencies are still high, and the turbomachines are still working in a near-optimum zone (Fig. 6): the isentropic efficiency variation is below 5 percent at about 60 percent speed.

The circumstance that the cycle efficiency remains high at very low pressure ratios is however typical of recuperative gas turbine cycles. Without considering the electrical losses, the gross efficiency map (here not represented) would show also an expected reduction of the optimum pressure ratio at lower turbine inlet temperatures.

The recuperator effectiveness has a relatively high value (≈89 percent) at design conditions, whose effects on the plant economics are not discussed here; a similar value is reported by Carnö et al. [17].

2.2 The SOFC Model: Part-Load Operation. The model makes reference to the latest generation of the tubular SOFC, the Siemens-Westinghouse Air Electrode Supported (AES) fuel cell, with operating temperature of 1000°C, which has been recently tested up to a 100 kW plant size, with the possibility of being easily upgraded to about 200 kW output [20,7].

The SOFC is fed by an oxidizer (air) and a fuel. The two fluxes flow in contact with cathode and anode porous surfaces, separated by a solid electrolyte which is a good $O^{=}$ ion-conductor at the high SOFC operating temperatures. The reduction of molecular oxygen to $O^{=}$ takes place at the cathode, while the fuel is oxidized to steam and carbon dioxide at the anode. The prevailing oxidization reaction is the hydrogen consumption. Hydrogen is generated by internal steam reforming and water-gas shift reactions starting from the natural gas feeding and exploiting the fuel cell high-temperature heat production. Steam is obtained by recirculating a fraction of the anode exhaust gases. The SOFC model is based on these reactions [21], however the high temperature SOFCs sustain also a fraction of CO and CH_4 direct oxidization. The Siemens-Westinghouse tubular SOFC system operates following these principles; it is provided with anode recirculation, sustained by an ejector using fresh fuel as driving flow, and with a small pre-reforming step cracking the higher hydrocarbons and reducing carbon deposition problems. The exhaust air and fuel flow, partially consumed by the cell, react up to complete fuel oxidization with an auxiliary combustion; the high temperature gases preheat the inlet air flow before being delivered to external components [18,22]. The alternative of external reforming, often considered for planar SOFC feeding, is not discussed here, as it is not employed by the most advanced tubular technology and it adds complexity to the plant configuration.

The FC generates direct current electrical energy with an efficiency proportional to its voltage [9,21]. Fuel and air are not completely consumed at the electrodes to avoid the large voltage losses due to reactant concentration gradients and limited gas diffusivity near the electrodes active area; air and fuel utilization factors (see nomenclature) quantify the consumed fraction.

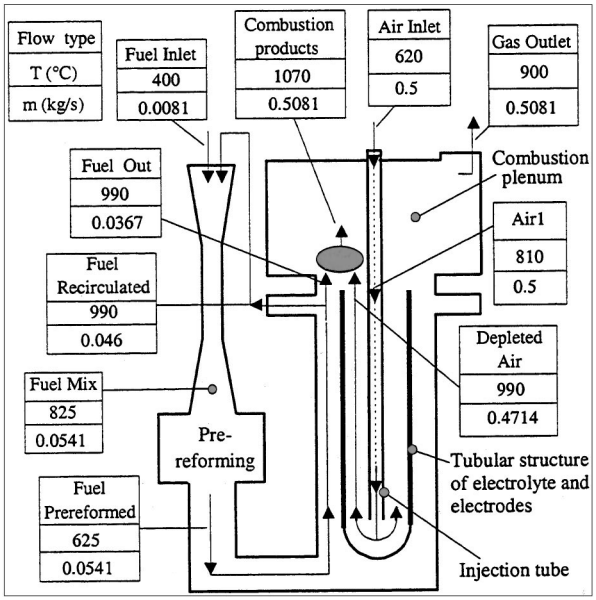

Fig. 7 Tubular SOFC module configuration: spent fuel is partially recirculated and the exhaust gases of the auxiliary combustion are used to preheat the inlet air flow

The SOFC schematic is shown in Fig. 7. The fuel is desulfurized natural gas, internally reformed by the SOFC itself; the fuel pressure is calculated to ensure the ejector operation. An external compressor rises the natural gas pressure from the 0.3 MPa available in any small network up to the requested pressure (i.e., 1 MPa). Other details about the cell model are discussed in Campanari and Macchi [23,6]. The fuel cell efficiency is positively affected by pressurized operation, with an increase proportional to the operating pressure, while the efficiency decreases by increasing the cell current density.

The model calculates the cell electric power production, heat generation and efficiency together with the thermodynamic properties and chemical composition of internal and external flows in all the representative points, as a function of the cell operating conditions (temperature, pressure, current density, fuel and oxidizer composition and utilization factors).

The cell power output is given by:

$$P = V \times I = V_c \times i_c \times A_c , \tag{5}$$

where i_c is the cell current density and A_c the cell active area. The equation shows that a reduction of the FC power output requires a reduction of the cell current density.[1]

In order to define the possible techniques for part-load operation of an integrated SOFC+GT plant, it is necessary to discuss the mutual dependence of the involved variables, which are the cell current density, the air utilization factor and the cell module exhaust temperature.

The temperature of the compressed air fed to the fuel cell module is generally in the range 500–700°C; the air flow is then preheated by the cell exhaust up to the temperatures required for the cell cooling (point ''Air1'' in Fig. 7). It should be noted that the calculation model considers that the depleted air temperature

[1]Another possibility, here not discussed further, is to reduce A_c with a by-pass system which excludes some of the cells during part-load operation; the system would be complicated by the necessity of keeping those cells at an adequate hot-stand-by temperature.

Downloaded 02 Jun 2010 to 171.66.16.119. Redistribution subject to ASME license or copyright; see http://www.asme.org/terms/Terms_Use.cfm

at the cathode outlet is almost constant (close to 1000°C), and that the temperature at the Air1 point of Fig. 7 follows the cell heat generation, with maximum variations of 50–100°C; the effective air temperature at the cell electrodes inlet (end of the injection tube) is by this way always close to 900°C, high enough to allow the solid electrolyte operation.

The cell air utilization can be expressed as:

$$U_a = \frac{m_{O_{2,\text{consumed}}}(\text{mol/s})}{m_{O_{2,\text{Inlet}}}(\text{mol/s})} = \frac{1}{X_{O_2} m_{\text{air,inlet}}(\text{mol/s})} \cdot \frac{i_c \cdot A_c}{4F}, \quad (6)$$

where F is the Faraday's constant (see nomenclature).

Any change of the air utilization factor at constant air flow will yield a variation of the cell exhaust temperature, as the cell heat generation is mainly discharged to the air flow (the remaining being partly taken by the fuel flow and partly lost to the ambient): lowering U_a will cause a reduction of the cell module exhaust temperature.

With these hypothesis the SOFC exhaust temperature is calculated as a function of the air/fuel inlet temperature, the air/fuel utilization factors and the cell voltage and efficiency. This model gives the possibility of predicting part-load operating conditions and performances.

Two different techniques for cell power reduction (part-load operation) have therefore been considered:

• **Constant air flow**. Starting from a design point condition, it is possible to reduce the cell current density with a constant air flow, lowering also the air utilization factor (Eq. (6)) with a linear proportion, and reducing the FC power output. A reduction of i_c and U_a will result in a certain increase of the cell voltage V_c calculated by the model (due to a reduction of resistance and cell polarization losses, as well as to the higher average oxygen concentration in the air flow), with a global efficiency gain parallel to the power output reduction. The effect of a reduction of U_a is also a reduction of the cell exhaust temperature. This first kind of power reduction is suitable for matching the gas turbine operation at constant speed, almost constant air flow and reduced TIT.

• **Constant U_a.** By this modality of part load operation, starting from a design point the air mass flow is progressively lowered. By lowering also the cell current density it is possible to keep the same air utilization (Eq. (6)). This would give the same cell exhaust temperature, provided that the cell air inlet temperature is kept constant. However, the gas turbine at reduced speed and mass flow operates with a lower pressure ratio and higher TOT (with constant TIT), delivering hotter gases to the recuperator and hotter air to the FC inlet. Therefore, it is necessary to reduce furthermore the cell current density in order to keep the same cell exhaust temperature at U_a constant. By this practice, the TIT can be kept to the desired values; the large reduction of i_c will also significantly increase the cell voltage and efficiency. This modality of part-load operation is therefore suitable for matching the gas turbine operation at reduced speed, reduced mass flow and constant TIT.

Table 2 SOFC model assumptions

Δp/p air/fuel side (design point)	5% / 2%
Δp/p auxiliary combustion	6%
Heat loss SOFC (design point; T_{amb}=15°C)	2%
Combustion efficiency	98.5%
DC-AC efficiency (design point)	96%
Fuel inlet temperature	400°C
Fuel utilization factor (single passage)	80%
Air utilization factor (design point)	25%
Current density (design point)	350 mA/cm^2
Steam-to-carbon ratio for recirculation	1.8
Fuel composition	as by Tab.1
Available fuel pressure	3 bar
Δp/p fuel preheater hot/cold side	2%
Fuel preheater min. ΔT	45°C

The main assumptions in the SOFC model are shown in Table 2; the calculated reference cell voltage is 0.7 V at design conditions. In order to avoid overestimated cell efficiencies at low loads, the maximum cell voltage has been set to the value corresponding to 100 mA/cm^2 (minimum value of i_c in Fig. 9).

The same considerations discussed for the efficiency of the gas turbine inverter system apply to the fuel cell DC/AC conversion. Natural gas is preheated at about 400°C to obtain the best efficiency in H_2S and sulfur compounds (mercaptans, odorizing substances) adsorption by mean of catalytic Zinc-Oxide beds; the H_2S concentration must be kept under 0.1 ppmv to avoid any cell degradation effect, even if 1 ppmv gives a limited and recoverable voltage reduction [18,24].

The air and fuel pressure losses are changed with mass flow and density as described by Eq. (4). The SOFC total heat loss amount resulting from design point calculation (which includes the auxiliary combustion heat loss) is kept constant and independent of the load; the auxiliary combustion pressure loss percentage is also kept constant at part-load.

3 Plant Configuration and Thermodynamic Results

The proposed plant configuration is represented in Fig. 8 with the corresponding energy balances and with the thermodynamic conditions of all the relevant cycle points. It is basically a recuperative gas turbine cycle, where the SOFC receives the preheated and compressed air and delivers hot exhaust gases to the turbine. The main differences with respect to the original microturbine plant of Fig. 3 are the following:

• The pressure losses in the air loop are larger: before reaching the gas turbine, the air flow passes through the recuperator, the SOFC and the auxiliary combustion process, with a total pressure drop of about 14 percent (versus 9 percent for the GT cycle). The gas turbine operates therefore with a lower pressure ratio and a lower power output.

• The SOFC fuel flow is larger than the GT combustor fuel flow, thereby increasing the mass flow in the gas turbine.

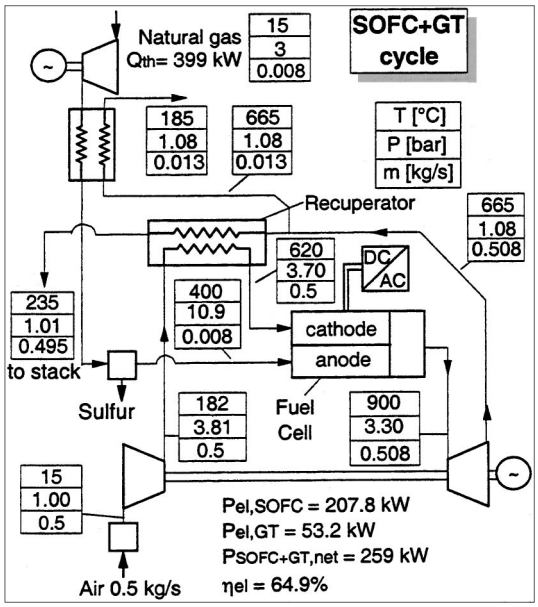

Fig. 8 The recuperative SOFC+GT cycle at design conditions; components assumptions as from Tables 1 and 2

Downloaded 02 Jun 2010 to 171.66.16.119. Redistribution subject to ASME license or copyright; see http://www.asme.org/terms/Terms_Use.cfm

Table 3 SOFC+GT and GT plant characteristics; (*)T stack =75°C

Plant characteristics	SOFC+GT	GT
Fuel flow in × LHV (kW)	399	185
Air flow at filter inlet (kg/s)	0.5	0.5
Combustor / FC outlet temperature (°C)	900	900
SOFC system power (kW)	209	-
GT power (kW)	53.5	56
Auxiliary power (kW)	3.0	0.5
Net total power (kW)	259.5	55.5
T exhaust (°C)	235	235
Turbine exhaust temperature (°C)	665	650
η_{el} (LHV)	64.9%	29.9%
Thermal power of exhaust gases(*) (kW)	83	83
I law efficiency with cogeneration(*)	86%	76%

Table 4 Second law losses for the GT cycle and for the plant configuration of Fig. 8

II law efficiency loss (%)	SOFC+GT	GT
SOFC	18.5	-
Combustor GT (including ΔP, η_{th})	0	33.0
Compressor (including ΔP air filter)	2.9	6.2
Gas Turbine	2.0	4.4
Recuperator (ΔT,Δp,η_{th})	3.5	7.3
Other heat exchangers (ΔT,Δp,η_{th}, mix)	0.3	-
Aux, organic, electric GT and fuel compressor	2.0	4.3
Stack (exhaust gas)	7.7	15.6
η_{II} total	63.1	29.2

• A fraction (about 3 percent) of the turbine exhaust flow is used to preheat the pressurized natural gas before the desulfurization process, up to about 400°C; hence the thermal capacity of the hot flow in the recuperator is a little lower.

• The conventional combustor is absent: this leads to substantial advantages for NO_x and CO emission abatement.

The analysis of SOFC+GT based power cycles is made with a simulation code already described in Campanari and Macchi [6] and Consonni et al. [25]. The SOFC+GT performances were calculated in two steps: (1) the GT part load model discussed in 2.1 was used to calculate all the cycle parameters and component performances of the recuperative GT cycle; and (2) the same operating conditions (GT pressure ratio and inlet/outlet temperatures, heat exchangers pressure drops etc., taking into account the design point parameters of Table 2) were used as input for the SOFC+GT model, providing point-by-point the corresponding performances of the SOFC+GT cycle.

Previous works have shown the possibility of obtaining net electrical efficiencies up to 75 percent (LHV) for medium (5–50 MW) or large scale (>100 MW) power plants adopting advanced gas turbines and SOFC systems with configurations similar or more complex than the cycle represented in Fig. 8: these plants benefit of both advanced GT cycles (intercooled, regenerative, reheated cycles) and the advantage of adopting high efficiency turbomachines [4], often with the addition of complex heat recovery bottoming cycles [26,6,27].

The thermodynamic performances of the smaller size and simpler cycle proposed here are nevertheless really remarkable: the net LHV efficiency reaches 65 percent with a total power output of about 250 kW, generated with a 4:1 ratio respectively by the SOFC and the gas turbine; exhaust gases leave the plant at about 230°C, giving the possibility of recuperating useful heat for cogeneration (see Table 3). These results confirm the possibility of obtaining high efficiencies with low pressure ratio SOFC and recuperated gas turbine cycles already investigated in a previous work [6].

The reversible work losses of this cycle, are represented in Table 4 and compared to the GT cycle losses. The irreversibilities occurring in the fuel cell include power conditioning, heat exchange, auxiliary combustion and heat losses, and pressure drop losses. It is possible to note that (i) the SOFC losses are about 15 points lower than the combustion losses occurring in the GT cycle; the large combustion loss is absent in the SOFC+GT cycle (the auxiliary combustion process loss weights for only one fourth of the total SOFC losses); and (ii) the losses related to compressor, turbine, recuperator and stack in the GT cycle are more than double with respect to the SOFC+GT cycle: this happens because in the SOFC plant the majority of the plant electric power is

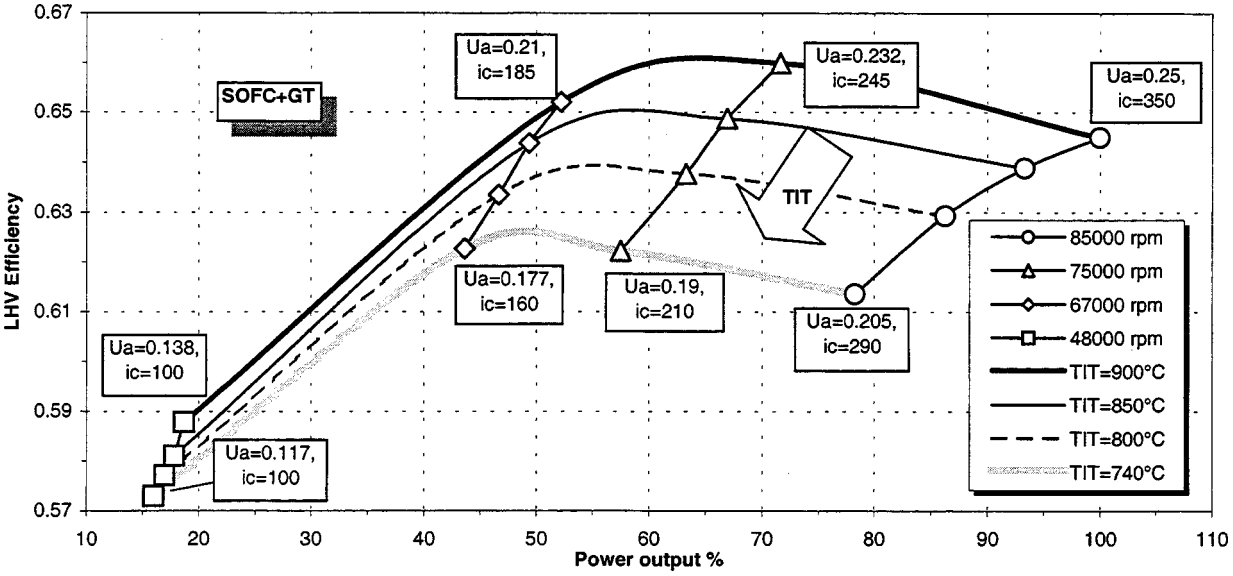

Fig. 9 Partial load performances of the SOFC+GT cycle. The cell current density is reduced according to Eq. (5), with lower limit at 100 mA/cm^2.

Downloaded 02 Jun 2010 to 171.66.16.119. Redistribution subject to ASME license or copyright; see http://www.asme.org/terms/Terms_Use.cfm

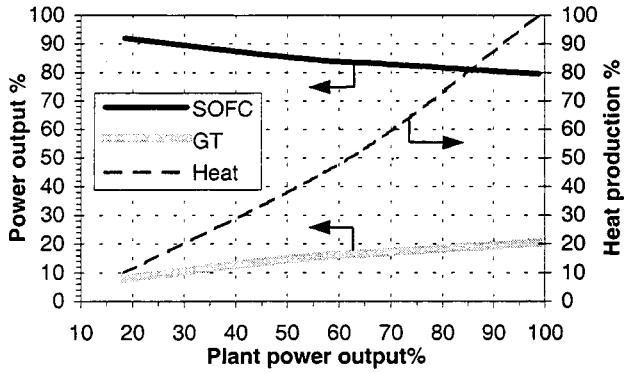

Fig. 10 SOFC+GT plant power distribution and heat production as a function of the load, for constant TIT operation

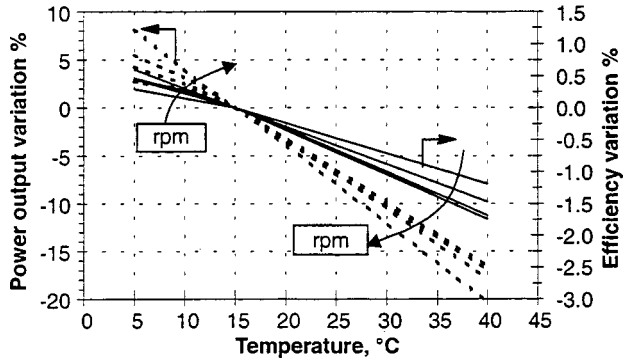

Fig. 11 Effects of ambient temperature on power output (dashed line) and cycle efficiency (solid line); the TIT is set to 900°C and each group of four lines is traced for 48,000, 67,000, 75,000, and 85,000 rpm

generated by the fuel cell, and the resulting higher fuel input reduces the weight of the losses related to the gas turbine section.

Figure 9 shows the results of the SOFC+GT cycle calculations at partial load: it is interesting to note how the fuel cell capability of achieving higher efficiencies at partial load is reflected on the total system efficiency, raised of about 3 percentage points at 60 percent of the full power output. The power distribution between the fuel cell and the gas turbine is shown in Fig. 10: at reduced output the fuel cell weight increases, raising up to more than 6:1 the power ratio with the gas turbine; by this way, thanks to the FC inherent performance gain, the system attains still a high electric efficiency. The heat production associated with the exhaust gases is almost linearly reduced at lower power outputs, with a little reduction of the exhaust temperature due to the lower compressor pressure ratio and to the more effective gas cooling in the recuperator.

Figure 11 deals with the calculated effects of changing the ambient temperature on the cycle performances; at nominal rpm, the surge margin decreases at lower temperatures, but it remains always over 12 percent.

4 Conclusions

Detailed calculations for the integration of SOFC and microturbine lead to a 250 kW-class plant with 65 percent net electrical efficiency (LHV). The possibility of demonstrating such performances on such a small scale plant, based on the available and existing 100 kW-class SOFC technology, could open wide and interesting markets for the future commercialization of these technologies.

The partial load analysis carried out in this paper demonstrates the possibility of obtaining very high system electric efficiency even at reduced plant electrical output, exploiting the fuel cell characteristic performance improvement at low current densities and microturbine variable-speed optimization. The energy-savings deriving by the application of such a system to cogeneration on small capacity plants are discussed in Campanari and Macchi [8].

5 Acknowledgments

The reported research was conducted at the Energetics Department of Politecnico di Milano as a part of the author's doctoral research under the supervision of Professor Ennio Macchi. The author thanks him for his guidance and constant support.

Nomenclature

A_c = cell active area (cm^2)
$c_{p,0}$ = specific heat at ambient temperature (kJ/(kg·K))
F = Faraday's constant (96439 Coulomb/mol of electrons)
i_c = cell current density (mA/cm^2)
m = mass flow rate (kg/s)
n = rotation speed (rpm)
p = pressure (Pa)
P_{el} = electric power (MW)
Q_{th} = thermal power (MW)
T = temperature (°C or K)
U_a = cell air utilization factor: $U_a = O_{2,consumed}/O_{2,inlet}$
U_f = cell fuel utilization factor: $U_f = (H_{2,consumed})/H_{2,inlet} + CO_{inlet} + 4CH_{4,inlet}$
V_c = cell voltage (V)
W_{el} = electric specific work (kJ/kg)
X_{O2} = oxygen molar fraction
β = pressure ratio
Δh = enthalpy change (kJ/kg)
ε_R = recuperator effectiveness
η = isentropic efficiency
η_p = polytropic efficiency
η_{el} = electric efficiency
η_{th} = thermal efficiency
ρ = density (kg/m^3)

Subscripts

c, t = compressor, turbine respectively
r = corrected conditions
re = real
ref = reference conditions (15°C, 101325 Pa)

Acronyms

DC/AC = direct/alternating current
FC = fuel cell
GT = gas turbine
LHV = lower heating value (kJ/kg)
SOFC = solid oxide fuel cell
TIT = turbine inlet temperature (total conditions)
TOT = turbine outlet temperature (total conditions)

References

[1] Barker, T., editor, 1997, ''Power-Gen International '96: Micros, Catalysts and Electronics,'' Turbomachinery International, **38**, pp. 19–21.
[2] De Biasi, V., 1998, ''Low Cost and High Efficiency Make 30 to 80 kW Microturbines Attractive,'' Gas Turbine World, No. **1-1998**, Pequot Publishing Inc. pp. 28–31.
[3] Harvey, S. P., and Ritcher, H. I., 1994, ''Gas Turbine Cycles With Solid Oxide Fuel Cells—Part I and II,'' ASME J. Energy Resour. Technol., **116**, pp. 305–318.
[4] Stephenson, D., and Ritchey, I., 1997, ''Parametric Study of Fuel Cell and Gas Turbine Combined Cycle Performance,'' ASME Paper 97-GT-340.
[5] Massardo, A. F., and Lubelli, F., 1998, ''Internal Reforming Solid Oxide Fuel Cell-Gas Turbine Combined Cycles (IRSOFC-GT)—Part A: Cell Model and Cycle Thermodynamic Analysis,'' ASME Paper 98-GT-577.
[6] Campanari, S., and Macchi, E., 1998, ''Thermodynamic Analysis of Advanced Power Cycles Based Upon Solid Oxide Fuel Cells, Gas Turbines and Rankine Bottoming Cycles,'' ASME Paper 98-GT-585.
[7] Veyo, S., and Forbes, C., 1998, ''Demonstrations Based on Westinghouse's

Downloaded 02 Jun 2010 to 171.66.16.119. Redistribution subject to ASME license or copyright; see http://www.asme.org/terms/Terms_Use.cfm

Prototype Commercial AES Design,'' *Proceedings of the Third European Solid Oxide Fuel Cell Forum*, pp. 79–86.
[8] Campanari, S., and Macchi, E., 1999, ''The Combination of SOFC and Microturbine for Civil and Industrial Cogeneration,'' ASME Paper 99-GT-084.
[9] Bessette, N. F., George, R. A., 1996, ''Electrical Performance of Westinghouse's AES Solid Oxide Fuel Cell,'' 2nd International Fuel Cell Conference (IFCC 4-12) Japan.
[10] 1998, Elliott Energy Systems—The TA Series Turbo Alternator® preliminary specifications of TA turbogenerators, Elliott Energy Systems Inc., Stuart, FL.
[11] O'Brien, P., 1998, ''Development of a 50-kW, Low-Emission Turbo-Generator for Hybrid Electric Vehicles,'' ASME Paper 98-GT-400.
[12] Uchida, H., Shiraki, M., Bessho, A., and Yagi, Y., 1994, ''Development of a Centrifugal Compressor for 100 kW Automotive Ceramic Gas Turbine,'' ASME Paper 94-GT-73.
[13] Pullen, K. R., Baines, N. C., Hill, S. H., 1992, ''The Design and Evaluation of a High Pressure Ratio Radial Turbine,'' ASME Paper 92-GT-93.
[14] Jones, A. C., 1994, ''Design and Test of a Small, High Pressure Ratio Radial Turbine,'' ASME Paper 94-GT-135.
[15] Kim, S. Y., Park, M. R., and Cho, S. Y., 1998, ''Performance Analysis of a 50 kW Turbogenerator Gas Turbine Engine,'' ASME Paper 98-GT-209.
[16] Holbrook, J. D., 1998, personal communications with Elliott Energy Systems Inc.
[17] Carnö, J., Cavani, A., and Liinanki, L., 1998, ''Micro Gas Turbine for Combined Heat and Power in Distributed Generation,'' ASME Paper 98-GT-309.
[18] Ray, E. R., and Ruby, J. D., 1992, ''Evaluation of the Westinghouse Solid Oxide Fuel Cell Technology for Electric Utility Applications in Japan,'' EPRI TR-100713.
[19] Fimet, 1998, personal communications with Fimet Motori & Riduttori Co., Bra, Italy.
[20] Singhal, S. C., 1997, ''Recent Progress in Tubular SOFC Technology,'' *Proceedings of the V Int. Symposium on Solid Oxide Fuel Cells* (SOFC-V), Vol. 97–40, The Electrochemical Society Inc., Pennington, NJ.
[21] Hirschenhofer, J. H., Stauffer, D. B., and Engleman, R. R., 1994, *Fuel Cells, A Handbook, Rev. 3*, Gilbert Commonwealth Inc. for U.S. Department of Energy (DOE), Report DOE/METC-94/1006, published by U.S. Dept. of Energy, Morgantown.
[22] Veyo, S., 1996, ''The Westinghouse SOFC Program—A Status Report,'' *Proceedings of the 31st IECEC*, no. 96570, pp. 1138.
[23] Campanari, S., and Macchi, E., 1997, ''Integrated Cycles With Solid Oxide Fuel Cells and Gas-Steam Combined Cycles,'' (in Italian), IX Congress Technologies and Complex Energy Systems ''Sergio Stecco,'' Milano, June 1997.
[24] Lundberg, W. L., 1990, ''System Applications of Tubular Solid Oxide Fuel Cells,'' *Proceedings of the 25th IECEC*, pp. 218–223.
[25] Consonni, S., Lozza, G., Macchi, E., Chiesa, P., and Bombarda, P., 1991, ''Gas-Turbine-Based Advanced Cycles for Power Generation—Part A: Calculation Model,'' International Gas Turbine Conference, Yokohama 1991, Vol. III, pp. 201–210.
[26] Bevc, F. P., Lundberg, W. L., and Bachovchin, D. M., 1996, ''Solid Oxide Fuel Cell Combined Cycles,'' ASME Paper 96-GT-447.
[27] Lobachyov, K., and Richter, H. J., 1996, ''Combined Cycle Gas Turbine Power Plant With Coal Gasification and Solid Oxide Fuel Cell,'' ASME J. Energy Resour. Technol., **118**, pp. 285–292.

Downloaded 02 Jun 2010 to 171.66.16.119. Redistribution subject to ASME license or copyright; see http://www.asme.org/terms/Terms_Use.cfm

Fuel Gas Cleanup Parameters in Air-Blown IGCC

Richard A. Newby
Wen-Ching Yang
Science & Technology Center,
Siemens Westinghouse Power Corporation,
1310 Beulah Road,
Pittsburgh, PA 15235-5068

Ronald L. Bannister
Emerging Technologies,
Siemens Westinghouse Power Corporation,
4400 Alafaya Trail,
Orlando, FL 32826-2399

Fuel gas cleanup processing significantly influences overall performance and cost of IGCC power generation. The raw fuel gas properties (heating value, sulfur content, alkali content, ammonia content, ''tar'' content, particulate content) and the fuel gas cleanup requirements (environmental and turbine protection) are key process parameters. Several IGCC power plant configurations and fuel gas cleanup technologies are being demonstrated or are under development. In this evaluation, air-blown, fluidized-bed gasification combined-cycle power plant thermal performance is estimated as a function of fuel type (coal and biomass fuels), extent of sulfur removal required, and the sulfur removal technique. Desulfurization in the fluid bed gasifier is combined with external hot fuel gas desulfurization, or, alternatively with conventional cold fuel gas desulfurization. The power plant simulations are built around the Siemens Westinghouse 501F combustion turbine in this evaluation. [S0742-4795(00)00502-0]

Introduction

Various forms of coal and biomass gasification combined-cycle (IGCC) power generation are currently being demonstrated throughout the world to establish the general technical and economic viability of the technologies [1–3]. These demonstration projects are applying variations in the following several major process parameters:

- entrained (single and two-stage), fluid bed, and fixed bed gasification
- oxygen and air-blown gasification
- fuel gas cooling techniques (quench, indirect steam generation)
- conventional cold fuel gas cleaning and advanced hot fuel gas cleaning
- combustion turbine type, firing conditions, and equipment adaptations
- air separation integration and steam integration alternatives

Coal and biomass-derived fuel gases must be cleaned to meet power plant environmental requirements (SOx, NOx, and particulate emissions) and to satisfy turbine protection specifications (particulate, alkali vapors, several metals). It has been demonstrated that conventional cold fuel gas cleaning techniques can meet both of these requirements. Two Westinghouse 501Ds were operated at the Dow Chemical, Plaquemine, Louisiana coal gasification plant (predecessor to Destec gasifier) starting in 1987. The cold fuel gas cleaning system on this oxygen-blown, entrained gasifier met Westinghouse turbine specifications and resulted in more than 125,000 h of operation of the turbines with greater than 95 percent availability.

Cold fuel gas desulfurization systems, operating at about 38°C (100°F), have improved their performance and reduced operating costs by adding a hot gas filter operating at 300 to 540°C (570 to 1000°F) to remove particulates before the fuel gas is desulfurized [4,5]. Hot fuel gas desulfurization, operating at 430°C to 540°C (800 to 1000°F) has also been developed because of its potential improvements in overall power plant efficiency. Hot fuel gas cleaning systems (zinc-based regenerative sorbents) are being demonstrated in U.S. Clean Coal Technology programs [6,7].

Contributed by the International Gas Turbine Institute (IGTI) of THE AMERICAN SOCIETY OF MECHANICAL ENGINEERS for publication in the ASME JOURNAL OF ENGINEERING FOR GAS TURBINES AND POWER. Paper presented at the International Gas Turbine and Aeroengine Congress and Exhibition, Stockholm, Sweden, June 2–5, 1998; ASME Paper 98-GT-341. Manuscript received by IGTI March 18, 1998; final revision received by the ASME Headquarters October 20, 1999. Associate Technical Editor: R. Kielb.

While hot fuel gas cleaning is expected to provide thermal performance advantages over conventional cold fuel gas cleaning, there currently exists limited understanding of the magnitude of their relative merits and the influence of key fuel and process parameters. Siemens Westinghouse Power Corporation (SWPC) has conducted previous studies to assess the integration and performance of IGCC with their fleet of combustion turbines [8–11]. This paper describes IGCC sulfur removal considerations for an air-blown, fluidized bed gasification process coupled with a SWPC 501F combustion turbine and assesses the estimated power plant performance results as a function of several fuel properties and sulfur removal parameters.

IGCC Gas Cleaning/Sulfur Removal Process Options

In air-blown, fluidized bed gasification of coal, it has been demonstrated that bulk fuel gas desulfurization can be performed directly within the fluid bed gasifier by feeding dolomite or limestone to the gasifier, at temperatures of 815 to 1038°C (1500 to 1900°F), to sulfur removal levels as high as about 95 percent. The reaction conversion performance and rates have been studied extensively in the literature [12]. The reaction solid product, CaS, must be transformed into an environmentally stable solid waste by oxidation to $CaSO_4$, or by conversion to some other stable product [13]. The use of dolomite or limestone in the fluid bed gasifier has the added benefits of increasing the carbon gasification rate, reducing the carbon content of the gasifier ash, and reducing the content of tars and other higher hydrocarbons in the raw fuel gas.

Downstream of the gasifier, the fuel gas can be cooled to an appropriate temperature for second-stage, or polishing desulfurization within an external fuel gas cleaning system. Second-stage desulfurization can be performed by using a commercial, cold gas desulfurization process operating at about 38°C (100°F), or an advanced, hot gas desulfurization process operating at about 540°C (1000°F). The commercial, cold gas desulfurization process is preceded by a hot gas filtration device that removes nearly all of the particulate from the fuel gas. Other fuel gas cleaning functions, such as HCl removal and hydrolysis, are also integrated into the cold fuel gas cleaning process. The advanced, hot fuel gas cleaning processes use regenerable solid sorbents based on zinc oxide combined with other metal carriers (e.g., various forms of zinc titanate, or commercial Z-Sorb®—Phillips Petroleum Co.). Other gas cleaning functions, such as HCl removal might also be performed in the process to enhance the durability of the regenerative desulfurization sorbent. The hot fuel gas desulfurization may be either preceded by a hot gas filter or followed by a hot gas filter depending on the nature of the desulfurizer process. Fluid bed, transport bed, and moving bed forms of the desulfurizer have

Copyright © 2000 by ASME

Downloaded 02 Jun 2010 to 171.66.16.119. Redistribution subject to ASME license or copyright; see http://www.asme.org/terms/Terms_Use.cfm

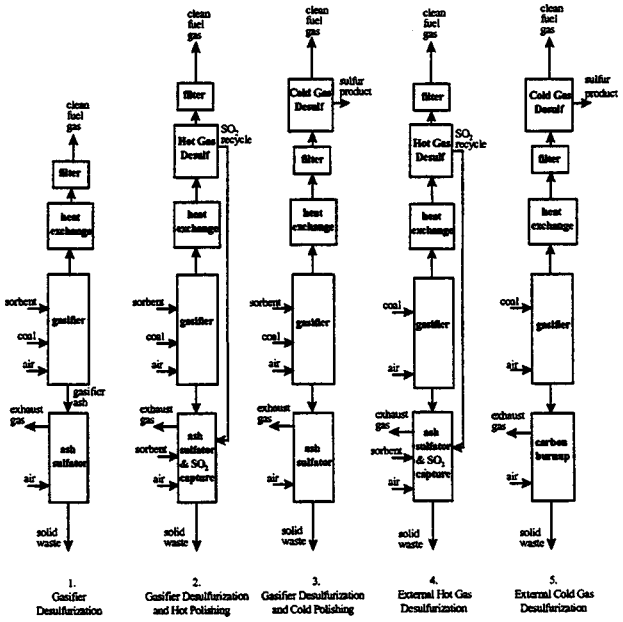

Fig. 1 Process schematics for alternative IGCC sulfur removal approaches

been under development and are currently being demonstrated. Alternative hot fuel gas regenerable sulfur sorbent types continue to be developed [14].

Thus, it is possible to conceive of several fuel gas desulfurization schemes for fluid bed gasification that might be applied to IGCC depending on the coal sulfur content and the level of desulfurization required in the power plant. Five of these schemes are illustrated in Fig. 1:

1 bulk desulfurization within the gasifier only
2 bulk desulfurization within the gasifier followed by second-stage, hot fuel gas regenerative desulfurization
3 bulk desulfurization within the gasifier followed by second-stage, conventional cold fuel gas desulfurization
4 external, hot fuel gas regenerative desulfurization only
5 external, conventional cold fuel gas desulfurization only

The figure shows only the main process steps and the main inlet and outlet steams for each scheme. The functions of the gasifier ash processing system change with each scheme and are listed in the figure. The overall sulfur removal capabilities of the first scheme, in-gasifier sulfur removal, is limited to about 95 percent, while the other schemes can achieve greater than 99 percent sulfur removal. Each scheme may have a significant influence on the air-blown IGCC power plant process complexity, availability, thermal performance, and economics. These influences would be expected to differ for an oxygen-blown, fluidized bed IGCC power plant.

Air-Blown IGCC Plant Process Integration

The air-blown, fluid bed IGCC consists of the four major process sections illustrated in Fig. 2: (1) the coal/sorbent feeding block, (2) the gasification block, (3) the fuel gas cleaning block, and (4) the power island. Another plant system of importance is the water treatment system. Figure 2 indicates the relationships between these sections in this air-blown IGCC process. The IGCC plant integrates these process sections in several areas:

• The power island's combustion turbine utilizes the fuel gas generated by the gasification block.

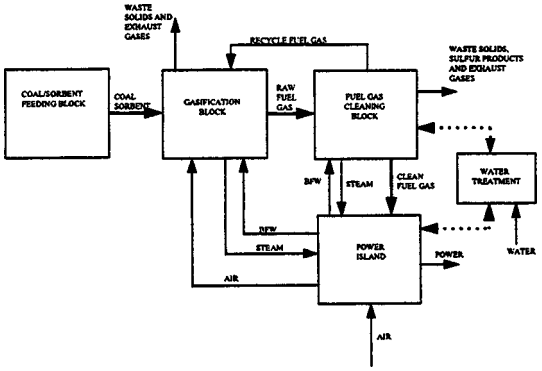

Fig. 2 Air-blown IGCC power plant process blocks

• The power island's combustion turbine supplies pressurized air through booster compressors to the gasifier block's gasifier, the fuel gas cleaning block's sorbent regenerator, and the coal/sorbent feeding block for pressurization and transport.

• The power island's steam bottoming power cycle supplies pressurized feed water to the gasification block and the fuel gas cleaning block, and intermediate pressure steam to the gasification block's gasifier. It subsequently receives steam at several pressure levels from the gasification block and the fuel gas cleaning block.

• The condensate system of the power island's steam bottoming cycle is integrated with the gasification block and the fuel gas cleaning block by serving as a heat sink for the low level waste heat generated.

• The fuel gas cleaning block provides recycle fuel gas to the gasification block for various solids transport needs.

• The water treatment system handles the integrated needs of the fuel gas cleaning block and the power island.

In general, sulfur removal is performed in two process steps, as in Fig. 1, schemes 2 and 3. Bulk sulfur removal is first conducted within the gasifier block by feeding a cheap, once-through sorbent, limestone, into the fluid bed gasifier. Subsequently, polishing or second-stage sulfur removal is conducted at high temperature in the fuel gas cleaning block using an advanced, regenerative sulfur sorbent system. Polishing sulfur removal using conventional cold fuel gas cleaning is also evaluated. While the power plant process integration considerations are substantial in this air-blown IGCC power plant, they are far simpler than in the equivalent oxygen-blown IGCC power plant.

Evaluation Basis

The parameters in this evaluation are the fuel properties (coals and biomass), the fuel gas desulfurization scheme, and the level of sulfur removal required. The basis for the power plant simulation is described below.

Fuel Properties. The four fuels listed in Table 1 are considered in the evaluation. Three coals, a high-sulfur, U.S. Eastern bituminous coal (Pittsburgh #8), a low-sulfur bituminous Austra-

Table 1 Coal and biomass compositions

	Pgh #8 (U.S.)	Blair Athol (Australia)	Lignite (India)	Bagasse (Hawaii)
	As received (wt%)	As received (wt%)	As received (wt%)	As received (wt%)
C	69.4	74.0	48.0	29.12
H	4.5	4.5	4.0	3.10
O	6.1	5.0	12.3	23.37
N	1.2	1.7	0.6	0.25
S	2.9	0.4	2.1	0.03
Ash	9.9	9.9	8.0	3.84
Moisture	6.0	4.5	25.0	40.29
Volatile matter	35.9	29.4	36.1	48.67
Fixed carbon	48.2	56.2	30.9	7.20
LHV- MJ/kg (Btu/lb)	28.9 (12,450)	30.1 (12,950)	19.1 (8,222)	10.6 (4,580)

Downloaded 02 Jun 2010 to 171.66.16.119. Redistribution subject to ASME license or copyright; see http://www.asme.org/terms/Terms_Use.cfm

lian coal (Blair Athol), and a representative Indian lignite were considered. Also, a biomass fuel, bagasse from Hawaii was considered. Both the as-received and as-fed compositions and heating values of the fuels are listed. It is unlikely that biomass (bagasse) could be supplied in sufficient quantity for the power plant application evaluated here, and this case is simply treated as a hypothetical study parameter relating to the composition of the biomass fuel.

Fuel Gas Cleaning Parameters. The IGCC power plant utilizes the fuels listed in Table 1 while satisfying representative environmental emissions standards for modern, greenfield power plants in the U.S. relating to sulfur oxides, nitrogen oxides, particulate, solid waste, and liquid effluents. Fuel gas cleaning block processes based on both advanced, hot fuel gas cleaning and on conventional, cold fuel gas cleaning were evaluated. Table 2 lists the sulfur removal performance factors applied in the evaluation as well as the sulfur removal process options considered, in Fig. 1. In the biomass case, it is assumed that no sulfur removal is required. Particulate and NOx power plant stack emissions are controlled by hot gas particulate filters and dry, low-NOx combustors. The high ammonia content expected in the biomass-derived fuel gas will make low-NOx performance more difficult to achieve, and additional ammonia cracking in the fuel gas may be required. In the case of biomass, limestone is used as an inert fluid bed material, and only a small makeup for system losses is needed. The gasifier sorbent type is a representative limestone having 86 wt percent calcium carbonate content. The analogous cold fuel gas cleaning performance factors are listed in Table 3. The cold fuel gas concepts are illustrated in Fig. 1.

Combustion Turbine. The combustion turbine applied in this evaluation is the SWPC 501F. The 501F engine is a 3600-rpm heavy duty combustion turbine designed to serve the 60-Hz power generation needs. The technologically advanced engine represents one of the latest in the evolutionary cycle that continues a long line of large single-shaft, heavy duty combustion turbines [15].

Table 2 Hot gas desulfurization parametric cases performance factors

	Pgh #8 (U.S.)			Blair Athol (Australia)			Lignite (India)			Bagasse (Hawaii)
Sulfur Removal Scheme	2	4	1	2	4	1	2	4	1	None
Gasifier sulfur removal (%)	90	0	95	75	0	70	90	0	95	0
Limestone Ca/S molar feed ratio	2.0	0	3.0	1.5	0	1.5	2.0	0	3.0	small makeup
Second-stage (hot) desulfurizer sulfur removal (%)	95	99.5	0	80	95	0	95	99.5	0	0
Second-stage (hot) sorbent Zn/S molar feed ratio	0.03	0.03	0	0.03	0.03	0	0.03	0.03	0	0

1: Bulk desulfurization in gasifier only
2: Bulk desulfurization in gasifier plus second-stage, hot desulfurization
4: External, hot desulfurization only

Table 3 Cold gas desulfurization parametric cases performance factors

	Pgh #8 (U.S.)		Blair Athol (Australia)		Lignite (India)	
Sulfur Removal Scheme	3	5	3	5	3	5
Gasifier sulfur removal (%)	90	0	75	0	90	0
Limestone Ca/S molar feed ratio	2.0	0	1.5	0	2.0	0
Second-stage (cold) desulfurizer sulfur removal (%)	95	99.5	80	95	95	99.5

3:: Bulk desulfurization in gasifier plus second-stage, conventional, cold desulfurization
5: External, conventional, cold desulfurization only

Some major 501F characteristics based on natural gas fuel are

- Air flow, kg/s (lb/s): 436 (961)
- Number of compressor stages: 16
- Compression ratio: 14.6
- Number of combustor cans: 16
- Rotor inlet temperature, °C (F): 1316 (2400)
- Number of turbine stages: 4
- Number of cooled turbine rows: 6
- Turbine exhaust gas flow, kg/s (lb/s): 445 (981)
- Exhaust temperature, °C (F): 607 (1125)
- Output—simple-cycle (MW): 164
- Output—combined-cycle (MW): 260
- Efficiency—simple cycle (percent LHV): 36.0
- Efficiency—combined-cycle (percent LHV): 56.8

To date, 77 of the 501F/701F machines have been sold, and the 38 units currently operating have accumulated a combined, approximate 250,000 operating hours. The longest operating 501Fs are located at the FPL, Lauderdale plant. The four units at this site have operation for more than four years, accumulating about 132,000 h with an average reliability of 99.6 percent and an average availability of 94.6 percent.

Plant Conditions. The power plant is assumed to be a new, combined-cycle plant located at a greenfield site. It is operated as a base loaded plant. Ambient conditions were fixed at ISO conditions for the evaluation. The power plant boundaries in the evaluation encompass the entire coal and sorbent receiving, handling and preparation systems (the coal/sorbent feeding block), all power plant normal auxiliaries, and the solid waste handling and storage systems.

Process Assumptions. The fluidized bed gasifier used is representative of several types being developed, such as the KRW/Kellogg fluid bed gasifier, the IGT U-Gas fluid bed gasifier, and the Rheinbraum HTW. Several aspects of the gasification block and fuel gas cleaning block (hot fuel gas cleaning) process flow diagrams are similar to the KRW/Kellogg process flow diagrams for the Sierra Pacific, Pinon Pine IGCC power plant [16].

A process flow diagram for a cold fuel gas cleaning system used for polishing sulfur removal was developed from information available in the open literature [17–19].

The IGCC power plant was simulated on ASPEN PLUS™, a process simulator providing state-of-the-art process estimation capabilities for such process applications. A detailed stage-by-stage model of the 501F combustion turbine was applied in the simulation. Equilibrium gasifier behavior was assumed except for carbon conversion and sulfur removal, where empirical conversion criteria was applied.

The process and cycle conditions were not optimized in the evaluation, but acceptable conditions were selected and applied and only limited cycle variations were considered.

The gasifier assumptions in Table 4 were selected based on prior fluid bed gasifier experience with similar coals and biomass. The gasifier inputs of air, steam, and recycled fuel gas, relative to the coal feed, were selected to produce the desired gasifier temperature and reaction kinetic conditions suitable for each fuel. The range in gasifier temperatures evaluated for the bagasse fuel results from tradeoffs between carbon conversion, tar formation and cracking, and the tendency for ash agglomeration in the fluid bed. Estimates of handling/feeding, gasification and cleanup component pressure drops, heat losses, auxiliary power consumption, auxiliary fuel consumption, steam consumption and generation, etc. were made as a function of the process of stream rates and conditions from available process information for similar components and applications. Standard assumptions used in Westinghouse commercial cycle estimates for power island component heat losses, pressure drops, mechanical losses, efficiency factors, and auxiliary losses have been applied.

Downloaded 02 Jun 2010 to 171.66.16.119. Redistribution subject to ASME license or copyright; see http://www.asme.org/terms/Terms_Use.cfm

Table 4 Fluid bed gasifier conditions and performance assumptions

	Pgh #8 (U.S.)	Blair Athol (Australia)	Lignite (India)	Bagasse (Hawaii)
Gasifier temperature -°C (°F)	982 (1800)	982 (1800)	927 (1700)	760 (1400) 816 (1500) 871 (1600)
Gasifier steam rate (% of carbon feed rate)	15 - 25	15 - 25	15	5 - 10
Carbon Conversion (%)	94	94	96	95
Coal feed drying required (wt% moisture in coal feed)	None	None	10	15

The fuel gas particulate device is a ceramic candle barrier filter type. It operates at a filter temperature of 538°C (1000°F) and is designed to maintain a maximum pressure drop of 5 psi. The polishing, or second-stage hot fuel gas sulfur removal system, is an advanced hot fuel gas desulfurization system using regenerative Z-Sorb (Phillips Petroleum Co.) in a fluidized bed contactor. The steam bottoming cycle steam conditions are: 69 bar/510°C/510°C (1000 psia/950°F/950°F).

IGCC Plant Description

The power plant description is built around the IGCC process with in-gasifier desulfurization and second-stage hot or cold fuel gas cleaning (schemes 2 and 3 in Fig. 1). Process modifications needed for the other variations in IGCC schemes are also described (Fig. 1, schemes 1, 4 and 5). It should be noted that the ASME is developing a performance test code (PTC) that will define the procedures for the performance testing of gasification combined cycle plants [20]. This code will define the boundaries of the overall power plant and of the two major plant sections, the gasification block, and the power island.

Coal/Sorbent Feeding Block. The equipment and processes in this block are based on dry feeding and are commercially available with significant industrial experience. The block consists of coal/sorbent receiving and handling, coal/sorbent crushing, sizing and drying, and coal/sorbent pressurization and feeding units. The coal/sorbent receiving and handling facilities are conventional systems, which are similar to those being used in many existing coal-fired plants.

Coal and sorbent are crushed to $<$6.35 mm (1/4 in.) size. Crushed and dried coal is pneumatically transported to the coal pressurization and feeding system. This system includes receiving vessels, lock hoppers, and feed hoppers. The receiving vessels separate the coal from its transport gas and then transfer the coal to the lock hoppers. The pressurized coal is metered using a screw conveyor and is transported to the gasifier pneumatically using pressurized air provided by the power island equipment. A similar system is used for sorbent (limestone) feeding to the gasifier. It is important to include this block in IGCC power plant performance estimates so that auxiliary power losses and auxiliary fuel consumption can be properly estimated. This block may utilize significantly different fuel feeding equipment with biomass fuel.

Gasification Block. The gasification process can handle a wide variety of fuels and produces a low-thermal-value fuel gas. A typical configuration for the gasification block is shown in Fig. 3. It consists of the gasifier and the equipment needed for processing the gasifier waste solids (ash, char, and spent limestone sorbent).

The gasifier is a refractory-lined pressure vessel with inlet and outlet nozzles for feed gases and solids, and exit gases and solids. The gasifier also utilizes a set of recycle cyclones to maintain sufficient particle residence times in the reactor. The gasifier operating pressure is selected to satisfy the pressure requirement of the combustion turbine. Coal, limestone (sulfur sorbent), steam, air, and recycle fuel gas are fed to the fluid bed gasifier. Coal and sorbent are fed pneumatically with transport air. Sorbent is fed to the gasifier to accomplish bulk sulfur removal within the vessel. The recycle fuel gas acts as an inert gas for purges, as a transport gas for reactive solids, and as a solids stream coolant.

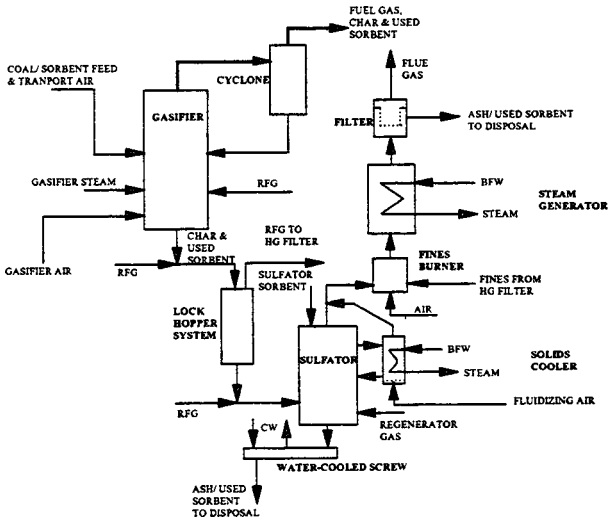

Fig. 3 Gasification block process schematic

The solids drained from the gasifier contain char and spent sorbent in the form of CaS that must be processed to render it environmentally acceptable. The carbon in the solid drain must also be utilized to achieve acceptable plant performance. The drained gasifier solids are depressurized and reacted in a fluidized bed reactor (the sulfator) with exhaust gas from the polishing sulfur removal system regenerator (see Fig. 4). The regenerator exhaust gas contains oxygen and sulfur oxides that react with the gasifier waste solids to convert the spent sorbent into an inert form of $CaSO_4$. The process also captures the polishing sulfur in the form of $CaSO_4$ so that normal sulfur products (elemental sulfur or sulfuric acid) need not be generated. Additional sorbent may be added to the sulfator for this purpose. Most of the carbon in the gasifier drain is also combusted in either the sulfator or in the fines burner that follows the sulfator. The flyash removed by the fuel gas filter in the fuel gas cleaning block is also recycled to the sulfator to utilize its contained carbon (see Fig. 4). Steam is generated from the sulfator and fines burner exhaust gas for export to

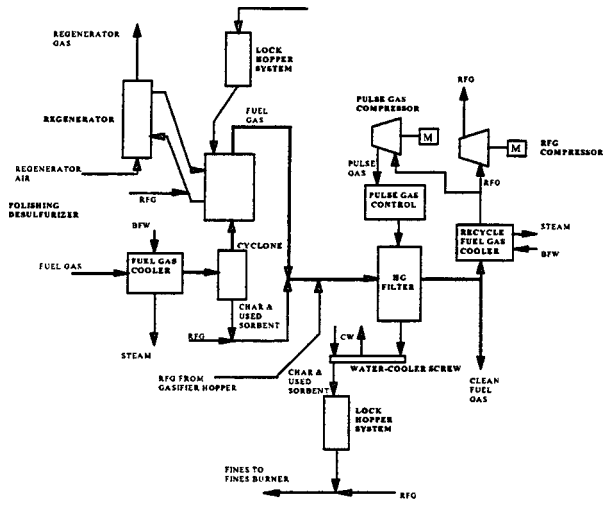

Fig. 4 Hot gas cleaning block process schematic

Downloaded 02 Jun 2010 to 171.66.16.119. Redistribution subject to ASME license or copyright; see http://www.asme.org/terms/Terms_Use.cfm

the power island. The temperature of the sulfator is controlled by a fluidized bed solids cooler and solids recirculation loop.

Hot Fuel Gas Cleaning Block. Figure 4 describes the fuel gas cleaning block for the hot fuel gas cleaning process. It contains a fuel gas cooler, a polishing sulfur removal system, a hot gas filter system, and a recycle fuel gas system. Each of these are briefly described.

Fuel Gas Cooler. The hot, raw fuel gas leaving the gasification block is cooled to 538°C (1000°F) in the fuel gas cooler. The design may be either a fire-tube design or a water-tube design depending on the designers preference with respect to the control of heat transfer surface fouling. High-pressure, super-heated steam is raised in the cooler.

Polishing Sulfur Removal System. In Fig. 4, the hot fuel gas cleaning system contains a fluidized bed desulfurizer that reacts to the fuel gas H_2S with a zinc-based polishing sulfur sorbent. The polishing sorbent is circulated by dense-phase pneumatic transport to a fluidized bed regenerator. The regenerator operates at about 649°C (1200°F) and reacts air with the utilized sorbent to generate an SO_2-rich regenerator gas and a reusable sorbent. The reactions may need to be moderated by the addition of steam also. The regenerated polishing sorbent is circulated back to the desulfurizer. Makeup polishing sorbent is also added to the desulfurizer. Economics demand that the polishing sorbent losses be very small. The sorbent regenerator produces a concentrated, gaseous sulfur oxide stream that is suitable for conversion to elemental sulfur, sulfuric acid using processing similar to that used in low-temperature fuel gas cleaning. In the evaluated process, gypsum is generated for final disposition as part of the gasification block (Fig. 3). No HCl removal, ammonia removal, or hydrolysis is performed in the selected process.

Hot Gas Filter. The desulfurized fuel gas is passed through a ceramic filter at 538°C (1000°F) to remove particulate to levels needed to satisfy environmental and turbine protection requirements. The particulate collected in the desulfurizer cyclone and entrained flyash from the gasifier hopper (Fig. 3) are sent to the hot gas filter to improve the filter performance and to improve the process economics.

A ceramic candle filter system has been used in the evaluation. The filter system includes a pulse gas compression system that uses recycle fuel gas as the pulse gas media.

Recycle Fuel Gas System. A portion of the cleaned fuel gas is utilized for inert gas and transport gas purposes. It is withdrawn following the ceramic filter and is cooled and compressed to provide for this need.

Cold Fuel Gas Cleaning Block. In the cold fuel gas cleaning process diagram, Fig. 5, the fuel gas is first cooled to 538°C (1000°F), just as in the hot fuel gas cleaning case. The 538°C fuel gas then passes through a ceramic filter to remove particulate. The partially cleaned fuel gas from the filter is then cooled further, down to about 38°C (100°F), both raising steam and preheating cleaned fuel gas. The cleaned fuel gas is available at a temperature of about 41°C (105°F) and is preheated to the extent possible. The pressure drop across the gas-gas heat exchanger would be fairly large to keep the equipment compact.

Typically, the fuel gas from the particulate removal unit would be routed to a catalytic hydrolyzer to convert the minor nitrogen contaminant (HCN) to NH_3 and COS to H_2S. The fuel gas would be heated before entering the hydrolyzer to the appropriate conversion temperature using medium pressure steam. No ammonia removal or hydrolysis is performed in the selected process.

In the cold fuel gas sulfur removal process, the partially cleaned fuel gas sulfur contaminants (primarily H_2S and COS) are removed by the selexol process. A portion of the fuel gas carbon dioxide, about 15 percent, is removed as well. The partially cleaned fuel gas enters at about 100°F, and exits at about 105 F to go to the fuel gas preheater.

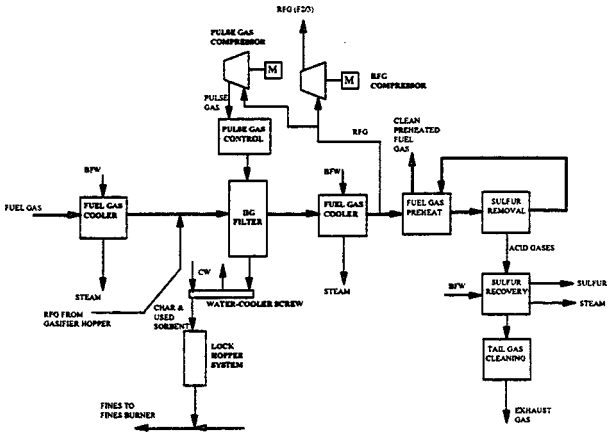

Fig. 5 Cold fuel gas cleaning block process schematic

The removed acid gases are treated in a conventional Claus sulfur recovery process. The Claus sulfur recovery unit is a two-stage catalytic unit where acid gases are combusted and reacted to produce salable elemental sulfur. Acid gases containing NH_3 and H_2S are combusted in the Claus furnace. NH_3 is combusted to form molecular nitrogen (N_2) and one-third of the H_2S is converted to SO_2. SO_2 and the remaining H_2S react in two catalytic stages to form elemental sulfur and water. The process generates steam for export to the power island.

The tail gases from the Claus plant go to a Beavon/Stretford tail gas cleaning process. In this unit, the small amount of unconverted sulfur compounds in the tail gas from the Claus unit are completely converted to H_2S. Gas from the reactor is cooled and treated for H_2S removal by absorption with solvent. The H_2S is then recycled back to the Claus sulfur recovery unit for conversion to elemental sulfur. The process consumes a small amount of auxiliary fuel provided by clean gasifier fuel gas. The process also generates a small amount of steam for export to the power island. The vent gas from the tail gas process contains a small content of H_2S and is incinerated before being exhausted.

Process Modifications for Alternative Sulfur Removal Schemes and Biomass. The Biomass fuel, bagasse, is assumed to require no desulfurization, and the process was modified to reflect this. The sulfator and external desulfurization systems were eliminated in this case, and the only fuel gas cleaning function was the hot gas filter for particulate control. At the cleanup temperature of 540°C (1000°F) the alkali vapor content of the fuel gas is expected to be acceptable for turbine corrosion specifications.

The IGCC plant descriptions presented above considered the cases where both the gasifier sulfur removal and the external, second-stage sulfur removal functions were operated simultaneously. In the alternative sulfur removal schemes considered, the following process modification were made:

- In-gasifier sulfur removal only (Fig. 1, Scheme 1): the gasifier ash sulfation system was retained, but without additional limestone feeding since no second-stage sulfur removal system was present to feed regenerator SO_2 to the sulfator. The external, second-stage desulfurization system was eliminated from the process diagram in this case.
- External sulfur removal only (Fig. 1, Schemes 4 and 5): even though gasifier ash sulfation was not required in these cases, the sulfation system was retained as a fluidized bed reactor to burn ungasified carbon in the ash and to capture sulfur (SO_2) from the external desulfurization regenerator as $CaSO_4$. A small makeup

Downloaded 02 Jun 2010 to 171.66.16.119. Redistribution subject to ASME license or copyright; see http://www.asme.org/terms/Terms_Use.cfm

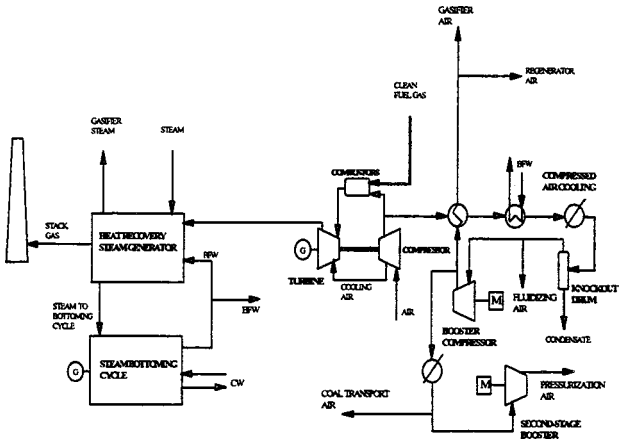

Fig. 6 Power island schematic

feed of limestone was maintained to the gasifier in this case, and limestone in a sufficient amount for capturing the regenerator SO_2 in the sulfator was used.

Power Block. The combined cycle portion of the IGCC power plant is based upon the SWPC 501F combustion turbine, a three pressure level reheat heat recovery steam generator (HRSG), and a two case, axial exhaust steam turbine. Figure 6 shows the process diagram of the combined cycle. Steam is generated in the gasification block, the fuel gas cleaning block, and in the power island. The high exhaust energy from the combustion turbine lends itself to a three pressure-level type HRSG system in which high pressure (HP), intermediate pressure (IP), and low pressure (LP) steam is produced. In addition, a reheat section is provided in the HRSG to improve overall cycle efficiency. The HP steam is admitted directly into the HP steam turbine element, the IP steam is admitted into the cold reheat steam header, and the LP steam is admitted directly into the IP/LP steam turbine element. The power island also contains the compressor equipment needed to provide gasifier air, coal/sorbent transport air, pressurization air, and regenerator air.

The heat sink for the cycle is a wet type condenser/cooling tower arrangement. The condenser design is optimized to maximize cycle performance and to allow for 100 percent steam turbine bypass operation.

IGCC Power Plant Performance

The estimated clean fuel gas heating value for the four study fuels are listed in Table 5. The fuel gas composition is nearly identical for the corresponding hot fuel gas and cold fuel gas cleaning cases. The fuel gas composition estimated reflects a close approach to equilibrium at the gasifier outlet. Empirical conversion factors were also applied that relate to the approach of the water-gas-shift reaction to equilibrium, and the generation of methane, but these had little impact on the power plant thermal performance. The fuel gas heating value (LHV) listed in Table 5 is typical of air-blown, low-thermal-value fuel gases. The fuel gas low heating-value and diluted composition allows efficient combustion with low generation of NOx when applying properly designed combustors. Over the range of conditions considered, the fuel gas molecular weight ranges from 23.7 to 25.0.

Table 5 Clean fuel gas heating value

	Pgh #8 (U.S.)		Blair Athol (Australia)		Lignite (India)		Bagasse (Hawaii)
Gas Cleaning Type	Hot	Cold	Hot	Cold	Hot	Cold	Hot
Heating Value MJ/nm^3 (Btu/scf)	5.4-5.8 (145-157)	5.4-5.8 (144-154)	5.9-6.0 (158-160)	6.1-6.3 (165-168)	4.8-5.5 (129-149)	5.1-5.5 (136-149)	3,9-4.9 (105-132)

Table 6 IGCC power plant emissions

Nitrogen oxides at stack: 10 ppmv
Particulate at stack: 2-3 ppmw

Case	Fuel sulfur (wt%, daf)	Sulfur Removal Scheme	Sulfur Removal overall % (gasifier/external)	Solid Waste lb/lb of coal	Fuel Gas Sulfur Content (ppmv)	Stack Gas Sulfur (ppmv)	Stack Gas SO_2 ng/J (lb/MBtu)
Pgh #8							
	3.5	Hot In-gasifier - Hot External	99.5 (90/95)	0.33	28	13	10.3 (0.024)
		Hot In-gasifier	95 (95/0)	0.39	298	140	99.9 (0.232)
		Hot External	99.5 (0/99.5)	0.25	25	11	10.3 (0.024)
		Hot In-gasifier - Cold External.	99.5 (90/95)	0.32	29	15	10.3 (0.024)
		Cold External	99.5 (0/99.5)	0.17	26	13	10.3 (0.024)
Blair Athol							
	0.5	Hot In-gasifier - Hot External	95 (75/80)	0.13	41	18	13.3 (0.031)
		Hot In-gasifier	70 (70/0)	0.12			79.7 (0.185)
		Hot External	95 (0/95)	0.12	32	14	13.3 (0.031)
		Hot In-gasifier - Cold External.	95 (75/80)	0.12	37	17	13.3 (0.031)
		Cold External	95 (0/95)	0.11	35	16	13.3 (0.031)
Lignite							
	3.1	Hot In-gasifier - Hot External	99.5 (90/95)	0.29	30	15	11.0 (0.255)
		Hot In-gasifier	95 (95/0)	0.35	364	190	109.8 (0.255)
		Hot External	99.5 (0/99.5)	0.23	25	14	11.0 (0.255)
		Hot In-gasifier - Cold External.	99.5 (90/95)	0.29	30	15	11.0 (0.255)
		Cold External	99.5 (0/99.5)	0.16	27	14	11.0 (0.255)
Bagasse							
	0.05	Hot/ No desulfurization	0	0.05	114-133	70	56.4 (0.131)

Fuel gas constituents influencing the turbine maintenance, such as particulate and alkali vapor, were estimated to be at acceptable content in the fuel gas to satisfy existing turbine specifications for both the hot fuel gas cleaning and cold fuel gas cleaning cases. Development testing of hot gas filters in gasification fuel gases confirm the small-scale, short-term capability of hot gas cleaning to meet turbine protection requirements, but full-scale demonstration is needed to establish this as a reliable, long-term capability.

The estimated emissions from the power plant are listed in Table 6. These estimated emissions are consistent with the capabilities of the equipment as claimed in the literature and have yet to be demonstrated at a large scale. The emissions shown are representative of both the hot and cold fuel gas cleaning under the design conditions established for this evaluation. The emissions for SOx, NOx, and particulate are expressed in the forms of volume or mass fraction at the stack and mass per unit of fuel energy input, and are significantly lower than current standards require.

Solid waste generated by the power plant, listed in Table 6, is relatively large, being almost twice the power plant coal ash mass rate. The solid waste rate in the plant is sensitive to the coal sulfur content and the nature of the bulk sulfur sorbent used. While cold gas cleaning has the potential to be applied to reduce emissions to levels lower than assumed as the design basis for this evaluation and lower than the capabilities of hot gas cleaning, these lower emissions require the consumption of more energy and result in lower plant thermal efficiency.

The thermal performance results for the described IGCC power plant are listed in Table 7. Some results from previous IGCC

Downloaded 02 Jun 2010 to 171.66.16.119. Redistribution subject to ASME license or copyright; see http://www.asme.org/terms/Terms_Use.cfm

Table 7 Combined-cycle performance sensitivity to sulfur removal requirements

Gasifier	Oxidant	Turbine	Fuel sulfur (wt%, daf)	Sulfur Removal System	Sulfur Removal overall % (gasifier/external)	Net Plant Efficiency (% LHV)
Entrained (Fluor, 1978)	Oxygen	501F	Ill #6 (4.3)	Cold External	80.2 (0/80.2)	39.2
					98.6 (0/98.6)	37.8
Entrained (Newby et al., 1996)	Oxygen	501F	Bituminous (1.2)	Cold External	99.3 (0/99.3)	44.7
				Hot External		46.0
	Oxygen	501G	Bituminous (1.2)	Cold External	99.3 (0/99.3)	48.2
				Hot External		49.7
Fluid bed (Yang et al., 1997)	Air	501F	Pgh #8 (3.5)	Hot In-gasifier + cold External	98 (86/85)	43.9
				Hot In-gasifier + Hot External		45.0
Fluid bed (this study)	Air	501F	Pgh #8 (3.5)	Hot In-gasifier + Hot External	99.5 (90/95)	44.0
				Hot In-gasifier	95 (95/0)	43.8
				Hot External	99.5 (0/99.5)	45.2
				Hot In-gasifier + Cold External	99.5 (90/95)	41.6
				Cold External	99.5 (0/99.5)	37.9
	Air	501F	Blair Athol (0.5)	Hot In-gasifier + Hot External	95 (75/80)	46.4
				Hot In-gasifier	70 (70/0)	
				Hot External	95 (0/95)	46.5
				Hot In-gasifier + Cold External	95 (75/80)	45.2
				Cold External	95 (0/95)	44.5
	Air	501F	Lignite (3.1)	Hot In-gasifier + Hot External	99.5 (90/95)	42.5
				Hot In-gasifier	95 (95/0)	41.8 .
				Hot External	99.5 (0/99.5)	44.0
				Hot In-gasifier + Cold External	99.5 (90/95)	40.1
				Cold External	99.5 (0/99.5)	36.2
	Air	501F	Bagasse	Hot/ No desulfurize	0	35.4-37.6

process evaluations for entrained oxygen-blown gasification and for a 501G combustion turbine are also shown in the table. The table lists results as a function of the fuel type, fuel gas cleaning type (hot or cold), showing the net plant efficiency (LHV).

The net electrical outputs are

- U.S. Bituminous coal with hot second-stage fuel gas cleaning: 261–262 MWe
- U.S. Bituminous coal with cold second-stage fuel gas cleaning: 243–274 MWe
- Australian Bituminous coal with hot second-stage fuel gas cleaning: 259 MWe
- Australian Bituminous coal with cold second-stage fuel gas cleaning: 269–272 MWe
- Indian Lignite with hot second-stage fuel gas cleaning: 246–247 MWe
- Indian Lignite with cold second-stage fuel gas cleaning: 259–276 MWe
- Bagasse with hot fuel gas cleaning: 234–236 MWe

The estimated net electrical output of the power plant is greater with cold fuel gas cleaning, reflecting the greater generating capacity of the steam turbine bottoming cycle in this case.

Examination of Table 7 shows that the net plant efficiency is related to the fuel properties (beating value, moisture content, sulfur content) and the required sulfur removal load by Blair Athol (Australia)>Pgh #8 (U.S.)>lignite (India)>bagasse (Hawaii) which is consistent with general expectations. Compared to the equivalent natural gas-fired power plant, the net plant efficiency is lower than the natural gas power plant as:

Blair Athol (Australia): 10.3–12.6 percentage points,
Pgh #8 (U.S.): 11.6–18.9 percentage points,
lignite (India): 12.8–20.6 percentage points,
bagasse (Hawaii): 19.2–21.4 percentage points.

The comparison of the sulfur removal schemes was consistent for all of the fuels and their ranking with respect to net power plant efficiency is:
hot external fuel gas cleaning>hot internal plus hot external>hot internal>hot internal plus cold external>cold external.

It should be noted that in this comparison the hot internal desulfurization was required to achieve a less stringent level of sulfur removal than the other schemes due to the performance limitations of this scheme. The net plant efficiency variation for each coal over all five schemes was:

Blair Athol (Australia, 0.5 wt percent sulfur): 2.0 percentage points,
Pgh #8 (U.S., 3.5 wt percent sulfur): 7.3 percentage points, and
lignite (India, 3.1 wt percent sulfur): 7.8 percentage points.

The lower the sulfur content of the coal, the less important the choice of sulfur removal scheme becomes to the IGCC plant efficiency.

Overall, the hot gas cleaning schemes show significant advantage over the cold fuel gas cleaning schemes with respect to net plant efficiency. The hot internal plus hot external scheme shows the following advantages over the hot internal plus cold external scheme:

Blair Athol (Australia, 0.5 wt percent sulfur): 1.3 percentage points,
Pgh #8 (U.S., 3.5 wt percent sulfur): 2.4 percentage points.
lignite (India, 3.1 wt percent sulfur): 2.4 percentage points.

The hot external scheme shows the following advantages over the cold external schemes:

Blair Athol (Australia, 0.5 wt percent sulfur): 2.0 percentage points,
Pgh #8 (U.S., 3.5 wt percent sulfur): 7.3 percentage points,
lignite (India, 3.1 wt percent sulfur): 7.8 percentage points.

The biomass fuel (bagasse) showed a significant 2.2 percentage point variation in net plant efficiency with respect to the choice of gasifier temperature, with the efficiency increasing as the gasifier temperature is decreased. This trend must be weighed against the tendency for the formation of tars in the fuel gas and increased gasifier ash carbon content as the temperature is decreased versus the tendency for greater bed agglomeration and greater alkali vapor release as the gasifier temperature is increased.

Hot fuel gas cleaning has claimed potential economic benefits over cold fuel gas cleaning, as well as the potential for significant power plant thermal efficiency improvement as is listed in Table 7, but its reliability and environmental performance are currently uncertain. The power plant capital investment and cost-of-electricity have not been estimated in this evaluation, so the relative cost impacts of hot and cold gas cleaning cannot be addressed. The Sierra Pacific, Pinon Pine IGCC, using the air-blown, KRW fluid bed gasifier will be the first integrated hot fuel gas cleaning demonstration. Its operation, starting in late-1997, will provide the full-scale performance data required to reduce the uncertainty in this technology.

Comparison of these results with other projected plant net thermal efficiencies from other reported studies or demonstration plant results must be made with caution since the scope and bases of reported evaluations and the related boundaries of the plant are frequently not well defined.

Downloaded 02 Jun 2010 to 171.66.16.119. Redistribution subject to ASME license or copyright; see http://www.asme.org/terms/Terms_Use.cfm

Conclusions

Combustion turbines can be adapted for the utilization of low-thermal-value fuel gases generated by coal gasification. The fuel gas cleaning system must achieve contaminant levels that satisfy the combustion turbine requirements, as well as emissions performance that can satisfy future, stringent environmental demands. The ability of conventional cold fuel gas cleaning to achieve these technical requirements has been demonstrated. Hot fuel gas cleaning is now being demonstrated in the U.S. in Clean Coal Technology Programs.

Within this study, it has been shown that IGCC power plant fuel properties (heating value, moisture content, sulfur content) and the plant sulfur removal requirement has significant impact on the power plant net efficiency. Lower sulfur content and lower sulfur removal requirement will increase the net plant efficiency. The sulfur removal scheme applied also significantly influences the plant efficiency. Hot fuel gas cleaning schemes are favored over cold fuel gas cleaning schemes with respect to net plant efficiency by greater than seven percentage points for high-sulfur coals. It is also expected that hot fuel gas cleaning schemes are favored over cold fuel gas cleaning schemes with respect to the economics of power generation. In fluid bed gasification, the use of in-gasifier desulfurization for bulk sulfur removal can enhance the emissions performance that can satisfy future stringent environmental demands.

The coal-fired IGCC plant efficiencies with the SWPC 501F combustion turbine are estimated to be as high as 46.5 percent (LHV) for low sulfur coal, and 45.2 percent (LHV) for high-sulfur coal, about 10 percentage points lower than the equivalent natural gas-fired power plant. Advanced combustion turbines, such as the 501G, are expected to approach IGCC power plant efficiencies of 50 percent (LHV).

References

[1] EPRI, 1995, Proceedings of the Conference on New Power Generation Technology, San Francisco, CA, October 1995.

[2] EPRI, 1996, Proceedings of the 1996 Gasification Technologies Conference, San Francisco, CA, October 1996.

[3] Bridgwater, A. V., and Boocock, D. G. B., eds., 1997, *Developments in Thermochemical Biomass Conversion* IEA Bioenergy, Blackie Academic & Professional, London.

[4] Zon, G. D., 1996, ''Present Status and Operation Experiences IGCC Buggenum,'' presented at the 1996 Gasification Technologies Conf., San Francisco, CA, October.

[5] Breton, D., and Stultz, J., 1996, ''Initial Operating Experiences at the Wabash River Coal Gasification Repowering Project,'' presented at the 1996 Gasification Technologies Conf., San Francisco, CA, October.

[6] Demuth, J., 1996, ''The Pinon Pine Gasification Project—Construction and Startup/Commissioning Experience,'' presented at the 1996 Gasification Technologies Conf., San Francisco, CA, October.

[7] Black, C. R., and McDaniel, J., 1996, ''IGCC Startup/Commissioning Experiences at Tampa Electric's Polk Power Station,'' presented at the 1996 Gasification Technologies Conf., San Francisco, CA, October.

[8] Newby, R. A., Archer, D. H., and Bannister, R. L., 1995, ''Conversion of an Advanced Natural Gas-Fueled Combustion Turbine to Coal-Based Fuel Applications,'' ASME Paper 95-GT-162.

[9] Newby, R. A., Bannister, R. L., and Miao, F., 1996, ''Westinghouse Combustion Turbine Performance in Coal Gasification Combined Cycles,'' ASME Paper 96-GT-231.

[10] Bannister, R. L., Newby, R. A., and Lippert, T. E., 1996, ''Westinghouse Status of Coal and Biomass Fueled Combustion Turbine Systems for Power Generation,'' ASME Paper 96-TA-5.

[11] Yang, W. C., Newby, R. A., and Bannister, R. L., 1997, ''Effect of Fuel Gas Cleanup Options on Air-Blown IGCC Power Plant Performance,'' ASME Paper 97-AA-17.

[12] Abbasian, J., and Rehmat, A., 1991, ''Reaction of Calcium-Based Sorbents with Sulfur Compounds During Gasification,'' final report (Oct. 1986–June 1991), GRI-91/0396.

[13] Katta, S., et al., 1994, ''Studies of In-Situ Calcium Based Sorbents In Advanced Pressurized Coal Conversion Systems,'' final report, June 1991-Oct. 1994, DOE/MC/27233-3919.

[14] DOE, FETC, 1997, ''Proceedings of the Advanced Coal-Based Power and Environmental Systems '97 Conference,'' July.

[15] Scalzo, A. J., Bannister, R. L., DeCorso, M., and Howard, G. S., 1996, ''Evolution of Westinghouse Heavy-Duty Power Generation and Industrial Turbines,'' ASME J. Eng. Gas Turbines Power, **118**, pp. 316–330.

[16] Sierra Pacific Power Company, 1994, ''Tracy Power Station—Unit No. 4, Pinon Pine Power Project, Public Design Report,'' DOE/MC/29309—4056.

[17] Biasca, F. E. et al., 1987, ''Process Screening Study of Alternative Gas Treating and Sulfur Removal Systems for IGCC Power Plant Applications,'' EPRI AP-5505.

[18] Bechtel Group, Inc., and Burnes & Roe, 1983, ''Design of Advanced Fossil Fuel Systems (DAFFS),'' ANL/FE-83-16.

[19] Fluor Engineers and Constructors, Inc., 1978, ''Effects of Sulfur Emission Control on the Cost of Gasification Combined Cycle Power Systems,'' EPRI AF-916.

[20] Bannister, R. L., et al., 1997, ''ASME PTC47—Development of a New Code for Integrated Gasification Combined Cycle Performance Testing,'' presented at the ASME IJPC Conference, Denver, CO, Nov. 3–5, 1997.

Downloaded 02 Jun 2010 to 171.66.16.119. Redistribution subject to ASME license or copyright; see http://www.asme.org/terms/Terms_Use.cfm

Eric D. Larson
Center for Energy and Environmental Studies,
School of Engineering and Applied Science,
Princeton University,
Princeton, NJ 08540

Stefano Consonni
Departimento di Energetica,
Politecnico di Milano,
Milan, Italy

Thomas G. Kreutz
Center for Energy and Environmental Studies,
School of Engineering and Applied Science,
Princeton University,
Princeton, NJ 08540

Preliminary Economics of Black Liquor Gasifier/Gas Turbine Cogeneration at Pulp and Paper Mills

Black liquor, the lignin-rich byproduct of kraft pulp production, is burned in boiler/steam turbine cogeneration systems at pulp mills today to provide heat and power for onsite use. Black liquor gasification technologies under development would enable this fuel to be used in gas turbines. This paper reports preliminary economics of 100-MW_e scale integrated black-liquor gasifier/combined cycles using alternative commercially proposed gasifier designs. The economics are based on detailed full-load performance modeling and on capital, operating and maintenance costs developed in collaboration with engineers at Bechtel Corporation and Stone & Webster Engineering. Comparisons with conventional boiler/steam turbine systems are included. [S0742-4795(00)00402-6]

Introduction

In 1994, the U.S. pulp and paper industry consumed 1.2 EJ (10^{18} J), or 38,000 MW, of black liquor, the lignin-rich byproduct of fiber extraction from wood in kraft pulp production. This exceeded the 1.0 EJ of total fossil fuel used by the industry [1]. Kraft mills burn black liquor today in Tomlinson recovery boilers that feed back-pressure steam turbine cogeneration systems supplying process steam and electricity to mills. Tomlinson boilers also recover pulping chemicals (sodium and sulfur compounds) from the black liquor for reuse [2]. As replacements for aging Tomlinson boilers, technologies for gasifying black liquor are under development. Black liquor gasifier/combined cycle (BLGCC) systems prospectively offer improvements in power generating capability, environmental profile, safety, and capital investment characteristics, as well as new possibilities for improving the kraft process itself [3,4].

Previous work [5,6] has quantified the large increases in power generation that are possible with BLGCC technology relative to Tomlinson systems. Relatively little has been published, however, on the prospective economics of BLGCC systems. This paper reports on work undertaken with inputs from Bechtel National, Inc. and Stone & Webster Engineering, with the support of the U.S. Department of Energy and the Weyerhaeuser Company, to assess the prospective performance and cost of alternative BLGCC powerhouse cogeneration technologies. For reference, self-consistent performance and cost estimates were also made for conventional Tomlinson-based powerhouses. Using a consistent set of input assumptions, including information from gasifier developers, detailed heat and mass balances were developed for each powerhouse configuration at hypothetical kraft pulp mills having approximately the same production capacity and process steam demand. The heat and mass balances were used by engineers at Bechtel and Stone & Webster as a basis for estimating capital costs (with accuracy of $\pm 20-50$ percent) and operating and maintenance costs, assuming commercially mature technology.

Contributed by the International Gas Turbine Institute (IGTI) of THE AMERICAN SOCIETY OF MECHANICAL ENGINEERS for publication in the ASME JOURNAL OF ENGINEERING FOR GAS TURBINES AND POWER. Paper presented at the International Gas Turbine and Aeroengine Congress and Exhibition, Stockholm, Sweden, June 2–5 1998; ASME Paper 98-GT-346. Manuscript received by IGTI March 18, 1998; final revision received by the ASME Headquarters January 3, 2000. Associate Technical Editor: R. Kielb.

Powerhouse Performance Modeling

Powerhouse cogeneration systems were designed around a Tomlinson boiler and each of three gasifier designs representing designs that are under commercial development for BLGCC applications: high-temperature, oxygen-blown gasification; high-temperature, air-blown gasification; and low-temperature, indirectly-heated gasification. The performance of alternative powerhouse cogeneration systems was calculated using a computation model originally developed to predict the full-load, design-point performance of complex gas-steam power cycles [7] and modified to accommodate black liquor as a fuel. Details of the computational modeling, including black liquor gasification modeling, are described elsewhere [5,8].

For each BLGCC system, the turbomachinery included a gas turbine representing a 70 MW_e class of machine typified by the Seimens V64.3a unit and a single-extraction back-pressure steam turbine. The black liquor throughput rate required to fuel a 70 MW_e class machine is in the range that is typically generated at kraft mills in the U.S. today—2300–2460 tonnes dry solids per day (tds/day). This corresponds to a mill production rate of about 1315–1415 tonne of pulp per day (tp/day). The liquor throughput in each case was set to match the turbine fuel requirements. The throughput in the case of the Tomlinson system was set to be roughly comparable to those with the BLGCC systems.

A perfect match between black liquor available at a mill and the fuel requirements of a specific gas turbine will be rare, because black liquor availability is largely determined by considerations related to pulp and paper production, while the size of the gas turbine is determined by the few models available on the market. One practical operating strategy at a mill (not considered here) might involve supplementing the available gasified black liquor with natural gas or gasified biomass to provide the full fuel requirement of a gas turbine. Alternatively, the gas turbine might be undersized relative to the gasifier, and the excess gasified black liquor might be used for supplementary firing of the HRSG.

Total process steam delivered by each cogeneration system per unit of black liquor throughput was fixed at a level representative of a typical U.S. kraft pulp mill: 28.4 GJ/tds, or equivalently, 16.3 GJ/tp. Each system delivers process steam at 10 bar and 4 bar in a mass ratio of 1:2. In all four cases process steam production from the black liquor alone is insufficient to meet the mill's demand. A supplemental boiler burning biomass is included in each case to augment steam production. For the Tomlinson cycle, peak steam pressure is 60 bar, a common level in practice to minimize

Copyright © 2000 by ASME

Downloaded 02 Jun 2010 to 171.66.16.119. Redistribution subject to ASME license or copyright; see http://www.asme.org/terms/Terms_Use.cfm

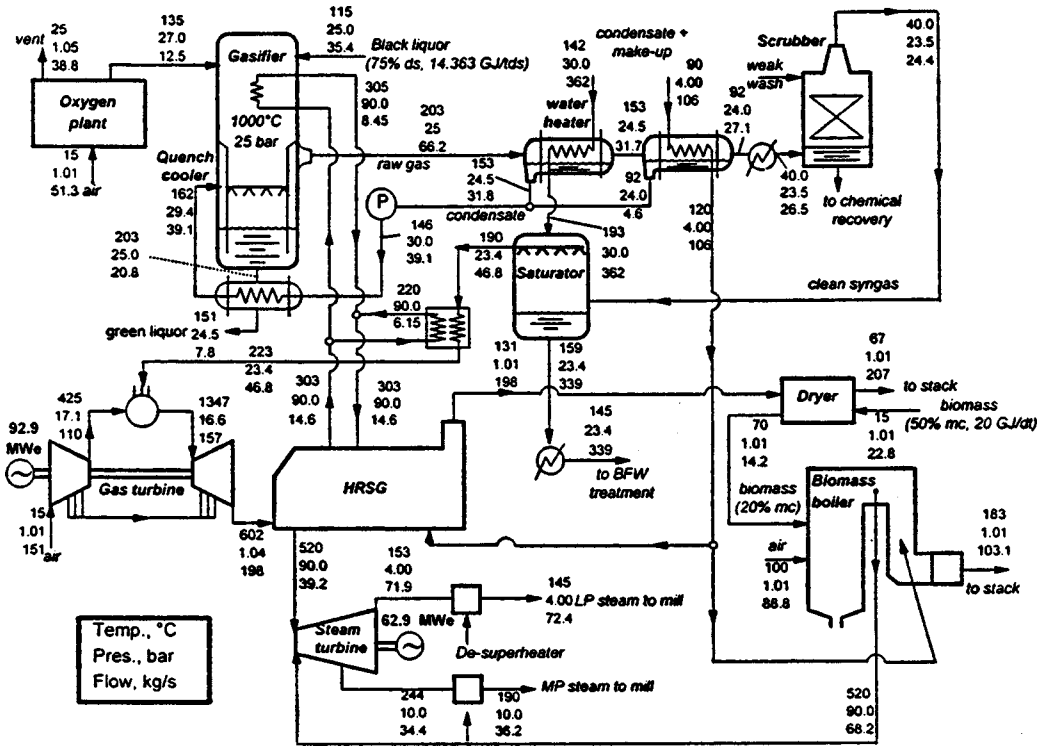

Fig. 1 Heat/mass balance used as basis for cost estimate of a BLGCC system with high-temperature, oxygen-blown gasifier

corrosion concerns. For BLGCC systems, a higher peak steam pressure is feasible in the HRSG (90 bar) because corrosion concerns are negligible.

Heat and Mass Balances

High-Temperature, Oxygen-Blown BLGCC. The basic plant configuration with the pressurized, oxygen-blown, high-temperature gasifier is shown in Fig. 1. The gasifier modeled in this case is nonadiabatic, based on the proposed Noell gasifier design, which includes steam recovery from a reactor cooling jacket [9]. The gasifier product gas passes through an integral quench bath and is further cooled by preheating makeup and condensate return water. Water condenses from the product gas in this process and is recirculated to the quench bath. The quench bath water preheats the recirculated condensate. A trim cooler drops the gas temperature to 40°C, the operating temperature for the caustic scrubbing stage that is assumed to capture H_2S from the gas. The heat content in the fuel gas leaving the scrubber is sufficiently high that a saturator can be included upstream of the gas turbine to increase overall power output and generating efficiency. The gas is modestly superheated before firing in the gas turbine combustor. Steam is raised at 90 bar in the HRSG from relatively clean turbine exhaust. The HRSG exhaust is used to dry biomass in advance of it being fired in the biomass boiler.

High-Temperature, Air-Blown BLGCC. The basic plant configuration with air-blown gasification (Fig. 2) is similar to the previous system, with oxygen replaced by air bled from the gas turbine compressor. There is no active cooling of the gasifier, but low-pressure steam is raised and boiler feedwater is preheated during gas cooling. A saturator is not used due to the lower heat content of the gases leaving the scrubber, but the syngas is preheated after the scrubber before firing in the gas turbine. Preheating does not appreciably improve cycle efficiency, but because of the low heating value of the fuel gas it is important in increasing combustion stability.

Low-Temperature, Indirectly-Heated BLGCC. This plant configuration (Fig. 3) is based on the fluidized-bed gasifier design of MTCI, which operates below the melting temperature of the inorganic solids [10]. Heat for gasification is provided by in-bed heat exchanger tubes. Combustion products from a pulse combustor burning part of the cleaned gasifier product gas flow inside the tubes. With steam as the primary fluidizing agent, the gasifier acts essentially as a black liquor steam reformer. The configuration here includes substantial heat exchange between various flows. Raw syngas at 600°C and 1.4 bar is cooled first by raising high-pressure steam and then by pre-heating air for the pulse combustor. After scrubbing, about half of the syngas goes to the pulse combustor. The rest is compressed and delivered to the gas turbine combustor. After releasing heat inside the gasifier, the pulse combustor flue gases (at 700°C) are cooled first by superheating gasifier fluidizing steam, then by raising steam in a boiler connected in parallel with the syngas cooler, then by pre-heating the pulse combustor fuel, and finally by preheating boiler feedwater. Some steam is also generated in the cooling circuit of the pulse combustor. The steam generated by the syngas cooler and the pulse combustor flue gases are fed to the gas turbine HRSG. Some 6 percent by mass of carbon input to the gasifier is not gasified. It is assumed that 75 percent of this carbon is recovered and burned in the biomass boiler. As in all other plant schemes, the steam cycle of the gas turbine HRSG is integrated with that of the biomass boiler to optimize heat recovery and allow use of a single steam turbine and condenser. The absence of air and oxygen in the feed to the gasifier substantially reduces the flow of syngas that must be compressed for injection into the gas turbine combustor, thereby reducing the parasitic consumption of the syngas compressor.

Tomlinson Boiler. To provide a consistent comparison between gasification-based systems and Tomlinson boiler cogeneration systems, the Tomlinson technology has been modeled at a

Downloaded 02 Jun 2010 to 171.66.16.119. Redistribution subject to ASME license or copyright; see http://www.asme.org/terms/Terms_Use.cfm

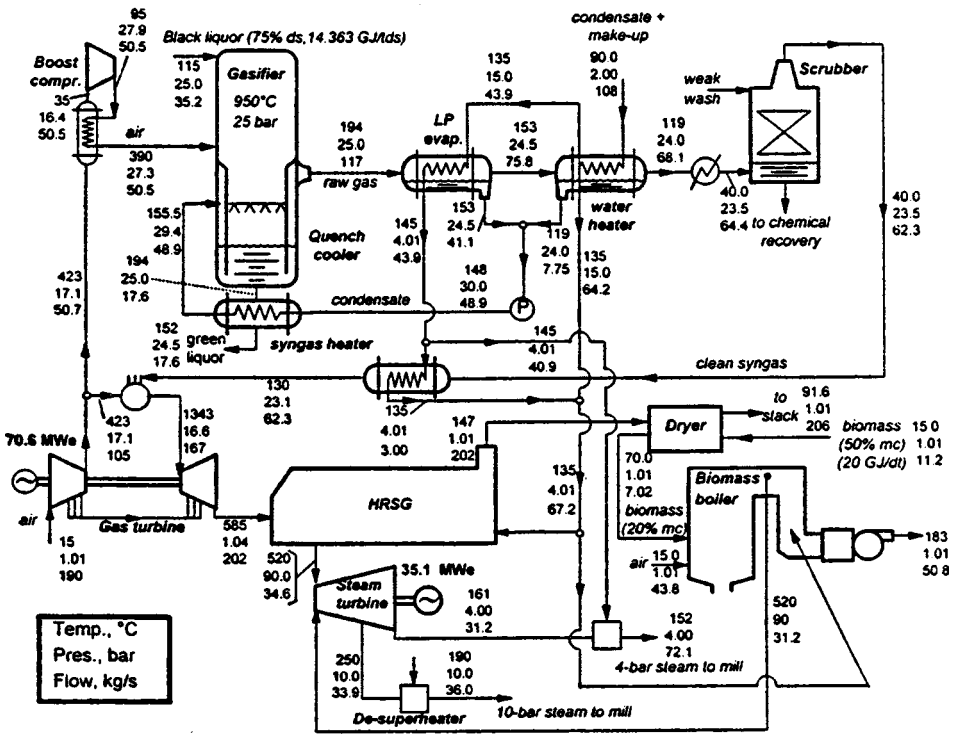

Fig. 2 Heat/mass balance used as basis for cost estimate of a BLGCC system with high-temperature, air-blown gasifier

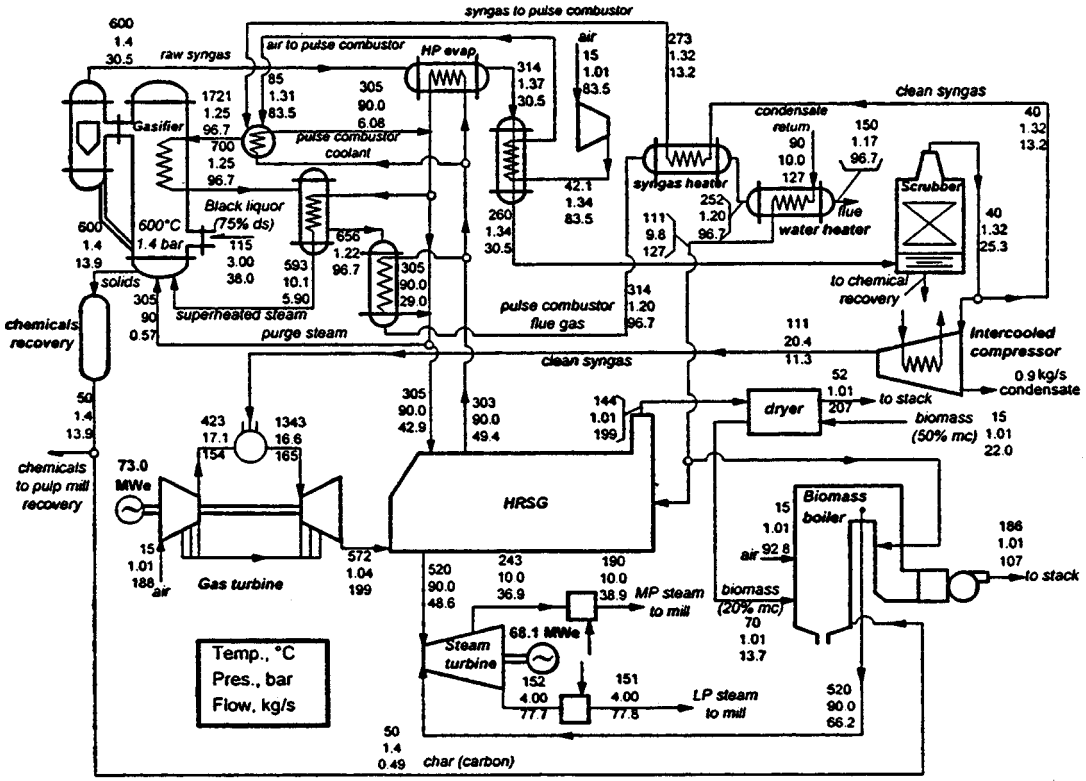

Fig. 3 Heat/mass balance used as basis for cost estimate of a BLGCC system with low-temperature, indirectly heated gasifier

Downloaded 02 Jun 2010 to 171.66.16.119. Redistribution subject to ASME license or copyright; see http://www.asme.org/terms/Terms_Use.cfm

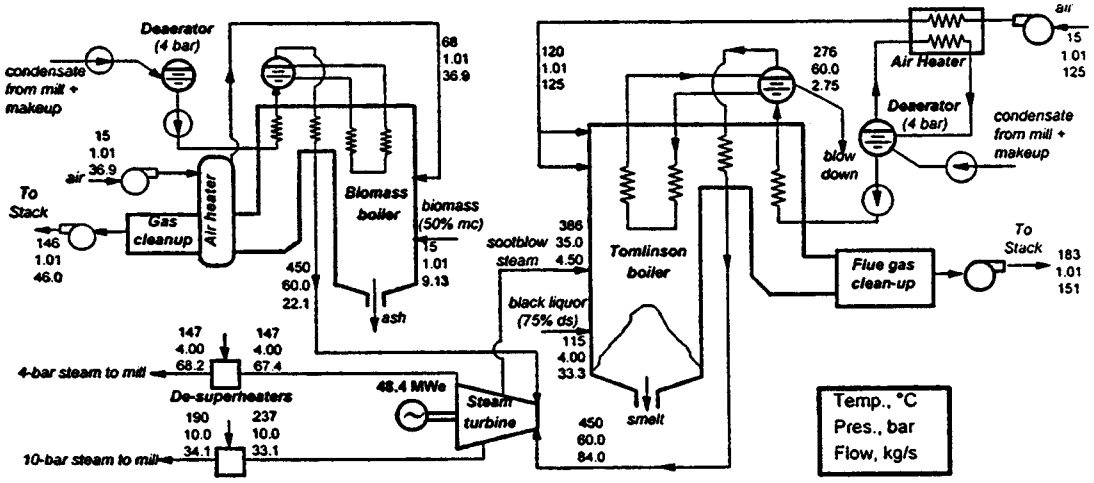

Fig. 4 Heat/mass balance used as basis for cost estimate of a conventional Tomlinson-based recovery powerhouse system

comparable level of detail (Fig. 4). A deaerator is included in all four systems modeled, but is only shown explicitly in the process flow diagram for the Tomlinson boiler case.

Preliminary Economics

The final heat and mass balance configurations (Figs. 1–4), summarized in Table 1, were developed taking into consideration recommendations of engineers from the Bechtel Corporation and Stone & Webster Engineering aimed at insuring that each case represented a feasible, practical system. Modifications made to the balances to address these recommendations led to a larger spread in black liquor throughput among the four cases than initially targeted. However, the throughput in all four cases falls within a range of ± 7 percent (Table 1), so that comparisons on a per-unit basis (e.g., kWh/tp or $/kW) are reasonable.

Engineers from Bechtel and Stone and Webster were engaged to develop capital, operating and maintenance cost estimates for the cogeneration systems based on the final heat and mass balances and assuming BLGCC technology to be commercially-mature, *N*th-plant technology. Bechtel provided estimates for the two high-temperature BLGCC cases and for the Tomlinson case [11]. Stone & Webster provided estimates for the low-temperature BLGCC and for the Tomlinson case [12]. Having both firms provide an estimate for a Tomlinson system provided a cross-check on the consistency of estimates from the two firms. The firms solicited vendor quotes for some major equipment and relied on in-house cost databases for others.

A set of general study criteria intended to be representative of conditions at a typical bleached kraft pulp mill in the U.S. were developed and used by both firms to provide a consistent, reasonable, and fair basis for each cost estimate (Table 2). The study criteria were defined to make cost comparisons between technologies as consistent and transparent as possible. For example, ''greenfield replacement'' of an existing Tomlinson powerhouse was assumed, i.e., the costs were developed to represent new construction without including costs for demolition, site remediation, and other factors that tend to be mill-specific, while not being especially relevant to a comparison between technologies. A Southeastern U.S. site was selected for geographic specificity.

An important implicit assumption in the BLGCC cost analysis

Table 1 Summary of calculated heat and mass balances for alternative black liquor co-generation technologies

	Tomlinson	BLGCC		
		O_2	Air	Indirect
Pulp Mill Parameters				
Pulp production (air-dry tp/day)	1240	1318	1311	1415
Process steam demand (GJ/tp)	16.3	16.3	16.3	16.3
Powerhouse Fuel Consumption				
Black liquor,[a] tds/day	2,158	2,294	2,281	2,462
MW	359	381	379	409
Biomass,[b] dry t/day	395	985	484	950
MW	91	228	112	220
Electricity Generation				
Gross gas turbine power (MW_e)	n.a.	92.9	70.6	73.0
Gross steam turbine power (MW_e)	48.4	62.9	35.1	68.1
Auxiliaries (MW_e)	1.6	20.4	4.3	12.1
Net power output (MW_e)	46.8	135.4	101.4	129.0
Net electricity prod. (kWh/tp)	906	2,465	1,856	2,188
Process steam production and power-to-steam				
Process steam, GJ/hour	842	895	890	961
Process steam, GJ/tp	16.3	16.3	16.3	16.3
Elec.-to-process steam (kWh/GJ)	56	151	114	134

(a) Black liquor is generated at a rate of 1.74 tds/tp, with an assumed higher heating value of 14.363 GJ/metric tonne, dry solids.
(b) Each system includes a biomass boiler generating additional steam to meet process demand. The assumed higher heating value of biomass is 20 GJ/dry tonne.

Table 2 Main criteria/guidelines for costing studies

Scope: - "Greenfield replacement" of existing powerhouse (no demolition, site remediation, salvage, etc.). - Black liq. delivered from mill; green liq. return to mill. - Biomass supply from mill. - Process steam delivered to mill; condensate from mill. - Makeup water supply from mill. - Pipeline natural gas available for backup/startup at 28 bar. - Wastewater delivery to mill for treatment (as required). - Fire protection water available from mill. - Switchyard and transmission equipment already in place except on high voltage side of transformers.
Key Design Features - Utility grid voltage of 115/138 kV. - "Open plant" design (enclosures only where needed for maintenance, noise, etc.). - Mechanical draft cooling tower (incremental to that already required at the mill). - One building for combined control room/elec. equip. area. - Admin./warehouse/maintenance area provided by mill (no capital cost).
Site Related Issues - North Carolina site/moderate ambient conditions (temperature, precipitation, etc.). - Clear, level site, no extensive excavation or dewatering. - Spread footing foundations (no piles).
Environmental Issues - NO_x target of 25 ppmvd w/o SCR or CO catalyst on HRSG. - Standard noise abatement provisions - Continuous emissions monitoring for CO, NO_x, oxygen - SNCR on biomass boilers for NO_x control.
Cost Issues - "N^{th} plant" (commercially mature—no development costs) - "Simplified" capital cost estimate, as defined by Electric Power Research Institute (TAG): ±20-50% accuracy. - Wages, productivities, distributable costs, and field non-manual costs typical for Southeast U.S. construction. - Taxes and permit costs excluded. - Mid-1997 dollars.

Downloaded 02 Jun 2010 to 171.66.16.119. Redistribution subject to ASME license or copyright; see http://www.asme.org/terms/Terms_Use.cfm

Table 3 Capital cost estimates (1997$) based on work by the Bechtel Corporation [11] for pulp mill powerhouse systems shown in Fig. 1 (with O2-blown back liquor gasification), Fig. 2 (air-blown gasification), and Fig. 4 (Tomlinson recovery boiler)

	Capacity[a]	Equip. (10^6 $)	Install.[b] (10^6 $)	Totals[c] (10^6 $)
COMBINED CYCLE WITH OXYGEN GASIFIER AND BIOMASS BOILER				
Gasification Island				**66.08**
Oxygen plant	1100 tO2/day	vendor quote total		27.00
Black liq. tank	270,000 gal	0.36	0.500	0.86
Black liq. charge pumps (28 bar)	6,108 tpd	1.95	1.469	3.41
Gasifier + green liq. cooler (25 bar)	6,108 tpd	15.09	11.46	26.55
2-stage syngas water heater (25 bar)	335 GJ/hr	1.43	1.43	2.85
Syngas trim cooler (25 bar)	11.9 GJ/hr	0.07	0.07	0.13
H2S scrubber (24 bar)	26.5 kg/s gas in	1.23	1.67	2.90
Syngas saturator (24 bar)	24.4 kg/s gas in	0.09	0.07	0.16
Saturator exit water cooler (24 bar)	71.2 GJ/hr	0.56	0.56	1.13
Syngas superheater (24 bar)	9.3 GJ/hr	0.59	0.48	1.07
Combined Cycle Island				**69.69**
Gas turbine generator[d]	70 MW_e (nom.)	20.07	13.35	33.42
HRSG (90 bar, 520°C)	39.2 kg/s steam	6.33	5.34	11.67
Steam turb/gen, 1 extr., 4 bar exh.	62.9 MW_e	7.55	7.91	15.46
Balance of plant	62.9 MW_e	4.47	4.68	9.14
Biomass Boiler Island				**37.68**
Boiler w/fans, dctwk, steel (90 bar)	68.2 kg/s steam	7.51	10.43	17.93
Biomass dryer (50% 20% mc)	22.8 kg/s bio_{50}	2.07	2.46	4.53
Material handling (biomass, ash)	22.8 kg/s bio_{50}	3.49	3.18	6.68
BOP (ESP, stack, water treatment,...)	68.2 kg/s steam	4.47	4.07	8.54
TOTAL				**173.44**
COMBINED CYCLE WITH AIR GASIFIER AND BIOMASS BOILER				
Gasification Island				**48.21**
Air-air heat exchanger (17 bar)	75.5 GJ/hr	0.31	0.16	0.47
Boost compressor	3 MW	1.40	0.94	2.34
Black liquor tank	270,000 gal	0.36	0.49	0.85
Black liq. charge pumps (28 bar)	4056 tpd	2.67	2.07	4.74
Gasifier & green liq. cooler (25 bar)	4056 tpd	15.24	14.88	30.12
Syngas cooler/LP evaporator (25 bar)	343 GJ/hr	1.22	1.22	2.44
Syngas cooler/water heater (25 bar)	73.9 GJ/hr	0.38	0.38	0.76
Syngas trim cooler (24 bar)	54.6 GJ/hr	0.13	0.13	0.25
H2S scrubber (24 bar)	64.4 kg/s gas in	2.10	2.86	4.96
Syngas superheater (23 bar)	23.5 GJ/hr	0.72	0.59	1.30
Combined Cycle Island				**62.80**
Gas turbine generator[d]	70 MW_e (nom.)	20.07	13.53	33.42
HRSG (90 bar, 520°C)	34.6 kg/s steam	5.50	4.64	10.14
Steam turb/gen, 1 extr., 4 bar exh.	35.1 MW_e	5.40	5.66	11.06
Balance of plant	35.1 MW_e	4.00	4.19	8.19
Biomass Boiler Island				**24.81**
Boiler w/fans, dctwk, steel (90 bar)	31.2 kg/s steam	4.79	6.67	11.45
Biomass dryer (50% 20% mc)	11.2 kg/s bio_{50}	1.40	1.66	3.06
Material handling (biomass, ash)	11.2 kg/s bio_{50}	2.55	2.32	4.87
BOP (ESP, stack, water treatment,...)	31.2 kg/s steam	2.84	2.59	5.43
TOTAL				**135.82**
TOMLINSON RECOVERY BOILER PLUS BIOMASS BOILER				
Tomlinson Boiler Island				**154.14**
Boiler (ESP, fans, dctwk, stl, conc...)	2880 tpd	56.50	57.19	113.69
Steam turb/gen, 1 extr., 4 bar exh.	48.4 MW_e	6.20	7.10	13.30
Balance of plant	48.4 MW_e	7.90	9.05	16.95
Minor equipment/bulks allowance	48.4 MW_e	4.76	5.45	10.21
Biomass Boiler Island				**16.24**
Boiler w/fans, dctwk, steel (60 bar)	22.4 kg/s steam	4.23	5.87	10.10
Material handling (biomass, ash)	9.13 kg/s bio_{50}	1.80	1.64	3.44
BOP (ESP, stack, water treatment,...)	22.4 kg/s steam	1.41	1.29	2.70
TOTAL				**170.38**

(a) Cost driving parameter used to adjust original estimates that were made by Betchel for slightly different unit capacities. A scaling factor of 0.6 was assumed in making adjustments. Each piece of equipment indicated is a single unit handling the full indicated capacity, with following exceptions. For the oxygen-blown case, 2 x 100% gasifiers and 2 x 100% black liquor pumps. For the air-blown case, 4 x 33% gasifiers and 4 x 33% black liquor pumps.
(b) Installation and indirects includes all non-equipment costs, including engineering and contingencies.
(c) Totals may not add due to rounding.
(d) Based on cost estimates for a Siemens KWU V64.3a gas turbine generator.

Table 4 Capital cost estimates (1997$) based on work by Stone & Webster Engineering [12] for pulp mill powerhouses in Fig. 3 (with indirectly-heated black liquor gasification) and Fig. 4 (with Tomlinson recovery boiler)

	Capacity[a]	Material (10^6 $)	Install. (10^6 $)	Totals[b] (10^6 $)
COMBINED CYCLE WITH INDIRECT GASIFIER AND BIOMASS BOILER				
Gasification Island			**10.72**	**37.02**
Site preparation	modest, nominal	0.20	0.10	0.30
Concrete work	black liquor rate	1.02	2.50	3.52
Structural steel	black liquor rate	1.90	1.10	3.00
Equipment				
Gasifiers (5 x 20% each)	3,283 tpd	10.24	1.70	11.94
H_2S scrubber	38.1 m^3/s gas in	0.76	0.05	0.81
Superheater	19.9 GJ/hr	0.33	0.04	0.36
Flue gas cooler	147 GJ/hr	3.66	0.73	4.39
Syngas heater	25.4 GJ/hr	0.10	0.02	0.12
Water heater	40.5 GJ/hr	0.14	0.03	0.17
HP evaporator	71.4 GJ/hr	2.00	0.40	2.39
Syngas cooling	83.0 GJ/hr	0.14	0.05	0.19
Air fan	2.44 MW	0.32	0.05	0.37
Piping	black liquor rate	1.50	1.00	2.50
Electrical	black liquor rate	0.40	0.25	0.65
Architecture/building	black liquor rate	0.49	0.31	0.80
Instrumentation	black liquor rate	2.50	1.50	4.00
Insulation/painting	black liquor rate	0.60	0.90	1.50
Power Island		**73.73**	**27.02**	**100.75**
Site preparation	modest, nominal	0.20	0.10	0.30
Concrete work	gross MW_e (141)	1.29	3.40	4.69
Structural steel	gross MW_e (141)	1.78	1.03	2.81
Equipment				
Intercooled compressor	8.61 MW	5.72	0.57	6.29
Gas turbine generator[c]	73 MW_e (nom.)	21.56	1.00	22.56
HRSG (90 bar, 520°C)	345 GJ/hr	4.42	2.88	7.30
Steam turb/gen.	68.1 MW_e	13.60	1.10	14.70
Biomass boiler	13.7 kg/s bio_{20}	10.00	6.60	16.60
Boiler ID fan	1.18 MW_e	0.26	0.04	0.30
Biomass dryer	22.0 kg/s bio_{50}	5.60	3.40	9.00
Piping	gross MW_e (141)	1.32	1.00	2.32
Electrical	gross MW_e (141)	5.90	3.50	9.40
Architecture/building	gross MW_e (141)	0.60	0.40	1.00
Instrumentation	gross MW_e (141)	1.14	0.73	1.87
Insulation/painting	gross MW_e (141)	0.34	1.27	1.61
Total Direct Cost (TDC)		**100.02**	**37.74**	**137.77**
Start-up	nominal			0.60
Engineering	10% of TDC			13.78
Contingency	10% of all other			15.21
TOTAL				**167.36**
TOMLINSON RECOVERY BOILER PLUS BIOMASS BOILER				
Tomlinson recovery system	2,880 tpd			87.00
Steam turbine	48.4 MW_e			16.00
Biomass boiler	22.4 kg/s steam			11.09
Total Direct Cost				**114.09**
Startup	nominal			0.600
Engineering	10% of TDC			11.41
Contingency	10% of all other			12.61
TOTAL				**138.71**

(a) Cost-driving parameter used to adjust original estimates that were made by Stone and Webster for slightly different unit capacities. A scaling factor of 0.6 was assumed in making adjustments.
(b) Totals may not add due to rounding.
(c) Based on cost estimates for a Siemens KWU V64.3a gas turbine generator.

is that these systems would not require any changes at the mill outside of the boundaries of the powerhouse defined in this study, especially that each BLGCC system would fulfill the same chemical recovery function as a Tomlinson boiler. A brief elaboration of this point is warranted. The design of a Tomlinson unit is such that essentially all of the inorganic pulping chemicals are recovered as a smelt of sodium sulfide (Na_2S) and sodium carbonate (Na_2CO_3). This smelt is dissolved in water to form ''green liquor.'' Green liquor is delivered from the powerhouse to the ''causticizing'' area of a mill, where it is reacted with calcium hydroxide ($Ca(OH)_2$) formed by mixing calcium oxide (CaO) with water in a causticizer. This reaction converts the Na_2CO_3 to NaOH, thereby regenerating the pulping chemical, a mix of Na_2S and NaOH. The precipitate from the causticizer, calcium carbonate ($CaCO_3$), is heated in a lime kiln (typically by burning residual oil or natural gas) to regenerate CaO.

Compared with firing black liquor in a Tomlinson boiler, more sulfur will leave a gasifier in the vapor phase as H_2S [5]. As a result, less of the condensed-phase Na will be present as Na_2S and more will be present as Na_2CO_3. Also, additional Na_2CO_3 may be formed at the H_2S scrubber, since any CO_2 removed with the H_2S will react with the green liquor scrubbing medium to form Na_2CO_3. Both the condensed-phase from the gasifier and the scrubber effluent would be delivered to the causticizing area. Na_2CO_3 present in these streams in excess of that delivered from a Tomlinson system will require a larger causticizing area. Alternative strategies for recovery of H_2S are possible to minimize or eliminate this impact [4], with modest cost consequences.

Capital and O&M Cost Estimates. Tables 3 and 4 detail the ''overnight'' capital cost estimates for the three BLGCC systems and the Tomlinson system. In these tables, the cost-driving parameter for each major unit is shown, e.g., heat duty for heat exchangers. The estimates assume 100 percent gasifier over-capacity in the oxygen-blown case, 33 percent over-capacity in the air-blown case, and no over-capacity in the indirectly-heated case. In the air-blown case, the physical size of the individual gasifier units is constrained by their transportability to the site. The difference in the Tomlinson cost estimates made by the two engineering firms appears to be larger than might be expected. Because insufficient

Downloaded 02 Jun 2010 to 171.66.16.119. Redistribution subject to ASME license or copyright; see http://www.asme.org/terms/Terms_Use.cfm

Table 5 Operation and maintenance cost estimates for black liquor recovery systems in Figs. 1–4, by Bechtel [11] and Stone & Webster [12]

	(BECHTEL)		(STONE & WEBSTER)	
BLGCC POWERHOUSE (all costs are thousand 1997 $ per year)				
Gasifier design >	O_2	Air	Indirect	
Gasification Island	**5,356.0**	**4,607.0**	**Gasification Island**	**2,550.0**
Variable O&M	1,785.0	2,454.0	*Variable O&M*	1,450.0
Contract maintenance	196.0	293.0	Non-rout. maint.	500.0
Routine maintenance	510.0	765.0	Routine maint.	400.0
Major overhaul (yearly avg)	534.0	801.0	Utilities	100.0
Replacement parts	included	incl.	Insurance	100.0
Spare parts	100.0	150.0		
Consumables/waste disp.	195.0	195.0		
Startup fuel (1% input GJ)	250.0	250.0		
Fixed Labor	2,621.0	2,153.0	***Fixed Labor***	1,450.0
Oxygen plant total	950.0	0.0		
Combined Cycle Island	**3,596.0**	**3,596.0**	**Power Island**	**3,580.0**
Variable O&M	1,916.0	1,916.0	*Variable O&M*	1,770.0
Contract maintenance	320.0	320.0	Non-rout. maint.	850.0
Routine maintenance	17.0	17.0	Routine maint.	700.0
Major overhaul (yearly avg)	452.0	452.0	Utilities	100.0
Replacement parts	294.0	294.0	Insurance	120.0
Tools/equipment	161.0	161.0		
Spare parts	280.0	280.0		
Consumables/waste disp.	392.0	392.0		
Fixed Costs	1,680.0	1,680.0	***Fixed Labor***	1,810.0
Labor	936.0	936.0		
Material	52.0	52.0		
Other	692.0	692.0		
Biomass Boiler Island	**2,559.0**	**2,359.0**	**Biomass Boiler**	
Variable O&M	1,155.0	955.0	(included above)	
Contract maintenance	w/routine	w/rout.		
Routine maintenance	510.0	375.0		
Major overhaul (yearly avg)	385.0	320.0		
Replacement parts	included	incl.		
Spare parts	75.0	75.0		
Consumables/waste disp.	185.0	185.0		
Fixed Labor	1,404.0	1,404.4		
TOTAL O&M	**11,511.0**	**10,562.**	**TOTAL O&M**	**6,130.0**
Fixed	4,856.0	5,325.0	*Fixed*	2,870.0
Variable	6,655.0	5,237.0	*Variable*	3,260.0
TOMLINSON POWERHOUSE (all costs are thousand 1997 $ per year)				
Tomlinson Boiler		**5,873.0**	**Tomlinson Island**	**2,650.0**
Variable O&M		3,720.0	*Variable O&M*	1,200.0
Contract		w/routine	Non-rout. maint.	400.0
Routine maintenance		2,310.0	Routine maint.	600.0
Major overhaul (yearly avg)		778.0	Utilities	100.0
Replacement parts		included	Insurance	100.0
Spare parts		182.0		
Consumables/waste disp.		450.0		
Fixed Labor		2,153.0	*Fixed Labor*	1,450.0
Biomass Boiler Island		**2,149.0**	**Power Island**	**2,450.0**
Variable O&M		745.0	*Variable O&M*	1,000.0
Contract		w/routine	Non-routine	350.0
Routine maintenance		240.0	Routine	500.0
Major overhaul (annual avg.)		245.0	Utilities	50.0
Replacement parts		included	Insurance	100.0
Spare parts		75.0		
Site		185.0		
Fixed Labor		1,404.0	*Fixed Labor*	1,450.0
TOTAL O&M		**8,022.0**	**TOTAL O&M**	**5,100.0**
Fixed		4,465.0	*Fixed*	2,200.0
Variable		3,557.0	*Variable*	2,900.0

Table 6 Capital and operating cost summary and calculated costs of electricity for black liquor cogeneration systems shown in Figs. 1–4 and detailed in Table 1 and Tables 3–5

					BLGCC	
	Tomlinson			O_2	Air	Ind.
Performance Parameters						
Pulp prod., air-dry t/day		1240		1318	1311	1415
Process steam, GJ/hour		842		893	890	961
Black liquor, tds/day		2,158		2,294	2,281	2,462
Biomass, dry t/day		395		985	484	950
Net power output, MW_e		46.8		135.4	101.4	129.0
Net electricity, kWh/tp		906		2,465	1,856	2,188
Electricity, 10^6kWh/yr[a]		373.1		1,079	808.3	1,028
Cost Parameters	Low[b]	High[b]	Avg.			
Overnight capital ($10^6$$)	138.7	170.4	154.5	173.4	135.8	167.4
IDC[c] ($10^6$$)	10.75	13.21	11.98	13.45	10.53	12.96
Total capital ($10^6$$)	149.5	183.6	166.5	186.9	146.4	180.3
Unit capital costs (overnight)						
$/kg liquor solids/day	69	85	77	81	64	73
$/net kW_e	3194	3923	3556	1380	1444	1398
O&M cost ($10^6$$/year)	5.10	8.02	6.56	11.51	10.56	6.13
Busbar Cost of Electricity Generation, ¢/kWh[a]						
O&M	1.4	2.2	1.8	1.1	1.3	0.6
Fuel[d]	1.1	1.1	1.1	0.9	0.6	0.9
Capital, with annual charge:						
10 % per year, real	4.0	4.9	4.5	1.7	1.8	1.8
15 % per year, real	6.0	7.4	6.7	2.6	2.7	2.6
20% per year, real	8.0	9.8	8.9	3.5	3.6	3.5
Total, with annual charge:						
10% per year, real	6.4	8.1	7.3	3.7	3.7	3.3
15% per year, real	8.4	10.6	9.5	4.6	4.6	4.1
20% per year, real	10.4	13.0	11.7	5.4	5.5	5.0

(a) Assuming a 91% capacity factor (7972 full-load hours/year).
(b) The low and high estimates are from Stone and Webster (Table 4) and Bechtel (Table 3), respectively.
(c) Interest during construction, assuming semi-annual construction expenditures over a 2 year period and a 10% real interest rate.
(d) The revenue from process steam and green liquor delivered from the powerhouse to the process is assumed to be offset by the cost of black liquor delivered from the process to the powerhouse. Biomass fuel is charged at $30 per dry tonne, or $1.5/GJ.

recent industry costs for actual installed Tomlinson units were available to reconcile the difference between the two estimates, both are carried through the analysis here, and an average of the two is used where needed.

Table 5 shows O&M cost estimates developed by Bechtel and Stone & Webster for all systems. Stone and Webster's estimates are considerably lower than those made by Bechtel, both for gasification systems (upper portion of the table) and for Tomlinson technology (lower portion of the table). Similar labor rates were used by both firms, but different sub-classifications of the variable costs make direct comparisons between the Bechtel and Stone and Webster estimates difficult.

Overall Economics. The overall performance and costs of the four alternative black liquor cogeneration systems are summarized in Table 6. High, low, and average cost parameter values are shown for the Tomlinson technology, representing the range of estimates developed by Bechtel and Stone & Webster. Interest during construction, assuming a two-year construction period, accounts for about 7 percent of the total installed cost.

Capital costs are shown in Table 6 normalized by the black liquor throughout (kg liquor solids/day) and by the net electricity generating capacity (kW_e) to eliminate complications of comparing absolute capital costs for systems that each process black liquor at slightly different rates. The capital cost per kg of black liquor solids processed is within ± 14 percent for the three BLGCC systems and the two Tomlinson systems. Thus, all systems are roughly equally capital intensive considering them strictly as chemical recovery units, which is primarily how they are viewed by pulp producers. Because of the much higher power output with the BLGCC systems, however, their costs per kW_e are substantially lower than for the Tomlinson systems: $\$1380-1440/kW_e$, compared to $3190-3920/kWe for the Tom-

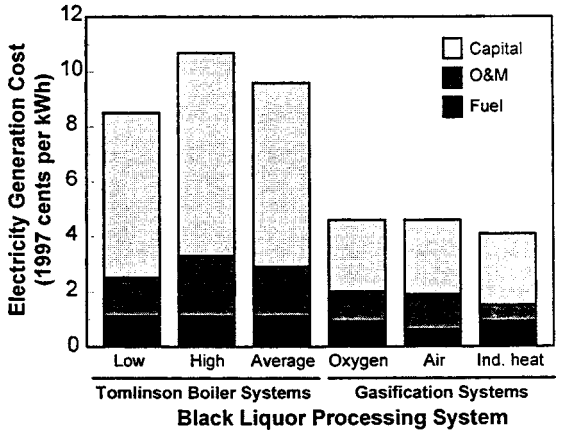

Fig. 5 Calculated costs of electricity generation, assuming 91 percent capacity factor, 15 percent per year capital charge rate, and $30/dry tonne biomass. See Table 6.

Downloaded 02 Jun 2010 to 171.66.16.119. Redistribution subject to ASME license or copyright; see http://www.asme.org/terms/Terms_Use.cfm

Table 7 Cost and value of incremental electricity with BLGCC relative to conventional Tomlinson recovery

	BLGCC System		
	O_2	Air	Indirect
Cost of Incremental Electricity[a,b] (¢/kWh)			
O&M	0.70	0.92	- 0.07
Fuel	0.83	0.20	0.85
Capital (@ 15%/yr)	0.43	- 0.70	0.32
TOTAL	2.0	0.4	1.1
Value of Incremental Electricity[a,c] (10^6/year)			
@ 2 ¢/kWh	14.13	8.70	13.11
@ 4 ¢/kWh	28.25	17.41	26.21
@ 6 ¢/kWh	42.38	26.11	39.32

(a) Incremental electricity generated = kWh generated by the gasification-based system (Table 6) less the kWh generated by the Tomlinson-based system (Table 6).
(b) The costs charged to incremental power are the costs for the gasification-based systems (Table 6) less the average costs for the Tomlinson-based system (Table 6).
(c) The value of the incremental power is the total annual revenue that would accrue to a mill when selling this power at the indicated unit prices.

linson systems. Thus, considered strictly as power generators, the BLGCC systems have considerable capital cost advantages over the Tomlinson technology.

The high net power output with the BLGCCs is due to the inherently higher electricity-to-process steam (E/S) production ratio for a combined cycle cogeneration system relative to a steam turbine-based system. The higher E/S ratios for the BLGCCs necessitates a greater reliance on supplementary biomass fuel in order to meet the same process steam demand as with the Tomlinson technology. The air-blown BLGCC is the best process steam generator among the BLGCC systems and thus requires the least amount of supplemental biomass among the BLGCC systems (Table 6). The larger biomass boilers needed with the BLGCC systems are accounted for in the capital cost estimates (Tables 3 and 4), and the higher costs associated with greater biomass consumption are included in the calculation (discussed below) of the total lifecycle costs associated with each powerhouse option.

Total lifecycle cost for each option is presented in Table 6 in terms of the busbar cost of electricity generation, including capital, operation and maintenance, and biomass cost. In this calculation, the cost of the black liquor delivered from the mill to the powerhouse is assumed to be equal to the value of the process steam and green liquor delivered from the powerhouse back to the mill. Biomass fuel is valued at $30 per dry tonne ($1.5/GJ), a typical cost for wood residues available at many pulp mills in North America. Total busbar electricity costs are calculated in Table 6 for real capital recovery rates of 10 percent, 15 percent, and 20 percent per year.

Because of the lower per-kW_e capital costs for the BLGCC systems compared to the Tomlinson technology, the calculated busbar costs are lower. For example, with a 15 percent/year capital charge rate, the BLGCC systems produce power for 4.1 to 4.6 ¢/kWh compared to more than double this (9.5 ¢/kWh average) for the Tomlinson system (Fig. 5).

The relative costs of the different powerhouse options can alternatively be assessed by calculating the costs for power generated with the BLGCC systems in excess of the power generated with the Tomlinson system. The costs charged against this incremental power are the difference in capital, O&M, and biomass expenditures between the BLGCC and Tomlinson systems. Considering a 15 percent capital charge rate, the cost of incremental power ranges from 0.4 ¢/kWh to 2.0 ¢/kWh for the BLGCC systems (Table 7). For the powerhouse owner, the value of this incremental electricity would be substantial, e.g., $13 to $21 million if the electricity were sold for 3 ¢/kWh or, equivalently, were replacing purchased electricity costing 3 ¢/kWh (Table 7). If the very low incremental cost estimates shown in Table 7 are approximately realized in practice, an investment in a BLGCC system in lieu of a Tomlinson system should be a very profitable venture.

The assumption that the BLGCC systems can fulfill the role of the Tomlinson technology implies that they would be able to provide the same chemical recovery function. (The capital costs in Table 6 were estimated on this basis.) While there appear to be technological strategies for achieving this [4], they have yet to be demonstrated. It is instructive to ask, therefore, how much additional capital could be expended on the BLGCC systems (e.g., to insure its chemical recovery function) before the total busbar costs of power generation would exceed the busbar costs with the Tomlinson system. The answer is that the capital costs for BLGCC systems could double or triple before busbar costs exceed the average busbar cost calculated for the Tomlinson technology. The allowable capital expenditures in excess of those shown in Table 6 are $260, $360, and $370 million for the air-blown, oxygen-blown, and indirectly-heated gasification cases, respectively.

Conclusions

The analysis in this paper indicates that when *N*th-plant costs are achieved for BLGCC systems, gasification-based black liquor processing at a kraft pulp mill will involve capital costs per unit of liquor processed that are comparable to those for conventional Tomlinson-based systems. However, because the BLGCC systems will generate double to triple the amount of electricity for the same black liquor throughput, the total cost of electricity generation per kWh will be about half that with Tomlinson-based technology.

Acknowledgments

The authors thank the Office of Industrial Technologies of the U.S. Department of Energy, the Weyerhaeuser Company, and the Union Camp Corporation for financial support of this work. S. Consonni also thanks the Italian National Research Council.

References

[1] AFPA, 1996, *Fact Sheet on 1994 Energy Use in the U.S. Pulp and Paper Industry*, American Forest & Paper Association, Wash., DC.
[2] Adams, T. N., Frederick, W. J., Hupa, M., Iisa, K., Jones, A., and Tran, H., 1997, *Kraft Recovery Boilers*, Tappi Press, Atlanta, GA.
[3] Larson, E. D., and Raymond, D., 1997, ''Commercializing Black Liquor and Biomass Gasifier/Gas Turbine Technology,'' Tappi J., **80**, No. 12, pp. 50–57.
[4] Larson, E. D., Yang, W., McDonald, G., Frederick, W. J., Malcolm, E. W., McDonough, T. J., Iisa, K., Kreutz, T. G., and Brown, C., 1998, ''Impacts of Integrated Gasification—Combined Cycle Recovery Technology on the Chemical Aspects of Kraft Pulping and Recovery,'' *Proceedings of the 1998 Int'l. Chemical Recovery Conf.*, Tappi Press, Atlanta, GA, pp. 1–18.
[5] Consonni, S., Larson, E. D., Kreutz, T. G., and Berglin, N., 1998, ''Black Liquor-Gasifier/Gas Turbine Cogeneration,'' ASME J. Eng. Gas Turbines Power, **120**, pp. 442–449.
[6] Larson, E. D., and Consonni, S., 1997, ''Performance of Black Liquor Gasifier/Gas Turbine Combined Cycle Cogeneration in the Kraft Pulp and Paper Industry,'' *Proceedings, 3rd Biomass Conf. of the Americas*, Overend and Chornet, eds., Elsevier Science Inc., Tarrytown, NY, pp. 1495–1512.
[7] Consonni, S., 1992, ''Performance Prediction of Gas/Steam Cycles for Power Generation,'' Ph.D. thesis 1893-T, Mechanical and Aerospace Eng. Dept., Princeton Univ., Princeton, NJ.
[8] Larson, E. D., Consonni, S., Berglin, N., and Kreutz, T., 1996, ''Advanced Technologies for Biomass-Energy Utilization in the Pulp and Paper Industry,'' report to U.S. Dept. of Energy from Center for Energy and Environmental Studies, Princeton Univ., Princeton, NJ.
[9] Lorson, H., Schingnitz, M., White, V. F., and Dean, D. R., 1996, ''Black Liquor Recovery by Pressurized Oxygen-Blown Gasification,'' *Proceedings, 1996 Engineering Conference*, Tappi Press, Atlanta, GA, pp. 557–565.
[10] Aghamohammadi, B., Mansour, M. N., Durai-Swamy, K., Steedman, W., Rockvam, L. N., Brown, C., and Smith, P., 1995, ''Large Scale Pilot Testing of the MTCI/Thermochem Black Liquor Steam Reformer,'' *Proceedings, 1995 Int'l. Chemical Recovery Conf.*, Tappi Press, Atlanta, GA, pp. B297–B301.
[11] Pietruszkiewicz, J., 1997, ''Final Report for Costing High-Temperature Black Liquor Gasifier/Gas Turbine Cogeneration Systems,'' prepared by Bechtel National, Inc. (Gaithersburg, MD) for Center for Energy & Environmental Studies, Princeton Univ., Princeton, NJ.
[12] Gastwirth, G., 1997, ''Costing Study of the Stonechem Black Liquor Gasifier/Gas Turbine Combined Cycle Cogeneration System,'' prepared by Stone and Webster Engineering Corp. (New York, NY) for Center for Energy & Environmental Studies, Princeton Univ., Princeton, NJ.

Downloaded 02 Jun 2010 to 171.66.16.119. Redistribution subject to ASME license or copyright; see http://www.asme.org/terms/Terms_Use.cfm

Sub-Scale Demonstration of the Active Feedback Control of Gas-Turbine Combustion Instabilities

Stanley S. Sattinger
Siemens-Westinghouse Power Corporation,
Science & Technology Center,
1310 Beulah Road,
Pittsburgh, PA 15235

Yedidia Neumeier
Aharon Nabi[1]
Ben T. Zinn
Georgia Institute of Technology,
School of Aerospace Engineering,
Atlanta, GA 30332

David J. Amos
Douglas D. Darling
Siemens-Westinghouse Power Corporation,
Orlando, FL 32826

Described are sub-scale tests that successfully demonstrate active feedback control as a means of suppressing damaging combustion oscillations in natural-gas-fueled, lean-premix combustors. The control approach is to damp the oscillations by suitably modulating an auxiliary flow of fuel injected near the flame. The control system incorporates state observer software that can ascertain the frequency, amplitude, and phase of the dominant modes of combustion oscillation, and a sub-scale fuel flow modulator that responds to frequencies well above 1 kHz. The demonstration was conducted on a test combustor that could sustain acoustically coupled combustion instabilities at preheat and pressurization conditions approaching those of gas-turbine engine operation. With the control system inactive, two separate instabilities occurred with combined amplitudes of pressure oscillations exceeding 70 kPa (10 psi). The active control system produced four-fold overall reduction in these amplitudes. With the exception of an explainable control response limitation at one frequency, this reduction represented a major milestone in the implementation of active control. [S0742-4795(00)00702-X]

Introduction

Perspective. Strong instabilities can occur in the combustors utilized in propulsion and industrial applications when the combustion process couples with the acoustic field in a way that excites one or more natural acoustic modes of the system [1]. Utilized approaches for eliminating these instabilities often consist of one or more of the following:

- modification of the combustion process to reduce the magnitude and/or change the frequency dependence of its driving
- increasing the combustor's damping
- preventing the excitation of unstable combustor modes (e.g., by welding in baffles, etc.)
- shifting the frequencies of the combustor's unstable modes away from the range where the combustion process driving is maximized

Unfortunately, implementation of these passive control approaches can be costly and time consuming, and they often fail to adequately damp the instability. Consequently, interest in developing active control systems (ACS) for stabilizing propulsion systems has increased in recent years. These efforts started with theoretical considerations of the subject in the 1950s [2–4], and were followed by the eventual demonstration of the feasibility of active control of combustion instabilities in the 1980s [5–7].

Interest in practical control of combustion instabilities in commercial gas turbines grew significantly when lean-premix combustors evolved as a means for reducing NOx (oxides of nitrogen) emissions from gas turbines without injecting steam or water into the combustor. In those combustors fuel and air are uniformly mixed in a lean stoichiometry before entering the combustion zone. At the leanest conditions, small changes in stoichiometry can cause marked changes in the chemical reaction rates, giving rise to combustion instabilities that may develop pressure amplitudes of damaging levels. Of particular concern in the lean premixed combustor is the coupling of the combustion chamber pressure oscillations with the dynamics of the premix feed system.

Control Considerations. A typical actively controlled combustor may consist of the combustion chamber, a sensor that detects the instability, analysis software (the observer) that determines the state of the system, a controller that modifies the observer's output to provide a signal for the actuator, and an actuator that perturbs the system in a controlled manner. Ideally, such a controller provides flexibility that will permit its effective application in different systems with different operating conditions that change with time. In addition, such a controller should be capable of controlling the performance of systems whose behavior is not fully understood. Finally, it must be significantly less expensive and more dependable than existing approaches for suppressing combustion instabilities.

A recent publication by Neumeier and Zinn [8] includes a survey of the active control approaches that have been taken in the suppression of combustion instabilities in recent years. Limitations to control effectiveness have included the inability to deal with closely spaced modes; the destabilization of stable combustor modes; the inability to adapt to suddenly changed conditions; difficulty in estimating modal parameters in implementing model-based control; and highly complex actuator behavior. The authors proceed to describe an improved control approach that addresses these problems. It is based upon a novel observer that can rapidly identify the frequencies, amplitudes and phases of several excited combustor modes without a priori knowledge of the mechanism of the instability. Furthermore, this observer can rapidly respond (i.e., follow) the changes in the characteristics of the instability. The information acquired by this observer is then used by the controller to optimally attenuate each unstable combustor mode without destabilizing other modes. The present paper describes the implementation of this control approach on a sub-scale gas-turbine combustor.

[1]Visiting Scholar.

Contributed by the International Gas Turbine Institute (IGTI) of THE AMERICAN SOCIETY OF MECHANICAL ENGINEERS for publication in the ASME JOURNAL OF ENGINEERING FOR GAS TURBINES AND POWER. Paper presented at the International Gas Turbine and Aeroengine Congress and Exhibition, Stockholm, Sweden, June 2–5, 1998; ASME Paper 98-GT-258. Manuscript received by IGTI March 8, 1998; final revision received by the ASME Headquarters January 3, 2000. Associate Technical Editor: R. Kielb.

 Copyright © 2000 by ASME

Downloaded 02 Jun 2010 to 171.66.16.119. Redistribution subject to ASME license or copyright; see http://www.asme.org/terms/Terms_Use.cfm

Experimental Facilities

Combustion Stabilization Test Section and Test Combustor The combustion stabilization test section shown in Fig. 1 was specially designed and fabricated for these experiments and was installed in a high-pressure, preheated combustion facility at the Siemens-Westinghouse Science & Technology Center. It includes an inlet air vessel that acoustically isolates the combustor from the upstream compressed-air supply system and a spray cooler plenum that isolates it from the exhaust system. The test section was intended to sustain acoustically coupled combustion instabilities so that the active control system's performance could be evaluated.

The sub-scale combustor that forms an integral portion of this test section was designed to meet the following requirements:

- The main combustion was to take place under conditions representative of a gas turbine operating with lean-premix, natural gas combustion. The premix fuel gas was to be introduced through a single primary fuel manifold and nozzle assembly.
- A modulated auxiliary flow of fuel gas for the active control system was to be introduced through a separate manifold and nozzle assembly.
- A central assembly with integral igniter was to be provided for flame holding.

The test combustor itself, shown in Fig. 2, resembles, in simplified form and small scale, a developmental gas turbine combustor design. Its radial dimensions are scaled down about 10-fold, but it has full axial dimensions to keep the longitudinal acoustic-mode natural frequencies representative of full-scale combustors. Two water-cooled piezoelectric transducers sense pressure fluctuations within the combustor.

Control System. A schematic of the ACS used to control instabilities in the sub-scale gas-turbine combustor is shown in Fig. 3. The developed ACS is based upon an observer that can rapidly identify the frequencies, amplitudes and phases of the combustion oscillations, which are generally not known in advance, and a fast fuel actuator that modulates an auxiliary fuel stream to produce combustion process heat release oscillations within the combustor. The feasibility and performance of this ACS were initially investigated using numerical simulations and subsequently demonstrated on an unstable gas rocket setup under the sponsorship of the Air Force Office of Scientific Research [8].

The Observer. A critical element in the ACS is the novel observer that analyzes the measured instability signal to determine in real time the amplitude, phases and frequencies of the unstable combustor modes. Theoretical details and illustrations of the fast convergence of the observer are described in the foregoing reference. The observer provides the capability of rejecting random noise and generating a reconstructed signal that closely follows the underlying dynamic content of the input signal.

Auxiliary Fuel Actuator. The actively controlled auxiliary fuel actuator introduced an oscillatory fuel flow into the combustion zone. High-pressure fuel was supplied to the actuator and forced through an annular orifice between the outer wall of the needle's base and its seat before flowing through a feed tube and slot-shaped nozzle into the combustor at the downstream end of the flame holder (see Fig. 2). A magnetostrictive actuator, supplied by Etrema Inc., was attached to the needle and used to oscillate the needle along its axis in response to changes in an electrical control signal. The oscillatory axial motion of the needle produced periodic changes of the annular cross sectional area between the needle's base and its seat, resulting in a controlled, modulated, auxiliary fuel flow rate through the annular orifice. The electrical signal to the actuator consisted of a steady and an oscillating component, which controlled the magnitudes of the steady and oscillating flow rates through the fuel nozzle actuator, respectively. Both signals were generated in the control computer, separately amplified, and then combined into a single control signal that was fed to the actuator.

The acoustic impedance and pneumatic resistance of the auxiliary nozzle's elements that carried the fuel from the supply line to the combustor were sized to maximize the fuel flow rate oscillations at the nozzle's exit and minimize the effect of the combustor pressure oscillations upon the nozzle's performance over a wide frequency range. The actuator used in this study was a three-fold scaled-up version of that used by Neumeier [9] to demonstrate active control of combustion instabilities in the gas rocket engine.

Early performance prediction and recent simulation and measurements [10] proved that the utilized auxiliary fuel actuator can produce fuel flow modulation amplitudes of the order of 0.6 grams per second over a 0–1000 Hz frequency range. Such fuel flow modulations can produce 60 kW peak-to-peak heat release rate oscillations if they are ''fully'' converted into heat release oscillations. The overall performance of the actuator, however, depends upon the conversion of these auxiliary fuel modulations into heat release oscillations. Indeed, one would expect this conversion to be strongly dependent on the nozzle/flame holder configuration. As discussed in a later section, we did not have the opportunity to quantify any ''blurring'' of these fuel flow modulations that may have occurred by mixing and transport between the nozzle and flame front in this sub-scale combustor.

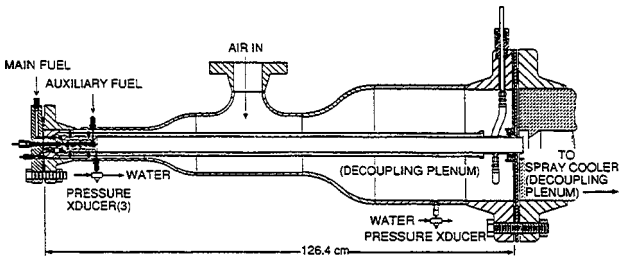

Fig. 1 Sub-scale combustion stabilization test section. Plenums at the upstream and downstream ends decouple the combustor acoustically from the air supply and exhaust lines.

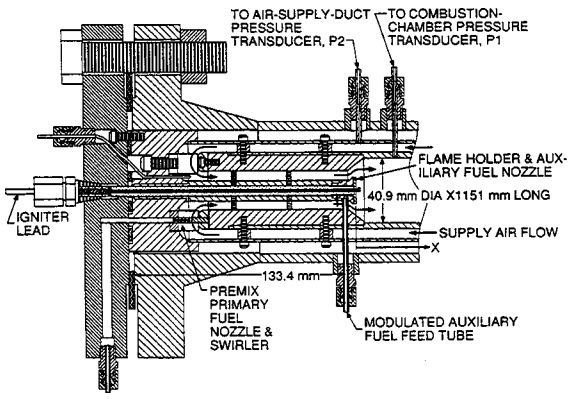

Fig. 2 Enlarged view of combustor portion of test section

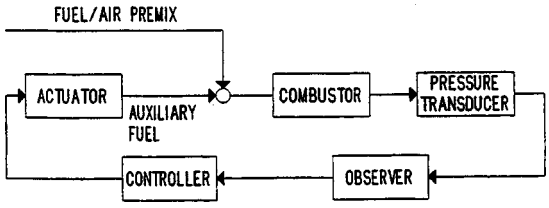

Fig. 3 Schematic of the active control system

Downloaded 02 Jun 2010 to 171.66.16.119. Redistribution subject to ASME license or copyright; see http://www.asme.org/terms/Terms_Use.cfm

Analytical Model

The acoustic characteristics of the sub-scale combustor with the ACS inactive were predicted using the acoustic impedance model described in Fig. 4. This model was originally created to predict the values of the combustor's natural frequencies, near which instabilities could develop, but it was not intended to predict explicitly which of these modes would be driven. However, as will be shown later, the model turned out to be useful for interpreting the observed control performance.

Acoustic impedance is defined as the ratio of the complex amplitude of pressure to the complex amplitude of volume velocity (volume of a fluid swept through a given plane per unit time). The impedances of the test section include compact elements such as orifices and plenums, which are modeled with lumped resistances, inertances, and compliances, in addition to wave transmission elements, whose length dimensions are of the order of magnitude or larger than the acoustic wavelength in the relevant frequency range [11].

Standard techniques for circuit analysis were used to combine the element impedances. One-dimensional (axial-direction) wave propagation was assumed for the wave transmission lines over the 0–500 Hz frequency range of interest. Any effects of steady flow velocity on sound speeds were ignored, as were any effects of products of combustion; i.e., the sound speed values used were those of still air, adjusted for temperature. The temperature distributions throughout the test section were estimated from a limited number of thermocouple measurements at the operating conditions that produced the strongest instabilities (described later). The acoustic resistance values for the air supply line and the exhaust discharge line were obtained by treating them as infinite sinks, while others were simply estimates.

In this modeling approach, the injection of oscillating volume velocity, i.e., volume expansion rate of oscillatory combustion, is used as an alternate to unsteady heat release. Based partly on earlier CFD modeling of the combustor, the effective center or ''lumped'' axial location of the flame front, i.e., the location at which the acoustic impedance seen by the volume-velocity source would be calculated, was taken as 75 mm (3.0 in) downstream of the flame holder.

The following is a listing of the acoustic natural frequency values in the range of 0 to 800 Hz as inferred from peaks in the magnitude of acoustic impedance as a function of frequency. As will be seen later, instabilities actually occurred in the vicinity of only two of these modes.

Acoustic Natural Mode Number	Calculated Natural Frequency
1	122 Hz
2	196 Hz
3	378 Hz
4	593 Hz

Results and Discussion

Combustor Operation Without ACS. With the control system inactive (except for steady flow of auxiliary fuel), we identified a set of operating conditions that would provide strong instabilities for subsequent tests on the ACS. These conditions were as follows:

Combustion Chamber Pressure:	862 kPa (125 psig)
Air Flow:	54 g/s (0.12 lbm/s)
Air Supply Temperature:	322°K (120°F)
Primary Fuel Flow:	1.4 g/s (0.0031 lbm/s)
Auxiliary Fuel Flow:	0.68 g/s (0.0015 lbm/s) (steady component only)
Equivalence Ratio:	0.61 (based on total fuel flow)
Estimated Flame Temperature:	2030°K (3200°F)

The chosen equivalence ratio was about midway between the limits of lean blowoff (about 0.5) and maximum intended wall temperature (about 0.7) for this combustor. The steady component of auxiliary fuel flow was set at a large fraction (about 1/3) of total fuel for purposes of cooling the flameholder in this sub-scale design, and not for reasons of control authority. We briefly

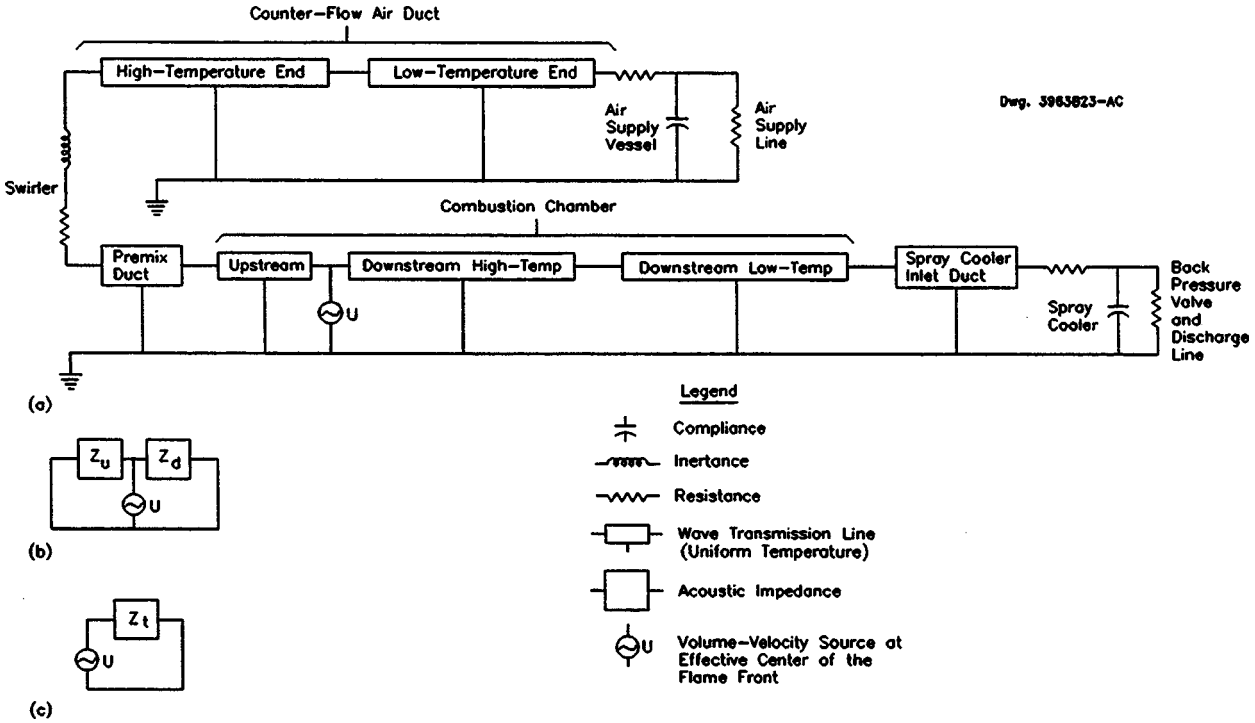

Fig. 4 Acoustic impedance model used to calculate natural acoustic modes and frequency-response quantities for the test section. (*a*) Detailed model. (*b*) Impedence elements combined upstream and downstream of the volume-velocity source. (*c*) Upstream and downstream impedances combined.

Downloaded 02 Jun 2010 to 171.66.16.119. Redistribution subject to ASME license or copyright; see http://www.asme.org/terms/Terms_Use.cfm

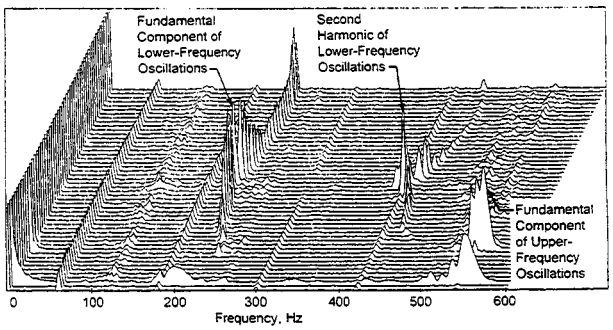

Fig. 5 Typical ''waterfall'' frequency-spectrum plot of combustion-chamber pressure oscillations (Transducer P1) for the lower-frequency (230 Hz vicinity) and upper-frequency (550 Hz vicinity) instabilities of the combustor without active control

changed the fraction of the steady component by more than ± 10 percent in the tests without ACS and found no effect on the strength of instability. Emissions were not sampled in conjunction with these experiments.

Two separate instabilities (combustion oscillations), having frequencies in the vicinity of 230 Hz and 550 Hz, were observed at these conditions. As shown in the Fig. 5 ''waterfall'' spectrum plot, these two instabilities tended to alternate—sometimes appearing together but usually appearing separately, each one disappearing and then reappearing. This pattern tended to be cyclic and may have involved thermal lags associated with the counterflow cooling of the combustor walls. The observed frequencies were reasonably close to the calculated acoustic-mode natural frequencies (230 versus 196 Hz and 550 versus 593 Hz). The maximum amplitudes of the pressure oscillations during periods of instability were in some instances greater than 70 kPa (10 psi) peak. Of the two pressure transducers, the combustion-chamber pressure fluctuation transducer, P1 (see Fig. 2), tended to show the stronger response to the standing pressure wave at 230 Hz. Transducer P1 and the air-supply-duct transducer, P2, showed roughly comparable responses to the 550 Hz pressure wave. Most of the pressure oscillation data shown in this paper are from the chamber transducer, P1.

Open-Loop Control Experiments. Open-loop tests are needed to evaluate the response of the combustion heat release to variable-frequency, sinusoidal actuator command signals, yielding the transfer function of the actuator in terms of gain and phase. The gain is the ratio of the amplitudes of the generated heat release oscillations to the current excitation in the actuator coil, and the phase measures the overall time delay contributed by the complex mixing and chemical reaction processes. Neumeier [9] had described such open loop tests where radical (CC and CH) radiation from the flame zone was measured to determine the combustion heat release. However, an accurate heat release measurement requires a window that can capture the global radiation from the reaction zone. Such a window was not available in the sub-scale combustor, making it unfeasible to measure the transfer function of the auxiliary fuel injection. The open-loop tests were thus limited to qualitative confirmation of pressure response in the combustor to actuator excitation at various frequencies.

Shown in Fig. 6 are time traces and spectra of the pressure fluctuations measured by Transducer P1 at various auxiliary fuel modulation frequencies. The operating conditions of the combustor for this test had been altered from those listed above, just enough to provide stable combustion (same flows, but 20 percent higher absolute pressure) to aid in detecting the oscillations induced by the fuel modulations. Fig. 6(*a*) shows the pressure oscillations with no modulations on the auxiliary fuel. The pressure spectrum indicates weak (note that scale is linear) but clear resonant peaks near 200, 520, and 820 Hz. When modulations of 200

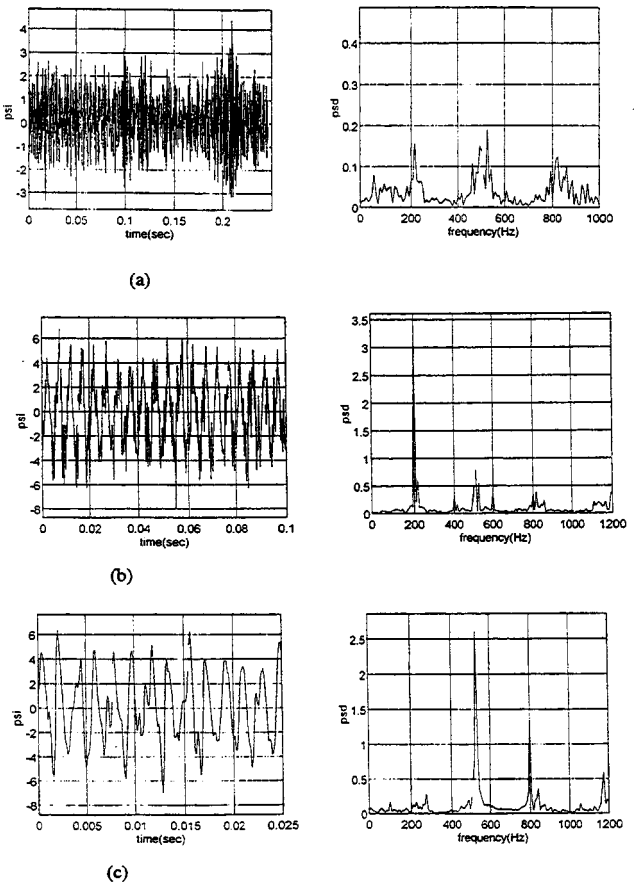

Fig. 6 Sample time histories and frequency spectra of combustion-chamber pressure fluctuations in open-loop active control tests (Transducer P1). (*a*) With no modulation of auxiliary fuel flow. (*b*) With modulation of auxiliary fuel flow at 200 Hz. (*c*) With modulation of auxiliary fuel flow at 800 Hz.

Hz are introduced to the auxiliary fuel stream by the actuator, a clear, dominant tone appears at 200 Hz in the pressure spectrum (see Fig. 6(*b*)). The modulating frequency is apparent also in the time trace of the pressure oscillations.

Clear pressure response is indicated also for modulation frequency as high as 800 Hz (see Fig. 6(*c*)). Interestingly, the resonance mode, distinguishable as a small peak just to the right of the 800 Hz exciting frequency, has not been excited by the fuel modulations, yet, the oscillation at 520 Hz shows the strongest response—likely the return of the higher-frequency combustion instability sustaining itself simultaneously with, but not necessarily caused by, the 800 Hz auxiliary fuel modulation. (We did not turn off the 800 Hz modulation to confirm this explanation; it is possible that the two oscillations may have actually been coupled by nonlinearities.)

Especially significant is the fact that there was poor coherence (cause/effect relationship) between the command signals and the resultant pressure oscillations, as determined with the use of a dual-channel spectrum analyzer, when the fuel modulator was driven in the 500–600 Hz range. Also, the pressure responses swung erratically from weak to strong in this range. A later section argues that this behavior was related to the placement of the auxiliary fuel nozzle in relation to the acoustic wave shapes in that range of frequencies.

Closed-Loop Control Experiments. After verifying that auxiliary fuel modulations indeed excite heat release oscillations within the combustor in the open-loop tests, we initiated closed-loop active control of the combustion oscillations. For this mis-

Downloaded 02 Jun 2010 to 171.66.16.119. Redistribution subject to ASME license or copyright; see http://www.asme.org/terms/Terms_Use.cfm

sion, the primary and nominal (without modulations) auxiliary fuel flow rate were set at the levels identified above, where strong instabilities occurred. All closed-loop testing was focused on this single set of conditions. The steady component of auxiliary fuel flow was controlled constant at the 0.68 g/s level throughout. Because an accurate heat-release transfer function was unavailable, the appropriate phase shift and gain were determined using the following manual adaptive procedure in conjunction with the Transducer P1 signal:

(a) set a high gain
(b) sweep phase until maximum pressure oscillation amplitude is obtained
(c) subtract 180 degrees from the phase of maximum oscillation amplitude; this is the phase that will provide maximum attenuation
(d) change gain to a value above which no significant attenuation is obtained

Figure 7(*a*), a sample time history of pressure oscillations measured by the combustion-chamber transducer (P1) with and without operation of the ACS, clearly demonstrates effective control action. Figure 7(*b*) shows the RMS level of the Transducer P1 and P2 signals, instantaneously averaged by an analog mixer before RMS averaging. A four-fold reduction in pressure oscillation level by the ACS is seen in both plots. The alternating pattern of the two modes persisted when ACS was optimally adjusted, but the oscillation amplitudes were at much lower levels. In testing with all possible phase shifts per the above-described procedure it was found that the ACS had much less influence on the 550 Hz mode than on the 230 Hz mode, consistent with the above-described lack of open-loop coherence in the 550–600 Hz range.

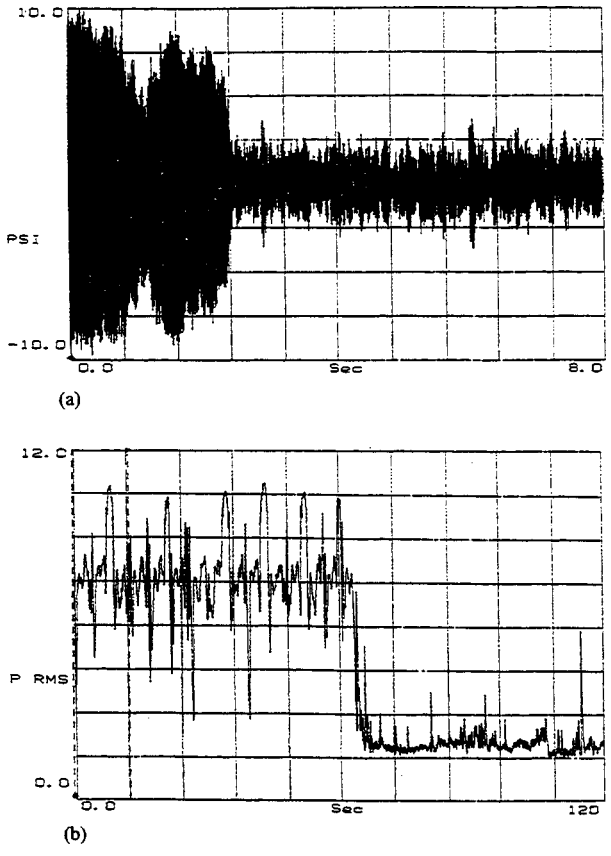

Fig. 7 Sample time histories of pressure fluctuations in closed-loop control tests without and with active control. The major reduction in amplitude level occurs less than 100 ms after the ACS is activated. (*a*) Raw signal from Transducer P1 without and with active control. (*b*) RMS level of mixed signals from Transducers P1 and P2 without and with active control.

Post-Test Analysis of Control Behavior. The open-loop testing showed that intentional sine-wave modulation of the auxiliary fuel flow by the control system could produce strong and coherent pressure oscillations in the combustion chamber at almost all frequencies from zero to 500 Hz and from 600 to 1000 Hz. It followed that closed-loop control was very effective in damping out the sub-scale combustor's 230 Hz, lower-frequency instability. However, the pressure oscillations generated in open-loop testing in the 500 to 600 Hz range lacked coherence with the actuator command signal, and the closed-loop control effectiveness in the instability that occurred in this range was limited.

We used results from the acoustic impedance modeling to seek an explanation for this finding. Baade [12] showed that the Rayleigh Criterion could be recast into a form which leads to exactly the same requirements for instability as derived using classical methods for analyzing the stability of servocontrol systems (see Fig. 8). For compact-flame, premix combustors with one-dimensional modes, acoustically coupled combustion instability occurs at frequencies where both of the following criteria on complex frequency-response quantities are satisfied:

$$|Z_t||H||G|>1 \tag{1}$$

and

$$\angle Z_t+\angle H+\angle G=0^\circ \text{ or integral multiples of } 360^\circ, \tag{2}$$

where

Z_t is the combined upstream and downstream acoustic driving-point impedance seen by the volume-velocity source at the location of the flame (see Fig. 4)

$H=-1/Z_u$ is the negative of the acoustic admittance (reciprocal of acoustic impedance) looking upstream at the location of the flame

G is the flame transfer function (the ratio of oscillatory volume velocity of combustion-product release during unsteady combustion to the volume velocity of the oscillating premix flow)

$\|$ denotes magnitude of a complex quantity

$\angle$ denotes phase angle of a complex quantity.

The servocontrol loop shown in Fig. 8 (not to be confused with the ACS) models premix combustion dynamics assuming that the flame is compact. Earlier CFD modeling of the sub-scale combustor, however, gave predictions of reaction-zone lengths as long as five combustion-chamber diameters. This compact-flame servocontrol analogy nonetheless provides useful insight into the results of the present active control tests.

Figures 9 and 10 show the dependence of the acoustic impedance Z_t and admittance H upon the axial location with respect to the flame holder. Figure 9 shows that at the frequency of the lower instability, relatively small changes in these quantities occur with changes in location along the flame. However, Fig. 10 indicates a dramatic sensitivity to changes in position at the frequency of the

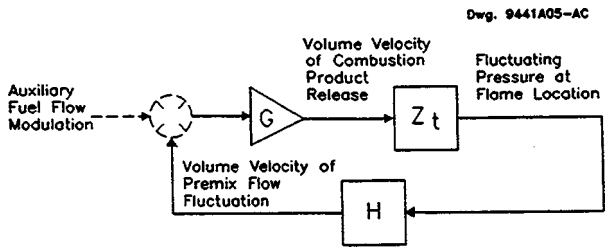

Fig. 8 Servocontrol-loop model of acoustically coupled combustion dynamics in a compact-flame, premix combustor. Auxiliary fuel flow modulation is represented as an optional input to the system.

Downloaded 02 Jun 2010 to 171.66.16.119. Redistribution subject to ASME license or copyright; see http://www.asme.org/terms/Terms_Use.cfm

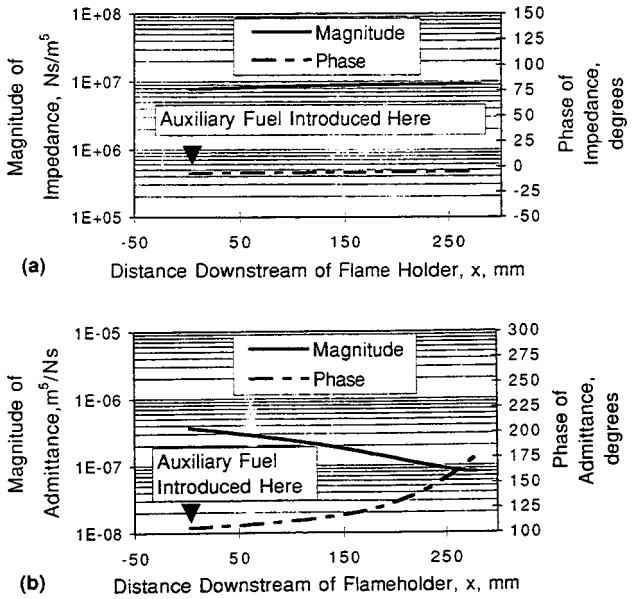

Fig. 9 Variation of the magnitude and phase of the acoustic frequency-response functions with axial position at the lower-frequency instability (196-Hz calculated natural mode). (*a*) Combined impedance, Z_t, seen by a volume-velocity source at location *x*. (*b*) Negative upstream admittance, *H*, at location *x*.

higher instability. At this frequency, the calculated upstream admittance drops to a minimum magnitude and undergoes a reversal of phase at a location close to the flame holder.

Recognizing that richer mixtures promote higher burning velocities, we can assume that combustion of the modulated auxiliary fuel stream introduced volume-velocity fluctuations, or heat release, over a region much closer to the flame holder than the long-length premix flame. (The actual effective location of heat release could not be measured.) Thus we speculate that two simultaneous but separate combustion processes occurred. The higher-frequency pressure oscillations resulting from the modulated auxiliary fuel combustion were probably large, considering the high combined impedance magnitude close to the flame holder. However, owing to the magnitude trough and very steep phase variation of the upstream admittance in this region, these pressure oscillations would create premix flow velocity fluctuations lacking consistent magnitude and phase, assuming a degree of spatial randomness in the heat release. (Recall the erratic pressure fluctuations and lack of coherence in the open-loop testing). In contrast, combustion-product release from the long-length premix flame occurred further downstream in a separate process, where the upstream admittance has higher magnitude and consistent phase, providing the high servocontrol loop gain that would sustain instabilities. This is our hypothesis for the support of the high-frequency instability by the main flame on the one hand, and the lack of controllability by the auxiliary fuel flow modulations on the other.

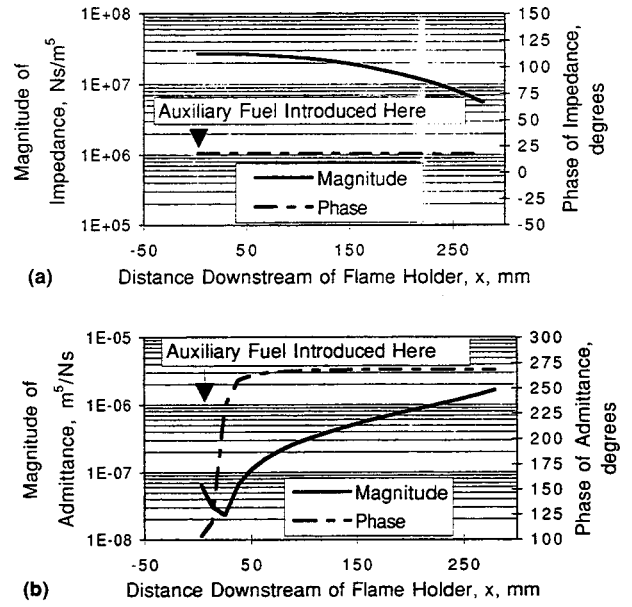

Fig. 10 Variation of the magnitude and phase of the acoustic frequency-response functions with axial position at the higher-frequency instability (593 Hz calculated natural mode). (*a*) Combined impedance, Z_t, seen by a volume-velocity source at location *x*. (*b*) Negative upstream admittance, *H*, at location *x*.

Conclusions

The active feedback control of lean-premix combustion instabilities has been demonstrated through a 4:1 reduction of pressure oscillations from amplitudes greater than 70 kPa (10 psi) peak, in a natural-gas-fired, sub-scale combustor at gas-turbine pressure and temperature conditions. This reduction has been achieved by a control system that uses novel observer software to continuously identify modes of combustion oscillation and a high-response flow modulator to introduce flows of auxiliary fuel for control actuation. The active control approach used in the present work provides the major advantage of removing combustion instabilities without a priori knowledge of the mechanism of the instability. The observer can rapidly respond (i.e., follow) the changes in the characteristics of the instability, and the controller can optimally attenuate each unstable combustor mode without destabilizing other modes.

These sub-scale test results show that the performance of the active control system can be strongly affected by the placement of the auxiliary fuel nozzle in relation to the acoustic wave-shape patterns. In these tests there was inconsistent combustion response to auxiliary fuel flow modulation at the frequency of the higher of two modes of instability because of a phase reversal in the velocity wave near the nozzle. This reversal limited the optimum overall reduction in oscillation amplitude to four-fold. Finding an auxiliary fuel nozzle location that provides strong control of all modes of instability will present a continuing challenge to active control system designers.

Unacceptable pressure fluctuations often prevent operation of combustors at conditions where the lowest NOx would otherwise be produced. The present work was focused on the evaluation of active control performance in a sub-scale apparatus that required high fractions of steady auxiliary fuel flow for cooling reasons. In a full-scale application we would expect the active control system to be able to operate effectively at much lower auxiliary fuel fractions, i.e., just enough to achieve control, or even less to maintain it, such that low NOx operation would be supported. Further development work is planned with concentration on scale-up of the fuel flow modulation to larger amplitudes.

Acknowledgments

This work was sponsored in part by the Power Generation Business Unit of the Siemens-Westinghouse Power Corporation and in part by the U.S. Department of Energy's National Energy Technology Laboratory (NETL) and South Carolina Institute for Energy Studies (SCIES). The encouragement and support of Dr. Richard A. Johnson, FETC Program Manager, and Dr. Dan Fant, SCERDC Program Manager, are appreciated. The combustion stabilization test section was designed by Richard Holm, and the test combustor CFD modeling was performed by

Downloaded 02 Jun 2010 to 171.66.16.119. Redistribution subject to ASME license or copyright; see http://www.asme.org/terms/Terms_Use.cfm

Brigitte Bouvier of the Siemens-Westinghouse Science & Technology Center. Technicians Tony Kramer and George Schneider assembled and instrumented the test section and conducted the tests.

References

[1] Harjee, D., and Reardon, F., eds., 1972, *Liquid Propellant Rocket Combustion Instability*, NASA SP 194.
[2] Tsien, H. S., 1952, ''Servo-Stabilization of Combustion in Rocket Motors,'' Am. Rocket Soc. J., **22**, p. 256.
[3] Marble, F. E., and Cox, D. W., Jr., 1953, ''Servo-Stabilization of Low-Frequency Oscillations in a Liquid Bipropellant Rocket Motor,'' Am. Rocket Soc. J., **23**, p. 63.
[4] Crocco, L., and Cheng, S. I., 1956, ''Theory of Combustion Instability in Liquid Propellant Rocket Motors,'' AGARD Monograph No. 8, Butterworths Scientific Publications, London.
[5] Bloxsidge, G. J., Dowling, A. P., Hooper, N., and Langhorne, P. J., 1988, ''Active Control of Reheat Buzz,'' AIAA J., **26**, p. 783.
[6] Poinsot, T., Veynante, D., Bourienne, F., Candel, S., Esposito, E., and Surget, J., 1988, ''Initiation and Suppression of Combustion Instabilities by Active Control,'' Proceedings of the 22nd Symposium (International) on Combustion, p. 1363.
[7] Langhorne, P. J., Dowling, A. P., and Hooper, N., 1990, ''Practical Active Control System for Combustion Oscillations,'' J. Propul. Power, **6**, No. 3, p. 324.
[8] Neumeier, Y., and Zinn, B. T., 1996, ''Active Control of Combustion Instabilities with Real Time Observation of Unstable Combustor Modes,'' AIAA Paper 96-0758.
[9] Neumeier, Y., 1996, ''Investigation of the Open Loop Performance of an Active Control System Utilizing a Fuel Injector Actuator,'' 32nd AIAA/ASME Joint Propulsion Conference, Lake Buena Vista, FL.
[10] Neumeier, Y., and Zinn, B. T., 1998, ''Theoretical and Experimental Investigation of the Performance of an Actively Controlled Fuel Actuator,'' AIAA-98-0355, presented at the 36th Aerospace Sciences Meeting and Exhibit, Reno, NV.
[11] Kinsler, L. E., and Frey, A. R., 1962, *Fundamentals of Acoustics*, 2nd ed., John Wiley & Sons, Inc., New York, pp. 186–216.
[12] Baade, P. K., 1978, ''Design Criteria and Models for Preventing Combustion Oscillations,'' ASHRAE Trans., **84**, pp. 449–465.

Downloaded 02 Jun 2010 to 171.66.16.119. Redistribution subject to ASME license or copyright; see http://www.asme.org/terms/Terms_Use.cfm

Combustion System Damping Augmentation With Helmholtz Resonators

D. L. Gysling
G. S. Copeland
D. C. McCormick
W. M. Proscia
United Technologies Research Center,
411 Silver Lane,
MS 129-16,
E. Hartford, CT 06108

This paper describes an analytical and experimental investigation to enhance combustion system operability using side branch resonators. First, a simplified model of the combustion system dynamics is developed in which the large amplitude pressure oscillations encountered at the operability limit are viewed as limit cycle oscillations of an initially linear instability. Under this assumption, increasing the damping of the small amplitude combustion system dynamics will increase combustor operability. The model is then modified to include side branch resonators. The parameters describing the side branch resonators and their coupling to the combustion system are identified, and their influence on system stability is examined. The parameters of the side branch resonator are optimized to maximize damping augmentation and frequency robustness. Secondly, the model parameters for the combustor and side branch resonator dynamics are identified from experimental data. The analytical model predicts the observed trends in combustor operability as a function of the resonator parameters and is shown to be a useful guide in developing resonators to improve the operability of combustion systems.
[S0742-4795(00)00602-5]

Introduction

Emissions regulations for land-based gas turbines are an order of magnitude more stringent than for aeroengines. This has necessitated the development of dry low NOx (DLN) combustion technology which premixes the fuel and air prior to burning. The lean premixed combustion process is susceptible to combustion instability, which under certain conditions, can result in unacceptable pressure fluctuation levels in the combustor. To avoid the high oscillatory pressure associated with combustion instabilities, lean premixed combustors are typically stabilized with diffusion flame pilots. However, operability is gained at the cost of elevated emissions of NOx.

Background

The combustor of a gas turbine, like any cavity or chamber, has a variety of acoustic modes—bulk or Helmholtz modes, longitudinal, and circumferential. In the absence of combustion, these acoustic modes have some degree of damping due to various loss mechanisms which dissipate acoustic energy. However, with combustion present, the unsteady heat release process can couple with the acoustic pressure and velocity oscillations and alter the system damping, potentially resulting in instability. The nature of this coupling depends on the magnitude and phase of the heat release fluctuations relative to the pressure fluctuations. The well-known Rayleigh criterion states that self-excited oscillations will be likely if the heat release is in phase with the acoustic pressure disturbances. Combustion instability occurs when driving from this interaction exceeds the inherent acoustic damping of the combustor.

This view suggests the two conventional approaches to enhancing combustion system operability: (1) augment acoustic damping and (2) modify flame structure. This paper is directed at the first approach. Specifically, using auxiliary side branch resonators to augment system damping. The second approach, modifying flame structure through mixing nozzle design, to reduce or eliminate the driving [1] is viewed as somewhat orthogonal to augmenting system damping and is not addressed in this paper.

In addition to these conventional approaches, novel approaches involving active control have recently been developed and demonstrated. An example of this approach is presented by other authors in which active control is used to enhance the operability of a liquid-fueled premixed combustor operating at realistic engine conditions [2].

Model Development

The goal of this section is to develop a low order model of the combustion system to assess the coupling between a combustion system and side branch resonators. The frequencies associated with the combustion instabilities of interest are sufficiently low such that a bulk mode model of the combustion system adequately captures the relevant dynamics. This modeling approach is similar to that developed by other authors for combustion [3,4] and compression system [5] instabilities.

The dynamics of the combustion system and of the side branch resonators are modeled as coupled Helmholtz resonators. The model is shown schematically in Fig. 1.

In this representation, the volume of the combustor provides the compliance and the mass of fluid in the fuel/air mixing nozzle provides the inertia for the resonator modeling the combustor. As developed below, the details of the heat release process are ignored and the model only recognizes the effect of combustion empirically through an effective combustion damping term. The flow into the nozzle is assumed to originate in a large volume, and the flow through the exit of the burner into the turbine is modeled as a quasi-steady orifice flow. Additionally, a pressure loss is modeled at the plane in which the flow exits the nozzle and dumps into the burner.

The side branch resonators are modeled in a similar manner [6]. The throat of each resonator, directly connected to the main volume of the combustor, provides the inertia and the volume provides the compliance for the side branch resonators. A quasi-steady pressure loss models the flow losses within the throat of the resonator.

Contributed by the International Gas Turbine Institute (IGTI) of THE AMERICAN SOCIETY OF MECHANICAL ENGINEERS for publication in the ASME JOURNAL OF ENGINEERING FOR GAS TURBINES AND POWER. Paper presented at the International Gas Turbine and Aeroengine Congress and Exhibition, Stockholm, Sweden, June 2–5, 1998; ASME Paper 98-GT-268. Manuscript received by IGTI March 8, 1998; final revision received by the ASME Headquarters October 20, 1999. Associate Technical Editor: R. Kielb.

Copyright © 2000 by ASME

Downloaded 02 Jun 2010 to 171.66.16.119. Redistribution subject to ASME license or copyright; see http://www.asme.org/terms/Terms_Use.cfm

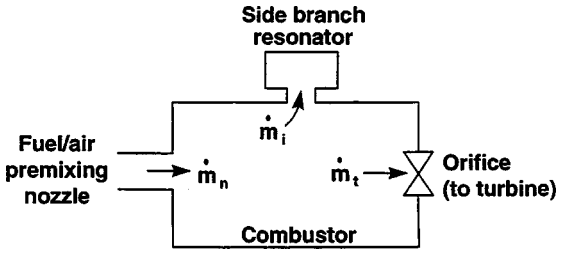

Fig. 1 Schematic of combustor with side-branch resonator

The model allows for large temperature variations between the components. Within each control volume however, the fluid properties are assumed to be spatially uniform.

Governing Equations

Balancing net mass flow into the combustor, entering from the premixing nozzle, exiting to the turbine and being exchanged with the side branch resonator, with the rate of change of mass within the combustor yields the following expression:

$$\dot{m}_n - \dot{m}_t - \sum_{i=1}^{R} \dot{m}_i = \frac{d}{dt}(\rho_p V_p). \tag{1}$$

The mass flow exiting to the turbine is modeled as a linear function of combustor pressure,

$$\dot{m}_t = K_t P_p. \tag{2}$$

The fluid within the combustor is assumed to behave isentropically.

$$\frac{\partial P_p}{\partial \rho_p} = a_p^2 \tag{3}$$

Combining the above relations results in the following expression for mass continuity in the combustor:

$$\frac{d}{dt}(\rho_p V_p) = \frac{V_p}{a_p^2}\dot{P}_p - \rho_p\left(A_n u_n - \sum_{i=1}^{R} A_i u_i\right) = -K_t P_p. \tag{4}$$

Applying conservation of axial momentum to the flow within the nozzle results in the following expression:

$$-P_p = \rho_n L_n \dot{u}_n + \rho_n K_d u_n. \tag{5}$$

The densities in the nozzle and combustor plenum may vary considerably.

Similarly, the equations for mass and momentum conservation for the i^{th} resonator, driven by combustor pressure results in the following expressions:

$$\begin{aligned} \frac{d}{dt}(\rho_{pi} V_i) &= \frac{V_i}{a_{pi}^2}\dot{P}_i - \rho_{pi} A_i u_i = 0, \\ P_p - P_i &= \rho_{ni} L_i \dot{u}_i + \rho_{ni} K_i u_i. \end{aligned} \tag{6}$$

Unsteady Heat Release

The destabilizing mechanism associated with the combustion process is modeled as a negative damping term in the oscillator equation for the combustion system dynamics.

As developed by other authors [3,7–9], the negative damping term results when the unsteady heat release is in phase with pressure oscillations within the combustion chamber. Modeling the details of the unsteady heat release mechanisms is beyond the scope of this paper. It is assumed that the resonators do not modify the destabilizing mechanism of the combustion process. Since we are interested in augmenting the damping of nominally unstable systems, we assume that the combustion damping is nominally negative. A more complete treatment of unsteady heat release models for premixed combustion is described by other authors [10,11].

Oscillator Equations

The above relations can be expressed as a system of coupled oscillators for the pressures within each of the volumes:

$$\ddot{P}_p + 2(\zeta_d + \zeta_t + \zeta_c)\dot{P}_p + \left(1 + \zeta_d\zeta_t + \sum_{i=1}^{R} \Gamma_i Q_i^2\right) P_p = \sum_{i=1}^{R} \Gamma_i [2(\zeta_i Q_i - \zeta_d)\dot{P}_i + Q_i^2 P_i], \tag{7}$$

$$\ddot{P}_i + 2\zeta_i Q_i \dot{P}_i + Q_i^2 (P_i - P_p) = 0. \tag{8}$$

ζ_c is destabilizing if negative. The temporal variations of the oscillator equations are non-dimensionalized by the Helmholtz frequency of the combustor.

Optimization of Damping Augmentation

The stability of the compression system can be evaluated by solving the eigenvalue problem defined by the coupled resonator equations [12]. The effect of the Helmholtz resonators on a given combustion system are characterized by three main parameters, the damping ratio (ζ_i), the Helmholtz frequency ratio (Q_i), and the volume ratio (Γ_i). The equations of motion were analyzed parametrically to optimize the damping augmentation obtained from the side branch resonators for a representative combustion system. For this study, the sum of the damping contribution from the throttle and from the combustion process was set to negative ten percent ($\zeta_t + \zeta_c = -10$ percent) and the damping ratio contribution from the dump plane was set to zero ($\zeta_d = 0$). For this study, damping augmentation is defined as the difference between the damping ratios associated with the least stable eigenvalues for the combustor with and without side branch resonators.

The effect of a single side branch resonator on system damping is illustrated in the two root locus plots shown in Fig. 2 in which system eigenvalues are plotted parametrically as the volume ratio (Γ) is varied from zero to twenty percent. Volume ratios of specific interest are denoted with symbols. In the limit of zero volume ratio, the eigenvalues represent those of two uncoupled systems, the baseline combustion system and the side branch resonator. As the volume ratio is increased, the damping of the eigenvalues primarily associated with the combustor increase while the damp-

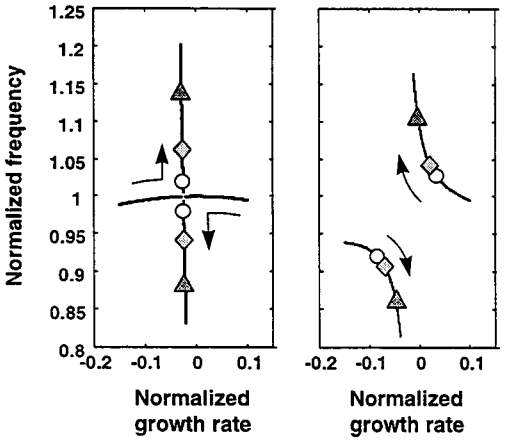

Fig. 2 Rootlocus plots of system eigenvalues as Γ is increased from 0 percent to 20 percent. Combustor with one resonator, $\zeta_H = 0.10$. (*a*) Tuned resonator, $Q = 1$. (*b*) Mistuned resonator, $Q = 0.95$. ($\Gamma = 6.4, 7.7, 12.8$ percent indicated by ○, ◇, and △, respectively).

Downloaded 02 Jun 2010 to 171.66.16.119. Redistribution subject to ASME license or copyright; see http://www.asme.org/terms/Terms_Use.cfm

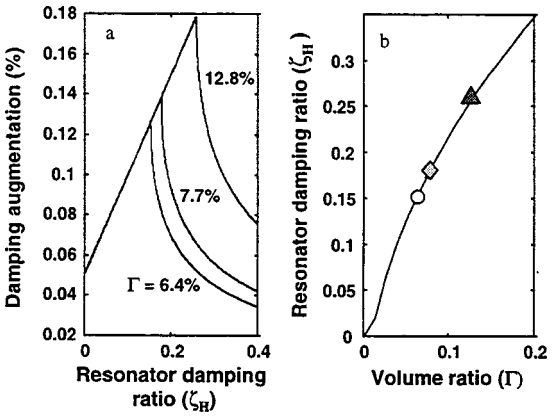

Fig. 3 Dependence of optimal resonator damping ratio on volume ratio for the tuned resonator. (*a*) Damping augmentation versus resonator damping for Γ=6.4, 7.7, and 12.8 percent. (*b*) Optimal damping ratio versus volume ratio.

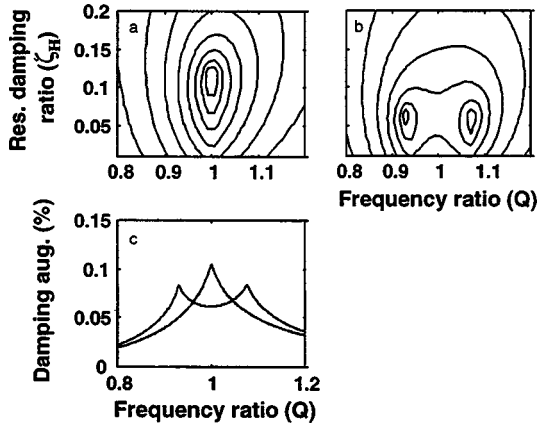

Fig. 4 Dependence of damping augmentation on frequency ratio and damping ratio. (ΣΓ=5 percent). (*a*) Single resonator. Optimal ζ_H is 11 percent. (*b*) Two resonators, $\zeta_1=\zeta_2=\zeta_H$, $\omega_1=1.1\omega_H$, $\omega_2=0.9\omega_H$. Optimal ζ_H is 7 percent. (*c*) Damping augmentation versus frequency ratio at optimal ζ_H for single resonator and two resonator configurations.

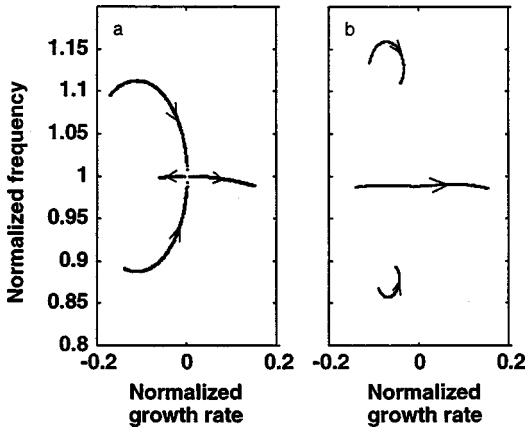

Fig. 5 Rootloci of eigenvalues as combustor damping ($\zeta_t+\zeta_c$) is varied from 20 percent damping to 20 percent growth. Arrows indicate direction of decreasing stability. Resonator configurations identical to those of Fig. 4.

ing of the eigenvalues primarily associated with the side branch resonator decrease. In the case of a tuned resonator, Fig. 2(*a*), this trend with volume ratio increases until the eigenvalues coalesce. At this volume ratio, the frequencies of the two systems begin to separate and the damping of the least damped mode begins to decrease with increasing volume ratio indicating that for these system parameters, additional increases in volume ratio reduce overall system stability.

For cases with frequency mistuning, the qualitative behavior of the eigenvalues is similar. However, the maximum system damping augmentation obtained from a given volume ratio is significantly reduced from that obtained from a frequency-aligned system.

The optimal damping ratio is dependent on the value of the volume ratio of the resonator. This dependence is illustrated in Fig. 3. Larger volume ratio resonators require more damping.

Although not explicitly recognized in the simplified model, the frequency of the pressure oscillations in the baseline combustion system varies to some degree over the operating conditions of interest. Thus, from an operability perspective, an optimal design should provide sufficient robustness with respect to frequency misalignment. One approach is to use multiple resonators of differing frequencies. In Fig. 4, the damping augmentation is plotted against frequency ratio and against damping coefficient at fixed volume ratio for a single resonator and a two-resonator configuration.

The damping augmentation also depends on the amount of unstable damping contributed by the combustion process. This value is assumed constant for each set of operating conditions. Rootloci corresponding to the configurations of Fig. 4 are plotted below in Fig. 5 as the damping contribution for the combustion process is varied from 20 percent to −20 percent. The Helmholtz resonators also influence the natural frequency of the combustion system and how the natural frequency varies with combustion damping.

The general conclusions for the system optimization studies were that for a given combustor operating at fixed conditions (1) the natural frequency of the resonators should be aligned with the natural frequency of the system, (2) the volume ratio should be as large as possible, (3) the optimal damping ratio for the side branch resonator increases with increasing volume ratio, and (4) the amount of negative damping of the combustion process influences the optimal side branch resonator parameters.

Design of Resonators

Three resonator configurations were designed for a combustion system with a natural frequency of 260 Hz. The design intent of the resonator frequencies are presented in Table 1. The damping augmentation of the three resonators predicted by the system model is shown in Fig. 6.

Experiments

Experiments were conducted in the UTRC Sector Rig which is a three nozzle segment of the sixteen nozzles that comprise the full annular burner. The rig includes engine geometry for the prediffuser, diffuser, fuel/air premixing nozzles, and combustor. Two resonators were attached to the sector case with the resonator neck passing through the shroud area such that the opening at the end of the resonator neck was flush with the combustor liner wall. The geometry of the resonators was configuration specific. High pressure (150 psia) preheated air is supplied to the prediffuser

Table 1 Optimized resonator design parameters

Case	Number of Resonators	Resonator Frequency (Hz)	Volume Ratio (Γ_I)	Damping Ratio (ζ_I)
I	1	260	6.4%	15%
II	1	260	7.7%	17%
III	2	260 260	7.7% 5.1%	25% 25%

Downloaded 02 Jun 2010 to 171.66.16.119. Redistribution subject to ASME license or copyright; see http://www.asme.org/terms/Terms_Use.cfm

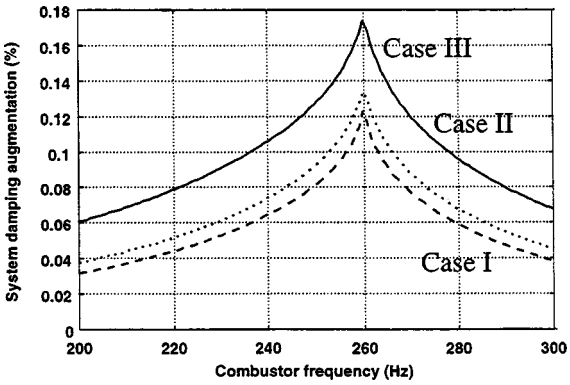

Fig. 6 Design intent of three resonator configurations

inlet through a large volume inlet plenum. The inlet temperature could be varied from 575 to 900 F to simulate engine operation over an ambient temperature range of −40 to +120 F at 60–100 percent power. A choked vane pack at the combustor exit approximately simulates the acoustic boundary condition of the turbine. Pressure oscillations were measured in the diffuser, combustor, and resonator cavities using Infinite Transfer Probes (ITPs) [13]. Dynamic data were acquired with a PC-based multi-channel simultaneous sample and hold data acquisition system. The signals were sampled at 5000 Hz and filtered using single-pole, 1 kHz, anti-aliasing filters. Data was also acquired using a 4-channel HP spectrum analyzer permitting on-line examination of pressure spectra and resonator transfer functions.

Identifying System Parameters

The natural frequency of the baseline combustor was assumed to correspond to the predominant frequency of the pressure oscillations within the combustor operating without resonators. In addition to changes in sidebranch resonator geometry, the damping (ζ_i) and natural frequency (Q_i) of the side branch resonators varied with combustion system operating parameters. The factors affecting these parameters were changes in (1) the natural frequency of the combustion system with operating conditions (ω_c), (2) the natural frequency of the sidebranch resonators depended on resonator neck temperature and (3) the critical damping ratio of the resonator was strongly affected by the acoustic velocity in the neck of the resonator. Thus, to accurately characterize the effect of the resonators on the combustion system, the resonator properties were identified for each operating condition by fitting the frequency domain transfer function from combustor pressure to resonator pressure.

An example of a measured transfer function and parametric fit used to characterize the resonator dynamics is shown in Fig. 7. There was ample noise within the combustor to adequately identify the resonator dynamics over the relevant frequency range. As shown, the low order parametric fit accurately captures the frequency domain transfer function providing a practical method to accurately identify the natural frequency and critical damping ratio of the side branch resonators. Additional information on techniques to characterize the dynamics of acoustic cavities is provided by [14].

Effect of Side Branch Resonators on Combustor Pressure Oscillations

The resonators enhanced combustor operability enabling operation at reduced emission levels and acceptably low oscillatory pressure levels. To illustrate this, the effect of three configurations of side branch resonators on the pressure oscillations within a combustor operating at a full power (a) and at part power (b) condition are shown in Figs. 8(*a*) and 8(*b*), respectively. The resonator parameters for each case are presented in Table 2. The pressure sprectra are normalized to the baseline spectra for each operating condition. The amplitude of the rms of the pressure oscillations in the baseline configurations exceeded 1 psi. The natural frequency of the baseline combustion system varied from 232 Hz at part power to 278 Hz at full power. Despite this variability in combustor natural frequency, each of the resonator configurations significantly reduced the pressure oscillations at both power settings.

Case III, the largest volume ratio configuration at $\Gamma = 12$ percent, was the most effective, reducing the pressure oscillation by roughly an order of magnitude below those of the baselines for both conditions. Cases I and II are similar in volume ratio and illustrate the effect of frequency alignment on resonator effectiveness. At 100 percent power, Case I is more effective in reducing the pressure oscillation than Case II, despite being smaller in volume ratio. This is reconciled by observing that the natural frequency of the resonators in Case I is more closely aligned with the combustor frequency ($Q = .90$) than that in Case II ($Q = .86$).

At the part power condition, the natural frequency of the baseline system decreases and frequency alignment of Case II ($Q = .95$) becomes comparable with that of Case I ($Q = 1.06$) and the larger volume ratio resonator is more effective in reducing the pressure oscillations.

Comparison With System Model Predictions

The results presented in Fig. 8 can be compared with model predictions. The natural frequencies of the baseline combustion

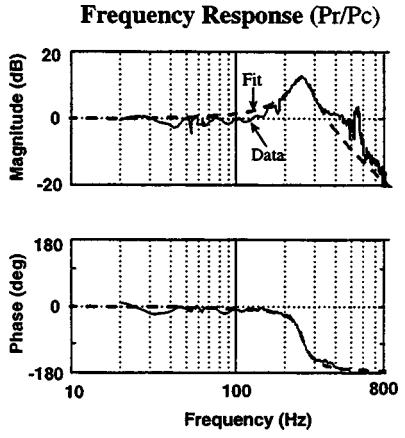

Fig. 7 Example of transfer function from combustor pressure to resonator pressure and the frequency domain curve fit used to identify resonator frequency and damping ratio

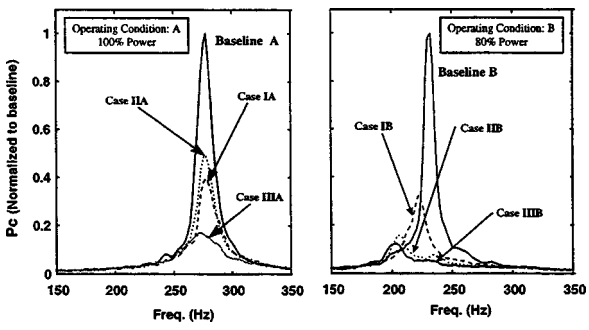

Fig. 8 Combustor pressure spectra for the baseline combustor without resonators and the same combustion system with three resonator configurations operating at two power levels.

Downloaded 02 Jun 2010 to 171.66.16.119. Redistribution subject to ASME license or copyright; see http://www.asme.org/terms/Terms_Use.cfm

Table 2 Combustion system and side branch resonator parameters identified from experimental data

Resonator Configuration	Combustor Operating Condition	Baseline Combustor Frequency (Hz)	Volume Ratio (Γ) (%)	Resonator Frequency (Hz)	Resonator Damping Ratio (ζ)
I	A	278	6.2	249	14%
II	A	278	7.1	237	9%
III	A	278	7.7 5.1	218 262	8% 11%
I	B	232	6.2	249	14%
II	B	232	7.7	223	9%
III	B	232	7.7 5.1	219 245	8% 9%
IV	C	260	5.1	257	11%
V	C	260	11.5	262	10%

system and the resonator frequencies and damping ratios were measured for each operating point and input into the system model. The predicted damping augmentation versus frequency for the three resonator configurations at the two operating conditions is presented in Fig. 9. Qualitatively, the configurations with the largest amount of damping augmentation at the natural frequency of the combustor should correspond to the largest reduction in pressure levels in the combustor.

As shown in Fig. 9(*a*), all three of the resonator configurations were operating with roughly 10 percent frequency misalignment. Due to this misalignment the resonators were providing roughly half of their optimal damping augmentation. At the natural frequency of the baseline combustor, configuration IIIA provides the most damping augmentation, followed by configuration IA and IIA, respectively. This ordering of predicted performance among the configuration is in agreement with the reduction in pressure fluctions achieved in the experiment (Fig. 8(*a*)).

At the 80 percent power level, a similar assessment can be made. At this operating condition, configuration IIIB is aligned in frequency; however, with a damping ratio of $\zeta_h = 8$ percent to 9 percent, case IIIb is substantially under damped compared to the optimal damping ratio. Referencing Fig. 3(*a*), the optimal damping ratio for a resonator with $\Gamma = 12.8$ percent is approximately $\zeta_h = 22$ percent. However, despite this lack of optimal damping, Case IIIb is predicted to achieve the largest system damping augmentation at the natural frequency of the baseline combustor. Case IIb is predicted to be the next most effective and Case Ib the least effective. This trend is consistent with the experimental trend observed in Fig. 8(*b*).

Frequency Robustness

The effect of frequency robustness of a resonator configuration is illustrated in Fig. 10. Figure 10(*a*) shows the spectra of the pressure fluctuations within the combustor for two resonator configurations operating at the 90 percent power condition. The identified resonator and combustion system parameters are listed in Table 2. As indicated, Case VC is significantly more effective than Case IVC in reducing the pressure oscillations. The system damping augmentation predicted for configuration IVC and VC are shown in Fig. 10(*b*). At the combustion system natural frequency (256 Hz), the two resonator configurations are predicted to produce roughly equivalent amounts of system damping augmentation. This is consistent with the pressure spectra at this frequency. However, as shown, configuration VC is more effective in reducing pressure oscillations over a broader range of frequencies.

Conclusions

A simplified model for bulk mode thermoacoustic instability in a combustor coupled with side-branch Helmholtz resonators has been developed and used to determine the influence of system parameters on damping augmentation achievable with resonators. The general conclusions for the system optimization studies were that for a given combustor operating at fixed conditions: (1) the natural frequency of the resonators should be aligned with the natural frequency of the system, (2) the volume ratio should be as large as possible, (3) the optimal damping ratio for the side branch resonator increases with increasing volume ratio,

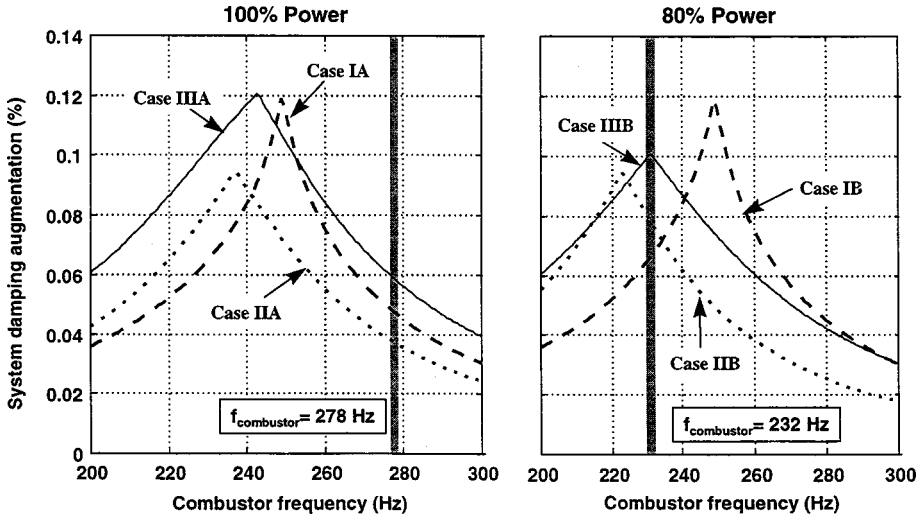

Fig. 9 Damping augmentation predictions for the three resonator configuration presented in Table 1 for the combustion system operating at two power levels. Combustion system and sidebranch resonator parameters identified from experimental data.

Downloaded 02 Jun 2010 to 171.66.16.119. Redistribution subject to ASME license or copyright; see http://www.asme.org/terms/Terms_Use.cfm

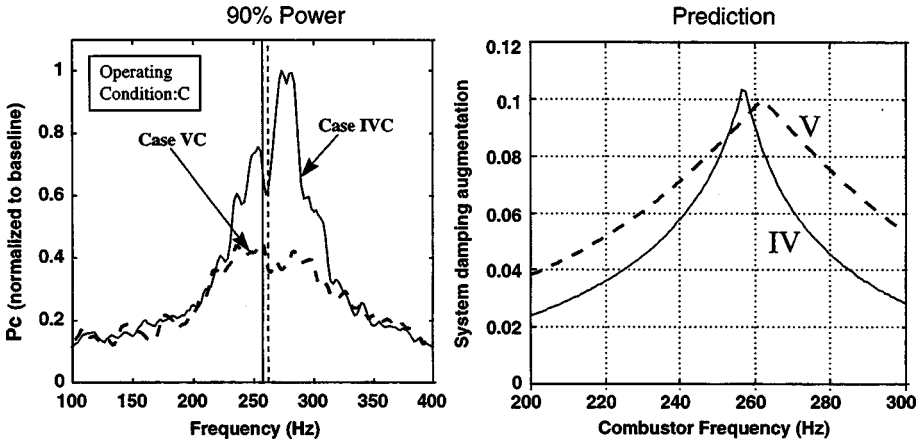

Fig. 10 Effect of frequency robustness on pressure fluctuations in combustor. Data and system damping augmentation predicted by model.

and (4) the amount of negative damping of the combustion process influences the optimal side branch resonator parameters.

Resonator configurations designed using the system model were shown to significantly reduced pressure oscillations within the combustor. The degree of operability enhancement correlated well with the system damping augmentation predicted by the system model. The system model was also useful in interpreting the robustness of resonator configurations towards variations in system parameters.

Acknowledgments

This work represents one aspect of a project which required contributions from numerous individuals within United Technologies Corporation. The authors wish to acknowledge their contribution and specifically acknowledge the support of Ed Greitzer and Bill Sowa of United Technologies Research Center and Dennis Sullivan, Dave Kwoka, and Seyf Tanrikut of Pratt and Whitney.

Nomenclature

A_n = cross-sectional neck area of nozzle
A_i = cross-sectional neck area of i^{th} resonator
a_{pi} = sonic velocity within plenum of i^{th} resonator
a_p = sonic velocity within combustor
K_i = coefficient of pressure loss at dump plane of i^{th} resonator
K_d = coefficient of pressure loss at nozzle dump plane
K_t = throttle coefficient
L_n = length of nozzle
L_{ni} = neck length of i^{th} resonator
$\dot{m}_i$ = mass flow into i^{th} side-band resonator
$\dot{m}_n$ = mass flow into combustor through nozzle
$\dot{m}_t$ = mass flow from combustor through orifice (throttle)
P_i = pressure fluctuation in i^{th} side-band resonator
P_p = pressure fluctuation in combustor
u_i = velocity in neck of i^{th} side-band resonator
u_n = nozzle velocity
V_i = volume of i^{th} resonator
V_p = volume of combustor
$Q_i = \omega_i / \omega_p$ = frequency ratio for the i^{th} resonator
$\Gamma_i = V_i / V_p$ = volume ratio for the i^{th} resonator
ρ_n = density within nozzle
ρ_p = density within combustor
ρ_{ni} = density within neck of i^{th} resonator
ρ_{pi} = density within plenum of i^{th} resonator
ζ_c = empirical contribution to damping due to combustion
$\zeta_d = K_d / 2L_n\omega_p$ = contribution to damping from nozzle dump plane
$\zeta_t = K_t a_p^2 / V_p \omega_p$ = contribution to damping from the throttle
$\zeta_i = K_i / 2L_i\omega_i$ = contribution to damping from the i^{th} resonator
$\omega_i = a_{ni}\sqrt{A_i / V_i L_i}$ = temperature-corrected Helmholtz frequency for the i^{th} resonator
$\omega_p = a_n\sqrt{A_n / V_p L_n}$ = temperature-corrected Helmholtz frequency for the combustor and nozzle.

References

[1] Kendrick, D. W., Anderson, T. J., Sowa, W. A., and Synder, T. S., ''Acoustic Sensitivities of Lean-Premixed Fuel Injectors in a Single Nozzle Rig,'' ASME Paper 98-GT-382.
[2] Cohen, J. M., et al., 1998, ''Active Control of Combustion Instability in a Liquid-Fueled Low-NO_x Combustor,'' ASME Paper 98-GT-267.
[3] Culick, F. E. C., 1989, ''Combustion Instabilities in Liquid-Fueled Propulsion Systems—An Overview,'' AGARD CP-450.
[4] Dowling, A. P., and Ffowcs Williams, J. E., 1983, *Sound and Sources of Sound*, Wiley, New York.
[5] Greitzer, E. M., 1983, ''The Stability of Pumping Systems—The 1980 Freeman Scholar Lecture,'' J. Fluids Eng., **103**, pp. 193–242.
[6] Ingard, Uno, 1953, ''On the Theory and Design of Acoustic Resonators,'' J. Acoust. Soc. Am., **25**, No. 6, pp. 1037–1061.
[7] Culick, F. E. C., 1971, ''Non-Linear Growth and Limiting Amplitude of Acoustic Oscillations in Combustion Chambers,'' Combust. Sci. Technol., **3**, No. 1, pp. 1–16.
[8] Culick, F. E. C., 1994, ''Some Recent Results for Nonlinear Acoustics in Combustion Chambers,'' AIAA J., **32**, No. 1, p. 146.
[9] Jahnke, C. C., and Culick, F. E. C., 1994, ''Application of Dynamical Systems Theory to Nonlinear Combustion Instabilities,'' J. Propul. Power, **10**, No. 4, p. 508.
[10] Peracchio, A. A., and Proscia, W. M., 1998, ''Nonlinear Heat-Release/Acoustic Model For Thermoacoustic Instability In Lean Premixed Combustors,'' ASME Paper 98-GT-269.
[11] Murray, R. M., Jacobson, C. A., Casas, R., Khibnik, A. I., Johnson, C. R., Jr., Bitmead, R., Peracchio, A. A., Proscia, W. M., 1998, ''System Identification For Limit Cycling Systems: A Case Study for Combustion Instabilities,'' Proceedings of the American Control Conference, Philadelphia, PA.
[12] Meirovich, L., 1985, *Introduction to Dynamics and Control*, John Wiley and Sons, New York.
[13] Nyland, T., Englund, D., and Anderson, R., 1971, ''On the Dynamics of Short Pressure Probes: Some Design Factors Affecting Frequency Response,'' NASA TN D-6151.
[14] Laudien, E., et al., 1995, ''Experimental Procedures Aiding the Design of Acoustic Cavities,'' *Liquid Rocket Engine Combustion Instabilities*, V. Yang and W. E. Anderson, eds., AIAA, Washington DC.

Downloaded 02 Jun 2010 to 171.66.16.119. Redistribution subject to ASME license or copyright; see http://www.asme.org/terms/Terms_Use.cfm

Marouan A. A. Nazha

Hobina Rajakaruna

Department of Mechanical and Manufacturing Engineering,
De Montfort University,
Leicester LE1 9BH, UK

Roy J. Crookes
Department of Engineering,
Queen Mary and Westfield College (L.U.),
London E1 4NS, UK

An Effective Property, LHF-Type Model for Spray Combustion

A mathematical model capable of describing the evaporation, mixing and burning characteristics of a confined reacting two-phase flow is presented. The flow field is described by solving the partial differential equations of continuity, momentum, and energy transport, together with the k-ε equations of turbulence. Evaporation is accounted for via a droplet evaporation sub-model which runs in parallel with the gas-phase solver exchanging data with it. Effective properties are calculated in each control volume and the property changes resulting from the evaporation are allowed to propagate according to the turbulent mixing model. Combustion follows the mixing process and is assumed to proceed to equilibrium. The model is validated against experimental results, and its applicability over a wide range of conditions is investigated. [S0742-4795(00)03002-7]

Introduction

The wide-spread application of spray combustion motivated many workers to strive continuously towards improving their understanding of the processes involved, and their ability to simulate and model these processes. Early attempts were by necessity crude and oversimplified. As experimental techniques improved and new sophisticated diagnostic equipment became available more reliable experimental data contributed towards an improved understanding of the phenomenon. This, coupled with rapid increases in computing power enabled more sophisticated models to be explored. Despite these advances, predictive models remain in their infancy. This is due to many factors; prominent amongst these are the complexity and multiplicity of the processes involved, the wide-ranging operating conditions encountered in the applications of spray combustion, insufficient data regarding the physical properties of combustion gases, and, finally, the lack of a full understanding of many aspects of the subject.

The two-phase spray models developed so far can be broadly classified into two groups: Locally Homogeneous Flow (LHF) and Separated Flow (SF) [1]. The basic premise of the LHF approach is that transfer processes between the two phases are fast in comparison to the rate of development of the flow field as a whole. This implies that the two phases are in dynamic and thermodynamic equilibrium. In general, the evaporation from the droplets is not accounted for directly in such models; instead the fuel vapor fraction in each control volume is evaluated from the saturation vapor pressure in the volume. In the SF approach the transfer of mass, momentum and energy between the two phases are considered [2–4]. The models in this group can be either deterministic in nature or stochastic. In both cases the spray is assumed to be dilute enough to make the volume fraction occupied by the liquid droplets sufficiently small to enable droplet-droplet interaction to be neglected. This assumption gives rise to a major disadvantage of the current SF models limiting their applicability to disperse regions of the spray away from the injector and the churn flow zone [5]. The process by which a churn flow is generated from a liquid sheet is part of the atomization problem which has not been fully understood so far. Only few attempts have been made to model this initial drop break up [6].

It has been suggested [7] that LHF type models can be used in the near injector regions in the absence of complex SF type models applicable to dense sprays. A study carried out at elevated pressures demonstrated that LHF type models provide reasonable estimates of the lateral spread of the spray. Measurements of velocities of pressure atomized sprays, using LDA, were also given as evidence that LHF ideas may be pertinent in the near injector region [8].

Based on the above it can be argued that although the LHF analysis is a simplification of the true physics of the spray, it could still be used as a good design tool on its own or in conjunction with more advanced SF models. Furthermore, it is reasonable to assume that LHF results can be improved significantly by including a droplet evaporation module within the LHF formulation [9,10]. This allows droplet properties with the most significant effects on the gas-phase flow development to be accounted for while maintaining the essential characteristics of the LHF type formulation in a manner that can be best described as an *effective property* LHF model. Such a formulation is described below.

Formulation of the Model

The two-dimensional, steady-state finite volume type model developed below is capable of describing the mixing and burning characteristics of a confined two-phase flow in a cylindrical combustion chamber. The fuel and air enter the chamber co-axially through two concentric tubes with the fuel injected via the inner tube. The length and diameter of the chamber and the diameter of each inlet tube can be varied. The fuel type can also be changed by supplying the relevant critical properties (t_c, v_c), acentric parameter, molar mass and a temperature based function for the isobaric specific heat capacity of the fuel. Other chemical and thermodynamic data can be derived by the program.

In LHF type formulation the differences between the two phases within each control volume are neglected in the mixing analysis. This requires that average values of the relevant properties are determined for the flow (deemed homogeneous) in each volume. This is achieved, in this model, via appropriate functions of the corresponding property values of liquid fuel, fuel vapor and air present in the volume. The property changes resulting from the evaporation of the liquid phase are allowed to propagate according to the turbulent mixing model affecting thus the overall mixing process.

In most LHF type models, the evaporation from the liquid phase is calculated via a saturation vapor-pressure function. This arises from the need to assume thermodynamic and phase equilibrium within the volume. It results, however, in overestimating the evaporation rate by neglecting the significant heating up period experienced by the fuel droplets [11]. The present model accounts for this by incorporating a fuel droplet evaporation model running in parallel with the mixing analysis. In this evaporation model the differences between the two phases are taken into account since their effects on the evaporation are quite significant. Thus the properties of the two phases are treated in different ways in the mixing analysis and in the evaporation analysis according to their relevance and effectiveness.

Contributed by the International Gas Turbine Institute (IGTI) of THE AMERICAN SOCIETY OF MECHANICAL ENGINEERS for publication in the ASME JOURNAL OF ENGINEERING FOR GAS TURBINES AND POWER. Manuscript received by IGTI May 31, 1999; final revision received by the ASME Headquarters February 14, 2000. Associate Technical Editor: J. E. Peters.

Copyright © 2000 by ASME

Downloaded 02 Jun 2010 to 171.66.16.119. Redistribution subject to ASME license or copyright; see http://www.asme.org/terms/Terms_Use.cfm

Table 1 Source terms of the generalized flow equation

ϕ	S_ϕ
1	-
u	$-\frac{\partial P}{\partial x}+\frac{\partial}{\partial x}(\mu_e\frac{\partial u}{\partial x})+\frac{1}{r}\frac{\partial}{\partial r}(r\mu_e\frac{\partial v}{\partial x})+s_u$
v	$-\frac{\partial P}{\partial r}+\frac{\partial}{\partial x}(\mu_e\frac{\partial u}{\partial r})+\frac{1}{r}\frac{\partial}{\partial}(r\mu_e\frac{\partial v}{\partial r})-2\mu_e\frac{V}{r^2}+s_v$
T	s_T
m_f	-
k	$G - C_D\rho\varepsilon + s_k$
ε	$C_1\frac{\varepsilon}{k}G - C_2\frac{\rho}{k}\varepsilon^2 + s_\varepsilon$

where $G=\mu_e\{2[(\frac{\partial u}{\partial x})^2+(\frac{\partial v}{\partial r})^2+(\frac{v}{r})^2]+(\frac{\partial u}{\partial r}+\frac{\partial v}{\partial x})^2\}$

Solution Technique. The gas-phase is solved via a Navier-Stokes solver based on the SIMPLE algorithm [12]. The transport equations of the flow variables in a cylindrical co-ordinate system are solved simultaneously with a droplet evaporation model. The evaporation from the spray is assumed to be represented by the evaporation from a Sauter Mean Diameter (SMD) droplet travelling along the axis of symmetry.

The generic form of the gas-phase equation set is as follows:

$$\frac{\partial(\rho u\phi)}{\partial x}+\frac{1}{r}\frac{\partial(r\rho v\phi)}{\partial r}-\frac{\partial\left(\Gamma\frac{\partial\phi}{\partial x}\right)}{\partial x}-\frac{1}{r}\frac{\partial\left(r\Gamma\frac{\partial\phi}{\partial r}\right)}{\partial r}=S_\phi, \quad (1)$$

where ϕ is the generalized flow variable, and S_ϕ is the source term which is explicitly given in Table 1 (the lower case s_ϕ term in each source term is there to account for the wall boundary conditions).

The droplet evaporation model is of transient, variable property, quasi-steady gas-phase and finite liquid diffusivity type [11]. It is programmed as a separate module which can be called from the main solver as needed. The set of equations solved by the droplet module is as follows:

$$\frac{\partial T}{\partial t}=\alpha\left(\frac{\partial^2 T}{\partial r^2}+\frac{2}{r}\frac{\partial T}{\partial r}\right), \quad (2)$$

where

$$\alpha=\frac{k_L}{C_{p_L}\rho_L} \quad (3)$$

subject to the following boundary conditions at the droplet surface and center respectively,

$$4\pi r^2 k_L\left(\frac{dT}{dr}\right)_s=h_c 4\pi r^2(T_\infty-T_s)\frac{Z}{e^z-1}+\frac{dm}{dt}L \quad (4)$$

$$\left(\frac{\partial T}{\partial r}\right)_{r=0}=0 \ ; \quad (5)$$

where,

$$\frac{dm}{dt}=-AK_c P_{fl}\alpha_c \quad (6)$$

General Overview of the Mixing Analysis. Attempting to start the analysis from the injector outlet causes numerical instabilities. The high liquid mass fraction results in large density differences between the flows in the control volume and outside the spray domain. For this reason the flow analysis begins a short distance downstream of the injector. At this distance the spray spreads sufficiently to have a diameter much larger than that of the injector. With this diameter as the initial fuel inlet (sometimes referred to as an injector equivalent diameter) the density differences mentioned earlier become manageable, avoiding the numerical instabilities. Over this short length the fuel is assumed to experience no evaporation; this is justified by the fact that the fuel temperature near the inlet is relatively low and the velocity of the flow is very high resulting in a negligible residence time.

This distance depends on the system and injector used and it is, in general, of the order of few millimeters. It is calculated from consideration of the conservation of injected mass, injected momentum, and the initial fuel mass fraction (taken as 1). Assumed profiles [13] are used at the section of initial conditions to facilitate the analysis and to generate the entry boundary conditions as follows:

Inlet u-Velocity Profile.

$$u(j)=u_{\text{air}}+(u_{c\_\text{in}}-u_{\text{air}})\left(1-\left(\frac{r(j)}{r_{\text{tot}}}\right)^{3/2}\right)^2 \quad (7)$$

Inlet Temperature Profile.

$$T(j)=T_{\text{air}}+(T_{c\_\text{in}}-T_{\text{air}})\left(1-\left(\frac{r(j)}{r_{\text{tot}}}\right)^{3/2}\right) \quad (8)$$

Inlet Mass Fraction Profile.

$$f(j)=C_{\text{int}}\left(1-\left(\frac{r(j)}{r_{\text{tot}}}\right)^{3/2}\right) \quad (9)$$

Inlet Density Profile.

$$\rho(j)=\left((1-f(j)\frac{R_{\text{air}}T_{\text{air}}}{P_{\text{air}}}+\frac{f(j)}{\rho_{\text{lqd}}}\right)^{-1} \quad (10)$$

where,

u_{air}=inlet air velocity; u_{c_in}=center line fuel velocity

r_{tot}=radius of the fuel tube; $r(j)=j$th radial point

T_{air}=air temperature; T_{c_in}=center line fuel temperature

C_{int}=initial concentration; P_{air}=inlet air pressure

ρ_{lqd}=liquid fuel density; f=mass fraction

These calculations are carried out in a pre-processing module which delivers the boundary conditions to the main solver. The computational grid is also established in this pre-processor. The grid used is a structured expanding type which is adequate for the geometry used in the runs carried out so far. The choice of the grid and the expansion factor ensures that a large number of grid points exists within the spray domain near the injector.

A droplet evaporation model is run in parallel with the flow solver. Evaporation is assumed to begin at the first x-grid location inside the computational domain. Data regarding the flow conditions and the rate of evaporation in the control volume are exchanged between the droplet model and the flow solver. The fuel vapor to liquid ratio obtained from the droplet analysis is assumed to prevail in all the control volumes within the cross section. The fuel mass fraction (both liquid and vapor) varies however according to the mixing rules. The overall mixture density and specific heat capacities are derived, in each control volume, using the following equations:

$$\rho=\left(\frac{\left(1-f\frac{m_{\text{new}}}{m_{\text{init}}}\right)}{\left(\frac{(1-f)}{\left(1-\frac{m_{\text{new}}}{m_{\text{init}}}f\right)}R_{\text{air}}+\frac{f\left(1-\frac{m_{\text{new}}}{m_{\text{init}}}\right)}{\left(1-\frac{m_{\text{new}}}{m_{\text{init}}}f\right)}R_{\text{fuel\_vap}}\right)}\right)^{-1}\Bigg/\left(\frac{T}{P}+\frac{f\frac{m_{\text{new}}}{m_{\text{init}}}}{\rho_{\text{lqd}}}\right) \quad (11)$$

Downloaded 02 Jun 2010 to 171.66.16.119. Redistribution subject to ASME license or copyright; see http://www.asme.org/terms/Terms_Use.cfm

$$C_P = \frac{m_{\text{new}}}{m_{\text{init}}} f C_P(T)_{\text{lqd}} + \left(1 - \frac{m_{\text{new}}}{m_{\text{init}}}\right) f C_P(T)_{\text{fuel\_vap}} + (1-f) C_P(T)_{\text{air}} \quad (12)$$

where,

f = mass fraction; $R_{\text{fuel\_vap}}$ = gas constant for fuel vapor

m_{init} = original droplet mass; m_{new} = current droplet mass; and $C_P(T)_{\text{fuel\_vap}}$ = heat capacity of fuel vapor.

Energy Transfer Considerations. In a burning liquid fuel spray, the evaporation process causes a reduction in the gas-phase cell temperatures (due to the enthalpy of evaporation); and the combustion process results in a significant increase in the cell temperatures due to the enthalpy of combustion. Both of the above processes can be incorporated into the gas-phase energy equation as a sink term and a source term respectively. However, appropriate choice of an average air temperature ensures accurate prediction while minimizing the execution time. Thus for an evaporating spray, the gas-phase temperature can be taken as an average temperature derived from the actual air temperature and the temperature after all the fuel has evaporated. For a burning spray, the flame temperature is taken into consideration. Care should be taken to ensure that the evaporation process is not over-estimated, nor under-estimated by the wrong choice of gas-phase temperature. The droplet evaporation module, where the choice of gas-phase temperature is extremely important, is run with accurate, variable temperature based on the temperature rise resulting from the combustion process.

Combustion Calculation. Combustion is carried out in a ''mixed-is-burnt'' manner. Once the mixing process has converged, the equivalence ratio map is passed to a combustion module, where the flame temperature is calculated; together with the equilibrium mole fractions of combustion product species. This is achieved by minimizing the total Gibbs free energy of the system [14].

Results and Discussion

The model is very versatile and a large number of predicted data for different fuels, conditions and geometry could be obtained. All these results could not be reproduced in this paper, however, two significant sets are presented: the first is related to a case study where the model is run simulating conditions for which experimental results are known, while the second set is a parametric study demonstrating the model's response to changes in certain parameters such as pressure, temperature,...etc.

Case Study. The experimental results against which the model was tested were obtained by Nazha and Crookes using a high-pressure steady-state combustion facility [15]. The facility consisted of cylindrical combustion chamber, 800 mm long and 150 mm in diameter. The air and fuel flows inside the chamber were co-axial and both air and fuel were introduced at room temperature (288 K). The fuel (Shell-gasoil) was injected continuously and ignited by a gas-turbine type igniter. Atomization was achieved using a fuel injector having a single hole with 0.2 mm diameter giving a Sauter Mean Diameter (SMD) of 20 μm. The predicted results were obtained for runs at a constant pressure of 653 kPa and an input equivalence ratio[1] of 1.08. The model was run simulating the conditions of the experimental tests.

The properties of gas-oil with chemical formula and molecular mass of *n*-dodacane were used as representative of the test fuel. To account for the effects of combustion temperature on the mixing and evaporating processes a constant average air temperature of 1500 K was assumed and a temperature function, derived from the experimental temperature measurements on the spray axis, was incorporated in the droplet evaporation module. Similarly, the effects of heat transfer to the chamber cooling-water were also incorporated in the flame temperature calculation. The results are presented in Figs. 1 and 2 (all axial distances are measured from the injector). Figure 1 shows the predicted iso-contours of the vapor equivalence ratio, flame temperature, and the concentrations of carbon dioxide (CO_2) and carbon monoxide (CO) within the chamber. The effects of recirculation can be deduced from these plots, particularly from the CO_2 concentrations. The presence of recirculation was observed by Nazha and Crookes in their experimental results. The predicted results show reasonable agreement with the experimental ones, particularly in the peak positions and values and in the distributions on the axis. The predicted axial distributions are reproduced in Fig. 2 with the experimental points superimposed on the plots. The model appears to under predict the vapor equivalence ratio in the early stages (between 0.18 m, start of experimental significant evaporation, and 0.24 m, start of significant predicted evaporation), which results in underprediction of the flame temperature and the combustion products in this region. This is probably due to the fact that predicted evaporation is based on heat transfer from the gas within the control volume; radiation effects from the flame downstream and from adjacent volumes are not considered and these may have a significant contribution in this region. However, the model very quickly catches up with the experimental results at about 0.28 m from the injector.

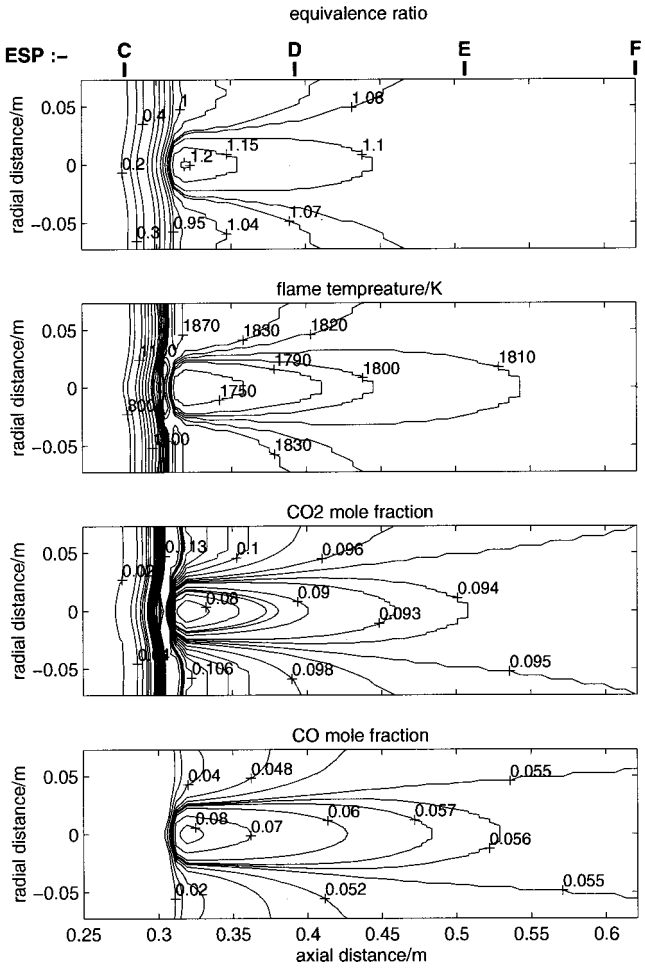

Fig. 1 Predicted iso-contour maps

Parametric Study. The ability of the model to detect the effects of pressure, temperature, input equivalence ratio, and fuel droplet size distribution on the burning spray behavior was studied. Several runs were carried out using the same conditions as those of the case study for all parameters except the one under

[1]equivalence ratio=(fuel mass/air mass)/(fuel mass/air mass)$_{\text{stoichiometric}}$

Downloaded 02 Jun 2010 to 171.66.16.119. Redistribution subject to ASME license or copyright; see http://www.asme.org/terms/Terms_Use.cfm

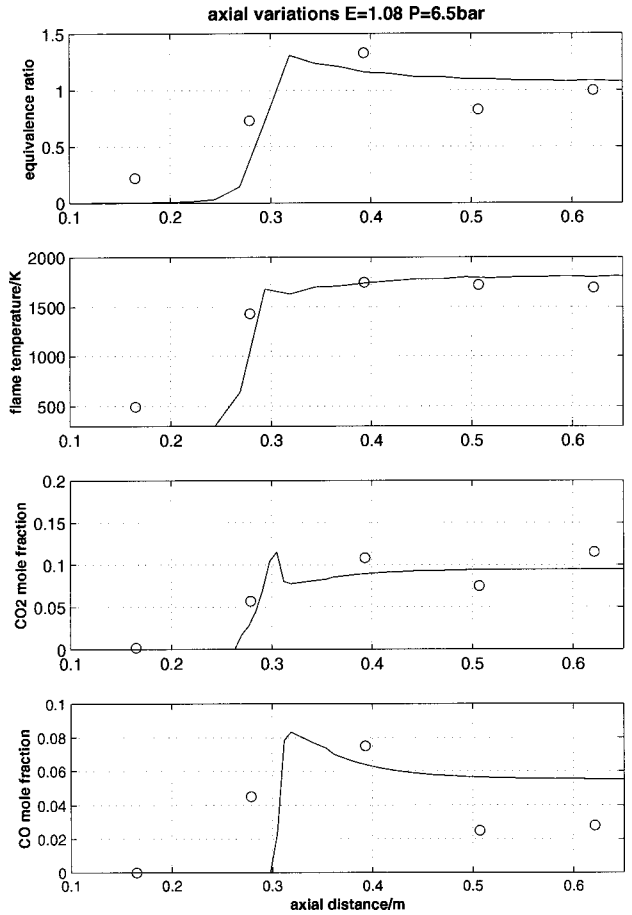

Fig. 2 Predicted axial distributions with superimposed experimental values

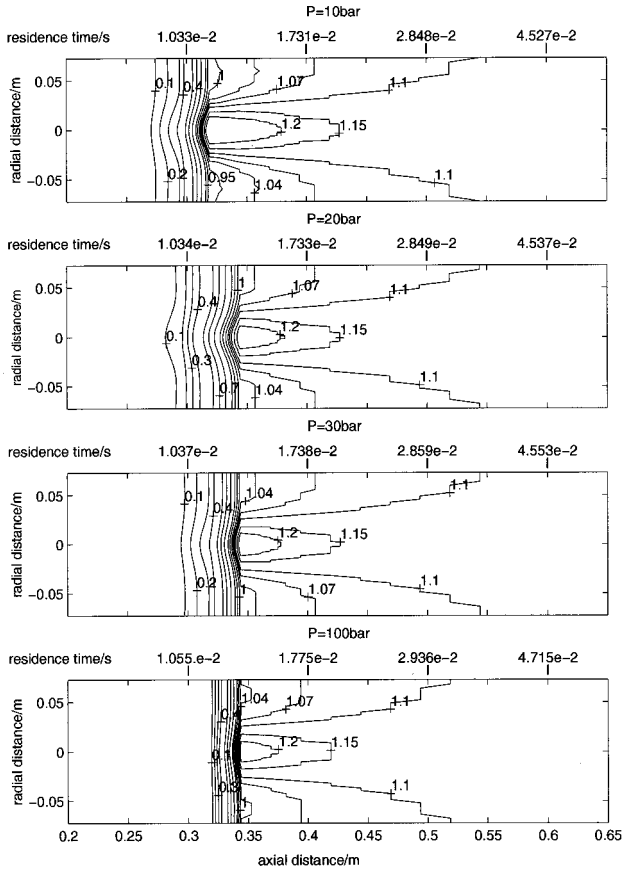

Fig. 3 Effects of ambient pressure on the local vapor equivalence ratio distribution

consideration. Only the predicted vapor equivalence ratio distributions are presented here (Figs. 3–5).

Figure 3 shows the effects of pressure on the evaporating, mixing spray. The model was run for four different pressures (1, 2, 3, and 10 MPa) with all other conditions kept constant. The 1 MPa is sub-critical, the 2 MPa is close to the critical point of the fuel used and the final two are super-critical. It is clear that increasing the system pressure delays the start of meaningful evaporation; however, as the droplets heat up the evaporation rate increases rapidly suggesting that temperature effects on evaporation are more significant than pressure effects. When the droplet's temperature reaches the critical value (in the super-critical runs) the fuel evaporates instantaneously. These pressure effects are more significant when considered against residence time (shown on the plots) which increases with pressure.

The effects of the input equivalence ratio were investigated and the predicted results are presented in Fig. 4. Three runs were carried out for equivalence ratios of 0.8, 1.0, and 1.2. All other conditions were kept constant. It appears from the predicted results that a decrease in the equivalence ratio causes complete mixing to occur further downstream of the injector. This is a direct result of the increase in air momentum accompanying the decrease in equivalence ratio for a fixed geometry and a fixed fuel mass flow rate.

The higher momentum of the air impedes the radial mixing and increases the constraint on the jet spread. The other significant finding from these runs (not shown explicitly here but can be deduced from the results) is to do with the recirculation zone. Increasing the equivalence ratio causes recirculation to be more pronounced and to occur earlier on, i.e., nearer to the injector. The higher the input equivalence ratio, the less air is available for entrainment.

The effects of air temperature on the evaporating spray were also investigated. Two runs were carried out for air temperature of 800 K and 1000 K. All other conditions being equal. The results (not shown here) indicate that, as expected, an increase in the system temperature causes the evaporation to begin earlier. This results in higher fuel vapor concentrations giving rise to higher

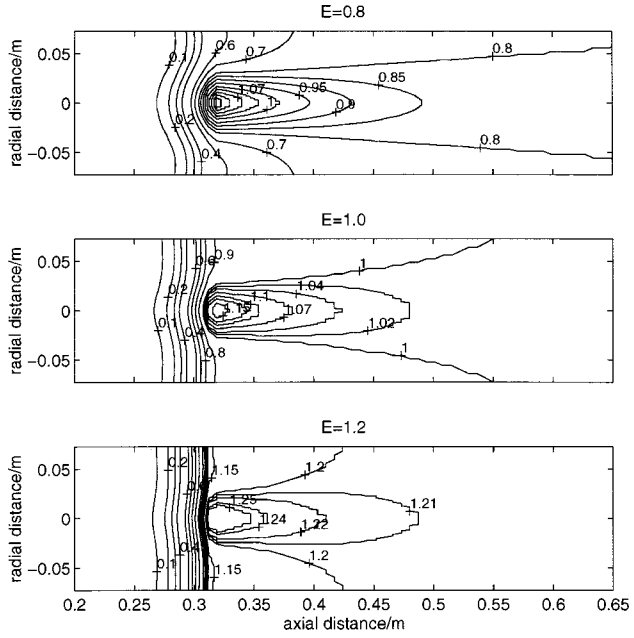

Fig. 4 Effects of input equivalence ratio on local vapor equivalence ratio distribution

Downloaded 02 Jun 2010 to 171.66.16.119. Redistribution subject to ASME license or copyright; see http://www.asme.org/terms/Terms_Use.cfm

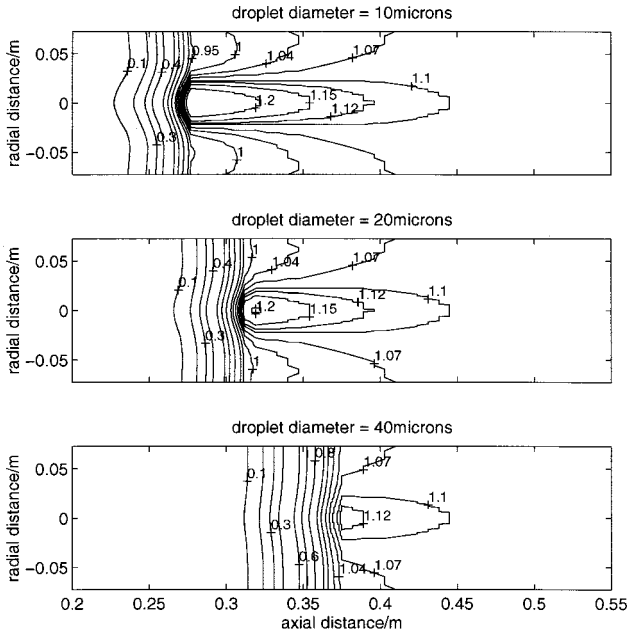

Fig. 5 Effects of droplet diameter on local vapor equivalence ratio distribution

peak values of the vapor equivalence ratio. These rich regions are likely to have significant effects on pollutant formation, particularly on soot formation.

Finally the effects of fuel droplets size distribution were studied by running the model for three different Sauter Mean Diameter droplets (10, 20, and 40 μm). The results predicted by these runs are shown in Fig. 5. As expected, increasing the droplet diameter causes the liquid phase to persist further downstream of the injector. These changes in the relative concentrations of the fuel vapor and the liquid affect the mixing process and the overall distribution of the injected mass and eventually the combustion products. This is an important feature of the present model. Most existing LHF type models are not sensitive to droplet size distribution since they depend on the saturation pressure function to calculate the fuel vapor mass fraction in each control volume. This insensitivity to fuel droplet size has resulted in the predictions from these models departing from those found experimentally as the experimental mean droplet size increases. It has been shown [16,17] that such LHF type models are only applicable to sprays with droplet average diameter below 10 μm. The present model guards against droplet size insensitivity and increases the applicability of LHF type formulation by the use of the droplet evaporation module.

Conclusions

An LHF type, two-phase mathematical model, applicable to high pressure combustion flows has been formulated. The model has the advantage over most existing LHF type formulations in that it accounts for the disperse phase evaporation via a simultaneous solution of a droplet module with the gas-phase equations. A case study using the two-phase model has demonstrated its suitability for predicting axial and radial distributions of combustion products, temperature and vapor equivalence ratio in a burning liquid fuel spray with reasonable accuracy.

The effects of system pressure, temperature, input equivalence ratio, and droplet size on the evaporation and mixing processes as reflected in the local vapor equivalence ratio (or mass fraction) distribution have been demonstrated in a parametric study. The versatility of the model and its ability to cover a wide range of conditions has thus been highlighted.

Nomenclature

A = droplet surface area
h_c = surface heat transfer coefficient
K_c = mass transfer coefficient
k = turbulent kinetic energy
k_L = liquid thermal conductivity
L = latent heat of gasification
m = droplet mass
m_f = fuel mass fraction
P = Pressure
P_{fl} = saturation vapor pressure of the fuel
P' = Pressure correction term
r = droplet radius
T = Temperature
u = axial velocity
v = radial velocity
z = correction for mass transfer

Greek Symbols

α = liquid thermal diffusivity
α_c = correction for mass transfer
ε = turbulent dessipation rate
ρ = density
Γ = diffusion coefficient

Subscripts

s = surface
0 = initial
∞ = ambient

References

[1] Faeth, G. M., 1983, ''Evaporation and Combustion of Sprays,'' Prog. Energy Combust. Sci., **9**, pp. 1–76.
[2] Crowe, C. T., 1978, ''A Numerical Model for the Gas-Droplet Flow Field Near an Atomiser,'' Proceedings of the 1st international Conference on Liquid Atomisation and Spray Systems, Tokyo, Japan.
[3] Huang, X., and Lixing, Z., 1991, ''Simulation of Three Dimensional Turbulent Recirculating Gas Particle Flows by an Energy Equation Model of Particle Turbulence,'' *Gas-Solid Flows*, FED-V **121**, ASME, New York, pp. 261–265.
[4] Lixing, Z., 1993, *Theory and Numerical Modelling of Turbulent Gas-Particle Flows and Combustion*, Science Press, Boston, MA.
[5] Karlsson, J., and Andres, J., 1995, ''Modelling Auto-Ignition, Flame Propagation and Combustion in Non-Stationary Turbulent Sprays,'' Ph.D. thesis, Dept. of Thermo and Fluid Dynamics Chalmers, University of Technology, Sweden.
[6] O'Rourke, P. J., and Amsden, A. A., 1987, ''The TAB Method for Numerical Calculations in Thick Sprays and Comparison with Experiments,'' SAE 872089.
[7] Faeth, G. M., 1987, ''Mixing and Transport and Combustion in Sprays,'' Prog. Energy Combust. Sci., **13**, pp. 293–345.
[8] Wu, K. J., Su, C. C., Steinberger, R. L., Santavicca, D. A., and Bracco, F. V., 1983, ''Measurements of Spray Angle of Atomisation Jets,'' J. Fluid Eng., **105**, pp. 406–413.
[9] Crookes, R. J., and Nazha, M. A. A., 1990, ''Measurement and Prediction of Soot and Gaseous Species in a Burning Fuel Spray at Elevated Pressure,'' *Archivum Combustionis*, Vol. 10 (Nos. 1–4), pp. 49–69.
[10] Nazha, M. A. A., Rajakaruna, H., and Crookes, R. J., 1997, ''Soot and Gaseous Species Formation in a Water-in-Liquid Fuel Emulsion Spray—A Mathematical Approach,'' Fourth International Conference on Combustion Technologies for a Clean Environment (FLOWERS97), Florence, Italy.
[11] Rajakaruna, H., 1997, ''A Mathematical Model for Liquid Fuel Spray Combustion,'' Ph.D. thesis, Dept. of Mech. Engineering, De Montfort University, United Kingdom.
[12] Patankar, S. V., 1980, *Numerical Heat Transfer and Fluid Flow*, Taylor and Francis, London.
[13] Abramovich, G. N., 1963, *The Theory of Turbulent Jets*, MIT Press, Cambridge, MA.
[14] Nazha, M. A. A., 1983, ''Burning Sprays of Water-in-Fuel Emulsions,'' Ph.D. thesis, University of London.
[15] Nazha, M. A. A., and Crookes, R. J., 1984, ''Effects of Water Content on Pollutant Formation in a Burning Spray of Water-in-Diesel Fuel Emulsion,'' 20th Symp. (*Int.*) on Comb., p. 2001.
[16] Shearer, A. J., and Faeth, G. M., 1979, ''Evaluation of Locally Homogeneous Model for Spray Evaporation,'' NASA Contractor Report 3198.
[17] Mao, C. P., Wakamatsu, Y., and Faeth, G. M., 1981, ''A Simplified Model for High Pressure Spray Combustion,'' 18th Symposium (*Int.*) on Combustion, The Combustion Institute, Pittsburgh, PA.

Downloaded 02 Jun 2010 to 171.66.16.119. Redistribution subject to ASME license or copyright; see http://www.asme.org/terms/Terms_Use.cfm

Industrial Trent Combustor—Combustion Noise Characteristics

Thomas Scarinci
John L. Halpin
Rolls-Royce Canada,
9545 Cote-de-Liesse,
Dorval, Quebec,
Canada H9P 1A5

Thermoacoustic resonance is a difficult technical problem that is experienced by almost all lean-premixed combustors. The Industrial Trent combustor is a novel dry-low-emissions (DLE) combustor design, which incorporates three stages of lean premixed fuel injection in series. The three stages in series allow independent control of two stages—the third stage receives the balance of fuel to maintain the desired power level—at all power conditions. Thus, primary zone and secondary zone temperatures can be independently controlled. This paper examines how the flexibility offered by a 3-stage lean premixed combustion system permits the implementation of a successful combustion noise avoidance strategy at all power conditions and at all ambient conditions. This is because at a given engine condition (power level and day temperature) a characteristic ''noise map'' can be generated on the engine, independently of the engine running condition. The variable distribution of heat release along the length of the combustor provides an effective mechanism to control the amplitude of longitudinal resonance modes of the combustor. This approach has allowed the Industrial Trent combustion engineers to thoroughly ''map out'' all longitudinal combustor acoustic modes and design a fuel schedule that can navigate around regions of combustor thermoacoustic resonance. Noise mapping results are presented in detail, together with the development of noise prediction methods (frequency and amplitude) that have allowed the noise characteristics of the engine to be established over the entire operating envelope of the engine. [S0742-4795(00)00802-4]

1 Introduction

Recent years have seen the emergence of combustion noise resonance as a central technical problem in the design of Dry Low Emissions (DLE) combustors. Despite the variety of technical approaches used in the design of DLE combustors (annular versus can combustors, parallel versus series staging of fuel and/or air, various flame stabilization strategies, etc.) the problem has been experienced by almost all gas turbine manufacturers.

The practical combustion noise problem can be summarized by the following fundamental question: given a set of combustor operating conditions, will the combustor exhibit a resonant acoustic mode and if so, what will be the frequency and amplitude of the pressure oscillations?

Most theoretical attempts at answering the above question have focused on the identification of the unstable modes of the combustor, using linear stability analysis. The recent work of Hubbard et al. [1] is a good example. Typically, the conservation equations are linearized for small amplitudes, so that a dispersion relation that predicts the linear growth of the unstable modes can be obtained. The result of this type of analysis is a prediction of the frequencies of the unstable mode(s), but nothing is obtained in terms of the resulting limit-cycle amplitude, or the effect of the engine cycle on the onset of the instability. Furthermore, linear stability models provide limited predictive capability, since a key ingredient to the approach is some information about the dynamic response of the flame when subjected to acoustic perturbations. A so-called ''flame model'' is necessary and usually needs to be obtained experimentally [2].

Yet, to the development engineer, the maximum amplitude of the instability is a key parameter that needs to be quantified, together with a reliable prediction of the engine conditions at which the resonance will occur. Under certain conditions (if not most conditions), a linear stability analysis will predict more than one unstable mode in the combustor. In these circumstances, the result is of no immediate practical value since it will fail to identify which of the unstable modes will be selected by the combustion system.

Work on liquid rocket motor instability has long established that, at first order, the frequency of the resonance always corresponds to a natural acoustic mode of the combustor [3]. Thus, the possible frequencies of the unstable modes are easily predicted with reasonable accuracy. On the other hand, Chu [4] established the relationship between a fluctuation in the rate of heat release and the amplitude of the resulting pressure wave. Considering a control volume that encloses a region of heat release inside an infinite tube, and a perturbation in the rate of energy release inside the control volume, Chu [4] obtained the following result:

$$q' = \frac{\Delta w}{w} = \frac{1}{\gamma M_1} \frac{\left(1+\left(\frac{c_2}{c_1}\right)\right)}{\left(\frac{T_2}{T_1}-1\right)} \left[\frac{\left(1+\left(\frac{\Delta p_1}{p_1}\right)\right)\left(\frac{\Delta p_1}{p_1}\right)}{\sqrt{\frac{\gamma+1}{2\gamma}\left(\frac{\Delta p_1}{p_1}\right)+1}} \right] \quad (1)$$

where q' is a fluctuation in the rate of heat release (percent), w is the rate of energy released per unit area, Δw is a *finite* perturbation in the rate of heat release, M_1 is the incoming Mach number, γ is the ratio of specific heats, Δp is the amplitude of the generated pressure wave and c, T, and p denote the sound speed, temperature, and pressure, respectively. The indices 1 and 2 refer to the unburned and burned states, respectively.

Clearly, Chu's result has no link whatsoever to any of the possible resonant frequencies associated to a tube (combustor) of finite dimensions. Interestingly enough (and contrary to what is sometimes observed in DLE combustors) the above relationship predicts that the pressure amplitude *decreases* as the temperature ratio is decreased. The above relationship, although rigorously correct, does not incorporate the feedback mechanism necessary for the prediction of an unstable condition.

The necessary condition for combustion instability is of course the well-known Rayleigh criterion, which says that the pressure waves need to be in phase with the heat release [5]. The distribu-

Contributed by the International Gas Turbine Institute (IGTI) of THE AMERICAN SOCIETY OF MECHANICAL ENGINEERS for publication in the ASME JOURNAL OF ENGINEERING FOR GAS TURBINES AND POWER. Paper presented at the International Gas Turbine and Aeroengine Congress and Exhibition, Indianapolis, IN, June 7–10, 1999; ASME Paper 98-GT-9.

Manuscript received by IGTI March 9, 1999; final revision received by the ASME Headquarters January 3, 2000. Associate Technical Editor: D. Wisler.

 Copyright © 2000 by ASME

Downloaded 02 Jun 2010 to 171.66.16.119. Redistribution subject to ASME license or copyright; see http://www.asme.org/terms/Terms_Use.cfm

tion of heat release along the length of the tube is therefore an important consideration on whether or not instability will occur.

One key difference between lean, premixed combustors and conventional combustors is the distribution of heat release within the combustor volume. In DLE combustors (using lean premixed technology), heat release occurs abruptly across a flame front whereas in traditional combustors the heat release is *smeared* across a much wider region. The abrupt heat release at the flame front in a premix system allows for the occurrence of a narrow range of time delays between fuel injection and heat release. This makes it possible for a large fraction of the heat release to satisfy Rayleigh's criterion. In a diffusion flame type combustor, there is a large collection of time delays between heat release and fuel injection and only a small fraction of the heat release can satisfy Rayleigh's criterion.

It is interesting to note that thermoacoustic oscillations are routinely observed in cryogenic systems [6] where they are the result of large temperature gradients along the length of tubes of finite length. Theoretical analysis of this phenomenon shows that the thermoacoustic instability in this case is strongly affected by the distribution of temperature along the length of the tube.

In this paper, it will be shown that the frequency and amplitude of the resonant axial modes in a DLE combustor are strongly affected by the axial distribution of heat release and temperature inside the combustor. The Industrial Trent combustor is a 3-stage lean premixed combustor. This design has allowed us to identify the frequencies and amplitudes of all the resonant modes of the combustor, independently of engine running conditions.

After a brief introduction to the 3 axial stage concept, noise-mapping results are presented. Correlations for each of the unstable modes are then presented, followed by a discussion of the predictive capabilities of the approach.

2 Axial Staging of Heat Release

A cross-section of the Industrial Trent combustor is shown in Fig. 1. The combustor consists of three premixing channels, which are respectively referred to as the primary, secondary, and tertiary premixers. The primary premix system is the only premix system that is self-stabilized. That is, the primary system can be operated alone, whereas the secondary and tertiary systems cannot. The secondary and tertiary premixed streams are ignited by the upstream stages, as they mix inside the combustor. If the primary stage flames out, the whole combustor flames out.

Flame temperatures associated to each of the premix stages can be calculated on the basis of ''cold flow'' effective areas (which provide combustor air splits) and measured fuel flows to each of the fuel stages.

The practical implication of the design is that the secondary and tertiary stages can be operated at much lower flame temperatures than what is normally required for flame stabilization. The result is a large turndown ratio in the achievable fuel-air ratios of the secondary and tertiary premixers.

Part of the secondary fuel-air mixture is entrained into the primary zone, to mix with the primary premix stream. Once the flame temperature associated with the secondary premix stream reaches a certain level, this entrainment effect will result in an improvement in the weak extinction limit of the primary system. This is because it is the average temperature resulting from the mixing of the two streams that governs the weak extinction of the primary zone. The improvement in primary zone stability resulting from secondary stream entrainment is shown in Fig. 2. The amount of secondary fuel-air mixture entrained into the primary zone of the combustor can be estimated from the slope of the line above 1400 K in Fig. 2.

At a given power level, the total amount of fuel inside the combustor is prescribed. The combustion engineer is left with the choice of the allocation of the total fuel between the three premix stages. The possible fuel splits are limited by a series of constraints: the primary weak extinction temperature, the maximum temperature for any of the three stages due to NOx reasons, and a minimum temperature of the last stage (tertiary) due to CO requirements. The secondary stage does not really have a minimum temperature, provided the tertiary stage is hot enough to accomplish CO burnout. There are no practical limits imposed by combustor metal temperatures or by limitations on the combustor temperature exit profile.

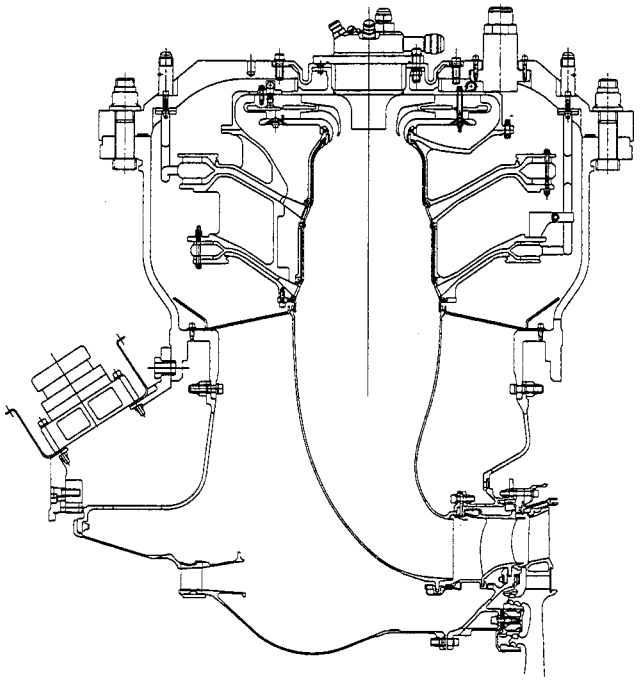

Fig. 1 Industrial Trent combustor

At a given power level, the ensemble of possible ways to allocate the fuel inside the combustor actually defines an operating envelope, whose axes are best defined in terms of premixer (or zone) temperatures. For instance, once a primary temperature is chosen (say, 1750 K), a secondary temperature (say, from 1200 K to 2000 K) can then be chosen. The amount of fuel to be allocated to the tertiary then falls out from the total amount of fuel required by the engine. Note that no fuel at all to the tertiary is also an option.

Figure 3 shows typical possible operating envelopes for the Trent combustor at different power levels. The temperatures of the *y*-axis and *x*-axis are the primary and secondary flame temperatures, from which a reference temperature was subtracted. Hence, the *bias* of the primary and secondary temperatures from a reference temperature is used to represent the results.

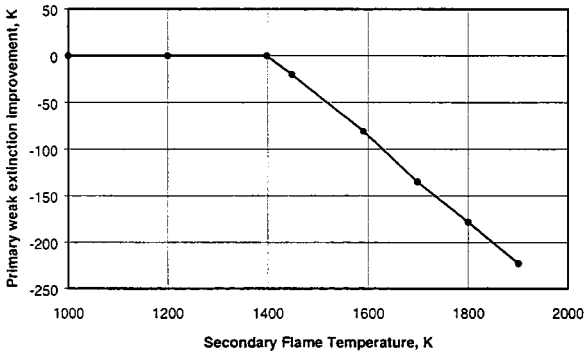

Fig. 2 Primary weak extinction characteristics

Downloaded 02 Jun 2010 to 171.66.16.119. Redistribution subject to ASME license or copyright; see http://www.asme.org/terms/Terms_Use.cfm

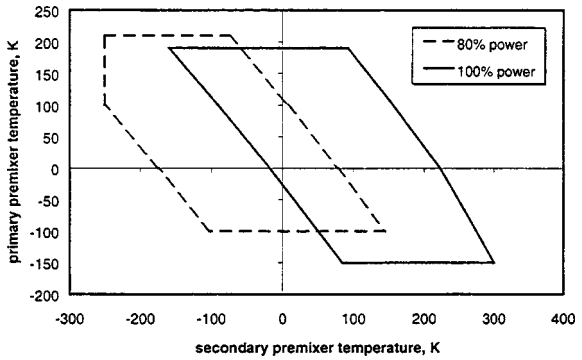

Fig. 3 Typical operating envelopes for the industrial Trent combustor (ISO day)

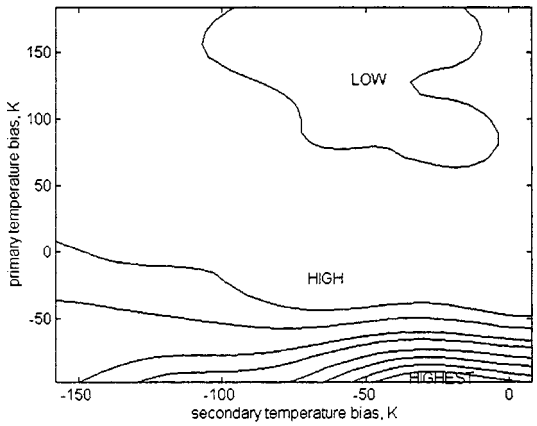

Fig. 5 Noise amplitude contour map near 80 percent power

3 ''Noise Mapping''

In order to assess the noise and emissions characteristics of the engine, a detailed mapping exercise was undertaken at a variety of power levels and ambient conditions, and on different engines.

Depending on the ambient conditions, the relationship between combustor inlet and outlet temperatures can vary quite significantly. Thus, at different engine operating conditions, the allocation of fuel between primary, secondary, and tertiary that gives the best combination of NOx, CO, and noise will vary. The objective of the development testing of the combustion system was the definition of a combustor fuel schedule. The *fuel schedule* is essentially a look-up table, which is a function of power level and ambient temperature that the control system can use to split the total fuel between the three stages.

Shown in Figs. 4, 5, and 6 are the results of measurements of the observed noise amplitude at various power levels. Again, at a given power level, the primary and secondary temperatures can be controlled independently, while the tertiary takes the balance of the total fuel.

Each of the noise maps shown below is the result of an interpolation of 25 to 35 measurement points. More than 10 noise maps were obtained (different power level, different day condition, different engines) during development. Thus, more than 300 test cases were obtained. In all cases it was found that the resonant frequency of pressure fluctuations always corresponded to a natural acoustic mode of the combustor.

The amplitudes measured in the noise maps are the RMS value of the signal from piezoelectric transducers, filtered from 10 Hz to 2000 Hz. The detailed frequencies corresponding to the regions high noise will be discussed below.

What is seen from the contour maps is that at any power condition it is always possible to find regions of high noise and low noise. In other words, the RMS level of pressure fluctuations is clearly affected by the axial distribution of heat release inside the combustor (this is assuming that changing the fuel splits will change the distribution of heat release). In general, the noise amplitude appears to scale linearly with the combustor inlet pressure. Thus, the potential for structural damage is a lot higher at high engine pressure ratios. This represents a difficult challenge for the Trent, since the inlet pressure can reach a level of up to 40 atm.

Depending on the power level and on the ambient conditions, the regions of high noise will be located in a different region of the operating envelope. In Fig. 6, there are two regions of high noise; both located in the region of low primary temperatures. However, as the secondary temperature is varied, it becomes possible to find an optimum condition that will minimize the noise amplitude.

It turns out that the two distinct regions of high noise in Fig. 6 correspond to two different acoustic modes of the combustor. For the specific geometry of the Industrial Trent (i.e., L/D is relatively large) the modes that can be excited in the range of 10–2000 Hz are only longitudinal modes. The noise mapping results presented above can be somewhat condensed when plotted in terms of a non-dimensional amplitude ($\Delta p/P$) and a non-dimensional wavelength (L/λ). That is, the single sided RMS noise amplitude Δp is non-dimensionalized by the combustor inlet pressure P and the sound wavelength λ is non-dimensionalized by the length of the combustor L. This is shown in Fig. 7.

The data from Fig. 7 are obtained from two different engines, at five different power levels, and from a range of ambient condi-

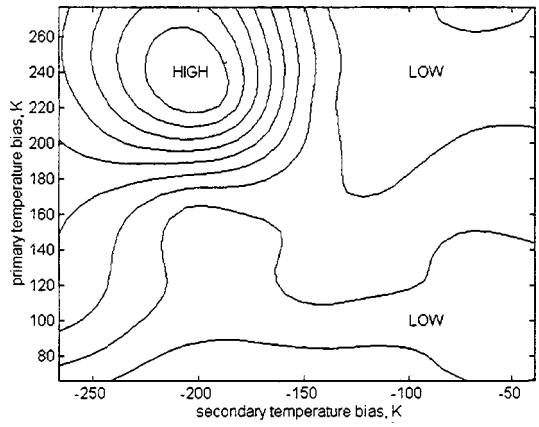

Fig. 4 Noise amplitude contour map near 50 percent power

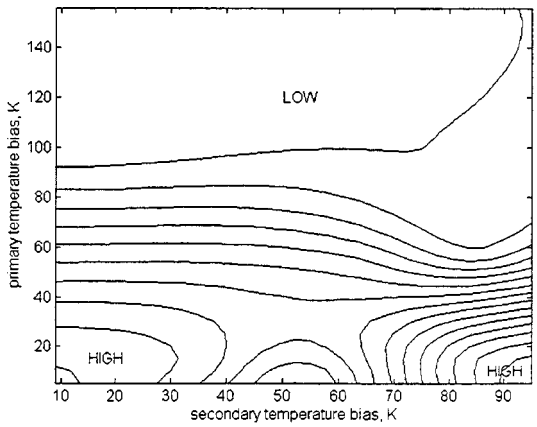

Fig. 6 Noise amplitude contour map near 100 percent power

Downloaded 02 Jun 2010 to 171.66.16.119. Redistribution subject to ASME license or copyright; see http://www.asme.org/terms/Terms_Use.cfm

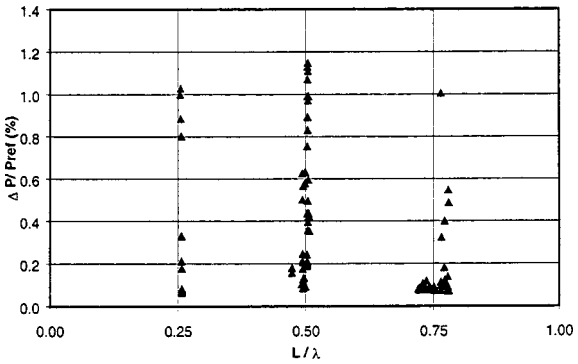

Fig. 7 Non-dimensional representation of the measured combustion noise amplitudes and frequencies

tions and combustor fuel splits. Yet, all results are clearly grouped into three well-defined acoustic modes. At a given condition, there may not be any resonant mode, although there will always be a dominant frequency. In such a case, the level of pressure fluctuations is of the order of 0.1–0.2 percent of the reference pressure. This represents the ''no noise'' cases. When resonance sets in, it will always select the frequency of one of the natural acoustic modes. Depending on the operating conditions, the fuel split at which resonance appears and the frequency and amplitude of the selected mode will vary.

Each of the resonant modes identified in Fig. 7 appears to correspond to a specific pattern of heat release and temperature distribution along the length of the combustor. This is illustrated in Fig. 8. Because the Industrial Trent incorporates three fuel stages in series, the choice of fuel splits will in principle affect the axial distribution in heat release and gas temperature along the length of the combustor. These distributions were not experimentally mea-

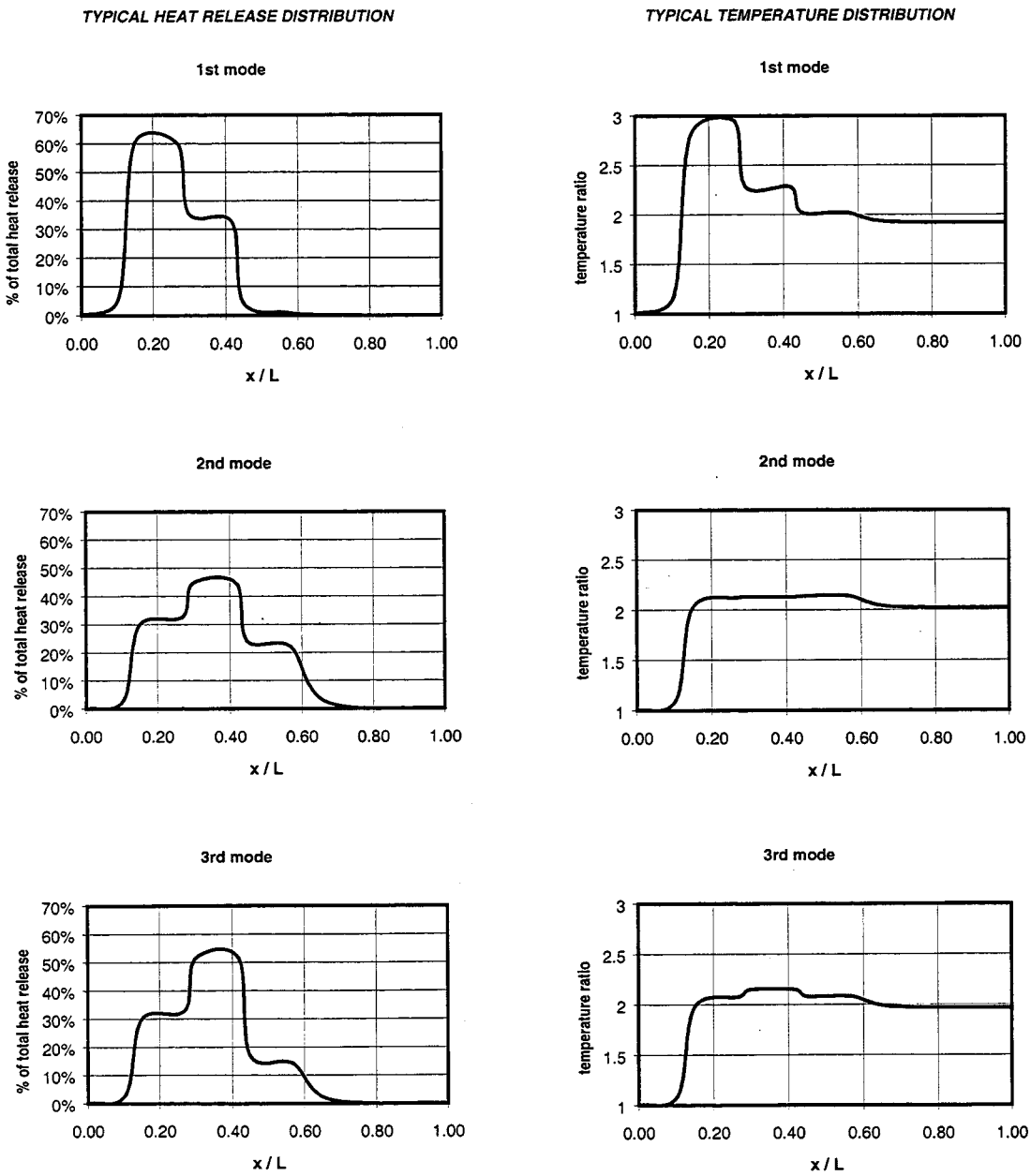

Fig. 8 Typical (calculated) heat release and temperature distribution along the length of the combustor for each of the unstable longitudinal acoustic modes. $x/L=1$ corresponds to the combustor exit.

Downloaded 02 Jun 2010 to 171.66.16.119. Redistribution subject to ASME license or copyright; see http://www.asme.org/terms/Terms_Use.cfm

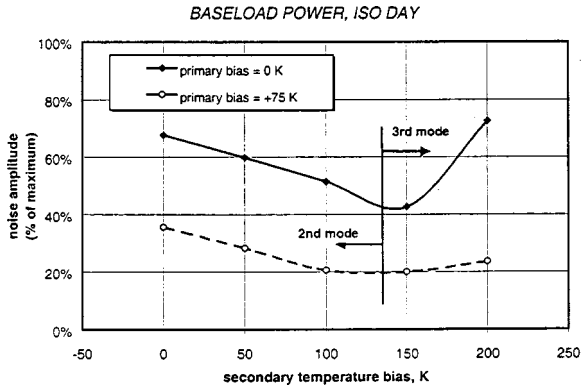

Fig. 9 Change in acoustic mode and noise amplitude as the combustor fuel split is varied at a steady engine operating condition

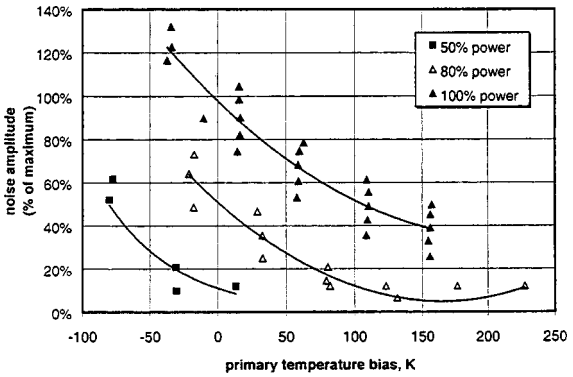

Fig. 10 Amplitude characteristics of the 2nd unstable mode ($L/\lambda = 0.5$). The data in this figure are obtained at engine power levels ranging from 50 percent to 100 percent power.

sured but were instead calculated, with the assumption that the combustor air splits are not changed as the fuel split is varied.

The first mode is usually observed at low power when the tertiary is not lit and hence it corresponds to a heat release distribution concentrated near the ''head'' of the combustor. For the second and third mode, all three stages are in operation and the energy release is distributed along a wider region of the combustor. The heat release distribution of the second and third mode are of a similar ''topology,'' i.e., most of the energy is released within the secondary zone. However, the resulting temperature distributions are different, as clearly seen from Fig. 8.

What is the relationship between the information shown in Fig. 7 and the noise maps of Figs. 4–6? A partial answer is presented in Fig. 9. This is effectively the equivalent of a slice through the noise map of Fig. 6. As the secondary bias is increased, the noise amplitude decreases until it reaches a minimum. Once the minimum is reached, the frequency of the resonance switches from the second to the third acoustic mode. It can also be seen that the overall noise levels can be reduced if the primary bias is increased.

Figure 9 is a good illustration of the flexibility offered by the 3-stage design. At a fixed engine running condition, a small change in the primary and/or secondary temperature can reduce the combustion noise amplitude by 50 percent and/or select the frequency at which resonance takes place.

The ability to ''select'' the frequency of the resonance is a unique feature of the system, which offers a significant advantage to reduce the vulnerability of the combustor against combustion noise. The combustor hardware will usually be more susceptible to certain frequencies, depending on the structural modes of the mechanical design. It is usually possible to ''design out'' some of the natural structural modes, but not all. Being able to also select the frequency of the resonance offers additional margins for mechanical integrity.

4 Correlations and Predictions of Noise

The objective of the noise mapping test was to allow the definition of a fuel schedule for the engine. In other words, what is the best fuel split between primary, secondary, and tertiary for a given power level (on a given ambient condition) which will avoid combustion noise?

To answer this question it was necessary to develop an empirical correlation for each of the possible resonant modes of the combustor. This way, not only the amplitude, but also the frequency of the combustion resonance could be predicted. The assumption that was made was that of *a principle of superposition*. That is, the unstable mode selected by the combustor is simply the one that is predicted to have the highest amplitude.

The behavior of each of the unstable modes was quite different. For instance, the dependence of the amplitude of the second longitudinal mode ($L/\lambda = 0.5$) on combustor fueling conditions and engine power is shown in Fig. 10. The noise amplitude (in psi-RMS) is non-dimensionalized by the maximum noise amplitude acceptable to the requirements of durability of the hardware.

The amplitude of the second mode always decreases as the primary bias is increased. What appears to be large scatter at a given primary bias is actually the effect of the secondary bias being changed. Even though the noise amplitude is non-dimensionalized by the combustor reference pressure, all the curves do not collapse into one. Thus, the 2nd mode depends to a certain degree on the total energy being released inside the combustor.

The 3rd unstable mode ($L/\lambda = 0.75$) has amplitude characteristics which are completely different from what was observed with the 2nd mode. As seen from Fig. 11, whenever the dominant frequency of the spectrum was that of the 3rd mode, it was possible to collapse all of the observations onto a single curve. It appears that a necessary condition for the appearance of the 3rd mode is that the secondary zone temperature must exceed the primary zone temperature. This condition can be achieved in a number of ways, and at different power levels.

Under most combustor operating conditions, the primary zone temperature is slightly above the secondary zone temperature. This is because the primary zone needs to keep a small margin above weak extinction, whereas the secondary doesn't. However, at high power the primary does have a large margin above weak extinction (see Fig. 2) so it becomes possible to have a condition where the secondary zone temperature exceeds the primary zone

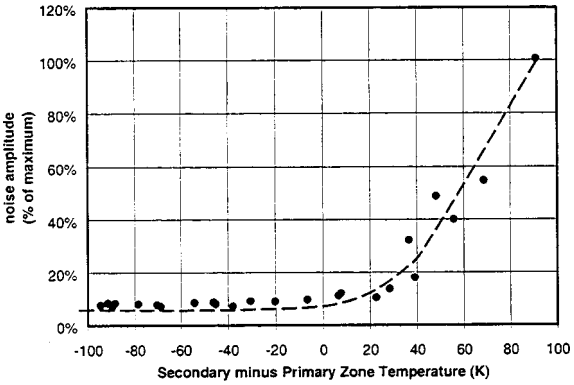

Fig. 11 Amplitude characteristics of the 3rd unstable mode ($L/\lambda = 0.75$). The data in this figure are obtained at engine power levels ranging from 30 percent to 100 percent power.

Downloaded 02 Jun 2010 to 171.66.16.119. Redistribution subject to ASME license or copyright; see http://www.asme.org/terms/Terms_Use.cfm

temperature. Although this is a necessary condition for the existence of the 3rd mode, it is not a sufficient one. Note that the data points shown in Fig. 11 all correspond to engine conditions where the dominant frequency in the frequency spectrum corresponded to that of the 3rd mode.

Depending on the power level and day temperature, an unstable mode may or may not manifest itself. It is quite possible (depending on combustor operating conditions) to have situations where neither the 2nd nor the 3rd mode (nor the 1st mode) are present. In these cases, the background noise level in the combustor is comparable to what would be measured in say, a diffusion flame combustor.

Having obtained some indications of the behavior of the unstable modes, an attempt was made to predict the amplitude of each of the unstable modes using empirical correlations. As mentioned in the Introduction, the work by Chu [4], although not linked to any mechanism of resonance, is ''exact'' in terms of establishing a nonlinear relationship between heat release fluctuations and the amplitude of the resulting pressure waves. This is because the conservation equations for a control volume enclosing a region of heat release are solved analytically.

If one makes the assumption that a given level of pressure fluctuations have a one-to-one correspondence with a level in heat release fluctuations, then it is expected from Eq. (1) that the nondimensional amplitude of the noise is predominantly a function of the temperature ratio across the region of heat release. In the case of a three-stage (axially staged) combustor there are three regions of heat release, and hence there are at least three important temperature ratios that will affect noise amplitude. It might also be argued that the overall heat release in the combustor (and the corresponding temperature ratio from combustor inlet to combustor exit) might also be a controlling parameter.

For these reasons, the assumed functional form of the empirical correlations that were used for each of the unstable modes was

$$\frac{\Delta p}{p} = K_1 + K_2 P_3^A \sum_{i=1}^{N} \left[\frac{(T_i - T_3)}{k_i} \right]^{\alpha_i}, \qquad (2)$$

where K_1, K_2, A, k_i, and α_i are all arbitrary constants. The summation index i, which runs from 1 to N, refer to each of the three combustion zones of the combustor, in addition to the overall heat release inside the combustor. The arbitrary constants were obtained from linear regression of engine data for each of the unstable modes.

What were obtained then are three independent empirical correlations for each of the longitudinal resonant modes. The assumption that was then made was that the mode observed would be the one having the highest amplitude of the three, given the combustor operating conditions. Note that this approach permits prediction of not only the amplitude but also the frequency of the combustion resonance.

The capabilities of the correlations were tested on development engines, where fuel schedule changes were made so as to deliberately create noise during engine acceleration to baseload. Two sets of results from two different engines at two different ambient conditions (+20°C and −5°C) are shown in Fig. 12.

When a combustion resonance sets in, it sets in abruptly. This is manifested by a sharp ''kink'' in the curves in Fig. 12. Note that the empirical correlations capture this feature quite well. In other words, the empirical correlations developed are able to predict relatively well the boundaries beyond which combustion noise will be encountered.

The occurrence of combustion noise is dependent on the ambient conditions. This is because a given power level on the engine is achieved quite differently depending on the day conditions. The combustor inlet pressure and temperature and combustor exit temperature will be quite different at say, 40 MW, if the ambient temperature is at 20°C or −5°C. Furthermore, it should be kept in mind that the *fuel schedule* will also be different, depending on power level and day conditions.

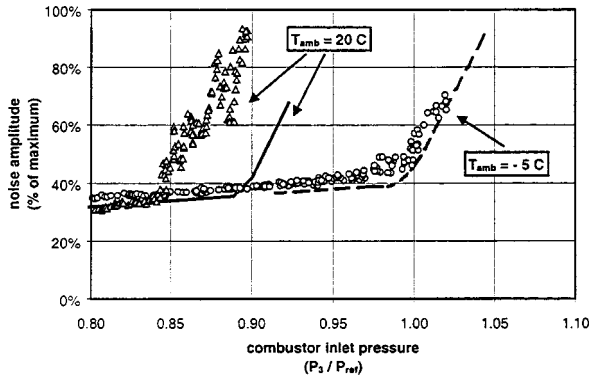

Fig. 12 Comparison between predictions and engine results during slow engine acceleration to baseload, at two different ambient conditions. The lines represent the prediction, whereas the symbols represent the engine data.

Nonetheless, Fig. 12 indicates that the correlations are able to capture relatively well the effects of engine cycle, ambient conditions and changes in fuel schedule (or equivalently, variations in combustor fuel splits). The correlations were able to reproduce the noise mapping results (e.g., Figs. 4, 5, and 6) within approximately 10 percent accuracy (i.e. the standard error of the estimate was 10 percent of the maximum allowable pressure amplitude inside the combustor).

One of the most difficult tasks in DLE combustor design, particularly for the entry-in-service of the engine, is to be able to predict the conditions under which the combustor will experience thermoacoustic resonance. The empirical correlations developed during development of the Industrial Trent allowed such predictions to be made so that the fuel schedule could be designed to avoid regions of high combustion noise across the entire operating range of the engine.

5 Conclusions

Axial staging of the heat release inside the Industrial Trent combustor allows a wide turndown of flame temperatures for the purpose of emissions control, but this also permits a direct influence on the amplitudes and frequency of combustion thermoacoustic resonance. At a fixed engine condition, the variation in fuel splits among the three stages effectively allows a direct control of combustion noise. The large flexibility of the three axial stages is such that the noise avoidance strategy for the Industrial Trent is really one of an *adaptive fuel schedule* (i.e., variation of combustor fuel splits in response to measured noise amplitudes) rather than one of *active noise control* (e.g., fast modulation of a small amount of the combustor fuel flow to suppress the instability).

The ''noise mapping'' capability of the three axial stages made it possible to obtain reliable empirical correlations for the occurrence of the unstable acoustic modes of the combustor. Today, it is possible to predict how a fuel schedule change will affect combustion noise on the engine from −30°C to +30°C. Both the frequency and the limit-cycle amplitude of the resonance can be predicted with reasonable accuracy.

6 Acknowledgments

We would first like to offer a heart-felt thanks to Tony Jackson who held the position of Director of Technology in Montreal during the first four years of the Industrial Trent project and is now enjoying a well-deserved retirement. Jeff Willis (Chief Combustion Technologist at RR) must be credited for always keeping us on our toes, thanks to numerous (and enjoyable!) heated debates.

Downloaded 02 Jun 2010 to 171.66.16.119. Redistribution subject to ASME license or copyright; see http://www.asme.org/terms/Terms_Use.cfm

We would also like to acknowledge the support and contribution of the Industrial Trent Combustion Team: merci à Henry, Eric, Leo, Karen, Maxime, Michel, Luc et Ritchie.

References

[1] Hubbard, S, and Dowling, A. P., 1998, ''Acoustic Instabilities in Premix Burners,'' AIAA Paper 98-2272, presented at the *4th AIAA/CEAS Aeroacoustics Conference*, June 1998, Toulouse, France.
[2] Paschereit, C. O., and Polifke, W., 1998, ''Investigation of the Thermoacoustic Characteristics of a Lean Premixed Gas Turbine Burner,'' ASME Paper 98-GT-582, presented at the International Gas Turbine & Aeroengine Congress & Exhibition, Stockholm, Sweden.
[3] Williams, F. A., 1985, *Combustion Theory*, Benjamin/Cummings, Menlo Park, CA, USA.
[4] Chu, B. T., 1953, ''Mechanism of Generation of Pressure Waves at Flame Fronts,'' Technical Note 3683, National Advisory Committee for Aeronautics.
[5] Candel, S., 1992, ''Combustion Instabilities Coupled by Pressure Waves and their Active Control,'' 24th Symposium (International) on Combustion, The Combustion Institute, pp. 1277–1296.
[6] Rott, N., 1980, ''Thermoacoustics,'' Adv. Appl. Mech., **20**, pp. 135–175.

Downloaded 02 Jun 2010 to 171.66.16.119. Redistribution subject to ASME license or copyright; see http://www.asme.org/terms/Terms_Use.cfm

The Role of Carbon Monoxide in NO_2 Plume Formation

Alan S. Feitelberg
Sanjay M. Correa
GE Corporate Research and Development,
One Research Circle,
Niskayuna, NY 12309

Through a series of computational studies, carbon monoxide has been identified as an important promoter of NO oxidation to NO_2 in combustion turbine exhaust gas at intermediate temperatures (450 to 750°C). NO_2 formation is accompanied by enhanced CO burnout at these temperatures. Perfectly stirred reactor and plug flow reactor calculations indicate that concentrations of CO as low as 50 ppmv in exhaust gas containing 25 ppmv NO can result in the conversion of 50 percent of the NO to NO_2 in less than 1 s. NO_2 concentrations as low as 15 ppmv can result in visible, yellow-brown plumes from large diameter exhaust stacks. If NO_2 plumes are to be prevented, then designers of gas turbines and heat recovery steam generators need to be aware of the relationships between time, temperature, and composition which cause NO_2 to form in exhaust gas. Reaction path analysis indicates that the mutually promoted oxidation of CO and NO occurs through a self-propagating, three-step chain reaction mechanism. CO is oxidized by OH ($CO+OH \rightarrow CO_2+H$), while NO is oxidized by HO_2: $NO+HO_2 \rightarrow NO_2+OH$. In a narrow temperature range, the H-atom produced by the first reaction can react with O_2 in a three body reaction to yield the hydroperoxy radical needed in the second reaction: $H+O_2+M \rightarrow HO_2+M$, where M is any third body. The observed net reaction is $CO+O_2+NO \rightarrow CO_2+NO_2$, which occurs stoichiometrically at temperatures below about 550°C. As the temperature increases, additional reaction pathways become available for H, HO_2, and OH which remove these radicals from the chain and eventually completely decouple the oxidation of CO from NO. An abbreviated set of elementary chemical reactions, including 15 species and 33 reactions, has been developed to model CO-enhanced oxidation of NO to NO_2. This reaction set was derived from a larger reaction set with more than 50 species and 230 elementary chemical reactions, and was validated by comparison of PSR and PFR calculations using the two sets.
[S0742-4795(00)01402-2]

Introduction

The fractional distribution of NO_x between NO and NO_2 in the exhaust from combustion systems is of considerable importance. The toxicity of NO_2 is greater than the toxicity of NO, and some localities have regulated the color and/or opacity of exhaust gas plumes (NO is colorless, while NO_2 is red-brown in color). NO_2 can be found in the exhaust from boilers, reciprocating engines, and combustion turbine engines. However, NO_2 is generally not produced in significant quantities within combustors themselves. The principal in-combustor formation mechanism is the mixing of hot gases containing NO with cooling or dilution air in the latter portion of the combustor, leading to the production of HO_2 and then NO_2 via $NO+HO_2=NO_2+OH$ [1]. The resulting NO_2 formed is usually a small fraction (less than 5 percent) of the total NO_x present. Furthermore, this pathway is physically removed in lean premixed gas turbine combustion systems because there is no wall (or ''liner'') film cooling and there is no dilution jet air. Measurements made in the bottoming cycle equipment downstream of these gas turbines tend to confirm the hypothesis that there is initially little or no NO_2 present in the gas turbine exhaust, but a large fraction (more than 50 percent) of the NO may be oxidized to NO_2 as the gas is cooled from the gas turbine exhaust temperature (about 600°C) to the stack exit temperature, resulting in visible NO_2 plumes [2]. At typical stack diameters, NO_2 should become visible at a concentration of about 10–15 ppmv.

One potential pathway identified in the literature is the reaction of unburned fuel with flame-generated NO downstream of the combustor. Previous experimental and theoretical studies [3–6] have shown that low concentrations (1 to 1000 ppm) of fuels can be strong promoters of NO oxidation to NO_2 at intermediate temperatures (300 to 700°C). Hydrocarbons vary in their effectiveness in promoting NO oxidation to NO_2, with C_3 and C_4 species generally being more effective than C_1 and C_2 species and H_2. CO has been reported to be relatively ineffective at promoting NO oxidation [6].

However, observations from gas turbine power plants equipped with lean premixed combustion systems suggest that installations operating at part load with high CO emissions (~50 ppmv) can have visible yellow-brown exhaust plumes, even when total NO_x is relatively low (~25 ppmv) and significant quantities of unburned hydrocarbons are not found. Since the unburned fuel pathway to NO_2 can be ruled out in these cases, the question of the importance of CO in converting NO to NO_2 is reopened.

Glarborg et al. [7] recently completed an experimental and theoretical study of interactions between CO, NO, NO_2, and H_2O in a flow reactor. They concluded that the presence of NO may enhance or inhibit CO oxidation, depending upon the exact temperature and composition of the exhaust gas mixture. However, their experimental test conditions were somewhat different from the conditions expected in turbine exhaust. For example, their CO concentrations (450 to 1600 ppm) were much higher than typically found in turbine exhaust, and their O_2 concentrations (2.0 to 4.3 percent) were lower than usually found.

The purpose of the present computational study was to extend the analysis of Glarborg et al. to more closely match the conditions found in gas turbine exhaust, with the overall objective of gaining a better understanding of the role of CO in the oxidation of NO to NO_2 at intermediate temperatures (400 to 850°C). Perfectly stirred reactor (PSR) and plug flow reactor (PFR) calcula-

Contributed by the International Gas Turbine Institute (IGTI) of THE AMERICAN SOCIETY OF MECHANICAL ENGINEERS for publication in the ASME JOURNAL OF ENGINEERING FOR GAS TURBINES AND POWER. Paper presented at the International Gas Turbine and Aeroengine Congress and Exhibition, Indianapolis, IN, June 7–10, 1999; ASME Paper 99-GT-53. Manuscript received by IGTI March 9, 1999; final revision received by the ASME Headquarters January 3, 2000. Associate Technical Editor: D. Wisler.

Copyright © 2000 by ASME

Downloaded 02 Jun 2010 to 171.66.16.119. Redistribution subject to ASME license or copyright; see http://www.asme.org/terms/Terms_Use.cfm

tions, as well as a reaction path analysis, were completed with both Miller and Bowman's [8] detailed chemical reaction set (more than 50 species and 230 elementary reactions) and a reduced reaction set (15 species and 33 elementary reactions) derived from their work. Predictions from both reaction sets were also compared to calculations using the reaction set proposed by Glarborg et al. [7,9] (54 elementary reactions) and the reaction set developed by Bowman et al. [10] for the Gas Research Institute (277 elementary reactions). Comparisons of the predictions of the four different reaction sets served to validate the reduced reaction set presented here. PFR calculations were performed because the cooling of turbine exhaust gas in a heat recovery steam generator (HRSG) is, to a first approximation, a plug flow process. The PSR calculations served as a convenient, second test case for comparing the complete reaction set with the reduced reaction set.

There have been reports (e.g., [11]) of brown NO_2 plumes forming far downstream (0.5–5.0 km) of power plant exhaust stacks. These NO_2 plumes result from reactions between NO in the exhaust and ambient ozone (O_3). The mechanism described in this paper explains the visible NO_2 plumes sometimes observed at the immediate exit (0–1 m) of an exhaust stack.

PSR and PFR Calculations

The initial gas composition used for all PSR and PFR calculations was determined by assuming complete combustion of methane in air (21 percent O_2, 79 percent N_2) at a particular equivalence ratio (φ). CO and NO were then added to the mixture at the desired concentrations. Unless otherwise indicated, the only species present in the initial mixture were O_2, N_2, CO_2, and H_2O, as well as any added CO and NO.

PSR and PFR calculations were completed on a VAX 7610 computer using the Chemkin II package of subroutines and associated programs [12,9,13]. The Chemkin software allowed adjustment of absolute and relative tolerances to insure computed mole fractions contained roughly four significant digits, even for species with concentrations as low as 10^{-6} ppm. For calculations at $P=1$ atm, four different reaction sets were used: (1) the well-known reaction set of Miller and Bowman [8]; (2) a reduced, 33-step reaction set derived from Miller and Bowman's work (see Table 1); (3) the reaction set developed by Glarborg et al. [7]; and (4) the most recent version of the Gas Research Institute reaction set, GRI-Mech 2.11 (Bowman et al.). For calculations at elevated pressures, the modifications recommended by Michaud et al. [14] were added to the Miller and Bowman reaction set. The reaction path analysis aided in the selection of the key reactions to be retained in the reduced reaction set in Table 1. This reduced set consists of reactions 61-64, 130-139, 143, 145-150, 166, 188-191, 204-207, and 232-234 in Appendix A of Miller and Bowman [8].

Results

The results from typical constant temperature and pressure PSR calculations are shown in Figs. 1 and 2. The inlet composition for the PSR calculations shown in Figs. 1 and 2 is burned gas resulting from complete combustion of methane in air at $\varphi=0.5$ (5 percent CO_2, 10 percent H_2O, 10 percent O_2, 75 percent N_2) with 50 ppmv of CO and either 25 ppmv (solid lines and symbols) or 0 ppmv (dashed lines) of NO added. PSR pressure was set to $P=1$ atm and the residence time was 0.5 s. For these conditions the fractional conversion of NO to NO_2 peaks at about 650°C, with about 30 percent of the NO converting into NO_2 and total NO_x remaining constant. CO decreases monotonically as temperature increases.

The solid and dashed lines in Figs. 1 and 2 indicate results using the Miller and Bowman (MB) reaction set. Symbols represent calculations with either the reduced reaction set in Table 1 (■), the 1995 Glarborg et al. (G et al.) reaction set (●), or the GRI-Mech 2.11 reaction set (▲). Figures 1 and 2 show that calculations with the reduced reaction set in Table 1 are indistinguishable from calculations with the complete MB reaction set. In addition, the four different reaction sets are in excellent qualitative agreement for all species and very good quantitative agreement for most species. Differences between reaction sets are largest for HO_2, with a maximum difference of about a factor of 3 at high temperatures. Notice, however, that the differences between reaction sets are much smaller for the important species of interest: CO, NO, and NO_2.

With the inlet NO concentration set to 0 ppmv (the dashed lines in Figs. 1 and 2), CO oxidation is greatly suppressed at low temperatures, but is almost unaffected at temperatures above 850°C. At low temperatures, the presence of 25 ppm NO in the inlet gas increases the OH concentration by almost a factor of 1000. NO has a similar effect on H atom concentrations, while HO_2 concentrations are only slightly affected by the presence of NO in the inlet gas. At high temperatures, the presence of NO in the inlet gas has no effect on these radical species concentrations.

A reaction path analysis provides useful insight into the chemical mechanisms causing the effects observed in Figs. 1 and 2. Under all conditions, the primary pathway for CO oxidation is reaction *R*2 in Table 1:

$$CO+OH\rightarrow CO_2+H, \qquad (R2)$$

and the primary pathway for NO oxidation is

$$NO+HO_2\rightarrow NO_2+OH. \qquad (R23)$$

However, key differences are observed in the reaction pathways for radical species. At low temperatures (450–650°C), when NO is present in the inlet, almost all of the H atom is destroyed through

$$H+O_2+M\rightarrow HO_2+M. \qquad (R9)$$

Under these conditions *R*2, *R*23, and *R*9 form a self-sustaining set of chain reactions. The sum of the three reactions is the overall reaction

$$CO+NO+O_2\rightarrow NO_2+CO_2$$

with no net consumption of radical species. The key chain initiation step is not thermal dissociation of stable species, but rather the slow reaction

$$CO+O_2\rightarrow CO_2+O. \qquad (R3)$$

O atom produced through *R*3 then participates in an important chain branching reaction,

$$H_2O+O\rightarrow 2OH, \qquad (-R13)$$

which produces the OH needed for *R*2, thus initiating the three-step chain reaction. Reactions *R*2, *R*23, and *R*9 then propagate the chain reaction, and proceed to oxidize NO and CO, with no net consumption of radicals. At temperatures below 550°C, almost every mole of CO oxidized to CO_2 also results in one mole of NO oxidized to NO_2.

At very low temperatures (below 450°C), *R*3 is too slow to provide sufficient quantities of O atom for the chain reactions to proceed at a significant rate. At high temperatures (above 650°C), *R*3 and the reverse direction of *R*13 are still the key chain initiation and chain branching reactions. However, additional reaction pathways become available for H, HO_2, and OH. These reactions remove radicals from the chain and decouple the oxidation of CO from NO. For example, as temperature increases, *R*9 becomes a less important pathway for H atom destruction as the alternate $H+O_2$ pathway

$$H+O_2\rightarrow OH+O \qquad (-R7)$$

becomes more important. At 850°C, about 50 percent of the H atom destruction occurs through *R*9, the remainder being destroyed through the reverse direction of *R*7. In addition, only 20 percent of the HO_2 that is consumed results in oxidation of NO to NO_2 through *R*23 (versus almost 100 percent at 500°C). The remainder of the HO_2 is being destroyed through

Downloaded 02 Jun 2010 to 171.66.16.119. Redistribution subject to ASME license or copyright; see http://www.asme.org/terms/Terms_Use.cfm

Table 1 Rate parameters for 33-step reduced reaction set

	REACTION	Forward rate parameters A	b	E
1.	$CO + O + M = CO_2 + M$	6.17×10^{14}	0.00	3000.
2.	$CO + OH = CO_2 + H$	1.51×10^{07}	1.30	–758.
3.	$CO + O_2 = CO_2 + O$	1.60×10^{13}	0.00	41000.
4.	$HO_2 + CO = CO_2 + OH$	5.80×10^{13}	0.00	22934.
5.	$H_2+O_2 = 2\ OH$	1.70×10^{13}	0.00	47780.
6.	$H + H_2= H_2O + H$	1.17×10^{09}	1.30	3626.
7.	$O + OH = O_2 + H$	4.00×10^{14}	–0.50	0.
8.	$O + H_2 = OH + H$	5.06×10^{04}	2.67	6290.
9.	$H + O_2 + M = HO_2 + M$	3.61×10^{17}	–0.72	0.
	Enhanced third-body efficiencies: $H_2O = 18.6$, $CO_2 = 4.2$, $H_2 = 2.9$, $CO = 2.1$, $N_2 = 1.3$			
10.	$OH + HO_2 = H_2O + O_2$	7.50×10^{12}	0.00	0.
11.	$H + HO_2 = 2\ OH$	1.40×10^{14}	0.00	1073.
12.	$O + HO_2 = O_2 + OH$	1.40×10^{13}	0.00	1073.
13.	$2\ OH = O + H_2O$	6.00×10^{08}	1.30	0.
14.	$H + H + M = H_2 + M$	1.00×10^{18}	–1.00	0.
	Enhanced third-body efficiencies: $H_2 = 0.0$, $H_2O = 0.0$, $CO_2 = 0.0$			
15.	$H + OH + M = H_2O + M$	1.60×10^{22}	–2.00	0.
	Enhanced third-body efficiencies: $H_2O = 5.0$			
16.	$O + O + M = O_2 + M$	1.89×10^{13}	0.00	–1788.
17.	$H + HO_2 = H_2 + O_2$	1.25×10^{13}	0.00	0.
18.	$2\ HO_2 = H_2O_2 + O_2$	2.00×10^{12}	0.00	0.
19.	$H_2O_2 + M = 2\ OH + M$	1.30×10^{17}	0.00	45500.
20.	$H_2O_2 + H = HO_2 + H_2$	1.60×10^{12}	0.00	3800.
21.	$H_2O_2 + OH = H_2O + H$	1.00×10^{13}	0.00	1800.
22.	$CO_2 + N = NO + CO$	1.90×10^{11}	0.00	3400.
23.	$HO_2 + NO = NO_2 + OH$	2.11×10^{12}	0.00	–479.
24.	$NO_2 + H = NO + OH$	3.50×10^{14}	0.00	1500.
25.	$NO_2 + O = NO + O_2$	1.00×10^{13}	0.00	600.
26.	$NO_2 + M = NO + O + M$	1.10×10^{16}	0.00	66000.
27.	$N_2O + H = N_2 + OH$	7.60×10^{13}	0.00	15200.
28.	$N_2O + M = N_2 + O + M$	1.60×10^{14}	0.00	51600.
29.	$N_2O + O = N_2 + O$	1.00×10^{14}	0.00	28200.
30.	$N_2O + O = 2\ NO$	1.00×10^{14}	0.00	28200.
31.	$N + NO = N_2 + O$	3.27×10^{12}	0.30	0.
32.	$N + O_2 = NO + O$	6.40×10^{09}	1.00	6280.
33.	$N + OH = NO + H$	3.80×10^{13}	0.00	0.

Note: forward rate coefficients (k_f) are of the form $k_f = A\,T^b \exp(-E/RT)$, where the dimensions of A are mole-cm-sec-K, the units of E are cal/mole, T is absolute temperature, and R is the ideal gas constant.

$$HO_2 + OH \rightarrow H_2O + O_2 . \qquad (R10)$$

NO_2 production reaches a maximum and then slows down as temperature increases, and CO oxidation increases monotonically with temperature, because as temperature increases (i) $R10$ consumes HO_2 that would have produced NO_2 at lower temperatures through $R23$, and (ii) the reverse direction of $R7$ produces the OH needed for CO oxidation that $R23$ produced at lower temperatures.

If NO is not present at low temperatures, CO oxidation slows considerably, as shown in Fig. 1. $R3$ and the reverse direction of $R13$ are still the important chain initiating and chain branching reactions. OH produced through the reverse direction of $R13$ still oxidizes CO, and the H from $R2$ reacts through $R9$ to form HO_2. However, without NO to convert HO_2 back to OH through $R23$, OH concentrations remain depressed (see Fig. 2) and CO oxidation slows down. At higher temperatures, new sources of OH become available (primarily through the reverse direction of $R7$), allowing CO oxidation to proceed without NO.

The results from typical constant temperature and pressure PFR calculations using the Miller and Bowman [8] reaction set are shown in Figs. 3 and 4. The initial condition for the calculations shown in Figs. 3 and 4 is again burned gas resulting from complete combustion of methane in air at $\varphi = 0.5$ (5 percent CO_2, 10 percent H_2O, 10 percent O_2, 75 percent N_2) at $P = 1$ atm, $T = 600°C$, with 50 ppmv CO added, and either 25 or 0 ppmv NO. For all of the species shown, the curves produced using the reduced reaction set in Table 1 are indistinguishable from the curves produced using the full MB reaction set, and so have not been shown. Calculations performed using the Glarborg et al. [7] reaction set and GRI-Mech 2.11 were again in good agreement with the MB and Table 1 reaction sets, but have not been shown for clarity.

When NO is present (the solid lines in Figs. 3 and 4), there is a short induction period (about 0.2 s) during which time radical species build up to relatively high concentrations. The end of the induction period is marked by the onset of a period of relatively

Downloaded 02 Jun 2010 to 171.66.16.119. Redistribution subject to ASME license or copyright; see http://www.asme.org/terms/Terms_Use.cfm

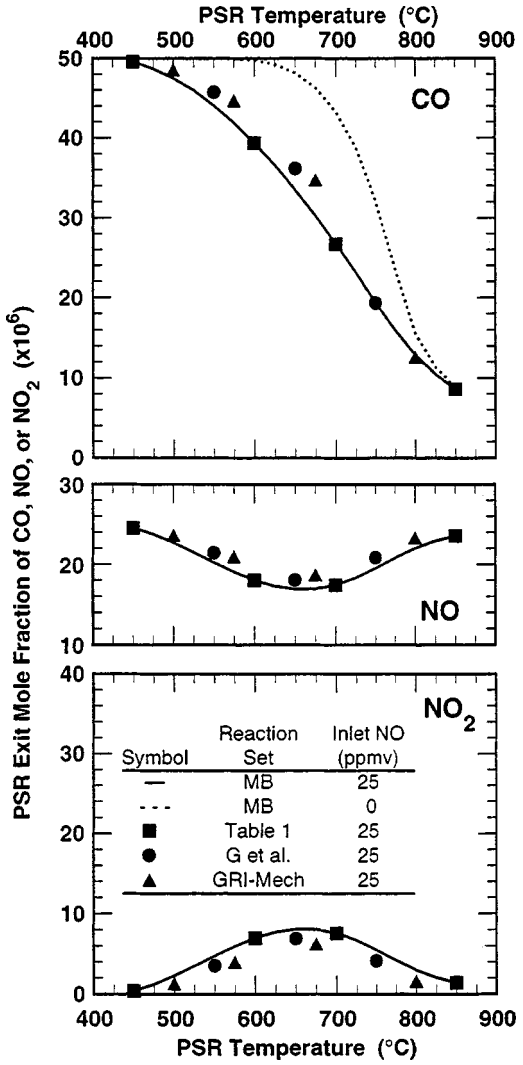

Fig. 1 Calculated concentrations of CO (top), NO (middle) and NO_2 (bottom) in constant pressure ($P=1$ atm) perfectly stirred reactors (PSRs) at various temperatures. Inlet gas composition=75 percent N_2, 10 percent O_2, 10 percent H_2O, 5 percent CO_2, 50 ppmv CO, and either 25 ppmv NO (solid lines and symbols) or 0 ppmv NO (dashed line). Solid and dashed lines indicate calculations using the Miller and Bowman reaction set. Symbols are points calculated using the reaction set in Table 1 (■), Glarborg et al (●), or GRI-Mech 2.11 (▲).

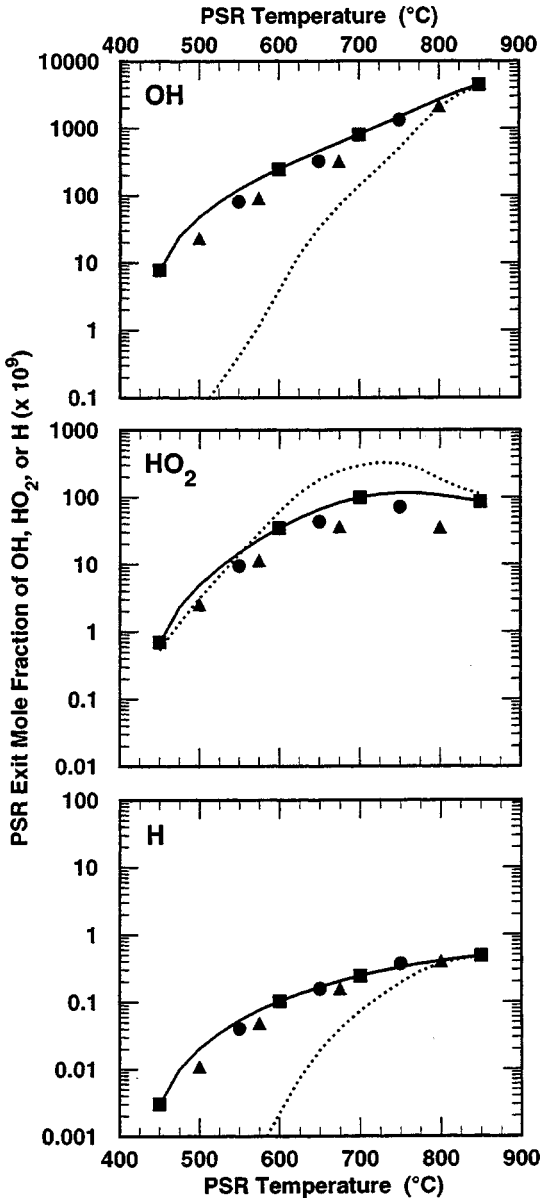

Fig. 2 Calculated concentrations of OH (top), HO_2 (middle), and H (bottom) at the same conditions as shown in Fig. 1

rapid CO and NO oxidation and a gradual decrease in radical species concentrations. In this particular case, approximately 0.6 moles of NO are oxidized to NO_2 for every mole of CO oxidized to CO_2. After about 1 s, 50 percent of the NO has been oxidized to NO_2. When NO is not present (the dashed lines in Figs. 3 and 4), the chemistry of the PFR is quite different. Concentrations of H, OH, and O are initially suppressed, while HO_2 concentrations increase by nearly a factor of 10. Without NO, overall CO burnout is reduced by a factor of 2. Additional calculations (not shown in Figs. 3 and 4) indicate that if CO is not present, NO oxidation does not occur under these conditions.

A careful examination of Figs. 1–4 reveals that both with and without NO, the composition of the PFR at 0.5 s is very similar to a 0.5 s residence time PSR operating at the same temperature. This similarity arises because (1) the reactions in the PSR and the PFR are the same and relatively slow, and (2) total conversion of CO and NO is low at 0.5 s.

Discussion

At typical gas turbine exhaust temperatures, NO is rapidly oxidized to NO_2 if CO is present. This observation has substantial consequences for the design of downstream process equipment, including HRSG's in bottoming cycles. The gas residence time in a typical HRSG is approximately 2 s, which is more than sufficient time to produce 10–15 ppmv of NO_2 if gas cooling is slow (see Fig. 5). Under part load conditions, when CO is relatively high, rapid quenching of turbine exhaust gas may be needed to prevent the formation of visible NO_2 plumes.

Because the net rate of NO oxidation to NO_2 in exhaust gas is of considerable importance to the designers of boilers (and other downstream process equipment) trying to minimize NO_2 formation, Fig. 5 has been prepared. Figure 5 is intended as an engineering tool that provides quick estimates of maximum NO_2 formation rates (due to only CO-enhanced oxidation) in exhaust gas as a function of temperature, pressure, and initial CO:NO mole ratio. Figure 5 is not intended to be a substitute for more detailed model calculations. The net rates of NO_2 production shown in Fig.

Downloaded 02 Jun 2010 to 171.66.16.119. Redistribution subject to ASME license or copyright; see http://www.asme.org/terms/Terms_Use.cfm

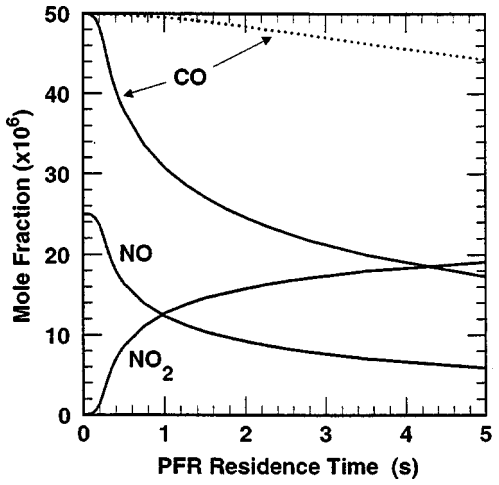

Fig. 3 Calculated composition profiles in a constant temperature (600°C) and pressure (1 atm) PFR. Initial gas composition=75 percent N_2, 10 percent O_2, 10 percent H_2O, 5 percent CO_2, 50 ppmv CO, and either 25 ppmv NO (solid lines, ——) or 0 ppmv NO (dashed line, – – –).

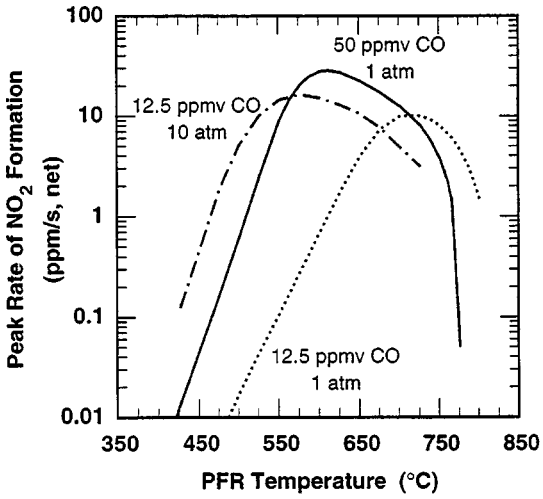

Fig. 5 Peak rates of NO_2 formation in a constant temperature and pressure PFR at various conditions. Initial gas composition=75 percent N_2, 10 percent O_2, 10 percent H_2O, 5 percent CO_2, and 25 ppmv NO. Solid line (——): initial CO concentration=50 ppmv, P=1 atm. Dotted line (···): initial CO concentration=12.5 ppmv, P=1 atm. Dot-dashed line (–·–·): initial CO concentration=12.5 ppmv, P=10 atm.

5 are taken from the maximum slope of NO_2 profiles computed in constant temperature and pressure PFR calculations at the indicated conditions. The maximum slope typically occurs immediately after the induction period, typically between 0.2 and 0.4 s (see Fig. 3). NO_2 production rates greater than 10 ppmv per second are possible at temperatures between 575 and 725°C.

The net rate of NO_2 formation shown in Fig. 5 exhibits extremely non-Arrhenius behavior and unusual pressure dependence. At $P=1$ atm, the rate of NO_2 formation reaches a maximum at temperatures between 600 and 750°C, depending upon the initial CO:NO ratio, and then decreases rapidly as temperature increases. This non-Arrhenius temperature dependence is not surprising, once the competition between $R7$ and $R9$ is recognized as a major factor in joint CO/NO oxidation. Elementary reaction $R9$ is a well known addition/stabilization reaction which has been widely reported to exhibit non-Arrhenius behavior [15]. The non-Arrhenius behavior of $R9$ explains the unusual temperature dependence of NO_2 formation from NO. The slow rate of NO_2 formation at high temperatures also explains why NO_2 is typically not found in exhaust gas immediately exiting a gas turbine. The residence time in the combustor and the turbine is too short (on the order of 25 ms), and the temperature is too high, for significant NO_2 formation to take place.

At temperatures below 550°C, the net rate of NO_2 formation is roughly proportional to P^2. At higher temperatures the pressure dependence becomes more complex as additional reaction pathways become available. At temperatures above 675°C, the net rate of NO_2 production can actually decrease as pressure increases. Again, the unusual pressure dependence of the overall reaction is a direct result of the non-Arrhenius behavior and pressure dependence of $R9$.

The coupling of CO and NO oxidation at low temperatures also has important implications for modeling chemistry in turbulent flow. A typical approach used to include chemistry in turbulent flow models is to determine the flow, temperature, and species concentration fields using only the fuel and air chemistry, and initially neglecting NO_x formation. Once the flow field has been solved, NO_x chemistry is ''overlaid'' on top of the existing solution, the assumption being that small concentrations of NO_x will not perturb the composition or temperature fields significantly. While NO_x and CO chemistry can be decoupled at high temperatures, this work shows that this assumption is poor at low temperatures. If NO is present, models that decouple CO and NO_x chemistry will under-predict CO burnout at low temperatures (450–750°C).

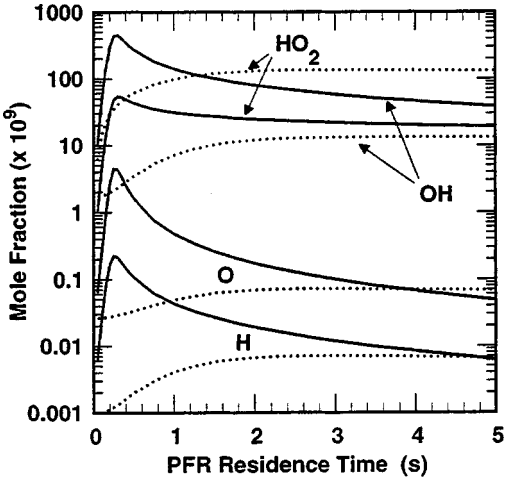

Fig. 4 Calculated PFR composition profiles of important radical species at the conditions of Fig. 3

Conclusions

The yellow-brown plumes sometimes observed in the exhaust from gas turbine power plants are caused by 10–15 ppmv of NO_2. Measurements and prior experience indicate that the NO_2 is not formed in the gas turbine combustor itself. This work has shown that CO plays a critical role in forming NO_2 downstream of the gas turbine. PSR and PFR calculations with four different reaction sets have shown that at temperatures below 800°C, the oxidation reactions of CO and NO are linked together through a chain reaction mechanism. The presence of each enhances the oxidation of the other. Below 550°C, the net reaction stoichiometry of

$$CO+NO+O_2 \rightarrow CO_2+NO_2$$

Downloaded 02 Jun 2010 to 171.66.16.119. Redistribution subject to ASME license or copyright; see http://www.asme.org/terms/Terms_Use.cfm

is expected. CO and NO_x chemistry cannot be decoupled in this temperature regime, and this observation has important implications for designers of boilers and exhaust gas systems trying to minimize NO_2 plume formation.

Acknowledgments

The authors gratefully acknowledge Robert A. Corr, currently with Catalytica, Inc., for introducing them to this problem.

References

[1] Sano, T., 1985, Combust. Sci. Technol., **38**, pp. 129–144.
[2] Corr, R. A., 1995, personal communication.
[3] Jaasma, D., and Borman, G., 1980, Combust. Sci. Technol., **23**, p. 83.
[4] Bromly, J. H., Barnes, F. J., and Little, L. H., 1988, J. Inst. Energy, **61**, p. 89.
[5] Bromly, J. H., Barnes, F. J., Mandyczewsky, R., Edwards, T. J., and Haynes, B. S., 1992, *Twenty-Fourth Symposium (International) on Combustion*, The Combustion Institute, Pittsburgh, PA, pp. 899–907.
[6] Hori, M., Matsunaga, N., Malte, P. C., and Marinov, N. M., 1992, *Twenty Fourth Symposium (International) on Combustion*, The Combustion Institute, Pittsburgh, PA, pp. 909–916.
[7] Glarborg, P., Kubel, D., Kristensen, P. G., Hansen, J., and DamJohansen, K., 1995, Combust. Sci. Technol., **110–111**, pp. 461–485.
[8] Miller, J. A., and Bowman, C. T., 1989, Prog. Energy Combust. Sci., **15**, pp. 287–338.
[9] Glarborg, P., Kee, R. J., Grcar, J. F., and Miller, J. A., 1986, ''PSR: A FORTRAN Program for Modeling Well-Stirred Reactors,'' Sandia National Laboratories Report SAND86-8209.
[10] Bowman, C. T., Hanson, R. K., Davidson, D. F., Gardiner, Jr., W. C., Lissianski, V., Smith, G. P., Golden, D. M., Frenklach, M., and Goldenberg, M., http://www.me.berkeley.edu/gri_mech/.
[11] Melo, O. T., and Stevens, R. D. S., 1981, Atmos. Environ., **15**, p. 12.
[12] Kee, R. J., Rupley, F. M., and Miller, J. A., 1989, ''Chemkin-II: A Fortran Chemical Kinetics Package for the Analysis of Gas-Phase Chemical Kinetics,'' Sandia National Laboratories, Report SAND89-8009.
[13] Lutz, A. E., Kee, R. J., and Miller, J. A., 1988, ''SENKIN: A Fortran Program for Predicting Homogeneous Gas Phase Chemical Kinetics with Sensitivity Analysis,'' Sandia National Laboratories, Report SAND87-8248.
[14] Michaud, M. G., Westmoreland, P. R., and Feitelberg, A. S., 1992, *Twenty-Fourth Symposium (International) on Combustion*, The Combustion Institute, Pittsburgh, PA, pp. 879–887.
[15] Mallard, W. G., Westley, F., Herron, J. T., and Hampson, R. F., 1992, ''NIST Chemical Kinetics Database-Ver. 4.0,'' NIST Standard Reference Data, Gaithersburg, MD.

Downloaded 02 Jun 2010 to 171.66.16.119. Redistribution subject to ASME license or copyright; see http://www.asme.org/terms/Terms_Use.cfm

D. B. Fant
South Carolina Institute for Energy Studies,
Clemson, SC 29634

G. S. Jackson
Department of Mechanical Engineering,
University of Maryland,
College Park, MD 20742

H. Karim
Precision Combustion Inc.,
New Haven, CT 06511

D. M. Newburry
Siemens Westinghouse,
Orlando, FL 32826

P. Dutta
K. O. Smith
Solar Turbines Inc.,
San Diego, CA 92186

R. W. Dibble
Department of Mechanical Engineering,
University of California,
Berkeley, CA 94720

Status of Catalytic Combustion R&D for the Department of Energy Advanced Turbine Systems Program

This paper discusses some of the advanced concepts and research and development associated with implementing catalytic combustion to achieve ultra-low-NO_x emissions in the next generation of land-based gas turbine engines. In particular, the paper presents current development status and design challenges being addressed by Siemens Westinghouse Power Corp. for large industrial engines (>200 MW) and by Solar Turbines for smaller engines (<20 MW) as part of the U.S. Department of Energy's (DOE) Advanced Turbine Systems (ATS) program. Operational issues in implementing catalytic combustion and the current needs for research in catalyst durability and operability are also discussed. This paper indicates how recent advances in reactor design and catalytic coatings have made catalytic combustion a viable technology for advanced turbine engines and how further research and development may improve catalytic combustion systems to better meet the durability and operability challenges presented by the high-efficiency, ultra-low emissions ATS program goals. [S0742-4795(00)01502-7]

1 Introduction

A major goal for the DOE-ATS program is to demonstrate stable, quiet, ultra-low emission combustion systems for advanced land-based gas turbine engines. This goal presents a substantial challenge to combustion engineers when it is combined with the ATS goal of high cycle efficiencies, which for the most part demand high turbine firing temperatures (>1700 K). To meet these challenges, two combustor technology paths are being pursued within the ATS program: (1) lean-premixed combustion for an emissions target of <10 ppm NO_x and <20 ppm CO/UHC, and (2) catalytic combustion with a target goal of <5 ppm NO_x and <10 ppm CO/UHC. While lean-premixed combustion systems for ATS engines are nearing readiness for field applications, catalytic combustion systems for the high efficiency ATS engines are still under development because of their potential for much lower emissions. Recent progress in reactor implementation as presented in this paper suggest that catalytic combustion systems will soon be ready for the next generation of high efficiency gas turbine engines.

The main advantage of catalytic combustion rests on the fact that the catalytic reactions inhibit chemical pathways that lead to NO_x. Catalytic combustion systems have the potential for achieving NO_x emissions of <3 ppm. Furthermore, large pressure oscillations (at frequencies of 100 to 1000 Hz) that can occur in lean premixed combustors may be highly suppressed in catalytic combustors [1]. This paper describes the status, approaches, and challenges of developing operable catalytic combustion systems for advanced gas turbines.

The challenges for implementing reliable catalytic combustion in ultra-low emissions gas turbines are being addressed at many levels by catalyst/catalytic reactor companies, engine manufacturers, and academic researchers. Development efforts in the U.S., including those under the ATS program, are starting to produce catalytic combustor designs [e.g., [2–4]] that are nearing engine worthiness. The various design approaches rely on upstream fuel/air premixing and a two-stage, so-called ''hybrid'' catalytic combustor. Figure 1 presents two schematics of hybrid catalytic combustion systems that have been developed for advanced gas turbine cycles. The schematics show two different approaches to handle combustor operation when inlet temperatures are too low for catalyst light-off: 1(*a*) with inlet gas preheating in a preburner, and 1(*b*) with downstream pilot fuel injection for stable combustion in the gas phase burnout zone. When the combustor inlet temperature rises to the catalyst light-off point, both designs switch to an ultra-low emissions mode where combustion occurs in a two-stage process. In the first stage, the catalytic reactor oxidizes a fraction of the fuel and thereby raises the gas-phase temperature to an intermediate level. After the catalyst, a downstream second stage, called the ''homogeneous burnout zone'' completes the fuel conversion and heats the gases to the desired combustor exit temperature.

In a hybrid catalytic combustor, the second-stage gas-phase combustion can lead to NO and CO formation, and thus, minimizing the fuel fraction converted in the gas phase tends to minimize NO_x and CO emissions. This suggests maximum conversion in the catalyst, which presents the challenge of avoiding catalyst overheating/meltdown. The current hybrid designs are far from optimized both in terms of operability and ultra-low emissions capability because of the fraction of fuel that must be converted

Contributed by the International Gas Turbine Institute (IGTI) of THE AMERICAN SOCIETY OF MECHANICAL ENGINEERS for publication in the ASME JOURNAL OF ENGINEERING FOR GAS TURBINES AND POWER. Paper presented at the International Gas Turbine and Aeroengine Congress and Exhibition, Indianapolis, IN, June 7–10, 1999; ASME Paper 99-GT-57. Manuscript received by IGTI March 9, 1999; final revision received by the ASME Headquarters January 3, 2000. Associate Technical Editor: D. Wisler.

Copyright © 2000 by ASME

Downloaded 02 Jun 2010 to 171.66.16.119. Redistribution subject to ASME license or copyright; see http://www.asme.org/terms/Terms_Use.cfm

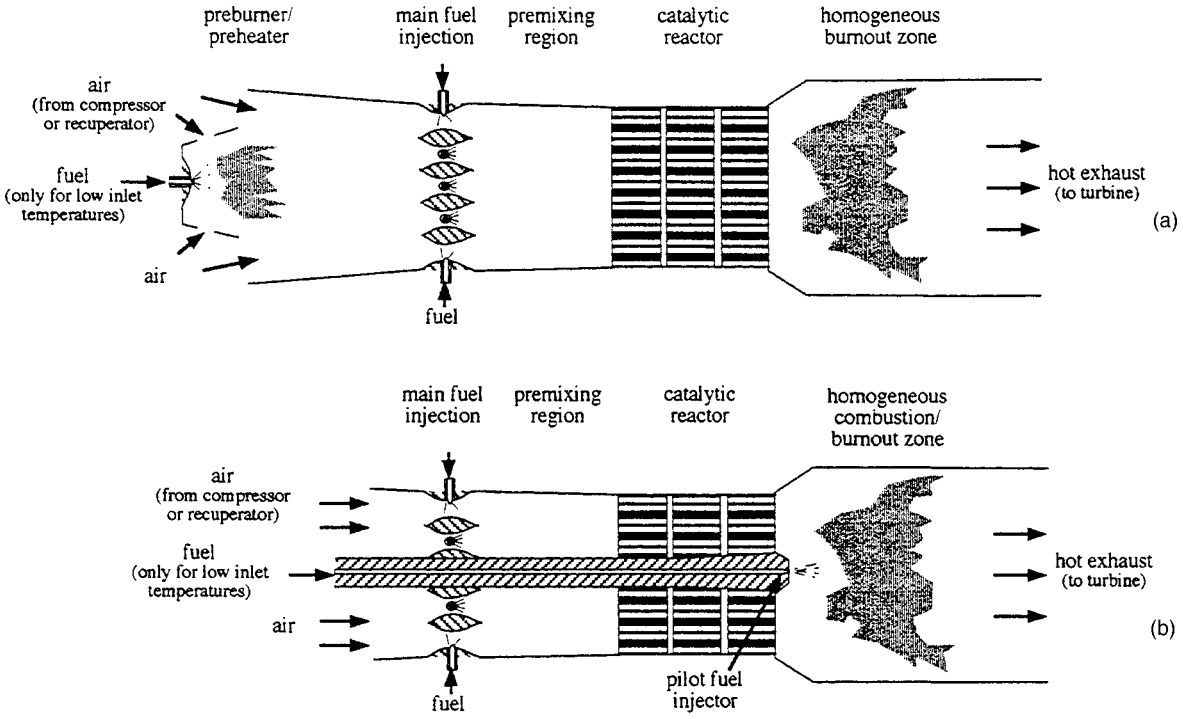

Fig. 1 Schematics of hybrid catalytic combustor designs for operation in advanced gas turbine engines (*a*) with preburner for low power operation, and (*b*) with downstream diffusion flame burner for low power operation

in the gas phase to avoid overheating of the catalyst/substrate. To fully realize the potential of catalytic combustion, further efforts in high-temperature materials development as well as reactor design (enhanced by advanced numerical models) must be undertaken.

Figure 2 shows a schematic operating window for a typical hybrid catalytic combustor in terms of combustor inlet temperature versus equivalence ratio. The operating window of a catalytic combustor is bounded by a low-temperature catalyst light-off limit (at the bottom), by a minimum adiabatic combustion temperature (to the left) below which low CO emissions and flame stability are difficult to maintain, and by a high-temperature catalyst or catalyst substrate limit (on the top). Figure 2 also indicates an approximate operating window for a typical dry-low-NO_x (DLN) combustion system. The respective operating windows suggest how the catalytic combustor offers advantages over DLN systems for operation at low adiabatic flame temperatures, and systems that operate in this range are now being demonstrated in small gas turbine engines [5]. Reliable operation at these low adiabatic flame temperatures is also critical for advanced ATS engines (with their higher firing temperatures) in order to avoid lean blowout during engine operation at low-power conditions (a problem for DLN systems). The advantages for catalytic combustion over DLN systems at high adiabatic flame temperatures due to improved combustor acoustics and lower NO_x emissions are not indicated in Fig. 2. The potential of reliable catalytic combustor operation at the high flame temperatures with NO_x and CO emissions below 5 and 10 ppm motivates the development efforts on catalytic combustion systems for ATS engines. Some of the key design challenges to improve operability and catalyst reliability and recent advances to address these challenges are summarized in the following sections.

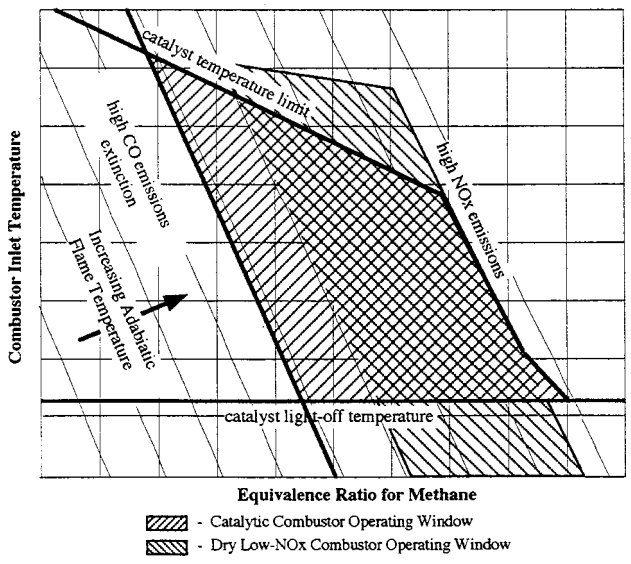

Fig. 2 Sketch showing representative operating windows of catalytic combustion system and dry low NO*x* combustion system

2 Catalytic Combustor Development at Solar Turbines

Solar Turbines has been developing a catalytic combustor design to meet the ATS emissions goals while providing firing temperatures necessary for the overall cycle efficiency goals [2]. The Solar Mercury 50 ATS gas turbine is the platform for catalytic combustor designs and is being developed for thermal efficiency >40 percent, for NO_x exhaust emissions <5 ppmv, and for high reliability and availability. The Mercury 50, which is designed to meet increasing distributed power generation needs and combined heat and power (cogeneration) demands in local communities, uses a recuperated cycle in order to achieve these goals.

Downloaded 02 Jun 2010 to 171.66.16.119. Redistribution subject to ASME license or copyright; see http://www.asme.org/terms/Terms_Use.cfm

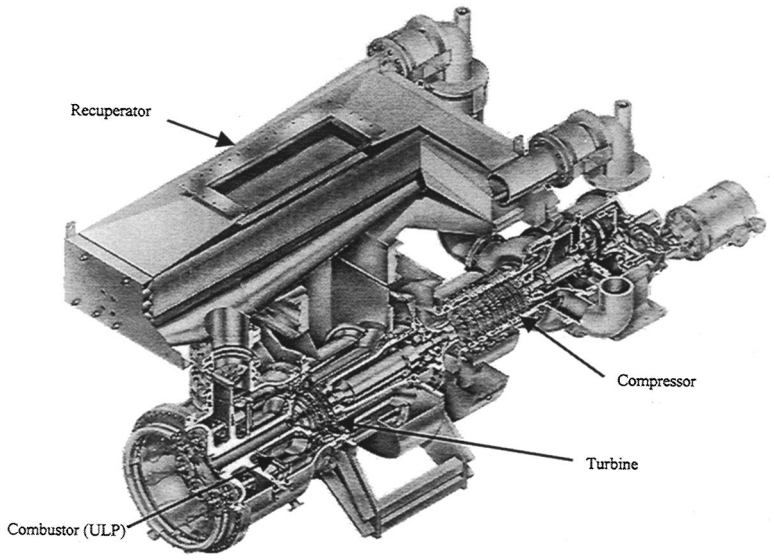

Fig. 3 Mercury 50 gas turbine with end-mounted combustor for lean-premixed or catalytic systems

The unique configuration of the Mercury 50 gas turbine, shown in Fig. 3, presents an ideal configuration for integrating a catalytic combustor into an engine previously designed for a more conventional combustor system. The compressor exit air travels through the recuperator from one side of the engine to the other where it then enters the combustion system, conveniently located at the end of the engine. This unique modular configuration allows for interchange between the annular ultra-lean premixed (ULP) combustion system and the future multi-can catalytic combustion system currently under development with virtually no impact on the rotating equipment in the engine.

The catalytic combustion system is being designed to exceed the low emissions performance of the ULP and to achieve <5 ppm NO_x and <10 ppm CO and UHC (corrected to 15 percent O_2) over the 50-to-100 percent load range. Development of the catalytic combustion system is divided into three phases: (1) sub-scale catalytic reactor ($\sim$10–12 cm dia.) testing at simulated engine conditions; (2) evaluation of system concept in a single-can, full-scale, high-pressure tests; and (3) multi-can hardware testing in high-pressure rigs followed by demonstration on the Mercury 50 engine. Current status of the catalytic combustor development process, and design challenges are summarized below.

Initial development of Solar's catalytic combustion system was based on sub-scale testing of various precious metal-based catalytic reactors (designed and fabricated by Catalytica). Designs followed the hybrid combustor concept discussed earlier where oxidation of a fraction of the fuel occurs in the catalyst bed and the remaining fuel is oxidized in a post catalyst homogeneous combustion region. The catalyst substrate temperatures are maintained at acceptable levels through use of a preferential substrate coating, and palladium-based catalysts were implemented to achieve reliable catalyst light-off at combustor inlet temperatures [6]. Results from the sub-scale testing have been summarized in an earlier paper [7].

Catalytic combustor testing at Solar has shown the need for very uniform fuel-air mixtures at the catalyst inlet in order to avoid locally high or low temperatures in the catalyst substrate. Regions of high temperature lead to catalyst deactivation and damage, while areas of low temperature lead to high CO and UHC emissions in the exhaust. The development of low-pressure drop premixers capable of achieving less than 10 percent peak-to-peak variation in fuel concentration is critical to avoid regions of catalyst overheating as well as regions of cold spots with low fuel conversion. The need for such uniform premixing is complicated by the variation in fuel-air splits as the engine changes operating conditions.

Sub-scale testing at Solar has also revealed the limited turndown (in terms of fuel-air equivalence ratios) of the catalytic reactor design. This necessitates the use of catalyst air modulation with variable geometry valves to maintain catalyst performance at off-design load conditions. Based on the catalyst performance in the sub-scale tests, concepts for reactor design and air flow modulation in the Mercury 50 catalytic combustion system were established. The concept design was largely empirical, based primarily on sub-scale testing results, since sufficient information is not available to model the heterogeneous oxidation of hydrocarbons (most notably CH_4) on the palladium-based catalyst surface. Homogeneous reactions downstream of the catalyst however can be modeled accurately, and one-dimensional flow models with detailed chemical kinetic information for the homogeneous burnout zone are integrated with empirical catalytic reactor models to predict system performance before final design. Upon completing fabrication of the full-scale catalytic reactor and homogeneous burnout zone, high-pressure tests of the single-can combustor are undertaken to define/optimize the operating window of the entire system.

The multi-can Mercury 50 catalytic combustion system concept follows the single-can combustor layout of Cowell and Roberts [8]. Figure 4 shows a schematic of the single-can combustor arrangement as tested in a high-pressure rig. The system incorporates a start-up/part-load fuel injector located at the center of an annular catalyst, and a variable geometry valve that regulates the flow of air into the catalyst. The start-up/part-load fuel injector is used to start the engine and operate it below 50 percent load. At 50 percent load, the combustor inlet temperature (recuperator discharge temperature) is sufficiently high for catalyst operation and the system transitions to catalyst operation mode. This catalytic combustion system configuration solves some of the operational difficulties with catalytic combustion systems. Firstly, the fuel flow bypasses the catalyst during engine light-off and initial acceleration, and avoids the complication of a preburner upstream of the catalyst. The lack of a preburner also allows the combustor to achieve the lowest levels of NO_x emissions and maintains a more uniform temperature profile at the catalyst inlet.

Downloaded 02 Jun 2010 to 171.66.16.119. Redistribution subject to ASME license or copyright; see http://www.asme.org/terms/Terms_Use.cfm

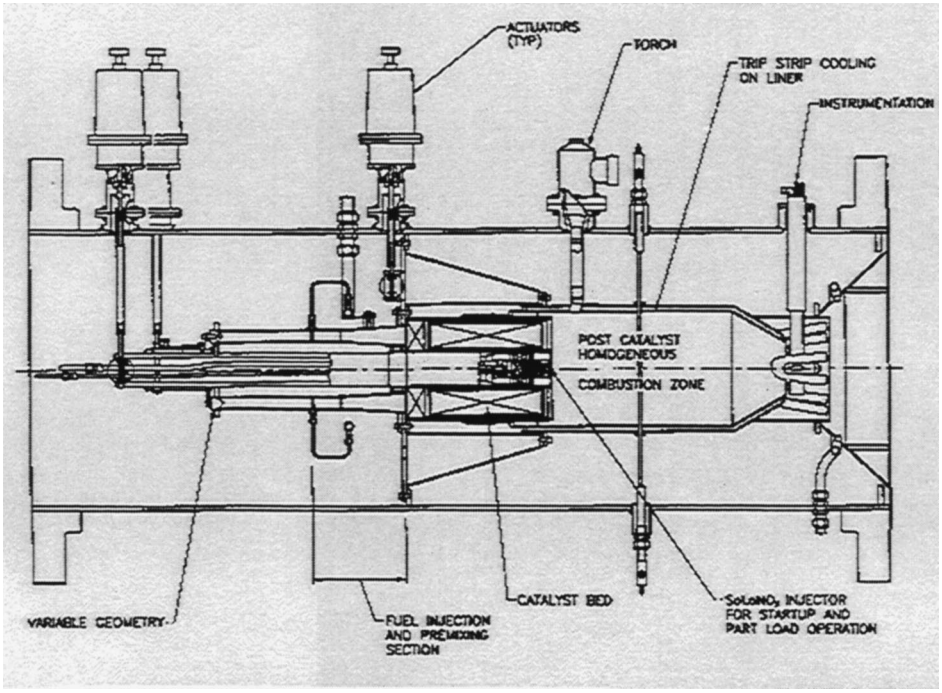

Fig. 4 Catalytic combustor system being tested and developed at Solar for ATS engine applications

Viability of the catalytic combustor was investigated under engine operating scenarios including system light-off, part-load conditions below 50 percent load using the central fuel injector, transition from part load to catalyst operating mode at 50 percent load, and active modulation of the air flow into the catalyst at high power conditions (>50 percent load) to meet <5 ppmv NO_x goals. Successful combustor operation over all of these scenarios was demonstrated in high pressure rig tests, and emissions goals were achieved over the 50–100 percent load range. Details of the design of the single-can catalytic combustor and results of rig tests are available elsewhere [2,7].

Design and fabrication of the complete multi-can catalytic combustion system is currently in progress, with an engine demonstration planned for late 1999. The design of the combustion system has to provide both uniform fuel concentrations and uniform air flows at the catalyst inlet. Even slight variations in can-to-can air mass flow rates could lead to catalyst damage at hot spots or high CO/UHC emissions in cold spots. To this end, the combustor needs the air flow modulation by the variable geometry valve to have minimal impact on the combustor aerodynamics. Likewise, the engine fuel controller must provide reliable and accurate transition of fuel flow from the start-up injector to the main catalyst premixer during switching from part-load to high-power operation.

In addition to the operability issues, concerns such as long term catalyst durability and mechanical integrity are also being addressed. Sub-scale tests of current state of the art palladium-based catalysts at simulated engine conditions have shown no deterioration in catalyst performance over approximately 1000 h. However, an accurate estimate of long term catalyst durability will not be available until a field demonstration is performed. Potential poisons/abrasives that may accelerate catalyst deterioration during field operation include lube oil, turbine wash solutions, compressor coatings, fuel contaminants (e.g., Na, S, Cl), and air-borne contaminants (e.g., silica, salts). Likewise, field demonstrations will test the mechanical integrity of the catalyst substrate at elevated temperature when subjected to engine vibrations. Addressing these issues in an engine field test is the next step for development of an ultra-low emissions catalytic combustor for the Mercury 50 ATS engine.

3 Catalytic Combustor Development for the Siemens Westinghouse ATS Engine

In contrast to Solar's Mercury 50 engine, the Siemens Westinghouse Power Corporation (formerly Westinghouse Power Generation) ATS engine shown in Fig. 5 is a large combustion turbine relying on high pressure ratios, instead of a recuperator, to achieve high cycle efficiencies. The engine contains sixteen can combustors located around the engine circumference between the compressor and the turbine, and efforts are ongoing to develop both lean-premixed (including catalytically enhanced) combustors and ultra-low emissions fully catalytic combustors for the engine. The high cycle efficiencies and associated high turbine firing temperatures require steam cooling in the transition ducts, which direct the hot combustor exit gases into the turbine. In order to minimize the need for cooling air and overall size of both the lean-premixed and fully catalytic combustors, the transition duct also serves as a homogeneous burnout zone where a significant fraction of the heat release takes place to achieve ultra-low CO and UHC emissions.

A major design goal of the Siemens Westinghouse catalytic combustor development program has been to incorporate catalytic combustion technology into the same-sized envelopes as existing lean premixed combustor designs. This goal presents a significant challenge to the catalytic combustor development since surface reactors usually are not amenable to high volumetric heat release rates. However, the size constraint has led to alternative approaches to catalytic combustion including unique approaches of integrating catalytic reactors with lean premixed combustion systems. To this end, catalytic combustor development efforts at Siemens Westinghouse have evolved into two development pro-

Downloaded 02 Jun 2010 to 171.66.16.119. Redistribution subject to ASME license or copyright; see http://www.asme.org/terms/Terms_Use.cfm

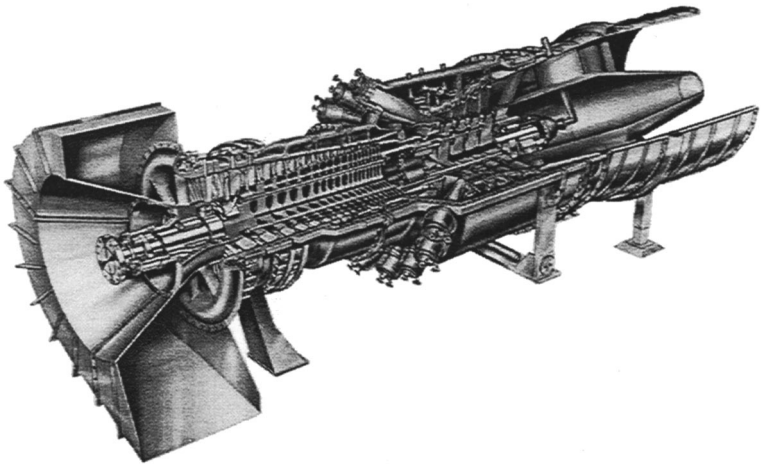

Fig. 5 Siemens Westinghouse ATS engine for which catalytic combustor development is ongoing

grams: one for a catalytic pilot in lean-premixed combustors and a second for a fully catalytic combustor with high operating space velocities.

Catalytic Pilot Development. The catalytic pilot concept seeks to address some of the limitations with conventional lean-premixed combustor operation (particularly at low adiabatic flame temperatures as indicated in Fig. 2) by providing improved combustor resistance to lean blowout and instabilities. The catalytic pilot consists of a unique radial inflow swirler with a central catalytic reactor. Fuel and air to the pilot are premixed upstream of the pilot with a small fraction of the mixture passing through the central catalytic reactor and the remainder passing through the swirler. The hot combustion products exiting from the central catalytic reactor stabilize combustion of the remaining pilot fuel, which subsequently sustains combustion in the entire lean-premixed combustor.

The catalytic pilot was developed as a stand-alone premixed burner (at Precision Combustion, Inc.), and development efforts began with atmospheric pressure testing and validation of CFD modeling, which was then used to predict high-pressure engine performance. Difficulties in predicting the heterogeneous surface reaction rates at the very high pressure ratios (>20 to 1) in the Westinghouse ATS engine made it difficult to assess the high-pressure performance of the catalytic reactor. In general, this difficulty currently limits the reliability of CFD modeling as a tool for designing catalytic reactors for combustion systems that operate at extremely high pressures. Nonetheless, the CFD studies can be integrated with empirical catalytic reactor models to study the downstream gas-phase fluid flow and chemistry interactions in the homogeneous combustion zone. Such an approach was used in the catalytic pilot development and once satisfactory atmospheric testing and high-pressure CFD results were achieved, the selected catalytic pilot design was incorporated into an existing full-scale, lean premixed combustor and successfully tested at atmospheric pressure. Currently, the full-scale combustor with catalytic pilot stabilization is being tested at high-pressure engine conditions. The catalytic pilot approach offers a unique solution to lean-premixed combustor operational difficulties, but initial testing suggests that this approach does not offer the potential for emissions as low as a fully catalytic combustor because of the reduced amount of heterogeneous reactions, which inhibit NO_x formation pathways in the combustor.

Fully Catalytic Combustor Development. Unlike the small catalytic pilot reactor, which only converts a small fraction of the entire combustor fuel flow, the fully catalytic combustor is designed to convert a significant fraction of the fuel and thereby provide ultra-low NO_x emissions (<5 ppm). The Siemens Westinghouse catalytic combustor, like the Solar design, relies on a hybrid combustor approach (discussed in Section 1) where the conversion in the catalyst is limited and combustion is completed in a downstream homogeneous burnout zone. Because the catalytic reactor plays such a large role in the fully catalytic combustor, the development efforts have been focused largely on the design and construction of a suitable catalytic reactor.

Because of the high firing temperatures required by the ATS engine (>1700 K), the catalytic reactor must operate at a relatively high fuel/air ratio. This presents the risk of overheating of the catalytic reactor, as current state-of-the-art catalyst/catalytic substrates are not capable of withstanding adiabatic flame temperatures required for the ATS turbine cycle. However, to achieve NO_x emissions below 5 ppm and stable downstream burnout with ultra-low CO and UHC emissions, a substantial fraction of the fuel must be converted in the catalyst bed. Because this is primarily a catalytic reactor problem, it is amenable to sub-scale testing, and thus, significant emphasis has been placed on small-scale catalyst bed design and testing, both in atmospheric and high pressure test rigs. The reactor designs tested in the sub-scale rigs have been guided by models of the catalytic reactor, which integrate simple surface chemistry models with CFD.

The sub-scale testing has led to some suitable catalytic reactor designs which limit the conversion of fuel inside the catalyst bed, even under the high fuel-air stoichiometries required by the Siemens Westinghouse ATS engine. The catalytic combustor development is now moving into full-scale combustor testing by integrating the reactor designs developed from the sub-scale tests into a single-can combustor, similar in size to the lean-premixed combustion system constructed for the engine. The fully catalytic combustor will operate without a preburner at high power conditions (above 50 percent load). At low power conditions where the combustor inlet temperature is too low to light off the catalytic reactors, a diffusion flame pilot is used to provide stable (though with high emissions) homogeneous combustion downstream of the catalyst beds. This arrangement is represented well by the schematic in Fig. 1(*b*). The diffusion flame pilot will also provide start-up capabilities. On the other hand, at high loads, when the catalytic reactors can provide adequate fuel conversion and ultra-low emissions are critical, the diffusion flame is shut off, and fuel will be premixed into the pilot air for minimum NO*x* emissions. Testing of this combustor concept will focus on combustor operability and catalytic reactor operation within the long-term durability limits of both the catalyst and the substrate.

Downloaded 02 Jun 2010 to 171.66.16.119. Redistribution subject to ASME license or copyright; see http://www.asme.org/terms/Terms_Use.cfm

4 Research and Development Issues

Substantial issues associated with catalytic combustor development have been raised by the catalytic combustor development efforts under the ATS program. Some of those issues were raised in the previous two sections and will be discussed further in this section. This section will look at how fundamental research and development in areas such as low and high temperature catalysts and catalytic reactor modeling is still needed for catalytic combustion technology to meet the challenges posed by the next generation of high-efficiency, ultra-low-emissions gas turbine engines.

Low Temperature Light-Off Catalysts. One of the outstanding issues in catalytic combustion is the development of oxidation catalysts, particularly for natural gas (i.e., methane), that maintain low light-off temperatures ($<$400°C) for several thousand hours. Due to the current limit of methane catalysts (which require inlet temperatures around 400°C for adequate performance in gas turbine combustor applications), various approaches, as discussed in the previous sections, have been adopted to operate catalytic combustion systems during conditions where combustor inlet temperatures are below the effective catalyst light-off temperature. Whereas the Solar and Siemens Westinghouse (as well as the Rolls Royce Allison) ATS engines provide adequate combustor inlet temperatures at high power conditions for current state-of-the-art palladium-based catalysts, availability of durable, lower-temperature catalysts would greatly simplify the approaches to catalytic combustor design.

One approach to operating a catalytic combustor at low inlet temperatures is the use of a non-premixed ''preburner,'' ahead of the catalyst (as shown in Fig. 1(*a*)). The non-premixed flame increases the temperature of gases flowing into the catalyst so that adequate light-off is maintained at low power conditions. The preburner may also be used to start the engine. However, control of the temperature distribution upstream of the catalyst and unwanted NO_x emissions that result from the non-premixed flame have caused designers to look for alternative approaches for low temperature operation. One alternative shown in Fig. 1(*b*) involves secondary fuel injection downstream of the catalytic. This approach, which has been adopted in different ways by both Solar Turbines and Siemens Westinghouse, also suffers from unwanted NO_x emissions at low power conditions but avoids the risk of the preburner upstream of the catalyst. In both the recuperated cycle of the Solar ATS engine and the high pressure ratio cycle of the Siemens Westinghouse engine, combustor inlet temperatures are adequate for catalyst light-off at high power conditions ($>$50 percent load), and thus the downstream fuel injection is not used at high power conditions.

Significant complexities in combustor geometry and fuel scheduling must be incorporated for the low power catalytic combustor operation where combustor inlet temperatures drop below 400°C. These complexities, as discussed in the previous paragraphs, have also included variable geometry as in the Solar engine [9] or downstream burners that must run relatively rich while the catalyst is not supplied with fuel [3]. Improved low-temperature catalysts would minimize the need for these complex additions used for start-up and low-power conditions and thereby would greatly improve the operability of the entire catalytic combustion system.

For the most part, supported palladium (Pd) based catalysts have been implemented for low-temperature light-off catalysts in natural gas combustors. As of yet alternative non-precious metal catalysts such as perovskites and substituted hexaluminates have not shown sustainable low temperature activity needed for natural gas combustor applications [10]. With Pd-based catalysts, the supports are generally an oxide ''washcoat,'' which provides a high surface-area for sufficient dispersion of the precious metal for low temperature light-off. However, the high surface area support becomes less critical during steady-state, high-temperature operation because the increased rate of oxidation reactions at the exposed surface exceeds the rate at which gas diffusion brings the reactants to the washcoat [11]. Research may still be done to provide guidelines for reducing precious metal loading through selective placement of high surface area supports without impacting reactor light-off or steady-state performance.

In the U.S., many researchers have used low-pressure, temperature-programmed microreactors to study supported Pd catalysts for methane oxidation. These studies have indicated that under oxygen-rich conditions, surface Pd is primarily in an oxidized state (PdO) below temperatures ranging from 600 to 900°C (depending primarily on O_2 partial pressure). At higher temperatures, PdO is reduced to Pd, and if temperatures rise high enough, the Pd metal undergoes particle restructuring with loss of active surface area. When the temperature falls back, the supported Pd catalyst exhibits a region of apparent negative activation energy as the catalyst begins to return to its oxidized state. Some have suggested that the transition from PdO to Pd can be used to control catalyst temperatures—i.e., as the temperature rises, PdO will revert to Pd and the reaction will slow down. However, reduced Pd can also promote methane oxidation at high temperatures, and methane oxidation reactions do not necessarily stop as PdO is converted to Pd, particularly at high pressures [12]. Nonetheless, reduction of PdO at intermediate temperatures and restructuring of Pd catalysts at high temperatures can result in catalyst behavior that depends on past operating conditions. The change in Pd catalyst behavior presents a challenge to combustor designers when consistent fuel conversion in the catalyst bed is necessary for low CO and UHC emissions.

A better understanding of the Pd/PdO system is needed at high pressures and at reacting conditions where surface oxides may be much more difficult to reduce than at the low-pressure conditions of most micro-reactor studies. Recent studies suggest that methane oxidation on Pd/PdO is promoted by CH_4 adsorption onto reduced Pd molecules with nearby PdO molecules promoting *H*-abstraction and subsequent CO_2 formation and desorption [13]. Assuming such a model is correct, it is not surprising that catalytic combustors have more difficulty lighting-off as pressure increases because the higher O_2 pressures will result in more extensive oxygen coverage of the catalyst. A better understanding of how Pd/PdO behaves under light-off and reacting conditions at high pressures will help researchers to determine how to enhance the long-term durability of the catalyst features that can provide high activity below 400°C. For example, if it is critical to maintain some fraction of reduced Pd for good low temperature activity, efforts might focus on the potential of bimetallic Pd-based catalysts to sustain some reduced palladium at combustor light-off conditions. The need for advanced processing techniques to ensure durable bimetallic catalysts will assist that effort. The development of durable, low-temperature, light-off catalysts for natural gas combustion may allow engine manufacturers to focus on simpler more reliable catalytic combustor designs than currently being developed for the ATS engines.

High Temperature Combustion Catalysts and Durability. Supported Pd-based catalysts, which work well as low temperature catalysts, have high temperature durability limits due to surface sintering (sintering means loss of surface active area), change in surface chemical composition (e.g., formation of aluminates), or catalyst volatilization [11]. The sintering process, which is accelerated by temperature excursions above 1000°C and by water produced from combustion reactions, may involve recrystallization/agglomeration of the supported precious metals and/or their support (i.e., washcoat restructuring such as the γ-Al_2O_3 to α-Al_2O_3 transition). To this end, washcoat stabilizers have been developed with rare-earth metals, which reduce the loss of washcoat surface area and thus exposed catalyst [14]. Researchers have looked at the effectiveness of more sintering resistant materials such as stabilized zirconia [15] and low surface area α-Al_2O_3 [16] to provide durable catalyst performance at higher temperatures.

Downloaded 02 Jun 2010 to 171.66.16.119. Redistribution subject to ASME license or copyright; see http://www.asme.org/terms/Terms_Use.cfm

Catalyst volatilization at high temperatures is correlated with the vapor pressure of the metal and/or its oxide. Catalyst volatilization and particle ''restructuring'' at high temperatures involve complex kinetic problems that are not well understood and thus difficult to control. Although Pd is thought to be least susceptible to catalyst volatilization of the precious metals, it is generally accepted Pd can only provide adequate resistance to temperatures of 1050 ± 100°C for long-term gas turbine applications. These temperatures are far below firing temperatures for advanced gas turbines, e.g., 1450°C, and thus catalytic combustor designs with conventional precious metal catalysts must leave some fuel conversion for the downstream homogeneous burnout zone. Accordingly, there is a search for catalysts that will survive higher temperature. Many researchers, principally in Japan and Europe, have investigated the use of non-precious metal, high-temperature catalysts, such as substituted hexaluminates. Recent advances in substituted-hexaluminate catalysts [17] suggest that catalytic reactor exit temperatures as high as 1200°C may be achievable, but these catalysts are still prone to deactivation from high temperature excursions that may be caused by poor upstream fuel/air distribution.

Thus far, catalytic combustion systems for ATS engines have not employed these alternative high temperature catalysts but have rather used precious metal catalysts, limited catalyst temperatures, and the hybrid combustor concept with the downstream homogeneous combustion. The absence of high temperature non-precious-metal catalysts in ATS catalytic combustor designs may be motivated in part by the desire for low combustor pressure drop. However, a large factor for not using these alternative catalysts concerns long-term durability of the catalytic reactor. Until high temperature catalysts can demonstrate durability for several 1000 h with typical fluctuations in fuel/air ratios from premixers, engine manufacturers will restrain from their use. Research aimed at high temperature catalyst development must clearly address sintering and volatilization of active components in the high temperature steam-laden flows experienced in catalytic combustors. Potential advantages of reduced NO_x emission from converting more of the fuel through the catalyst [18] should provide the motivation for continued materials development for high temperature combustion catalysts.

Catalytic Reactor Design and Operating Conditions. Consideration of reactor design and performance at actual engine conditions has been the focus of many scientists and engineers working on catalytic combustion issues for ATS gas turbine engines. The U.S. patent literature has many proposed reactor designs for addressing problems associated with catalyst overheating. Approaches include diffusion barrier coatings, selective coatings to reduce mass transfer-limited catalyst temperatures [6,19], and short segmented monoliths to increase mass transfer rates [20]. A brief discussion is presented here on how operating conditions and scenarios impact the study of catalytic combustors and their design.

Catalytic combustors face system integration issues such as uneven air flow and fuel/air ratios from the upstream premixer [1]. A large effort in the ATS program has gone into the development of improved premixers both for dry-low NO_x as well as catalytic combustors [21]. Catalytic combustor designs must include careful specifications of the limits in variation of fuel/air ratios and reactor velocities entering the catalytic monoliths. This is critical to avoid high temperature runaway or loss of long-term catalyst durability. Unlike heterogeneous reactors utilized in the chemical process industry, gas turbine catalytic combustors operate at high throughput velocities with relatively low pressure drop and low residence times. The high velocity throughputs reduce the risk of gas phase pre-ignition upstream and within the catalyst bed, which is exacerbated by higher pressures and temperatures [22]. The high velocities, however, also reduce the catalysts' ability to light-off at low temperatures and achieve adequate conversion. Thus, gas turbine combustion catalysts must have high activities to make up for the relatively low reactant residence times inside the catalyst bed.

For the high-pressure ratio ATS engines, pressures in the catalytic monoliths may lead to a transition to turbulent flow inside the catalytic reactor channels. Transition to turbulent flow may increase the risk of flashback inside the catalyst due to the increase in flame speeds caused by the turbulence. On the other hand, the increased mass transfer to the surface may serve to blunt autocatalytic reactions by radical recombination on the washcoat. The ways in which the high velocities impact catalytic combustor performance may be addressed to a large extent by improved computational models that combine fluid dynamics with gas phase chemistry and surface reactions. Such models are discussed in the next section.

The higher pressures of the ATS gas turbine cycles may also influence the heterogeneous chemistry on the catalyst surface since the higher pressures may result in increased oxygen coverage on the catalyst and changes in the active mechanism on palladium-based catalysts for methane oxidation. While low-pressure studies have indicated that CH_4 oxidation on Pd catalysts is first order in CH_4 concentration and zeroth order in O_2 concentration [23], simple Langmuir-Hinshelwood kinetics raises the question of whether the first-order dependence on CH_4 will fall off as the pressure increases to 30 atmospheres. High pressure tests have indicated that conversion does fall off with a $P^{-0.1}$ to $P^{-0.2}$ dependence suggesting that the conversion is controlled by mass transfer or chemical kinetics which increases by $P^{0.8-0.9}$ [23]. It should be noted that this power dependence may not be operative over the entire pressure range and that light-off tests over these pressure ranges indicate an increase in light-off temperature as pressure increases. To improve our understanding of the applicability of simple scaling laws, improved computational models may play a significant role as discussed in the final section of the paper.

Potential for Modeling to Impact the Design Process. The expense and risk of testing catalytic combustion systems at actual engine conditions, and even more so in actual gas turbines, encourages the development of reliable and validated computational models for providing performance expectations and risk assessments of a given catalytic combustor design. Although several models have been presented in the literature as reviewed in previous references [24,25], these models for the most part are not well suited for simulating critical interactions between the catalyst and the channel flows which dictate overall trends in catalyst/combustor performance.

As implied in the previous section, changes in flow characteristics particularly at high pressure inside the catalytic reactor channels can greatly impact reactor performance. The inability of previous models to simulate properly the velocity profiles inside catalytic channels and the effects of complex surface chemistry suggests that these models have limited value in extrapolating catalytic reactor performance from controlled low-pressure experiments to the high-pressure conditions experienced in the engine. Thus, a challenge particularly for catalytic combustion research is to build computational models of catalytic channel flows which will adequately capture the coupling between heat release from the catalytic surface and the gas-phase velocity field (and gas-phase transport). Examples of such emerging models include Deutschmann et al. [26] and Bond et al. [27], but these models have focused primarily on platinum chemistry. The more pertinent (and more difficult) chemistry models for methane oxidation on palladium catalysts are still under development. Improved computational flow models, that may incorporate large eddy simulation models for capturing transition to turbulence in catalytic channels, may provide better prediction of conversion trends and assessment of the risk of preignition and fuel/air unmixedness for proposed catalytic reactor/combustor designs.

Another place where advanced modeling may significantly im-

Downloaded 02 Jun 2010 to 171.66.16.119. Redistribution subject to ASME license or copyright; see http://www.asme.org/terms/Terms_Use.cfm

prove the combustor design process involves predicting transient reactor performance, such as during light-off or oscillatory behavior in Pd-based catalyst systems. Such phenomena are generally driven by complex changes in surface chemistry and thus will only be understood as improved surface chemistry models are developed and incorporated into appropriate catalytic combustor models. Since low temperature activity is extremely important in determining the operability of a catalytic combustion system, developing validated transient models will improve our understanding of the driving mechanisms in catalytic combustor light-off and thus hopefully of critical design parameters for improving low temperature catalytic reactor light-off. Improved surface chemistry models particularly of Pd/PdO systems may also increase designer's capability to predict unwanted combustor oscillations as well as steady-state performance. Development of these models will require close collaboration between experimentalists, who have helped to build the large database on Pd-based catalyst behavior, and computational model builders. The cost benefits of using computer models to assess the feasibility of a catalytic combustor design for a high pressure engine should motivate a collaborative effort to build better surface chemistry models for critical catalyst compositions as well as improved flow models for catalytic monoliths in high temperature combustor applications.

5 Conclusion

Although significant engineering and R&D challenges remain to successfully integrate and operate catalytic combustion systems in advanced gas turbines, the ATS engine manufacturers are actively pursuing the technology and its long-term demonstration in full-scale engine tests. Results to date have been very encouraging, and once optimized, catalytic combustion has the potential to provide a cleaner alternative to lean-premixed combustion systems for advanced turbine engines. Further research in low temperature catalysts, high temperature materials, and advanced catalytic reactor models can play a critical role in pushing the development further so that catalytic combustors will be available for advanced power generation systems.

Acknowledgments

This paper was written with partial support from the U.S. DOE-ATS program. The authors kindly recognize Ms. Abbie Layne and Dr. Norman Holcombe: ATS Product Manager and Contracting Officer Representative, respectively. The authors sincerely appreciate the paper invitation from RTA/NATO through Dr. Klaus Schadow of the Navy/China Lake, and coordination of the U.S. paper clearance process through Richard Hill of Wright-Patterson Air Force Base.

References

[1] Schlegel, A., Strichsbier, M., Mongia, R., and Dibble, R. W., 1996, ''A Comparison of the Influence of Fuel/Air Unmixedness on NO*x* Emissions in Lean Premixed, Non-Catalytic and Catalytically Stabilized Combustion,'' ASME Paper 96-GT-306.
[2] Dutta, P., Cowell, L. H., Yee, D. K., and Dalla Betta, R. A., 1997, ''Design and Evaluation of a Single-Can Full Scale Catalytic Combustion System for Ultra-Low Emissions Industrial Gas Turbines,'' ASME Paper 97-GT-292.
[3] Smith, D. A., Frey, S. F., Stansel, D. M., and Razdan, M. K., 1997, ''Low Emissions Combustion System for The Allison ATS Engine,'' ASME Paper 97-GT-311.
[4] Etemad, S., Karim, H., Smith, L. L., and Pfefferle, W. C., 1999, Catal. Today, **47**, Nos. 1–4, pp. 305–313.
[5] Dalla Betta, R. A., Schlatter, J. C., Nickolas, S. G., Yee, D. K., Shoji, T., 1997, ''Single-Digit in a Full-Scale Catalytic Combustor,'' ASME Paper 97-GT-57.
[6] Dalla Betta, R. A., et al., 1993, U.S. Patent No. 5,248,251.
[7] Dutta, P., 1997, *Proc. of the Quadrennial Intl. Conference on Power Stations*, Association des Ingenieurs de Montefiore, Liege, Belgium, pp. 267–272.
[8] Cowell, L. H., and Roberts, P. B., 1995, U.S. Patent No. 5,452,574.
[9] Dutta, P., Yee, D. K., and Dalla Betta, R. A., 1997, ''Catalytic Combustor Development for Ultra-Low Emissions Industrial Gas Turbines,'' ASME Paper 97-GT-497.
[10] Quinlan, M. A., Wise, H., and McCarty, J. G., 1989, GRI-Report No. 89/0141.
[11] Heck, R. M., and Farrauto, R. J., 1995, *Catalytic Air Pollution Control*, Van Nostrand Reinhold, New York.
[12] McCarty, J. G., and Chang, Y., 1994, Scr. Metall. Mater., **31**, No. 8, pp. 1115–1120.
[13] Su, S. C., Carstens, J. N., and Bell, A. T., 1998, J. Catal., **176**, pp. 125–135.
[14] Trimm, D. L., 1993, *Proc. of Intl. Workshop on Catalytic Combustion*, H. Arai, ed., Catalysis Society of Japan, Tokyo, pp. 46–55.
[15] Rodriguez, N. M., Oh, S. G., Dalla Betta, R. A., and Baker, R. T. K., 1995, J. Catal., **157**, pp. 676–686.
[16] Lyubovsky, M., Weber, R., and Pfefferle, L., 1996, *Twenty-Sixth Symp. (Intl.) on Combustion*, The Combustion Institute, Pittsburgh, PA, pp. 1779–1787.
[17] Sadamori, H., Tanioka, T., and Matuhisa, T., 1993, *Proc. of Intl. Workshop on Catalytic Combustion*, H. Arai, ed., Catalysis Society of Japan, Tokyo, pp. 158–161.
[18] Schlegel, A., Buser, S., Benz, P., Bockhorn, H., and Mauss, F., 1994, *Twenty-Fifth Symp. (Intl.) on Combustion*, The Combustion Institute, Pittsburgh, PA, pp. 1019–1026.
[19] Chou, T. C., Kennelly, T., and Farrauto, R. J., 1992, U.S. Patent No. 5,102,639.
[20] Pfefferle, W. C., et al., 1995, U.S. Patent No. 5,601,426.
[21] Mongia, R. K., Dibble, R. W., and Lovett, J., 1998, ''Measure of Air-Fuel Ratio Fluctuations Caused by Combustor Driven Oscillations,'' ASME Paper 98-GT-304.
[22] Spadaccini, L. J., and Colket, III, M. B., 1994, Prog. Energy Combust. Sci., **20**, pp. 431–460.
[23] Fredrik, A., Ahlstom-Silversan, C., and Odenbrand, C., 1997, Appl. Catal., A, **157**, pp. 157–175.
[24] Cybulski, A., and Moulin, J. A., 1994, Catal. Rev. Sci. Eng., **36**, No. 2, pp. 179–270.
[25] Kolaczowski, S. T., 1995, Trans. Inst. Chem. Eng., **73(A)**, pp. 168–190.
[26] Deutschmann, O., Gorablski, C. T., Schmidt, L. D., Raja, L. L., Kee, R. J., and Warnatz, J., 1998, ''Comparison of Navier–Stokes, Boundary-Layer, and Plug-Flow Models for Simulating Flow in a Catalytic-Combustion Honeycomb Channel,'' Poster presented to *27th Symposium (Intl.) on Combustion*, Boulder, Colorado.
[27] Bond, T. C., Noguchi, R. A., Chou, C. P., Mongia, R. K., Dibble, R. W., Chen, J. Y., 1997, *Twenty-Sixth Symp. (Intl.) Comb.*, The Combustion Institute, Pittsburgh, PA, pp. 1771–1778.

Downloaded 02 Jun 2010 to 171.66.16.119. Redistribution subject to ASME license or copyright; see http://www.asme.org/terms/Terms_Use.cfm

Performance of a Reduced NO_x Diffusion Flame Combustor for the MS5002 Gas Turbine

Alan S. Feitelberg
GE Corporate Research and Development,
One Research Circle,
Niskayuna, NY 12309

Michael D. Starkey
Richard B. Schiefer
Roointon E. Pavri
GE Power Systems,
Schenectady, NY 12301

Matt Bender
John L. Booth
Gordon R. Schmidt
British Petroleum,
Prudhoe Bay, Alaska 99734

This paper describes a reduced NO_x diffusion flame combustor that has been developed for the MS5002 gas turbine. Laboratory tests have shown that when firing with natural gas, without water or steam injection, NO_x emissions from the new combustor are about 40 percent lower than NO_x emissions from the standard MS5002 combustor. CO emissions are virtually unchanged at base load, but increase at part load conditions. The laboratory results were confirmed in 1997 by a commercial demonstration test at a British Petroleum site in Prudhoe Bay, Alaska. The standard MS5002 gas turbine is equipped with a conventional, swirl stabilized diffusion flame combustion system. The twelve standard combustors in an MS5002 turbine are cylindrical cans, approximately 27 cm (10.5 in.) in diameter and 112 cm (44 in.) long. A small, annular, vortex generator surrounds the single fuel nozzle that is centered at the inlet to each can. The walls of the cans are louvered for cooling, and contain an array of mixing and dilution holes that provide the air needed to complete combustion and dilute the burned gas to the desired turbine inlet temperature. The new, reduced NO_x emissions combustor (referred to as a ''lean head end,'' or LHE, combustor) retains all of the key features of the conventional combustor; the only significant difference is the arrangement of the mixing and dilution holes in the cylindrical combustor can. By optimizing the number, diameter, and location of these holes, NO_x emissions were substantially reduced. The materials of construction, fuel nozzle, and total combustor air flow were unchanged. The differences in NO_x emissions between the standard and LHE combustors, as well as the variations in NO_x emissions with firing temperature, were well correlated using turbulent flame length arguments. Details of this correlation are also presented. [S0742-4795(00)01602-1]

Introduction

The simple cycle MS5002 gas turbine is a mechanical drive model which is widely used in pumping applications. The MS5002 turbine has two shafts (a high pressure turbine powers the air compressor and a low pressure turbine drives the desired load), a pressure ratio of about 8.5:1, a compressor discharge temperature of about 290°C (555°F), and a net power output of about 28 MW. NO_x emissions from an unabated, natural gas fired MS5002B turbine equipped with standard combustors are about 100 ppmv (on a dry, 15 percent O_2 basis) at base load and ISO conditions. The base load combustor exit temperature for an MS5002B is 953°C (1747°F) at ISO conditions. The MS5002C turbine is an uprated version of the MS5002B unit with a 39°C (70°F) increase in firing temperature.

Increasingly stringent environmental regulations continue to drive emissions reductions from almost all combustion turbines. Dry low NO_x (DLN) combustion systems (that is, systems that do not require water or steam injection) remain one of the most popular methods of reducing emissions, because of the demonstrated potential for high reliability, minimal impact on turbine performance, and extremely low emissions. These systems routinely achieve emissions of 25 ppmv NO_x (on a dry, 15 percent O_2 basis) or less, usually through lean premixing of the fuel and air to eliminate high temperature, stoichiometric combustion zones. One drawback is that lean premixed combustion systems are often more complex and, therefore, more costly than the older style, diffusion flame combustors they replace.

Although DLN combustors are generally preferred for new units, there are applications in which the low emissions (and high cost) of lean premixed combustion systems are not essential. For example, when modifying an existing turbine to increase turbine power output and/or efficiency (often by increasing the pressure ratio and/or turbine inlet temperature), frequently the only requirement is that emissions do not increase after the modifications. Increasing the pressure ratio and/or turbine inlet temperature will tend to increase NO_x emissions, but since the available modifications to existing units are often relatively minor, the resulting increases in emissions are typically small (10–15 percent). In these situations, there exists a need for low cost combustion system modifications with relatively modest emissions reductions.

To fill this need, GE has been developing lead head end (LHE) combustors. Although somewhat similar in appearance to the standard combustors they replace, NO_x emissions from LHE combustors are about 40 percent lower. Nevertheless, combustion occurs in a swirl-stabilized turbulent diffusion flame in both combustors.

The essence of the LHE concept is best understood by comparing the standard and LHE MS5002 combustors. The MS5002 turbine is equipped with twelve cylindrical can-type combustors (see Fig. 1). Each standard (and LHE) combustor is approximately 27 cm (10.5 in.) in diameter and 112 cm (44 in.) long. A small, annular, vortex generator surrounds the single fuel nozzle that is centered at the inlet to each can. The walls of the cans are louvered for cooling, and contain an array of mixing and dilution holes that provide the air needed to complete combustion and dilute the burned gas to the desired combustor exit temperature.

The MS5002 LHE combustor retains all of the key features of the conventional combustor; the only significant difference is the

Contributed by the International Gas Turbine Institute (IGTI) of THE AMERICAN SOCIETY OF MECHANICAL ENGINEERS for publication in the ASME JOURNAL OF ENGINEERING FOR GAS TURBINES AND POWER. Paper presented at the International Gas Turbine and Aeroengine Congress and Exhibition, Indianapolis, IN, June 7–10, 1999; ASME Paper 99-GT-58. Manuscript received by IGTI March 9, 1999; final revision received by the ASME Headquarters January 3, 2000. Associate Technical Editor: D. Wisler.

Copyright © 2000 by ASME

Downloaded 02 Jun 2010 to 171.66.16.119. Redistribution subject to ASME license or copyright; see http://www.asme.org/terms/Terms_Use.cfm

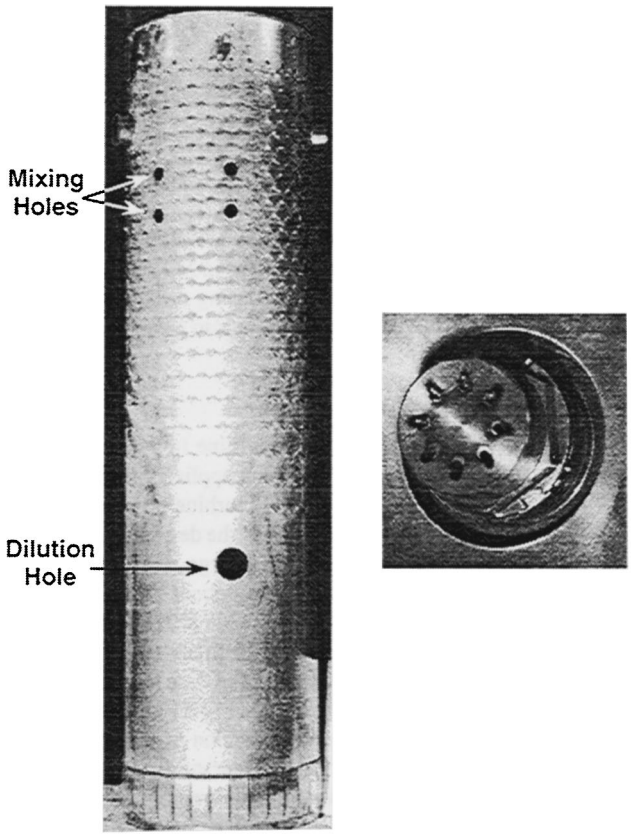

Fig. 1 Standard MS5002 combustor liner (left) and gas fuel nozzle (right)

arrangement of the mixing and dilution holes in the cylindrical combustor can. The number and diameter of the mixing holes have been increased; both the mixing holes and the dilution holes have been moved closer to the fuel nozzle, resulting in a more fully aerated diffusion flame. This reduces both the turbulent flame length and the time in the flame spent at stoichiometric conditions, thereby reducing NO_x emissions. For a given firing temperature, the total combustor air flow and the overall fuel/air ratio in the combustor are unchanged.

Development of an LHE combustor for the MS5002 turbine began in early 1997. After a series of laboratory tests at GE Corporate Research and Development, a turbine test was successfully conducted in September 1997 at a British Petroleum site in Prudhoe Bay, Alaska. To minimize unit-to-unit variation, the same turbine was tested with both standard combustors and LHE combustors. LHE combustors are now being developed for the simple cycle MS3002 turbine series.

Laboratory Testing and Results

The laboratory test stand used for development of the MS5002 LHE combustor is shown in Fig. 2 and has been described previously [1]. The combustor liner is housed in a 40.5 cm (16 in.) diameter pressure vessel, which is supplied with up to 7.3 kg/s (16 lb_m/s) of preheated, non-vitiated, oil-free air. Air enters the vessel through 24 holes uniformly distributed around the circumference of an air distribution plenum. The air flows over a simulated transition piece and continues upstream, towards the combustor liner and fuel nozzle, mimicking the reverse-flow configuration of the MS5002 turbine. The vessel pressure is set by an orifice plate which has an effective area approximately equal to one-twelfth (since there are 12 combustors) of the total first stage nozzle area in an MS5002 turbine. The backpressure orifice is cooled by a water spray injected into the exhaust gas just upstream of the orifice. Exhaust gas is sampled with an uncooled stainless steel probe located upstream of the water spray and analyzed for CO, CO_2, O_2, and NO_x with continuous emissions analyzers. The gas sample probe extends across a diameter of the duct, and has inlet holes equally spaced along its entire length. Using this arrangement, the sampled gas represents an integrated average across the duct.

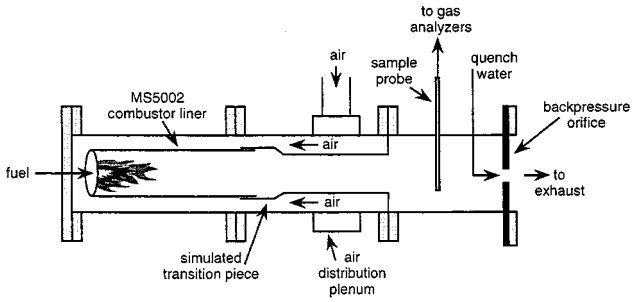

Fig. 2 The laboratory MS5002 combustor test stand

Results from laboratory tests of the standard and LHE MS5002 combustors are shown in Figs. 3 and 4. Each combustor was tested at two different total air flow rates and pressures, because the total air flow through an MS5002 combustor (about 9.5 kg/s, or 21 lb_m/s at base load) exceeds the capacity of the laboratory air compressors. The variations in air flow between the lab tests of the standard and lean head end combustors are due to day-to-day variations in the settings of the laboratory air compressors. Since lab emissions must be scaled to full pressure regardless of the air

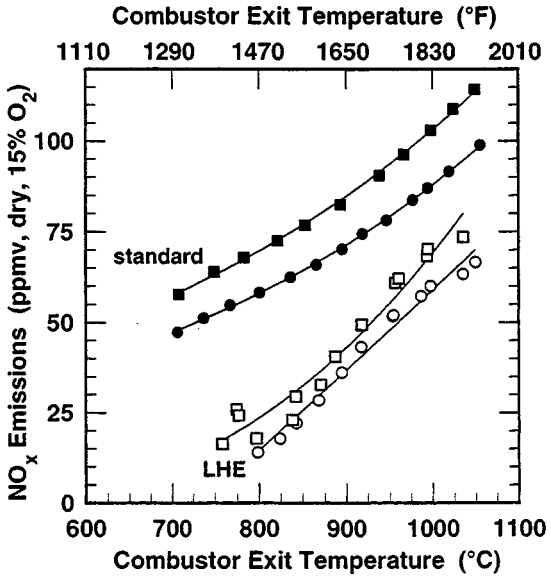

Symbol	Combustor	Air Flow (kg/s)	Pressure (bar)
■	standard	5.4	5.0
●	standard	3.3	3.1
□	LHE	6.0	5.4
○	LHE	4.2	3.8

Fig. 3 Laboratory measurements of NO_x emissions from standard and LHE combustors at reduced total flows. Combustion air temperature=294±3°C for all points. Combustor exit temperature for the MS5002B turbine is 953°C at base load ISO conditions.

Downloaded 02 Jun 2010 to 171.66.16.119. Redistribution subject to ASME license or copyright; see http://www.asme.org/terms/Terms_Use.cfm

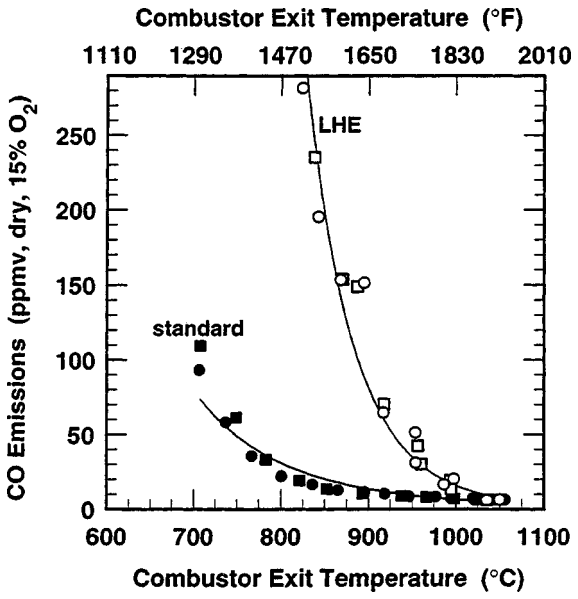

Fig. 4 Laboratory measurements of CO emissions from standard and LHE combustors at the same conditions as shown in Fig. 3

Table 1 Field and laboratory natural gas compositions

Species	Concentration (mole %)	
	Field Test	Laboratory
N_2	0.6	0.6
CH_4	76.0	95.8
CO_2	12.2	0.7
C_2H_6	6.2	2.2
C_3H_8	3.2	0.7
isobutane	0.4	<0.1
n-butane	0.9	<0.1
isopentane	0.2	<0.1
n-pentane	0.2	<0.1
C_6+	0.1	<0.1
Higher Heating Value (kJ/kg)	40,650	53,700

flow, no attempt was made to exactly duplicate the air flow from day to day. In general, we find laboratory NO_x emissions are proportional to P^n, where P is the absolute pressure and $0.3<n<0.5$. Through testing at two different air flow rates and pressures, we can determine the pressure exponent n for each combustor, and scale lab NO_x emissions to full flow and pressure. This result in not surprising; Lefebvre [2] recently summarized several studies in which NO_x from diffusion flame combustors was found to be proportional to P^n. Laboratory CO emissions are generally found to be insensitive to total flow rate and pressure, and do not require scaling.

Figure 3 shows that NO_x emissions decrease as the fuel flow and combustor exit temperature decrease. This is typical behavior for diffusion flame gas turbine combustors. At the base load combustor exit temperature for an MS5002B turbine (953°C or 1747°F at ISO conditions) and at similar pressures, lab NO_x emissions decreased from about 94 ppmv (dry, 15 percent O_2) for the standard combustor to about 58 ppmv (dry, 15 percent O_2) for the LHE combustor, a decrease of 38 percent. The percent reduction in NO_x emissions was even larger at part load conditions. A regression analysis of the data in Fig. 3 showed that NO_x emissions from the standard combustor were proportional to $P^{0.36}$, while NO_x emissions from the LHE combustor were proportional to $P^{0.40}$.

CO emissions from laboratory tests of the standard and LHE combustors are shown in Fig. 4. As expected, CO increases as the fuel flow and combustor exit temperature decrease. LHE CO emissions were substantially higher than CO emissions from the standard combustor at part load conditions, but were similar at base load MS5002C conditions. Figure 4 also shows that laboratory CO emissions are insensitive to the total air flow rate and pressure.

Field Testing and Results

The first field test of a simple cycle, natural gas fired MS5002 turbine equipped with LHE combustors was conducted during September, 1997, at a British Petroleum site in Prudhoe Bay, Alaska. An MS5002B turbine equipped with standard combustors was tested just before a scheduled outage. LHE combustors were installed during the outage, and the same unit was tested again just after being restarted. During both tests, data points were collected at both base load and part load conditions. The lower load limit was determined by the operating limits of the load compressor being driven by the MS5002B turbine, not by the turbine itself. Turbine operating parameters such as compressor inlet temperature, compressor discharge temperature, fuel flow rate, etc., were collected from the turbine data logging system. After the tests were completed, these parameters and the measured natural gas composition at the site (see Table 1) were used to calculate the combustor exit temperature for each field test point.

As might be expected from the lean head end design, the fuel flow rate required for ignition increased by approximately 5 percent after the LHE combustors were installed. No problems with lean blow out, crossfiring, or stability were detected during startup or acceleration. Part load and base load operations were also uneventful.

A gas sample probe was inserted into an existing flanged port on the turbine exhaust stack and positioned along a stack diameter. The sample probe had 3 mm (1/8 in.) diameter inlet holes, spaced approximately 30 cm (12 in.) apart, along its entire length. In this manner the gas sample approximated an integrated average across the exhaust stack. The sample gas was dried and sent to a portable gas analyzer (an Environmental Equipment, Inc. IMR 2800-P) which measured concentrations of CO, O_2, NO, and NO_2. Results from the field tests are shown in Figures 5, 6, and 7.

As expected from the laboratory tests, base load NO_x emissions from the LHE combustor were about 36 percent lower than NO_x emissions from the standard combustor, with the percent reduction increasing at part load conditions (see Fig. 5). The dashed lines in Fig. 5 represent the NO_x emissions expected in the field, based upon the laboratory data from the standard and LHE combustors. Reduced pressure lab NO_x emissions were first scaled to full field pressures using the P^n pressure dependence determined in the lab tests. Additional corrections were then applied to account for the differences in combustion air temperature and fuel composition between the lab and the field.

To apply these corrections, the stoichiometric flame temperature was calculated for each lab and field test point. Flame temperatures were calculated using *CET89*, the NASA chemical equilibrium code [3]. Stoichiometric flame temperatures were calculated because in an diffusion flame, most of the NO_x can be assumed to have formed through the thermal NO_x reaction pathway at the stoichiometric fuel/air interface. If this assumption is correct, the rate of NO_x formation should follow an Arrhenius-type rate expression of the form:

Downloaded 02 Jun 2010 to 171.66.16.119. Redistribution subject to ASME license or copyright; see http://www.asme.org/terms/Terms_Use.cfm

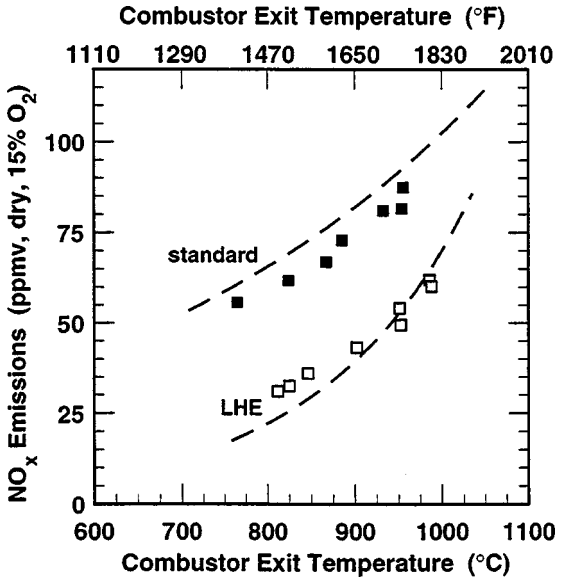

Fig. 5 NO_x emissions from an MS5002B turbine equipped with standard and LHE combustors. Compressor discharge temperature=269±9°C for all points. Symbols represent field measurements, while dashed lines represent expected values, based on laboratory measurements corrected to field fuel composition, pressure, and compressor discharge temperature.

$$\frac{d}{dt}[\mathrm{NO}_x] \propto \exp\left\{\frac{-E_{\mathrm{act}}}{RT_{\mathrm{stoic}}}\right\}, \tag{1}$$

where

$d/dt[\mathrm{NO}_x]$ = NO_x formation rate [moles/(unit volume) (time)]
E_{act} = activation energy for thermal NO_x formation [energy/mole],
R = ideal gas constant [energy/(mole) (K)], and
T_{stoic} = stoichiometric flame temperature [K].

Assuming the residence time in the flame zone is the same in both the lab and the field, Eq. 1 can be used to derive an expression relating the difference in NO_x emissions between the lab and the field to the difference in stoichiometric flame temperature:

$$\frac{\mathrm{NO}_{x,\mathrm{field}}}{\mathrm{NO}_{x,\mathrm{lab}}} = \frac{\exp\{-E_{\mathrm{act}}/RT_{\mathrm{stoic,field}}\}}{\exp\{-E_{\mathrm{act}}/RT_{\mathrm{stoic,lab}}\}}. \tag{2}$$

Rearranging (2) gives

$$\mathrm{NO}_{x,\mathrm{field}} = \mathrm{NO}_{x,\mathrm{lab}} \exp\left\{\frac{-E_{\mathrm{act}}}{R}\left[\frac{T_{\mathrm{stoic,lab}} - T_{\mathrm{stoic,field}}}{T_{\mathrm{stoic,lab}} \times T_{\mathrm{stoic,field}}}\right]\right\}. \tag{3}$$

Equation 3 was used to project field test NO_x emissions from the laboratory measurements (the dashed lines in Fig. 5). E_{act} was taken to be 76 kcal/mole based on Hanson and Salimian's 1984 review [4].

At the same combustor exit temperature, stoichiometric flame temperatures during the field test were 25–35°C (45–60°F) lower than stoichiometric flame temperatures in the lab. The difference was due in part to the lower compressor discharge temperature in the field (due to the low ambient temperature), and in part due to the lower heating value of the field test natural gas (see Table 1). Figure 5 shows that after applying corrections for pressure and stoichiometric flame temperature, the overall agreement between the lab and field NO_x measurements is fairly good.

Figure 6 shows that most of the emitted NO_x was in the form of NO at base load, with the fractional contribution of NO_2 increasing at part load conditions. This result was not surprising, since CO emissions also increase at part load. Recent studies (e.g., [5]) have indicated that if significant concentrations of CO are present, NO can convert into NO_2 relatively rapidly at typical turbine exhaust temperatures. CO emissions measured during the field test are shown in Fig. 7. Comparing Figs. 4 and 7 shows that the laboratory test stand slightly over-predicts field CO emissions. This over-prediction may be caused by differences in the time-temperature history of the burned gas downstream of the combustor. In the lab, the burned gas is rapidly quenched in the gas sample probe. There may be a greater opportunity for CO burnout to occur during the initial stages of expansion in the turbine than in the gas sample probe.

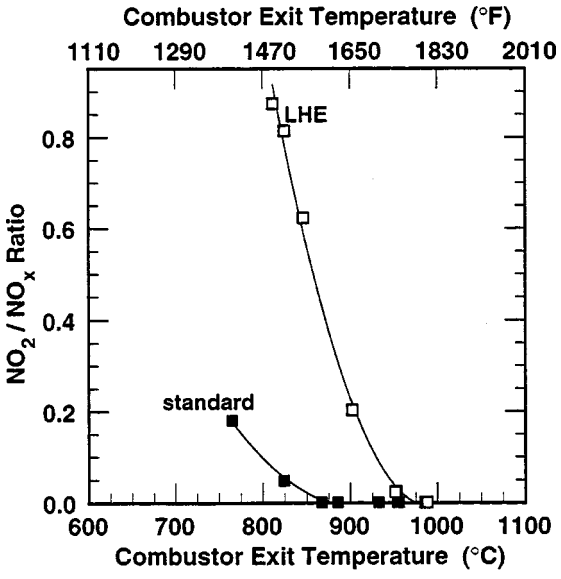

Fig. 6 Ratio of NO_2/NO_x in the MS5002B field test exhaust gas at the same conditions as shown in Fig. 5

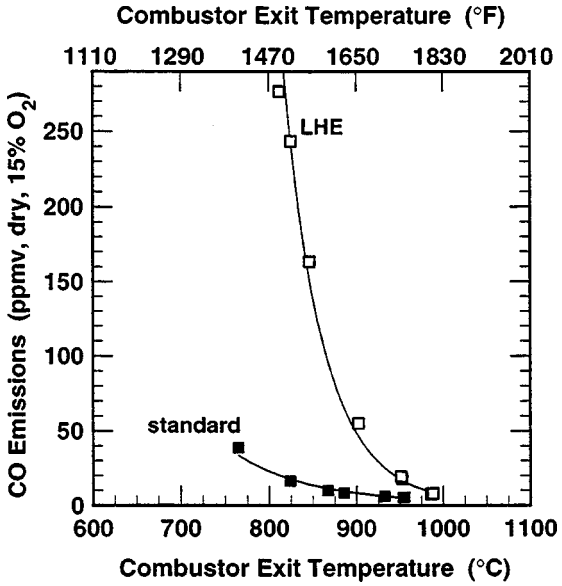

Fig. 7 CO emissions from an MS5002B turbine equipped with standard and LHE combustors at the same conditions as shown in Figs. 5 and 6

Discussion

The LHE MS5002 combustor liner design demonstrates the trade-off between NO_x emissions reductions and increases in CO

Downloaded 02 Jun 2010 to 171.66.16.119. Redistribution subject to ASME license or copyright; see http://www.asme.org/terms/Terms_Use.cfm

emissions. At a given firing temperature, the standard and LHE combustors have the same overall fuel/air ratio, but different fuel/air ratios in the primary zone (that is, the zone within the combustor that is closest to the fuel nozzle). Increasing primary zone aeration decreases NO_x emissions but also increases CO emissions. Additional increases in primary zone aeration, beyond the LHE design presented here, would begin to significantly increase base load CO emissions. In this regard, the LHE MS5002 combustor represents a design optimized for the minimum possible NO_x emissions with negligible increase in base load CO emissions.

To aid in the development of LHE combustors for other turbines, we have developed a semi-empirical model which relates liner features to NO_x emissions. This model can be used as a tool for rapidly evaluating the impact of combustor liner design alternatives on NO_x emissions. The starting point for the model is the well known relationship (e.g., [6]) between flame length (L_f), fuel flow rate (W_{fuel}), and primary air flow rate ($W_{\text{primary air}}$) for a confined, turbulent diffusion jet flame:

$$L_f \propto \frac{W_{\text{fuel}}}{W_{\text{primary air}}}. \tag{4}$$

The key hypotheses in the model are: (1) most of the NO_x is formed at the stoichiometric fuel/air interface, and (2) residence time in the stoichiometric flame zone is proportional to flame length. If these hypotheses are correct, then we should be able to infer a stoichiometric flame zone residence time (τ) from the measured NO_x emissions. Furthermore, this residence time should be proportional to fuel flow rate and inversely proportional to the primary air flow rate.

The first step in applying the model is to infer τ from the NO_x emissions measured in the lab. NO_x formation rates in stoichiometric flame zones were estimated by calculating NO_x emissions from stoichiometric, perfectly stirred reactors (PSRs) at the same pressure and inlet temperature. PSR calculations were performed using the Chemkin II package of programs and subroutines [7,8] and the set of ~250 elementary chemical reactions recommended by Michaud et al. [9]. The calculated relationship between PSR residence time and NO_x emissions for one set of lab conditions (the solid squares ■ in Figs. 3 and 4) is shown in Fig. 8. Using this approach, a residence time τ can be found that corresponds to each data point shown in Fig. 3.

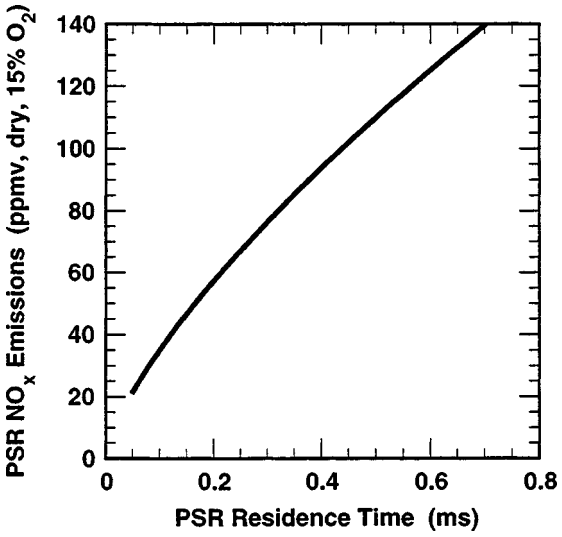

Fig. 8 Calculated NO_x emissions from a stoichiometric PSR for the high air flow rate, standard combustor conditions shown in Fig. 3 (P=5.0 bar, combustion air temperature =294°C)

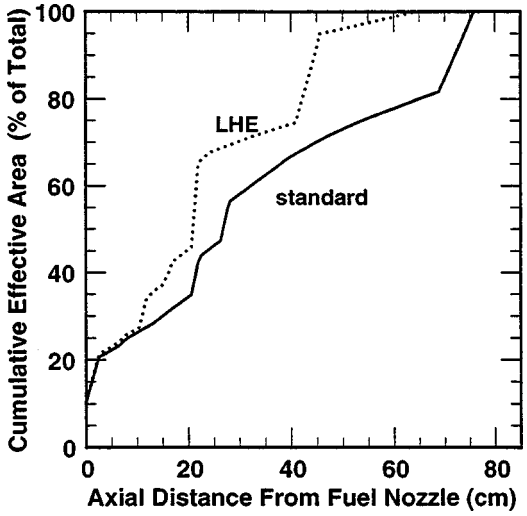

Fig. 9 Axial distribution of effective area in the standard and LHE MS5002 combustor liners

The second step in applying the model is to determine the primary air flow rate. Figure 9 shows the axial distribution of effective area, expressed as a percentage of the total effective area, for both the standard and LHE combustors. Effective areas of distinct liner features (louvers, mixing holes, etc.) were measured separately in a flow stand at atmospheric pressure and temperature. The cumulative effective area at each axial location was then determined by a simple linear combination of the liner features and open areas upstream of that location. The step increases in effective area shown in Fig. 9 correspond to mixing holes and dilution holes. The gradual increases in effective area in other portions of the curves correspond to regions of the liner with louvers, but no holes. For reasons that will be shown below, the primary air will be defined as the air that enters the liner within one combustor diameter (27 cm or 10.5 in.) of the fuel nozzle. With this definition, primary aeration increased from about 51 percent for the standard combustor to about 69 percent for the LHE combustor. Using this definition, and the known test conditions, $W_{\text{fuel}}/W_{\text{primary air}}$ can be calculated for each data point shown in Fig. 3.

Figure 10 shows the resulting linear correlation between residence time τ and $W_{\text{fuel}}/W_{\text{primary air}}$ for the standard and LHE combustor laboratory test NO_x data. The correlation is remarkably good ($R^2=0.99$) if primary air is defined as described above. Figure 11 shows the value or R^2 that would be calculated for a range of definitions of the primary zone. The model is most nearly linear, as predicted by the hypotheses outlined above, when the primary zone is defined as the region of the combustor within one combustor diameter (27 cm or 10.5 in.), of the fuel nozzle.

One somewhat surprising observation from this model is that a single definition of primary zone is suitable for both the standard and LHE combustors. Since the same definition of the primary zone is acceptable for both combustors, the proportionality constant implied by Eq. 4 is about the same for both combustors. Significant changes in the number, location, and diameter of the holes in the liner, especially holes located in the primary zone, might be expected to lead to different values of this proportionality constant for each combustor. Figure 10 shows that this is not the case, and the modeling approach outlined here is relatively insensitive to these aerodynamic difference.

The value of this model is that by measuring NOx emissions from a single liner design over a range of fuel flow rates, the effect of varying the hole diameter and location (and, therefore, the primary zone aeration) can also be evaluated. Other, more radical liner modifications would probably not be well fit with this

Downloaded 02 Jun 2010 to 171.66.16.119. Redistribution subject to ASME license or copyright; see http://www.asme.org/terms/Terms_Use.cfm

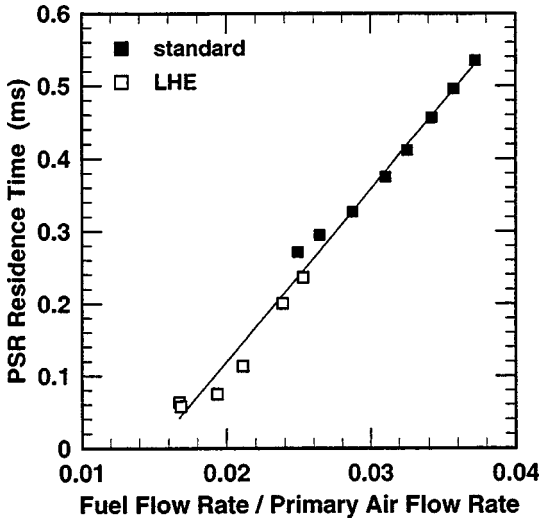

Fig. 10 Correlation between PSR residence time and $W_{fuel}/W_{primary\ air}$ when the primary air is defined as the air entering the combustor through the first 27 cm of the combustor liner. Data points correspond to the high air flow rate, standard and LHE combustor laboratory NO_x measurements shown in Fig. 3. The straight line is a best fit through the data. With this definition of primary air flow, $R^2=0.99$.

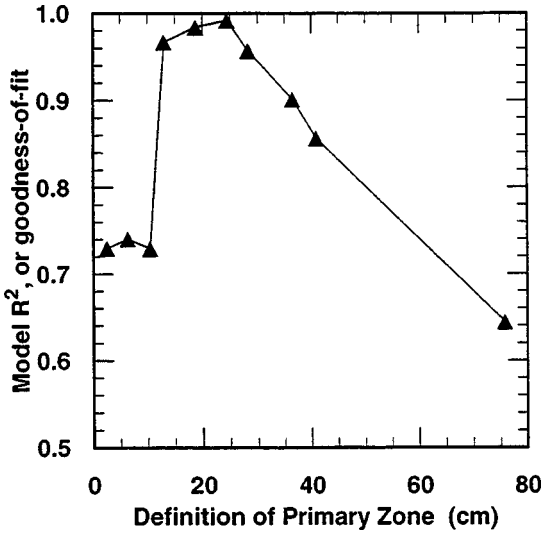

Fig. 11 Model goodness-of-fit for various definitions of the primary zone. The correlation between PSR residence time and $W_{fuel}/W_{primary\ air}$ is most nearly linear when the primary air is defined as the air entering the combustor through the first ~27 cm (10.5 in.) of the combustor liner. To generate this figure, the data points in Fig. 10 were recalculated with the range of primary zone definitions shown here, and then refit to a straight line.

approach. Modifications that resulted in significant changes to the aerothermal pattern, such as partially premixing the fuel and air, or dramatically changing the swirl number, would fall into this category.

The methodology for applying the model is fairly straightforward. Figures 8 and 10 can be used to estimate NO_x emissions from combustor liners with designs similar to the designs presented here, with primary aerations between 50 and 70 percent and over a range of combustor exit temperatures. First, the cumulative effective area at the 27 cm (10.5 in.) axial location must be estimated for the proposed design. $W_{fuel}/W_{primary\ air}$ can then be calculated. Figure 10 can then be used to estimate the residence time, and Fig. 8 indicates the expected NO_x emissions. Of course, if the pressure and/or inlet temperature are changed, then Figure 8 must be recalculated at the new conditions. This model is semi-empirical because the slope of the line in Figure 10 will also change if the pressure and/or inlet temperature change. Radical changes to the aerothermal pattern are also likely to change the slope of the line. Since the slope cannot be predicted a priori, NO_x emissions data will be required from at least one liner design, either standard or LHE, to determine the slope of the line.

Conclusions

A diffusion flame combustor has been developed with ~40 percent lower NO_x emissions than the standard combustor for the natural gas fired, simple cycle MS5002 turbine. This new lean head end (LHE) combustor design offers modest NO_x reductions with a negligible increase in base load CO emissions, and at a substantially lower cost than lean premixed combustors. The LHE combustor is intended primarily for the retrofit market, where moderate NO_x reductions are needed to offset NO_x increases that would otherwise occur when uprating an existing unit.

Reduced flow laboratory development tests are in reasonably good agreement with the results from the first field test. The differences in NO_x emissions between the standard and LHE combustors, as well as the variations in NO_x emissions with firing temperature, were well correlated with a semi-empirical model that was developed using turbulent flame length arguments. This model relates combustor liner features to NO_x emissions and can be used as a rapid design tool. GE is currently adapting the LHE combustor concept to the MS3002 series of gas turbines.

Acknowledgments

The authors gratefully acknowledge James F. Dalpe and Steven G. Goebel of GE Corporate Research and Development, as well as George W. Probert of GE Power Systems, for their assistance in completing the field tests in Prudhoe Bay, Alaska.

References

[1] Maughan, J. R., Luts, A., and Bautista, P. J., 1999, ''A Dry Low NO_x Combustor for the MS3002 Regenerative Gas Turbine,'' ASME Paper 94-GT-252.
[2] Lefebvre, A. H., 1999, *Gas Turbine Combustion, Second Edition*, Taylor & Francis, Philadelphia, PA.
[3] McBride, B., 1989, *CET89—Chemical Equilibrium with Transport Properties*, software available from COSMIC, The University of Georgia, Athens, GA.
[4] Hanson, R. K., and Salimian, S., 1984, ''Survey of Rate Constants in the N/H/O System,'' *Combustion Chemistry*, W. C. Gardiner, Jr., ed., Springer-Verlag, New York.
[5] Feitelberg, A. S., and Correa, S. M., 1999, ''The Role of Carbon Monoxide in NO_2 Plume Formation,'' ASME Paper 99-GT-53.
[6] Beér, J. M., and Chigier, N. A., 1983, *Combustion Aerodynamics*, Krieger Publishing, Malabar, FL. (1983).
[7] Glarborg, P., Kee, R. J., Grcar, J. F., and Miller, J. A., 1986, ''PSR: A FORTRAN Program for Modeling Well-Stirred Reactors,'' Sandia National Laboratories, Report SAND86-8209.
[8] Kee, R. J., Rupley, F. M., and Miller, J. A., 1989, ''Chemkin-II: A Fortran Chemical Kinetics Package for the Analysis of Gas-Phase Chemical Kinetics,'' Sandia National Laboratories, Report SAND89-8009.
[9] Michaud, M. G., Westmoreland, P. R., and Feitelberg, A. S., 1992, *Twenty-Fourth Symposium (International) on Combustion*, The Combustion Institute, Pittsburgh, PA, pp. 879–887.

Downloaded 02 Jun 2010 to 171.66.16.119. Redistribution subject to ASME license or copyright; see http://www.asme.org/terms/Terms_Use.cfm

Channel Height Effect on Heat Transfer and Friction in a Dimpled Passage

H. K. Moon
T. O'Connell
B. Glezer
Solar Turbines Incorporated,
San Diego, CA 92101

The heat transfer enhancement in cooling passages with dimpled (concavity imprinted) surface can be effective for use in heat exchangers and various hot section components (nozzle, blade, combustor liner, etc.), as it provides comparable heat transfer coefficients with considerably less pressure loss relative to protruding ribs. Heat transfer coefficients and friction factors were experimentally investigated in rectangular channels which had concavities (dimples) on one wall. The heat transfer coefficients were measured using a transient thermochromic liquid crystal technique. Relative channel heights (H/d) of 0.37, 0.74, 1.11, and 1.49 were investigated in a Reynolds number range from 12,000 to 60,000. The heat transfer enhancement (Nu_{HD}) on the dimpled wall was approximately constant at a value of 2.1 times that (Nu_{sm}) of a smooth channel over $0.37 \leqslant H/d \leqslant 1.49$ in the thermally developed region. The heat transfer enhancement ratio ($\overline{Nu}_{HD}/Nu_{sm}$) was invariant with Reynolds number. The friction factors (f) in the aerodynamically fully developed region were consistently measured to be around 0.0412 (only 1.6 to 2.0 times that of a smooth channel). The aerodynamic entry length was comparable to that of a typical turbulent flow ($x_o/D_h=20$), unlike the thermal entry length on dimpled surface which was much shorter ($x_o/D_h<9.8$). The thermal performance ($(\overline{Nu}_{HD}/Nu_{sm})/(f/f_{sm})^{1/3} \cong 1.75$) of dimpled surface was superior to that ($1.16 < (Nu_{HD}/Nu_{sm})/(f/f_{sm})^{1/3} < 1.60$) of continuous ribs, demonstrating that the heat transfer enhancement with concavities can be achieved with a relatively low-pressure penalty. Neither the heat transfer coefficient distribution nor the friction factor exhibited a detectable effect of the channel height within the studied relative height range ($0.37 \leqslant H/d \leqslant 1.49$). [S0742-4795(00)02802-7]

Background

Advanced cooling techniques are essential for further improvement of the gas turbine durability and efficiency. Sophisticated cooling designs are commonly found throughout engine hot sections such as combustor liners, turbine vanes, and blades. The type of heat transfer augmentor is selected by considering enhancement level, available pressure ratio, cost, and complexity. Most heat transfer augmentations affect the boundary layer in such a way as to make it thinner or partially break it, which often result in a higher flow resistance. Excessive pressure loss can result in a more complex air supply system and higher cost or its application may be totally precluded. The surface heat transfer enhancement using concavity (dimple) recently attracted interest due to its relatively low pressure-loss characteristics. Surface dimples are expected to promote turbulent mixing in the flow and enhance the heat transfer, as they behave as a vortex generator.

The aerodynamic effect of dimples has been studied by a number of investigators to reduce the drag coefficient of a golf ball. Bearman and Harvey [1] studied the balls with round dimples and hexagonal dimples, and stated their advantages over a smooth sphere. The same authors [2] conducted further investigations and were able to identify a specific Reynolds number range where a dimpled circular cylinder has a lower drag coefficient than a smooth cylinder. Kimura and Tsutahara [3] conducted numerical investigations for several types of circular arc cross sections. Gromov et al. [4] carried out flow visualizations and reported a partial recirculatory flow exists in the depression and some of the streamlines leave the depression.

Although the concept of using depression for heat transfer augmentation dates back to the early 1970's [5], the heat transfer data on dimpled surface are very limited and most of the previous studies have been conducted in Russia. Kesarev and Kozlov [6] conducted a convective heat transfer test with a single concavity. Their study was limited to the concavity inside surface and reported that the total heat flux was about a factor of 1.5 times that of a plane circle of the same diameter at a freestream turbulence level of 0.5 percent. This study therefore failed to address the heat transfer enhancement outside of the concavity. Afanasyev et al. [7] experimentally studied the friction and heat transfer in a dimpled channel and reported a 30 to 40 percent heat transfer enhancement without any appreciable effect on the hydrodynamic loss. This investigation, however, was very localized at mid point (outside of concavity) of a staggered dimpled plate. Terekhov et al. [8] concentrated on the surface within a concavity and concluded the existence of an optimum concavity depth. The potential gas turbine applications of concavity designs were recently mentioned by Schukin et al. [9] and later by Chyu et al. [10]. Schukin et al. [9] provided the limited data downstream of the single concavity in a diffuser channel. Chyu et al. [10] measured a local heat transfer distribution on a surface imprinted with a staggered array of two different shapes of concavities. Chyu et al. also measured pressure losses and concluded that the pressure losses were nearly one-half of the protruding elements. The effect of channel height on heat transfer and pressure losses, however, has not been addressed in the open literature and is experimentally investigated herein for the thermally and aerodynamically fully developed region.

Four different channel heights with a fixed concavity pattern on one side were investigated. The local heat transfer coefficients

Contributed by the International Gas Turbine Institute (IGTI) of THE AMERICAN SOCIETY OF MECHANICAL ENGINEERS for publication in the ASME JOURNAL OF ENGINEERING FOR GAS TURBINES AND POWER. Paper presented at the International Gas Turbine and Aeroengine Congress and Exhibition, Indianapolis, IN, June 7–10, 1999; ASME Paper 99-GT-163. Manuscript received by IGTI March 9, 1999; final revision received by the ASME Headquarters January 3, 2000. Associate Technical Editor: D. Wisler.

Copyright © 2000 by ASME

Downloaded 02 Jun 2010 to 171.66.16.119. Redistribution subject to ASME license or copyright; see http://www.asme.org/terms/Terms_Use.cfm

were measured with a transient thermochromic liquid crystal imaging system. The equivalent friction factor was measured using static taps and compared to that of a smooth channel.

Experimental Apparatus and Procedures

The local heat transfer coefficient was measured with a Thermochromic Liquid Crystal (TLC) technique. The present TLC technique, which is based on a transient heat transfer solution of the semi-infinite medium suddenly exposed to a convective boundary condition, has been previously used by a number of different investigators [11–15]. The basic methodology of a transient technique was also demonstrated with use of melting paint surface coatings [16–17].

Figure 1 shows a schematic of the test apparatus. Compressed air was filtered, dried, and monitored with a turbine flow meter. The plenum was equipped with a flow deflector to avert the incoming jet from the supply line reaching the channel inlet. The plenum is wedge-shaped in streamwise direction to avoid a sudden contraction at the inlet. The air is preheated to the desired temperature and diverted away from the test section until it reached steady state. A thermal transient is initiated by using a pneumatic 3-way valve to suddenly route the heated airflow through the test section. The pneumatic 3-way valve also triggered a ''time zero'' light on the test section for the image processing system. The image processing system, which included a Y-C camera (Cohu 82100) and a Silicon Graphics workstation (R4000SC), digitally recorded the images of the surface pixels as they experienced a color transition during the test. The composite signal was decomposed into red, green, and blue components. The time of color change to green at each point on the test surface was the measured quantity. Green color was chosen for its signal strength and sharpness. As the wall surface does not experience a pure step change in air temperature, the actual air temperature rise is represented by a superposed set of elemental steps in T_m and the fundamental solution is modified accordingly.

$$T_s - T_i = \sum_{i=1}^{N} U(\theta - \tau_i)\Delta T_m, \tag{1}$$

where

$$U(\theta - \tau_i) = 1 - \exp\left[\frac{h^2\alpha(\theta - \tau_i)}{k^2}\right] erfc\left[\frac{h\sqrt{\alpha(\theta - \tau_i)}}{k}\right]. \tag{2}$$

In the present experiments, separate air temperature profile measurements were conducted in a transient mode. From this air temperature profile data and the five thermocouples located in the spanwise direction at the upstream and one thermocouple downstream of two arrays of concavities (see Fig. 2) during the test, a mixed mean air temperature (T_m) was obtained.

The entire test section was constructed from a 1.27 cm thick transparent acrylic. The test surface was machined to have a staggered array of concavities as shown in Fig. 2. The test surface had a total of 15 rows of concavities. All the concavities had the same imprint diameter, depth and were equally spaced. Heat transfer coefficients were measured in the vicinity of thirteenth and fourteenth rows of concavities to insure a fully developed thermal boundary layer. Chyu et al. [10] took data at the downstream of the third row and claimed a thermally fully developed flow. Four different channel heights (2.5, 1.9, 1.3, and 0.6 cm) were tested while its channel width and length were kept at 9.6 cm and 33.0 cm, respectively. Only one side of the channel was equipped with concavities during the entire investigation. The test surface first was coated with a TLC (Hallcrest, R35C1W) and then spray-painted black (Hallcrest, BB-G1) to provide an optimum contrasting visual background for the TLC color display. For the pressure loss experiments, separate 127 cm long test sections were constructed and instrumented with static taps in 10.2 cm intervals. The static taps, therefore, were placed on the channel side-wall, not in particular locations relative to the dimple rows.

A diffuse-light source was mounted on the camera to eliminate view-angle dependency of the TLC color transition as discussed by Herrold and Wiegel [18]. Green color to temperature calibration was done on a copper coupon with TLC coating at the rep-

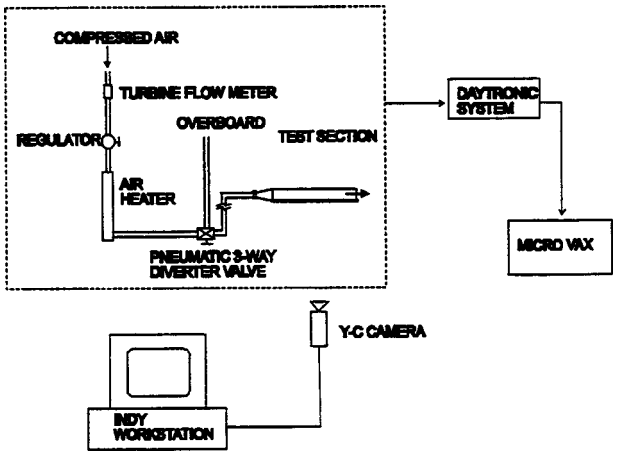

Fig. 1 Schematic view of test apparatus

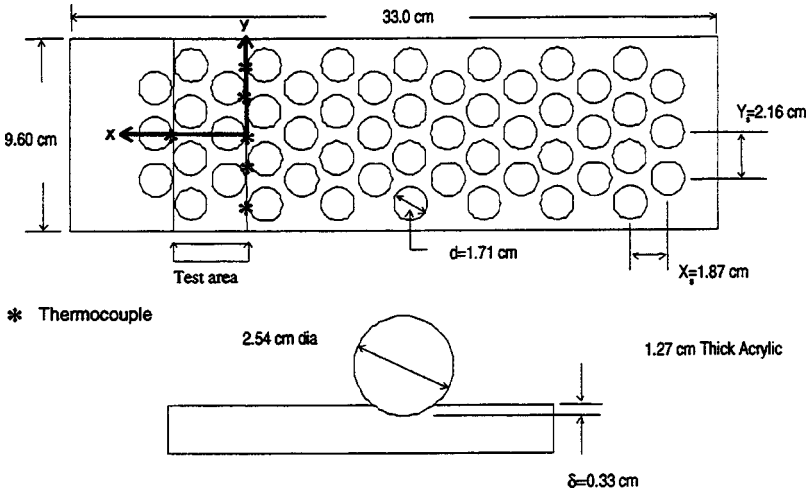

Fig. 2 Schematic view of dimpled side

Downloaded 02 Jun 2010 to 171.66.16.119. Redistribution subject to ASME license or copyright; see http://www.asme.org/terms/Terms_Use.cfm

resentative view angle at the beginning of each test. The experimental uncertainty for the present measurement of the average Nusselt number was within ±12 percent and was largest with the narrowest gap experiments due to their relatively high heat transfer coefficients (up to 964 w/m^2-°K). The heat transfer level (transient time) is directly related to the experimental uncertainty, as described by Höcker [19] who investigated the optimization of the transient TLC technique on error estimation in detail. Considering the air supply system stability and pressure transducer accuracy, the uncertainty in friction factors was estimated to be within ±10 percent. Uncertainties were calculated using the single sample methods of Kline and McClintock [20] and Moffat [21].

Results and Discussion

Figure 3 shows a typical air temperature profile within the channel gap at the middle of the twelfth and thirteenth rows of concavities. As expected, the air temperature is skewed toward the concavity side due to its high heat transfer rate. A typical Nusselt number distribution, which was reduced based on a local mixed mean temperature, is plotted in a projected view of the CCD camera as shown in Fig. 4. In order to help the understanding of the relative position, the concavities were overlaid on the same plot. It is clear that most of the heat transfer enhancement occurs outside of the concavities. The heat transfer enhancement is lowest on the concavity wall facing the streamwise direction and highest in the vicinity of the downstream rim (edge) of the concavity. The lowest heat transfer region ($Nu_{HD}<81$), which appears square-looking due to the camera resolution (pixels/area), is limited to a small area within the concavity. It is, therefore, supports Terekhov et al. [8] that even the average heat transfer coefficient within the concavity at $\delta/d=0.19$ (present design) is higher than that ($Nu_{sm}=81$, Dittus-Boelter correlation) of a smooth channel. The relative heat transfer rate from a smooth wall can be accessed from the surface area near the side wall. The heat transfer coefficient distribution exhibited a similar pattern throughout the studied H/d range ($0.37\leqslant H/d<1.49$) and Reynolds number range ($29000<Re_{HD}<56000$). This indicates that the heat transfer mechanism does not change significantly over the studied channel height range. In other words, the channel height needs to be further reduced before the opposite wall significantly affects heat transfer on the dimpled wall. Low heat transfer coefficients on the concavity floor indicate the possibility of recirculating flow covering a significant portion of the concavity. Three distinct contour fringes in the vicinity of the downstream edge as shown in Fig. 4

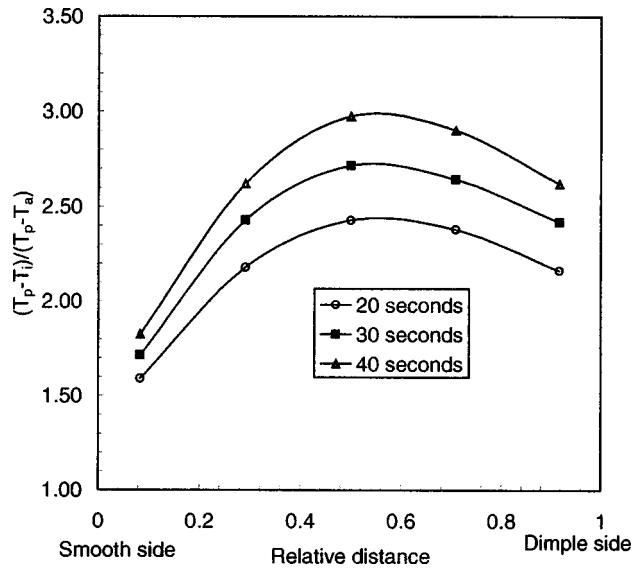

Fig. 3 Normalized air temperature profile

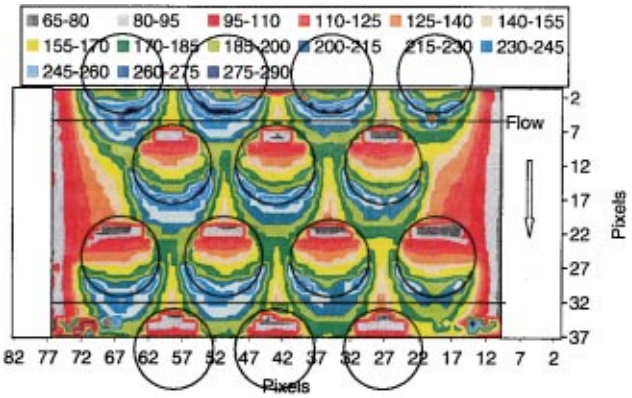

Fig. 4 Local Nusselt number (Nu_{HD}) distribution, $H/d=0.74$, $Re_{HD}=31216$

indicate the existence of secondary vortex streaks as discussed by Gromov et al. [4]. The central one may correspond to a reattachment point of the separated shear layer. Figures 5–8 show the streamwise-averaged Nusselt numbers over $0<x<2X_s$, plotted in the spanwise direction. The asymmetrical profiles in the spanwise direction, which became noticeably flat for a narrow channel height, were caused by the inlet flow profile. Although the inlet profile was not measured, it is expected to be somewhat asymmetrical even with a flow deflector in the plenum. The overall shape (parabolic) of streamwise-averaged Nusselt number distribution is similar to that of a typical rectangular channel flow. The lowest points of the streamwise-averaged Nusselt number distribution are aligned with a row of concavities and are due to a low heat transfer enhancement within the concavity. Despite seven concavity centers presented in the spanwise direction, only five distinct lowest points exist due to the effects of a lesser number of concavity edges (one instead of two) near the side walls and the side wall itself. The spanwise-averaged Nusselt numbers over $-2.2Y_s<y<2.2Y_s$, plotted in Figs. 9–12, show a lowest value at a quarter distance ($x/X_s=0.25$) within the concavity surface and a peak value just before downstream edge. This was resulted from the two high heat transfer locations on the concavity downstream

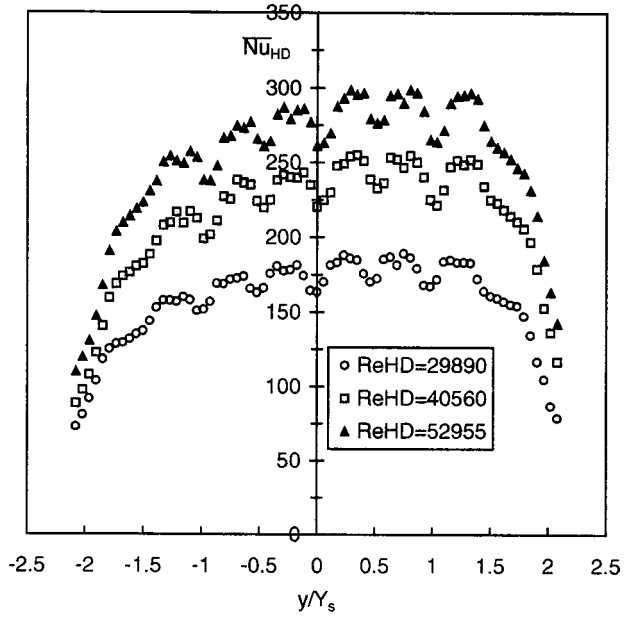

Fig. 5 Streamwise-averaged Nusselt number distribution, $H/d=1.49$

Downloaded 02 Jun 2010 to 171.66.16.119. Redistribution subject to ASME license or copyright; see http://www.asme.org/terms/Terms_Use.cfm

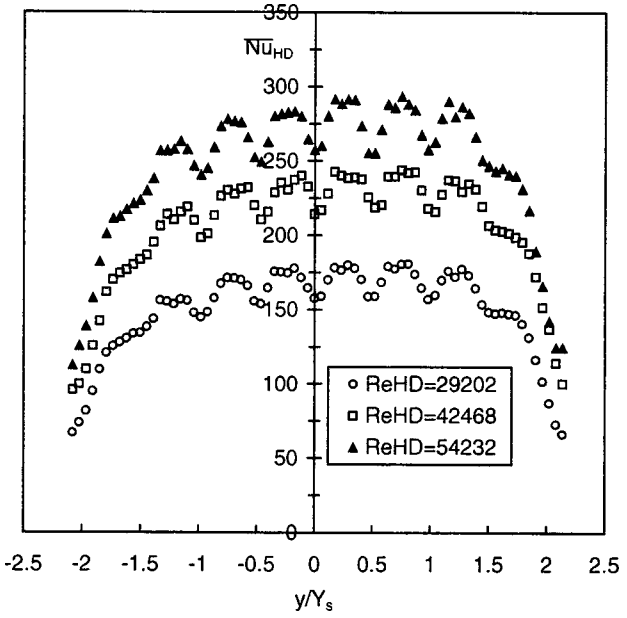

Fig. 6 Streamwise-averaged Nusselt number distribution, $H/d=1.11$

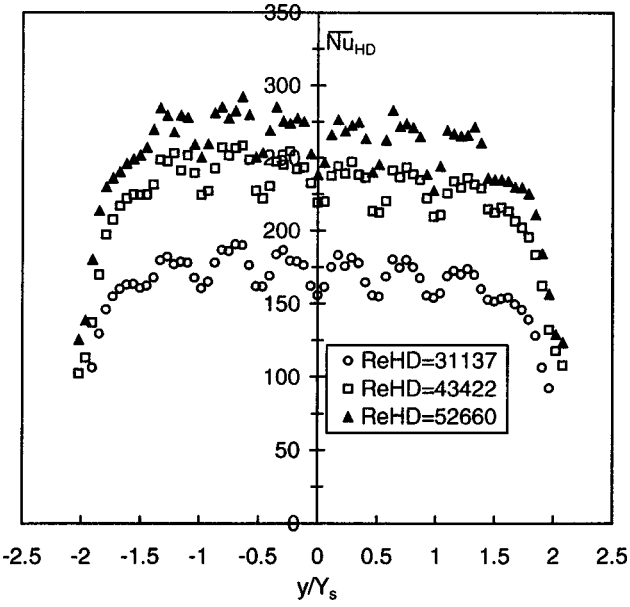

Fig. 8 Streamwise-averaged Nusselt number distribution, $H/d=0.37$

edge neighboring the central one. This consistent location of a peak value indicates that the basic flow structure is independent of the studied channel height and Reynolds number. As expected, the first peak which spanwise-averaged over the location with three concavities is consistently lower than the second peak which spanwise-averaged over the location with four concavities as shown in Figures 9–12. The present spanwise-averaged data shows rather a blunt shape of periodic data distributions compared to those of Chyu et al. [10]. This blunt periodic data distribution may have resulted from a difference in the spanwise spacing (Y_s) of the concavities in relation to the streamwise spacing (present $Y_s/X_s=1.15$ versus $Y_s/X_s=1.0$ Chyu et al. [10]). The heat transfer distribution near the lowest value, which corresponds to the concavity centers is directly related to the concavity depth (present $\delta/d=0.19$ versus 0.29 Chyu et al. [10]). The deeper concavity shows a sharper gradient in the heat transfer coefficient.

The overall average Nusselt numbers, which have accounted for the concavity area, are normalized to that of a smooth channel and are plotted as a function of Reynolds numbers in Fig. 13. It is clear from Fig. 13 that the normalized Nusselt number ($\overline{Nu}_{HD}/Nu_{sm}$) is not a function of Reynolds numbers at least in a range of $0.37 \leqslant H/d \leqslant 1.49$. The same data are plotted in Fig. 14 as a function of the relative channel height (H/d) to show that all the normalized Nusselt numbers are within 5 percent of their mean value of 2.1. The normalized Nusselt number and, therefore, the dominant heat transfer mechanism did not significantly change over $0.37 \leqslant H/d \leqslant 1.49$. Since the experimental uncertainty was 12

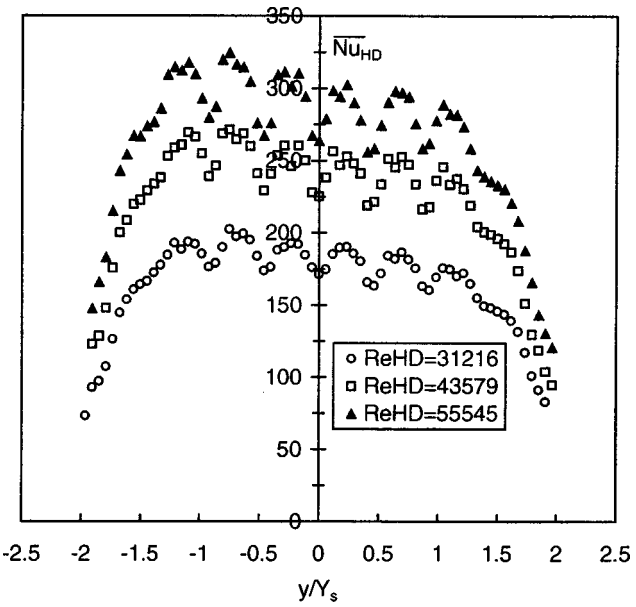

Fig. 7 Streamwise-averaged Nusselt number distribution, $H/d=0.74$

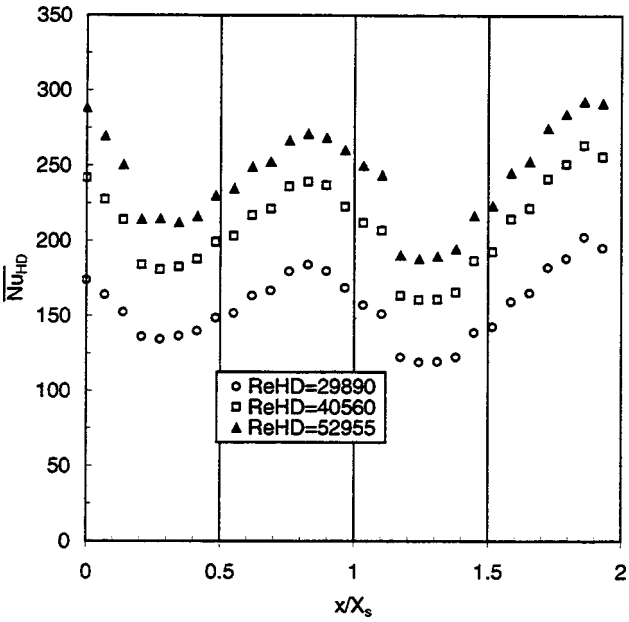

Fig. 9 Spanwise-averaged Nusselt number distribution, $H/d=1.49$

Downloaded 02 Jun 2010 to 171.66.16.119. Redistribution subject to ASME license or copyright; see http://www.asme.org/terms/Terms_Use.cfm

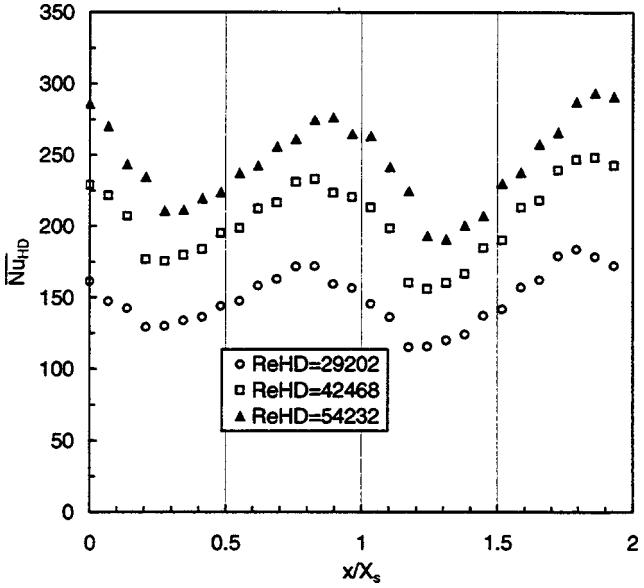

Fig. 10 Spanwise-averaged Nusselt number distribution, *H/d* = 1.11

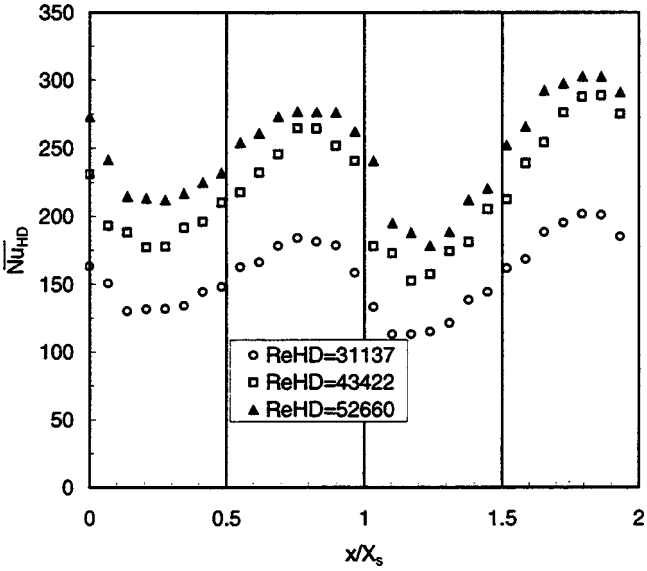

Fig. 12 Spanwise-averaged Nusselt number distribution, *H/d* = 0.37

percent, this also confirms that the data were obtained in a thermally fully developed region and that the repeatability was better than 5 percent. The thermal entry length, therefore, is shorter than the thirteenth row which corresponds to 9.8 times the hydraulic diameter for the largest studied channel height ($H/d = 1.49$). The relative heat transfer enhancement ($\overline{\mathrm{Nu}}_{HD}/\mathrm{Nu}_{sm}$) of 2.1 compared to 2.25 of Chyu et al. [10] may have resulted from a geometric difference in both the spanwise spacing (Y_s) of the concavities in relation to the streamwise spacing ($Y_s/X_s = 1.15$ versus $Y_s/X_s = 1.0$) and the concavity depth ($\delta/d = 0.19$ versus 0.29), although the difference is within the present experimental uncertainty (12 percent).

Some experiments were conducted with a further channel height decrease beyond the limit commonly considered as practical for the certain gas turbine cooling applications. The preliminary data indicated that a narrow channel height comparable to the dimple-depth resulted in a substantial heat transfer increase.

Figure 15 shows a typical static pressure distribution along the channel. The uneven distribution, especially more noticeable with higher Reynolds numbers, was caused by the static tap placements relative to the dimple rows as it consistently occurred at the same locations regardless of the flow rates (Reynolds numbers). More detailed measurements of static pressure distribution are beyond the present work scope. A least square fitted line was drawn through the data points and corresponding Darcy friction factors (f) were calculated. The Darcy friction factors for the fully developed region, which consistently occurred at a x_o/D_h of about 19, are plotted in Fig. 16. This demonstrates that the aerodynamic entrance length is comparable to that of a turbulent smooth channel flow unlike the thermal entrance length. The friction factors (f) are relatively constant at about 0.0412 regardless of the Reynolds number and channel height. The friction factors were nor-

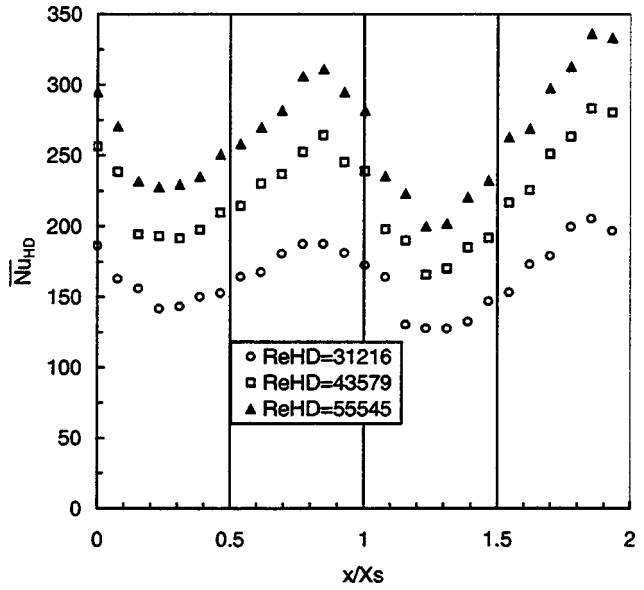

Fig. 11 Spanwise-averaged Nusselt number distribution, *H/d* = 0.74

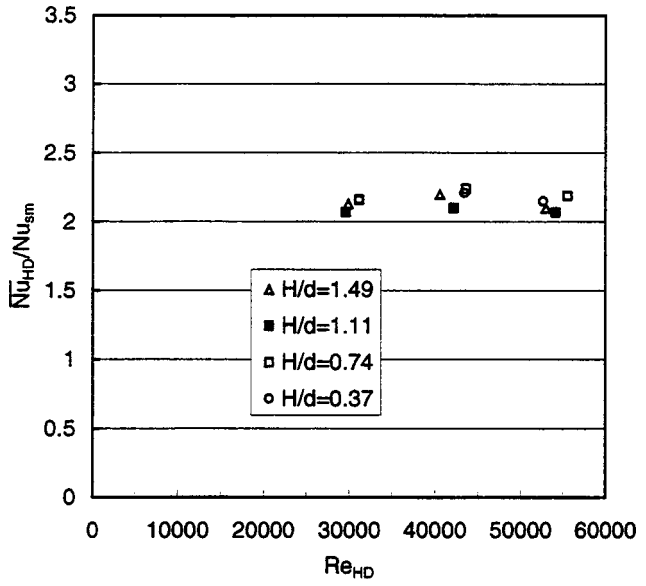

Fig. 13 Heat transfer enhancement with different Reynolds numbers

Downloaded 02 Jun 2010 to 171.66.16.119. Redistribution subject to ASME license or copyright; see http://www.asme.org/terms/Terms_Use.cfm

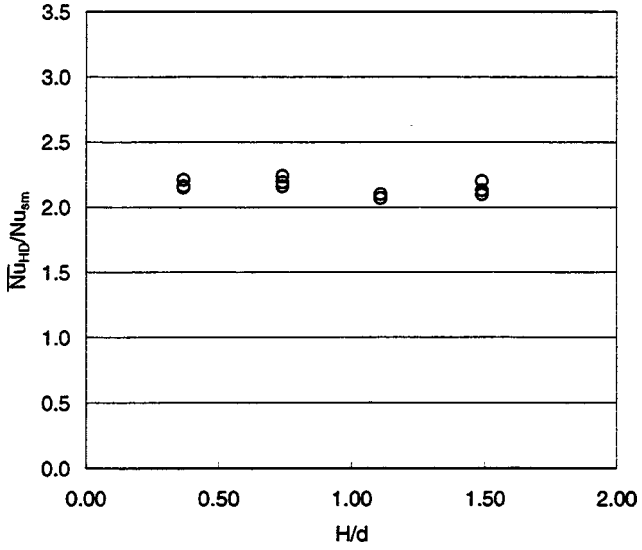

Fig. 14 Heat transfer enhancement with different channel heights

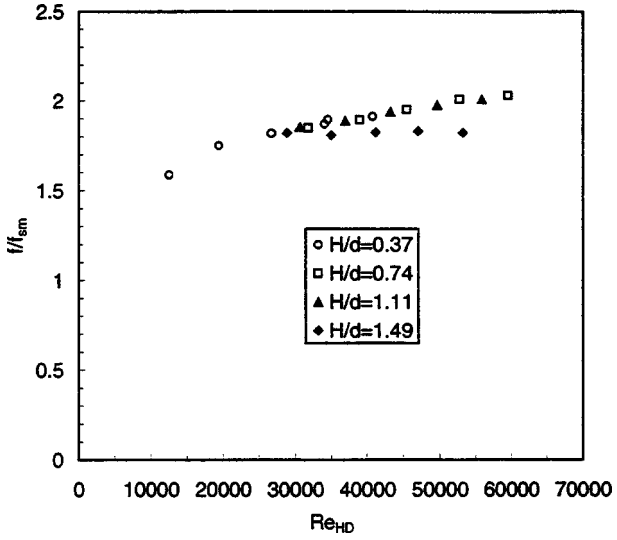

Fig. 17 Normalized friction factors

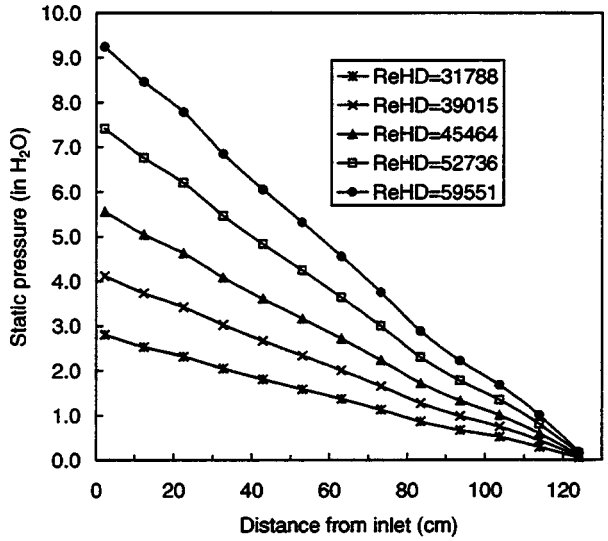

Fig. 15 Static pressure distribution, $H/d=0.74$

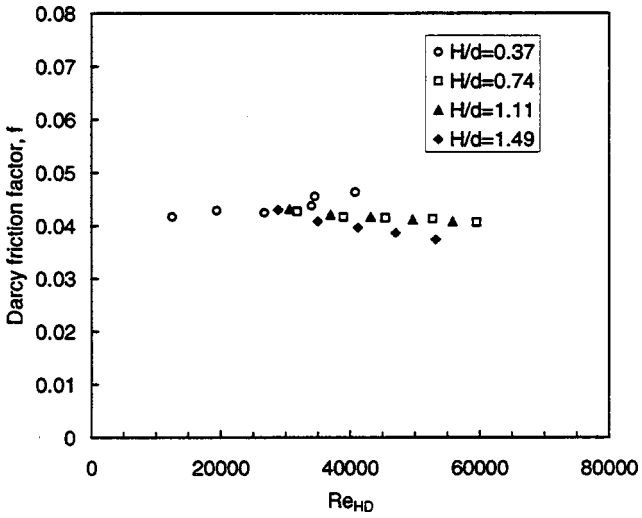

Fig. 16 Friction factors

malized to that (Moody Chart) of a smooth channel and plotted in Fig. 17. The average relative friction factors (f/f_{sm}) range from 1.6 to 2.0.

The present investigation resulted in a thermal performance $(\overline{Nu}_{HD}/Nu_{sm})/(f/(f_{sm})^{1/3})$ of 1.75, which is 38 percent higher than a 90 deg continuous rib and 13 percent higher than 60 deg continuous rib at a Reynolds number (Re_{HD}) of 40,000. Kizuka et al. [22] summarized the heat transfer studies on turbulence promoter ribs from different investigators [23–26] and plotted the Nusselt numbers and friction factors as a function of the Reynolds number. The 90 deg and 60 deg continuous rib data for the present comparisons were based on a P/e ratio of 10 and an e/D_h ratio of 0.04 to 0.1.

These findings are encouraging for the application of dimpled surface to gas turbine components such as combustor liner, certain airfoil areas, and turbine gas path structures.

Summary and Conclusions

The surface heat transfer augmentation with an array of concavities in a rectangular channel was experimentally investigated using a transient Thermochromic Liquid Crystal technique. Only one side of the rectangular channel had concavities during the study. The channel aspect ratio was varied, as well as Reynolds number. Corresponding friction factors were also measured. The heat transfer coefficients were measured in the thermally fully developed region and the friction factors were measured in the aerodynamically fully developed region. The principal conclusions of the present study are summarized as follows:

- The heat transfer enhancement occurs mostly outside of the concavities.
- The heat transfer enhancement is lowest on the upstream concavity wall and highest in the vicinity of the downstream rim (edge) of the concavity.
- The heat transfer coefficient distribution exhibited a similar pattern throughout the studied H/d range ($0.37 \leqslant H/d \leqslant 1.49$).
- The normalized Nusselt number ($\overline{Nu}_{HD}/Nu_{sm}$) is not a function of Reynolds number.
- The normalized Nusselt number ($\overline{Nu}_{HD}/Nu_{sm}$) is approximately constant at a value of 2.1 over $0.37 \leqslant H/d \leqslant 1.49$.
- The aerodynamic entrance length of a concavity-designed channel is comparable to that of a typical turbulent smooth channel flow.
- The friction factor is relatively independent of the Reynolds number and channel height.

Downloaded 02 Jun 2010 to 171.66.16.119. Redistribution subject to ASME license or copyright; see http://www.asme.org/terms/Terms_Use.cfm

• The high thermal performance $((\overline{\mathrm{Nu}}_{HD}/\mathrm{Nu}_{sm})/(f/f_{sm})^{1/3} \cong 1.75)$ of a dimpled channel makes its application attractive for the cooled turbine components where the pressure losses of other convective cooling techniques are unacceptable.

Nomenclature

d = concavity imprint diameter
D_h = hydraulic diameter
e = height of turbulence promoter rib
f = Darcy friction factor, $2D_h\Delta p/L\rho U^2$
f_{sm} = Darcy friction factor of smooth channel (Moody Chart)
h = heat transfer coefficient
H = channel height
K = thermal conductivity
L = length of the channel
P = pitch distance between turbulence promoter ribs
Δp = pressure drop
x = streamwise coordinate (see Fig. 2)
x_0 = streamwise distance from the inlet
y = spanwise coordinate (see Fig. 2)
T = temperature
U = mean velocity in the smooth channel
W = width of channel
X_s = streamwise distance between concavities
Y_s = spanwise distance between concavities
Nu_{HD} = local Nusselt number, hD_h/k
$\overline{\mathrm{Nu}}_{HD}$ = average Nusselt number, $\overline{h}D_h/k$
Nu_{sm} = smooth-channel Nusselt number
Re_{HD} = Reynolds number, $\rho UD_h/\mu$
α = thermal diffusivity
δ = concavity depth
μ = dynamic viscosity
θ = time
τ = time step

Subscripts

a = air
i = initial
m = mixed mean
p = plenum
s = surface

References

[1] Bearman, P. W., and Harvey, J. K., 1976, ''Golf Ball Aerodynamics,'' Aeronaut. Q., **27**, pp. 112–122.
[2] Bearman, P. W., and Harvey, J. K., 1993, ''Control of Circular Cylinder Flow by the Use of Dimples,'' AIAA J., **31**, No. 10, pp. 1753–1756.
[3] Kimura, T., and Tsutahara, M., 1991, ''Fluid Dynamic Effects of Grooves on Circular Cylinder Surface,'' AIAA J., **29**, No. 12, pp. 2062–2068.
[4] Gromov, P. R., Zobnin, A. B., Rabinovich, M. I., and Sushchik, M. M., 1986, ''Creation of Solitary Vortices in a Flow Around Shallow Spherical Depressions,'' Sov. Tech. Phys. Lett., **12**, No. 11, American Institute of Physics, New York, pp. 547–549.
[5] Kuethe, A. M., 1971, ''Boundary Layer Control of Flow Separation and Heat Exchange,'' US Patent No. 3,578,264.
[6] Kesarev, V. S., and Kozlov, A. P., 1993, ''Convective Heat Transfer in Turbulized Flow Past a Hemispherical Cavity,'' Heat Transfer-Sov. Res., **25**, No. 2, Scripta Technica Inc, pp. 156–160.
[7] Afnasyev, V. N., Chudnovsky, Ya. P., Leontiev, A. I., and Roganov, P. S., 1993, ''Turbulent Flow Friction and Heat Transfer Characteristics for Spherical Cavities on a Flat Plate,'' Exp. Therm. Fluid Sci., **7**, Elsevier Science Publishing Co., pp. 1–8.
[8] Terekhov, V. I., Kalinina, S. V., and Mshvidobadze, Y. M., 1995, ''Flow Structure and Heat Transfer on a Surface with a Unit Hole Depression,'' Russ. J. Eng. Thermophys., **5**, pp. 11–34.
[9] Schukin, A. V., Kozlov, A. P., and Agachev, R. S., 1995, ''Study and Application of Hemispherical Cavities for Surface Heat Transfer Augmentation,'' ASME Paper 95-GT-59.
[10] Chyu, M. K., Yu, Y., and Ding, H., 1997, ''Concavity Enhanced Heat Transfer in an Internal Cooling Passage,'' ASME paper 97-GT-437.
[11] Ireland, P. T., and Jones, T. V., 1985, ''The Measurement of Local Heat Transfer Coefficients in Blade Cooling Geometries,'' *Proceedings of AGARD Conference on Heat Transfer and Cooling in Gas Turbines*, CP. 390 Paper 28, Bergen.
[12] Vedula, R. I., and Metzger, D. E., 1991, ''A Method for the Simultaneous Determination of Local Effectiveness and Heat Transfer Distributions in Three Temperature Convection Situations,'' ASME Paper 91-GT-345.
[13] Camci, C., Kim, K., Hippensteele, S. A., and Poinsatte, P. E., 1993, ''Evaluation of Hue Capturing Based Transient Liquid Crystal Method for High-Resolution Mapping of Convective Heat Transfer on Curved Surfaces,'' ASME J. Heat Transfer, **115**, pp. 311–318.
[14] Yu, Y., and Chyu, M. K., 1996, ''Influence of a Leaking Gap Downstream of the Injection Holes on Film Cooling Performance,'' ASME Paper 96-GT-175.
[15] Ekkad, S. V., Zapata, D., and Han, J. C., 1995, ''Heat Transfer Coefficients Over a Flat Surface With Air and CO2 Injection Through Compound Angle Holes Using a Transient Liquid Crystal Image Method,'' ASME Paper 95-GT-10.
[16] Larson, D. E., 1983, ''Transient Local Heat Transfer Measurements in 90° Bends Using Surface Coatings Having Prescribed Melting Points,'' M.S. thesis, Arizona State University, Tucson, AZ.
[17] Larson, D. E., and Metzger, D. E., 1986, ''Use of Melting Point Surface Coatings for Local Convection Heat Transfer Measurements in Rectangular Channel Flows With 90-deg Turns,'' Transaction of the ASME, **108**, pp. 48–54.
[18] Herold, W., and Wiegel, D., 1980, ''Problems of Photographic Documentation of Liquid Crystalline Thermographs,'' *Advances in Liquid Crystal Research and Applications*, L. Bata, ed., Pergamon Press, Oxford, pp. 1255–1259.
[19] Höcker, R., 1996, ''Optimization of Transient Heat Transfer Measurements Using Thermochromic Liquid Crystals Based on Error Estimation,'' ASME Paper 96-GT-235.
[20] Kline, S. J., and McClintock, F. A., 1953, ''Describing Uncertainties in Single Sample Experiments,'' *Mechanical Engineering*, **75**, pp. 3–8.
[21] Moffat, R. J., 1988, ''Describing the Uncertainties in Experimental Results, Exp. Therm. Fluid Sci.,'' **1**, pp. 3–17.
[22] Kizuka, N., Sagae, K., Anzai, S., Marushima, S., Ikeguchi, T., and Kawaike, K., 1998, ''Conceptual Design of the Cooling System for 1700 C-class Hydrogen-Fueled Combustion Gas Turbines,'' ASME Paper 98-GT-345.
[23] Han, J. C., Park, J. S., and Lei, C. K., 1985, ''Heat Transfer Enhancement in Channels with Turbulence Promoters,'' ASME J. Eng. Gas Turbines Power, **107**, pp. 629–635.
[24] Kukreja, R. T., Lau, S. C., and Mcmillin, R. D., 1991, ''Effects of Length and Configuration of Transverse Discrete Ribs on Heat Transfer and Friction for Turbulent Flow in a Square Channel,'' ASME/JSME Thermal Engineering Proceeding, **3**, pp. 213–218.
[25] Anzai, S., Kawaike, K., Kawaike, K., and Takehara, I., 1991, ''Effects of Turbulence Promoter Rib Shape on Heat Transfer and Pressure Loss Characteristics,'' J. of the Gas Turbine Society of Japan, **20**, No. 75, pp. 65–73 (in Japanese).
[26] Taslim, M. E., Li, T., and Kercher, D. M., 1994, ''Experimental Heat Transfer and Friction in Channels Roughened with Angled, V-Shaped and Discrete Ribs on Opposite Walls,'' ASME Paper 94-GT-163.

Downloaded 02 Jun 2010 to 171.66.16.119. Redistribution subject to ASME license or copyright; see http://www.asme.org/terms/Terms_Use.cfm

Internal Bearing Chamber Wall Heat Transfer as a Function of Operating Conditions and Chamber Geometry

Stefan Busam
Lehrstuhl und Institut für Thermische Strömungsmaschinen, Universität Karlsruhe (T.H.), Kaiserstr. 12, 76128 Karlsruhe, Germany

Axel Glahn
United Technologies Research Center, 411 Silver Lane, East Hartford, CT 06108

Sigmar Wittig
Lehrstuhl und Institut für Thermische Strömungsmaschinen, Universität Karlsruhe (T.H.), Kaiserstr. 12, 76128 Karlsruhe, Germany

Increasing efficiencies of modern aero-engines are accompanied by rising turbine inlet temperatures, pressure levels and rotational speeds. These operating conditions require a detailed knowledge of two-phase flow phenomena in secondary air and lubrication oil systems in order to predict correctly the heat transfer to the oil. It has been found in earlier investigations that especially at high rotational speeds the heat transfer rate within the bearing chambers is significantly increased with negative effects on the heat to oil management. Furthermore, operating conditions are reached where oil coking and oil fires are more likely to occur. Therefore, besides heat sources like bearing friction and churning, the heat transfer along the housing wall has to be considered in order to meet safety and reliability criteria. Based on our recent publications as well as new measurements of local and mean heat transfer coefficients, which were obtained at our test facility for engine relevant operating conditions, an equation for the internal bearing chamber wall heat transfer is proposed. Nusselt numbers are expressed as a function of non-dimensional parameter groups covering influences of chamber geometry, flow rates and shaft speed. [S0742-4795(00)02202-X]

Introduction

Aero-engine rolling element bearings have to be lubricated by oil and, as a consequence, measures must be taken to prevent oil ingestion into the hot zones of the engines. Therefore, bearings are incorporated in chamber geometries and the gap between the chamber housing and the rotating shaft is sealed, e.g., by air-pressurized labyrinths or brush seals. As reported in one of our recent studies [1], the flow field inside bearing chambers can be characterized by a rotating wall film of oil interspersed with gas bubbles, and by oil droplets in the turbulent rotating air flow, which drives the film in the circumferential direction. It has been noted that the flow pattern is highly affected by the shaft speed. At low rotational speeds gravity forces cause a non-uniform oil film distribution, whereas at high speed conditions the increasing interfacial shear as well as the higher momentum of impinging oil particles lead to a more homogeneously distributed flow field and to droplet removal from the wall film. The latter contributes to higher oil concentrations in the core flow.

For a calculation of lubrication oil flow rates, which should be kept as small as possible in order to reduce parasitic losses due to larger pumps, filters and coolers, a sufficient knowledge of all heat transfer phenomena involved in bearing chamber flows is required. Additional heat sources are the bearing friction, the dissipation due to churning and windage, and the heat transfer from the bearing chamber walls to the oil which is bounded, to a substantial degree, in the rotating wall film at the inner side of the housing wall.

In order to overcome uncertainties in the design process, which were stated, e.g., by Zimmermann et al. [2], a bearing chamber test facility has been developed at the Institut für Thermische Strömungsmaschinen (ITS), University of Karlsruhe. The unique rig described first by Wittig et al. [3] allows detailed investigations of all relevant flow and heat transfer processes. Examples of successful work on the challenging tasks described above were presented by Glahn and Wittig [1], who characterized the momentum transfer in bearing chamber oil film flows, and Glahn et al. [4], who performed a study on the droplet flow in bearing chambers. Chew [5] as well as Glahn and Wittig [6] presented analytical approaches for the characterization of oil films and associated heat transfer phenomena. Both used the experimental data acquired at the bearing chamber test rig at the University of Karlsruhe for a comparison. They found some good qualitative and quantitative agreement, but uncertainties remained and, therefore, more experimental heat transfer data for representative bearing compartment operating conditions were still demanded.

A systematic investigation of internal bearing chamber wall heat transfer phenomena covering effects of flow rates and rotational speeds was performed by Glahn et al. [7]. However, their discussion of local and mean heat transfer coefficients did not include a sufficient variation of geometry parameters. As a continuation of the Glahn et al. [7] work, the present paper deals with the impact of the bearing chamber geometry on the internal wall heat transfer. By studying these effects, it was also possible to derive a non-dimensional empirical correlation for the internal wall heat transfer.

The outline of this paper is as follows. A brief description of the experimental arrangement is presented, followed by a sample discussion of local and mean heat transfer coefficients. Next, heat transfer coefficients and operating conditions are reduced to Nusselt and Reynolds numbers, respectively, and individual dependencies are shown. Finally, the empirical correlation for non-dimensional heat transfer coefficients is introduced.

Experimental Setup and Measuring Technique

Bearing Chamber Rig. The test rig, shown in a co-axial sectional view in Fig. 1, is already the second modification for smaller heights of a setup that was introduced by Wittig et al. [3]. At each side of the squeezefilm-damped roller bearing (1), separate chambers (III, IV) are formed. The rotor (2) is supported by

Contributed by the International Gas Turbine Institute (IGTI) of THE AMERICAN SOCIETY OF MECHANICAL ENGINEERS for publication in the ASME JOURNAL OF ENGINEERING FOR GAS TURBINES AND POWER. Paper presented at the International Gas Turbine and Aeroengine Congress and Exhibition, Indianapolis, IN, June 7–10, 1999; ASME Paper 99-GT-249. Manuscript received by IGTI March 9, 1999; final revision received by the ASME Headquarters January 3, 2000. Associate Technical Editor: D. Wisler.

 Copyright © 2000 by ASME

Downloaded 02 Jun 2010 to 171.66.16.119. Redistribution subject to ASME license or copyright; see http://www.asme.org/terms/Terms_Use.cfm

use of a Radial Drive Shaft location ball bearing (3), which was taken from a production engine and tolerates axial loads and rotational speeds that are high enough to compensate thrusts and rotational loads occurring during rig operation. The chambers are bounded by a thick-walled housing (4), the roller bearing support (5), the rotor, a flange (6) realizing the sealing air supply of chamber III and the support of the housing, and a cover (7) for chamber IV. It can be readily concluded from Fig. 1 that the bearing chamber geometries of our test rig were abstracted from the very complex arrangements given by a real engine to a more or less rectangular shape.

Air and oil flows are arranged in the same way as in the real engine. An under-race lubrication (8) supplies the roller bearing with preheated oil. This system is capable of flow rates of $\dot{V}_{F,t} \leqslant 400$ l/h. Typical oil temperatures were set to $T_F = 423$ K. To prevent oil leakage, the chambers were sealed using three-fin labyrinth seals (9(*a*,*b*)). Both labyrinth seals were pressurized by air, which was preheated to the same temperature level as the lubrication oil. The airflow to each labyrinth can be controlled independently and ranged between $5\ \text{g/s} \leqslant \dot{m}_L \leqslant 20\ \text{g/s}$. Air/oil mixtures are discharged through the vent line (10) at the top of each chamber, while the oil sump at the bottom is scavenged out via the radial port by use of revolution controlled oil pumps.

The test rig has been optimized with respect to the heat transfer analysis. As explained by Wittig et al. [3], the water-cooled housing wall was adjusted and the thermocouples were artificially aged and individually calibrated in order to minimize uncertainties of the determination of the heat transfer coefficients. Therewith, the relative error of all the h-numbers is less than 5 percent.

Whereas the Wittig et al. [3] arrangement was basically used as a test vehicle for the development of measuring techniques its successors were fully instrumented for flow and heat transfer measurements using the equipment identified as suitable in the preliminary study. The reader is referred for details to the second generation bearing chamber test rig to Glahn et al. [7]. The additional experiments presented in this paper were acquired with an almost identical arrangement. Differences between both configurations are shown in Fig. 2. Configuration 1, which was used by Glahn and Wittig [1,6] and by Glahn et al. [7], consists of two chambers (I, II) of the same height, *h*, but different width, *b*. Furthermore, Chamber I introduced a step change in the rotor contour line. The disk face was shown to have a strong impact on the local heat transfer inside Chamber I, because it acts as a rotary atomizer and pumps oil radial outward. Droplets impinging at the stationary wall opposite to the disk cause a strong increase of local heat transfer coefficients. In contrast, Configuration 2 deals with strongly rectangular cross-sectional bearing chamber shapes and, in addition, both chambers have a different height. Dimensions for the four chambers are summarized in Table 1. Note that the hydraulic diameter was calculated from

$$D_h = \frac{4 \cdot A}{U} = \frac{2 \cdot b \cdot h}{b + h}. \tag{1}$$

The instrumentation survey included in Fig. 2 shows four different heat transfer instrumentation planes TE1-4 as well as circumferential locations where gas and oil film temperatures were taken. TE1-4 were chosen for the heat transfer investigations based on the observations made in flow visualization studies using the preliminary arrangement. They exhibit distinct bearing chamber heat transfer phenomena described in detail by Glahn et al. [7]. By defining an averaged heat transfer coefficient based on measurements at these locations, i.e., by covering all effects expected to occur along the internal housing wall, it is believed that a representative aero-engine bearing chamber heat transfer coefficient is obtained. The next section gives a description of the measuring techniques used and shows how average values were obtained first for each measuring plane and then for each chamber.

Heat Transfer Measuring Technique. In the present study, the heat flux and heat transfer coefficients have been measured

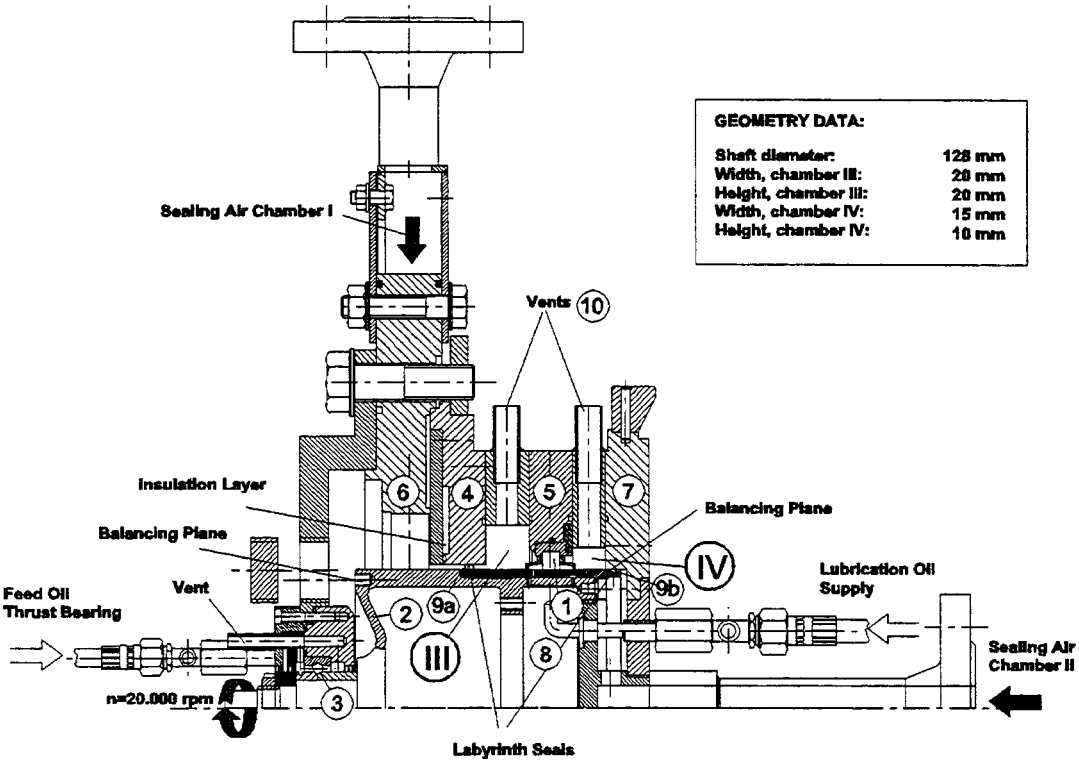

Fig. 1 High Speed Bearing Chamber Test Rig: (1) squeeze-film-damped roller bearing; (2) rotor; (3) ball bearing; (4) housing; (5) roller bearing support; (6) flange; (7) chamber cover; (8) under-race lubrication; (9(*a*,*b*)) three-fin labyrinth seals; and (10) vent

Downloaded 02 Jun 2010 to 171.66.16.119. Redistribution subject to ASME license or copyright; see http://www.asme.org/terms/Terms_Use.cfm

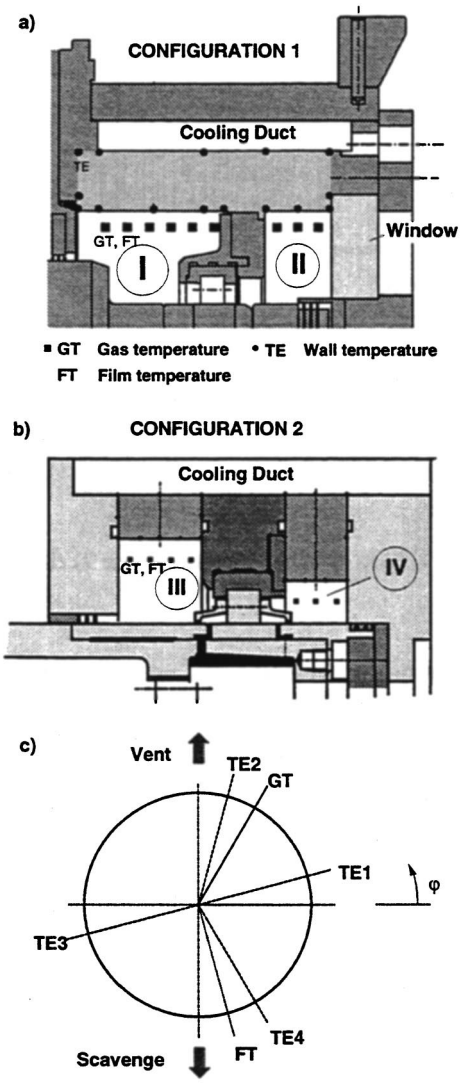

Fig. 2 Bearing Chamber Configurations and Heat Transfer Instrumentation: (*a*) co-axial sectional view of chamber configurations; (*b*) co-axial sectional view of present chamber configuration; and (*c*) heat transfer instrumentation survey

Table 1 Dimensions of the different bearing chambers

	Ch I	Ch II	Ch III	Ch IV
h [m]	0.028	0.028	0.020	0.010
b [m]	0.046	0.020	0.020	0.015
r_s [m]	0.062	0.062	0.064	0.064
D_h [m]	0.034	0.023	0.020	0.012

utilizing the temperature gradient method. It is the same experimental approach as chosen in our previous bearing chamber heat transfer studies [7] and, therefore, this section gives only a brief outline on the measuring principle rather than a detailed description. However, it should be pointed out that it is a stationary technique, which is based on a two-dimensional finite element calculation procedure [8]. Note that the assumption of a locally two-dimensional temperature field, which was generated by a water-cooling scheme, was verified earlier in our preliminary investigation [3].

The calculation of the temperature distribution was conducted for planes, which were located at positions TE1-4. Figure 2(*a*, *b*) shows samples of the cross-sections, which were discretized utilizing TRIM6 elements. Local temperature measurements taken with embedded thermocouples in these areas provided boundary conditions for the solution of the thermal conductivity equation. Temperature dependent material properties were considered in an iterative manner. Following Fourier's law, the local heat transfer rate can be calculated readily from the temperature distribution inside the wall.

$$\dot{Q}_{W,j}(z) = -\lambda A_j(z) \nabla T|_{W,j}(z). \tag{2}$$

This was done for each boundary element, *j*, of the underlying computational grid, i.e., for the elements facing a bearing chamber. By using Newton's law, the corresponding heat transfer coefficient results from

$$h_{\mathrm{CH}}(z) = \frac{\dot{Q}_{W,j}(z)}{A_j(z)(T_{\mathrm{CH}}(z) - T_{W,j}(z))}. \tag{3}$$

Flow temperatures were determined from local measurements inside the bearing chambers (5 mm apart from the internal wall surface corresponding to the thermocouples for the gas temperatures GT in Fig. 2) and interpolated in order to obtain the flow temperature distribution, $T_{\mathrm{CH}}(z)$, which was needed for the definition of local heat transfer coefficients.

The local data at each of the four heat transfer measurement planes TE1-4 were used to calculate mean heat transfer coefficients for each plane:

$$\overline{h}|_{TEi} = \left.\frac{\dot{Q}_W}{A(\overline{T}_{\mathrm{CH}} - \overline{T}_W)}\right|_{TEi}, \tag{4}$$

where the total heat transfer rate was calculated from

$$\dot{Q}_W = \sum_j h_{\mathrm{CH}} A_j (T_{\mathrm{CH}} - T_{W,j}) \tag{5}$$

and

$$\overline{T}_W = \frac{1}{A} \sum_j A_j T_{W,j} \tag{6}$$

$$\overline{T}_{\mathrm{CH}} = \frac{1}{A} \sum_j A_j T_{\mathrm{CH}} \tag{7}$$

$$A = \sum_j A_j \tag{8}$$

were introduced as new wall and flow reference temperatures which consider variations in each element's size. Finally, the mean heat transfer coefficient for the entire chamber was calculated as the arithmetic mean from the *h*-numbers at the four measuring planes:

$$\overline{h}_{\mathrm{CH}} = \frac{1}{4} \sum_{TEi} \overline{h}|_{TEi}. \tag{9}$$

Heat Transfer Coefficients

The analysis of heat transfer phenomena in bearing chambers is based on engine relevant operating conditions characterized in terms of sealing air mass flows, lubrication oil flows, and rotational speeds. Since the impact of these operating parameters on the local heat transfer was already discussed in detail by Glahn et al. [7], only sample results are given here. The main objective of the present paper is the non-dimensional characterization of the internal bearing chamber wall heat transfer. Individual relationships between flow and rotational Reynolds numbers and Nusselt numbers will be highlighted for different geometries and, finally, a generalized heat transfer correlation will be introduced, which covers for the first time operating conditions as well as characteristic dimensions.

Downloaded 02 Jun 2010 to 171.66.16.119. Redistribution subject to ASME license or copyright; see http://www.asme.org/terms/Terms_Use.cfm

Local Heat Transfer in Bearing Chambers. Glahn et al. [7] presented results for local heat transfer coefficients, h, and discussed relationships to specific features of the chamber geometry. A sample is given in Fig. 3 for two speed conditions and lubrication flow rates to each chamber. The sealing airflow rate was kept constant. Data are displayed for the heat transfer measuring plane TE2 ($\varphi = 75$ deg), whereas a coaxial sectional view of the bearing chamber at the position of $\varphi = 90$ deg has been selected in order to demonstrate significant locations of the setup, e.g., those of vent and scavenge ports, respectively.

With respect to Chamber I, two regions with extreme values of the local heat transfer distribution can be seen. Maximum heat transfer coefficients are located at an axial position corresponding to the sudden diameter reduction of the rotor and in the middle of the chamber. The significant heat transfer augmentation is attributed to a pumping of fluid at the disk and to higher flow velocities in the middle of the chamber superimposed by an acceleration of fluid next to the vent. Note also that impingement of hot oil droplets emanated from the bearing is likely to occur in these regions. Although the range of h-numbers in Chamber II corresponds to those in Chamber I, the qualitative distribution shows different trends. Obviously, differences in the chamber geometry—width, sealing air supply at a different radial location, and the presence of the support flange aside the roller bearing—have a decisive influence on local heat transfer coefficients. Summarizing the experimental findings of Glahn et al. [7] the following can be stated:

- Local heat transfer coefficients along the internal bearing chamber housing walls vary in the range of $2000\ \mathrm{W/(m^2\ K)} \leq h \leq 6000\ \mathrm{W/(m^2\ K)}$.
- An increase of either sealing mass flow, lubrication oil flow, or rotational speed will increase the heat transfer. Effects of sealing air and speed were stronger than those of oil flow rates.
- The circumferential heat transfer distribution is strongly dependent on the rotational speed. At moderate speed conditions of 9000 rpm, the deviation of heat transfer coefficients in circumferential direction was in the same order as the average heat transfer coefficient. At high-speed conditions of 16,000 rpm this nonuniformity was still about 20 percent of the average value.
- Local heat transfer coefficients in regions next to disk arrangements vary significantly with the momentum flux ratio of the flow pumped radial outward to the flow superimposed axially at the rim of the disk.

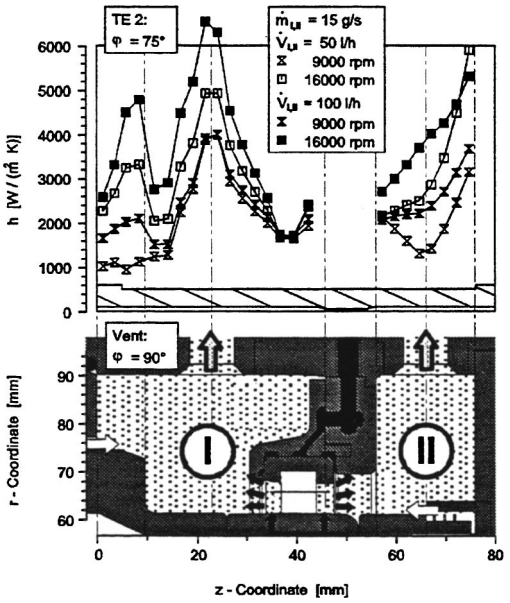

Fig. 3 Local Heat Transfer Coefficients Versus Chamber Geometry of Configuration 2 [7]

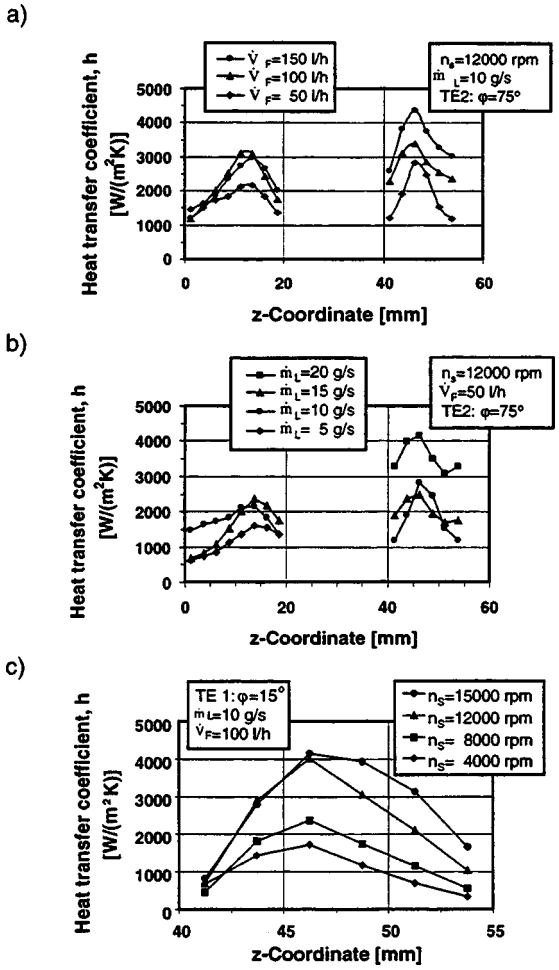

Fig. 4 Local Heat Transfer Coefficient in Chamber III, IV Versus Operating Conditions: and (*a*) Impact of lubrication oil flow; (*b*) Impact of sealing airflow; and (*c*) Impact of rotational speed

Local heat transfer distributions for rig Configuration 2 (Fig. 4) reveal the same trends. As mentioned before, disk arrangements were not part of the present bearing chamber configuration, but dependencies from operating conditions were studied analogous to our previous heat transfer investigations. As expressed in Fig. 4, the level of local heat transfer coefficients appears to be on the lower end of the range given above. However, the qualitative distributions show the familiar characteristic of high heat transfer in the vent and scavenge plane, i.e., in the middle of the chamber, and the increasing effects of all operating parameters. Note that in Fig. 4 the level of heat transfer coefficients is higher for Chamber IV, which is the chamber with the smallest height. Note also that Chambers I and II, which showed even higher heat transfer coefficients (Fig. 3), have the largest chamber height of all geometries tested. Obviously, an explanation of the geometry impact on the heat transfer cannot be obtained from a discussion of dimensional quantities and, therefore, the subsequent analysis is based on nondimensional parameters.

Non-Dimensional Mean Heat Transfer Coefficients as a Function of Operating Parameters. As shown by relation (10), heat transfer coefficients, flow rates, rotational speeds and fluid properties have to be combined with geometrical boundary

Downloaded 02 Jun 2010 to 171.66.16.119. Redistribution subject to ASME license or copyright; see http://www.asme.org/terms/Terms_Use.cfm

conditions in order to express the heat transfer at bearing chamber walls as a function of non-dimensional quantities.

By introducing the hydraulic diameter defined in Eq. (1) as the characteristic length, a definition for the Nusselt number has been obtained from the mean heat transfer

$$\left.\begin{array}{l}\overline{h}_{\mathrm{CH}}\\ \dot{m}_{\mathrm{CH}}\\ \dot{V}_{\mathrm{CH}}\\ n_S\\ \textit{fluid properties}\\ \textit{geometry}\end{array}\right\}\Rightarrow\left\{\begin{array}{l}\mathrm{Nu}\\ \mathrm{Re}_U\\ \mathrm{Re}_L\\ \mathrm{Re}_F\end{array}\right. \tag{10}$$

coefficient calculated according to Eq. (9):

$$\mathrm{Nu}_{Dh}=\frac{\overline{h}_{\mathrm{CH}}\cdot D_h}{\lambda(\overline{T}_{\mathrm{CH}})}. \tag{11}$$

The rotational speed has been transferred into a circumferential Reynolds number based on the shaft speed and the same characteristic length:

$$\mathrm{Re}_U=\frac{2\cdot\pi\cdot n_S\cdot r_S\cdot D_h}{\nu_F(\overline{T}_{\mathrm{CH}})}. \tag{12}$$

Based on these parameters, the heat transfer may be related to the rotational speed in a manner that takes temperature dependent fluid properties into account. The remaining operating conditions, i.e., sealing air flow and lubrication oil flow, can be expressed in terms of hydraulic Reynolds numbers

$$\mathrm{Re}_L=\frac{\overline{c_L}\cdot D_h}{\nu_L}=\frac{4\cdot\dot{m}_L}{\mu_L\cdot U} \tag{13}$$

and

$$\mathrm{Re}_F=\frac{\overline{c_F}\cdot D_h}{\nu_F}=\frac{4\cdot\dot{V}_F}{\nu_F\cdot U} \tag{14}$$

with c_i as averaged velocities and D_h and U as the hydraulic diameter and the wetted circumference, respectively. However, the definition of a cross-section for the flow inside a bearing chamber is not trivial. Although we conclude from rig investigations as well as from numerical studies that the flow inside the bearing chamber is dominated by rotation, the flow direction is a priori unknown. Therefore, it has to be noted that in the absence of any better knowledge, we only postulate the use of Eq. (1) for the definition of the hydraulic diameter and use prime notations for the flow Reynolds numbers given in Eqs. (15) and (16):

$$\mathrm{Re}'_L=\frac{4\cdot\dot{m}_{\mathrm{CH}}}{\mu_L(\overline{T}_{\mathrm{CH}})\cdot D_h} \tag{15}$$

$$\mathrm{Re}'_F=\frac{4\cdot\dot{V}_{\mathrm{CH}}}{\nu_F(\overline{T}_{\mathrm{CH}})\cdot D_h}. \tag{16}$$

In order to find relationships of the kind

$$\mathrm{Nu}_{Dh}=\mathrm{A}_i\cdot\mathrm{Re}_i^{m_i},i=L,F,U \tag{17}$$

the impact of each operating parameter was investigated separately by systematic variations of the individual quantity, while all other conditions were held constant.

Sealing Mass Flow Versus Heat Transfer. Figure 5 summarizes operating conditions characterized by a constant oil flow of $\dot{V}_F=50$ l/h and a constant rotational speed of $n_S=12{,}000$ rpm in order to show the influence of the sealing air mass flow on the non-dimensional mean heat transfer. Nusselt numbers are plotted as a function of non-dimensional air mass flows, Re'_L for the four bearing chamber geometries (Fig. 2(*a*, *b*)), which are characterized by hydraulic diameters (Table 1). As it is expressed in the same exponent $m_L=0.48$, cf. Eq. (17), all chambers tested show the same impact of the sealing airflow on the heat transfer. Note that Nusselt numbers increase with increasing hydraulic diameters. Thus, the correlation parameter A_L is a function of the hydraulic diameter and the relationship $A_L=f(D_h)$ has to be identified. As shown in Fig. 6, $A_L=f(D_h)$ is a polynomal function. It can be approximated by $A_L=350\cdot D_h^{1.56}$ and, therefore, Eq. (17) is equal to

$$\mathrm{Nu}_{Dh}=450\cdot D_h^{1.56}\,\mathrm{Re}_L^{0.48} \tag{18}$$

for the sealing air flow.

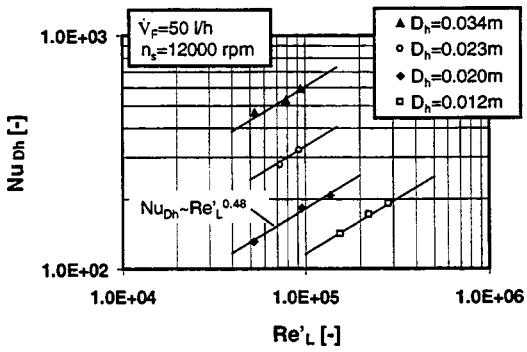

Fig. 5 Influences of the Non-Dimensional Sealing Air Flow on Averaged Nusselt Numbers

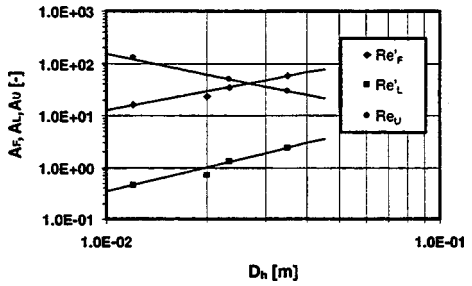

Fig. 6 Geometry Impact on the Correlation Coefficients

Lubrication Oil Flow Versus Heat Transfer. Similar results as observed for the sealing airflow were obtained for the analysis of the impact of oil flow rates on the heat transfer. A plot of Nu_{DH} as a function of Re'_F is shown in Fig. 7. Data is presented for a constant air mass flow $\dot{m}_L=10$ g/s and a rotational speed of $n_S=12{,}000$. Again, the Nusselt numbers increase with the non-dimensional flow rate and the hydraulic diameter. As it is expressed in a lower value for the exponent ($m_F=0.32$), the impact of oil flow rates appears to be weaker, which is consistent with the

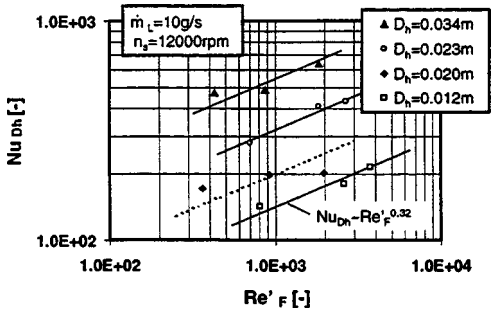

Fig. 7 Influences of the Non-Dimensional Lubrication Flow Rate on Averaged Nusselt Numbers

Downloaded 02 Jun 2010 to 171.66.16.119. Redistribution subject to ASME license or copyright; see http://www.asme.org/terms/Terms_Use.cfm

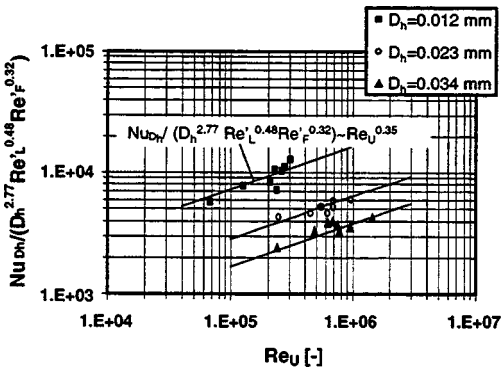

Fig. 8 Influences of the Circumferential Reynolds Numbers on Averaged Nusselt Numbers

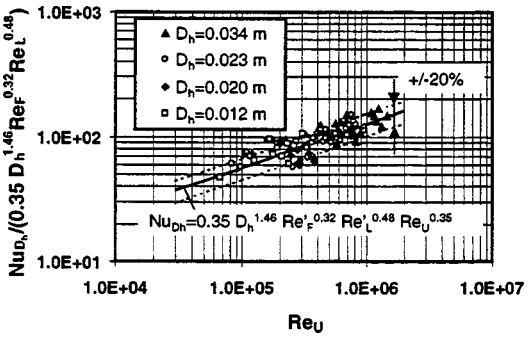

Fig. 9 Heat Transfer Correlated With Operating Conditions

observations reported before [7]. As for the sealing air flow, a functional relationship according to Eq. (18) must be found to account for the geometry impact. Analogous to the procedure outlined above, the correlation coefficient is obtained as $A_F = 3350 \cdot D_h^{1.21}$ (Fig. 6) and the correlation of the Nusselt number as a function of lubrication oil flows to the chamber becomes

$$\mathrm{Nu}_{Dh} = 3350 \cdot D_h^{1.21}\,\mathrm{Re}_F^{0.32}. \tag{19}$$

Rotational Speed Versus Heat Transfer. The investigation of the impact of the third operating parameter, namely the rotational speed, n_S, on the mean heat already incorporates the knowledge gained from the analysis of flow rate dependencies. In order to broaden the database, Nusselt numbers obtained for different sealing and lubrication flows were reduced for the impact of hydraulic diameters:

$$\mathrm{Nu}^*_{Dh} = \mathrm{Nu}_{Dh}/(D_h^{2.77}\,\mathrm{Re}_F'^{0.32}\,\mathrm{Re}_L'^{0.48}). \tag{20}$$

In Fig. 8, reduced Nusselt numbers, Nu^*_{Dh}, are plotted as a function of circumferential Reynolds numbers. As it is expressed by the characteristic $\mathrm{Nu}^*_{Dh} \sim \mathrm{Re}_U'^{0.35}$, the heat transfer shows the expected increases with rotational speed. Note that the heat transfer increases with decreasing hydraulic diameter. As it was done for the other operating parameters (Fig. 6), the relationship between the correlation coefficient, A_U, and the hydraulic diameter, D_h, was determined by assuming a logarithmic function. It is included in Fig. 6 and was determined to

$$A_U = 0.35 \cdot D_h^{-1.32}. \tag{21}$$

The heat transfer speed relationship reads then

$$\mathrm{Nu}^*_{Dh} = 0.35 \cdot D_h^{-1.32}\,\mathrm{Re}_U^{0.35}. \tag{22}$$

Generalized Empirical Formula for the Internal Bearing Chamber Heat Transfer. From individual relationships between heat transfer and operating conditions, which were provided in the last paragraphs, a generalized heat transfer correlation can be derived readily. Substituting Eq. (20) into Eq. (22) and rearranging for Nu_{Dh} reads

$$\mathrm{Nu}_{Dh} = 0.35 \cdot D_h^{1.46} \cdot \mathrm{Re}'^{0.48}_L \cdot \mathrm{Re}'^{0.32}_F \cdot \mathrm{Re}_U^{0.35}. \tag{23}$$

Equation (23) is shown in Fig. 9 and comparison is made with experimental data that cover a sealing mass flow range of

$$5.3\ \mathrm{g/s} \leqslant \dot{m}_L \leqslant 20.5\ \mathrm{g/s},$$

lubrication oil flows of

$$24.4\ \mathrm{l/h} \leqslant \dot{V}_F \leqslant 175.8\ \mathrm{l/h},$$

and rotational speeds in the range of

$$4000\ \mathrm{rpm} \leqslant n_S \leqslant 16{,}000\ \mathrm{rpm}.$$

As it was pointed out before, measurements were taken for four different geometries with hydraulic diameters defined by Eq. (1) ranging from

$$0.012\ \mathrm{m} \leqslant D_h \leqslant 0.034\ \mathrm{m}.$$

Most of the measured data fall into a scatter band of ± 20 percent of the line representing Eq. (23).

Conclusions

The current paper describes heat transfer measurements inside an experimental bearing chamber rig, designed for ''not-end'' rear bearing chambers sealed by means of labyrinths. These measurements extend the heat transfer database of our bearing chamber studies and include for the first time variations of the most dominant geometrical parameter, the chamber height. Therefore, it was not only possible to study the impact of operating conditions such as flow rates and rotational speed, but also the geometry impact on the heat transfer along the internal bearing compartment wall. The successful outcome of this investigation is reflected by the introduction of a generalized correlation for the mean heat transfer coefficient at the internal bearing chamber housing wall. It includes all relevant parameters, i.e., Nusselt number, hydraulic diameter, flow Reynolds numbers and rotational Reynolds numbers, and is expected to give a major contribution to the design process of bearing compartments by reducing uncertainties in both the mechanical integrity calculation and the heat to oil analysis.

Acknowledgments

The work reported was partly sponsored within the Brite-Euram project BRE2–CT94-0538 as well as by grants from Rolls-Royce, Bristol, and MTU Munich. Special thanks are due to R. M. Coleman and M. Turner, Rolls Royce, as well as to H. Zimmermann, MTU, for open-minded technical discussions and continuous support.

Nomenclature

A = correlation coefficient
A = area, m^2
b = width, m
c = velocity, m/s
D_h = hydraulic diameter, m
h = heat transfer coefficient, $\mathrm{W/(m^2 \cdot K)}$
h = chamber height, m
m = correlation coefficient
$\dot{m}$ = mass flow, kg/s
Nu = Nusselt number
n_S = rotational speed, s^{-1}
Q = heat transfer rate, W
Re = Reynolds number
r,φ,z = cylindrical coordinates, m,°,m
T = temperature, K

Downloaded 02 Jun 2010 to 171.66.16.119. Redistribution subject to ASME license or copyright; see http://www.asme.org/terms/Terms_Use.cfm

U = circumference, m
$\dot{V}$ = volume flow, m^3/s
λ = thermal conductivity, $W/(m \cdot K)$
μ = dynamic viscosity, $kg/(m \cdot s)$
ν = kinematic viscosity, m^2/s

Subscripts

CH = chamber
F = film, oil
j = element number
L = air
S = shaft
t = total
TEi $(i=1-4)$ = heat transfer measuring plane
U = circumference
W = wall

Superscripts

$-$ = mean value
$'$ = modified
m_i = exponents

References

[1] Glahn, A., and Wittig, S., 1996, ''Two-Phase Air Oil Flow in Aero Engine Bearing Chambers—Characterization of Oil Film Flows,'' ASME J. Eng. Gas Turbines Power, **118**, No. 3, pp. 578–583.

[2] Zimmermann, H., Kammerer, A., Fischer, R., and Rebhahn, D., 1991, ''Two-Phase Flow Correlations in Air/Oil Systems of Aero Engines,'' ASME Paper 91-GT-54.

[3] Wittig, S., Glahn, A., and Himmelsbach, J., 1994, ''Influence of High Rotational Speeds on Heat Transfer and Oil Film Thickness in Aero Engine Bearing Chambers,'' ASME J. Eng. Gas Turbines Power, **116**, pp. 395–401.

[4] Glahn, A., Kurreck, M., Willmann, M., and Wittig, S., 1996, ''Feasibility Study on Oil Droplet Flow Investigations inside Aero-Engine Bearing Chambers—PDPA Techniques in Combination with Numerical Approaches,'' ASME J. Eng. Gas Turbines Power, **118**, No. 4, pp. 749–755.

[5] Chew, J., 1996, ''Analysis of the Oil Film on the Inside of an Aero-Engine Bearing Chamber Housing,'' ASME Paper 96-GT-300.

[6] Glahn, A., and Wittig, S., 1996, ''Two-Phase Air/Oil Flow in Aero-Engine Bearing Chambers—Assessment of an Analytical Prediction Model for the Internal Wall Heat Transfer,'' ISROMAC-6, Honolulu, Hawaii, February 25–28, 1996.

[7] Glahn, A., Busam, S., and Wittig, S., 1997, ''Local and Mean Heat Transfer Coefficients along the Internal Housing Walls of Aero Engine Bearing Chambers,'' ASME Paper 97-GT-261.

[8] Marsal, D., 1976, ''Die numerische Lösung partieller Differentialgleichungen,'' Bibliographisches Institut, Zürich.

Downloaded 02 Jun 2010 to 171.66.16.119. Redistribution subject to ASME license or copyright; see http://www.asme.org/terms/Terms_Use.cfm

Richard A. Layton
North Carolina A&T State University,
Department of Mechanical Engineering,
1601 E. Market Street,
Greensboro, NC 27411
e-mail: rlayton@ncat.edu

John J. Marra
Pratt & Whitney,
V2500 Systems Design,
400 Main St., M/S 169-15,
East Hartford, CT 06108
e-mail: marraj@pweh.com

Conceptual Basis for a New Approach to Bladed-Disk Design

A central issue in gas turbine engine design today is the demand for higher performance, greater reliability, shorter lead times, and lower cost. The design of bladed disks (fans, compressors and turbines) is one area in which suitable design tools are sought to meet this demand. In this paper is presented the conceptual basis for a new, energy-based approach to design and an outline for future development of the approach as a software-based design tool. Technical tasks and risks associated with this development are summarized. It is hoped that this study will facilitate dialogue among practitioners of the various disciplines involved in bladed-disk design. [S0742-4795(00)00302-1]

1 Introduction

A central issue in gas turbine engine design today is reducing the cost of developing and deploying new products. Both commercial and military customers of engine manufacturers demand improved performance and greater reliability with shorter lead times at lower cost.

Manufacturers have succeeded in reducing time to market by improving the fidelity of analysis, integrating design and manufacturing, and initiating modern quality control. However, some aspects of design have benefited only incrementally at best from these initiatives. And incremental improvements, while desirable, are insufficient to insure continued corporate competitiveness.

The design of bladed-disk assemblies (fans, compressors, and turbines) is one area in which manufacturers are eager to realize order-of-magnitude time savings. The basic obstacle to progress in this area is a lack of adequate design tools. First, current design methods incorporate knowledge-based rules (often contradictory) which could possibly be relaxed or eliminated if the physical aspects of engine technology were better understood. Second, current design methods require seemingly endless iterations among functional design groups, particularly between aerodynamic and structural groups.

A typical bladed disk, shown in Fig. 1, comprises on the order of 100 blades attached to a disk, where each blade is typically a single forging comprising an airfoil, platform, and attachment. The disciplines involved in designing such an assembly include gas dynamics, structural mechanics, and heat transfer, with a substantial expenditure of effort in the areas of materials, airfoil design, vibration, fatigue, and manufacturability. Final designs are typically feasible rather than optimal and design procedures are not fully integrated among functional groups.

Current research efforts to address these issues tend to focus on specific problems within a discipline. For example, Zboinski and Ostachowicz [1,2] model friction at the contact surface between attachment and disk, an important issue not well understood. Csaba and Andersson [3] optimize the design of friction dampers used to reduce the vibratory blade response at resonance. Frischbier et al. [4] optimize blade thickness to avoid resonance at fundamental engine orders. Natalini and Sciubba [5] optimize the configuration of a cooled blade by minimizing entropy production in the fluid flow. Goel et al. [6] develop an airfoil design procedure for reducing aerodynamic design time. Kodiyalam et al. [7] minimize disk volume subject to stress allowables, laying a foundation for reducing structural design time. However, important as such investigations are, they are unlikely (in our opinion) to significantly reduce design-cycle time because they approach design from a traditional, discipline-specific perspective. Such approaches do not systematically account for the strong coupling among mechanical, aerodynamic, and thermal processes in modern engines.

Developing approaches for systematic, multidisciplinary design requires a better understanding of the physical phenomena associated with the dynamics of bladed disks. Several recent studies recognize this need. For example, Srinivasan [8] gives an in-depth study of blade vibration problems and concludes by emphasizing that design goals cannot be met unless ''a dialogue is promoted and maintained among experts in analyses and testing in the fields of structures, aerodynamics, materials, fatigue and fracture, statistics, controls, and diagnostics.'' In a similar spirit, Narayan et al. [9] develop a blade shape optimization procedure integrating aerodynamic efficiency and heat transfer. Kao et al. [10] propose an iterative procedure in which aerodynamic design is optimized subject to structural constraints followed by a structural optimization subject to aerodynamic constraints. The sequence repeats until a design converges. New design ideas such as these, however, have not fully matured and integrated design tools have not been realized.

In this paper is presented a conceptual basis for a new, systematic, unified approach to bladed-disk design and an outline for future development of the approach as a software-based design tool. Technical tasks and risks associated with this development are summarized. The basic contribution of this paper is to present

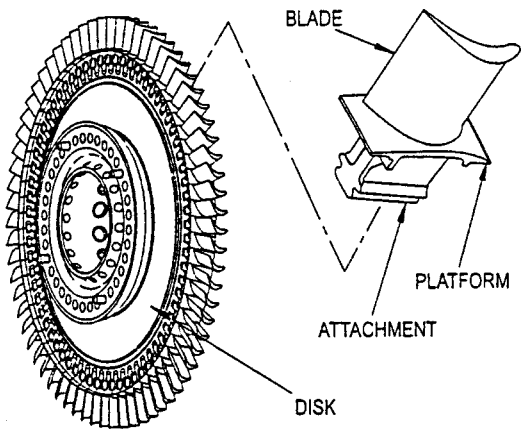

Fig. 1 Typical bladed disk from the turbine section of a gas turbine engine (courtesy of Pratt & Whitney)

Contributed by the Gas Turbine Division of THE AMERICAN SOCIETY OF MECHANICAL ENGINEERS for publication in the ASME JOURNAL OF ENGINEERING FOR GAS TURBINES AND POWER. Manuscript received by the Gas Turbine Division, October 19, 1998; final revision received by the ASME Headquarters October 25, 1999. Technical Editor: H. D. Nelson.

Copyright © 2000 by ASME

Downloaded 02 Jun 2010 to 171.66.16.119. Redistribution subject to ASME license or copyright; see http://www.asme.org/terms/Terms_Use.cfm

the problem of bladed-disk design from a non-traditional perspective and to lay a conceptual foundation for true integration of design among traditional functional groups.

2 Conceptual Basis for a New Approach

In this section are presented the core concepts underlying the new approach to bladed-disk design. An energy-based perspective of physical systems is described and the design of bladed disks is posed as a numerical optimization problem. The relationship of this approach to prior research and current industry practice is discussed.

2.1 A Physical Systems Perspective. A tenet of modern system dynamics is that the fundamental processes underlying a physical system's dynamic behavior are the storage, transmission, and transformation of energy among the components of a system and between a system and its surroundings. Physical components are thought of as energy manipulators which, based on the manner in which they are interconnected, process energy injected into the system in a characteristic manner which is observed as the system's dynamic response [11]. Analysis of a system begins, therefore, by classifying the constitutive behavior of system components, describing interconnections, and identifying inputs and outputs, all according to the manner in which energy is manipulated.

For the purpose of illustrating how this approach is applied to the design of a bladed-disk assembly, consider a turbine rotor assembly of a gas turbine engine. As illustrated in Fig. 2, a turbine is a power-transformation system. A large fraction of the fluid power, where the fluid is air and power is the product of pressure and volumetric flow rate, is transformed by the action of the turbine into shaft power, where power is the product of torque and angular speed. The result of this energy-transfer process is that air at the turbine outlet has a lower energy state than the air at the turbine inlet and that the shaft power is sufficient to operate the compressor, fan, and auxiliary machinery.

Power extracted from this energy-transfer process is both stored in and dissipated by the bladed-disk assemblies. Energy storage takes the forms of kinetic energy due to rotation, kinetic energy due to vibration, potential energy due to strain, and internal energy associated with thermal capacitance. Energy dissipation through cooling, as well as mechanical damping, is an entropy production process where the product of entropy flow rate and temperature is thermal power. Dissipation via noise can be described in terms of acoustic power. Designing the bladed-disk assemblies to reduce the total amount of energy stored and dissipated via these mechanisms improves the efficiency of the turbine's essential function—the transmission and transformation of power. This perspective of turbine operation constitutes a basic framework for the systematic treatment of the entire physical system.

2.2 Proposed Optimization Problem. It is proposed that the design of a bladed-disk can be formulated as a numerical optimization problem where, for a given part or assembly, the objective function is a function of all energy stored in and dissipated by the part. Constraints include limits on stress, deflection, temperature, manufacturing dimensional limits, and so forth. The solution of the optimization problem is the geometry or shape of the part. In essence, the design problem is to determine a geometry that minimizes the energy extracted from the energy flow through the rotating assembly while satisfying limits imposed by material properties, manufacturing, performance, and robustness.

The design problem can be stated in the form of a standard optimization problem as follows. Given the loads P acting on the solid body of a bladed-disk, determine the set S of geometric parameters that minimizes an energy-based objective function subject to a set of equality and inequality constraints C.

The form of the objective function is being investigated. A possible formulation, neglecting dissipation, is total energy E, given by

$$E = T + U + V, \tag{1}$$

where T is total kinetic energy due to rotation and vibration, U is internal energy associated with thermal capacitance, and V is potential energy due to strain. Load set P can be the result of an approximate or detailed aerodynamic analysis. The set S can include such parameters as blade attachment geometry, rim width and depth, web thickness and depth, and spacer diameter. The constraint set C include limits imposed by material properties and manufacturing, performance limits such as those described on a frequency-speed diagram (Campbell diagram), and heuristic limits representing a manufacturer's knowledge base. However, care must be taken in posing such a knowledge base as a set of firm constraints. Each heuristic rule must be interpreted in terms of the physics of the bladed-disk so that such rules that prevent innovative design can be identified and reformulated or eliminated.

The level of complexity of the design problem can be tailored to suit the task—from the relative simplicity (!) of designing a blade attachment to the seeming intractability of optimizing an entire turbine section. These tasks, vastly different in scope, are conceptually similar in kind when considered from the energy-

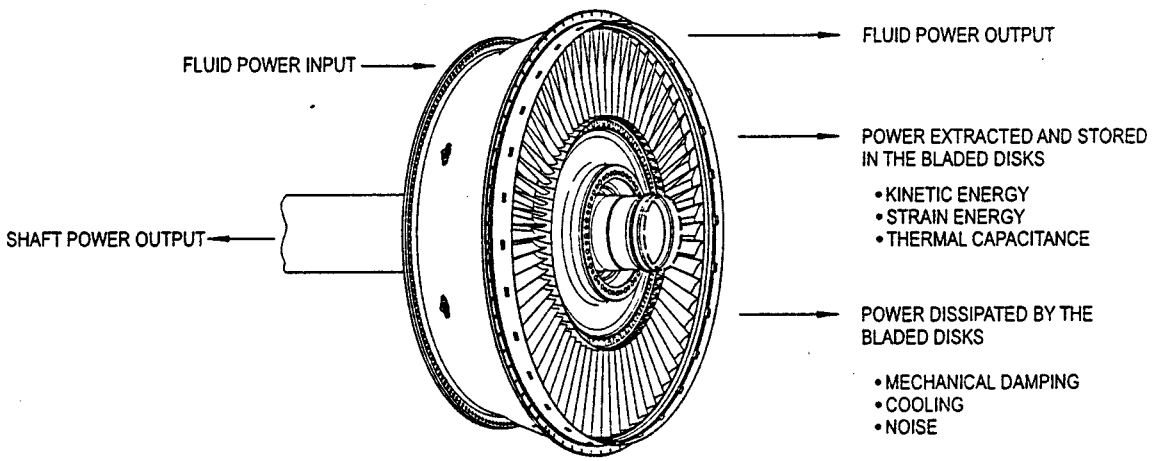

Fig. 2 Typical turbine rotor assembly, considered as a power-transformation system (courtesy of Pratt & Whitney)

Downloaded 02 Jun 2010 to 171.66.16.119. Redistribution subject to ASME license or copyright; see http://www.asme.org/terms/Terms_Use.cfm

based perspective described above. It is this unifying aspect of the proposed strategy that both illuminates the underlying physics of the dynamic bladed-disk system and promises to enable an innovative approach to integrating design among functional groups (aero, structures, heat transfer, and so forth).

2.3 Relationship to Existing Design Strategies. The proposed energy-based optimization problem unifies essential aspects of current design strategies. First, consider the problem of minimizing structural mass. In structural shape optimization, volume, subject to stress allowables, is often selected as the objective function to minimize mass, as in Botkin [12] or Kodiyalam [7]. In some cases, mass is minimized directly, as in Zhang et al. [13]. For rotating structures such as a turbine, the mass moment of inertia is an appropriate mass-related objective function. All these properties are subsumed by the kinetic energy component of an energy-based objective function. In its simplest form, the kinetic energy T of a structure rotating about a fixed axis is given by

$$T=\tfrac{1}{2}\dot{Q}^T M\dot{Q}, \tag{2}$$

where M is a consistent mass matrix and $\dot{Q}$ is a velocity vector. Thus, minimizing kinetic energy inherently minimizes the mass of a structure at the rotational speeds of interest.

Second, consider deflection as a design criterion. A rotating structure such as a turbine engine rotor deflects radially when acted on by precessional input such as an aircraft pitching maneuver, producing strain in both the rotor and the bearing supports. The resulting strain energy is tuned via stiffness and damper selection to minimize deflection between the blade tip and the case. In addition, tuning rotor dynamic frequencies out of the engine operating range generally requires that strain energy be minimized. In its simplest form, the strain energy (a form of potential energy V) of a structure is given by

$$V=\tfrac{1}{2}Q^T KQ, \tag{3}$$

where K is a generalized stiffness coefficient, and Q is a global displacement vector. For a given value of K, minimizing strain energy minimizes Q. An upper limit Q_0 on deflection is imposed as the inequality constraint

$$Q-Q_0\leqslant 0. \tag{4}$$

Note that an energy-based objective function containing both kinetic and potential terms inherently contains a tradeoff among mass, stiffness and deflection, as follows. Stiffness K is reduced is two ways: (1) minimizing strain energy reduces K, and (2) minimizing kinetic energy reduces mass, which reduces K. As stiffness becomes small, deflections Q become large, increasing strain energy, which the optimization routine opposes. Consequently, deflections are reduced by increasing mass and stiffness until a balance is attained in accordance with some constrained, lowest energy-state criterion.

Third, a common criterion for assessing a bladed-disk design is stress concentration. Both high stress concentrations and particular patterns of stress contours can be predictors of structural failure. The quantity that subsumes these stress-based design criteria is again strain energy V, this time in the form

$$V=\int \sigma d\varepsilon, \tag{5}$$

where σ is stress and ε is strain and the integral is simply the area under a stress-strain curve. In this case, stress concentrations are reduced by minimizing or constraining energy density and stress contours are reduced by minimizing or constraining energy contours.

Fourth, bladed-disk design is assessed according to thermal criteria involving temperature distribution and temperature gradients. A simple form of thermal energy (a form of internal energy U) for solids is given by

$$U=CT, \tag{6}$$

where C is specific heat and T is temperature. By minimizing this component of an energy-based objective function, either temperatures or temperature gradients can be included in the general optimization problem.

Fifth, vibration, a critical aspect of bladed-disk design, can be expressed in terms of kinetic energy, as follows. Axial displacement $Q(t)$ associated with the vibration of a differential mass m can be represented by

$$Q(t)=uf(t), \tag{7}$$

where u is a constant coefficient and $f(t)$ is a harmonic function, possibly represented by a discrete Fourier series [14]. It follows that the kinetic energy T, due to vibration, of a solid body comprising many discrete differential masses can be represented by

$$T=\tfrac{1}{2}(u^T Mu)\dot{f}^2, \tag{8}$$

where u is a vector of coefficients, and M is a mass matrix. By including a function of this form in the general objective function of the proposed optimization problem, vibratory blade response at resonance can be addressed.

Last, the interaction between the blade and the airstream, encompassing gas dynamics, thermodynamics, and aerodynamics, is expressible in terms of kinetic, potential, and internal energy. Thus a single energy-based objective function can incorporate both gas dynamics and structural mechanics, leading possibly to breakthrough advances in reducing the lengthy, iterative design cycle that characterizes current practice. This is a significant and difficult task, and is beyond the scope of this preliminary study. However, this concept of energy-based design clearly facilitates the needed dialogue among the discipline-specific experts involved in bladed-disk design.

As shown by these examples, significant aspects of bladed-disk design can be treated systematically and concurrently by expressing the basic physics of each in terms of energy and constraint. But this list is not exhaustive, the examples of energy expressions are over-simplified, and a specific objective function has not been identified. Herein lie the main analytical challenges to be overcome in developing an energy-based design tool: to determine physics-based expressions for all important design considerations in terms of energy and constraint and to determine an energy-based objective function that produces feasible part geometry.

3 An Outline for Future Development

In this section are presented a description of a proposed design procedure, technical tasks to be accomplished to realize the procedure, and risks associated with the development.

3.1 Attributes of a New Design Procedure. A design procedure having the following attributes is proposed. In future work this procedure would be implemented using commercially available software.

(a) Generate a parametric three-dimensional solid model of the part as an initial estimate for the optimization problem, using a CAD package for basic geometry. Since part geometry changes with each iteration of the optimization routine, new models and meshes are generated each iteration.
(b) Automatically generate a finite element (FE) mesh.
(c) Apply design loads to the solid model and compute resulting stress, strain, deflections, temperature gradients, and so forth for every differential volume in the model, using appropriate software for analysis.
(d) Compute the terms of the energy-based objective function for every differential volume and sum over the entire model.
(e) Determine a set of geometric parameters that reduces the objective function, check convergence criteria, iterate.

The new design procedure does not, however, obviate the need for experienced designers and engineers. The procedure cannot add features or create new designs; it can only optimize a given

Downloaded 02 Jun 2010 to 171.66.16.119. Redistribution subject to ASME license or copyright; see http://www.asme.org/terms/Terms_Use.cfm

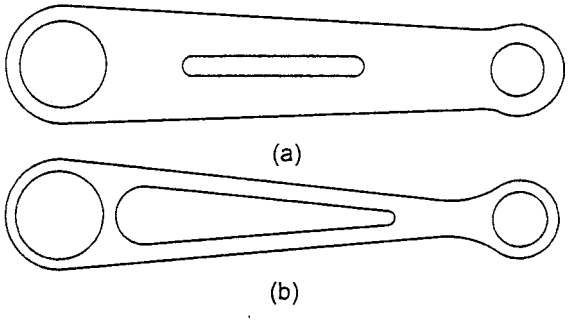

Fig. 3 Dependence of a typical structural optimization on initial parameters: (*a*) initial design; (*b*) final design

design. This is a characteristic typical of current structural optimization methods. For example, consider the structural member illustrated in Fig. 3, adapted from Zhang et al. [13]. The mass of the initial design (*a*) is minimized subject to stress allowables producing the final design (*b*). The optimization could not have enlarged the weight-saving slot in the member had not the designer defined a slot in the initial design. Similarly, bladed-disk design as described above cannot add new features nor create new designs. The method can only optimize a design based on the parameters initially defined. Thus effective use of the proposed design tool requires creative and knowledgeable users.

3.2 Technical Tasks to be Accomplished. Outlined below are the major technical tasks that would have to be accomplished to implement the new, energy-based design tool.

(a) **Physical Systems Theory**. Determine physics-based expressions for important, discipline-specific, three-dimensional design considerations in terms of energy and constraint.

(b) **Objective Function**. Determine an energy-based objective function that produces feasible part geometry.

(c) **Numerical Optimization**. Develop a numerical optimization routine suited to a computational problem of this magnitude. Conjugate gradient and method of feasible directions are candidate methods.

(d) **Computing Environment**. Select commercial software and develop the necessary architecture and interfaces to implement the prototype design tool. Write a supervisory program to control the flow of information among software packages and to and from the user.

Tasks (a) and (b) address the basic theory underlying the new approach and are both more challenging and more speculative than tasks (c) and (d). The second two tasks are areas of active research in turbine design and future work can draw extensively on recent advances in these areas.

3.3 Risks. In this section are described the risks associated with developing and implementing an energy-based approach to design and suggestions for risk mitigation are given. The list is not exhaustive but covers the significant obstacles to successful implementation of the new approach.

The first risk is that the new approach is speculative, and even if developed to maturity, may not be able to supplant well-established methods. After all, bladed-disk design is a complex topic that has been developed over many years and that produces operational engines. In mitigation of this risk, existing design processes are approaching a limit in their ability to meet customer requirements for new, high-performance products that are developed faster and are cheaper to operate and maintain. It is imperative that industry examine the process from a new perspective—one that is not entrenched in the iterative-aero-structures tradition, but that nevertheless captures the basic dynamics of the physical system. The systems perspective on which the new design approach is based, dating in contemporary form to the work of Paynter with classical roots in the work of Lagrange and Hamilton, meets this need [15].

The second risk is the difficulty of expressing important design considerations in terms of energy and constraint. In mitigation, physical systems theory supports the concept. The study of energy begins with the first and second laws of thermodynamics, and there is a demonstrable connection between these energy laws and the dynamic response of physical systems, as shown, for example, in [16]. Expressing important design considerations in terms of energy and constraint is not an easy task, but it is in accord with basic physics.

Third, it is possible that the problem posed will be numerically intractable. In mitigation, computing resources continue to become faster, cheaper, and more powerful. In our opinion, straightforward computing power is not an issue. However, numerical issues related to size, convergence, and existence of solutions could arise. One approach to mitigating this problem is to ensure that energy functions are quadratic as in Eqs. (2) and (3), since solution existence and uniqueness for quadratic functionals are well understood [17].

Fourth, an energy-based objective function has not been defined and cannot be assessed as a design tool. In mitigation, an energy-based objective function unifies existing design optimization strategies, as described in Section 2.3. The objective function may have the form of total energy, energy distribution or energy contours. It may be too that an all-inclusive energy-based objective function is too coarse a measure to be suited to all design issues. If so, a series of objective functions can be developed, each suited to the problem at hand (high stress at blade roots, crack initiation and propagation, damping, and so forth), but each based on the systematic treatment of the problem in terms of energy and constraint.

Fifth, differential equations of motion have not been accounted for in the new approach. In mitigation, it is uncertain that explicit ordinary differential equations (ODEs) or partial differential equations (PDEs) are required in the optimization problem, since energy and constraint expressions are sufficient to determine a system's dynamic response. However, should the satisfaction of ODEs be a necessary condition of solving the design problem, it is proposed to adjoin the ODEs to the optimization problem as a set of dynamic constraints, as first defined in Fabien and Layton [18] and used in the material-property design and optimization procedure exploited in Thielman [19]. Including PDEs is a more complex issue. However, numerical methods of solving PDEs, such as the method of lines, can lead to equations of motion expressed as a set of differential equations subject to algebraic constraints [20], a formulation readily incorporated in the structure of a constrained optimization problem with dynamic constraints.

Last, the typical corporate organizational structure, based on engineering discipline and functional task, hinders the implementation of multidisciplinary design methods. In mitigation, engineers, particularly team leaders and managers, are finding it increasingly important to acquire technical competence outside their core disciplines. Design is coming to be viewed as a systems engineering task instead of a collection of tasks in aerodynamics, thermodynamics, structural mechanics, and so forth. In our opinion, design procedures that purposely preserve traditional disciplinary groupings, such as the ''integrated optimization'' of Kao et al. [10] or the ''collaborative optimization'' of Braun et al. [21], for example, even though they improve analytical fidelity, are unlikely to satisfy the market-driven need for significant reductions in design-cycle time.

4 Conclusion

The new approach for bladed-disk design presented in this paper is consistent with the view that the dynamic response of a

Downloaded 02 Jun 2010 to 171.66.16.119. Redistribution subject to ASME license or copyright; see http://www.asme.org/terms/Terms_Use.cfm

physical system is a consequence of the energy transactions occurring in the system. The proposed numerical optimization problem is of the same order of complexity as current structural optimization strategies and so should be tractable, although the efficacy of an energy-based objective function is unproved. Expressing important design criteria in terms of energy and constraint is conceptually straightforward but may prove to be an arduous task.

The new method promises to unify important aspects of current design methods from many disciplines, laying a foundation for an integrated design approach that could lead to breakthrough advances in bladed-disk design. Assessing the approach waits on future development of a prototype design tool and a comparison of the results of energy-based design to the results of conventional design. The outline of such a development, including the technical tasks to be accomplished and risks associated with the development, suggests that developing such a design tool is feasible.

Lastly, the authors hope that this study will facilitate interaction among practitioners of the various disciplines involved in bladed-disk design. The manipulation of energy provides a common, physics-based language and perspective that should, to echo Srinivasan [8], promote and maintain a dialogue among experts to meet modern design goals.

Acknowledgments

Our thanks to our many colleagues at Pratt & Whitney who offered critical comments and suggestions, and to Frank Shurick and Bill Jobbagy in particular for initiating and supporting this study. Thanks are also due to Al Brockett at Pratt & Whitney, Ted Fecke at Wright Research Site, and Bob Brockman at University of Dayton Research Institute for their interest and comments.

References

[1] Zboinski, G., and Ostachowicz, W., 1997, ''General FE Algorithm for 3D Incremental Analysis of Frictional Contact Problems of Elastoplasticity,'' Finite Elem. Anal. Design, **27**, No. 4, pp. 289–305.

[2] Zboinski, G., and Ostachowicz, W., 1997, ''General FE Computer Program for 3D Incremental Analysis of Frictional Contact Problems of Elastoplasticity,'' Finite Elem. Anal. Design, **27**, No. 4, pp. 307–322.

[3] Csaba, G., and Andersson, M., 1997, ''Optimization of Friction Damper Weight, Simulation and Experiments,'' Proceedings, *ASME International Gas Turbine and Aeroengine Congress and Exposition*, ASME Paper 97-GT-115, ASME, New York.

[4] Frischbier, J., Schulze, G., Zielinski, M., and Ziller, G., 1996, ''Blade Vibrations of a High Speed Compressor Blisk-Rotor, Numerical Resonance Tuning and Optical Measurements,'' Proceedings, *ASME International Gas Turbine and Aeroengine Congress and Exposition*, ASME Paper 96-GT-24, ASME, New York.

[5] Natalini, G., and Sciubba, E., 1996, ''Choice of the Pseudo-Optimal Configuration of a Cooled Gas-Turbine Blade Based on a Constrained Minimization of the Global Entropy Production Rate,'' Proceedings, *ASME International Gas Turbine and Aeroengine Congress and Exposition*, ASME Paper 96-GT-509, ASME, New York.

[6] Goel, S., Cofer, IV, J., and Singh, H., 1996, ''Turbine Airfoil Design Optimization,'' Proceedings, *ASME International Gas Turbine and Aeroengine Congress and Exposition*, ASME Paper 96-GT-158, ASME, New York.

[7] Kodiyalam, S., Kumar, V., and Finnigan, P., 1992, ''Constructive Solid Geometry Approach to Three-Dimensional Structural Shape Optimization,'' AIAA J., **30**, No. 5, pp. 1408–1415.

[8] Srinivasan, A. V., 1997, ''Flutter and Resonant Vibration Characteristics of Engine Blades,'' ASME J. Eng. Gas Turbines Power, **119**, No. 4, pp. 742–775.

[9] Narayan, J., Chattopadhyay, A., Pagaldipti, N., and Zhang, S., 1995, ''Integrated Aerodynamics and Heat Transfer Optimization Procedure for Turbine Blade Design,'' Proceedings, *36th AIAA/ASME/ASCE/AHS/ASC Structures, Structural Dynamics, and Materials Conference and AIAA/ASME Adaptive Structures Forum*, AIAA Paper AIAA-95-1479-CP, AIAA, New York, pp. 2973–2982.

[10] Kao, P-J., Parthasarathy, V., and Kodiyalam, S., 1994, ''Coupled Aerodynamic-Structural Shape Optimal Design of Engine Blades,'' Proceedings, *35th AIAA/ASME/ASCE/AHS/ASC Structures, Structural Dynamics, and Materials Conference*, AIAA Paper AIAA-94-1479-CP, AIAA, New York, pp. 1317–1323.

[11] Wellstead, P., 1979, *Introduction to Physical System Modelling*, Academic Press, London.

[12] Botkin, M., 1992, ''Three-Dimensional Shape Optimization Using Fully Automatic Mesh Generation,'' AIAA J., **30**, No. 7, pp. 1932–1934.

[13] Zhang, W., Beckers, P., and Fleury, C., 1995, ''A Unified Parametric Design Approach to Structural Shape Optimization,'' Int. J. Numer. Methods Eng., **38**, pp. 2283–2292.

[14] Meirovitch, L., 1967, *Analytical Methods in Vibrations*, Macmillan, New York, pp. 76–81.

[15] Paynter, H., 1961, *Analysis and Design of Engineering Systems*, MIT Press, Cambridge, MA.

[16] Layton, R., 1998, *Principles of Analytical System Dynamics*, Springer-Verlag, New York, pp. 67–83.

[17] Gill, P., Murray, W., and Wright, M., 1981, *Practical Optimization*, Academic Press, London, pp. 59–82.

[18] Fabien, B., and Layton, R., 1997, ''Modeling and Simulation of Physical Systems III: An Approach for Modeling Dynamic Constraints,'' Proceedings, *IASTED International Conference in Applied Modelling and Simulation.*

[19] Thielman, S., 1997, ''*Design and Optimization of a Material Property Distribution in a Composite Flywheel*,'' Ph.D. dissertation, University of Washington, Seattle, WA, pp. 9–22.

[20] Brenan, K., Campbell, S., and Petzold, L., 1996, *Numerical Solution of Initial-Value Problems in Differential-Algebraic Equations*, Society for Industrial and Applied Mathematics (SIAM), Philadelphia, PA, pp. 10–13.

[21] Braun, R., Gage, P., Kroo, I., and Sobieski, I., 1996, ''Implementation and Performance Issues in Collaborative Optimization,'' Proceedings, *6th AIAA/NASA/ISSMO Symposium on Multidisciplinary Analysis and Optimization*, Paper AIAA-96-4017-CP, AIAA, Reston, VA, pp. 295–305.

Downloaded 02 Jun 2010 to 171.66.16.119. Redistribution subject to ASME license or copyright; see http://www.asme.org/terms/Terms_Use.cfm

Experimental Evaluation of a Metal Mesh Bearing Damper

Mark Zarzour
John Vance
Mechanical Engineering Department,
Texas A&M University,
1214-B Webhollow,
College Station, TX 77843

Metal mesh is a commercially available material used in many applications including seals, heat shields, filters, gaskets, aircraft engine mounts, and vibration absorbers. This material has been tested by the authors as a bearing damper in a rotordynamic test rig. The test facility was originally used to support the design of a turboprop engine, developing squirrel cages and squeeze film dampers for both the gas generator and power turbine rotors. To design the metal mesh damper, static stiffness and dynamic rap test measurements were first made on metal mesh samples in a specially designed nonrotating test fixture. These property tests were performed on samples of various densities and press fits. One sample was also tested in an Instron machine as an ancillary and redundant way to determine the stiffness. Using the stiffness test results and equations derived by a previous investigator, a spreadsheet program was written and used to size metal mesh donuts that have the radial stiffness value required to replace the squirrel cage in the power turbine. The squirrel cage and squeeze film bearing damper developed for the power turbine rotor was then replaced by a metal mesh donut sized by the computer code. Coast down tests were conducted through the first critical speed of the power turbine. The results of the metal mesh tests are compared with those obtained from previous testing with the squeeze film damper and show that the metal mesh damper has the same damping as the squeeze film at room temperature but does not lose its damping at elevated temperatures up to 103°C. Experiments were run under several different conditions, including balanced rotor, unbalanced rotor, heated metal mesh, and wet (with oil) metal mesh. The creep, or sag, of the metal mesh supporting the rotor weight was also measured over a period of several weeks and found to be very small. Based on these tests, metal mesh dampers appear to be a viable and attractive substitute for squeeze film dampers in gas turbine engines. The advantages shown by these tests include less variation of damping with temperature, ability to handle large rotor unbalance, and the ability (if required) to operate effectively in an oil free environment. Additional testing is required to determine the endurance properties, the effect of high impact or maneuver loads, and the ability to sustain blade loss loads (which squeeze films cannot handle). [S0742-4795(00)01002-4]

Introduction

Squeeze-film dampers (SFD) are used extensively in almost all aircraft turbine engines designed since 1970, and have been installed in more than 300 multistage industrial compressors to raise stability thresholds. However, the SFD has some shortcomings that are difficult to overcome. If the local rotor imbalance exceeds 2.3 times the damper clearance, the SFD actually increases the response. Also, nonlinear phenomena (bistable jump up) may occur. Twenty years of applied research on SFD has failed to produce analysis tools that can accurately predict the performance of any except the simplest geometry under laboratory conditions [1]. Testing of a full-scale prototype aircraft engine rotor with squeeze film dampers in the authors' laboratory showed a large increase in rotor response when the oil temperature was raised from 27°C to 119°C.

Two researchers in China, Wang and Zhu [2] publicized a replacement for the SFD that did not require fluid. They described this damper as a short hollow cylinder made of woven metal material. Xin and Zi-Gen called the woven metal ''metal rubber,'' and reported that it had good internal damping properties. They tested a metal mesh damper in a rotordynamic rig and a SFD in the same rig for comparison. The results are remarkable; they show the metal mesh damper controlling almost three times more unbalance than the SFD.

Joe Tecza [3] also reports tests of a metal mesh damper in a rotordynamic rig in the fall of 1991. The project was internally supported by Tecza's company in an effort to obtain an Air Force contract. The results were encouraging but the external funds were not obtained to continue the project so it was dropped. Although previously performed research has shown great promise for the metal mesh bearing dampers, test results have not been published to show the effect of temperature or the effect of an oil environment. Prediction tools for sizing a metal mesh damper are yet to be developed and made available to machine designers.

Test Apparatus

A nonrotating test apparatus was used to determine the static stiffness and damping of two densities of metal mesh. The test apparatus consisted of two concentric cylinders that were used to constrain the inner and outer boundary of the metal mesh. A steel ring was constructed to fix the outer dimension of the metal mesh contained between it and the inner cylinder. The diameters of these inner cylinders varied in size to put different press fits on the metal mesh. The inner cylinder was fixed to the top of a rigid concrete and metal slab. To fix the inner cylinder, an aluminum cap was placed on top of the inner cylinder and a bolt was placed through the center of the top into the table. The outer steel ring of the assembled rig did not rest on the table, therefore, it was free to move in the horizontal plane, parallel to the tabletop. This test setup is shown in Fig. 1.

Contributed by the International Gas Turbine Institute (IGTI) of THE AMERICAN SOCIETY OF MECHANICAL ENGINEERS for publication in the ASME JOURNAL OF ENGINEERING FOR GAS TURBINES AND POWER. Paper presented at the International Gas Turbine and Aeroengine Congress and Exhibition, Indianapolis, IN, June 7–10, 1999; ASME Paper 99-GT-15.
Manuscript received by IGTI March 9, 1999; final revision received by the ASME Headquarters January 3, 2000. Associate Technical Editor: D. Wisler.

 Copyright © 2000 by ASME

Downloaded 02 Jun 2010 to 171.66.16.119. Redistribution subject to ASME license or copyright; see http://www.asme.org/terms/Terms_Use.cfm

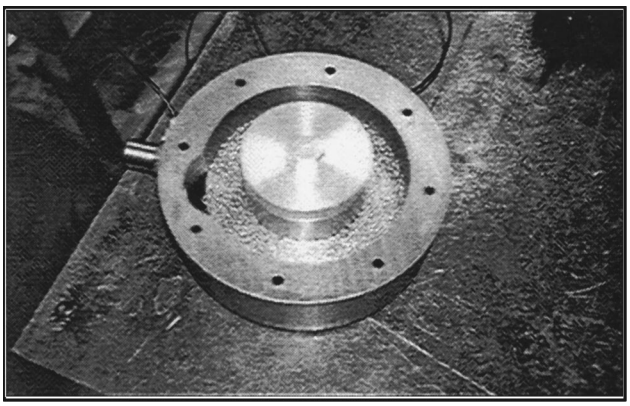

Fig. 1 Nonrotating test apparatus

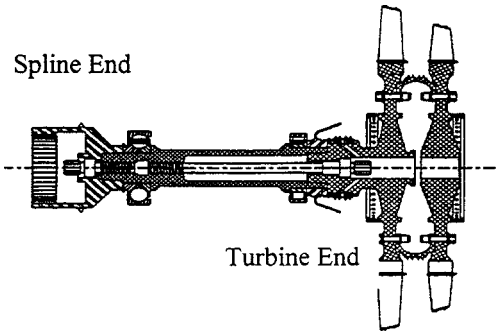

Fig. 2 Power turbine rotor

A power turbine test rig was used in the rotordynamic testing of the metal-mesh damper. The power turbine rotor assembly is made up of two turbine wheels, an Inconel shaft, and a steel spline. The assembly is press fitted together and fastened with two tie-bolts. A cross section of the assembled power turbine rotor is shown in Fig. 2.

The weight of the fully assembled rotor is 147.6 N. It is driven by an air turbine in the test cell. The power turbine test rotor has a ball bearing at the spline end and a roller bearing at the turbine end. The original test rotor used two squeeze film dampers to provide damping. A squirrel cage, which provided a specific stiffness, accompanied each squeeze film damper. The squirrel cage located at the spline end had a stiffness of approximately 5253 kN/m. The squirrel cage at the turbine end had a stiffness of approximately 4990 kN/m. For the metal-mesh testing, the squirrel cage at the spline end of the roller-bearing system was retained but the land of the squeeze film damper was removed to insure that this bearing had no damping. Thus, there was no damping in the system except that provided by the metal-mesh donut at the turbine end. The assembled power turbine test rotor can be seen in Fig. 3.

Preliminary Analysis and Results

To try and match the stiffness and damping of the squeeze-film dampers previously installed, stiffness testing, damping tests, and computer analysis were performed on two densities of metal mesh samples. Samples of 29 percent density were tested for stiffness using the nonrotating test apparatus in Fig. 1, with a hand held force gauge, and a dial indicator. The 29 percent density sample had dimensions 57.15 mm ID, 99.57 mm OD, and 12.7 mm thickness. The test was performed with press fits ranging from (1.27 mm) to (3.048 mm). These tests indicate that the stiffness of this material increases as the press fit is increased. The stiffness values for the two extremes of fit were not close to our target stiffness of 4,990 kN/m, (for rotordynamic testing to be done later).

To obtain a stiffness value closer to the target value, a sample of 57 percent density was tested. The 57 percent density sample had dimensions 58.42 mm ID, 95.76 mm OD, and 11.176 mm thickness. This sample was tested in an Instron machine where both loading and unloading could be graphed. To perform this test, the inner and outer surface of the mesh was fixed by cylinders. A solid rod was placed through the center of the inner cylinder (see Fig. 4). This test yielded a stiffness value close to 3502 kN/m, which was input into a spreadsheet program to obtain an equivalent modulus of elasticity. The metal-mesh spreadsheet program had been previously developed with support from a research consortium (see the Acknowledgements). It takes the dimensions and equivalent modulus of elasticity of the metal-mesh as input, and outputs the stiffness by curve-fitting a number of points. The equations used in these computer programs may be the subject of a future paper after refinement by further testing.

Since the stiffness was measured, the modulus of elasticity for the 57 percent density sample could be backed out of the program as approximately 1628 kN/m. This value along with the desired inner and outer diameter were input back into the equations leaving the stiffness as a function of width only. The width was then altered to obtain an acceptable value for stiffness. Using the dimensions for inner and outer diameter that are required for the power turbine hardware, a stiffness of 5734 kN/m was obtained from the metal mesh program. The dimensions for the final metal-mesh damper were then 76.2 mm ID, 108.6 mm OD, and 12.7 mm thickness.

In order to measure the damping of the metal mesh, the outer steel ring of the nonrotating test rig was rapped with a plastic hammer to obtain a time response and frequency spectrum. The free vibration data were collected using an accelerometer attached

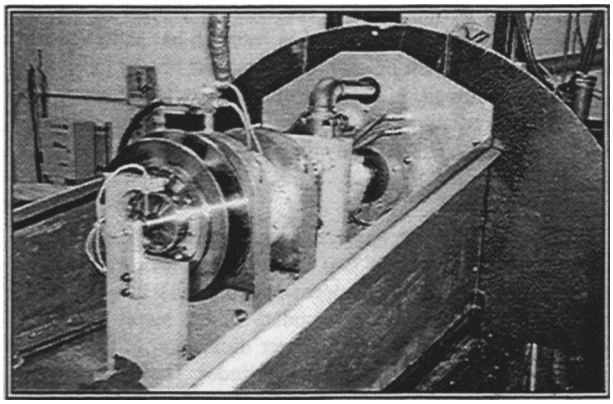

Fig. 3 Assembled power turbine test rig

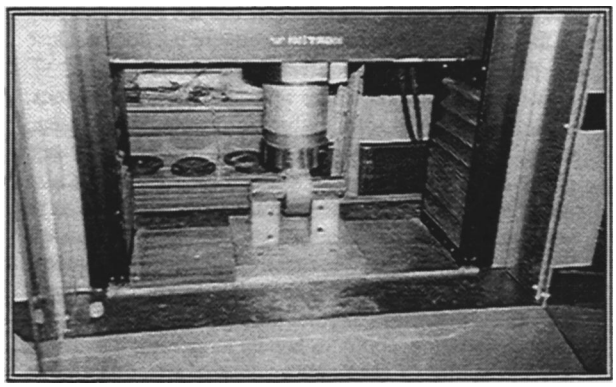

Fig. 4 Instron machine and test setup for stiffness testing

Downloaded 02 Jun 2010 to 171.66.16.119. Redistribution subject to ASME license or copyright; see http://www.asme.org/terms/Terms_Use.cfm

Table 1 Effects of press fit on damping

Configuration	Press fit	Log Dec	Damping Ratio
Press fit #1	1.27 mm	0.988	0.155
Press fit #2	1.905 mm	0.815	0.129
Press fit #3	2.54 mm	0.534	0.085
Press fit #4	3.048 mm	0.451	0.0702

to the outer ring. Ten raps were averaged using a Hewlett Packard signal analyzer. The time response was used to obtain the log decrement and the frequency spectrum identified the natural frequency of the system. Table 1 shows the log decrement and damping ratio for several different press fits. The decrease of the log decrement with tightness of fit is entirely due to an increase in stiffness, as can be deduced from Table 2. The increased stiffness raises the value of critical damping, which then produces a lower damping ratio. There is some evidence from the experimental data that the nature of the damping is predominantly hysteretic. Table 3 shows values of the loss coefficient β ($k\beta$ is the imaginary part of a complex stiffness) and the hysteretic damping coefficient h. These were computed from the measured data using $h=c\omega$, and $\beta=h/k$, where c is the equivalent viscous damping coefficient and the frequency ω is in rad/sec.

Experiments are currently underway to determine how the damping varies with frequency and to conclusively determine

Table 2 Effect of press fit on stiffness

Press Fit (D)	Stiffness k
1.27 mm	924 kN/m
3.048 mm	3021 kN/m

Table 3 Loss and hysteretic coefficients

Press Fit (D)	β	h
1.27 mm	0.319	295 kN/m
3.048 mm	0.097	293 kN/m

what mechanism is responsible for the damping. It is not currently known whether or not the damping and stiffness parameters would be affected by a static eccentricity due to an offset load.

Rotordynamic Testing and Results

Computer analysis of the power turbine mode shapes was performed to determine if the metal mesh would be needed at both bearings. The first critical speed of the rotor bearing system with the original squirrel cage configuration was at 3200 RPM. The mode shape associated with it shows large amplitude of vibration at the turbine end. It became apparent that metal-mesh would only need to be installed at the turbine end for a complete rotordynamic evaluation at the first critical speed. With high levels of vibration at the turbine end and no other form of external damping in the system, the metal-mesh donut is responsible for providing the damping necessary to transverse the first critical speed.

The power turbine test rig was run up to a speed of 7000 RPM, since it was only necessary to coast down through the first critical speed. The second mode shape has the largest amplitude at the spline end where there is no damping so the second critical speed

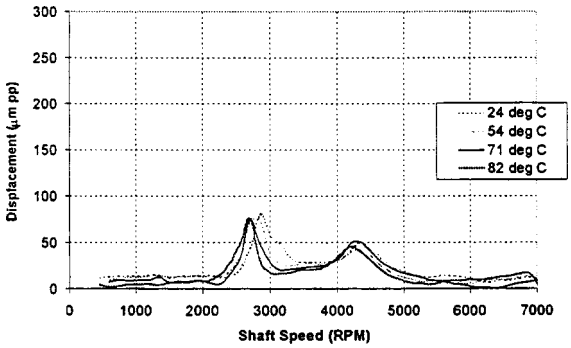

Fig. 5 Balanced condition @ Rx-probe with metal-mesh installed, multiple temperatures

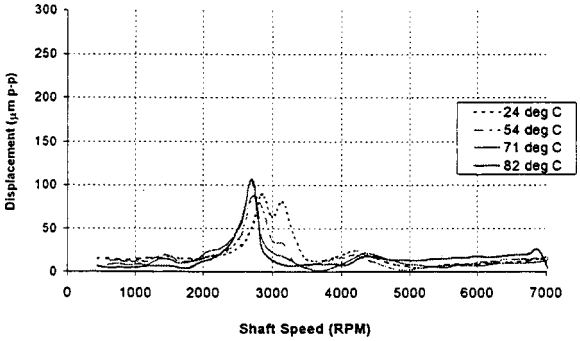

Fig. 6 Balanced condition @ Ry-probe with metal-mesh installed, multiple temperatures

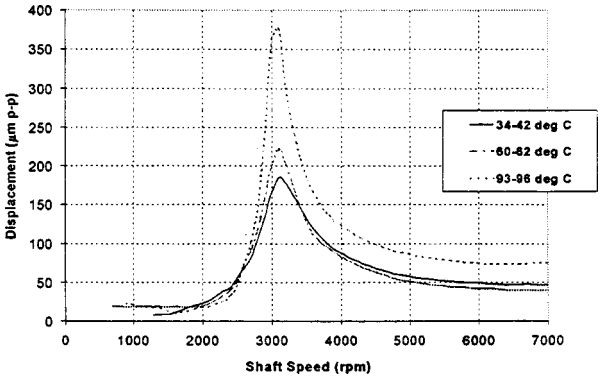

Fig. 7 Unbalanced condition @ Rx-probe with squeeze-film damper installed, multiple temperatures

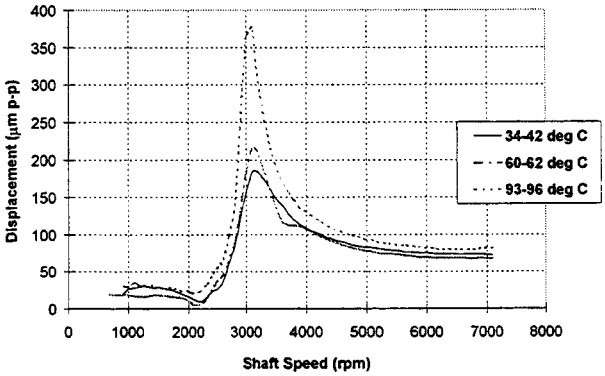

Fig. 8 Unbalanced condition @ Ry-probe with squeeze-film damper installed, multiple temperatures

Downloaded 02 Jun 2010 to 171.66.16.119. Redistribution subject to ASME license or copyright; see http://www.asme.org/terms/Terms_Use.cfm

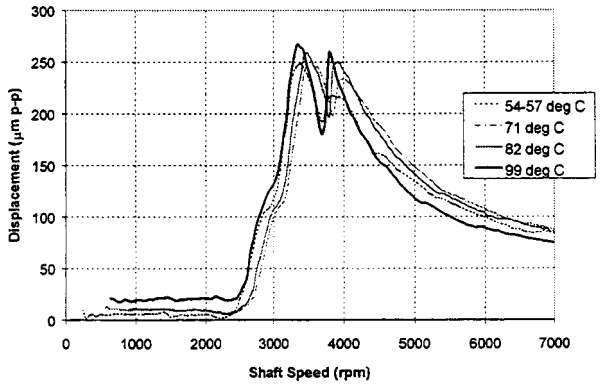

Fig. 9 Unbalanced condition @ Rx-probe with metal-mesh installed, multiple temperatures

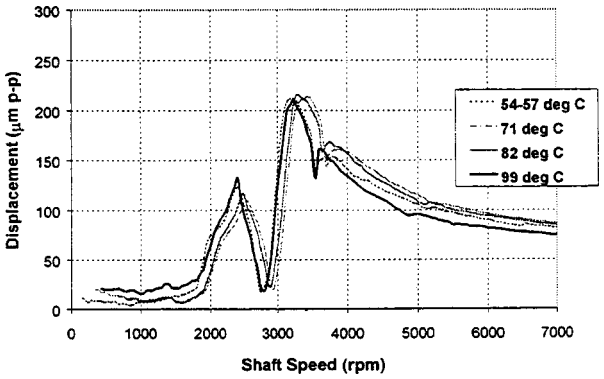

Fig. 10 Unbalanced condition @ Ry-probe with metal mesh installed, multiple temperatures

was to be avoided. All data presented is from the horizontal and vertical proximity probes at the turbine end of the rotor (X,Y).

The metal-mesh was tested under several conditions including hot, cold, balanced rotor, and unbalanced rotor. For tests requiring high temperatures the metal-mesh was heated with oil that flowed over it. The mesh was first tested dry and then soaked with room temperature oil to determine whether oil would affect the damping. It did not. A heating strip was then used to heat the oil that flowed from the pump to the test rig and through the metal mesh. A valve could be closed for tests not requiring high temperature oil. To monitor the temperature of the oil entering, a thermocouple was placed at the inlet of the bearing pedestal containing the metal-mesh donut.

A set of tests was performed with the rotor balanced. The rotor was balanced in one plane to achieve an acceptable level of vibration. The amplitude of vibration was reduced to 30 percent of its original unbalanced state. The test rig was run with the metal-mesh dry and with oil at 54°C, 71°C, and 82°C. The results of the balanced tests are shown in Figs. 5 and 6. They show the response at the turbine end where the highest vibration amplitudes exist. The critical speed peaks in Fig. 5 are slightly shifted to the left as the temperature increases. The RY amplitude increased approximately 20 percent at temperatures of 71°C and 82°C. Both Figs. 5 and 6 (RX, RY) show split critical speeds. This may be due to stiffness asymmetry in the metal-mesh.

The second and most important test condition was the unbalanced condition. This condition is important since the squeeze film damper had much larger levels of vibration with an unbalanced rotor at high temperatures. These tests were run with oil at 54°C, 71°C, 82°C, and 99°C. Results of these tests can be compared with those obtained with the squeeze film damper previously installed. Figures 7 and 8 show the measured response with the squeeze film dampers at an oil supply pressure of 1.034 bar. They show the response at the X and Y probes (turbine end). The amplitude of vibration with the squeeze film dampers increases dramatically at elevated temperatures. For comparison, tests were run at similar temperatures with the metal-mesh installed. Figures 9 and 10 show the results. Although the rotor unbalance is probably not exactly the same as it was with the squeeze-film dampers installed, the results can be compared as a percent increase in the level of vibration with increase in temperature. Observation of the response bandwidths suggests that the metal-mesh damping at all temperatures is about the same as the squeeze-film damper at room temperature. The results with metal-mesh show that there is no correlation between temperature and amplitude of vibration.

Conclusion

The following conclusions apply only to the parameters tested. However, it should be remarked that they are full scale parameters of a power turbine test rig used to develop a turboprop aircraft engine.

a Metal-mesh has useful damping properties that can be used to reduce rotordynamic amplitudes of vibration
b the damping provided by the metal-mesh is not significantly temperature dependent over the range of 54–99°C
c the damping provided by the metal-mesh is not affected by the presence of turbine oil
d higher temperatures appear to have a de-stiffening effect on the metal-mesh bearing damper under balanced conditions
e increasing the radial press-fit interference of the metal-mesh damper ring has a stiffening effect that decreases the free vibration damping ratio
f increasing the radial press-fit interference of the metal-mesh damper ring has a negligible effect on the hysteretic damping coefficient
g a spread sheet program is being developed that shows promise as a design tool for metal-mesh bearing dampers

Acknowledgments

The help of Metex Corporation in providing damper rings of several different densities is gratefully acknowledged. The help of Air Tractor Inc. in providing the test rotor and associated hardware is gratefully appreciated. This research was supported by the Turbomachinery Research Consortium at Texas A&M University.

References

[1] Zeidan, F. Y., San Andres, L. A., and Vance, J. M., 1996, ''Design and Application of Squeeze Film Dampers in Rotating Machinery,'' *Proceedings of the 25th Turbomachinery Symposium*, Houston, Texas, pp. 169–188.
[2] Wang, X., 1996, private internet communication.
[3] Tecza, J., 1997, private telephone and email communication, Mechanical Technology Incorporated.

Downloaded 02 Jun 2010 to 171.66.16.119. Redistribution subject to ASME license or copyright; see http://www.asme.org/terms/Terms_Use.cfm

Hybrid Brush Pocket Damper Seals for Turbomachinery

Hector E. Laos
John M. Vance
Steven E. Buchanan
Department of Mechanical Engineering,
Texas A&M University,
College Station, Texas 77843-3123

Pocket damper seals perform a dual function: both sealing the pressurized gas around a rotating shaft and providing large amounts of vibration damping. The annular cavity between the labyrinth seal teeth is subdivided into separate annular cavities around the circumference of the rotor by partitioning walls. Also, the upstream and downstream teeth have different radial clearances to the rotor. These seals have been shown to provide a remarkable amount of direct damping to attenuate vibration in turbomachinery, but they generally leak more than conventional labyrinth seals if both seals have the same minimum clearance. Conversely, brush seals allow less than half the leakage of labyrinth seals, but published test results show no significant amount of damping. They are considered to be a primary choice for the seals in new aircraft engine designs because of their low leakage. This paper will describe a recently invented hybrid brush/pocket damper seal that combines high damping with low leakage. Previous brush seal results were studied and calculations were made to select a brush seal to combine with the pocket damper design. The result is a hybrid seal with high damping and low leakage. A special design feature can also allow active vibration control as a bonus benefit. A computer code written for the original pocket damper seal was modified to include the brush element at the exit blade. Results from the computer code indicate that the hybrid seal can have less leakage than a six bladed (or 6 knives) labyrinth seal along with orders of magnitude more damping. Experimental evaluations of the damping and leakage performance of the hybrid seal are being conducted by the authors. The experimental work reported here tested the damping capability of the new hybrid brush seal by exciting the seal journal through an impedance head. A conventional six-bladed labyrinth seal of the same working dimensions was also tested. The brush hybrid pocket damper seal is found to leak less than the labyrinth seal while producing two to three times more damping than the original pocket damper seal (orders of magnitude more than the conventional labyrinth). [S0742-4795(00)01102-9]

Introduction

Rotating fluid seals are critical components affecting the performance and efficiency of modern turbomachines. For example, gas seals are employed in both the compressor and turbine sections of aircraft engines, where the stage pressures range up to eight bar. Gas seals with much higher pressures are used in oil industry compressors for natural gas reinjection and in petrochemical process plants. Traditionally, rotating seals have been designed solely to minimize leakage. In the case of steam turbines the destabilizing effects of the labyrinth seals were studied by Thomas [1]. Starting in the 1960s [2] rotating seals were found to have a major effect on rotordynamics and vibration in aircraft engine compressors. In the case of the space shuttle main engine turbopumps, rotating seals are the major mechanical component which allow stable operation [3–5]. The fluid mechanics theory of rotating seals is quite complex as the flow is turbulent and takes place through intricate and tortuous passages.

This paper describes continuing research on an innovative gas damper seal element whose potential benefits are revolutionary in terms of damping capability to attenuate rotor vibrations along with pressure sealing. It is a light weight, compact, and high temperature compatible mechanical element that can be used as a direct replacement for the common labyrinth seal at the most effective locations for rotor damping in turbomachines. The first published description of this gas damper seal [6] referred to it as the TAMSEAL™. In this paper the generic description will be ''pocket damper seal'' (PDS for short) and the particular advancement described here will be called the ''brush hybrid pocket damper seal'' or ''brush hybrid seal'' (BHS) for short. Test results and field applications to date suggest that the BHS may be an advance in vibration suppression for turbomachinery with significance similar to the invention of the squeeze film damper at Rolls Royce in 1959. The first patent granted on squeeze film dampers marked the beginning of extensive research on that device which still continues today and which has produced hundreds of technical publications addressing the basic scientific issues surrounding it. The internal fluid dynamics theory of the pocket damper seal is even more complex, involving fluid compressibility and flow turbulence. But the potential for effectiveness is greater since seals are often found at optimal locations for damping in turbomachines, whereas bearings are usually near the nodes of the modes of interest.

The most common type of pressure seal in high-speed turbomachinery is the labyrinth seal. This seal is composed of a series of circular blades and annular grooves which present a tortuous path for flow of the process fluid in regions of high to low pressures between stages in turbines and compressors. Although they are effective for leakage control, labyrinth seals show very little direct damping and their cross coupled stiffness can be the source of rotordynamic instabilities in rotating machinery [4]. Extensive experimental tests over the past two decades [7,8] have demonstrated the undesirable dynamic force characteristics of gas labyrinth seals. These experiments have shown the presence of significant cross-coupled stiffness force coefficients induced by the rotation of the seal journal. They can easily overcome the action of direct damping and produce unstable rotor whirling at frequencies well below the operating speed. The most direct and effective way to avoid this problem is to employ damper seals,

Contributed by the International Gas Turbine Institute (IGTI) of THE AMERICAN SOCIETY OF MECHANICAL ENGINEERS for publication in the ASME JOURNAL OF ENGINEERING FOR GAS TURBINES AND POWER. Paper presented at the International Gas Turbine and Aeroengine Congress and Exhibition, Indianapolis, IN, June 7–10, 1999; ASME Paper 99-GT-16. Manuscript received by IGTI March 9, 1999; final revision received by the ASME Headquarters January 3, 2000. Associate Technical Editor: D. Wisler.

 Copyright © 2000 by ASME

Downloaded 02 Jun 2010 to 171.66.16.119. Redistribution subject to ASME license or copyright; see http://www.asme.org/terms/Terms_Use.cfm

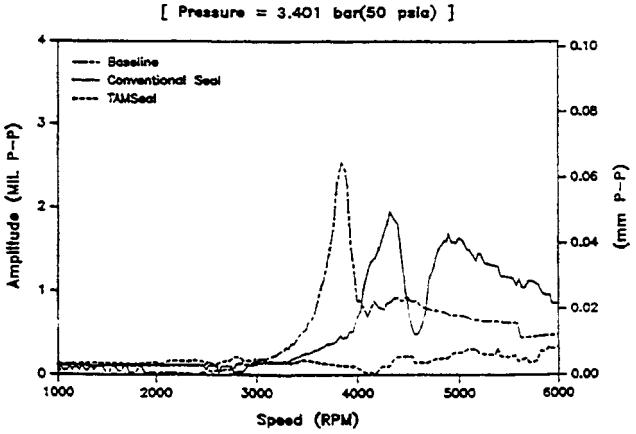

Fig. 1 Measured unbalance response with no seal, labyrinth seal, and a pocket damper seal (TAMSEAL™) [17]

such as the honeycomb type [9], or the pocket damper seal that is the subject of this paper. Laboratory testing has shown the pocket damper seal to have direct damping large enough to completely eliminate the appearance of critical speeds (see Fig. 1). They have successfully suppressed rotordynamic instabilities in several high-pressure compressors [10]. The main incentive for design improvement lies in the fact that the leakage so far has been larger than for a conventional labyrinth seal of the same dimensions and clearance. The brush hybrid aims to correct this deficiency.

Brush seals are a relatively new development that have been used to some extent in aircraft turbine engines [11] and are under serious consideration for steam turbines [12]. Most current aircraft turbine engine seals are labyrinth or brush types. The labyrinth seal has a high leakage rate, low damping capability to reduce blade rub, and allows undesirable fluid swirl, which is destabilizing. The brush seal exhibits very low leakage, but previous tests [13] have shown very little damping capacity. More recently, engine tests were made to compare the forward-facing labyrinth seal with dual-brush seals installed as compressor discharge seals [14]. The leakage of the brush seals was only 40 percent of the labyrinth leakage, so specific fuel consumption was improved three to five percent. The brush hybrid pocket damper seal combines the desirable low leakage of a brush seal with the high damping characteristics of the pocket damper seal.

Physical Description

Figure 2 shows a cross section of the brush hybrid pocket damper seal. The inlet blade, or upstream tooth, of this seal is identical to a labyrinth seal. The downstream blades are replaced by a brush seal element. Partition walls around the circumference form pockets that isolate regions of dynamically varying pressure. This design is meant to allow the journal vibration to modulate the flow into the pockets through the inlet blade clearance while minimizing the modulation of the exit flow (downstream) through the brush seal. In that case the dynamically varying pressure forces will always oppose the seal journal vibratory velocity, which is the very definition of a damping force. A secondary function of the pocket partition walls is to block the destabilizing circumferential swirl of the fluid around the journal. Optional bypass flow orifices are provided in case the brush leakage is too low to produce the desired pressure modulations, or they can be used with valves to implement active control of the damping.

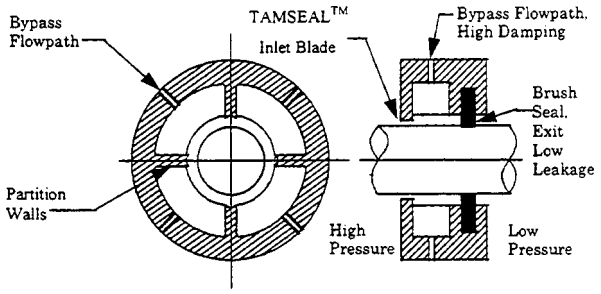

Fig. 2 The brush hybrid pocket damper seal with optional bypass flow paths

Development of the pocket damper seal began in the early 1990s when experimental and analytical research on gas damper actuators for bearing supports [15,16] led to a better understanding of the flow mechanics in gas sealing devices and to the discovery of a new mechanism for damping action. The pocket damper seal concept replaces the limited damping characteristics of conventional labyrinth seals without a major alteration of their geometry and without the addition of heavy and costly hardware. Modal analysis shows that the relative effectiveness of a damper at two different locations along a rotor is proportional to the square of the ratio of whirl amplitudes at the two locations. Rotor whirl amplitudes at seal locations are typically at least twice the amplitude at bearings, so a damper seal will be at least four times more effective than a bearing damper with the same damping coefficient.

In the original pocket damper seal, modulation of the exit flow was accomplished by making the exit (downstream) blade clearance larger, but this increased the leakage [6,17]. In the brush hybrid, much of the leakage flow passes through the bristles and is unmodulated by the journal vibration. Theory predicts that this will increase the damping. The leakage allowed by a brush is greatly reduced, down to values much less than allowed by a conventional labyrinth seal.

It is important to note that the pocket damper seal is unlike all other damping elements commonly used, in that it does not rely on viscosity of a fluid to dissipate energy. In fact, it would be more effective with a purely inviscid fluid, since fluid viscosity will slow the transfer of gas from pocket to pocket and produce unwanted time lags across the flow restricting clearances.

Computer Predictions

Although the primary objective of this paper is to show experimental results, it is instructive to briefly look at some computer predictions based on the theory described by Vance and Shultz, [6]. This theory considers only the continuity equations and compressibility effects for the gas flow into and out of the pockets in the axial (downstream) direction. Only the leakage and the direct force coefficients (K_{xx} and C_{xx}) are computed. Cross coupled coefficients are neglected by this code and their insignificance has been verified experimentally for the original pocket damper seal by Ransom et al., [18]. Li [19] has shown that spin of the seal journal has no significant effect on any of the force coefficients for this type of seal. The computer code has shown good agreement with large amplitude test data measured at pressure ratios up to 3.0 [6]. It has overpredicted test data measured at lower pressure ratios with smaller vibration amplitudes [20]. However, in all cases this code has correctly predicted the direction of trends when design parameters or operating conditions are changed, so it can be expected to show the relative effect of replacing the downstream blade with a brush.

Figure 3 shows computed damping coefficients versus computed leakage for the brush hybrid pocket damper seal (BHS), and also for the original pocket damper seal (PDS) with downstream blade clearances twice the upstream clearances. The varying leakage of the PDS is due to a variable number of labyrinth teeth (6, 4, and 2). The varying leakage of the two bladed BHS is due to a variable porosity of the brush element, or due to progressive opening of the bypass orifices evident in Fig. 2. Note that the two

Downloaded 02 Jun 2010 to 171.66.16.119. Redistribution subject to ASME license or copyright; see http://www.asme.org/terms/Terms_Use.cfm

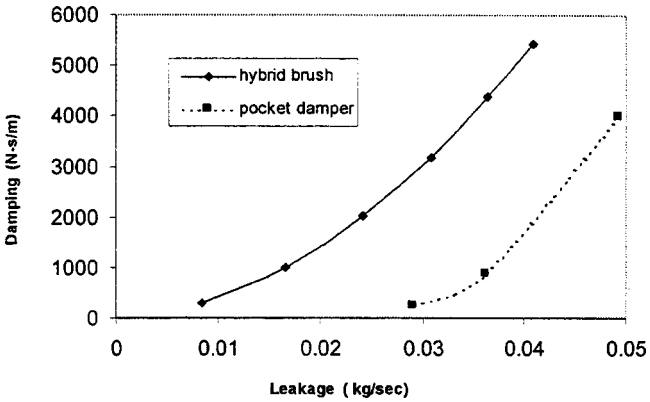

Fig. 3 Computed damping coefficient versus leakage for the brush pocket hybrid (two-bladed) and the original pocket damper seal (6 blades) (inlet pressure of 6.4 bar (80 psig))

bladed BHS is predicted to have an order of magnitude more damping at the smallest leakage value of the PDS (with six blades). These results do not include the mechanical damping of the brush itself, which was found to be considerable in the experiments described below.

Description of the Test Apparatus

A cross section of the test rig is shown on Fig. 4. The test rig consists of a solid frame (1) made of low carbon steel pipe welded to the test rig base (2). The mounting flange plate is welded to the top of the pipe. The test rig base has a centered hole that helps to position a flexible cantilever beam (3) or shaft. The seal (4), used for the experiments, is located on the mounting flange and is fixed by four quick release toggle clamps (10) and swivel pad positioning screws, which are set, as soon as the seal is centered relative to the journal (5). The journal (5) is connected to the shaft (3) with a bolt. Attached to the journal is a steel block (8), which was originally a reference for the proximity probes (9) as shown in Fig. 4. Figure 5 is a photo of the actual test rig configuration and it is observed that the two orthogonal proximity probes directly measure the journal (5) displacement. Therefore, the block (8) is actually a mounting point for the stinger, which connects the journal assembly to the shaker. A complete list of the parts of the test rig is shown on a table below Fig. 4.

Figure 5 shows the electromagnetic shaker connected to the block (8). The shaker contains an impedance head that outputs acceleration and force signals in time. As shown in Fig. 6, the shaker is suspended with four bungee cords to relieve the weight of the shaker on the stinger and to simplify the positioning of the stinger. The bungee cords are attached to a tubular steel frame surrounding the test rig.

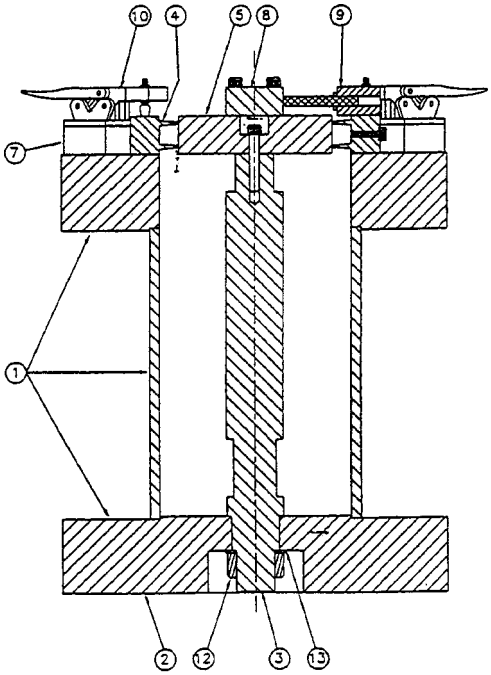

ITEM	DESCRIPTION
1	Test rig assembly
2	Test rig base
3	Shaft
4	Labyrinth seal stator
5	Labyrinth seal journal
6	Jacking crew stand
7	Clamp mounting spacers
8	Probe target
9	Probe stand
10	Toggle clamp
11	Socket set swivel-pad clamp steel
12	1-12 UNF steel hex nut
13	1" ground flat washer

Fig. 4 Cross section of the test apparatus

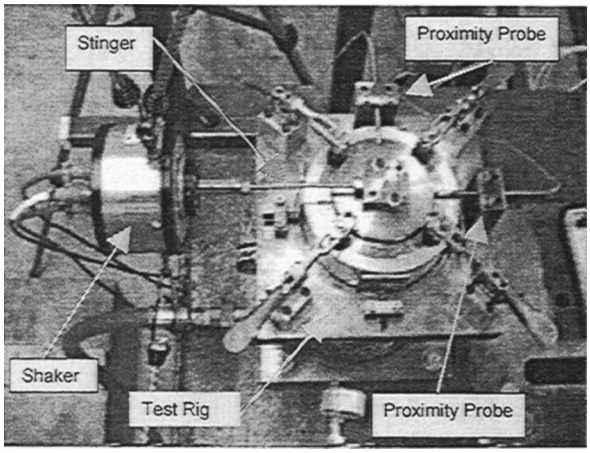

Fig. 5 Side view of the test apparatus

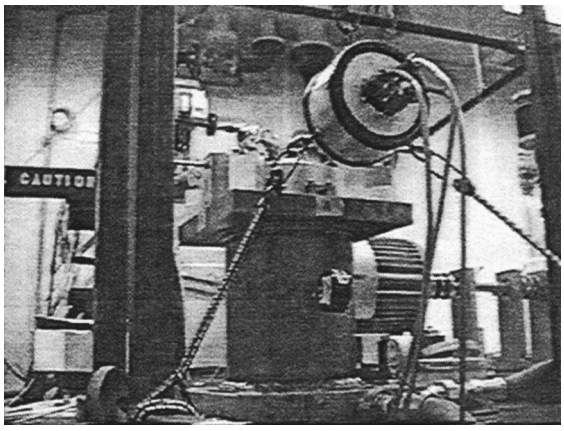

Fig. 6 Shaker supported on bungee cords

Downloaded 02 Jun 2010 to 171.66.16.119. Redistribution subject to ASME license or copyright; see http://www.asme.org/terms/Terms_Use.cfm

Instrumentation

The test rig instrumentation enabled the damping coefficients and leakage rate to be determined. The two orthogonal proximity probes are connected to the proximitors and then these signals are sent to the oscilloscope. The primary function of the proximity probes is to help center the seal and also to show an oscilloscope trace of the journal's orbit in the dynamic testing. The acceleration and force signals from the impedance head of the shaker were connected to a dynamic signal analyzer with ASCII storage capabilities. The impedance head has been calibrated recently at the manufacturer's facility. Table 1 shows the specifications of the shaker, impedance head and signal analyzer that were used for the uncertainty calculation [21]. A variable area flow meter was used to determine the flow rate through the seal. A Bourdon tube pressure gauge was placed at the test rig inlet to measure the inlet pressure of the seal. The flow rate is controlled by the use of a pneumatic control valve in the pressure range from 1 to 9.2 bar (0 to 120 psig).

Table 1 Specifications of the shaker, impedance head, and signal analyzer

DESCRIPTION	VALUE
Frequency range	20 to 5000 Hz.
Blocked force output	10 lb
Nominal accelerometer sensitivity	133 mV/g
Nominal force gauge sensitivity	283 mV/lb
Accuracy of impedance magnitude over specified frequency range	±10%
Accuracy of impedance phase angle over specified frequency range	±1 degree
Accuracy of the frequency on the signal analyzer.	±0.5 Hz

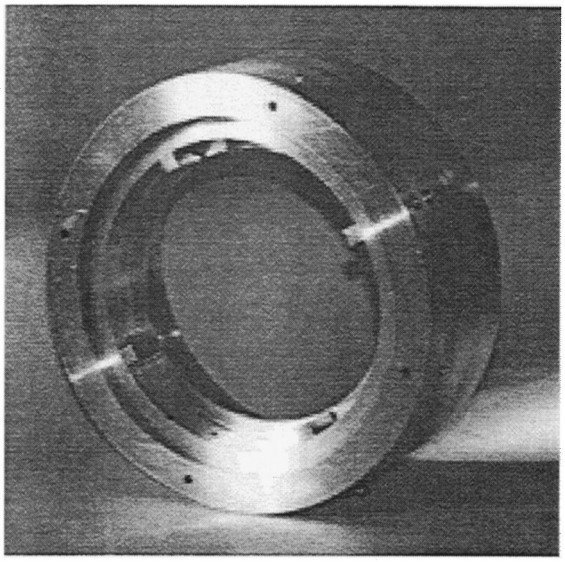

DESCRIPTION	SIZE mm	(in)
Internal diameter	101.60	(4.000)
Radial clearance at the exit	0.102	(0.004)
Rotor Diameter	158.75	(6.250)
Length of the seal	55.88	(2.200)
Thickness of the blade	3.175	(0.125)

Fig. 7 Two-bladed pocket damper seal assembly without brush elements

Seal Description

Figure 7 depicts the BHS used for the experiments. The four partition walls are made of 6.35 mm (0.25 in) square key stock. Also, a standard 6-bladed labyrinth seal with the same length as the short BHS was tested. The labyrinth seal tests were conducted for comparison purposes. Testing of a larger volume (longer) BHS was also begun until it was found that it had been fabricated with incorrect pocket depth, and also that the mode shape in the test apparatus was changed by the longer journal.

Test Procedure

The first operation was to center the seal. The journal was always within 0.013 mm (0.5 mils) of center. The experiments were performed in the range from 1 to 7.1 bar (0 to 90 psig) by adjusting the pneumatic control valve. In all tests the downstream pressure was atmospheric. Measurements of the steady flow rate and pressure were made prior to the dynamic testing. The dynamic signal analyzer sent a periodic chirp signal as input for the shaker's amplifier. The force generated in the impedance head excited the journal. The journal's orbit of motion was observed on the oscilloscope. The signals from the impedance head were collected by the dynamic signal analyzer and processed in the frequency domain. The transfer function Acceleration over Force was averaged 16 times and this data was saved in ASCII format along with other useful information such as the Phase and the Coherence plots.

Analysis of the Results

A computer was used to analyze the data on the ASCII files. Our objective was to extract the damping coefficient of the seals as a function of the inlet pressure. The experimental values of the transfer function, $H(\omega)$ (acceleration over force) at a phase angle of 90 deg corresponds to

$$H(\omega)=\frac{\omega}{C}, \tag{1}$$

where C is the direct damping coefficient and ω is the excitation frequency. Then, the damping coefficient C is solved using Eq. (1) at the excitation frequency where the phase angle is 90 deg. From Eq. (1) is calculated a value of ± 10 percent of uncertainty in the damping coefficients. In most of the experiments it was observed that the value of the coherence was nearly unity for frequencies above 30 Hz, as shown on Fig. 8. Some electrical noise is ob-

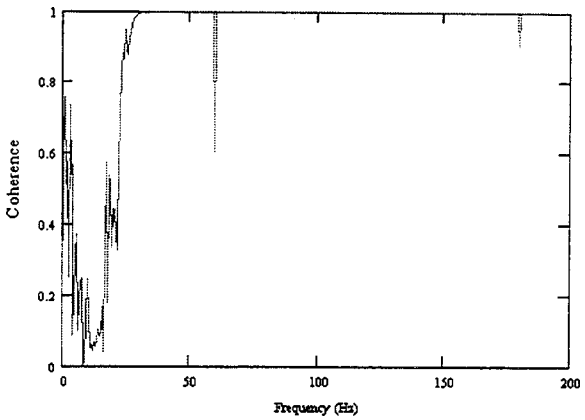

Fig. 8 Typical coherence for the transfer function measurements

Downloaded 02 Jun 2010 to 171.66.16.119. Redistribution subject to ASME license or copyright; see http://www.asme.org/terms/Terms_Use.cfm

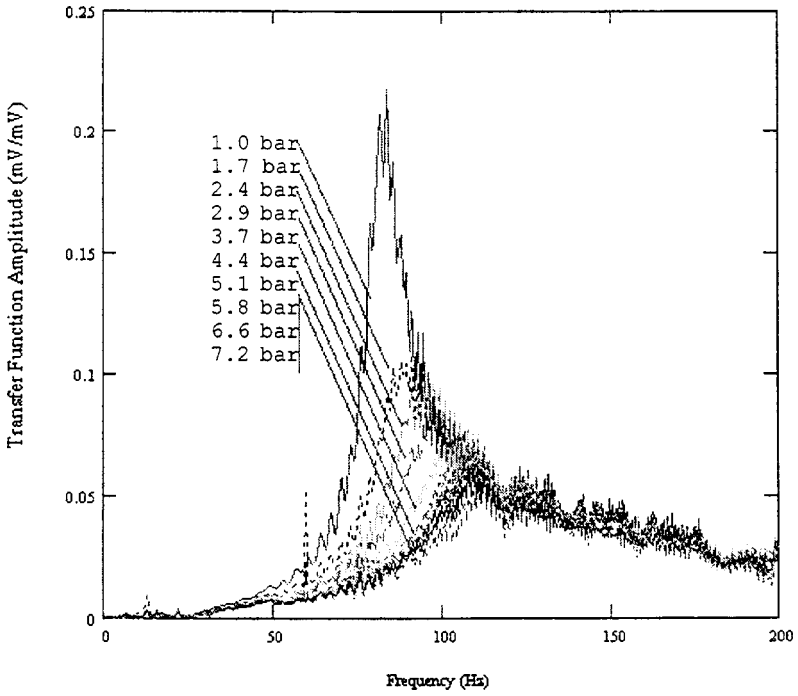

Fig. 9 Transfer function *a*/*F* for the brush hybrid pocket damper seal at various pressures

served at 60 and 180 Hz. It was not necessary to filter the data since no calculations were made near the electrical noise frequencies.

Figures 9 and 10 show experimental data on the full pressure range for a short BHS. Figure 9 shows steps of increasing resonant frequency and a corresponding decay of the transfer function amplitude. The increased frequency is due to a combination of the ''stiffening effect'' of the brush seal and the ''destiffening effect'' of the pocket pressures. Obviously, the brush seal effect is dominant and overcomes the other effect, which increases the resonance frequency. The amplitude decays because the damping is increasing.

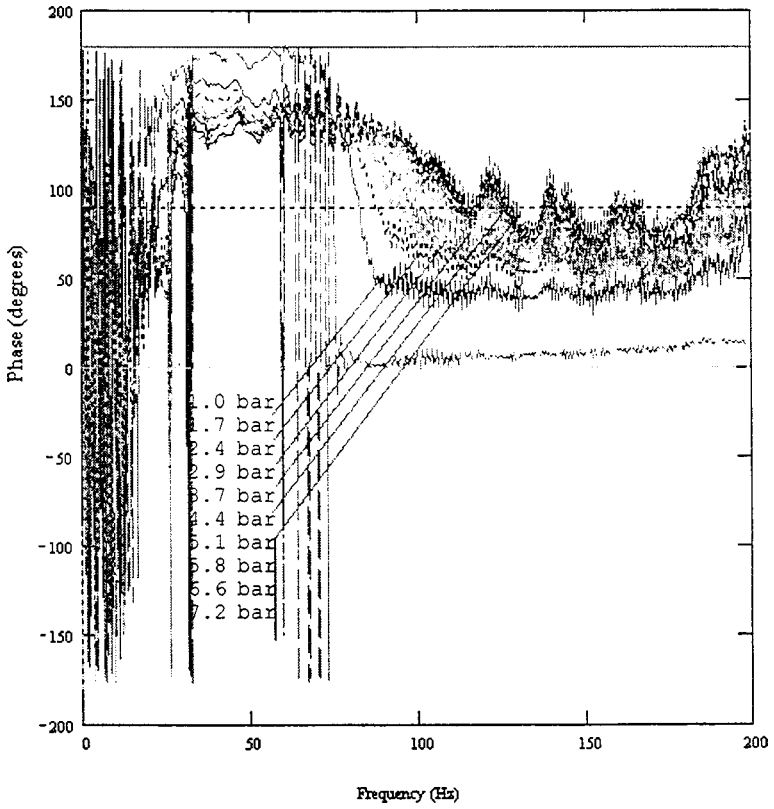

Fig. 10 Phase plots associated with Fig. 9

Downloaded 02 Jun 2010 to 171.66.16.119. Redistribution subject to ASME license or copyright; see http://www.asme.org/terms/Terms_Use.cfm

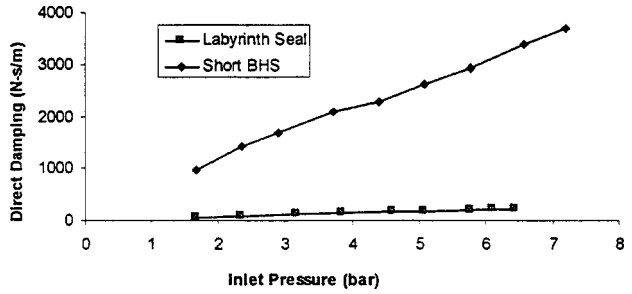

Fig. 11 Predicted damping coefficients for the hybrid brush (BHS) and labyrinth seal

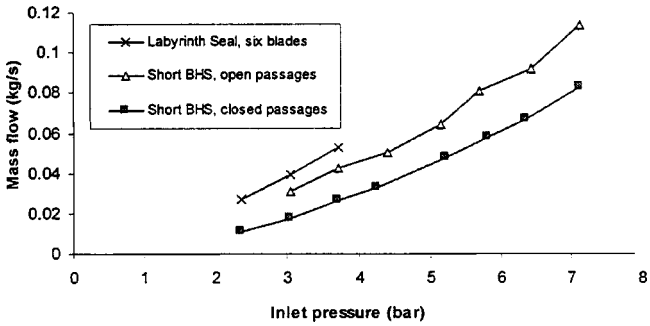

Fig. 13 Measured mass flow through the seals

Numerical and Experimental Results

The main objective of the experiments was to measure the damping and leakage of BHS seals and labyrinth seals for comparison. Figure 11 shows the predicted values for the damping coefficients of two seals that were used for the experiments. In this graph the BHS has closed bypass. The computer code predicts very low damping values for the labyrinth seal at all pressures when compared with the calculated damping for the BHS. The values for the damping of the BHS are calculated taking into consideration only the dynamic pressure effect of the modulated flow of air at the inlet and outlet of the seal. The mechanical properties of the brush seal are not included in this code. Figure 12 shows the damping values extracted from the experimental results. As predicted, the labyrinth seal has very low damping. The labyrinth seal could not be tested over 3.0 bar (30 psig) because the journal of the test rig became off-centered and started to rub against the wall of the labyrinth seal. In Fig. 12, the brush element alone (without the pockets) shows increasing damping values when pressurized. This damping is much larger than was measured for brush seals earlier by Conner and Childs [13], with fewer bristles and a different backing plate. It is hypothesized that the bristles became more packed together and held against the backing plate by the pressure drop [14]. The friction among bristles is thus augmented by the increase in pressure and this could be a mechanism that generates damping. The next step in the experiments was to test a BHS to observe the combined effect of the inlet blade with pockets and the brush element. The results for the experiments with the BHS (with pockets) are shown in Fig. 12. The damping values for the BHS tested are quite similar to the brush seal results up to a pressure of 5.8 bar (70 psig). The combined effect of the BHS (flow modulation plus brush) starts to become noticeable at a pressure over 5.8 bar (70 psig) and the difference of the damping values between the brush seal and the BHS (closed passages) is quite significant, about 40 percent at 7.1 bar (90 psig). The highest values of damping were obtained with the BHS in the ''open bypass'' configuration as shown in Fig. 12.

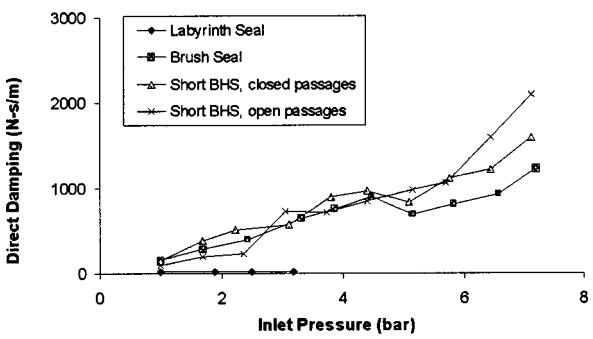

Fig. 12 Measured damping for the labyrinth seal, the brush element only, and the BHS with open and closed bypass

The authors have observed that the amount of damping obtainable from a PDS is proportional to its leakage rate, and the open passages provide a way for air to exit the seal with unmodulated flow. An explanation of why the graphs in Fig. 12 do not diverge appreciably until inlet pressures exceed 5.8 bar (70 psig) may be found in the nonlinear dependence of the brush damping on inlet pressure, combined with a different nonlinear dependence of the pocket damper effect on pressure. The lost damping from interpocket leakage of the dynamic pressures is certainly pressure dependent, and the bristle packing effect is seen to become a decreasing factor at an inlet pressure of 4.4 bar (50 psig). The mass flow observed during the experiments is shown in the Fig. 13. The uncertainty of the mass flow measurements is ± 2.5 percent. The BHS in the ''open passages'' configuration has lower leakage than the six bladed labyrinth seal, which is remarkable since the BHS has only one cavity and the labyrinth seal has five.

Conclusions

Of all the seals tested the labyrinth seal has the lowest damping (zero for practical purposes). The damping is overpredicted as shown in Figs. 11 and 12 for the short BHS with closed passages. At an inlet pressure of 6.4 bar (80 psig) the measured value of 3500 N-s/m (20 lb-s/in). All the seals tested with brush elements have roughly the same damping coefficients in the pressure range from 1 to 5.8 bar (0 to 70 psig). Over 5.8 bar (70 psig) the lowest was from the pure brush seal (no pockets). The hybrid brush seal with closed passages had more, since the damping was obtained from two combined effects: first, from the brush seal installed in the BHS and, second, from the air pressure in the pockets. The maximum damping available was obtained from the hybrid brush seal with the ''open passages'' configuration. Its leakage rate doubles the predicted leakage for the same hybrid brush seal with the closed passages, but the damping values are at least 30 percent higher and increase with pressure drop. The open passages configuration is a design that can be easily implemented in a control scheme where the damping would be immediately increased by just opening a valve.

Previous research with the pocket damper seal has shown the force coefficients and leakage to be independent of the shaft rotation, but the mechanical damping of the brush may decrease with bristle wear. Also, the pocket partition walls block circumferential swirl of the gas, so the cross-coupled effects of labyrinth seals are avoided. Rotating tests are now being planned to investigate these effects.

Acknowledgment

The Applied Technology Program of the Higher Education Coordinating Board of the State of Texas supported this research. Bearings Plus, Inc. of Houston, Texas has the patent license and donated some of the brush seals.

Downloaded 02 Jun 2010 to 171.66.16.119. Redistribution subject to ASME license or copyright; see http://www.asme.org/terms/Terms_Use.cfm

References

[1] Thomas, H., 1958, ''Instabile Eigenschwingungen von Turbinenläufern angefacht durch die Spaltströmungen Stopfbuschen und Beschauflungen,'' Bull de L'AIM, **71**, pp. 1039–1063.

[2] Alford, J. S., 1965, ''Protecting Turbomachinery from Self-Excited Rotor Whirl,'' ASME J. Eng. Power, **87**, pp. 333–344.

[3] Childs, D. W., 1978, ''The Space Shuttle Main Engine High Pressure Fuel Turbopump Rotordynamic Instability Problem,'' ASME J. Eng. Power, Jan., pp. 48–57.

[4] Childs, D., 1993, *Turbomachinery Rotordynamics, Phenomena, Modeling and Analysis*, John Wiley and Sons, New York.

[5] Von Pragenau, G. L., 1992 ''From Labyrinth Seals to Damping Seals/Bearings,'' presented at the Fourth International Symposium on Transport Phenomena and Dynamics of Rotating Machinery (ISROMAC-4), Honolulu, Hawaii, pp. 277–285.

[6] Vance, J. and Schultz, R., 1993, ''A New Damper Seal for Turbomachinery,'' *Vibration of Rotating Systems*, ASME DE, **60**, September 1993.

[7] Childs, D., and Scharrer, J., 1988, ''Theory versus Experiment for the Rotordynamic Coefficients of Labyrinth Gas Seals: Part II—A Comparison to Experiment,'' ASME J. Vibr. Acoust., **110**, pp. 281–287.

[8] Vance, J. M., Zierer, J. J., and Conway, E. M., 1993, ''Effect of Straight-Through Labyrinth Seals on Rotordynamics,'' presented at the 1993 ASME Vibration and Noise Conference, Albuquerque, NM.

[9] Childs, D., and Vance, J., 1994, ''Annular Seals as Tools to Control Rotordynamic Response of Future Gas Turbine Engines,'' AIAA Paper 94-2804.

[10] Richards, R. L., Vance, J. M., Paquette, D. J., and Zeidan, F. Y, 1995, ''Using a Damper Seal to Eliminate Subsynchronous Vibrations in Three Back to Back Compressors,'' *Proceedings of the 24th Turbomachinery Symposium*, Houston, Texas, September 26–28, 1995, pp. 59–71.

[11] Ferguson, J. G., 1988, ''Brushes as High Performance Gas Turbine Seals,'' ASME Paper 88-GT-182.

[12] Chupp, R., Short, J., and Loewenthal, R., 1997, ''Brush Seals: Lower Leakage Means Higher Efficiency,'' *Turbomachinery International*, March/April, pp. 58–61.

[13] Conner, K., and Childs, D., 1990, ''Rotordynamic Coefficient Test Results for a 4-Stage Brush Seal,'' AIAA Paper No. 90-2139.

[14] Hendricks, R. C., Griffin, T. A., Kline, T. R., Csavina, K. R., Pancholi, A., Sood, D., 1994, ''Relative Performance Comparison Between Baseline Labyrinth and Dual Brush Compressor Discharge Seals in a T-700 Engine Test,'' presented at the International Gas Turbine and Aeroengine Congress and Exposition, The Hague, Netherlands, June 13–16, ASME Paper 94-GT-266.

[15] Vance, J. M., Cardon, B., San Andrés, L., and Storace, A., 1993, ''A Gas Operated Bearing Damper for Turbomachinery,'' ASME J. Eng. Gas Turbines Power, **115**, No. 2, pp. 383–389.

[16] Sundararajan, P., and Vance, J. M., 1995, ''A Theoretical and Experimental Investigation of a Gas Operated Bearing Damper for Turbomachinery: Part I—Theoretical Model and Predictions,'' ASME J. Eng. Gas Turbines Power, **117**, pp. 742–749.

[17] Vance, J. M., and Li, J., 1996, ''Test Results of A New Damper Seal for Vibration Reduction in Turbomachinery,'' ASME J. Eng. Gas Turbines Power, **118**, No. 2, pp. 843–846.

[18] Ransom, D., Li, J., San Andrés, L., and Vance, J. M., 1998, ''Experimental Force Coefficients for a Two-Bladed Labyrinth Seal and a Four-Pocket Damper Seal,'' ASME J. Tribol., **121**, No. 2, pp. 370–376.

[19] Li, J., 1999, ''A Bulk Flow Model of Multiple-Blade, Multiple-Pocket Gas Damper Seals,'' Ph.D. dissertation, Texas A&M University, May College Station, TX.

[20] Li, J., Ransom, D., San Andrés, L., and Vance, J. M., 1998, ''Comparison of Predictions With Test Results for Rotordynamic Coefficients of a Four-Pocket Gas Damper Seal,'' ASME J. Tribol., **121**, No. 2, pp. 363–369.

[21] Wilcoxon Research, 1984, Operating Guide for the Model F4 Electromagnetic Shaker, Rockville, Maryland.

Downloaded 02 Jun 2010 to 171.66.16.119. Redistribution subject to ASME license or copyright; see http://www.asme.org/terms/Terms_Use.cfm

Experimental Measurements of Actively Controlled Bearing Damping With an Electrorheological Fluid

John M. Vance
Mechanical Engineering Department,
Texas A & M University,
College Station, TX 77843

Daniel Ying
Bently Nevada Corporation,
7651 Airport Boulevard,
Houston, TX 77059

Selection criteria and design evaluations of several types of bearing dampers with active control for application to aircraft engines were described in a companion paper. A disk type electrorheological (ER) damper was chosen for further study and testing. The results of the tests and the final conclusions of the study are described in this paper. Experimental results including stiffness and damping coefficients are presented for the ER bearing damper with two types of ER fluid, 350 CS and 10 CS (centistokes) viscosity. The vibration attenuation performance of the ER damper was measured on a rotordynamic test rig in the form of free vibration decay, rotor orbits, and runup unbalance responses. The results show that the ER fluid with lower viscosity has the better characteristics for rotordynamic applications. It was found that ER fluids produce both Coulomb and viscous damping. If only the damping is considered, the Coulomb type is less desirable, but with active control it can also achieve control of rotor stiffness. A feedback control system was developed and applied to the ER damper with the objective of improving the overall rotordynamic performance of the rotor bearing system, considering both vibration amplitudes and dynamic bearing forces. A ''bang–bang'' (on and off) simple control logic was found to work better in practice than more sophisticated schemes. The measured runup response of the rotor-bearing system with this control approximated the desired vibration response curves fairly well. The tests highlighted some of the practical considerations that would be important for aircraft engine applications, such as the ER fluid limitations, the electrical power supply requirements, the electrical insulation requirements, the nonlinear relationship between the voltage and the damping, and the relative benefits of active control. It is concluded that active control of bearing damping is probably not a practical improvement over the passive squeeze film dampers currently used in most aircraft gas turbine engines. [S0742-4795(00)01202-3]

Introduction

Selection criteria and design evaluations of several types of bearing dampers with active control were described in a companion paper by Vance et al. [1] for application to aircraft engines. A disk type electrorheological (ER) damper was chosen for further study and testing in a laboratory test rig (Fig. 1). The results of these experiments are described in this paper.

The function of bearing dampers (or vibration dampers) in turbomachines is to reduce rotor vibration. This is normally accomplished by introducing additional damping to the bearing support. A popular device for rotor vibration control in turbomachines is the squeeze film damper (SFD). The performance of a SFD is mainly restricted by the fluid viscosity, which normally is a function of temperature. Experimental research has also shown SFD to be influenced strongly by air entrainment and air bubbles, which are difficult to predict and control.

A novel electrorheological (ER) or electroviscous (EV) damper that is easily adapted to active control was initially developed by Nikolajsen [2]. Figure 2 shows a descriptive cross section. The damper contains ER fluid that thickens and provides combined Coulomb and viscous damping when an electric field is imposed across the fluid film. The ER fluid is a special fluid that has the electrorheological effect. When subjected to an electric field, typically from 500 V/mm up to 6000 V/mm, the fluid instantly turns from a liquid state to a gel-like solid within about 0.001 s. This effect increases the resistance to relative movement in the fluid. In other words, the stressed ER fluids provide more shear friction. Previous investigators including the present authors assumed that the dominant effect of the voltage would be to provide mainly a Coulomb type of damping. The rotordynamic effects of Coulomb damping are analyzed in a companion paper [3]. The results of the experiments to be described below will show that the damping model for a real ER fluid is actually quite complex and is yet to be precisely determined.

Objectives

The objectives of this research were as follows:

1 to experimentally explore the feasibility and performance of the ER damper at frequencies and whirl amplitudes typical of aircraft engine rotor systems
2 to obtain experimental data that would aid optimization of the design of an ER damper for the experimental engine described in the study by Vance et al. [1].
3 to develop and test a control system and software for the ER damper, and to explore the attractiveness of actively controlled dampers for possible application to turbomachinery

These objectives were pursued by carrying out the following major tasks:

1 modification of an existing test rig to raise the first critical

Contributed by the International Gas Turbine Institute (IGTI) of THE AMERICAN SOCIETY OF MECHANICAL ENGINEERS for publication in the ASME JOURNAL OF ENGINEERING FOR GAS TURBINES AND POWER. Paper presented at the International Gas Turbine and Aeroengine Congress and Exhibition, Indianapolis, IN, June 7–10, 1999; ASME Paper 99-GT-17. Manuscript received by IGTI March 9, 1999; final revision received by the ASME Headquarters January 3, 2000. Associate Technical Editor: D. Wisler.

Copyright © 2000 by ASME

Downloaded 02 Jun 2010 to 171.66.16.119. Redistribution subject to ASME license or copyright; see http://www.asme.org/terms/Terms_Use.cfm

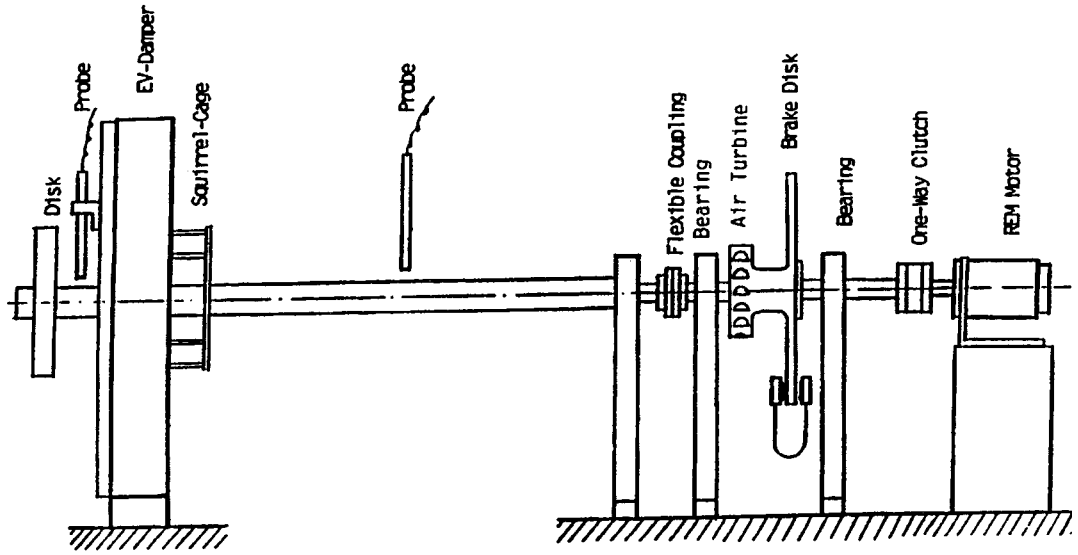

Fig. 1 Rotordynamic test rig for the ER damper

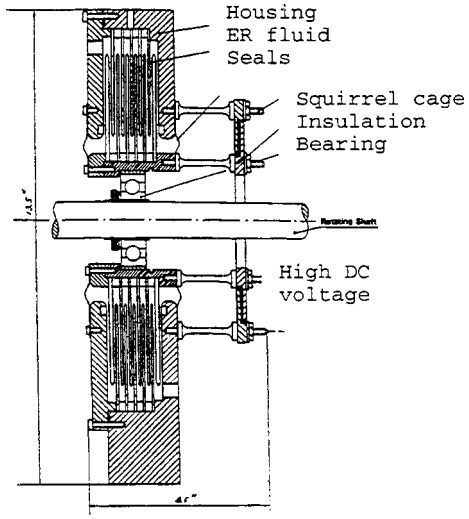

Fig. 2 Cross section of the ER damper

speed to 6000 rpm and to improve its vibration characteristics for the purpose of identifying stiffness and damping coefficients

2 identification of the rotordynamic characteristics (stiffness coefficients and equivalent viscous damping coefficients) of the ER damper through experimental techniques

3 development of a control system for the ER damper that produces significantly better performance than the passive system

4 operation of the test rig to produce Bode plots (imbalance response) with and without the control system active

Test Rig Modifications

Improvement of the test rig vibration characteristics was accomplished by a redesign of the rotor system and the squirrel cage bearing support. The main problem encountered with the original rig was a low critical speed (<3000 rpm.). The modified test rig reasonably simulates the speed and vibration characteristics of a wide range of turbomachinery including aircraft engines. Figure 1 shows a sketch of the test rig after modification. The rotor operates through its first critical speed at about 5800 rpm with a light viscosity ER fluid at no voltage. A second critical speed appears around 8000 rpm as the stiffness and/or damping at the left bearing is increased by using the ER fluid. The second critical speed involves more rotor bending than the first.

The damper (Fig. 2) houses five stationary plates and six whirling plates with a gap of 1.6 mm (1/16 in.) between them. The stationary plates were assigned to a negative electrode connected to the outer squirrel-cage beams and housing. The whirling plates were selected as the positive electrode joining the inner squirrel-cage beams and whirling sleeve. The stationary plates and whirling plates were electrically insulated and sealed by a pair of nonconducting sheets. The main shaft was insulated from the damper by a plastic pipe inserted between the outer race of the bearing and the whirling sleeve. The damper housing, bearing supports and motor were seated on plastic blocks. The whole rig was electrically insulated from the base plate by applying nonconducting bushings under the tie-down bolts. In spite of all these measures taken to guarantee good electrical insulation, arcing problems persisted during the tests and the rig had to be torn down and rebuilt at one point while taking data.

Figure 1 shows three sections of the test rig. Section one on the left includes an overhung disk, an ER damper actuator, a rotating shaft and bearing supports. Section two in the middle contains a pair of bearing supports, a jackshaft and an air turbine wheel with brake disk. Section three at the right has an adjustable frequency motor (0–25,000 rpm) with an accuracy of 1 rpm. The minimum controllable speed is 2000 rpm. A flexible coupling connects the main shaft and jackshaft to isolate the vibration transmitted from the motor. The air turbine is mounted on the jackshaft to help the rig start up and is also used for running speeds below 2000 rpm.

Another flexible coupling connects the jackshaft to the motor shaft. It contains a one-way clutch with maximum torque capacity of 8.3 N-m (73.6 lb-in.) in one direction and with free slip in the other direction. The diameter and thickness of the overhung rotor disk are 102 mm (4.0 in.) and 19 mm (0.75 in.), respectively. The length of the main shaft is 568 mm (22.37 in.). The bore edges of the damper housing were rounded to prevent arcing between the whirling sleeve and housing. The squirrel-cage beams are 37 mm (1.45 in.) long with a diameter of 7.6 mm (0.3 in.). Nine of these beams produce the desired first critical speed. The seals used to prevent the leakage of the ER fluid are made of a 0.8 mm (1/32 in.) thick nonconducting sheet to increase both the mechanical strength and breakdown voltage of the seal. A 4.8 mm (3/16 in.) wide straight slot was machined into the base plate for the purpose of maintaining rotor system alignment.

Downloaded 02 Jun 2010 to 171.66.16.119. Redistribution subject to ASME license or copyright; see http://www.asme.org/terms/Terms_Use.cfm

The ER Fluid

A good ER fluid for rotordynamic application in aircraft engines should have most of the following features:

1 chemically and physically stable, so the ER effect remains constant with time
2 low viscosity at zero voltage
3 high yield shear stress with applied voltage
4 low conductivity and high breakdown voltage
5 no sediment, i.e., no forced circulation of the fluid should be required
6 high operating temperature, i.e., not a water based fluid

Several donated samples of commercially available ER fluids were first used in the test rig without good results. Some were too viscous without voltage and some were too difficult to keep mixed. Obtaining a satisfactory ER fluid would be a major concern if the ER damper were to be adopted for operational use in aircraft engines. Two types of homemade ER fluids were found to work better in the laboratory and so were used in this research. They were formulated using cornstarch and polydimethylsiloxane fluid (silicon oil). The first one was a mixture of 350 CS liquid and cornstarch in 2:1 ratio by mass. This combination was chosen for its relative chemical simplicity and its successful previous application [4]. The results described below from the first ER fluid (350 CS) indicate that the 350 CS oil was too thick for use in this application because: (1) it was difficult to pump the ER fluid into the damper housing; (2) controllability of the damping was poor; and (3) the residual viscous damping was too high (the damping values are presented later). Therefore, a second ER fluid was made by mixing 10 CS fluid with cornstarch in 4:1 ratio by mass. This fluid turned out to be much better for the purpose of these tests. Its baseline viscosity was not too high but it could still be turned solid with a high voltage. It should be noted that these two formulations of ER fluid were used for purpose of this project only and would not have any of the other desirable operational properties listed above for aircraft engines (items 1, 4, 5, and 6).

Instrumentation

The basic instrumentation used in the tests included a pair of proximity probes, an optical probe, a shaker system with impedance head, a synchronous tracking filter, and a dynamic signal analyzer. The proximity probes were orthogonally mounted on the housing cover to measure the relative vibration between the shaft and damper housing. Most of the vibration measurements to be described below are from these horizontal and vertical probes mounted just outboard of the bearing pedestal containing the ER damper. They will be referred as bearing no. 1 probes, but it is important to remember that they are actually a slight distance outboard of the bearing. An optical probe was used to measure the rotating speed of the main shaft by placing a black marker on the shaft.

The tracking filter provides both synchronous vibration amplitude (2-channel) and phase, and speed of a rotating shaft. In these experiments, the tracking filter was first used to balance the rotor and later to provide the feedback control system signal. The impedance head was used to measure driving-point frequency response of the rotor, thus identifying the damping coefficients of the ER damper. The dynamic signal analyzer has a special feature that allows transfer function curve fits for parameter identification.

The extended instrumentation included a PC computer with a 12 bit A/D board and a computer controlled high-voltage amplifier. Maximum A/D throughput depends on the operating mode and can be up to 50,000 Hz. An on-board -5 volt reference can be used to provide analog outputs in the zero to $+5$ VDC range, or external references (max. 10 VDC) can be used for other desired output ranges. This analog output signal was used as the control signal for the voltage applied to the damper. In this study, channel zero was used to control the high-voltage amplifier.

The Control System

The control system requires a high-voltage amplifier, which has unique specifications for this application. The unit is designed to allow amplification of an analog voltage in the range zero to $+10$ V. The gain of this unit is set at 500, so that the maximum output is 5000 volts and 2 mA. The input terminal of the unit is a 3-pin DIN socket which accepts analog voltage in the range zero to $+10$ volts. The input circuit is fully isolated from the high voltage output to prevent ground loops and to protect the computer from high voltage transients. There is a set of binding posts on the side of the unit, which are provided to monitor the actual high voltage output. The scale factor for this output is 0.001, meaning that a one volt signal indicates 1000 V at the high voltage output. Although this unit is not perfect (about 350 V offset at 60 percent setting.), it did provide a controllable high voltage to the ER damper. Detailed specifications of the high voltage amplifier can be found in Ying [5]. The analog output signal from the computer (which determines the voltage applied to the ER damper plates) was regulated by special software written for this application. The control algorithms will be discussed below.

Bearing Support Stiffness

Static tests were performed on the rotor at each bearing of the main shaft to determine the bearing support stiffness. A force transducer was screwed onto a heavy steel block, and the block was placed under the shaft close to the bearing. A bolt was then placed between the shaft and block, one end reacting against the force transducer and the other end on the shaft. A dial gage (0.0005 in. resolution) was used to measure the deflection of the shaft where the force is applied. Turning the nut along the bolt varied the static force. This worked well and was repeatable for measuring the stiffness in the vertical direction. The rap tests described in a following section were used to determine the horizontal stiffness.

Figure 3 shows the static stiffness results for bearing 1 (the ER damper end). The straight line on the graph is a fit to the plot of the measured data (also shown on the graph). The same test procedure was performed for bearing 2 (coupling side). The uncertainty of this data is unknown, but the stiffness values agree well with those obtained from independent rap tests. The overall average stiffness of each bearing was obtained by averaging several static test results. The values were found to be 1.6×10^6 N/m (9148 lb/in.) for bearing 1 and 26.3×10^6 N/m (150, 276 lb/in.) for bearing 2. The rap test results presented below show that the horizontal and vertical stiffness values are closely similar.

Free Vibration Measurements

Rap tests (response to impact) were performed on the rotor to get the free vibration frequencies and logarithmic decrements in the time domain. Rap tests give satisfactory results for lightly damped mechanical systems with widely separated modes, but

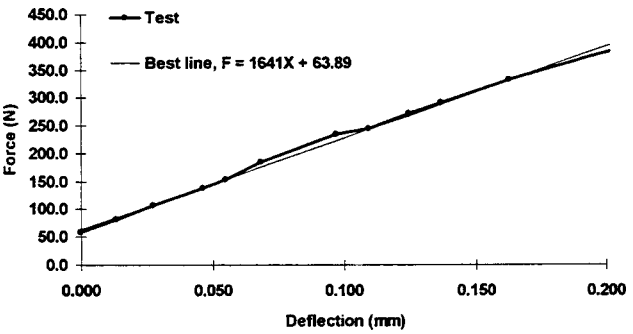

Fig. 3 Curve fit for bearing no. 1 stiffness

Downloaded 02 Jun 2010 to 171.66.16.119. Redistribution subject to ASME license or copyright; see http://www.asme.org/terms/Terms_Use.cfm

heavily damped mechanical systems with closely spaced modes create problems for the test. Ying [5] shows how the ER damping changes the mode shapes of the test rig.

With light damping the first mode of the test rig has only a small amount of shaft bending, due to the soft bearing support. In that case most of the relative displacement is at the support containing the damper. The rap tests with no ER fluid revealed a natural frequency of 101 Hz in the horizontal direction (*X*-probe) and 102.5 Hz in the vertical direction (*Y*-probe). The time trace showed that the vertical direction (*Y*) had a smaller damping ratio than that of the horizontal direction (*X*). A frequency spectrum of the rap test, from the horizontal probe at bearing 1 with no ER fluid, is shown in Fig. 4. Note that there are two close peaks, 101 and 120 Hz, respectively. The damping in this case was light, around six percent of the critical value for the system. The critical damping ratio was calculated by using the logarithmic decrements of the time trace where the first mode is the dominant frequency [5]. Selecting optimum impact locations to excite the desired modes can vary modal participation in rap tests. The critical damping ratio with no ER fluid was around 6 percent and 4 percent for the horizontal direction (*X*) and the vertical direction (*Y*), respectively.

The same rap tests were performed with zero to 2500 V applied to the ER damper, filled with the 350 CS fluid. The rap test spectrum with no voltage applied to the fluid is shown in Fig. 5. Two dominant peaks now appear in the rap test frequency spectrum of the damper with the ER fluid. This fluid is so viscous that it constrains the motion at the bearings, makes the bending mode more dominant, and raises its frequency. These effects become even more pronounced when voltage is applied. The time traces in these cases do not exhibit a pure frequency, so the logarithmic decrement is difficult to accurately determine. The damping is estimated from to be between 13 percent and 25 percent of the critical value, with high uncertainties.

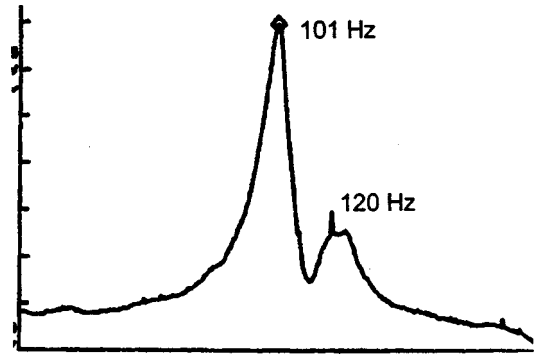

Fig. 4 Rap test spectrum, *X*, no ER fluid

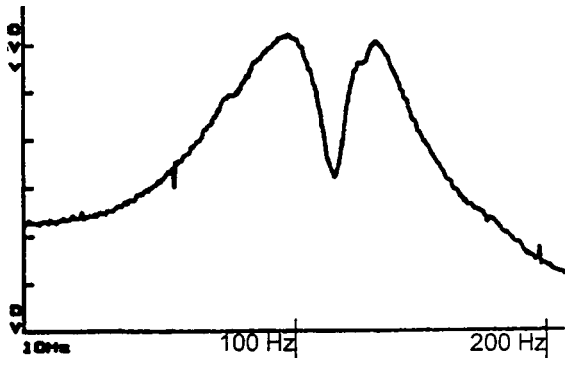

Fig. 5 Rap test spectrum, *X*, 350 CS fluid, no voltage

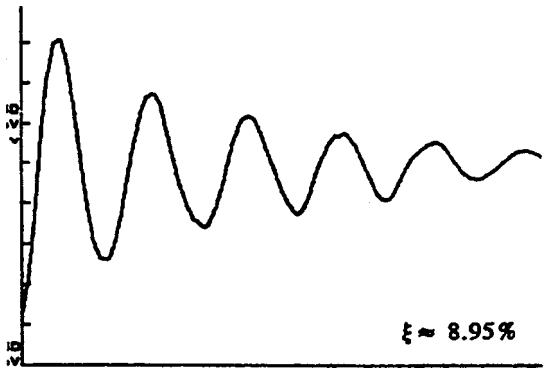

Fig. 6 Time trace, 10 CS fluid, 500 V

The rap tests were repeated for the 10 CS ER fluid. The damper had to be reassembled for changing the fluid. It was difficult to keep the same damper assembly conditions, e.g., tightness of the squirrel-cage beams, for every reassembly. Therefore, the natural frequency without the ER fluid was slightly different after reassembly but the damping was still about six percent of the critical value. A free vibration decay trace with 10 CS fluid and with applied voltage of 500 V is shown in Fig. 6. The first mode is seen to be dominant here. The percentage of critical damping is shown on the plot. Raising the voltage by a factor of five (to 2500 V) raises the damping ratio about 20 percent. Comparison of the rap test results at zero voltage showed that the 350 CS fluid provided much more damping than the 10 CS fluid because of the baseline fluid viscosity. This turns out to be a very important factor when developing an active control scheme. The 10 CS fluid is to be preferred (see [3] for some analytical insight).

Not shown here are the measured differences between the horizontal and vertical free vibration responses with the 10 CS fluid. They show an exponential decay in the horizontal direction (*X* probe) and a linear decay in the vertical direction (*Y* probe). The linear decay indicates that the system contains Coulomb damping [6]. It is unknown why the horizontal direction did not reflect a strong Coulomb damping effect. It is clear, however, that the ER fluid provides both viscous and Coulomb damping to the system.

It was also noted that the linear decays in the vertical direction appeared only for the first three peaks. The decay was exponential after the third peak. This suggests that the 10 CS fluid produced Coulomb damping for large displacements and viscous damping for small displacements in the vertical direction. For the Coulomb case (linear decay) an equivalent viscous damping coefficient and damping ratio can be calculated from the free vibration measurements. They are a function of the exciting frequency and response amplitude. These coefficients alone cannot limit the amplitude of unbalance response at the critical speed. Vance and San Andres [3] discuss proper use of these coefficients.

Effect of the ER Damper on the Imbalance Response of the Test Rig

Runup imbalance responses and whirl orbits were measured on the test rig at the damper location. These tests show how the ER damper affected the rotordynamic performance of the test rig. The test consists of two parts (1) the response without the ER fluid, and (2) the response with the ER fluid while applying various voltage levels. With no ER fluid, the maximum whirling amplitude occurred at 6000 rpm, which indicates that the baseline first critical speed is 6000 rpm (100 Hz). All the responses were synchronous with shaft speed.

The orbits of the rotor at 6000 rpm with and without ER fluid (350 CS fluid) are seen at the top of Fig. 7. The whirling amplitude at the first critical speed is reduced from a maximum of 0.3 mm (12 mils) *p-p* (empty damper) to 0.06 mm (2.3 mils) *p-p* (0 V

Downloaded 02 Jun 2010 to 171.66.16.119. Redistribution subject to ASME license or copyright; see http://www.asme.org/terms/Terms_Use.cfm

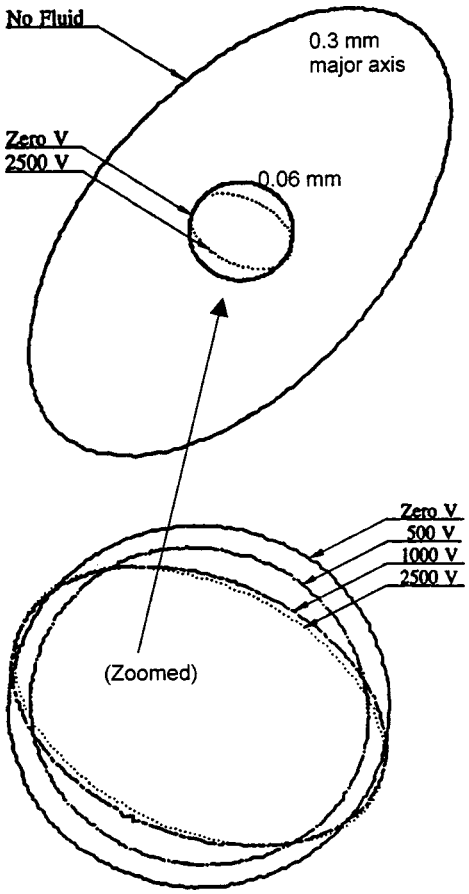

Fig. 7 Rotor orbits at the first critical speed with the 350 CS fluid

with 350 CS ER fluid). The effect of the applied voltage from zero to 2500 Volts is relatively small. The bottom of Fig. 7 zooms the inside portion of the orbits to show how they change with applied voltage. It is seen that 500 volts reduces the whirling amplitude down to 0.05 mm (2.1 mils) *p-p*, but the applied voltage does not reduce the whirling amplitude any more. The higher applied voltage only changes the shape of the orbit. There is no distinction of the orbits for applied voltages above 1500 V. This indicates that there is a value of optimum damping that has been exceeded with the 350 CS fluid.

The optimum damping minimizes the whirling amplitude at the critical speed. Since the ER fluid reduces the critical speed amplitudes, and since it is known that purely Coulomb damping cannot do this [3], it is clear that the ER fluid produces a considerable amount of damping that is not of the Coulomb type. This non-Coulomb damping is seen here to increase with applied voltage.

The orbits are also recorded at the second critical speed (8000 rpm) and shown in Fig. 8 for various applied voltages. It can be seen that the higher the applied voltage, the larger the whirling amplitude. The increased damping (or friction) of the 350 CS ER fluid with voltage is constraining the bearing support and causing the rotor to bend more, thus increasing the response of the second mode.

Figure 9 shows the orbits with various applied voltages for the 10 CS fluid at 5800 rpm (first critical speed). The whirling amplitude reduces from 0.19 mm (7.5 mils) *p-p* at 0 V down to 0.10 mm (4.1 mils) *p-p* at 2500 volt. This figure shows that, with the 10 CS fluid, the higher the applied voltage the smaller the whirling amplitude. The maximum whirling amplitude is reduced about 45 percent at 2500 V compared to the zero volt amplitude. At the second critical speed (8000 rpm), the 10 CS fluid with no voltage

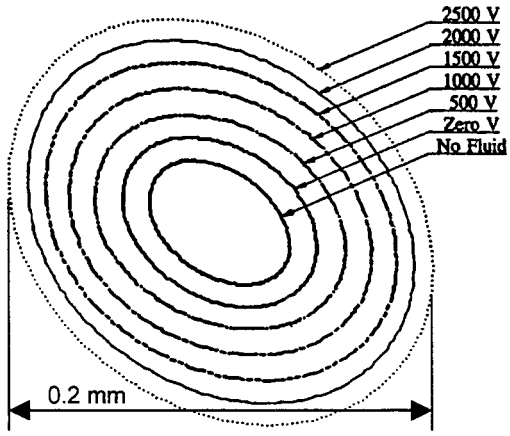

Fig. 8 Orbits at the second critical speed with the 350 CS fluid

does not increase the amplitude, but does increase it up to 80 percent higher than the baseline as the electric potential is raised to 2500 volts and the rotor is forced to bend in the second mode.

The orbits provide information only at a particular speed. The overall amplitude response for the entire operating speed range is shown in the rotor imbalance response curve, or the so-called Bode plot. Figure 10 shows a family of Bode plots, taken from the horizontal probe at bearing 1, with various applied voltages using

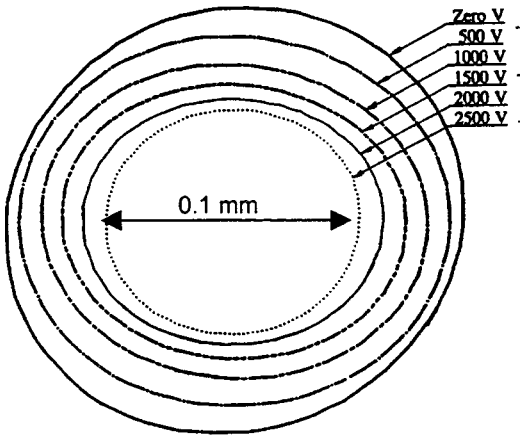

Fig. 9 Orbits at the first critical speed with the 10 CS fluid

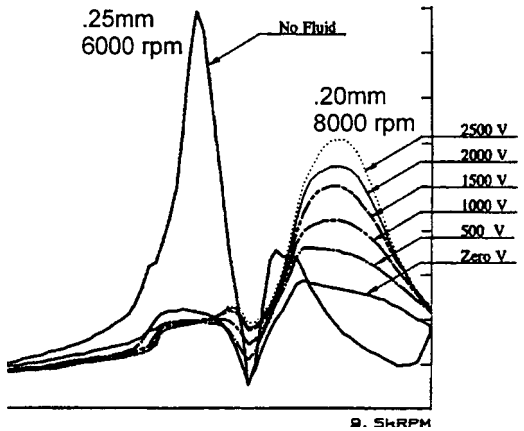

Fig. 10 Measured Bode plots with 350 CS fluid (*X*)

Downloaded 02 Jun 2010 to 171.66.16.119. Redistribution subject to ASME license or copyright; see http://www.asme.org/terms/Terms_Use.cfm

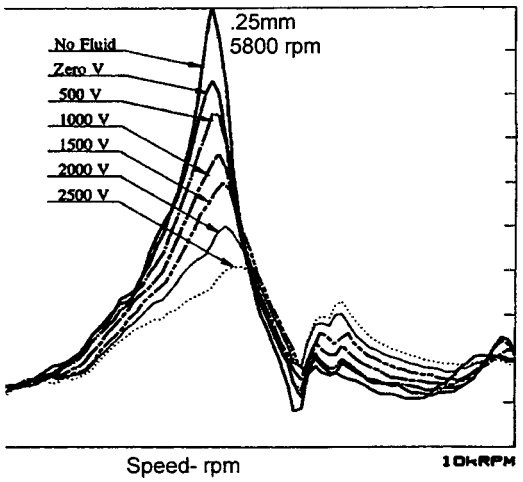

Fig. 11 Measured Bode plots with 10 CS fluid (*X*)

350 CS ER fluid at speeds ranging from 1000 rpm to 9500 rpm. The first critical speed is 6000 rpm, which corresponds to the first peak. The 350 CS ER fluid with increasing voltage suppresses vibration through the first critical speed and magnifies the vibration above the first critical speed.

The same runup tests were performed with the 10 CS ER fluid. It should be noted that the reassembled damper had a slightly different first natural frequency and modal damping with no fluid. Figure 11 shows all the imbalance responses in the *X* direction for different applied voltages. The peak amplitudes at the first critical speed decrease with the increasing applied voltage, but the vibration amplitudes around the second mode increase slightly with increasing applied voltage. It was found that the first critical speed (peak location) was increased by 400 rpm in the *X*-direction and by 200 rpm in the *Y*-direction, respectively, while increasing the applied voltage from 0 to 2500 V. Comparing the runup imbalance responses with the two fluids without active control, one can say that the 10 CS ER fluid is to be preferred in this test rig. Clearly, there is an optimum formulation of the ER fluid for a given application that has the best characteristics of both effective damping and effective stiffness.

Figures 10 and 11 were used later to help determine the best ''ON'' and ''OFF'' speeds of the bang–bang control logic for the control system. This is discussed in a following section.

Bearing Loads

Two potential benefits of using variable rate dampers in aircraft turbine engines are (1) the avoidance of rubs between the rotor and stator near the critical speeds, and (2) a reduction of the dynamic bearing loads for supercritical operations. Benefit 2 is illustrated in Fig. 12, the bearing force transmissibility plot for three values of viscous damping [7]. High bearing support damping decreases the imbalance response of the rotor at the first critical speed and reduces the dynamic load transmitted through the bearing at the critical and lower speeds. But for high operating speeds, bearing support damping should be as low as possible in order to reduce the dynamic bearing loads. The bearing loads with the 10 CS fluid were calculated at applied voltages of 0 and 2500 V, respectively, using the identified bearing stiffness and damping coefficients at various speeds. The bearing loads corresponding to 2500 V were found to be higher than those with zero voltage at speeds only slightly above the first critical speed, as shown in Fig. 13. This suggests that zero voltage (i.e., low damping) should be applied to minimize the dynamic bearing load at these speeds. This was one of the factors influencing development of the active control logic.

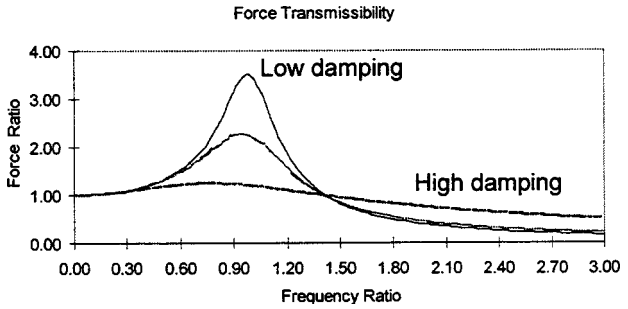

Fig. 12 Theoretical dimensionless bearing force versus frequency ratio for three damping ratios

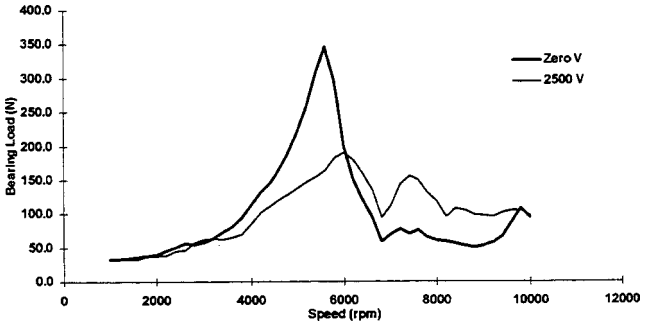

Fig. 13 Dynamic bearing loads calculated from the measured stiffness and damping coefficients, 10 CS fluid

Impedance Measurements and Curve Fitting

Frequency response transfer functions (FRF) were measured with the impedance head and curve-fitted to determine the undamped natural frequency and the critical damping ratio of the rotor-bearing system. The shaker was attached to the overhung disk and suspended by a pair of long rubber ropes. The shaker power amplifier was excited by random noise (frequency range from 50 to 450 Hz). The excitation force and response acceleration signals were fed into the signal analyzer. The power amplifier was manually adjusted so as to maintain the response amplitude around 0.025 mm (1.0 mil) *p-p*. The driving-point transfer functions were averaged 100 times. The frequency response functions in the range of 50 to 200 Hz were chosen for display and curve fitting. The signal analyzer listed the corresponding poles and zeros in a ''fit table.'' The user should be able to judge the selection of the pole(s) of interest based on experience or some other available information (e.g., runup results). This is not difficult to do for a lightly damped linear system with distinct and dominant peaks in the frequency spectrum. This system, however, was heavily damped with closely spaced resonances and the damping is not purely viscous. The results of this procedure therefore have a high uncertainty, probably in the range of $\pm$ 50 percent. The amplitude of the frequency response function at the undamped natural frequency was read from the FRF and the damping coefficient was computed as $C=\omega_n/\mathrm{FRF}$. The resulting damping coefficients with the 10 CS fluid are presented in Table 1.

Control Schemes Implemented for the ER Damper

One of the incentives to test the ER damper was to verify its suitability for a feedback control system. The control system consists of two parts. One is the control system hardware, which includes the damper actuator, probes, measuring instruments, computer, A/D board and high-voltage amplifier. The other is the software, i.e., the digitized control law. The project sponsor proposed the first version of control logic. After discussions with the

Downloaded 02 Jun 2010 to 171.66.16.119. Redistribution subject to ASME license or copyright; see http://www.asme.org/terms/Terms_Use.cfm

Table 1 Identified damping coefficients, 10 CS fluid

	No fluid	0 volts	500 v	1000 v	1500 v	2000 v	2500 v
Cxx N-s/m (lb-s/in)	560 (3.2)	963 (5.5)	1191 (6.8)	1366 (7.8)	1226 (7.0)	1243 (7.1)	1348 (7.7)
Cyy N-s/m (lb-s/in)	473 (2.7)	1068 (6.1)	1488 (8.5)	1453 (8.3)	1173 (6.7)	981 (5.6)	805 (4.6)

authors and several iterations, a final version of this control law was ready to try with the hardware. The basic concept of this control logic was to repeatedly compare the measured vibration with a predetermined reference level and vary the ER voltage to keep the rotor vibration level as close as possible to the reference without exceeding it. This control logic would minimize the bearing loads whenever the vibration level is below the reference level because the ER damper would be turned off. Although this appeared perfect on paper, numerous problems appeared when putting it into practice. There were some constants in the code that had to be determined by experiment, which turned out to be quite difficult. Some other ''fatal'' errors were detected while testing the code (e.g., dead loop in comparing measured vibration level with a predetermined reference level). In order to move the project along, a much simpler ''ON'' and ''OFF'' control logic (sometimes called a bang–bang control system) was developed. This logic uses vibration only or speed only or both vibration and speed as a reference to determine the desired state. It was found that choosing speed only as a ''ON'' and ''OFF'' reference was better than the others since the amplitude versus speed characteristic of the system was well known. The bang–bang control worked so well and was so simple that the initial logic was abandoned.

Studying Fig. 10 for the 350 CS fluid, one could see that the damper should be turned ''ON'' when the speed reaches 5400 rpm and turned ''OFF'' when the speed passes 7100 rpm. The ''ON'' condition means the applied voltage is not zero. The outline of the overlapped area on Fig. 10 (the envelope under all the curves after discounting the curve with no fluid) is the expected imbalance response which has minimum vibration for the entire speed range of 1000 rpm to 9500 rpm. The voltage applied in the ''ON'' condition with 350 CS fluid was chosen to be 1000 V because it gives a vibration level very close to minimum with just a moderate amount of applied voltage (saving power consumption). The ''OFF'' condition is supposed to be 0 V. But the high voltage power supply used in this research has about 350 V DC offset at zero input. Therefore, it made the actual controlled imbalance response, shown in Fig. 14, shift a little from the expected imbalance response. The dotted lines are the expected response and the solid lines are the measured runup imbalance responses using 350 CS ER fluid incorporated with the control system.

The same procedure implemented with the 10 CS fluid yielded the runup response shown in Fig. 15. In this case 2500 V was applied between 3800 rpm and 6800 rpm. There is more discrepancy here between the expected and actual curves because electrical arcing problems required the test rig to be disassembled and rebuilt immediately after the uncontrolled tests.

This actively controlled damper does not produce the same kind of damper forces as the on-off control scheme modeled by Vance and San Andres [3] because it turns out that ER damping is not purely Coulomb as had been earlier assumed. Nevertheless, it can be seen that the bang–bang control logic does produce results similar to the response predicted in that reference. It is simple, feasible, and works well to minimize the vibration amplitude response at the first critical speed and to minimize the dynamic bearing loads at higher speeds.

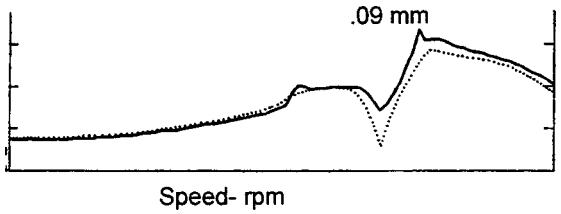

Fig. 14 Measured runup response with 350 CS fluid and the control system (solid line). Dashed line is expected.

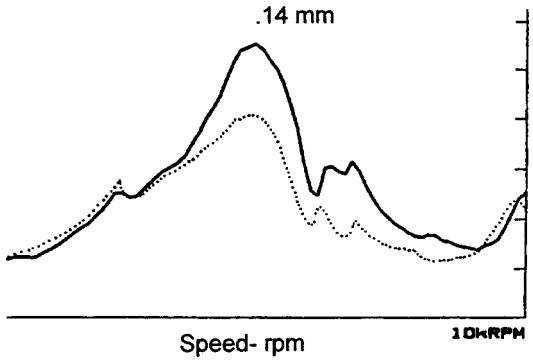

Fig. 15 Measured runup response with 10 CS fluid and the control system (solid line). Dashed line is expected.

Conclusions

1 A rotordynamic test rig was designed and constructed with an ER bearing damper that could be actively controlled by varying the voltage applied to the ER fluid.

2 Suitable ER fluids were not found to be commercially available (after considerable effort), neither for a bearing damper in aircraft engines nor for the conditions of the laboratory test rig. Fluids suitable for laboratory testing were concocted in the laboratory. Two fluids were concocted and used, with zero voltage viscosity of 10 CS and 350 CS.

3 The lower viscosity fluid was found to work better in the test rig because it amplified the second critical speed much less than the higher viscosity fluid, even at zero voltage. This finding would be generally true for rotor bending modes in aircraft engines as well because of their lightweight flexible structures (although the viscosity values could change with the application).

4 The ER fluids tested showed free vibration characteristics indicating Coulomb damping under some conditions and viscous under other conditions. The measured attenuation of critical speed peaks with increasing voltages indicates that there is a substantial amount of truly viscous damping produced by the ER damper. The type of damping observed could not be predicted a priori.

5 Equivalent viscous damping coefficients were measured using impedance transfer function methods, but the value uncertainty is large due to closely spaced resonances and the fact that the ER damping is not purely viscous.

6 An on–off (bang–bang) control logic was developed and implemented to actively control the bearing damping in the test rig. It proved to be successful, to the point of discouraging efforts to prove out a more sophisticated scheme.

Downloaded 02 Jun 2010 to 171.66.16.119. Redistribution subject to ASME license or copyright; see http://www.asme.org/terms/Terms_Use.cfm

7 The system tested was the best and most cost effective that could be identified in an extensive paper study by Vance et al. [1]. But the experiments reported here exposed practical problems with electrical arcing, poor availability of proper ER fluids, and the required physical size and weight of the ER damper. They all combine to raise serious questions as to whether this system could really be superior to the passive squeeze film damper as currently used in most aircraft engines.

Acknowledgment

These experiments were sponsored at Texas A&M University by the General Electric Co. under the capable direction of Al Storace. His contributions to this work are gratefully acknowledged.

References

[1] Vance, J. M., Ying, D. Z., and Nikolajsen, J. N., 1999, ''Active Control Of Bearing Damping for Aircraft Engine Applications,'' ASME Paper 99-GT-18.
[2] Nikolajsen, J. L., and Hoque, M. S., 1988, ''An Electroviscous Damper,'' NASA CP 3026, *Rotordynamic Instability Problems in High-Performance Turbomachinery*, pp. 133–141.
[3] Vance, J. M., and San Andres, L. A., 1999, ''Analysis of Actively Controlled Coulomb Damping for Rotating Machinery,'' ASME Paper 99-GT-175.
[4] Stevens, N. G., Sproston, J. L., and Stanway, R., 1988, ''Experimental Study of Electrorheological Torque Transmission,'' J. Mech. Trans. Automat. Design, **110**, No. 2, pp. 182–188.
[5] Ying, D. Z., 1993, ''Experimental Study of an Electrorheological Bearing Damper With a Parametric Control System,'' Master of Science thesis, Mechanical Engineering Department, Texas A&M University, College Station, TX.
[6] Thomson, W. T., 1993, *Theory of Vibrations With Applications*, 4th ed., Prentice Hall, Englewood Cliffs, NJ, pp. 35–36.
[7] Vance, J. M., 1988, *Rotordynamics of Turbomachinery*, John Wiley & Sons, New York.

Downloaded 02 Jun 2010 to 171.66.16.119. Redistribution subject to ASME license or copyright; see http://www.asme.org/terms/Terms_Use.cfm

1997 Soichiro Honda Lecture: Pathways to Achieving a New Generation of Engines for Personal Transportation

Gary L. Borman
University of Wisconsin,
4634 Gregg Road,
Madison, WI 53705

As we move into the twenty-first century the spread of affluence to a greater portion of an ever growing world population, coupled with dwindling reserves of crude oil, will make it imperative that we simultaneously protect our environment and enhance the fuel efficiency of transportation vehicles. Although reduced vehicle weight is the major contributor to conservation, it is argued that safety considerations limit vehicle size reduction. The engine thus remains an important component in meeting the needs of the new century; it is the primary subject of this lecture. The lecture first specifies those areas of engine design which provide the best opportunities for changes that will meet the needs of fuel economy and reduced emissions at an affordable cost. The discussion then concentrates on defining the pathways to achieving such goals. In particular, the tools available to perform the needed studies are discussed. The lecture ends with a discussion of the types of programs and methods of technical interchange required to produce a new generation of engines. [S0742-4795(00)00202-7]

Introduction

The focus of this lecture is to explore some of the directions that can be taken to develop engines for personal transportation vehicles to be used in the next generation. The timetable is uncertain, because technology is moving us toward more rapid change.

Because the vehicle is a complex system the best trade-off for engine characteristics depend on technology developments for all the vehicle components. For example, consider engine weight and its effect on fuel economy. We all know that vehicle weight is highly correlated to fuel economy, but in trading off engine cost and reliability against engine weight one might not change to a lighter design if the engine weight is a small fraction of the vehicle weight. But it must also be remembered that a heavy engine requires a stronger supporting frame so that it influences total vehicle weight more than just its own contribution. I'm sure that you can think of many other, perhaps more important, examples of such engine-system interactions such as the effects of engine torque-speed characteristics on the drive train. Of course engine efficiency and vehicle weight are not the only factors that determine fuel economy. Data supplied by USCAR show that for an intermediate size car operating over the federal driving cycle at 70 °F (21 °C) ambient, the fuel energy is distributed as shown in Table 1.

As can be seen the components other than the engine use 20.4 percent of the fuel energy. Because many advances have already been made in aerodynamics, tire design and drivetrain efficiency it is doubtful that more than a total 2 percent gain can be made due to further improvements. Braking energy can be recovered if a storage system is used, but although useful for buses, the application to personal cars is of doubtful cost effectiveness. The largest potential gains are therefore from engine improvements.

The point here is that any discussion of future engine technology cannot be isolated from the effects of other vehicle technologies. It is beyond my ability to cope with this broad question and thus this lecture is, at best, incomplete.

Contributed by the Internal Combustion Engine Division of THE AMERICAN SOCIETY OF MECHANICAL ENGINEERS for publication in the ASME JOURNAL OF ENGINEERING FOR GAS TURBINES AND POWER. Manuscript received by the ICE Division June 1, 1999; final revision received by the ASME Headquarters August 31, 1999. Technical Editor: D. Assanis.

Similarly, other external influences which will shape the nature of future vehicles must be considered; the effects of these influences are even less predictable. These influences are illustrated by

1 customer preferences
2 governmental regulations
3 transportation system infrastructure
4 energy source technology
5 global political stability
6 growth of domestic and global economics

I shall give a very brief heuristic discussion of these factors to set the stage for the main discussion of engine technologies.

Customer Preferences. In an invited lecture at Madison, Dr. Bill Agnew once stated that ''engines don't sell cars.'' As disagreeable as this is to engine engineers it is nevertheless a fact of life. In part, this is due to the excellent performance of today's engines and drive trains. Catch phrases such as ''thirty-two valves'' and ''raw power'' may help a car's image among some portions of the buying public, some may even worry about owning an under powered luxury car, but many other factors such as sticker price, dependability, dealer reputation, appearance and comfort play a more significant role. Certainly, fuel economy in the present U.S. market is not much of a factor given the low cost of fuel. If past observations hold, it is fuel availability concerns that can have the greatest effect and for now that is not a public concern.

With the reduction of size of even the ''full size'' cars the U.S. public has moved toward vans, sport utility vehicles and light

Table 1 Where the fuel goes (USCAR)

Accessories	2.2%
Aerodynamic Drag	2.6
Braking	5.8
Drivetrain	5.6
Engine (driving)	62.4
Engine (idling)	17.2
Rolling Resistance	4.2

Copyright © 2000 by ASME

Downloaded 02 Jun 2010 to 171.66.16.119. Redistribution subject to ASME license or copyright; see http://www.asme.org/terms/Terms_Use.cfm

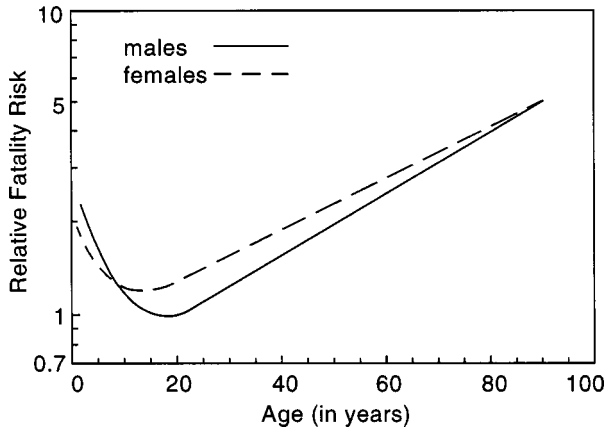

Fig. 1 Fatality risk from similar physical insults for males and females relative to the same reference case [1].

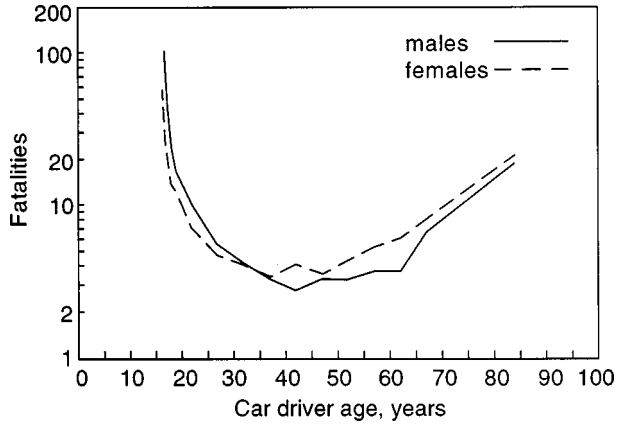

Fig. 2 Car driver fatalities per billion km of travel versus age and sex [2].

Table 2 Percentage of population over age 65 [3]

Year	% OVER 65	MEDIAN AGE
1995	12.8	34.3
2000	12.6	35.7
2005	12.6	36.6
2010	13.2	37.2
2015	14.7	37.3
2020	16.5	37.6
2025	18.5	38.0
2030	20.0	38.5

trucks. These vehicles serve the lifestyle of many baby boomers. We must recognize, however, that demographics show an aging, but more affluent population. Seniors favor larger cars for both comfort and safety. The safety issue is well founded, because larger cars are safer and older people are much more vulnerable to injury as shown in Fig. 1 [1]. In addition, the number of involvements per mile driven adds to fatalities. Both factors then contribute to the fatality data shown in Fig. 2 [2]. After 2005 the fraction of the U.S. population over age 65, will grow dramatically, as shown in Table 2 [3]. The health of the seniors will be very good and thus they will continue to affect the marketplace longer. At the same time it may be expected that the younger portion of the population will be more economically stressed by the need to support the less fortunate portion of the elderly. The challenge to automotive engineers is to meet these changing needs while continuing to meet the government imposed regulations on safety, fuel economy, and emissions.

Government Regulations. Government regulations for safety, corporate average fuel economy (CAFE) and emissions have continuously challenged the automobile industry and have undoubtedly also increased the sticker shock of consumers. But the result has been needed changes that might not have been made, given only the forces of consumer preference. Despite the dramatic reductions in emissions and significant improvements in fuel economy the nonattainment of air quality standards in cities and the growing consumption of foreign crude oil continues to plague the nation.

One must agree that increased taxation of fuel to European levels would help to solve these problems in the U.S, but it is doubtful that this is sufficient since Europe has high fuel prices, but air quality and consumption problems. It can also be argued that increased fuel taxation could be used to improve the transportation infrastructure in congested areas and thus improve fuel economy by changing the urban-driving cycle. Of course better highway infrastructure would also discourage the use of public transportation and thus its development. Because state governments are being encouraged to find ways to improve air quality we can expect more and more local restrictions, regulations and encouragements aimed at improving the very low 1.5 passenger-per-car average of U.S. commuters. Such interference in lifestyle will most likely find even more public resistance than higher taxation. Death and taxes are after all accepted as inevitable, but freedom of mobility is taken as a birthright.

Given the low probability of solving problems through taxation or changing human behavior it is most likely that the path will continue to be one of regulation by CAFE requirements and emissions standards.

The Tier II light duty vehicle (LDV) gram-per-mile pollution limits of the 1990 Amendments of the Clean Air Act of 1.7 for CO, 0.125 for nonmethane hydrocarbons, and 0.2 for NO_x can be expected to come about in 2004; EPA will find them necessary, feasible and cost effective. At the same time durability is already being extended to 100,000 miles. In addition, LDV cold start (20 °F) and evaporative emissions regulation will most likely become more stringent. Some states may even elect to follow the more stringent California standards. The California Ultra-low Emissions Vehicle (ULEV) requires particulate mass levels of 0.04 g/mile for diesels. At these low levels it would seem likely that other engines will also need to meet such a particulate standard.

The increase of CAFE requirements are not apt to be supported as strongly politically as are emissions reductions as long as fuel is available and more stringent emissions standards can be achieved. The current goal to produce an 80 mile per gallon car may be achieved, but unless such cars find consumer acceptance they may not have much effect on CAFE.

Transportation Systems Infrastructure. Keeping the current highway infrastructure in repair is the current challenge, dramatically improving it to take advantage of new technologies or to provide alternative transportation choices is improbable given economic restraints and the demographics already discussed. For larger cities some combination of an on-road hauler and small, electric or alternative-fuel-powered vehicles is technically feasible, but expensive. Such a system does allow use of a special personal vehicle designed for short, lower speed trips since the hauler would carry it and its passenger(s) for the longer high-speed portions of the journey. The concept is now available for intercity transport on Amtrak, but it is expensive and restricting.

Downloaded 02 Jun 2010 to 171.66.16.119. Redistribution subject to ASME license or copyright; see http://www.asme.org/terms/Terms_Use.cfm

An intracity version to be effective means purchase of a special personal vehicle, perhaps electric powered, which is of very restricted utility. Currently cost/benefits considerations do not favor such a system over more conventional public transport.

A second part of the transportation infrastructure is the fueling system which is currently designed to supply gasoline and to a limited extent diesel fuel at almost every location in the U.S. Supplying transportation power via the electric power grid would require an enormous change in the electric power production and delivery. The gasoline sold in the U.S. during 1996 had a total available energy of 5 billion MW-hr, and the total-net-energy-for-load of electricity produced was 3.25 billion MW-hr. If all cars were electric, and using an efficiency factor ratio of 3, the autos would have used about 50 percent of the produced electric power. To be realistic, we must consider hybrid systems where hydrocarbon fuel energy is converted to electric energy on board each vehicle. The advantages of such a system are probably restricted to urban driving where sustained high power demands are seldom encountered. The cost of the system is apt to be high for a special purpose vehicle. Still, local laws might force commuters to use such vehicles or all electric vehicles if severe environmental conditions similar to those in Southern California become common.

An alternative to more fuel efficient vehicles is to reduce travel by use of electronic communications. Teleconferencing, working at home using a computer, and shopping by electronic ordering are examples of travel-saving already being used. However, substantial changes in human social behavior will be needed to make such solutions productive and popular. If such technologies do have an impact, they will undoubtedly increase the percentage of shorter trips. Trips of under 15 miles are already most frequent [4]. Under urban driving conditions it takes about 15 miles of driving to reach fully warmed-up conditions. At 0°C ambient it took about 2 miles of travel to reach 50 percent of warmed-up fuel economy for 1960's era cars [5]. Undoubtedly this distance is shorter for modern cars, but I could find no similar data for 1990's cars.

Energy Source Technology. While the growth of free markets should bode well for the world economy it also indicates a potentially large increase in global fuel consumption. Even without such growth, it is expected that fuel costs will rise early in the next century due to competitive demand for crude oil. Those countries that have taken care to be efficient users of energy will have an economic advantage in the global markets. Unfortunately, technologies which have promised new energy sources, such as fusion power, have not progressed at the anticipated rate. Similarly competitive powerplant technologies, such as fuel cells and batteries, have also been slow to develop. Energy can be obtained from biomass, wind energy, and tidal energy, but the impact will remain small. Conversion of natural gas to liquid fuel offers a significant source, but uses a fuel already valuable in its natural form for stationary power and heating. Conversion of coal is a final solution, but a very expensive process with potentially undesirable environmental and social effects.

Table 3 shows data on energy reserves from these various sources. Based on the reserves and current use levels it would seem that we have no immediate problem, but it must be remembered that world use may rise sharply and that many reserves will be costly to recover. At a sustained global economic growth rate the reserves can be estimated to last about half as long as at the 1993 rate. North America has only 8 percent of the natural gas and crude oil reserves.

Although the comments above give little importance to alternative fuels, there is a place for a fuel such as DME,[1] produced from natural gas, for use in special nonattainment areas such as Southern California. Used in diesels it could allow the diesel to play a part in personal transportation providing both low emissions and excellent fuel economy. In the longer run its production would allow use of natural gas for transportation uses as crude oil becomes scarce [7].

[1]Dimethyl ether, CH_3OCH_3; data available since the lecture raise questions regarding degradation rates of DME.

Table 3 Global energy production and reserves [6]

Fuel	1993 Quantity Produced	Est. 1993 Energy Produced 10^{12} MJ	Est. Reserve 10^{15} MJ	Yrs. Reserve at 1993 Rates
Natural Gas	75 x 10^{12} ft^3	74	9.1	120
(Est) Gasoline, diesel and heating oil @58% of crude	13.1 x10^9 barrels	90	6.0	67
Coal (dry, ash free)	2.5 10^9 tons	71	16.4	230

Global Political Stability. One cannot help but notice that the largest oil reserves are located in areas of least political stability or under the ocean. Instability leading to internal strife can cause large losses in production; witness the drastic change in oil production from the former Soviet Union. While a global alliance of concerned countries may use military power, as in the Gulf War, to stop aggression by one state against another, it is more difficult and protracted to do so in the case of civil strife. It does not seem that there is any direct scientific solution to such problems, only the indirect use of technology to keep the armed forces of peaceful democratic countries far superior to all others.

Growth of Domestic and Global Economies. The ties between global economic growth and growth in use of energy have already been mentioned and are obvious. It is therefore important that the technologies developed to produce clean and efficient forms of personal transportation be available to all peoples, not only to the most affluent nations. This is especially true of technologies related to environmental concerns. Even now, some countries do not have unleaded gasoline and thus cannot use the three-way catalyst system to reduce pollutants from automobiles. If global warming is a legitimate concern, then it adds to all of the reasons discussed above to reduce consumption on a global basis.

Three Big Es

In his 1991 Honda Lecture, Karl Springer [8] discussed energy, efficiency, and the environment as the ''Three Big Es of Transportation.'' As discussed above, the concerns in general are much broader, but for engineers the issues often come down to the ''Big Es.'' Although as already discussed, vehicle efficiency depends on many factors, the engine is the primary determiner of the other two Es. A good engine may not sell the car, but a bad engine will certainly do the opposite. It is thus important that the new generation of engines not only solve the problems of the three Es, but also meet all the ''Three Big Ds,'' driveability, dependability and durability. At the present time the direction of engine type to achieve these goals is in a state of discussion with no ''super highway'' leading to a clear solution. From purely an efficiency standpoint the diesel engine is probably the short term choice. Table 4 was prepared with the help of friends in the industry. The numbers are probably contentious, but I believe the ranking is correct. It is not the purpose of this lecture to advocate a particular technology, but rather to explore the basic principles which may guide the way to a new generation of engines and then to suggest research pathways that may help to define the engine. Some technologies are, nevertheless, not considered because they do not appear practical. The fuel cell is one of these, because hydrogen is

Downloaded 02 Jun 2010 to 171.66.16.119. Redistribution subject to ASME license or copyright; see http://www.asme.org/terms/Terms_Use.cfm

Table 4 Estimations of best thermal efficiency for various powerplants

Powerplant Type	Efficiency (%)
Spark-ignited, port-injected, stoichiometric	31.5
Direct-injected, spark-ignited, stoichiometric	33.0
Direct-injected, spark-ignited, lean, early injection	34.5
Indirect-injected diesel	35.5
Direct-injected, spark-ignited, lean, late injection of gasoline	38.0
Gas Turbine	38.0
High-speed, direct-injected diesel	43.0
Heavy duty, direct-injected (HDDI) diesel	46.0
Fuel Cell (Using Hydrogen)	54.0
Turbo-compounded, HDDI diesel	54.0

not available in quantity and the technologies for producing and storing it appear to be quite unattractive. However, work on this technology has recently encouraged some to believe that solutions using gasoline conversion and storing hydrogen may soon be found. The system efficiency of such a process can be questioned; it is certainly less than the 54 percent shown in Table 4. Similarly, one could bet on a ''miracle cure,'' which will eliminate emissions by choice of fuel or fuel-with-additive, or by a new affordable aftertreatment device. Such considerations are discussed later, but not pursued in detail.

Selecting Pathways

Selecting the pathways to a future engine design would be made easier if an optimum engine design could be defined. It is recognized that the ''Three Big Es'' and ''Three Big Ds'' limit the multidimensional parameter space that defines the engine design. For example, emissions regulations determine one such boundary. Within such a restricted space the exact optimum depends on the weighting assigned to each factor that defines the optimum. Thus, for example, cost may be highly weighted for some vehicles and lowly weighted for others. In addition, design parameters are coupled by physical constraints. For example, four valves may be selected to improve volumetric efficiency and head design of a four stroke engine, but the total valve diameters are limited by the bore which in turn is determined by bore-stroke ratio for a given displacement and number of cylinders. In the days of thermodynamic cycle analysis [9] such design coupling was limited to simple considerations which could incorporate only qualitative predictions of combustion effects. Improvements in combustion analysis for port-injected-spark-ignited engines allowed some effects of geometry to be included [10]. However, the ability to handle direct injected engines remained limited. Progress on computational fluid dynamic (CFD) modeling of combustion widened opportunities for prediction, but it is only within recent years that CFD analysis including the fluid dynamics of the intake process has allowed full coupling of all parameters except some yet-to-be modeled aspects of two-phase flow and cycle-by-cycle variations of the intake process [11]. This is not to say that CFD models are now mature enough to be a complete design tool. Many aspects of the physics of injection, spray behavior, combustion, turbulence, emissions, etc., are not captured by current models. The subgrid model parameters are often empirically manipulated to produce results that agree with engine-out data. This should not limit the use of these models, but simply warn us that cautious application is prudent, and careful cross checks with experiment are required. In fact, models may be predictive for ensemble-averaged data even when they do not incorporate the correct single-cycle physics. An example of this is in-cylinder heat flux where gradient models of the boundary layer [12] imbedded in CFD programs can be quite accurate [13], but yet do not reflect some experimental observations of the physical processes [14,15].

The conclusions from the above discussion are four-fold.

1 the selection of a future engine type for personal transportation vehicles depends on the optimization definition selected, which is not unique

2 the design of a given engine type is complicated by many coupled parameters and thus analytical tools, including CFD models, must be combined with appropriate experiments to sort out designs

3 the current status of CFD modeling requires additional basic research to reduce the empirical manipulation of parameters based on engine-out data

4 because current CFD models are incomplete, some investigations along new pathways which are dead-ended may be unavoidable

These conclusions should not be taken as discouraging. Although the internal-combustion engine is technologically mature, much room exists for improvement and invention. Let us then begin by a critique of the good and the bad aspects of various engine designs. The first step is to define the engine design categories to be considered.

Engine Categories

Based on considerations of applicability to personal vehicles, the categories here exclude fuel cells, Stirling engines, gas turbines, and various combinations of gas turbine and/or other continuous burners combined with reciprocating engines. The remaining categories may be sorted out by; (A) geometry (open versus divided chamber), (B) ignition method (spark, jet, glow plug, compression). (C) fueling method (port injection, indirect injection, direct injection), (D) nature of the combustion process (premixed flame, homogeneous-charge oxidation, stratified-charge with mixing controlled combustion) and (E) type of fuel used. Certain unusual new engine concepts do not quite fit the above categories. For example, the use of an in-cylinder heat sink [16], an unconventional expansion mechanism [17], or a valved prechamber [18]. These and other unusual designs will thus be lumped together and discussed separately from the conventional designs. A review of older concepts is given in [19] and [20].

In considering the geometry, open-chambers (OC) are favored for fuel economy so that despite the many advantages of divided chamber (DC) diesels they are being replaced by OC designs. The DCs increased heat transfer and passage throttling losses might be overcome by use of a ceramic prechamber or by a ceramic prechamber combined with a ceramic valve in the passage. Currently cost considerations have limited the work on such designs although a natural gas stationary engine of the valved type is being developed in Japan [18]. The DC definition may be somewhat arbitrary. For example, a highly reentrant bowl-in-piston could be defined as either DC or OC. Similarly, small chambers of jet (plasma) igniters [21] or of jets for augmented mixing in diesels [22,23] could be classified as DC technologies, if the fuel burned in them is a significant fraction of total fuel burned. For this lecture I shall define DC as the traditional divided chambers where all or a significant amount of the charge first combusts in the prechamber. Because of the fuel economy issue all such DC designs will be excluded from the discussion. Table 5 thus lists only OC engine concepts for use in personal transportation. To further limit the discussion only four-stroke engines will be considered, even though two-strokes offer higher power density potential. The following abbreviations are used:

BR = broad-range fuel
CI = compression ignition
D = diesel fuel (high cetane fuel)
DISC = direct-injected, stratified charge

Downloaded 02 Jun 2010 to 171.66.16.119. Redistribution subject to ASME license or copyright; see http://www.asme.org/terms/Terms_Use.cfm

Table 5 Four-stroke, open-chamber engine categories

TYPE	REF.	IGN./FUELING/COMBUSTION MODE/FUEL	DESCRIPTION
1	24	SI/PI/PCF/G	Conventional automotive SI engine, Otto
2a	24	CI/DSPI/MCF/D	Conventional automotive CI engine, Diesel
2b	25	CI/DMPI/MCF/D	Diesel with split injection
2c	26	(SI or GP)/DSPI/MCF/BR	Diesel, but with forced ignition
3a	27	SI/DSPI/SCF/BR	Texaco-type-engine, late injection DISC
3b	28	SI/DMPI/PCF/G	PROCO-Ford type-engine early injection DISC
3c	29	SI/PI/SCF/G	Horizontally stratified charge
4	30	SI/DMPI/(SCF+PCF)/G	Mixed combustion mode DISI
5a	31	CI/PI/HBR/D	Flameless homogeneous autoignition
5b	32	CI/DSPI/HBR/D	Early injection with autoignition
6a		CI/DMPI/(HBR+MCF)/D	Flameless stratified autoignition followed by direct injection
6b	33	CI/(PI+DSPI)/(HBR+MCF)/D	Fumigation of diesel
7	34	JI/DMPI/MCF/G	Combustion-driven jet into early injected charge

DISI = direct-injected, spark-ignited
DMPI = direct-multi-pulse injection
DSPI = direct-single-pulse injection
G = gasoline (high octane fuel)
GP = glow plug
HBR = homogeneous-bulk reaction, ''flameless''
JI = jet ignition, ''torch or plasma''
MCF = mixing-controlled flame(s)
PCF = premixed-charge flame
PI = port injection
SCF = stratified-charge flame
SI = spark ignition

The list of Table 5 [24–34] could be expanded by the addition of engines, which use various valve and/or piston mechanisms. Piston mechanisms to replace the slider-crank [35,36], vary compression ratio [37], or provide different expansion and compression ratios [38] have not been used for various reasons, many of which include high retooling-cost-to-benefit-ratio and in the case of variation of compression ratio high friction outweighing the benefits.

Variable valve timing (VVT) can be used to improve the torque-speed curve shape, optimize volumetric efficiency, control peak pressure, reduce pumping work, and improve idle combustion. With two intake valves one can control the proportions of tumble and swirl flow at part-load in throttled engines. The largest gains from VVT are to reduce pumping. The Atkinson cycle [24], which uses late-intake-closing, allows a higher expansion ratio while keeping the compression ratio at its octane limited value. The addition of an intercooled supercharger helps to recover the power density and results in the Miller cycle [39]. For turbocharged diesels VVT to get early intake closing can result in a small improvement in efficiency and a reduction in NO_x due to lowering of the temperature at the start of combustion. Power density may suffer however.

Another valve control concept is to reduce engine power by deactivating the valves on some portion of the cylinders. This was used at one time by application of a simple valve deactivation mechanism applicable only to push-rod valve mechanisms. A similar simple mechanism is not available for overhead cam engines and the method is no longer in use. Note also that during deactivation oil tends to be pumped up into the cylinders which can lead to maintenance and emissions problems. The major problem is finding low friction, low cost VVT mechanisms, although a huge number of designs have been attempted [40] and some gasoline engines are now using electronic VVT. There is a good potential for such devices to improve SI engines, but the application to CI engines has less payoff.

A concept that allows very lean burning at part load in SI/PI/PCF/G engines is to burn rich in a few cylinders and then cool and mix the products from those cylinders with additional air and fuel and burn the resulting mixture in the other cylinders. The hydrogen produced from rich burning increases the ability to burn very lean [41]. If the rich burning is limited in equivalence ratio to prevent soot formation the hydrogen production is limited, but the use of a water-gas reaction catalyst can convert the carbon monoxide to carbon dioxide and hydrogen. This process is now being applied to some natural gas engines [42]. Unless the engine can be converted to run with the equivalent of stoichiometric mixtures in all cylinders at full load, the design limits the engine power density. The concept thus seems best suited to stationary engines where power density is typically not an issue.

Each type of engine in Table 5 offers some advantage, but all of the designs except the first two have limitations which have kept them from being used in the global personal vehicle market. All of the designs share some common limitations, these are discussed before going on to discuss the other specific design features.

Common Problems

As discussed by John Heywood in his 1990 Soichiro Honda Lecture [43], second-law analysis allows one to sort out the various causes of fuel availability destruction. Of the various causes the ones common in importance to all engines are combustion irreversibility, heat loss, and mechanical friction. The other losses due to combustion inefficiency, exhaust gas available energy and pumping-work loss vary considerably with engine type. The first two common losses amount to about 40 percent of the fuel available energy for a part-load SI/PI/PCF/G engine [43] and about 35 percent for a turbocharged heavy duty diesel engine [44] at part load. Unfortunately they are the losses that are also hardest to reduce.

Irreversibility is inherent to the process of converting chemical internal energy to thermal (sensible) internal energy by combustion. Reduction of the irreversibility is favored by very high temperature reactants and products, but such processes also produce high heat transfer, high peak pressure, and increased NO_x. A portion of the thermal energy is thus always unavailable, i.e., we cannot entirely convert it to useful work. The causes of irreversibility are fairly easy to understand for a homogeneous charge deflagration, but much more difficult to understand in detail for mixing controlled combustion where burning takes place at various conditions of fuel-air ratio, air to products ratio, and reactant temperature. In a typical modern diesel much of the fuel burns rich by mixing with hot products and air before mixing and combusting to a final lean condition. The mixing processes also pro-

Downloaded 02 Jun 2010 to 171.66.16.119. Redistribution subject to ASME license or copyright; see http://www.asme.org/terms/Terms_Use.cfm

duces a loss in available energy. The overall loss can be calculated, but the process path calculation requires a detail model of the combustion.

Heat loss due to both convection and radiation is not recovered in engines so it would seem prudent to insulate the combustion chamber. However, the concept does not work well for engines where knock limits the compression ratio [45]. In all cases a portion of the energy stored by the hot surfaces of the chamber is transferred to the intake charge and reduces the trapped masses. For a low heat rejection diesel the trapped mass is reduced by about 10 percent. With insulation, only a small fraction of the additional thermal energy in the cylinder gas during expansion goes to work, the rest goes out with the exhaust gas. Nevertheless fuel economy is improved if the combustion process and friction are not adversely affected by the higher temperature levels. Adverse combustion effects in diesels have been observed, and it is not understood if they can be avoided by design changes. They appear to be caused by the deterioration of the injection process due to the hot injector tip.

Friction between moving parts is unavoidable. In most engines about half is due to piston ring-cylinder hydrodynamic lubrication. High piston speeds increase the friction, the effect of increasing average cylinder pressure is a smaller effect. Improved piston and ring pack design combined with improved lube oil have already reduced friction in modern engines, but we may expect some further design improvements by application of computer models [46]. At a fixed speed, the mechanical friction loss increases as a percentage of fuel energy as the load is decreased, so again we see the importance of the driving cycle on efficiency.

Because significantly large improvements in the common losses discussed above are doubtful, it is very important to reduce the other half of the losses by improved design. Before discussing such improvements it is important to focus on the potentially best engines among those in Table 5.

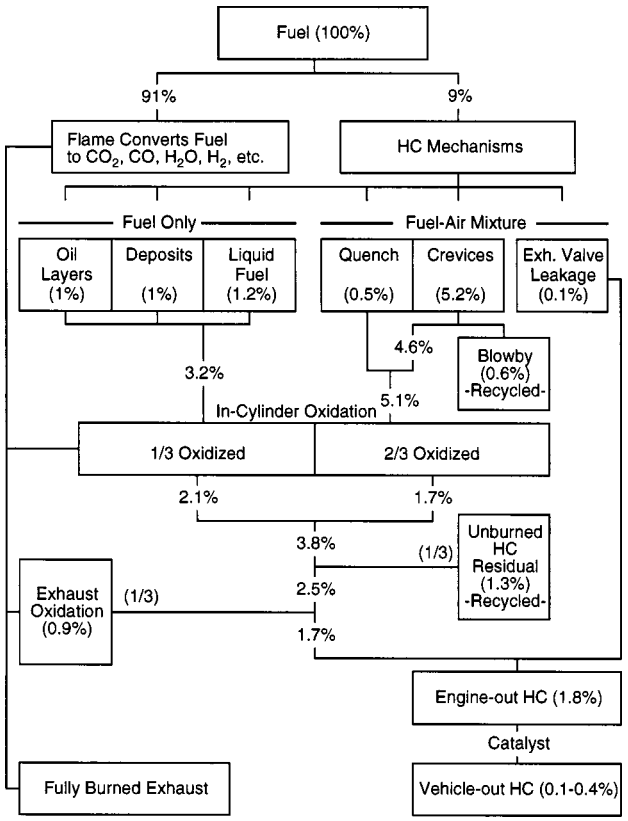

Fig. 3 Complete flow chart for the gasoline fuel, which enters each cylinder [47].

Removing the Clinkers

For those not familiar with coal combustion, I should explain that clinkers are fused lumps of uncombustibles formed in the ash—they get caught in the grate and must be removed. The clinkers in our combustion processes are combustion inefficiency, low power density, fuel property sensitivity, pumping losses, and the inability to reduce emissions to the atmosphere to regulated values. Of course the three ''Big Ds'' and cost must always be considered as well and provide additional clinkers.

Combustion Efficiency. Any combustion product constituents that are not equilibrium products represent a combustion inefficiency. All of the engine types except Type 2 engines have significant losses of combustion efficiency because fuel gets into crevice volumes or on surfaces where it does not combust. Cheng et al. [47] estimate that for a Type 1 engine about 9 percent of the fuel does not directly take part in the combustion flame process. Figure 3 shows their results for hydrocarbon losses. Note that both liquid phase and gas phase initial losses are significant, but that after in-cylinder oxidation they contribute about equally to the incomplete products leaving the cylinder. The liquid phase losses could be eliminated by prevaporization in the port. The total effect of hydrocarbons, carbon monoxide and hydrogen leaving the engine is a 4–5 percent loss in the available energy of the fuel at part load [24]. It is interesting to compare Fig. 3 with similar, but less substantiated, estimates for a Type 3 engine [48]. This is shown in Fig. 4 [48]. The numbers shown will vary a lot with the engine design. For example, late injection typically gives high values of unburned hydrocarbons (UHC) due to wall wetting, while early injection should give values smaller than those of a Type 1 engine. It is important to remember that the efficiency losses are higher than indicated by the cylinder-out UHC mass because of very late oxidation of the crevice hydrocarbons.

Engines of Type 4 combine aspects of Type 1 and Type 3, but during starting before catalyst light-off, where UHC really count, the engine referenced behaves like a Type 1 engine.

Type 5 engines are limited to dilute conditions, but have Type 1 crevice problems. More hydrocarbons are lost, lowering the efficiency, due to the higher compression ratio, but more will be

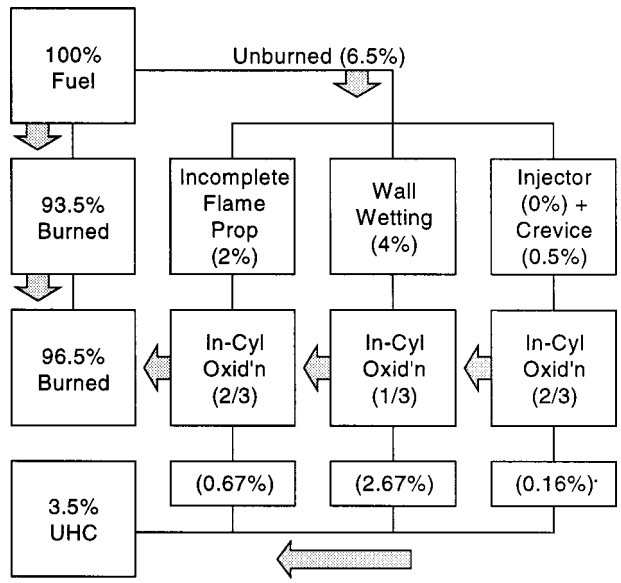

Fig. 4 Schematic of hydrocarbon emission sources for stratified charge engines. [48].

Downloaded 02 Jun 2010 to 171.66.16.119. Redistribution subject to ASME license or copyright; see http://www.asme.org/terms/Terms_Use.cfm

oxidized in the cylinder thus lowering cylinder-out UHC. Similar remarks apply to the fumigated fuel portion of the Type 6b engine.

Type 6a and Type 7 engines could have lower hydrocarbons than Type 1, more like Type 2, if stratification can be achieved. Like all stratified engines, the UHC problem will be a problem at low loads where exhaust temperature levels are low.

One may conclude that the diesel engine (Type 2), except for low loads, has the best combustion efficiency. The low load problem stems from either overpenetration because the boost is low or from overmixing in the case of high swirl engines. If the design is low swirl then Type 2b offers a possible solution by using split injection [49]. An alternative would be a high pressure injector that can vary spray penetration without sacrifice of droplet size and can also provide the mixing momentum required for a quiescent chamber design.

Power Density. To achieve desirable power density, fueling levels must be at least as high as the stoichiometric Type 1 engine with turbocharging. All engines which are subject to knock at full load must limit reactant temperature and surface temperatures in the end-gas if they are to avoid knock. Type 2 engines can be highly boosted, but are limited by peak pressure. Type 2b engines might avoid high peak pressure by injection strategy. Type 6a is a version of Type 2b and has a similar advantage. To achieve HBR combustion the initial charge must be well mixed, by, for example, spraying onto a target close to the injector. Ideally the injector would at first inject down through one very small hole and then radially outward as a normal diesel through multiple holes of larger size. A single injector with such attributes is (to my knowledge) unavailable.

The limits of power density of the DI engines depends on air utilization achieved without creating an end-gas. Novel combinations of air motion and innovative injector designs and/or operation offer potential improvements. Of course the automobile engine should not be heavy, so control of peak pressure and use of light-high-strength materials is key to power density increases. Two-stroke devotees would undoubtedly champion their cause at this juncture.

Fuel Sensitivity. Those engine types marked ''BR'' for fuel category are least sensitive to fuel quality. All of the types with ''HBR'' combustion are very sensitive to fuel quality and are thus currently impractical except for some nitch market where fuel quality can be carefully controlled. A method to use EGR with a control that can rapidly respond to fuel quality could of course greatly reduce the fuel sensitivity problem. Engines that are fuel insensitive may offer a wide appeal for a global market and for some future time when fuel is scarce, but given tight emissions regulations the use of a broad range of fuels seems unlikely and thus irrelevant. It is an attribute, however, if relaxation of engine combustion requirements allows new fuel formulations that can lower emissions, either from the tail pipe or from evaporative losses.

Pumping Losses. Types 1, 3, 4, and 7 all require throttling even if only to allow use of EGR. One must remember that although pumping losses are low for the Type 2 engines the loss of energy by blowdown of the exhaust (exhaust valve throttling) causes a loss of available energy that is significant—similar in magnitude to pumping losses of Type 1 at mid-load. The use of a VVT system could reduce this loss. Otherwise, the Type 2 engines offer the best hope for efficient idle-fuel-economy.

Emissions. The three-way catalyst combined with the Type 1 engine will be hard to beat for low emissions at a reasonable cost. Development of an efficient, low cost lean catalyst would of course allow improvements for all lean-burn engines [50]. The storage catalyst used in the Type 4 design causes many design limitations, but does give a temporary solution (of sorts) for SC gasoline engines. A Type 2b engine with a fuel additive to remove NO_x in the cylinder and with a reduced cost version of the current heavy duty oxidizing catalyst systems would of course provide an excellent solution.

The use of combined split injection, EGR and retarded timing offer methods to move the NO-particulate trade-off to low values for heavy duty engines with high pressure injection. To apply these concepts to smaller engines will, however, require cost reductions and perhaps the use of very small (below 0.1 mm) injector nozzle hole sizes. The problem aside from cost is that such designs may produce less particulate mass but greatly increase the number of particulates [51]. This challenges the current concept that total particulate mass is a sufficient measurement to judge health effects. Ultrasonics could perhaps be used to cause agglomeration of these small particles. The heterogeneous nature of SC combustion can produce pockets of rich mixture that when burned create soot. Thus the various stratified charge engines also produce engine-out particulates that may require regulation.

From these observations it would appear that a turbocharged diesel engine using DME as a fuel gives the best solution for low emissions and good efficiency. However, such a solution requires a large production of DME from natural gas—this will happen very slowly unless encouraged by some government actions that make the higher DME fuel cost competitive. Given market forces alone, the rise of fuel price with reduced reserves of crude oil should cause a natural shift to natural gas and fuels produced from it. However, the urgency of meeting ultra-low emissions standards works against such a slow pace and thus conventional fuels must be used in the near term solutions. The rational use of fuel resources suggests that conversion of a large fraction of personal vehicles to diesel fuel use is not consistent with current refinery product streams. In the near term, we need to find an engine which uses gasoline, but has the best attributes of a diesel engine. While the Type 2c engine can burn low cetane fuels and gasoline-diesel-fuel mixtures it cannot burn gasoline over the wide range of loads required [26]. The current revived interest in engines of Types 3 and 4 is thus rational, but frustrating because such designs are in fact fighting against the laws of Mother Nature. We thus ask how to emulate the diesel's fuel economy while avoiding its typically high NO_x and particulate emissions. Are there pathways to this goal suggested by the previous discussion, and if so, what R and D is needed to follow these pathways?

Pathways to a New Engine

Most of what has been said here so far is not new and certainly offers few revelations. Unusual new designs are best illustrated by Type 4 which combines previous concepts using a tour de force of sophisticated controls to manage the very complex system. While the use of controls offers great hope, controls cannot reverse the laws of physics.

In the diesel engine the high pressure spray provides early mixing without the cyclic behavior of the mixing provided by cylinder flows. However, once the injection stops the mixing decreases. One then needs more late mixing, but a gas phase solution to this requires some augmented mixing device which is not practical for small engines. Multiple-pulsed injection can help manage the mixing problem, but is limited by combustion duration considerations and the need for high pressure injection to provide momentum. A means to dynamically vary nozzle hole size seems difficult to achieve. Some means of introducing air into the fuel prior to compression and in a controlled manner, or a way to fluidically or electrically modulate the flow inside the injector could offer novel control methods. For example, a short duration spark could provide control within the injector. Also, recall that in the Cummins PT injector, combustion is thought to have occurred within the injector due to air present in the tip. This could have been the reason that this injector gave shorter than typical ignition delays. We have only begun to understand the connection between the flows within the injector and their influence on spray behavior. Such understanding combined with innovative designs appears to

Downloaded 02 Jun 2010 to 171.66.16.119. Redistribution subject to ASME license or copyright; see http://www.asme.org/terms/Terms_Use.cfm

be a pathway to improved stratified combustion. Similarly the use of CFD and experience, to explore a wide variety of unusual combinations of geometries and injection patterns and to evaluate ''what if'' ideas, may yet lead to lower emissions designs [52,53].

Injectors can be designed to produce very fine mists without the use of high pressure (see Ref. [54] as one of many examples), but penetration is a problem. The design must then return to the use of fluid mechanics to provide mixing variation with load and speed. The problems inherent to this are discussed next.

The stratified gasoline engine using low pressure injection (Types 3 and 4) typically requires an initial lack of mixing followed by more mixing all without use of divided chambers and with avoidance of wall wetting. Figure 5, which is reproduced from Ref. [55] shows some concepts of SC mixing. Ignition of the spray by a spark close to the nozzle is difficult and may provide fouling problems. Use of the piston to steer the spray encourages the wall wetting UHC problem. The use of air flow provides the best flexibility if port controls can provide the needed changes without excessive pumping losses, however cycle-by-cycle variations cause the process to be imprecise.

The needed time variation of mixing is backward to that obtained from tumble flow. Alternatively, swirl persists throughout the process and is hard to break down at the required time. This basic inability to provide the required fluid mechanics was pointed out by Bracco [20] more than two decades ago. The continuing lack of progress indicates we are indeed fighting against the laws of physics unless some divided chamber concept is used.

The creation of the stratified mixture by the fuel injection in CI engines allows very rapid spread of the combustion once ignition starts. The spread is probably by a multiple-compression-ignition process rather than by a flame propagation. Rapid surrounding and penetration of the outer surface of the fuel-air mixture by combustion reduces the chance for fuel-air mixtures to be pushed into the surrounding air-products mixture prior to burning. For the spark-ignition case the flame spreads out from a single point and the expanding products push the mixture into the surrounding unburned gas.

The amount of mixing of the unburned fuel-air charge depends on the geometry, turbulence, and rate of flame propagation—but mixing will occur. This is a potential source of unburned hydrocarbons due to formation of very lean zones of mixture not hot enough to oxidize before exhaust-valve-opening. Even the leanest gasoline mixtures will oxidize if hot enough, so mixing with hot, lean products will cause oxidation if the mixture temperature gas goes well above 1200 K and time to react is sufficient. The mixing rate of very lean end-gas and products will depend on the chamber geometry and turbulence level during the expansion stroke. A large interfacial surface area between products and end-gas should aid mixing. Obviously the temperature levels drop as load decreases and the chance of complete oxidation decreases. Even high-compression-ratio diesels experience white smoke emissions at low load if over-mixing or wall-wetting has taken place.

Rapid mixing of hot products with cooler air, cooler products or even cool dilute reactants will reduce the NO production. (For the latter case some scant evidence exists that NO may also be converted to nitrous oxide.) Of course such rapid mixing implies conditions which destroy stratification of the charge. Note again that the diesel case is different because of the way the initial combustion surrounds and penetrates the charge except close to the injector tip. In the heavy duty case the jet is vaporized over almost the whole length and is quite rich, with perhaps almost the whole jet volume undergoing pyrolysis or burning near the rich limit [56]. The production of NO as predicted by the U.W. version of KIVA and experiment [57] extends over a large portion of the heat release as rich products are leaned out by mixing and cooled by expansion. This is quite different from older data from naturally aspirated engines with MBT timing and moderate injection pressure where the products of premixed burning at near stoichiometric cause most of the NO produced and where NO production has leveled off by the time of peak pressure [58].

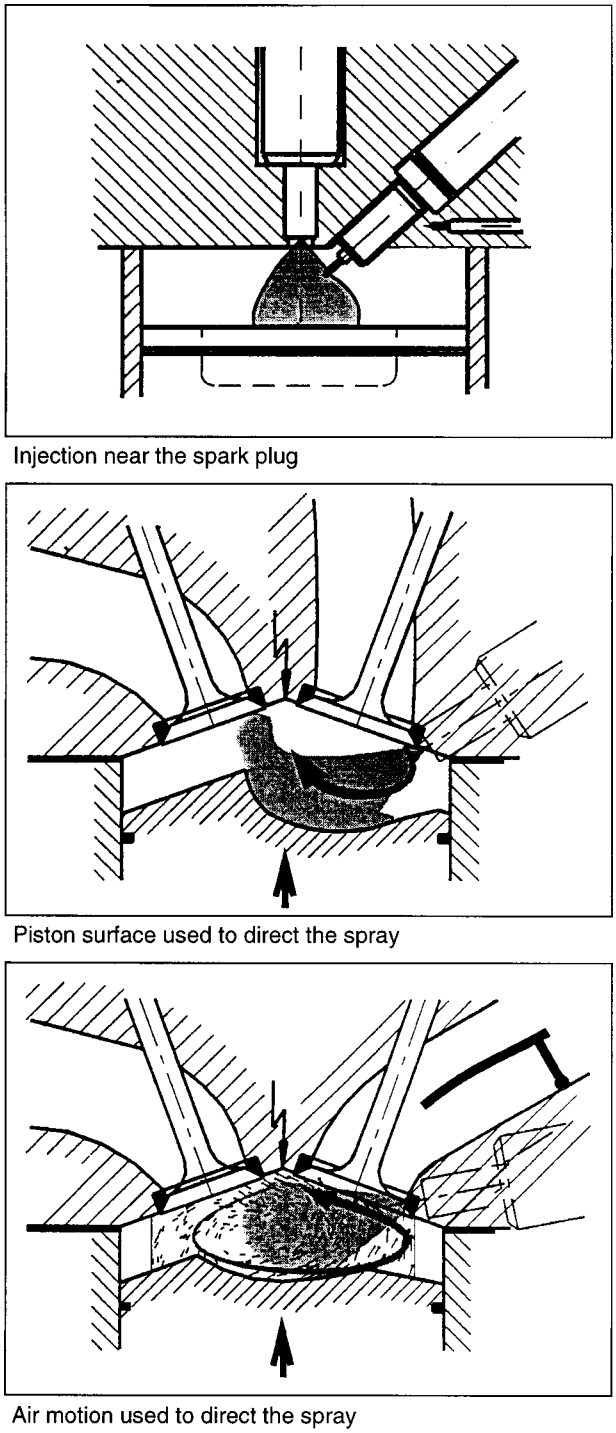

Fig. 5 Fuel stratification concepts [55].

Various impinging jet concepts have been used following the work of Kroeger [59]. The technique can use a raised portion of the piston or targets attached to the injector [26,60]. The method creates a cloud of droplets creating better air utilization than by jet breakup with multihole nozzles. Recent computations [52] indicate that with diesel fuel low levels of particulate and NO_x can be achieved, however the level of UHC could not be computed. One expects these designs may cause surface wetting at the target area resulting in high UHC values. Application of the concept to gasoline with spark ignition might be similar to the use of spark ig-

Downloaded 02 Jun 2010 to 171.66.16.119. Redistribution subject to ASME license or copyright; see http://www.asme.org/terms/Terms_Use.cfm

nited low cetane fuel [26] where good results were obtained. A spark plug that creates ignition at the injector which is on the cylinder axis would likely be good if flame spread over the fuel cloud can be maintained over the whole range of speeds and loads. Note that compression ignition aids this process for higher cetane fuels, but the spread is limited by flame speed for higher octane (gasoline) fuels. Introduction of a small amount of fuel followed by ignition during a pause in injection might be helpful. Again, turbocharging is critical to obtaining good power density.

The application of fuel formulation to the problems of Type 3 engines may offer a solution to the combustion management problem. Diesel combustion and emissions changes are very small due to fuels with the same distillation curves, but different chemical property distributions as a function of volatility [61]. However, addition of a single pure constituent that puts a spike in the distillation curve can affect the combustion and emissions [62]. Recent modeling which includes the droplet distillation process in the spray model shows how such effects can occur [63]. Preferential vaporization or a low octane blending agent might improve the characteristics of combustion spread in a late injection DISC engine but would increase the risk of knock. The concept is so complex that initial attempts to understand it are probably best done by modeling.

In the above discussion a few pathways have been suggested, but no clear path for gasoline engines without NO_x after treatment has been shown. At present the activity is hectic and thus this lecture, which was written before the August SAE Meeting in San Diego and is being presented while the ASME sponsored Foundation Conference is in progress, is undoubtedly behind the curve. However, given the difficulties discussed it is unlikely that any late breaking discovery will suspend the need for additional R and D. This lecture thus concludes with some brief remarks about research needs.

Research Needs

The downsizing of industrial research in the U.S. has been a subject of many papers and is a source of admiration by some and desperation by others. While I feel that not enough is being spent now, the new attempt to focus on results oriented outcomes is a move in the correct direction. I believe that universities need a similar reappraisal of their methods and attitudes. It is important to produce new methods of working with industry which do not jeopardize basic long-term approaches, but do focus on outcomes. It is in the best interest of industry to encourage and nurture such a reappraisal without being arrogant. We all need to learn what we each do best and respect each other for what we do.

The following research concepts are university (or government lab) oriented, given my background. Because the topics are numerous and my abilities very limited, I shall limit the suggestions to just seven broad topic areas in modeling since that topic is the theme of this ASME ICE Conference. I feel strongly that CFD modeling has now reached a point where it can be used to explore optimization of a given design concept in addition to sorting out various disparate designs. In doing so, the limitations of the models need to be constantly in mind.

The first suggestion is to define a methodology which allows optimum designs to be discovered in a systematic way. To do this one must first start with a definition of the factors and a weighting of each factor that defines the optimum design. Because so many factors determine what is defined as optimum it is likely that no CFD program can include them all. That limitation is important, but should not stop the process. The point of defining an optimum, even if it is limited in scope, is to provide a mathematical way to allow the computer to seek out pathways in the multi-parameter space. Such computational algorithms are well known and need not be discussed here. The project is large and would need the cooperative efforts of a number of groups. A working group on this effort would also help to define needed code and subgrid model improvements and their required supporting experimental programs.

The second suggestion is to apply the Second Law using CFD to compute the losses in available energy during stratified charge combustion. This is not a systems approach that has already been done, but is a look at the details of the process. The point of the exercise is to better understand in detail where combustion processes go wrong.

The third suggestion is to obtain a better basic understanding of combustion in prevaporized mixtures of fuel, products, and air which, contain composition gradients and are at temperatures and pressures typical of engines. This does not imply that vaporization is unimportant, but simply that one should start with a more manageable problem. Suggestion one (above) deals with sprays, etc., at a systems level. The modeling here should incorporate more detailed chemical kinetics as well as the physical issues typically included. Some of the work should include direct numerical simulation so that fundamentals can be properly included in the more empirical models. Again a working group is needed for a multidisciplinary approach.

The fourth suggestion is to continue research on modeling the internal flows within the injector with a focus on the ability to understand how those flows influence the spray behavior. Experimental evidence [64,65] shows that current models, which use only velocity and mass flow at the exit of the injector hole(s) as initial conditions are unable to predict some spray differences due to internal injector geometry. Such research might also help discovery of new injection control concepts.

The fifth suggestion is to model the processes that cause unburned hydrocarbon emissions due to wall wetting in direct injection engines. The models should include wall temperature and deposit effects. While avoiding wetting would appear to be the best strategy, designs which use impacting sprays offer advantages and need to be evaluated.

The sixth suggestion is to use modeling to evaluate the concept of distributed ignition at the injector tip to see if this would allow flame spreading that would encapsulate the whole spray from the very start of injection. Finding the appropriate mechanism for causing such ignition is an experimental project, but evaluation of this ''what if'' concept by modeling could encourage or discourage such experimental efforts.

The seventh suggestion is to model the combustion of stoichiometric fuel-to-oxygen ratio mixtures which contain very high amounts of exhaust products. Such mixtures would probably produce particulates for typical fuels, but may be soot-free for fuels containing oxygen, such as DME. The study must incorporate very high temperatures and pressures characteristic of high compression ratios, thus addition experimental work will be needed. The use of homogeneous compression ignition as well as flame propagation should be included. In looking at such mixtures it will be important to include NO measurements and modeling as the extended Zeldovich mechanism may no longer be adequate.

The above suggested projects are mostly computational, but I do not wish to end this lecture with the impression that experiments are to be abandoned. I assume that industry will attempt many engine designs and learn much in the process, however it is most important that fundamental experiments also be conducted to determine the correct inputs to the models. It does not take much perusal of past modeling efforts to see that simple comparisons to engine-out results can lead to serious conceptual errors.

References

[1] Evans, L., 1988, ''Risk of Fatality from Physical Trauma versus Sex and Age,'' J. Trauma, **28**, No. 3, pp. 368–378.

[2] Evans, L., 1994, ''The Older Driver Problem: An Epidemiological Overview,'' *Proc. of 14th Enhanced Safety of Vehicles Conference*, Munich, Germany, May 1994.

[3] U.S. Bureau of Census, Projected Population Breakdown by Age, Sex and Ethnic Origin, 1995–2050.

Downloaded 02 Jun 2010 to 171.66.16.119. Redistribution subject to ASME license or copyright; see http://www.asme.org/terms/Terms_Use.cfm

[4] Cole, D., 1984, ''Automotive Fuel Economy,'' in *Fuel Economy*, J. C. Hillard and G. S. Springer, eds., Plenum Press, New York.
[5] Niepoth, G. W., and Scheffler, C. E., 1965, ''Customer Fuel Economy Estimated from Engineering Tests,'' SAE Paper 650861.
[6] Borman, G., and Ragland, K., 1998, *Combustion Engineering*, McGraw Hill, New York.
[7] Fleish, T., McCarthy, C., Basu, A., Udovich, C., Charbonneau, P., Slodowske, M., Mikkelsen, S. E., and McCandless, J., 1995, ''A New Clean Diesel Technology: Demonstration of ULEV Emissions on a Navistar Diesel Engine Fueled With Dimethyl Ether,'' SAE Paper 950061.
[8] Springer, K. J., 1992, ''Energy, Efficiency, and the Environment: Three Big Es of Transportation,'' ASME J. Eng. Gas Turbines Power, **114**, pp. 445–458.
[9] Weber, H., and Borman, G., 1967, ''Parametric Studies Using a Mathematically Simulated Diesel Engine Cycle,'' SAE Paper 670480.
[10] Mattavi, J. A., Groff, E., Lienesch, J., Matekunas, F., and Noyes, R., 1980, ''Engine Improvements Through Combustion Modeling,'' in *Combustion Modeling in Reciprocating Engines*, Mattavi and Amann, eds., Plenum Press, New York.
[11] Reitz, R., and Rutland, C. J., 1995, ''Development and Testing of Diesel Engine CFD Models,'' Prog. Energy Combust. Sci., **21**, pp. 173–196.
[12] Yang, J., and Martin, J. K., 1989, ''Approximate Solution-1D Energy Equation for Transient, Low-Mach Number, Compressible, Turbulent Boundary Layer Flow,'' ASME J. Heat Trans.
[13] Reitz, R. D., 1991, ''Assessment of Heat Transfer Models for Premixed Charge Engines,'' SAE Paper 910267.
[14] Pierce, P., Ghandhi, J., and Martin, J., 1992, ''Near-Wall Velocity Characteristics in Valved and Ported Motored Engines,'' SAE Paper 920520.
[15] Boggs, D., and Borman, G., 1991, ''Calculation of Heat Flux Integral Length Scales from Spatially-Resolved Surface Temperature Measurements in an Engine,'' SAE Paper 910721.
[16] Ferrenberg, A. J., 1990, ''The Single Cylinder Regenerated Internal Combustion Engine,'' SAE Paper 900911. (See also SAE 961677.)
[17] Clarke, J., and Berlinger, W. G., 1996, ''A New Compression Ignition Engine Concept for High Power Density,'' *Proc. 18th Annual Fall Tech. Conf. of ASME ICE Div.*, ICE Vol. 27-1.
[18] Kawamura, H., Nakashima, K., and Miyagawa, T., 1996, ''Improvement of Thermal Efficiency and NO_x in CNG Engine with Ceramic Heat Insulation System,'' Paper P02, 14, FISITA.
[19] Uyehara, O. A., Myers, P. S., Marsh, E. E., and Cheklich, G. E., 1974, ''A Classification of Reciprocating Engine Combustion Systems,'' SAE Paper 741156.
[20] Bracco, F. V., 1974, ''Toward an Optimal Automobile Powerplant,'' Combust. Sci. Technol., **12**, (1/2/3), pp. 1–10.
[21] Edwards, C. F., Oppenheim, A. K., and Dale, J. D., 1983, ''A Comparative Study of Plasma Ignition Systems,'' SAE Paper 830479.
[22] Nagano, S., Kawazoe, H., and Ohsawa, K., 1991, ''Reduction of Soot Emission by Air-Jet Turbulence in a D.I. Diesel Engine,'' SAE Paper 912353.
[23] Konno, J., Chikahisa, T., and Murayama, T., 1993, ''An Investigation on the Simultaneous Reduction of Particulate and NO_x by Controlling Both the Turbulence and Mixture Formation in DI Diesel Engine,'' SAE Paper 932797.
[24] Heywood, J., 1988, *Internal Combustion Engines Fundamentals*, McGraw-Hill, New York.
[25] Han, Z., Uludogan, A., Hampson, G. J., and Reitz, R. D., 1996, ''Mechanism of Soot and NO_x Emission Reduction Using Multiple-Injection in a Diesel Engine,'' SAE Paper 960633.
[26] Enright, B., Borman, G., and Myers, P., 1988, ''A Critical Review of Spark-Ignited Diesel Combustion,'' SAE Paper 881317.
[27] Mitchell, E., and Alperstein, M., 1973, ''Texaco Controlled-Combustion System Multifuel, Efficient, Clean and Practical,'' Combust. Sci. Technol., **8**, (1–2), 39–50.
[28] Simko, A., Choma, M. A., and Repko, L. L., 1972, ''Exhaust Emission Control by the Ford Programmed Combustion Process-PROCO,'' SAE Paper 720052.
[29] Quader, A. A., 1982, ''The Axially-Stratified-Charge Engine,'' SAE Trans., **91**, pp. 479–504.
[30] Harada, J., Tomita, T., Mizuno, H., Mashiki, Z., and Ito, Y., 1997, ''Development of Direct Injection Gasoline Engine,'' SAE Paper 970540.
[31] Onishi, S., Hong, J., Shoda, P., Jo, D., and Kato, S., 1979, ''Active Thermo-Atmospheric Combustion-ATAC,'' SAE Paper 790501.
[32] Ryan, T. W., and Callahan, T. J., 1996, ''Homogeneous Charge Compression Ignition of Diesel Fuel,'' SAE Paper 961160.
[33] Shakal, J., and Martin, J. K., 1990, ''Effects of Auxiliary Injection on Diesel Engine Combustion,'' SAE Paper 900398.
[34] Hensinger, D. M., Maxson, J. A., Hom, K., and Oppenheim, A. K., 1992, ''Jet Plume Injection and Combustion,'' SAE Paper 920414.
[35] Beachley, N. H., and Lenz, M. A., 1988, ''A Critical Evaluation of the Geared Hypocycloid Mechanism for Internal Combustion Engines,'' SAE Paper 880660.
[36] McKisic, A. D., Smith, J., Wang, W., and Prucz, J., 1988, ''A Parametric Investigation of the Stiller-Smith Mechanism for Application in Internal-Combustion Engines,'' SAE Paper 880662.
[37] Basiletti, J. C., and Blackburne, E. F., 1966, ''High Output Diesel Engines-Recent Developments in Variable Compression Ratio Engines,'' SAE Paper 660344.
[38] Amann, C. A., 1985, ''The Powertrain, Fuel Economy and the Environment,'' Second Congress, Int. Assoc. for Vehicle Design, Geneva, Switzerland, 1985. Also GMR-4949, Feb. 15, 1985.
[39] Ma, T. H., 1988, ''Effect of Variable Engine Valve Timing on Fuel Economy,'' SAE Paper 880390.
[40] Ahmad, T. and Theobald, M. A., 1989, ''A Survey of Variable-Valve-Actuation Technology,'' SAE Paper 891674.
[41] Siewart, R. M., and Turns, S. R., 1975, ''The Staged Combustion Compound Engine: Exhaust Emissions and Fuel Economy Potential,'' SAE Paper 750889.
[42] Smith, J. A., Podnar, D., and Meyers, P., 1996, ''The Hybrid Rich Burn/Lean Burn Engine, Part II,'' ASME, ICE Vol. 27-4, Book G1011D-1996.
[43] Heywood, J. B., 1990, ''Future Engine Technology: Lessons from the 80's for the 1990's,'' ICE-Vol. 13, *New Technology in Large Bore Engines*, B. Chrisman, ed., Book No. 100306, ASME, New York.
[44] Primus, R. J., Hoag, K. L., Flynn, P. F., and Brands, M. C., 1984, ''An Appraisal of Advanced Engine Concepts Using Second Law Analysis Techniques,'' SAE Paper 841287.
[45] Siegla, D. C., and Amann, C. A., 1984, ''Exploratory Study of the Low-Heat-Rejection Diesel for Passenger-Car Application,'' SAE Paper 840435.
[46] Keribar, R., Dursunkaya, Z., and Flemming, M. F., 1991, ''An Integrated Model of Ring Pack Performance,'' ASME J. Eng. Gas Turbines Power, **113**, No. (3), pp. 382–389.
[47] Cheng, W. K., Min, K., Hochgreb, S., Heywood, J. B., and Norris, M., 1993, ''An Overview of Hydrocarbon Emissions Mechanisms in Spark-Ignited Engines,'' SAE Paper 932708.
[48] Anderson, R. W., Young, J., Brehhob, D. D., Yi, J., Han, Z., and Reitz, R. D., 1997, ''Challenges of Stratified Charge Combustion,'' *Conf. on Direkteinspritzung im Ottomotor*, March 12–13, 1997, Essen, Germany.
[49] Montgomery, D. T., and Reitz, R. D., 1966, ''Six-mode Cycle Evaluation of the Effects of EGR and Multiple Injections on Particulate and NO_x Emissions from a D.I. Engine,'' SAE Paper 960316.
[50] Heimrich, M. J., 1997, ''Demonstration of Lean NO_x Catalytic Converter Technology on a Heavy-Duty Diesel Engine,'' SAE Paper 970755.
[51] Baumgard, K. J., and Johnson, J. H., 1996, ''The Effect of Fuel and Engine Design on Diesel Exhaust Particulate Size Distributions,'' SAE Paper 960131.
[52] Senecal, P. K., 1977, ''Exploring Alternatives to Conventional DI Diesel Combustion Systems Using Computational Fluid Dynamics,'' M.S. thesis, University of Wisconsin-Madison, Department of Mechanical Engineering, Madison WI.
[53] Park, K., and Watkins, A. P., 1996, ''An Investigation of Combustion Chamber Shapes for Small Automotive Direct Injection Diesel Engines Employing Spray Impaction,'' Proc. I. Mech E, **210**, pp. 261–272.
[54] Snyder, H. E., and Reitz, R. D., 1996, ''Gas Efficient Liquid Atomization Using Micro-Machined Spray Nozzles,'' SAE Paper 960859.
[55] Wolter, A., and Grigo, M., 1997, ''Entwicklung von Ottomotoren mit Direkteinspritzung: Motor Konzepte und Entwicklung-swerkzeuge,'' Conf. on Direkteinspritzung in Ottomotor, March 12–13, 1997, Essen, Germany.
[56] Dec, J., 1997, ''A New Conceptual Model of D.I. Diesel Combustion Based on Laser-Sheet Imaging,'' SAE Paper 970873.
[57] Donahue, R. J., Borman, G. L., and Bower, G. R., 1994, ''Cylinder-Averaged Histories of Nitrogen Oxide in a D.I. Diesel with Simulated Turbocharging,'' SAE Paper 942046.
[58] Voiculescu, A., and Borman, G., 1978, ''An Experimental Study of Diesel Engine Cylinder-Averaged NO_x Histories,'' SAE Paper 780228.
[59] Kroeger, C. A., 1986, ''A Neat Methanol Direct Injection Combustion System for Heavy Duty Applications,'' SAE Paper 861169.
[60] Kato, S., and Onishi, S., ''New Mixture Formation Technology of Direct Fuel Injection Stratified Charge SI Engine (OSKA)—Test Result with Gasoline Fuel,'' SAE Paper 881241. (Also see SAE 900608 1990.)
[61] Bair, R. E., 1989, ''Ignition Quality and Composition of Fuel Volatile Fraction: Effects on Diesel Combustion,'' Ph.D. thesis, University of Wisconsin-Madison, Department of Mechanical Engineering, Madison, WI.
[62] Mueller, E., 1990, ''The Effects of Fuel Sulfur Volatility Range and Inlet Air O_2 Enrichment on Particulate Emissions in a Diesel Engine,'' M.S. thesis, University of Wisconsin-Madison, Department of Mechanical Engineering, Madison, WI.
[63] Lippert, A. M., 1999, ''Modeling of Multi-component Fuels with Application to Sprays and Simulation of Diesel Engine Cold Start,'' Ph.D. Thesis, Department of Mechanical Engineering, Universtiy of Wisconsin-Madison, Madison, WI.
[64] Montgomery, D. T., Chan, M., Chang, C. T., Farrell, P. V., and Reitz, R. D., 1996, ''Effect of Injector Nozzle Hole Size and Number on Spray Characteristics and the Performance of a Heavy Duty D.I. Diesel Engine,'' SAE Paper 962002.
[65] Su, T. F., Chang, C. T., Reitz, R. D., and Farrell, P. V., 1995, ''Effects of Injection Pressure and Nozzle Geometry on Spray SMD and D.I. Emissions,'' SAE Paper 952360.

Downloaded 02 Jun 2010 to 171.66.16.119. Redistribution subject to ASME license or copyright; see http://www.asme.org/terms/Terms_Use.cfm

Second-Moment Closure Model for IC Engine Flow Simulation Using Kiva Code[1]

S. L. Yang
B. D. Peschke
Mechanical Engineering-Engineering Mechanics Department,
Michigan Technological University,
Houghton, MI 49931

K. Hanjalic
Faculty of Applied Science,
Department of Applied Physics,
Thermofluids Section,
Delft University of Technology,
The Netherlands

The flow and turbulence in an IC engine cylinder were studied using the SSG variant of the Reynolds stress turbulence closure model. In-cylinder turbulence is characterized by strong turbulence anisotropy and flow rotation, which aid in air-fuel mixing. It is argued that solving the differential transport equations for each turbulent stress tensor component, as implied by second-moment closures, can better reproduce stress anisotropy and effects of rotation, than with eddy-viscosity models. Therefore, a Reynolds stress model that can meet the demands of in-cylinder flows was incorporated into an engine flow solver. The solver and SSG turbulence model were first successfully tested with two different validation cases. Finally, simulations were applied to IC-engine like geometries. The results showed that the Reynolds stress model predicted additional flow structures and yielded less diffusive profiles than those predicted by an eddy-viscosity model. [S0742-4795(00)00101-0]

Introduction

The performance, efficiency, and exhaust emissions of reciprocating engines are highly dependent on the air-fuel mixing process inside the combustion cylinder. For direct-injection (DI) engines, the complexity of the combustion process is further augmented due to the heterogeneous distribution of the liquid fuel inside the combustion chamber. Therefore, to increase the performance efficiency and to reduce the pollutant emissions, the air-fuel mixing process becomes essential to the design of DI engines. One standard practice is to increase the fluid turbulence, such as geometry-induced turbulence using bowl-in-piston, to enhance the air-fuel mixing. Accordingly, a better understanding of the turbulent flow structure inside the engine cylinder is essential for a better design.

The turbulent flow inside the reciprocating engine has several characteristics which cannot be described by any conventional eddy-viscosity turbulence model (EVTM), such as the two-equation k-ε and k-ω models. First, due to complex geometry, wall effects, and flow rotation, the turbulence is highly anisotropic. Because different stress components respond differently to these effects and, in particular, to a rapid compression and expansion, exhibiting different degrees of hysteresis, a proper reproduction of the mixing process requires an accurate modeling of the space and time evolution of the stress anisotropy tensor. The anisotropy of turbulence cannot be accounted for by any currently available conventional EVTM.

Without modifications, these EVTM also cannot properly account for flow rotation, which includes swirling and tumbling effects. Swirling flow is an important design feature for improving combustion and mixing. In addition, the influence of the cylinder wall and the flow characteristics of secondary fluid motions and streamline curvature are all important and need to be resolved by any turbulence model to correctly reproduce flow physics inside the engine cylinder.

Therefore, to better understand the physics of turbulent flow and to improve the engine design, a higher level turbulence model needs to be explored. Unfortunately, most of today's industrial and commercial codes for engine flow simulations use conventional EVTM turbulence models, due to simplicity and robustness.

Beyond the Boussinesq hypothesis, the next level of turbulence modeling is the Reynolds-stress (second-moment) turbulence model (RSTM). The RSTM is considered to be the natural and logical level of modeling turbulence within the framework of the Reynolds averaging approach. It provides the extra turbulent momentum fluxes from the solution of full transport equations. The RSTM represents the most comprehensive description for turbulent flows that can be employed for practical computations with the present generation of computers. The RSTM also naturally includes effects of anisotropy, streamline curvature, sudden changes in strain rate, secondary motions, flow rotation, etc.

The purpose of this research is to incorporate, investigate, validate, and modify an advanced RSTM for in-cylinder flowfield simulations using the KIVA-3 computer code [1]. In this paper, the performance of a RSTM, namely the SSG model [2], for simulating turbulence flow inside the cylinder of piston engine like geometries will be given. One major advantage of using the SSG model is that no wall distance parameter is needed as with the LRR model [3,4]. This feature is especially desirable and important for the piston engine flow simulation, due to the movement of the piston over time.

To validate the SSG model using KIVA-3, solutions of fully developed channel and pipe flows will be given first. These results were compared with the available experimental and DNS data. Afterwards, two engine like flows will be studied. The first case is an axisymmetric direct-injected stratified charge (DISC) engine with a bowl in the piston, which is used to study the effect of bowl-in-piston on the in-cylinder flow structure. A teapot geometry for a two-stroke engine with side ports is included as the second case. These are the baseline cases given for the KIVA-3 code. Finally, a flametube combustor flow case rounds out the application study. Details of fluid and flow properties, such as velocity, temperature, Reynolds-stresses, turbulence kinetic energy, etc. will also be given along with the comparison of the results among RSTM, k-ε model, and experimental data.

The Re-Stress Turbulence Model

In this section, the description of the modeling equations used in this research is given first. Numerical implementation of these equations in the KIVA code follows.

[1]Part of this research was undertaken while the lead author took sabbatical leave at Delft University of Technology, The Netherlands.

Contributed by the Internal Combustion Engine Division of THE AMERICAN SOCIETY OF MECHANICAL ENGINEERS for publication in the ASME JOURNAL OF ENGINEERING FOR GAS TURBINES AND POWER. Manuscript received by the Internal Combustion Engine Division June 1, 1999; final revision received by the ASME Headquarters August 31, 1999. Technical Editor: D. Assanis.

Copyright © 2000 by ASME

Downloaded 02 Jun 2010 to 171.66.16.119. Redistribution subject to ASME license or copyright; see http://www.asme.org/terms/Terms_Use.cfm

Modeling Equations. The transport equation for the Reynolds stresses $\widetilde{u_i u_j}$, written in Cartesian tensor notation, are

$$\frac{\partial(\overline{\rho}\widetilde{u_i u_j})}{\partial t}+\frac{\partial(\overline{\rho}\widetilde{U}_k\widetilde{u_i u_j})}{\partial x_k}=P_{ij}+D_{ij}+\varepsilon_{ij}+\Phi_{ij}, \tag{1}$$

where the overbar denotes the conventional Reynolds average and the over-tilde is shorthand for the Favre average (density-weighted average). In Eq. (1), the production P_{ij}, diffusion D_{ij}, dissipation rate of turbulence kinetic energy ε_{ij}, and pressure-strain redistribution Φ_{ij} tensors are

$$P_{ij}=-\left(\overline{\rho}\widetilde{u_i u_k}\frac{\partial\widetilde{U}_j}{\partial x_k}+\overline{\rho}\widetilde{u_j u_k}\frac{\partial\widetilde{U}_i}{\partial x_k}\right) \tag{2}$$

$$D_{ij}=\frac{\partial}{\partial x_k}\left(\frac{\mu_t}{\sigma_k}\frac{\partial\widetilde{u_i u_j}}{\partial x_k}\right)\quad \mu_t=\overline{\rho}C_\mu\frac{k^2}{\varepsilon} \tag{3}$$

$$\varepsilon_{ij}=-\frac{2}{3}\overline{\rho}\varepsilon\,\delta_{ij}\quad \delta_{ij}=\text{Kronecker Delta} \tag{4}$$

$$\Phi_{ij}=\Phi_{ij,1}+\Phi_{ij,2}+\phi_{ij,w}, \tag{5}$$

where $k=\widetilde{u_i u_i}/2$ is the turbulence kinetic energy, ε is the dissipation rate of turbulence kinetic energy, and $\widetilde{U}_i$ is the mean flow velocity vector.

Using the locally homogeneous approximation, the pressure-strain redistribution term is usually decomposed into three parts, as indicated in Eq. (5). The first term represents the ''slow'' pressure-strain due to the velocity fluctuations. This term causes the turbulence to approach an isotropic state by itself. It is also called the ''return to isotropy'' term and is normally modeled in terms of the stress anisotropy tensor $a_{ij}=(\widetilde{u_i u_j}/k)-(2/3)\delta_{ij}$ and its first $A_2=a_{ij}a_{ji}$ and/or second $A_3=a_{ij}a_{jk}a_{ki}$ invariants [5]. A general nonlinear model can be expressed as

$$\Phi_{ij,1}=-\overline{\rho}\varepsilon\left[C_1 a_{ij}-C_{1s}\left(a_{ik}a_{kj}-\frac{1}{3}A_2\delta_{ij}\right)\right]. \tag{6}$$

The second term in Eq. (5) represents the ''rapid'' pressure-strain due to the interactions between mean strain rate and velocity fluctuations. This term is often referred to as the ''isotropization of production'' term. For a linear or quasi-linear expression, $\Phi_{ij,2}$ can be written in terms of the mean rate of strain S_{ij}, mean vorticity Ω_{ij}, and stress anisotropy tensor a_{ij}:

$$\Phi_{ij,2}=C_2 P\overline{\rho}a_{ij}+(C_{3a}+C_{3b}A_2^{1/2})\overline{\rho}kS_{ij}+C_4\overline{\rho}k\left(a_{ik}S_{jk}+a_{jk}S_{ik}-\frac{2}{3}a_{kl}S_{kl}\delta_{ij}\right)+C_5\overline{\rho}k(a_{ik}\Omega_{jk}+a_{jk}\Omega_{jk}), \tag{7}$$

where

$$S_{ij}=\frac{1}{2}\left(\frac{\partial\widetilde{U}_i}{\partial x_j}+\frac{\partial\widetilde{U}_j}{\partial x_i}\right),\quad \Omega_{ij}=\frac{1}{2}\left(\frac{\partial\widetilde{U}_i}{\partial x_j}-\frac{\partial\widetilde{U}_j}{\partial x_i}\right),\quad P=\widetilde{u_i u_j}\frac{\partial\widetilde{U}_i}{\partial x_j}. \tag{8}$$

The last term in Eq. (5) is the wall-reflection (or pressure-echo) term due to the effect of solid walls. This term was introduced by Shir [6], Launder et al. [3], and Gibson and Launder [4] to compensate for the noticeable differences in stress anisotropy due to the presence of a solid wall. In order to introduce the damping effect with a selective orientation, all models use a function that is explicitly related to the normal distance from the wall and is not coordinate-frame invariant. This is obviously a very undesirable parameter for reciprocating engine flow simulations, since the computational domain changes constantly in time due to piston motion.

In 1991, Speziale, Sarkar, and Gatski (SSG) [2] proposed a quasi-linear $\Phi_{ij,2}$ model, in which some of the coefficients are dependent on the turbulent stress invariants and turbulence production. They found that the model satisfies both the homogeneous and wall-equilibrium flows without the need to introduce the wall-reflection correction. The SSG model is used in the current research and its modeling coefficients are given in Table 1 along with other correlation constants.

Table 1 Modeling constants

C_1	C_{1s}	C_2	C_{3a}	C_{3b}	C_4	C_5
1.7	1.05	.9	.8	-0.65	.625	.2
$C_{\varepsilon 1}$	$C_{\varepsilon 2}$	$C_{\varepsilon 3}$	C_μ	σ_k	σ_ε	
1.44	1.83	-1.0	.09	1.0	1.3	

It is noted that in Eq. (3), the simple isotropic form for the diffusion is used. Although more elaborate and/or complex models are available [6–9], a previous study for flow over the backward facing step indicated that Eq. (3) gives better numerical stability characteristics [10].

Equation (4) assumes that the dissipation rate tensor ε_{ij} is locally isotropic. The transport equation for ε is

$$\frac{\partial\overline{\rho}\varepsilon}{\partial t}+\frac{\partial}{\partial x_k}(\overline{\rho}\widetilde{U}_k\varepsilon)=-\left(\frac{2}{3}C_{\varepsilon 1}-C_{\varepsilon 3}\right)\overline{\rho}\varepsilon\frac{\partial\widetilde{U}_i}{\partial x_i}+\frac{\partial}{\partial x_k}\left(\frac{\mu_t}{\sigma_\varepsilon}\frac{\partial\varepsilon}{\partial x_k}\right)-\overline{\rho}\frac{\varepsilon}{k}(C_{\varepsilon 1}P+C_{\varepsilon 2}\varepsilon). \tag{9}$$

This is the standard ε-equation, except for the first term on the right-hand side. This term accounts for the length scale changes when there is velocity dilatation [11]. Modeling constants are given in Table 1.

In Eq. (9), as suggested by Speziale et al. [2], a value of $C_{\varepsilon 2}=1.83$ (as opposed to the more commonly quoted value of 1.92) should be used for better prediction of the power law decay in isotropic turbulence (with an exponent of 1.2). Using the constants stated in Table 1, the von Karman constant κ, defined as $\kappa=\sqrt{\sqrt{C_\mu}(C_{\varepsilon 2}-C_{\varepsilon 1})\sigma_\varepsilon}$ [11], has a value of 0.39 (the commonly accepted value is 0.4). However, if $C_{\varepsilon 2}=1.92$ is used, κ will be equal to 0.432661.

Numerical Implementation in the KIVA Code. The KIVA family CFD code [11–13] is an advanced computer program for the numerical calculation of transient, two and three-dimensional, chemically reactive fluid flows with sprays using a standard or a RNG variant k-ε model [13,14]. It is primarily written for solving reciprocating internal combustion engine problems. The numerical scheme is based on the arbitrary Lagrangian–Eulerian method with implicit continuous Eulerian modification for low Mach number flows. The code uses a semi-staggered grid layout, as opposed to the fully staggered grid arrangement used in the SIMPLE [15] type method. Velocity components are vertex centered quantities and all thermodynamic variables are defined at the cell centers. Governing equations are written for Cartesian coordinates and are discretized using the finite-volume method. For a cylindrical geometry, a wrapped around grid along with the periodic boundary condition in the azimuthal (y) direction is used. For details regarding the numerical method used in the KIVA code, please refer to Amsden et al. [11]. In this section, a description of how we implement the RSTM in the KIVA code is given.

Using RSTM, the six components of the Reynolds stress are now available for use in the mean flow calculations. Accordingly, the momentum equation is now read

$$\frac{\partial(\overline{\rho}\widetilde{U}_i)}{\partial t}+\frac{\partial(\overline{\rho}\widetilde{U}_j\widetilde{U}_i)}{\partial x_j}=-\frac{\partial p}{\partial x_i}-\frac{\partial(\overline{\rho}\widetilde{u_i u_j})}{\partial x_j}+\frac{\partial(\mu\chi_{ij})}{\partial x_j} \tag{10}$$

Downloaded 02 Jun 2010 to 171.66.16.119. Redistribution subject to ASME license or copyright; see http://www.asme.org/terms/Terms_Use.cfm

$$\chi_{ij}=\frac{\partial \tilde{U}_i}{\partial x_j}+\frac{\partial \tilde{U}_j}{\partial x_i}-\frac{2}{3}\frac{\partial \tilde{U}_k}{\partial x_k}\delta_{ij}, \tag{11}$$

where p and μ are the fluid pressure and molecular viscosity, respectively. For clarity, source terms due to sprays and gravity are not included in Eq. (10). All other governing equations, such as species, continuity, and energy equations, are the same as in the KIVA code, due to the passive influence of turbulence on these equations.

To preserve the KIVA code structure and hence minimize the code modification, the Reynolds stresses and ε are treated as cell-centered quantities. However, unlike the scalar thermodynamic quantities, care must be taken when applying the periodic boundary condition. Since the Re-stress is a second-order tensor, the following transformation matrix (and its transpose) was used for the rotation of the Re-stress for periodic boundaries or for the transformation between cylindrical and Cartesian coordinates for averaging

$$\begin{bmatrix} \cos\theta & \sin\theta & 0 \\ -\sin\theta & \cos\theta & 0 \\ 0 & 0 & 1 \end{bmatrix}, \tag{12}$$

where θ is either the two-dimensional/three-dimensional sector angle for rotation or the azimuthal angle of the grid location under consideration.

To maintain the diagonally dominant property and hence enhance the stability, source terms, such as the first element P_{11} in the production term P_{ij} in Eq. (1), were linearized using the following ''max'' and ''min'' functions (where superscript n denotes the cycle/time number),

$$P_{11}^{n+1}=P_{11}^{+}+P_{11}^{-}\cdot(\widetilde{u_1u_1})^{n+1}, \tag{13}$$

where P_{11}^{+} is a strictly positive quantity and P_{11}^{-} is a strictly negative quantity, and are defined as [16]

$$P_{11}^{+}=\max(P_{11}^{n},0) \quad \text{and} \quad P_{11}^{-}=\frac{\min(P_{11}^{n},0)}{(\widetilde{u_1u_1})^{n}}. \tag{14}$$

All other source terms in Eq. (1) are linearized accordingly. Linearization of the source terms in the ε-equation stays the same as in the original KIVA code.

Since no convection terms are involved in the Lagrangian phase B KIVA code calculation and the above source linearization procedure is used, the six equations of (1) are decoupled. However, these equations are still coupled through the periodic condition in the azimuthal direction due to Eq. (12). To maintain a time accurate solution, they should be solved simultaneously and were solved using the conjugate residual iterative method [17].

To calculate the cell face (face-centered) normal velocities for the Lagrangian phase (phase B) cell volume changes and fluxing volumes in phase C, accelerations due to the thermodynamic and turbulence pressures p and $(2/3)\overline{\rho}k$ were used in the KIVA code. This procedure has been found to reduce the checkerboarding effect in the pressure field due to the semi-staggered grid arrangement [12]. During the course of this research, through numerical experiments using pipe flow, only the thermodynamic pressure was included in the calculation of the face-centered normal velocities.

To increase the numerical stability further, the diffusion term in the momentum Eq. (10), was rearranged according to the following expression [18]

$$\frac{\partial(\mu\chi_{ij})}{\partial x_j}=\left[\frac{\partial(\mu_e\chi_{ij})}{\partial x_j}\right]^{n+1}-\left[\frac{\partial(\mu_t\chi_{ij})}{\partial x_j}\right]^{n}, \tag{15}$$

where the effective viscosity μ_e is the sum of the eddy and the molecular viscosities, $\mu_e=\mu_t+\mu$.

Since Eq. (1) are only valid for high-Re flow, wall functions were used for boundary conditions at the wall. This eliminates the necessity of very fine grids to resolve the flow features near the solid wall, which might become too expensive for the engine flow simulations. However, it is imperative that, when using the wall functions with RSTM, only the logarithmic wall functions should be used, irrespective of whether the first grid point next to the wall is located inside or outside the viscous sublayer. For multidimensional unsteady flows, implementation of the wall functions is crucial.

In the KIVA code, the wall function for the momentum equations is implemented in such a way that, for a control volume next to the solid wall, the control surface lies on the solid wall has contribution of shear stress (and hence wall friction) due to turbulence. This wall friction (obtained using a wall function) is then used to construct a momentum equation based on Newton's second law locally to obtain the time rate change of the fluid momentum. Contributions of momentum change due to friction are then added to the momentum equation for the calculation of velocities in phase A. A similar approach is used for the energy equation. This approach is considered appropriate for the multidimensional unsteady flow simulation with RSTM. Lien et al. [19] used Dirichlet conditions for nonzero stress components based on wall functions. Although their method is promising, the coefficients in their formulas are problem/model dependent. As a result, more studies are needed for multidimensional unsteady flows.

As in the KIVA code, diffusion fluxes on the solid walls are approximately zero, and

$$\varepsilon=\frac{c_\mu^{3/4}}{\kappa}\frac{k^{3/2}}{y_n}, \quad y_n \equiv \text{normal distance to the wall} \tag{16}$$

is used directly to calculate the value of ε next to the walls, even if this formula is only valid under wall-equilibrium conditions.

Code Validations

To validate the Re-stress model described using KIVA-3, a fully developed plane channel flow and a fully developed axisymmetric pipe flow were used. These results were compared with the available experimental and DNS data.

The Channel Flow. The first validation case is the plane channel flow due to its simple geometry. The channel flow considered has a channel half-width of 2.5 cm and is 1 cm long. Air enters the channel inlet with a uniform flow velocity of 463.16 cm/s, density of 1.1774 kg/m^3, and temperature of 300 K. This will yield a Re number of 13,750 based on the channel height and average velocity. An ambient pressure of 1 atm is specified at the outlet.

A numerical solution was obtained using a uniform grid with 25 computational cells across the channel half-width and 10 cells in the main flow direction. Although a denser grid (50 cells by 20 cells) was also used, the results are similar to those shown in Fig. 1. Computation was carried out using a periodic condition with volumetric flow rate correction between inlet and outlet until the flow fully developed. The volumetric flow rate correction is to assure that, when fully developed, the flow Re number is maintained at 13,750. This procedure proves to work well for this incompressible flow problem using a compressible flow code, such as the KIVA code.

Figure 1 shows the fully developed plane channel flow result. In this figure, the DNS data [20] are also included for comparison. Agreement is excellent. As can be seen in this figure, the wall damping effect produces a smaller normal wall component of the Reynolds normal stress ($u'u'$) than the tangential component ($v'v'$) and is well predicted by the model. This shows that the SSG model is able to capture the anisotropy of this flow. The linearity of the Reynolds shear stress ($u'v'$) and the turbulent boundary layer profile (u^+ versus y^+) are also well resolved. It is noted that in similar studies, reported by Lebrere et al. [21,22], a

Downloaded 02 Jun 2010 to 171.66.16.119. Redistribution subject to ASME license or copyright; see http://www.asme.org/terms/Terms_Use.cfm

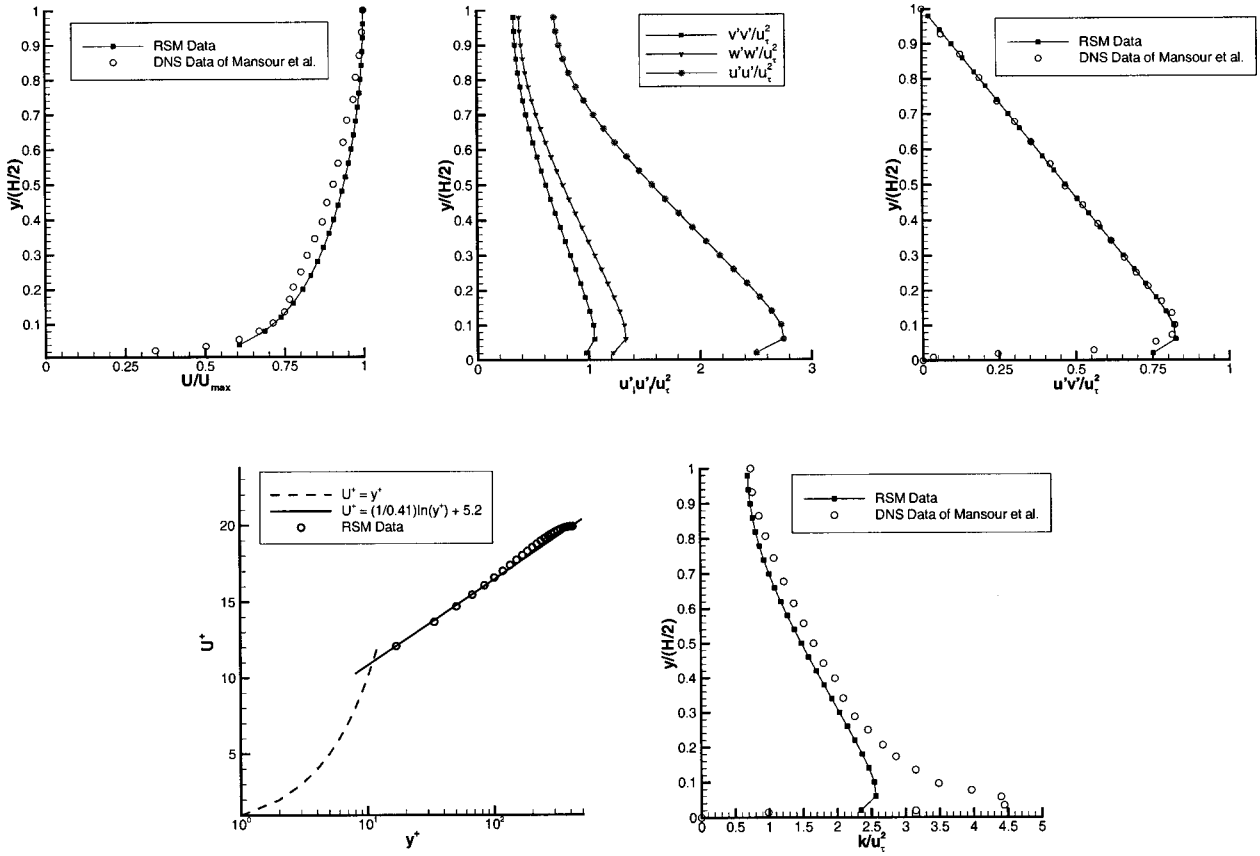

Fig. 1 Channel flow results

LRR model with and without wall-echo terms were used. Their results showed that the linearity of the Reynolds shear stress across the channel was not resolved.

The Pipe Flow. Validation for a Cartesian based CFD code requires the assessment of an axisymmetric pipe flow or similar geometry. The pipe flow considered has a radius of 2.5 cm and is 3 cm long. Air enters the pipe with a uniform flow velocity of 1347.4 cm/s, density of 1.1774 kg/m^3, and temperature of 300 K. This will yield a Re number of 40,000 based on the pipe diameter. At the outlet, an ambient pressure of 1 atm is specified.

There were 40 computational cells in the radial direction and 30 cells in the axial direction. The grid is slightly stretched in the radial direction using a two-sided stretching function [23], to better resolve the flow near the pipe wall and centerline. Again, computation was carried out using the periodic condition with volumetric flow rate correction between inlet and outlet. A denser grid was also used and the results are similar to those shown in Fig. 2.

Figure 2 shows the fully developed axisymmetric pipe flow result. In this figure, the experimental data of Laufer [24] are also included for comparison. Agreement is excellent. The linearity of the Reynolds shear stress and the turbulent boundary layer profile (u_z^+ versus r^+) are also well resolved.

Code Application to IC-Engines

The SSG RSTM is now applied to several IC-engine applications. These applications include two of the example problems from KIVA-3. The model is also applied to a flametube combustor. Calculations were obtained for both the k-ε and RSTM models for purposes of comparison.

DISC Engine. The first example is of a DISC engine chamber whose two-dimensional computational domain at $-60°$ ATDC is displayed in Fig. 3. The chamber has a bore of 9.843 cm and a stroke of 9.55 cm. A chamfered bowl is located in the piston, and its cavity depth is 3.3 cm. The piston is located at 90° ATDC when the calculation starts. At this time, the fluid inside the cylinder has the composition of pure stagnant air, which is composed of 22 percent of O_2, 76.5 percent of N_2, 1 percent of CO_2, and 0.5 percent of water vapor, at 400 K with a Bessel function swirl profile.

During the compression stroke, 11.6 mg of liquid gasoline in the form of a hollow cone spray is injected into the cylinder from an injector with a single half sine wave pulse, located close to the cylinder head axis. The injection begins at $-52°$ ATDC and has a duration of 12.672°. Figure 4 shows the k-ε and RSTM flowfield results at $-30°$ ATDC, shortly before ignition.

The fuel-air mixture is subsequently spark-ignited at $-27°$ ATDC. Although not shown here, the premixed fuel vapor begins to burn at about $-24°$ ATDC, the burning rate becomes rapid after $-20°$ ATDC, and the temperature and pressure increase dramatically. Drastic differences between RSTM and k-ε model results can be observed from the figures. The magnitude of the eddy viscosity is overpredicted by the k-ε model, which is expected since the k-ε model typically overpredicts μ_t. This can be seen in Fig. 4 for the effective viscosity and for k. Because of the smaller eddy viscosity, the RSTM results tend to show more distinct and localized profiles of temperature, effective viscosity, and k. For example, the cooler region corresponding to the fuel spray at $-30°$ ATDC is smaller and less diffuse for the RSTM model. In addition, the RSTM is able to perceive the spray in the dissipation rate and effective viscosity. Distinctive profiles also exist at later angles as in Fig. 5, which is focused only on the bowl region. Here the high temperature combustion gases are confined near the center of the bowl while several squish-induced circulation regions dominate the RSTM velocity profile. Highly diffusive variations in k are seen from the k-ε results while only a well defined

Downloaded 02 Jun 2010 to 171.66.16.119. Redistribution subject to ASME license or copyright; see http://www.asme.org/terms/Terms_Use.cfm

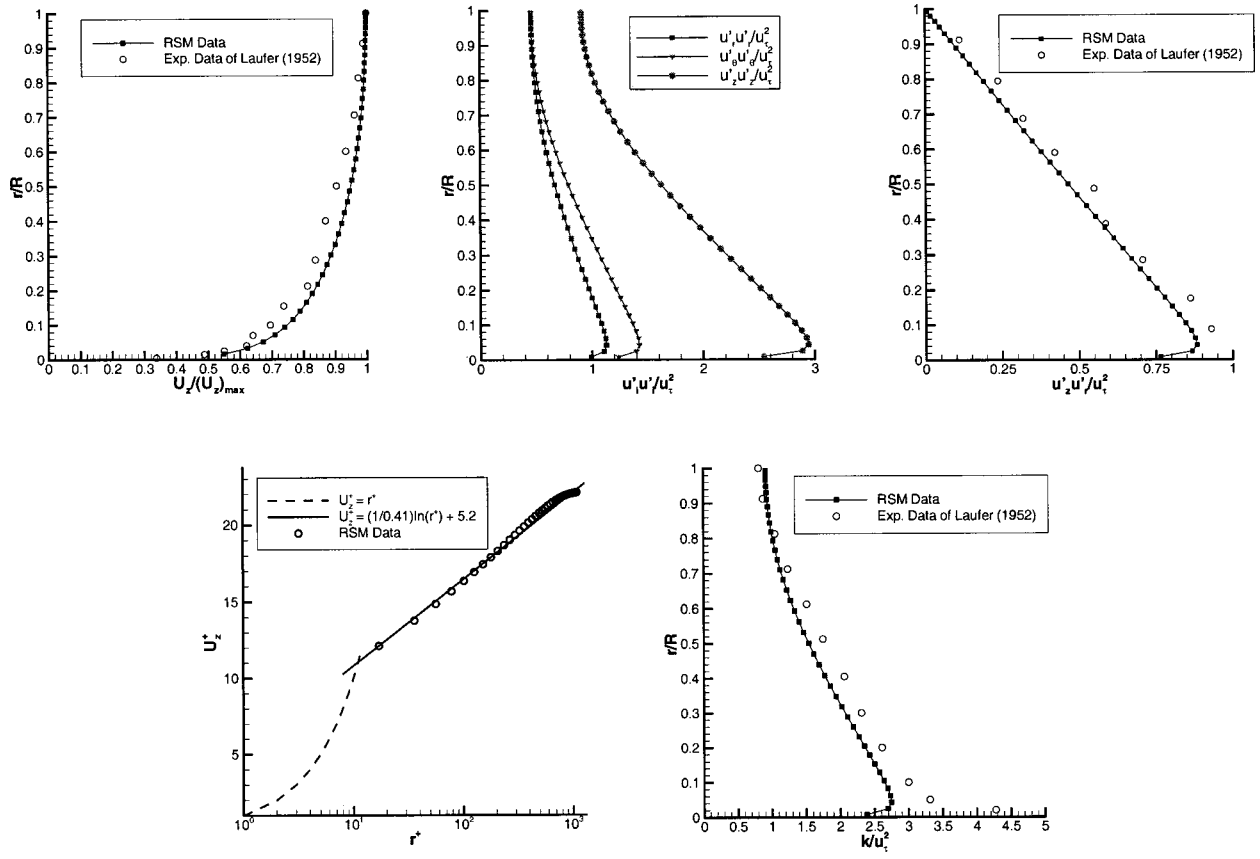

Fig. 2 Pipe flow results

structure appears from the RSTM. As shown, the anisotropic nature of the flowfield is resolved only by the RSTM.

Teapot Geometry. The second application example is of a teapot combustion cylinder for a two-stroke engine. Highlighting the ports, the flat head, and the flat piston face, the computational grid of this geometry is shown in Fig. 6. This example is used to display robustness for solving cases where the moving piston covers or reveals intake and exhaust ports. Cold flow calculations begin at-180° crank angle, and the *k-ε* and RSTM show similar results through the compression stroke and on into the power stroke. However, recirculation regions which form around +90° are located in different regions as shown in Fig. 7 at +120°

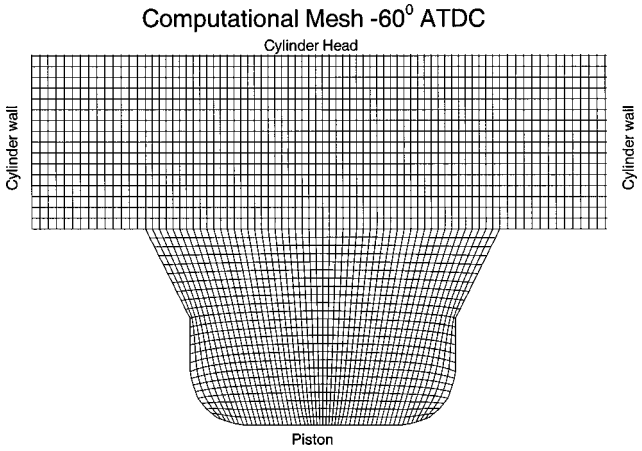

Fig. 3 DISC case computational mesh

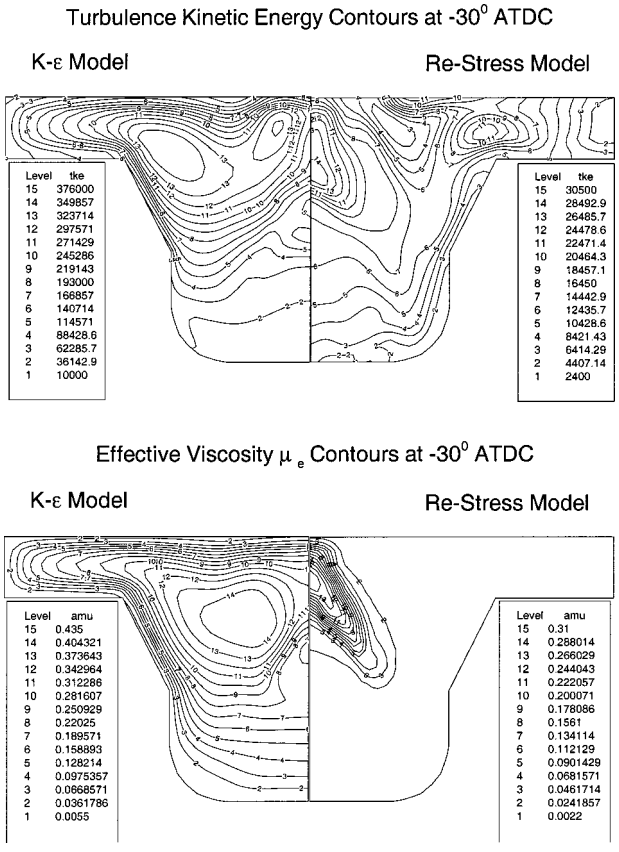

Fig. 4 Turbulence kinetic energy and effective viscosity at −30° ATDC

Downloaded 02 Jun 2010 to 171.66.16.119. Redistribution subject to ASME license or copyright; see http://www.asme.org/terms/Terms_Use.cfm

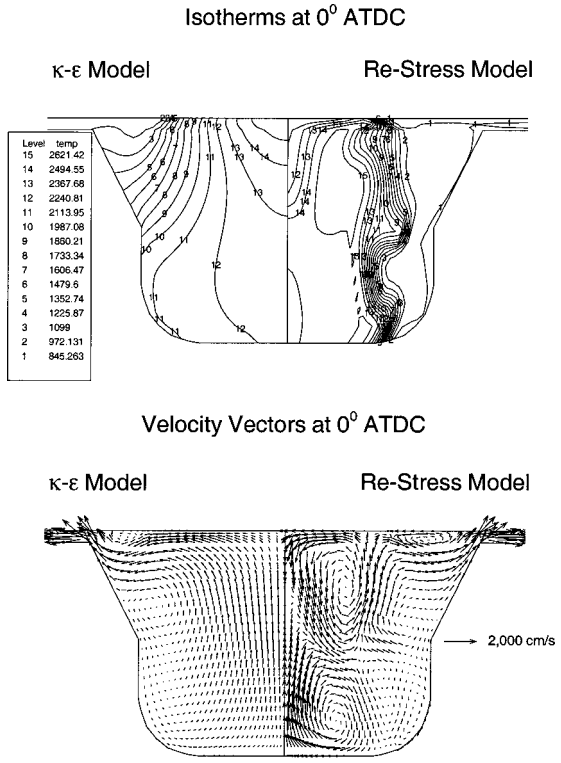

Fig. 5 Temperature and velocity at TDC

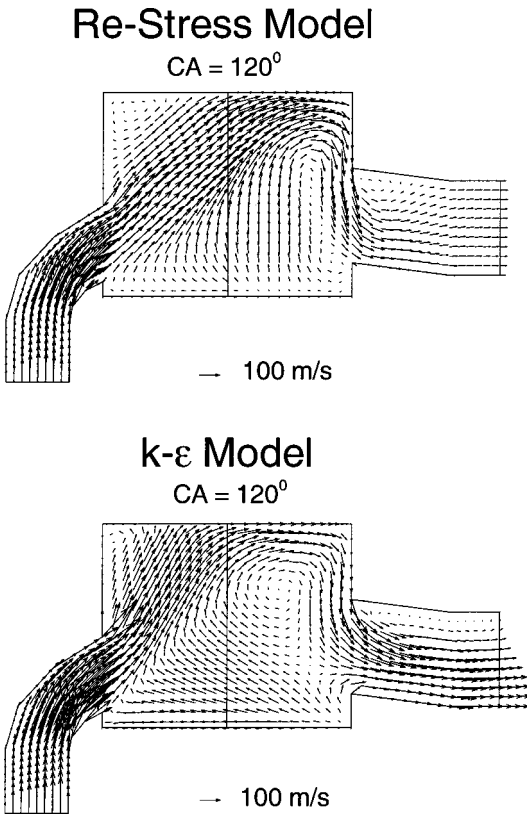

Fig. 7 Velocity profiles at +120° ATDC

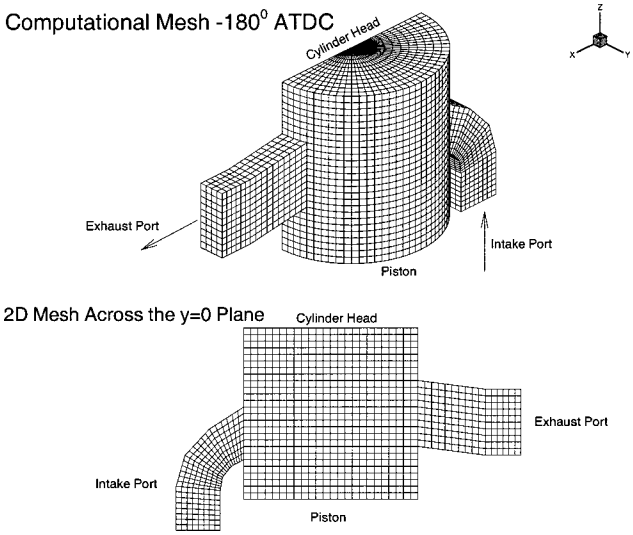

Fig. 6 Computational grid of teapot geometry −180° ATDC

ATDC. This difference continues beyond the crank angle of 150° probably because of the anisotropy produced in the rapid expansion process.

LPP Flametube. The RSTM was also applied to propane-air combustion in a lean, premixed, prevaporized (LPP) flametube [25]. A study has been recently performed by Kundu et al. [26] with the *k-ε* model and with a reduced reaction mechanism (23 kinetic reactions with 16 species) to simulate the combustion and to evaluate NOx emissions. The computational region displayed in Fig. 8 is 43 cm long and 10.2 cm in diameter. It includes the combustion zone, the flame holder, and a 10 cm length of the prevaporization/premixing zone. To reduce the domain into an axisymmetric model, the holes of the actual flame holder were approximated by several concentric rings. Therefore, only 4434 cells were required for a two-dimensional radial mesh. An inlet velocity of 2500 cm/s and temperature of 800 K were specified in addition to an equivalence ratio of 0.8. Since the KIVA code is designed for unsteady flow simulations, the results are constantly monitored over at least every 2000 iterations to ensure a converged solution.

The results show differences between the RSTM and *k-ε* models in terms of the velocity profile and NOx emission index. Results from the *k-ε* model in Fig. 9 indicate a similar velocity profile exiting from each radial flameholder ring as well as a slightly overestimated NOx emission index. In contrast, the RSTM results in Fig. 10 show unique velocity profiles downstream of each flameholder ring. These unique profiles permit recirculation regions near the holder which draw hotter combustion gases upstream. As a result, two regions of higher NOx formation stretch upstream to the flameholder. This shows that the RSTM is sensitive to the relative flow passage area of the rings, which increases in the radial direction. Emission index values agree better with experimental values along the flametube centerline.

Conclusions

In this study, the SSG Reynolds-stress turbulence model was implemented within the KIVA-3 code. The descriptions of implementing the RSTM into the KIVA code were given to guide interested users. Several validation and application cases were performed to ascertain the SSG performance and to compare it with the *k-ε* model and the experimental data (LPP case). Placed within the structure of the KIVA code, the SSG RSTM can successfully reproduce standard turbulent flow test cases which can include planar and axisymmetric flows. This provides confidence in applying the RSTM to IC-engine type cases. In these cases, the

Downloaded 02 Jun 2010 to 171.66.16.119. Redistribution subject to ASME license or copyright; see http://www.asme.org/terms/Terms_Use.cfm

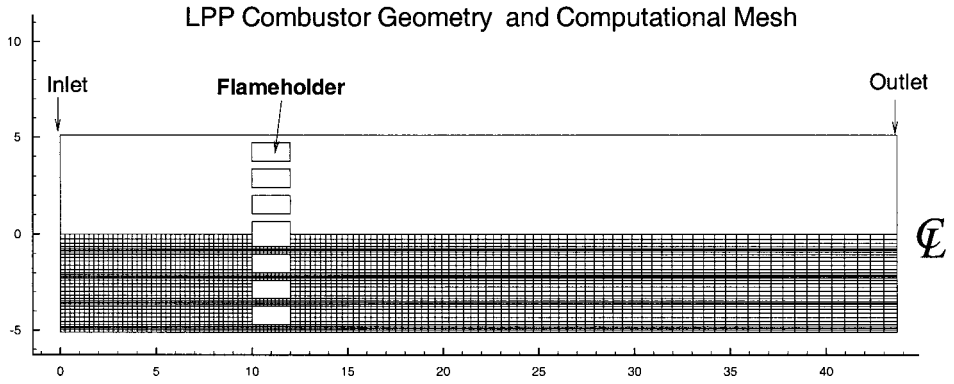

Flame Holder - Actual vs. 2D Axisymmetric Model

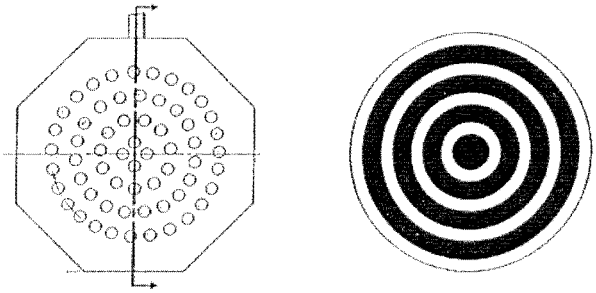

Fig. 8 Combustor computational mesh and flameholder

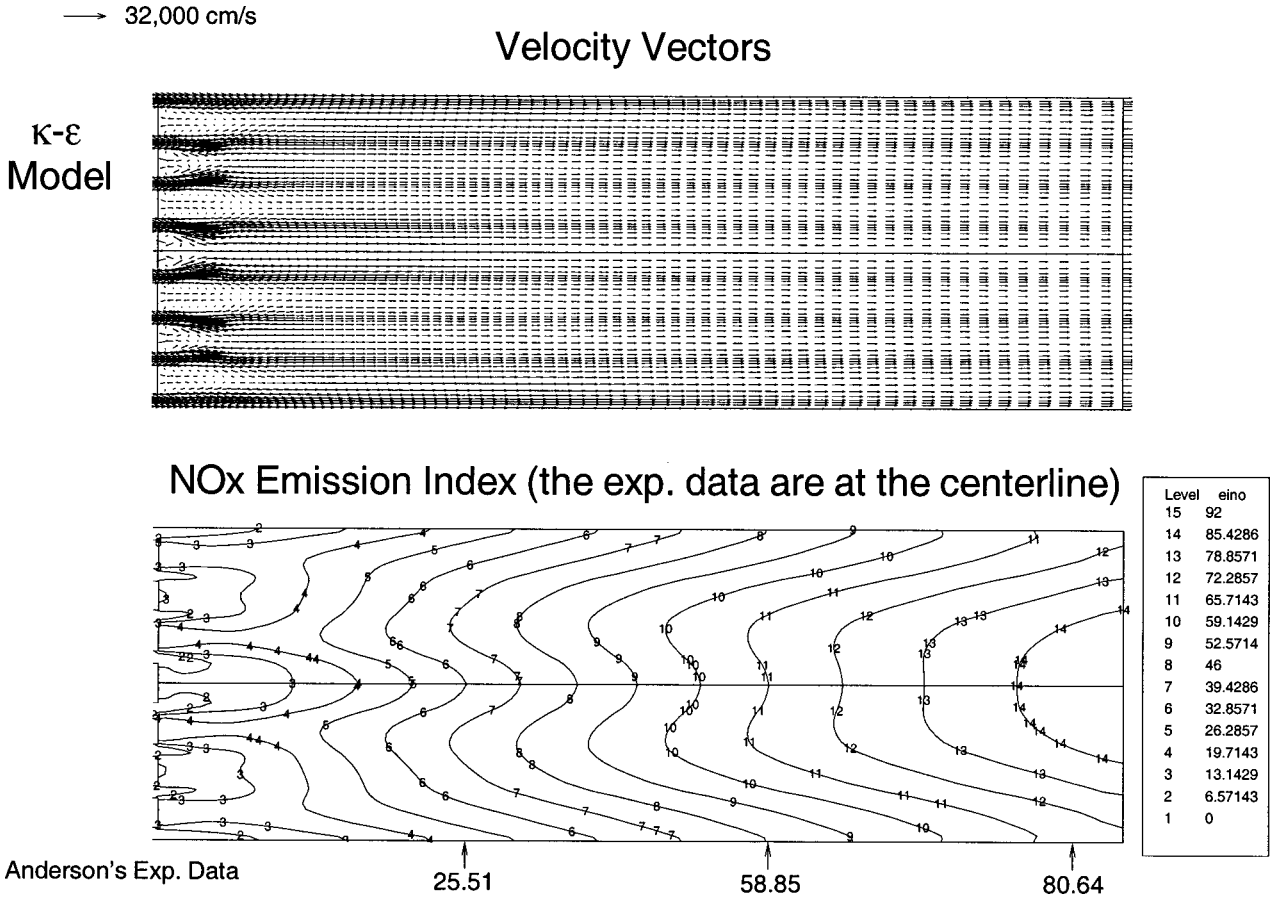

Fig. 9 Velocity and NOx emission index for $k-\varepsilon$ model

Downloaded 02 Jun 2010 to 171.66.16.119. Redistribution subject to ASME license or copyright; see http://www.asme.org/terms/Terms_Use.cfm

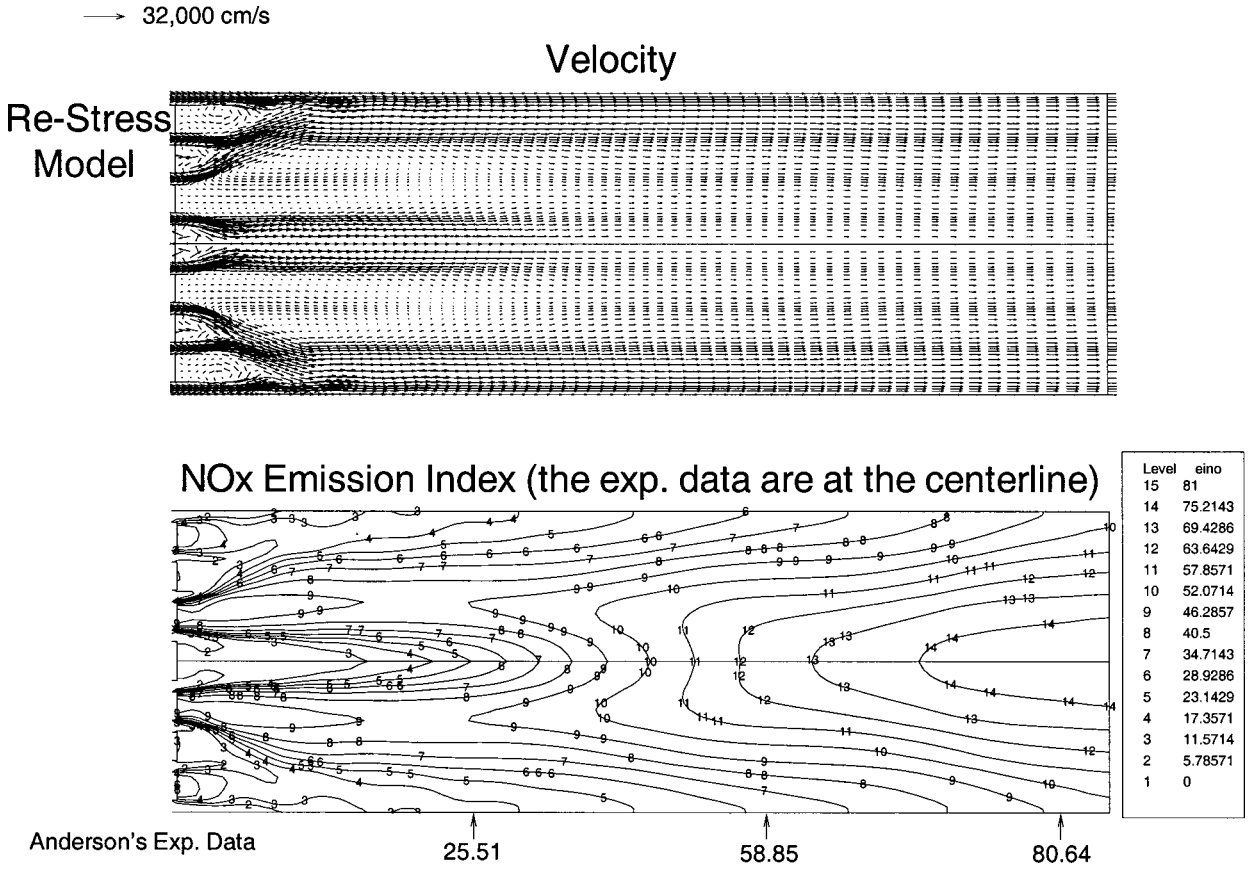

Fig. 10 Velocity and NOx emission index for RSTM

RSTM produces results which differ from the k-ε model in terms of turbulence kinetic energy and dissipation magnitudes. This results in profiles which are less diffusive and can reveal anomalies such as sprays. The RSTM often captures additional recirculation structures which the k-ε model ignores. In a recent study by Yang et al. [27] on a LDI (lean-direct-injection) combustor, the RSTM outperforms the k-ε model, when compared with the experimental data. Further conclusions on the RSTM will be obtained in the future once it is compared with experimental results from IC-engine tests.

Acknowledgments

The lead author would like to thank the Delft University of Technology (TU-Delft), The Netherlands, for supporting this work. He also wishes to thank Dr. S. Obi of the Keio University, Tokyo, and Dr. I. Hadzic of TU-Delft, for valuable comments and discussions. The reduced reaction mechanism chemistry model was provided by Dr. K. P. Kundu of NASA Lewis Research Center.

Nomenclature

Variables

A = invariant
a = anisotropy tensor
C = modeling constant
D = diffusion terms
k = turbulence kinetic energy
P = production terms
p = pressure
r = coordinate
S = strain rate
U = averaged velocity
u = fluctuating velocity
x = coordinate
ε = dissipation
θ = rotation angle
κ = von Karman constant
μ = viscosity
ρ = density
σ = Prandtl number
Φ = pressure-strain terms
χ = mean flow strain rate tensor
Ω = mean vorticity

Subscripts

e = effective
k = turbulence energy
n = normal
t = turbulent
z = coordinate
ε = turbulence dissipation
μ = viscosity

Superscript

n = time level

References

[1] Amsden, A. A., 1993, ''KIVA-3: A KIVA Program with Block-Structured Mesh for Complex Geometries,'' Los Alamos National Laboratory, Report No. LA-12503-MS.
[2] Speziale, C. G., Sarkar, S., and Gatski, T. B., 1991, ''Modelling the Pressure-Strain Correlation of Turbulence: An Invariant Dynamical Systems Approach,'' J. Fluid Mech., **227**, pp. 245–272.
[3] Launder, B. E., Reece, G. J., and Rodi, W., 1975, ''Progress in the Development of a Reynolds-Stress Turbulence Closure,'' J. Fluid Mech., **68**, Part 3, pp. 537–566.

Downloaded 02 Jun 2010 to 171.66.16.119. Redistribution subject to ASME license or copyright; see http://www.asme.org/terms/Terms_Use.cfm

[4] Gibson, M. M., and Launder, B. E., 1978, ''Ground Effects on Pressure Fluctuations in the Atmospheric Boundary Layer,'' J. Fluid Mech., **86**, Part 3, pp. 491–511.
[5] Hanjalic, K., 1994, ''Advanced Turbulence Closure Models: A View of Current Status and Future Prospects,'' Int. J. Heat Fluid Flow, **15**, No. 3, pp. 178–203.
[6] Shir, C. C., 1973, ''A Preliminary Numerical Study of Atmospheric Turbulent Flows in the Idealized Planetary Boundary Layer,'' J. Atmos. Sci., **30**, pp. 1327–1339.
[7] Daly, B. J., and Harlow, F. H., 1970, ''Transport Equations in Turbulence,'' Phys. Fluids, **13**, No. 11, pp. 2634–2649.
[8] Hanjalic, K., and Launder, B. E., 1972, ''A Reynolds Stress Model of Turbulence and Its Application to Thin Shear Flows,'' J. Fluid Mech., **52**, Part 4, pp. 609–638.
[9] Lumley, J. L., 1978, ''Computational Modeling of Turbulent Flows,'' Adv. Appl. Mech., **18**, pp. 123–176.
[10] Lien, F. S., and Leschziner, M. A., 1994, ''Assessment of Turbulence-Transport Models Including Non-Linear RNG Eddy-Viscosity Formulation and Second-Moment Closure for Flow Over a Backward Facing Step,'' Comput. Fluids, **23**, pp. 983–1004.
[11] Amsden, A. A., O'Rourke, P. J., and Butler, T. D., 1989, ''KIVA-II: A Computer Program for Chemically Reactive Flows with Sprays,'' Los Alamos National Laboratory, Report No. LA-11560-MS.
[12] Amsden, A. A., Ramshaw, J. D., O'Rourke, P. J., and Dukowicz, J. K., 1985, ''KIVA: A Computer Program for Two and Three-Dimensional Fluid Flows with Chemical Reactions and Fuel Sprays,'' Los Alamos National Laboratory, Report No. LA-10245-MS.
[13] Amsden, A. A., 1997, ''KIVA-3V: A Block-Structured KIVA Program for Engines with Vertical or Canted Valves,'' Los Alamos National Laboratory, Report No. LA-13313-MS.
[14] Han, Z., 1996, ''Numerical Study of Air-Fuel Mixing in Direct-Injection Spark-Ignition and Diesel Engines,'' Ph.D. thesis, University of Wisconsin-Madison.
[15] Patankar, S. V., 1980, *Numerical Heat Transfer and Fluid Flow*, Taylor and Francis, London.
[16] Huang, P. G. and Coakley, T. J., 1992, ''An Implicit Navier-Stokes Code for Turbulent Flow Modeling,'' AIAA Paper No. 92-0547.
[17] O'Rourke, P. J. and Amsden, A. A., 1986, ''Implementation of a Conjugate Residual Iteration in the KIVA Computer Program,'' Los Alamos National Laboratory, Report No. LA-10849-MS.
[18] Basara, B., 1993, ''A Numerical Study into the Effects of Turbulent Flows Around Full-Scale Buildings,'' Ph.D. thesis, City University, London, UK.
[19] Lien, F. S., and Leschziner, M. A., 1993, ''Second-Moment Modeling of Recirculating Flow with a Non-Orthogonal Collocated Finite-Volume Algorithm,'' Turbulent Shear Flows, **8**, 205–222.
[20] Mansour, N. N., Kim, J., and Moin, P., 1988, ''Reynolds Stress and Dissipation Rate Budgets in Turbulent Channel Flow,'' J. Fluid Mech., **194**, pp. 15–44.
[21] Lebrere, L., Buffat, M., Le Penven, L., and Dillies, B., 1996, ''Application of Reynolds Stress Modelling to Engine Flow Calculations,'' J. Fluids Eng., **118**, pp. 710–721.
[22] Lebrere, L., and Dillies, B., 1996, ''Engine Flow Calculations Using a Reynolds Stress Model in the KIVA-II Code,'' SAE Paper No. 960636.
[23] Hoffmann, K. A., and Chiang, S. T., 1993, *Computational Fluid Dynamics for Engineers—Volume 1*, Engineering Education System, Wichita, Kansas.
[24] Laufer, J., 1952, ''The Structure of Turbulence in Fully Developed Pipe Flow,'' NACA 1174.
[25] Anderson, D. A., 1975, ''Effects of Equivalence Ratio and Dwell Time on Exhaust Emissions from an Experimental Premixing Prevaporizing Burner,'' NASA TMX-71592.
[26] Kundu, K. P., Penko, P. F., and Yang, S. L., 1998, ''Reduced Reaction Mechanisms for Numerical Calculations in Combustion of Hydrocarbon Fuels,'' AIAA Paper No. 98-0803.
[27] Yang, S. L., Peschke, B. D., and Tacina, R. R., 1999, ''Numerical Simulation of a Lean Direct Injection Combustor Using a Reynolds Stress Closure Model,'' Int. Conference ICE99, Internal Combustion Engine: Experiments and Modeling, Capri-Naples, Italy, Sept. 12–16.

Downloaded 02 Jun 2010 to 171.66.16.119. Redistribution subject to ASME license or copyright; see http://www.asme.org/terms/Terms_Use.cfm

Journal of Engineering for Gas Turbines and Power

Discussion

Discussion: ''Internal Bearing Chamber Wall Heat Transfer as a Function of Operating Conditions and Chamber Geometry'' [ASME J. Eng. Gas Turbines Power, 122, No. 2, pp. 314–320][1]

A. V. Mirzamoghadam
Principal Engineer, Siemens Westinghouse Power Corporation, Orlando, FL 32826

The subject under investigation is very important to the gas turbine industry, and the derivation of a correlation for the oil chamber wall heat transfer coefficient is long past overdue. The complexity, however, is that the correlation needs to represent the two-phase flow regime (liquid oil + air) along the chamber wall which changes with engine operating conditions. Therefore, the proposed correlation in this paper requires further validation in order to delineate the effect of two-phase flow regime. Would the authors comment on why the definition of the Reynolds number (Eq. (12)) is not based on local tangential velocity ($n_s \times r_s$) but rather a pseudo tangential velocity based on circumference ($n_s \times 2\pi r_s$). Also, if the chamber circumference is $U=\pi D_h$, why are the Reynolds numbers of Eqs. (15) and (16) written without the π?

[1]Busam, S., Glahn, A., and Wittig, S., 2000, ASME JOURNAL OF ENGINEERING FOR GAS TURBINES AND POWER, **122**, No. 2, pp. 314–320.

Closure to ''Discussion of 'Internal Bearing Chamber Wall Heat Transfer as a Function of Operating Conditions and Chamber Geometry''' [ASME J. Eng. Gas Turbines Power, 122, No. 2, p. 366]

S. Busam
Lehrstuhl und Institut für Thermische, Strömungsmaschinen, Universität Karlsruhe (T.H.), Kaiserstr. 12, 76128 Karlsruhe, Germany

The authors appreciate Dr. Mirzamoghadam's comments and like to thank him for his interest in this work. The subject of two-phase flows in bearing chambers is indeed very complex. However, considering steady-state operation at various engine thrust settings, flow visualization studies as well as oil film velocity and thickness measurements along the internal bearing chamber housing walls have shown that flow regimes at the chamber walls do not change fundamentally over the flight envelope. Although it has been recognized for typical engine speeds that the gas liquid interface, i.e., the film surface, turns into a foamy air/oil layer, it has also been shown by oil film profile measurements [1,2] that the time-averaged flow behavior can be described even for highest speeds by analytical methods. In combination with core flow velocity information and local mass balances for the oil film, these methods can be applied to calculate heat transfer coefficients along the circumference of the internal housing wall. The present paper, however, deals with spatially averaged internal bearing compartment heat transfer. Based on our flow and heat transfer investigations at relevant engine conditions, we believe that the main drivers for this circumstance are the rotational speed, the flow rates, and geometrical boundary conditions. Therefore, the correlation, which aims at providing easy-to-use system-level information for calculating heat transfer to the oil, has been derived as a function of the appropriate non-dimensional quantities. Relative to the effect of rotational speeds on the heat transfer, a common definition of a gap Reynolds number, based on the rim speed of the shaft ($C_S=\omega_S r_S=2\pi n_S r_S$), has been used. All Reynolds numbers were based on the hydraulic diameter and not—as interpreted by Dr. Mirzamoghadam—on the chamber circumference.

References

[1] Glahn, A., and Wittig, S., 1996, ''Two-Phase Air Oil Flow in Aero-Engine Bearing Chambers—Characterization of Oil Film Flow,'' ASME J. Eng. Gas Turbines Power, **118**, No. 3, pp. 578–583.
[2] Glahn, A., and Wittig, S., 1999, ''Two-Phase Air/Oil Flow in Aero-Engine Bearing Chambers—Assessment of an Analytical Prediction Model for the Internal Wall Heat Transfer,'' Int. J. Rotating Machinery, **5**, No. 3, pp. 155–165.

 Copyright © 2000 by ASME

Downloaded 02 Jun 2010 to 171.66.16.119. Redistribution subject to ASME license or copyright; see http://www.asme.org/terms/Terms_Use.cfm